Mössbauer, EPR, and DFT Studies of Oxygen Activation in Enzymes and Biologically Relevant Synthetic Complexes

Dissertation by

Katlyn Kelli Meier

In Partial Fulfillment of the Requirements for the
Degree of Doctor of Philosophy

Thesis committee

Dr. Eckard Münck	Department of Chemistry, Carnegie Mellon University
Dr. Emile L. Bominaar	Department of Chemistry, Carnegie Mellon University
Dr. Catalina Achim	Department of Chemistry, Carnegie Mellon University
Dr. Michael P. Hendrich	Department of Chemistry, Carnegie Mellon University
Dr. Doros Petasis	Department of Physics, Allegheny College

Acknowledgements

I am incredibly thankful to have had the opportunity to complete my Ph.D. under the advisorship of Eckard Münck. Eckard has been a wonderful role model for me, and I have a tremendous amount of respect for him both as a scientist and as a person. I am grateful for the time he took to help me learn and develop as a researcher, and for his confidence in me, even when my confidence in myself waned. I am very thankful to have had the opportunity to have a truly unique graduate school experience where every day was a group meeting, where I developed critical thinking skills in each project I was involved in, and where I gained the technical skills necessary to disassemble and reassemble the dewar, electromagnetic system, diffusion pumps, etc. Finally, I am thankful for the numerous opportunities that Eckard offered for me to attend local, national, and international conferences to present my research.

I also wish to thank Emile Bominaar for his seemingly endless supply of patience. Although he was not officially my co-advisor, Emile provided me with guidance and support via countless valuable discussions. In the later stage of my Ph.D. career we worked together to develop an approach using the spectroscopically derived angular dependence relationships between multiple reference frames along with DFT to identify each frame with respect to the crystal structure. I greatly value all of our discussions and the time that he took to teach me about DFT – Emile has been an invaluable resource and mentor to me, and for that I am grateful.

I am honored to have Dr. Michael Hendrich and Dr. Catalina Achim on my Ph.D. committee. I have solicited career advice and feedback on talks, writing, etc. from them on numerous occasions over the past five years. I am grateful for their willingness to listen and offer assistance. During my time at Carnegie Mellon University I had the privilege to teach the recitation sections for the Physical Chemistry Thermo course when Mike was the course instructor, and to take Catalina's Transition Metal Chemistry course. I learned a great deal from their courses, and learned even more about effective teaching methods that will (hopefully) come in handy in the future.

I wish to thank the external member of my Ph.D. committee, and my undergraduate research advisor, Dr. Doros Petasis. Doros took me under his wing at Allegheny College, and introduced me to the world of research. I am grateful for his guidance and advice when it came time for me to choose a graduate program, and for believing that I could be successful at Carnegie Mellon University in the company of Eckard, Emile, and Mike. And lastly, as if coming full circle, I am thankful that he was able to serve as the external member of my committee – it seemed only appropriate that he be present for my defense since his opinions and advice were a large part of why I am here in the first place.

Over the course of the past five years I have worked on many projects, mostly in collaboration with the following people from the University of Minnesota. Firstly, I would like to acknolwedge my collaborators in the lab of Dr. Lawrence Que, Jr.: Feifei

Li, Matthew Cranswick, Katherine Van Heuvelen, Jai Prakash, Gregory Rohde, Williamson Oloo, Achintesh Biswas, Anna Komor, and Scott Kleespies. Together we have published nine papers (1 more near submission; 1 in review) of high impact work including the second-ever Fe(V)=O complexes. I would also like to acknowledge my collaborators from the lab of Dr. John D. Lipscomb: Mike Mbughuni, Tom Makris, Melanie Rogers, Elena Kovaleva, Brent Rivard, Rahul Banerjee. The culmination of our hard work resulted in six publications (2 near submission), with our work on the extradiol-cleaving dioxygenase, homoprotocatechuate 2,3-dioxygenase spanning my entire graduate school career, and accounting for the majority of these papers. In addition to our larger collaborations, I wish to acknowledge Dr. Jing Liu and Dr. Yi Lu of the University of Illinois, Urbana Champaign and Dr. Miquel Costas of the Universitat de Girona in Spain for our work on the Fe-Azurin system and highly reactive, high-valent iron systems, respectively.

I would like to acknowledge two former postdoctoral fellows; Yisong (Alex) Guo and Sebastian Stoian. Although our time in the Münck group only briefly overlapped, both Alex and Sebastian were tremendous mentors to me. They were approachable and were always eager and willing to share your knowledge with me. I greatly valued our discussions, their advice, and their willingness to share their time with me.

I am thankful and incredibly grateful for my friendships with Heather Stout, Sara Wainer, Jon Willcox, Chris Collins, Andrew Weitz, and Christian Legaspi. I greatly

value and appreciate each of them. I am thankful for our mutual support of one another, for our coffee breaks on Craig Street (Heather and Jon), and for being each other's running and yoga buddies (Sara, Jon, Chris). My graduate school experience would not have been the same without them.

I acknowledge my fourth grade teacher, Mrs. Yarros, who always encouraged me to "let my special shine". She always challenged me to be the best version of myself, on both a personal and academic level, and had a tremendous impact on my life and on my attitude towards my education. I am a better person for having had the privilege to be her student, and for living by her mantra: "let your special shine".

I am thankful for the support of my family; Grandma and Pappy, Aunt Patty and Uncle Dave, Uncle Bob and Aunt Lisa, Shane, Tim, and Patrick. They have always been there to support me through every obstacle and to celebrate my accomplishments no matter how big or small they were. I am especially grateful for my brother, Danny. I am so proud of him for sticking with his dreams and never giving up. I am thankful to have such a kind, intelligent, and loyal friend and brother who, reminds me not to take myself too seriously and to laugh.

Finally, I acknowledge my mom – words cannot begin to express how much all of her sacrifices, hard work, and seemingly endless supply of encouragement and love mean to me. She always encouraged me to believe in myself, to have faith that I can

accomplish anything I set my mind to, and to be thankful for each goal that I accomplish. I credit her with instilling in me the strong work ethic that, I feel, is what has been a major factor in my successes thus far. I could not imagine having a better role model.

Table of Contents

List of Tables

Chapter I

Chapter II

Chapter III

Chapter IV

Chapter V

Chapter VI

Chapter VII

Chapter VIII

Chapter IX

Chapter X

List of Figures, Schemes, and Charts

Introduction

Chapter I

Chapter II

Chapter III

Chapter IV

Chapter V

Chapter VI

Chapter VII

Chapter VIII

Chapter IX

Chapter X

Introduction

Long before Joseph Priestley's observation that heating lead and mercury oxides generates oxygen, Leonardo da Vinci proposed that one of the two main gases that make up air must be capable of supporting both flames and life. Today, nearly five hundred years after da Vinci's death, researchers are busy trying to understand the evolution and activation of oxygen in biochemical reactions, as well as the maladies that result when oxygen activation is not tightly regulated. At the forefront of the field of 'oxygen activation' are questions regarding how O_2 can be made to react with high specificity at ambient temperature and how we can understand nature's oxygen activation strategies.

Dioxygen is involved in key biological processes such as oxidative phosphorylation to yield energy-rich molecules for metabolic processes, and it is the source of most of the oxygen atoms found in steroid hormones, aromatic amino acids, neurotransmitters, signaling molecules, and regulatory factors. From an environmental standpoint, O_2 is involved in the recovery of carbon sequestered in plant lignin, and is crucial for the oxidation of methane to methanol (via methane monooxygenases).[1] Finally, a third area of interest is the conversion of dioxygen by aerobic organisms to produce highly specialized reagents used to synthesize important biomolecules such as penicillin-type antibiotics.

To fully appreciate the versatility of derived mechanisms of oxygen activation, there are a few points worth noting. The high *potential* reactivity of dioxygen is arrested in the molecular structure of its stable triplet ground state and can only be accessed under very specific conditions or in a particular environment. Consequently, activation of O_2 to its reactive singlet or doublet (radical) states is typically facilitated by oxidases or oxygenases. Once activated, cleavage of the O-O bond has the potential to generate highly reactive species. Nature has designed ways to regulate these reactions, both spatially and temporally, to promote specific chemistries that yield biomolecules compatible with the desired pathways or function.

When these mechanisms fail to properly regulate oxygen activation, reactive oxygen species form, which results in deleterious effects. To circumvent the undesirable production of promiscuous reactive oxygen species, nature has evolved oxidases and oxygenases that often contain transition metal ions such as copper, iron or molybdenum, and in some cases organic cofactors, that are able to selectively activate O_2. In order to understand biological oxygen activation mechanisms, researchers use a multipronged approach consisting of biochemical, genetic, chemical, structural, spectroscopic, and computational approaches.

Chapters I-X detail work on enzymes and biomimetic model systems, beginning with exhaustive studies on the enzyme homoprotocatechuate 2,3-dioxygenase (HPCD), and ending with the characterization of an exciting biomimetic system that puzzled us for

the better part of two years by disguising itself as an Fe(IV)=O complex, when in fact it was a novel Fe(V)=O species. The following is a brief introduction to these two systems that is accompanied by an overview of techniques relevant to my thesis work. As of April 2015, I have coauthored 19 publications while a graduate student in the Münck laboratory; a complete list of my publications can be found on page 537.

Biological non-heme Fe(II) centers and their roles in conferring specificity in oxygen activation reactions: Studies of HPCD. Dioxygen activation has attracted attention by researchers from many fields.[2-10] Interestingly crystal structures of several mononuclear nonheme iron(II) oxygen-activating enzymes reveal a common structural motif known as the 2-His-1-carboxylate facial triad binding motif, which consists of two histidyl groups and one carboxylate ligand that occupy a face of an octahedral iron(II) coordination sphere.[11,12] Members of this enzyme family include isopenicillin *N* synthase, 2,3-dihydroxybiphenyl 1,2-dioxygenase, soybean lipoxygenase, Fe-superoxide dismutase, tyrosine hydroxylase, taurine dioxygenase, and naphthalene dioxygenase, to name a few.[6,13] The broad utilization of the 2-His-1-carboxylate Fe(II) binding motif demonstrates nature's ability to adapt a structural building block to catalyze a remarkable variety of oxygen activation chemistries with exquisite control of the O-O cleavage site and the specific oxygenated and oxidized products that result.

Biological systems generally will not bind O_2 unless the substrate is present at the active site. Therefore, reductive O_2 activation is initiated by substrate binding, and is followed by O_2 binding at the metal center. Despite this common property, the means by which non-heme iron enzymes interact with their substrates and activate O_2 are remarkably diverse owing, perhaps, to factors such as the structure and geometry of the open metal coordination site. It follows that second coordination sphere residues have a large impact on the reaction mechanisms of these systems by forming a complex network of hydrogen bonds that optimally position the substrate and dioxygen for attack on the desired substrate (or co-substrate) bonds.[14]

Dioxygenases can be split into two main families, namely intradiol- and extradiol-cleaving enzymes.[15] Herein we focus on a member of the latter class, specifically, homoprotocatechuate 2,3-dioxygenase (HPCD) isolated from *Brevibacterium fuscum*. HPCD is undoubtedly the best-studied enzyme in its class with reports on the biochemistry, structure, spectroscopy, mechanism, and quantum chemical studies of the wild-type enzyme and various mutants.[5,8,16-24]

Extradiol dioxygenases cleave the aromatic ring of the catechol substrate at a position adjacent to the vicinal hydroxyl substituents and incorporate both atoms of O_2 into the ring cleaved muconic semialdehyde product (Figure 1). For HPCD the reaction is initiated by addition of substrate (here homoprototocatechate = HPCA), which binds via the two catecholic oxygens, displacing two of the water molecules coordinated to the Fe^{II}

resting enzyme complex. Figure 1 outlines the present consensus mechanism that is based mainly on the work of the Lipscomb lab[8,25,4] and expounded upon by density functional theory (DFT) calculations.[26,27,28,29,30]

In this scheme, O_2 binds to the metal center of the enzyme-substrate (ES) complex at a site adjacent to the substrate oxygen donors, displacing the weakly bound water in the sixth coordination site. Having the dioxygen and substrate in adjacent sites facilitates their synchronized activation via metal-mediated electron and proton transfers from the substrate to the dioxygen. Upon transfer of a proton from the substrate to the dioxygen and transfer of an electron from the iron to the substrate, reactive species is formed that then can attack the C_2 carbon of the substrate to generate an Fe^{II}-alkylperoxo intermediate. Figure 1 shows two possible mechanisms for the reaction of HPCD + substrate + O_2.[4,7,14] The distinguishing features of these two mechanisms (Pathway A or Pathway B) are the reactive species: a biradical in Pathway A, and a ferric hydroperoxo substrate radical in Pathway B. These possibilities are discussed in further detail in Chapters I-III. Either pathway relies on key second-sphere residues (His200, Tyr257, Asn157, His248), HPCA substrate, and surrounding solvent water molecules to carry out the necessary multiple protonation and deprotonation steps. Through an intricate network of hydrogen bonding and acid/base pair interactions, these second-sphere residues along with the HPCA substrate, and crystallographic waters guide the dioxygen/superoxo/hydroperoxo moiety into the correct position for attack on the C_2

carbon of HPCA. Suggestions for the subsequent alkylperoxo intermediate in HPCD have been substantiated via the seminal contributions of Kovaleva and Lipscomb, who have trapped this state in HPCD single crystals.[19] While several intermediates have been trapped and characterized in single crystal studies, the exact mechanism of oxygen activation is still unclear.

The current evidence suggests that the oxygen activation step likely proceeds through a short-lived Fe^{III}-superoxo intermediate that is formed via transfer of an electron from the Fe^{II} to the bound dioxygen. While the unstable superoxo moiety of the wild-type FeHPCD system may be too fleeting to be trapped on the millisecond time scale, a superoxo intermediate has been thoroughly characterized by Mössbauer and EPR spectroscopy for the His200Asn variant.[16] DFT studies of HPCD by Neese and coworkers suggest that the reactive form is an Fe^{III} (HOO^{-})(substrate radical) state that is thought to attack the HPCA-C_2 carbon to generate an alkyl-peroxo intermediate similar to that reported in the X-ray studies.[27,19] In a separate DFT study, Shaik and coworkers proposed that the reactive species is instead a hybrid state with both (catecholate)-Fe^{III}-($O\text{-}O^{\bullet -}$) and (semiquinone$^{\bullet}$)Fe^{II}-($O\text{-}O^{\bullet -}$) character, and a lower activation barrier for formation of the Fe^{II}-alkylperoxo intermediate than that of the mechanism proposed by Neese.[29]

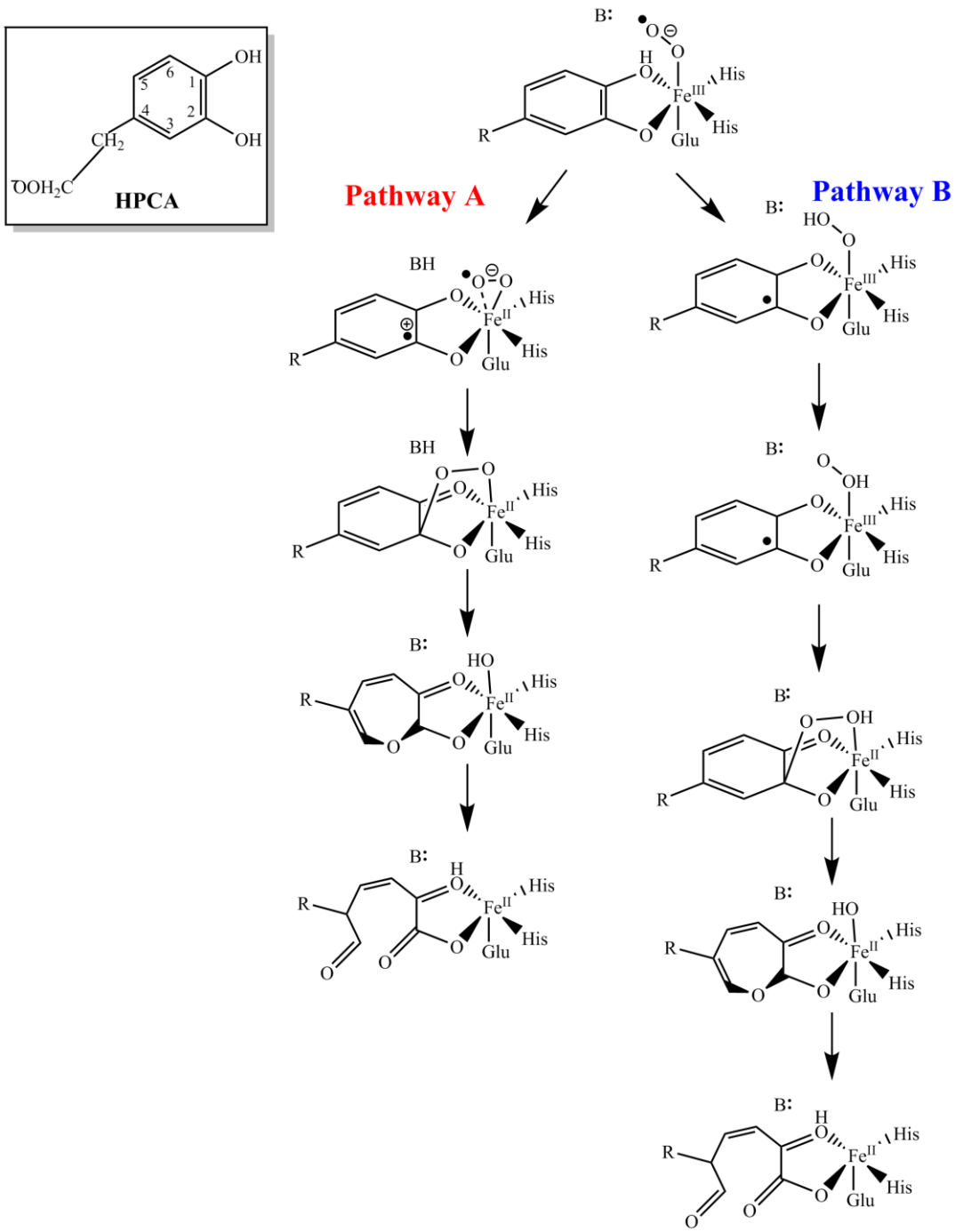

Figure 1. Cartoon depicting the proposed reaction mechanism of HPCD enzyme: substrate complex with O_2. The cartoon shows the entire reaction to yield the ring-cleaved product. "Pathway A" (red) is the reaction mechanism preferred by Lipscomb and coworkers.[1,4-6,10,13,15] "Pathway B" is a mechanism proposed by Neese and coworkers[14] in their computational investigation into the intermediates of HPCD that involves protonation of the proximal oxygen of the O_2 subunit. **Inset:** Cartoon of the homoprotocatechuate (HPCA) substrate with carbon atoms labeled.

In either case, the alkylperoxo state then undergoes a concerted Criegee rearrangement to yield a lactone intermediate. Heterolytic O-O cleavage is facilitated by protonation of the proximal oxygen of the O_2 moiety by an active site acid catalyst. Finally, hydrolysis of the lactone intermediate by the (former) proximal oxygen yields the ring-cleaved product.

In Chapter III I describe our most recent work on the HPCD variant His200Cys. High-resolution Mössbauer spectra and ^{17}O parallel mode EPR spectroscopy have allowed the characterization of the (semiquinone$^{\bullet}$) Fe^{III}(hydroperoxo) intermediate, H200C-$HPCA_{Int1}$ in unprecedented detail. Exploiting the wealth of experimental information we have extracted from biochemical/crystallographic/spectroscopic studies, we have performed exhaustive DFT studies, optimizing well over 100 DFT structures. Unlike previous DFT studies of HPCD, we considered numerous models that differed in (a) the orientation of the dioxygen subunit relative to the substrate catechol ring, (b) the protonation state of the substrate, (c) protonation site on the dioxygen moiety (i.e. proximal or distal), and (d) orientation of the proton on the distal oxygen (i.e. down toward the catechol ring, in the plane of the ring, or up toward position 200). In each case we focused on (i) the observed principal axis values and orientation of the electric field gradient (EFG) tensor at the iron relative to the zero-field splitting (ZFS) frame, (ii) the orientation of the calculated EFG frame relative to the crystal structure, and (iii) on establishing the relationship between the zero-field splitting (ZFS) frame and the crystal

structure. Additionally, drawing on our analysis of the g = 8.04 parallel mode EPR signal for samples prepared with $^{17}O_2$, we developed a novel approach for the analysis of ^{17}O hyperfine splittings. Using these properties, we have been able to exclude a number of computational models by comparison with our high-resolution spectroscopy and x-ray crystallographic data. Details of this approach are worked out in chapter III.

Studies of High-valent, Bio-inspired Synthetic Complexes.

Our collaborators in the groups of J. D. Lipscomb and L. Que, Jr., both at the University of Minnesota, have strong research programs focused on exploring high-oxidation states of iron-containing systems. In this effort, the Lipscomb group has been pursuing intermediates of benzoate 1,2 dioxygenase (BZDO) isolated from *Pseudomonas putida*. BZDO is an enzyme that contains a non-heme iron and a Rieske Fe_2S_2 cluster that provides two electrons for the cis-hydroxylation of the substrate.[32] In 2007, using a peroxide shunt reaction, the Lipscomb and Münck groups reported the trapping of a BZDO intermediate assigned as a side-on Fe^{III}-(hydro)peroxo species. This intermediate carries all the required redox equivalents, and ^{17}O-labeling experiments show that both oxygens of the peroxide are incorporated into the substrate. As an Fe^{III}-(hydro)peroxo species is electronically equivalent to an $Fe^{V}(O)(OH)$ moiety, there have been proposals for this and related enzymes such as napthalene-1,2-dioxygenase and phthalate dioxygenase that the catalytic cycle may involve an Fe^{V}=O intermediate.[4,33,34,35] Together

with the Lipscomb group I have searched for such an intermediate in BZDO. Unfortunately we were not able to dissect the Mössbauer spectra as the mononuclear site turned out to be rather labile, presenting us with a number of species reflecting "damaged" sites with iron trapped in various states. Further complicating the matter was the observation that a fraction of the mononuclear iron is lost during sample preparation and manipulations. The idea of an Fe^{V} (oxo)(hydroxo) intermediate has considerable support from bioinorganic studies of Que and coworkers, who showed with ^{16}O and ^{18}O labeling that an Fe^{V} intermediate must be present in *cis*-dihydroxylations of olefins.[36] To date such species have been proposed in C=C epoxidation, C-H hydroxylation and aromatic ring hydroxylation but have not been trapped for spectroscopic analysis.[37]

Given the high interest in trapping Fe^{V}=O intermediates in enzymes and bio-inspired model complexes and recent reports of such intermediates in water oxidation chemistry,[38,39] we, together with the Que lab, have been pursuing studies of oxidation chemistry involving the TMC ligand (TMC = tetramethylcyclam). In 2004, this neutral, tetradentate ligand yielded the first x-ray structure of a non-heme Fe^{IV}=O complex.[40]

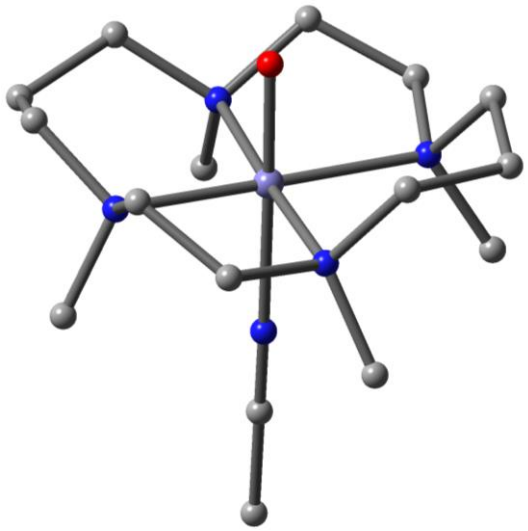

Figure 2. Ball-and-stick representation of the x-ray structure of the cation of *trans*-[Fe(IV)(O)(TMC)($NCCH_3$)]$(OTf)_2$.[40]

In order to study the oxygen activation process in the iron-TMC system, in 2011 our collaborators prepared a side-on Fe^{III}-peroxo complex as well as an end-on Fe(III)-hydroperoxo complex. We have studied both complexes by Mössbauer and EPR spectroscopy and have reported their characterization in *JACS*.[41]

Recently, the use of redox-inactive Lewis-acidic metal ions for influencing the reactivity of metal oxo complexes has attracted considerable attention. While similar chemistry has been reported for Photosystem II where Ca^{3+} and Sr^{2+} have been shown to be an integral part of the oxygen-evolving Mn_4O_5 cluster, it was a 2010 publication involving scandium that piqued our interest. In 2010, Fukuzumi and Nam reported the crystal structure of a Sc^{3+} bound Fe^{IV}(O)(TMC) adduct where Sc^{3+} is bound to the oxo group in a linear Fe-O-Sc geometry.[42] While this discovery initially generated a lot of excitement among researchers, further scrutiny of the crystallographic data by the Que

group and M. Swart raised concerns about the claimed oxidation state of the iron.[43] We therefore set out to prepare Mössbauer samples of *polycrystalline* material. Our studies entitled "Spectroscopic Identification of an Fe^{III} Center, not Fe^{IV}, in the Crystalline Fe-O-Sc adduct derived from $[Fe^{IV}(O)(TMC)]^{2+}$ " were published in *J. Am. Chem. Soc.* and provided conclusive evidence for the oxidation state of the iron center in the Fe-O-Sc adduct (Figure 3).[44]

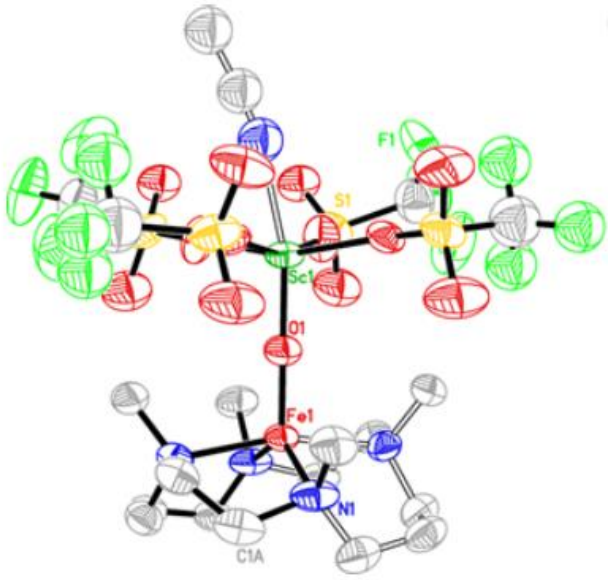

Figure 3. Structure of the Fe-O-Sc^{3+} adduct with ellipsoids drawn to the 50% probability level with the hydrogen atoms removed for clarity (Figure 1 in reference 44).[44]

Further studies exploiting the versatility of the TMC ligand led to our observation that the above mentioned Fe^{III}(OOH)(TMC) complex decays by proton-assisted O-O bond cleavage. This kind of chemistry is suggestive of heterolytic bond cleavage that would lead to formation of an Fe^{V}=O oxidant. To date, we have not observed this

putative intermediate, but we have been successful in characterizing a related Fe^{V}=O system.

In 2008 Dr. Xiaopeng Shan of the Que lab took a different approach. Dr. Shan wondered whether the Fe^{IV}(O)(TMC) complex of Figure 2 could be oxidized one electron further by addition of tert-butyl hydroperoxide. Indeed, addition of this oxidant produced an S = ½ species with g-values at g ≈ 2.04, 2.01 and 1.97.[45] The signals sharpened considerably (linewidth 0.4 mT) when the complex was dissolved in the glassing solvent mixture, 3:1 butyronitrile:MeCN, revealing ^{14,15}N, ^{57}Fe and ^{17}O hyperfine structure. Determination of the oxidation state of the iron in this complex was particularly challenging as the Mössbauer isomer shift, rRaman frequencies and DFT-B3LYP calculations appeared to suggest an exchange coupled Fe^{IV}-(aminyl radical) complex. However, the correct assignment of an Fe^{V} oxidation state emerged when the ^{57}Fe hyperfine tensor was analyzed. The presence of three contaminants that accounted for ≈ 45% of the iron in the sample prompted us to analyze difference spectra. Difference spectra were obtained by recording a spectrum of the sample where the applied magnetic field was oriented parallel to the direction of propagation of the γ radiation, and subtracting a spectrum collected under the same conditions, but with the applied magnetic field oriented perpendicular to the direction of propagation of the γ radiation. This trick allowed us to suppress unavoidable contaminants that yield the same spectra in parallel and perpendicular applied magnetic fields. Once the ^{57}Fe hyperfine tensor was

determined and compared with that of the bona fide Fe^{V}=O species of T. J. Collins' TAML ligand,[46] it became clear that our TMC complex was best described as an Fe^{V}=O center. Our Fe^{V}(O)(TMC)(imido) complex is only the second spectroscopically characterized non-heme Fe^{V}=O complex in the literature. One major difference between our TMC system and the TAML system of Tiago de Oliveira et al.[46] is that the TAML ligand contributes four negative charges from an external source to help stabilize the reactive iron center in the latter case. In contrast, the Fe^{V} state of the TMC system is the result of electron transfer from the metal to the ligand, transforming the transient aminyl radical into an imido ligand through an internal oxidation process. In this model one can readily rationalize that the significant *trans* effect of the imido group weakens the Fe=O bond, resulting in a larger isomer shift and a lower Fe=O rRaman frequency. For these reasons, we were misled as to the oxidation state of the iron. It took almost two years to come to this realization, and even then DFT calculations using the hybrid functional B3LYP preferred the Fe^{IV} model on the basis of an overestimation of the Hartree-Fock exchange contribution. Using the pure functional BP86 and 6-311g basis set, our final theoretical model for the O=Fe^{V}-N=R complex explains quite nicely the angular properties of the ^{57}Fe, ^{14}N and ^{17}O A-tensors observed experimentally by EPR and Mössbauer spectroscopy.

Characterization of species with Mössbauer and EPR Spectroscopy. The main experimental information reported in the present work was gleaned from the analysis of

EPR and Mössbauer spectra displaying paramagnetic hyperfine structure. Details and descriptions of these techniques are well documented in the literature.[47,48,49,50,51] The following is an introduction focused on very specific aspects of a combined Mössbauer and EPR approach employed in studies of HPCD (Chapters I-III) and the fleeting Fe^{V}=O(TMC) intermediate.

Methodology for studying HPCD states. In the nonheme iron system of HPCD we have studied several S = 2 complexes of resting enzyme, the enzyme: substrate complex with the catechol substrate, and several short-lived HPCD intermediates with S=2 ground states originating from antiferromagnetic exchange coupling between a high-spin ferric site (S_1 = 5/2) and an S_R = ½ radical. In both cases, the Mössbauer and EPR spectra can be described by the S = 2 spin Hamiltonian:

$$\widehat{\boldsymbol{H}} = \boldsymbol{D}\left[\widehat{\boldsymbol{S}}_{\boldsymbol{z}}^{\boldsymbol{2}} - \frac{1}{3}\boldsymbol{S}(\boldsymbol{S}+1)\right] + \boldsymbol{E}\left(\widehat{\boldsymbol{S}}_{\boldsymbol{x}}^{\boldsymbol{2}} - \widehat{\boldsymbol{S}}_{\boldsymbol{y}}^{\boldsymbol{2}}\right) + \beta\widehat{\boldsymbol{S}}\cdot\boldsymbol{g}\cdot\boldsymbol{B} + \widehat{\boldsymbol{S}}\cdot\boldsymbol{A}\cdot\widehat{\boldsymbol{I}} - g_N\beta_N\widehat{\boldsymbol{I}}\cdot B + \boldsymbol{H_Q} \quad (1)$$

where

$$\boldsymbol{H_Q} = \frac{\mathrm{eQV_{z'z'}}}{12}\left[3I_{z'}^2 - \frac{15}{4} + \eta\left(I_{x'}^2 - I_{y'}^2\right)\right] \quad \textbf{(2)}$$

In equation 1, D and E are the tetragonal and rhombic zero-field splitting (ZFS) parameters, respectively, (E is commonly expressed as the rhombicity parameter, E/D) and **g** is the electronic g-tensor (in the present description we can assume that the g-values are essentially isotropic). **A** is the ^{57}Fe magnetic hyperfine tensor, and **I** is the nuclear spin operator. **B** is an externally applied magnetic field that (in this case) is oriented parallel to the observed 14.4 KeV Mössbauer radiation. Lastly, H_Q describes the

quadrupole interactions of the I = 3/2 nuclear excited state with the traceless electric field gradient (EFG) tensor which has principal components V_{xx} , V_{yy} and V_{zz}, and asymmetry parameter $\eta = (V_{xx} - V_{yy})/V_{zz}$).

The spectra presented herein were collected in magnetic fields up to 8.0 T at temperatures between 4.2 K and 150 K. In order to simplify equation 1, we can consider a case in which the electronic Zeeman term is large compared to the magnetic hyperfine term (^{57}Fe A-values are typically 10^{-3} cm^{-1}). Under this condition the spin operator **S** of the magnetic hyperfine term can be replaced by its expectation value <**S**> which allows one to describe the interaction of the ^{57}Fe nucleus with the electron system by the *nuclear* Hamiltonian of equation 2.[49,52]

$$\widehat{\boldsymbol{H_N}} = -g_N\beta_N\hat{\boldsymbol{I}}\cdot\left(\frac{-\langle \boldsymbol{S}\rangle\cdot A}{g_N\beta_N} + \boldsymbol{B}\right) = -g_N\beta_N\hat{\boldsymbol{I}}\cdot(\boldsymbol{B_{int}} + \boldsymbol{B}) = -g_N\beta_N\hat{\boldsymbol{I}}\cdot\boldsymbol{B_{eff}} \qquad (3)$$

For an S = 2 system each of the five electronic levels as described in equation 1 is associated with an orientation-dependent internal magnetic field, $\mathbf{B}_{int} = -\langle \mathbf{S}\rangle\cdot A/g_N\beta_N$. By recording Mössbauer spectra at different temperatures and in different applied magnetic fields, one can extract the magnetic hyperfine tensor **A** as well as the ZFS parameters D and E/D through analysis of the magnetic splittings. Taking this one step further, one can also analyze the Mössbauer spectra to determine the orientation of the EFG tensor relative to the traceless ZFS tensor. Ideally, one would like to study samples of single crystals in order to extract information about the orientations of the various frames. Instead, we can use our experimental orientation-dependent analysis to relate our

experimental frames and parameters to the molecular structure that can then be compared to the EFG tensor calculated by DFT. In the following I use intermediate 1 of the His200Cys HPCD variant to elaborate on these considerations.

Intermediate 1 is obtained by reacting the high-spin ferrous H200C enzyme substrate complex, designated H200C-HPCA, with dioxygen. The resultant short-lived intermediate, H200C-HPCA$_{Int1}$, has a high-spin (S_1=5/2) Fe^{III} site that is antiferromagnetically coupled to an S_R = ½ semiquinone radical to yield an S = 2 ground state. The intermediate yields a parallel mode EPR signal at g = 8.04 that results from a transition within the M_S = ± 2 quasi-doublet. Variable temperature and variable field EPR and Mössbauer spectra showed that D = 1.6 cm^{-1} and E/D = 0.055. The temperature dependence of the EPR signal shows that the g = 8.04 resonance originates from an excited state. At 4.2 K the electronic spin of the S = 2 multiplet of Int1 is in the slow relaxation limit on the Mössbauer time scale, meaning that the relaxation rate is slow compared to the nuclear precession frequencies. In this limit, each spin level of the S = 2 multiplet contributes a distinct Mössbauer spectrum with intensities that depend on the population of the spin levels. Since E/D is near zero, the M_S = ± 2 doublet is uniaxial, i.e. $|\langle S_z \rangle| >> |\langle S_x \rangle, \langle S_y \rangle|$, and thus B_{int} is locked along the molecular z axis. For moderate applied fields, B < 0.5T in the present case, the two levels of the M_S = ± 2 doublet have an ‘easy axis’ along z that yields a 6-line Mössbauer spectrum (Chapter III, Figure 2D green curve) with an intensity ratio of 3:2:1:1:2:3. In the frame of the EFG the direction

$\mathbf{B}_{int}$ is described by the polar angles α and β. From the spacing of the six absorption lines one can constrain β to 55° < β < 70°, and from the fit to the entire data set one obtains α = 58° and β = 70°. One can then employ DFT geometry optimizations and 'property' calculations to determine the orientation of the EFG and, via a reverse rotation operation, the 'easy axis' in the molecular structure. Depending on the complexity of the system, in this case the hydrogen bonding interactions of the hydroperoxo moiety of H200C-$HPCA_{Int1}$, this last step can be remarkably difficult. The determination of α and β allows one to assess the ^{17}O hyperfine structure of the proximal oxygen of the hydroperoxo ligand.

We have studied the g = 8.04 parallel mode EPR signal using ^{17}O enriched dioxygen to probe the ^{17}O hyperfine structure of the proximal hydroperoxo oxygen. As a consequence of the uniaxial nature of the $M_S = \pm 2$ doublet, one measures the effective component of the ^{17}O hyperfine tensor, in $A_{eff}S_zI_z(^{17}O)$, that is along the direction of the easy axis. By comparison, the EPR result with the DFT calculated ^{17}O A-tensor component along the easy axis, one can assess the validity of a particular DFT solution. To my knowledge this is the first time that a combined Mössbauer, parallel mode EPR, and DFT methodology has by applied to studies of ^{17}O and ^{57}Fe hyperfine splittings.

Recovery of a nearly pure spectrum of a novel Fe^{V}=O complex from a sample plagued with contaminants using a 'parallel minus transverse applied field' difference spectrum.

The study of short-lived high-valent species in biochemical systems typically requires use of rapid-freeze techniques to trap the intermediates. In biomimetic synthetic chemistry, samples are generally prepared at cryogenic temperatures (~ -40 °C to – 90 °C). Unfortunately, even when preparation conditions are designed to optimize the yield of the species of interest, one often finds that there are various contaminants present. These contaminants may be associated with unreacted material, may be products from side reactions, or may be decay products. In some cases these contaminants are readily recognized and their spectra can be subtracted from the raw data. However, we have encountered cases where we had to rely on 'tricks' to remove the spectral contributions of unavoidable contaminants. As an example, our best sample of the novel S = ½ Fe^{V}=O species (details in Chapter XI) contained three contaminants that had to be removed from the experimental spectra before an exhaustive Mössbauer analysis could be attempted to characterize the S = ½ species. The following is a brief explanation, in simple terms, of the trick we used to deconvolve the Mössbauer spectra in the framework of the $[O=Fe^{V}=NR)]^{+}$ TMC project.

Consider an isotropic S = ½ system described by the Hamiltonian:

$$H = g_0\beta\mathbf{B}\bullet\mathbf{S} + A_0\mathbf{S}\bullet\mathbf{I} \qquad \textbf{(4)}$$

and suppose that we use Mössbauer spectroscopy to study a frozen solution sample in a weak applied field, such that the condition $\beta B >> |A_0|$ is satisfied. For ^{57}Fe this condition is generally fulfilled for B > 10 mT. Because the system is isotropic the spin expectation

value, $\langle \mathbf{S} \rangle$, as well as the internal field, $\mathbf{B}_{int} = -A_0 \langle \mathbf{S} \rangle / g_N \beta_N$, are oriented parallel to the applied field for every molecule in the sample, and the nuclear quantization axis is thus also parallel to the applied field. If we rotate the direction of the applied magnetic field by 90° so that the field is applied perpendicular (transverse) to the direction of propagation of the observed γ radiation, we would expect to see a 6-line spectrum as shown in Figure 4 (left panel, middle). The difference in orientation of the applied magnetic field relative to the direction of propagation of the observed γ radiation results in spectral intensity changes that are due to the nature of the magnetic dipole transitions.

Transitions between the $|I=1/2,m_g\rangle$ and $|I=3/2,m_e\rangle$ levels which are connected by magnetic dipole transitions are governed by the selection rules $\Delta m = 0, \pm 1$, where $\Delta m = m_g - m_e$. The intensities of these transitions have an angular dependence given by:

$$I(\Theta) \sim \sin^2\Theta \text{ for } \Delta m = 0 \text{ transitions}$$

$$I(\Theta) \sim (1 + \cos^2\Theta) \text{ for } \Delta m = \pm 1 \text{ transitions}$$

where Θ is the angle between the nuclear quantization axis and the propagation direction of the observed γ-rays. This means that in parallel applied fields the six absorption lines will display a 6:0:2:2:0:6 pattern as shown in Figure 4A, whereas a 3:4:1:1:4:3 pattern is observed for perpendicular fields (counting from the left in Figure 4B, lines 2 and 5 are nuclear $\Delta m = 0$ transitions). When we subtract the transverse spectrum from the parallel data we extract the spectrum of the $\Delta m = 0$ state with negative intensity. Figure 4C shows an example of a 'parallel minus transverse' difference spectrum. The problem becomes

slightly more complicated in the case of *anisotropic* magnetic hyperfine interactions for which the nuclear quantization axis is along <**S**>•**A**. In this case the intensities depend also on the anisotropy of the A-tensor. A further (generally weak for $\Delta E_Q < 0.5$ mm/s) modification occurs when quadrupole interactions are present. The right panel of Figure 4 illustrates the situation for our $[O=Fe^{V}=NR)]^{+}$ TMC complex, where we have an isotropic Zeeman term (g = 2.00) and a very anisotropic A-tensor (Figure 4, right panel). To further complicate the analysis, the sample with the highest yield of the $Fe^{V}=O$ complex also contained several S = 1 integer spin $Fe^{IV}=O$ species. Fortunately, difference spectra can also be used to handle integer spin species. Thus, species with integer spin, such as $Fe^{IV}=O$ complexes, generally yield quadrupole doublets for B = 0, and only slightly broadened lines in applied fields B < 0.1 T. For quadrupole doublets the $\Delta m = 0$ and $\Delta m = \pm 1$ lines overlap, and the parallel and perpendicular field spectra are therefore identical for small B. This feature allows us to unbiasedly cancel the contribution of these species by working with difference spectra.

Analysis of the $[O=Fe^{V}=NR)]^{+}$ TMC spectra was quite involved, requiring that we work in one difference spectrum after cancelling the absorption of two $Fe^{IV}=O$ minority species and one high-spin Fe^{III} contaminant. Further complicating matters was our observation that even at T = 150 K, the electronic spin relaxation was slow, preventing us from obtaining the ΔE_Q and isomer shift from high temperature data. Instead, we had to extract this information from a detailed analysis of the 4.2 K

difference spectrum. Details of this analysis, including the resonance Raman studies that hinted at an Fe^{IV} species, are included in Chapter XI.

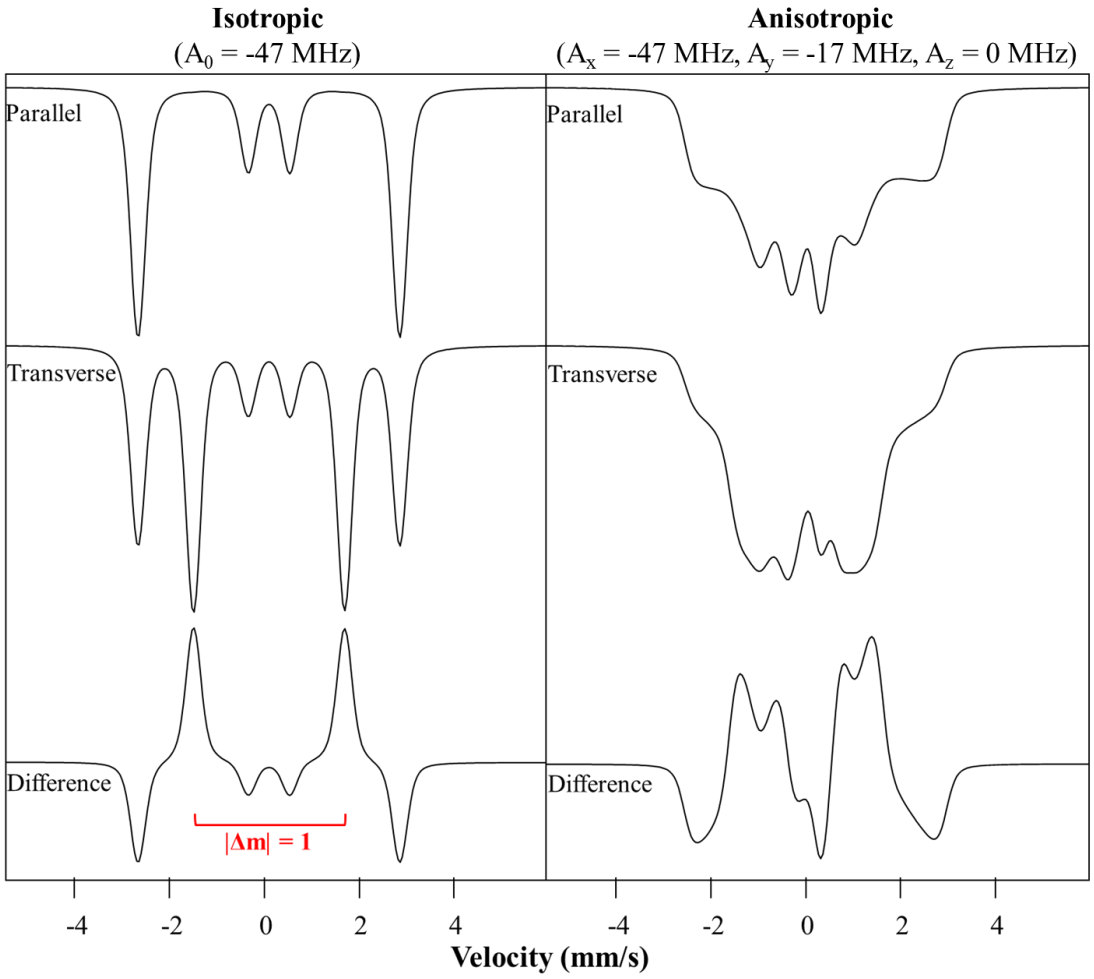

Figure 4. Schematic of the orientation dependence of the Mössbauer spectra for the case when the magnetic field is applied parallel (top) or transverse (middle) to the direction of propagation of the gamma-rays. Left panel: isotropic case with A_0 = -47 MHz. Right panel: theoretical spectra for the $[O=Fe^{V}=NR)]^{+}$ TMC complex using A_x = -47 MHz, A_y = -17 MHz, A_z = 0 MHz, ΔE_Q = -0.2. mm/s, η = 3.0 ; for details see Chapter XI. Because of the anisotropy in the A-tensor the magnetic splitting of the frozen solution spectra of the $[O=Fe^{V}=NR)]^{+}$ TMC complex is strongly orientation-dependent, yielding broad spectra rather than a clean 6-line pattern.

References

1. Dagley, S. (1987) Lessons from Biodegradation. *Ann. Rev. Microbiol. 41,* 1-23.

2. Klinman, J. P. (2007) How Do Enzymes Activate Oxygen without Inactivating Themselves? *Acc. Chem. Res. 40,* 325-333.

3. Lange, S. J.; Que Jr., L. (1998) Oxygen activating nonheme iron enzymes. *Current Opinion in Chem. Biol. 2,* 159-172.

4. Kovaleva, E. G.; Lipscomb, J. D. (2008) Versatility of biological non-heme Fe(II) centers in oxygen activation reactions. *Nat. Chem. Biol. 4,* 186-193.

5. Fielding, A. J., Lipscomb, J. D., Que Jr., L. (2014) A two-electron-shell game: intermediates of the extradiol-cleaving catechol dioxygenases. *J. Biol. Inorg. Chem. 19,* 491-504.

6. Solomon, E. I.; Brunold, T. C.; Davis, M. I.; Kemsley, J. N.; Lee, S.-K.; Lehnert, N.; Neese, F.; Skulan, A. J.; Yang, Y.-S.; Zhou, J. (2000) Geometric and Electronic Structure/Function Correlations in Non-heme Iron Enzymes. *Chem. Rev. 100,* 235-349.

7. Feig, A. L.; Lippard, S. J. (1994) Reactions of Non-Heme Iron(II) Centers with Dioxygen in Biology and Chemistry. *Chem. Rev. 94,* 759-805.

8. Lipscomb, J. D. (2008) Mechanism of extradiol aromatic ring-cleaving dioxygenases. *Curr. Opin. Struct. Biol. 18,* 644-649.

9. Que Jr., L.; Ho, R. Y. N. (1996) Dioxygen Activation by Enzymes with Mononuclear Non-Heme Iron Active Sites. *Chem. Rev. 96,* 2607-2624.

10. Wallar, B. J.; Lipscomb, J. D. (1996) Dioxygen Activation by Enzymes Containing Binuclear Non-Heme Iron Clusters. *Chem. Rev. 96,* 2625-2657.

11. Hegg, E. L.; Que Jr., L. (1997) The 2-His-1-carboxylate facial triad—An emerging structural motif in mononuclear non-heme iron(II) enzymes. *Eur. J. Biochem. 250,* 625-629.

12. Koehntop, K. D.; Emerson, J. P.; Que Jr., L. (2005) The 2-His-1-carboxylate facial triad: a versatile platform for dioxygen activation by mononuclear non-heme iron(II) enzymes. *J. Biol. Inorg. Chem. 10,* 87-93.

13. Solomon, E. I.; Decker, A.; Lehnert, N. (2003) Non-heme iron enzymes: contrasts to heme catalysis. *Proc. Natl. Acad. Sci. U S A 100,* 3589-3594.

14. Light, K. M.; Hangasky, J. A.; Knapp, M. J.; Solomon, E. I. (2014) First- and second-sphere contributions to Fe(II) site activation by cosubstrate binding in non-heme Fe enzymes. *Dalton Trans. 43,* 1505-1508.

15. Vaillancourt, F. H.; Bolin, J. T.; Eltis, L. D. (2006) The ins and outs of ring-cleaving dioxygenases. *Crit. Rev. Biochem. Mol. Biol. 41,* 241-267.

16. Mbughuni, M. M.; Chakrabarti, M.; Hayden, J. A.; Bominaar, E. L.; Hendrich, M. P.; Münck, E.; Lipscomb, J. D. (2010) Trapping and spectroscopic characterization of an FeIII-superoxo intermediate from a nonheme mononuclear iron-containing enzyme. *Proc. Natl. Acad. Sci. 107,* 16788-16793.

17. Mbughuni, M. M.; Chakrabarti, M.; Hayden, J. A.; Meier, K. K.; Dalluge, J. J.; Hendrich, M. P.; Münck, E.; Lipscomb, J. D. (2011) Oxy Intermediates of Homoprotocatechuate 2,3-Dioxygenase: Facile Electron Transfer between Substrates. *Biochem. 50,* 10262-10274.

18. Mbughuni, M. M.; Meier, K. K.; Münck, E.; Lipscomb, J. D. (2012) Substrate-Mediated Oxygen Activation by Homoprotocatechuate 2,3-Dioxygenase: Intermediates Formed by a Tyrosine 257 Variant. *Biochem. 51,* 8743-8754.

19. Kovaleva, E. G.; Lipscomb, J. D. (2007) Crystal Structures of Fe2+ Dioxygenase Superoxo, Alkylperoxo, and Bound Product Intermediates. *Science 316,* 453-457.

20. Kovaleva, E. G.; Lipscomb, J. D. (2012) Structural Basis for the Role of Tyrosine 257 of Homoprotocatechuate 2,3-Dioxygenase in Substrate and Oxygen Activation. *Biochem. 51,* 8755-8763.

21. Kovaleva, E. G.; Lipscomb, J. D. (2008) Intermediate in the O-O Bond Cleavage Reaction of an Extradiol Dioxygenase. *Biochem. 47,* 11168-11170.

22. Miller, M. A.; Lipscomb, J. D. (1996) Homoprotocatechuate 2,3-Dioxygenase from *Brevibacterium fuscum:* A DIOXYGENASE WITH CATALAST ACTIVITY. *J. Biol. Chem. 271,* 5524-5535.

23. Groce, S. L.; Lipscomb, J. D. (2005) Aromatic Ring Cleavage by Homoprotocatechuate 2,3-Dioxygenase: Role of His200 in the Kinetics of Interconversion of Reaction Cycle Intermediates. *Biochem. 44,* 7175-7188.

24. Groce, S. L.; Lipscomb, J. D. (2003) Conversion of Extradiol Aromatic Ring-Cleaving Homoprotocatechuate 2,3-Dioxygenase into an Intradiol Cleaving Enzyme. *J. Am. Chem. Soc. 125,* 11780-11781.

25. Bugg, T. D. H.; Ramaswamy, S. (2008) Non-heme iron-dependent dioxygenases: unravelling catalytic mechanisms for complex enzymatic oxidations. *Curr. Opin. Chem. Biol. 12,* 134-140.

26. Georgiev, V.; Borowski, T.; Blomberg, M. R. A.; Siegbahn, P. E. M. (2008) A comparison of the reaction mechanisms of iron-and manganese-containing 2,3-HPCD: an important spin transition for manganese. *J. Biol. Inorg. Chem. 13,* 929-940.

27. Christian, G. J.; Ye, S.; Neese, F. (2012) Oxygen activation in extradiol catecholate dioxygenases – a density functional study. *Chem. Sci. 3,* 1600-1611.

28. Dong, G.; Lai, W. (2014) Reaction Mechanism of Homoprotocatechuate 2,3-Dioxygenase with 4-Nitrocatechol: Implications for the Role of Substrate. *J. Phys. Chem. B 118,* 1791-1798.

29. Dong, G.; Shaik, S.; Lai, W. (2013) Oxygen activation by homoprotocatechuate 2,3-dioxygenase: a QM/MM study reveals the key intermediates in the activation cycle. *Chem. Sci. 4,* 3624-3635.

30. Borowski, T.; Georgiev, V.; Sigebahn, P. E. M. (2010) On the observation of a gem diol intermediate after O-O bond cleavage by extradiol dioxygenases. A hybrid DFT study. *J. Mol. Model 16,* 1673-1677.

31. Tinberg, C. E.; Lippard, S. J. (2010) Dioxygen Activation in Soluble Methane Monooxygenase. *Accounts of Chemical Research 44,* 280-288.

32. Wolfe, M. D.; Altier, D. J.; Stubna, A.; Popescu, C. V.; Münck, E.; Lipscomb, J. D. (2002) Benzoate 1,2-dioxygenase from Pseudomonas putida: single turnover kinetics and regulation of a two-component Rieske dioxygenase. *Biochem. 41,* 9611-9626.

33. Neibergall, M. B.; Stubna, A.; Mekmouche, Y.; Münck, E.; Lipscomb, J. D. (2007) Hydrogen Peroxide Dependent *cis*-Dihydroxylation of Benzoate by Fully Oxidized Benzoate 1,2-Dioxygenase. *Biochem. 46,* 8004-8016.

34. Tarasev, M.; Ballou, D. P. (2005) Chemistry of the Catalytic Conversion of Phthalate into Its *cis*-Dihydrodiol during the Reaction of Oxygen with the Reduced Form of Phthalate Dioxygenase. *Biochem. 44,* 6197-6207.

35. Wolfe, M. D., Parales, J. V., Gibson, D. T., and Lipscomb, J. D. (2001) Single Turnover Chemistry and Regulation of O2 Activation by the Oxygenase Component of Naphthalene 1,2-Dioxygenase. *J. Biol. Chem. 276,* 1945-1953.

36. Costas, M.; Mehn, M. P.; Jensen, M. P.; Que Jr., L. (2004) Dioxygen Activation at Mononuclear Nonheme Iron Active Sites: Enzymes, Models, and Intermediates. *Chem. Rev. 104,* 939-986.

37. Chen, K.; Costas, M.; Kim, J.; Tipton, A. K.; Que Jr., L. (2002) Olefin Cis-Dihydroxylation versus Epoxidation by Non-Heme Iron Catalysts: Two faces of an FeIII-OOH Coin. *J. Am. Chem. Soc. 124,* 3026-3035.

38. Fillol, J. L.; Codolà, Z.; Garcia-Bosch, I.; Gómez, L.; Pla, J. J.; Costas, M. (2011) Efficient water oxidation catalysts based on readily available iron coordination complexes. *Nature Chem. 3,* 807-813.

39. Prat, I.; Mathieson, J. S.; Güell, M.; Ribas, X.; Luis, J. M.; Cronin, L.; Costas, M. (2011) Observation of Fe(V)=O using variable-temperature mass spectrometry and its enzyme-like C-H and C=C oxidation reactions. *Nature Chem. 3,* 788-793.

40. Rohde, J.-U.; In, J.-H.; Lim, M. H.; Brennessel, W. W.; Bukowski, M. R.; Stubna, A.; Münck, E.; Nam, W.; Que Jr. L. (2003) Crystallographic and Spectroscopic Characterization of a Nonheme Fe(IV)=O Complex. *Science 299,* 1037-1039.

41. Li, F.; Meier, K. K.; Cranswick, M. A.; Chakrabarti, M.; Van Heuvelen, K. M.; Münck, E.; Que, L. (2011) Characterization of a high-spin non-heme Fe(III)-OOH intermediate and its quantitative conversion to an Fe(IV)=O complex. *J. Am. Chem. Soc. 133,* 7256-7259.

42. Fukuzumi, S.; Morimoto, Y.; Kotani, H.; Naumov, P.; Lee, Y.-M.; Nam, W. (2010) Crystal structure of a metal ion-bound oxoiron(IV) complex and implications for biological electron transfer. *Nature Chem. 2,* 756-759.

43. Swart, M. (2013) A change in the oxidation state of iron: scandium is not innocent. *Chem. Commun. (Camb.) 49,* 6650-6652.

44. Prakash, J.; Rohde, G. T.; Meier, K. K.; Jasniewski, A. J.; Van Heuvelen, K. M.; Münck, E.; Que Jr., L. (2015) Spectroscopic Identification of an Fe^{III} Center, not Fe^{IV}, in the Crystalline Sc-O-Fe Adduct Derived from [FeIV(O)(TMC)]2^{+}. *J. Am. Chem. Soc., Article ASAP.*

45. Van Heuvelen, K. M.; Fiedler, A. T.; Shan, X.; De Hont, R. F.; Meier, K. K.; Bominaar, E. L.; Münck, E.; Que Jr., L. (2012) One-electron oxidation of an oxoiron(IV) complex to form an [O=FeV=NR]+ center. *Proc. Natl. Acad. Sci U S A, 109,* 11933-11938.

46. Tiago de Oliveira, F. T.; Chanda, A.; Banerjee, D.; Shan, X.; Mondal, S.; Que Jr., L.; Bominaar, E. L.; Münck, E.; Collins, T. J. (2007) Chemical and spectroscopic evidence for an Fe(V)-oxo complex. *Science 315,* 835-838.

47. Hendrich, M. P.; Debrunner, P. G. (1989) Integer Spin Electron Paramagnetic Resonance of Iron Proteins. *BioPhysical Journ. 56,* 490-506.

48. Münck, E.; Surerus, K. K.; Hendrich, M. (1993) Combining Mössbauer Spectroscopy with Integer Spin Electron Paramagnetic Resonance. *Methods Enzym. 227,* 463-479.

49. Münck E (2000) Aspects of 57Fe Mössbauer spectroscopy. Physical Methods in Bioinorganic Chemistry, ed Que L, Jr. (University Science Books, Sausalito, CA), pp 287-319.

50. Münck, E.; Huynh, B. H. (1979) Iron Sulfur Proteins: Combined Mössbauer and EPR Studies. *ESR and NMR of Paramagnetic Species in Biological and Related Systems* (eds. I. Bertini and R. S. Drago) pp. 275-288, Reidel Publishing Company, Holland.

51. Krebs, C.; Bollinger Jr., J. M. (2009) Freeze-quench (57)Fe-Mössbauer spectroscopy: trapping reactive intermediates. *Photosynth. Res. 102,* 295-304.

52. Debrunner, P. G. (1996) Mössbauer Spectroscopy. Biophysical Techniques in Photosynthesis; *Advances in Photosynthesis and Respiration 3,* 355-373.

Chapter I – Oxy-intermediates of Homoprotocatechuate 2,3-dioxygenase: Facile Electron Transfer Between Substrates

Published: Mbughuni, M.M.; Chakrabarti, M.; Hayden, J.A.; **Meier, K.K.**; Dalluge, J.J.; Hendrich, M.P.; Münck, E.; Lipscomb, J.D. "Oxy-intermediates of homoprotocatechuate 2,3-dioxygenase: facile electron transfer between substrates." *Biochemistry*. 2011, 50, pp 10262-10274.

Author Contributions: M.M.M., M.C., J.A.H., K.K.M., J.J.D., M.P.H., E.M., and J.D.L. conceived and designed the experiments. M.M.M., M.C. (Mössbauer), J.A.H. (EPR), K.K.M. (Mössbauer), and J.J.D. performed the experiments. M.M.M., M.C., J.A.H., K.K.M., J.J.D., M.P.H., E.M., and J.D.L. analyzed the data. All authors participated in the writing of the paper.

Abstract

Substrates homoprotocatechuate (HPCA) and O_2 bind to the Fe^{II} of Homoprotocatechuate 2,3-dioxygenase (FeHPCD) in adjacent coordination sites. Transfer of an electron(s) from HPCA to O_2 via the iron is proposed to activate the substrates for reaction with each other to initiate aromatic ring cleavage. Here, rapid-freeze-quench methods are used to trap and spectroscopically characterize early intermediates in the reactions of the HPCA complexes of FeHPCD and the variant His200Asn (FeHPCD-HPCA and H200N-HPCA) with O_2. A blue intermediate forms within 20 ms after mixing O_2 with H200N-HPCA ($H200N_{Int1}{}^{HPCA}$). Parallel mode EPR and Mössbauer spectroscopies show that this intermediate contains high-spin Fe^{III}

(S=5/2) antiferromagnetically coupled to a radical (S_R=1/2) to yield an S=2 state. Together, optical and Mössbauer spectra of the intermediate support assignment of the radical as an HPCA semiquinone, implying that oxygen is bound as a (hydro)peroxo ligand. $H200N_{Int1}^{HPCA}$ decays over the next 2 s, possibly through an Fe^{II} intermediate ($H200N_{Int2}^{HPCA}$), to yield product and the resting Fe^{II} enzyme. Reaction of FeHPCD-HPCA with O_2 results in rapid formation of a colorless Fe^{II} intermediate ($FeHPCD_{Int1}^{HPCA}$). This species decays within 1 s to yield the product and the resting enzyme. The absence of a chromophore from a semiquinone or evidence for a spin-coupled species in $FeHPCD_{Int1}^{HPCA}$ suggests it is an intermediate occurring after O_2 activation and attack. The similar Mössbauer parameters for $FeHPCD_{Int1}^{HPCA}$ and $H200N_{Int2}^{HPCA}$ suggest these are similar intermediates. The results show that electron transfer from the substrate to the O_2 via the iron does occur leading to aromatic ring cleavage.

Introduction

Extradiol dioxygenases are a class of nonheme Fe^{II}- (or occasionally Mn^{II}-) containing enzymes that catalyze the cleavage of catecholic substrates adjacent to the vicinal OH functions with incorporation of both atoms of oxygen from O_2 (Scheme 1).[1-5] This reaction allows a host of aerobic microorganisms to channel carbon from naturally occurring and man-made aromatic compounds into the TCA cycle, facilitating biodegradation.[1,4,6,7] As such, the catechol ring-cleaving dioxygenases have roles in human health and maintenance of the global carbon cycle.

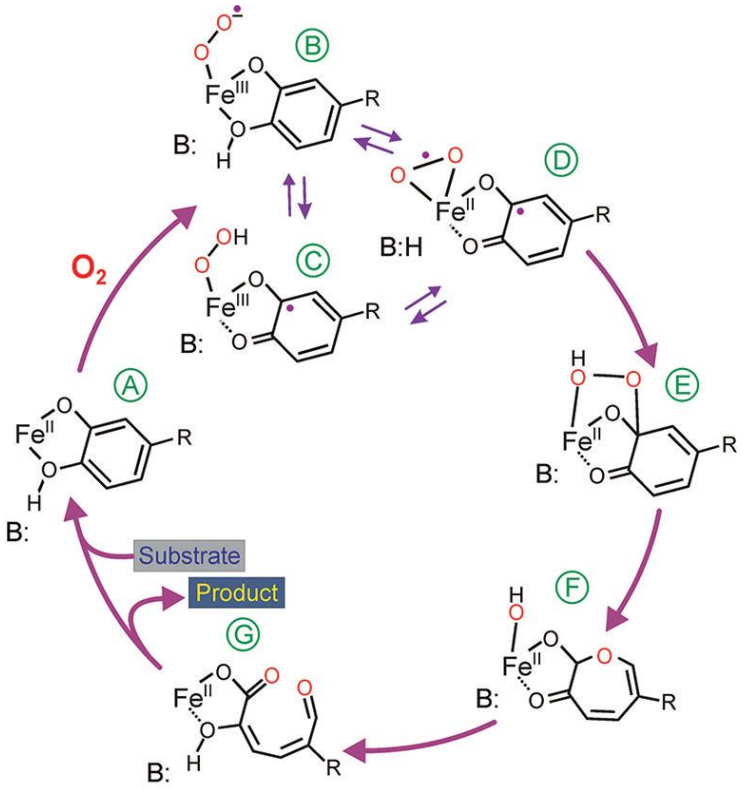

Scheme 1. Proposed Reaction Mechanism for Extradiol Dioxygenases. For the studies described here, R is either $-NO_2$ (4NC) or $-CH_2COO^-$ (HPCA).

Extradiol dioxygenases were the first members of the large class of so called 2-His-1-carboxylate facial triad enzymes to be recognized.[8] This enzyme class utilizes two His and one Asp/Glu residues to bind the divalent metal through one face of the coordination surface, leaving the other face free to bind solvents or reaction substrates.[9,10] Often a substrate or cofactor will bind to, or very near, the metal causing release of the solvents and opening a coordination site for O_2 (see examples[11]). It has been shown that, in the case of the extradiol dioxygenases, the catecholic substrates and O_2 bind to the metal in adjacent coordination sites (Scheme 1 A-D).[12] We and others have proposed that electron transfer from the substrate to the oxygen via the metal gives radical character to both the substrate and the oxygen (Scheme 1 B-D).[1,10,12-14] Recombination of the radicals to form a metal-bound alkylperoxo intermediate would initiate aromatic ring cleavage (Scheme 1 E-G).

An oxygen activation mechanism of this type does not require a formal change in oxidation state of the metal between the initial enzyme-aromatic substrate complex and postulated diradical reactive state (Scheme 1 D). Accordingly, it has recently been shown that the recombinant extradiol dioxygenase Homoprotocatechuate 2,3-dioxygenase originally isolated from *Brevibacterium fuscum* (FeHPCD, Scheme 1) functions with the same k_{cat}, and k_{cat}/K_{mO2} values within error when the Fe^{II} is replace by Mn^{II} (MnHPCD).[15] It exhibits even higher k_{cat} and K_{mO2} values when Co^{II} is substituted.[16] The fact that the enzyme is fully functional using metals with a redox potential range

spanning 1.15 V suggests either no change in metal oxidation state or no net change between the enzyme form that can bind O_2 and that which can irreversibly attack substrate. An indication that the metal transiently changes redox state prior to formation of the reactive species has come from a kinetic study of the reaction of MnHPCD with the natural substrate (HPCA) and O_2.[17] A species best described as Mn^{III}-$O_2^{\bullet-}$ is formed in low yield and then decays to a Mn^{II} species within 30 ms of the start of the reaction. This second intermediate may be the alkylperoxo intermediate of the reaction cycle, which then decays to yield ring-cleaved product.

Investigation of the native FeHPCD mechanism has been facilitated by discovery of methods to slow the rates of steps in the reaction cycle. One method has been to conduct the reaction in a single crystal using the slowly cleaved substrate, 4-nitrocatechol (4NC). It was found that the postulated 4NC-semiquinone ($SQ^{\bullet}$)-Fe^{II}-$O_2^{\bullet-}$ (Scheme 1D) and Fe^{II}-alkylperoxo- (Scheme 1E) intermediates, as well as the ring-cleaved product intermediate (Scheme 1G) were stabilized in different active sites of the asymmetric unit of the crystal.[12] This allowed them to be structurally characterized. Another approach to slow the reaction was to use active site variants of the postulated active site acid/base catalyst His200.[18,19] It was found when His200 was replaced by Asn (H200N), and 4NC was used as the substrate, O_2 bound to form a long-lived, antiferromagnetically coupled Fe^{III}-$O_2^{\bullet-}$ species ($H200N_{Int1}{}^{4NC}$). This species decayed during the following 100 s to another intermediate ($H200N_{Int2}{}^{4NC}$) postulated to be a 4NC $SQ^{\bullet}$-Fe^{III}-peroxo species.

Rather than undergo ring cleavage, this intermediate decayed to release 4NC quinone and H_2O_2 and restore the Fe^{II} center of the enzyme. This study showed that a change in the iron redox state can occur as O_2 binds, but the downstream chemistry deviates from normal catalysis, suggesting that the H200N mutation and/or the use of a substrate with an electron withdrawing substituent can uncouple O_2 activation from ring cleaving chemistry.

Transient kinetic studies of extradiol dioxygenase reactions that yield the correct ring-cleaved products have been carried out using HPCA as the substrate for FeHPCD and H200N.[18,20] These studies revealed at least four intermediates following addition of O_2 with a pre-formed enzyme-substrate complex. In the case of H200N, the O_2 binding step itself could be monitored because a visible absorption band associated with the complex was observed near 610 nm.

In the current study, we use rapid-freeze-quench (RFQ) methods to trap and spectroscopically characterize the intermediates from the reaction of FeHPCD- and H200N-HPCA complexes with O_2. The earliest trapped intermediates differ markedly from that identified in the H200N-4NC reaction with O_2.[19] Together, they support a mechanism in which facile electron transfer between bound HPCA and O_2 via the Fe^{II} forms the basis for O_2 activation and insertion chemistry.

Experimental Methods

Reagents and Enzymes. All chemicals were purchased from Sigma-Aldrich and were used without purification except for HPCA, which was recrystallized from water at 4 °C to remove minor contaminants. Anaerobic conditions were achieved by repeated cycling of solutions between argon gas and vacuum. Trace contaminating O_2 was removed from the Ar gas by passage through an Agilent GC-1 POP O_2 scrubbing cartridge, then through an Agilent GC-4 POP O_2 indicating cartridge. Formate dehydrogenase (FDH) was prepared as previously described.[21] The C_1 and C_2 *p*-hydroxyphenylacetate hydroxylase system from *Acinetobacter baumannii* was the generous gift of David P. Ballou. Recombinant *Brevibacterium fuscum* FeHPCD and the H200N variant were expressed and purified as previously described.[18,22] ^{57}Fe-enriched enzyme was prepared for RFQ/ Mössbauer experiments as previously described.[19] Mushroom Tyrosinase was purchased from Sigma.

Stopped-flow and Spectroscopy. All stopped-flow experiments were performed using an Applied Photophysics model SX.18MV stopped flow device at 4 °C. The reaction procedures were as previously described.[20] The kinetic data were analyzed to extract reciprocal relaxation times using the Applied Photophysics Pro-Data Viewer version 4.0.17. EPR spectra were collected using a Bruker Elexsys E-500 or Bruker ESP 300 spectrometer each equipped with a Bruker dual mode cavity and an Oxford ESR 910 liquid helium cryostat. Mössbauer spectroscopy was performed as previously

described.[19,23] Spectra were analyzed using the software WMOSS (SEE Co, Edina, MN, USA).

RFQ Methods. Anaerobic substrate complexes were prepared in a Coy glovebox as previously described.[19] RFQ syringes were loaded inside the anaerobic glovebox before transferring to the Update RFQ Instrument (Model 1019 RFQ) where they were equilibrated at 4 °C for 30 min using an ice bath. After rapid mixing and passage through a calibrated delay line, samples were collected by rapid freezing on counter-rotating aluminum wheels at Liq N_2 temperature. A programmed delay was used for time points > 0.4 s. For samples at times >1.5 s, the mixed sample was collected directly in an EPR tube or Mössbauer cup and frozen by rapid emersion in a dry ice/methanol bath (EPR) or Liq N_2 (Mössbauer) after the appropriate incubation time. We have observed that freezing on the counter-rotating wheels introduces a small splash artifact that becomes more prominent at the highest ram drive speeds. The splashed material falls into the Liq N_2 bath directly and freezes more slowly than the material on the wheel, causing the appearance of the spectrum of the product complex in early samples. The rate of product formation for the reactions investigated here is well known from stopped flow experiments,[20] and no product-complex is expected in the earliest RFQ samples collected.

Synthesis of HPCA Enriched with ^{17}O at the C3 Hydroxyl Functional Group. 3-^{17}OH-HPCA was prepared from p-hydroxyphenylacetate (HPA). The C_1 and C_2 hydroxylase from *Acinetobacter baumannii*[24] was used to catalyze conversion of HPA to

3-(^{17}OH),4-(^{16}OH)-dihydroxyphenylacetic using 70% enriched $^{17}O_2$ (Cambridge Isotopes). A 2 mL reaction mixture was prepared in a 5 mL pear shaped flask fitted with a 3-way valve in the anaerobic glovebox. Concentrations of the reactants were10 μM C_1, 20 μM C_2, 20 μM FDH, 100 μM NADH, 15 mM formate, and 10 mM HPA. The flask mouth was capped with a SUBA seal septa crimped with copper wire and the valve closed prior to removal from the glovebox. The 3-way valve was connected to a vacuum/argon line and to a tank of 70% enriched $^{17}O_2$ and the lines were evacuated and exchanged with argon several times. The system was opened to vacuum and the headspace of the pear shape flask evacuated for ~ 1 s. The vacuum line was closed and the flask was filled with 1-2 psi of 70% enriched $^{17}O_2$ to initiate the reaction. The reaction was allowed to proceed for 2 h at room temperature to reach completion, and then it was quenched with 3% H_2SO_4. The quenched reaction was centrifuged at 39,000 × g for 40 min to remove insoluble materials. The supernatant from centrifugation was assayed for HPCA using the catalytic activity of FeHPCD, which converts HPCA to the α-hydroxy δ-carboxymethyl *cis*-muconic semialdehyde, which has an extinction coefficient at 380 nm of 38,000 M^{-1} cm^{-1}.[20] The assay revealed nearly stoichiometric conversion of HPA to HPCA. The reaction supernatant containing 3-^{17}OH-HPCA was lyophilized and then dissolved in 50 mM MOPS buffer pH 7.5 and stored at -80 °C until used in RFQ experiments. LC/MS/MS analysis of the synthesized HPCA is described in

Supplemental Materials and shows nearly 68% enrichment of one atom of ^{17}O per HPCA molecule.

Preparation of HPCA Quinone. HPCA was oxidized using mushroom tyrosinase (Sigma) in 100 mM MES buffer pH 5.6 and 4 °C. The reaction was initiated and monitored using the stopped-flow spectrometer with diode-array detection. A solution of 2 mM HPCA was mixed with 10 mg/ml mushroom tyrosinase. The quinone product formed during the first 5 min of the reaction and then slowly decayed to an unidentified secondary species.

Results

Single-Turnover Studies of the H200N-HPCA + O_2 Reaction Reveal a Transient Intermediate. Our previous stop-flow studies revealed the accumulation of at least four reaction cycle intermediates after the pre-formed H200N-HPCA complex reacts with O_2 in a single-turnover reaction.[18] Improvements in the stopped-flow instrumentation and procedures[19] allow the first of these intermediates to accumulate in higher yield so that it can be studied in detail.

As shown in Figure 1A, for the reaction of a stoichiometric (per active site) H200N-HPCA complex with a slight excess of O_2 at pH 7.5, the previously described 610 nm transient intermediate ($H200N_{Int1}^{HPCA}$, $\varepsilon_{610\ nm} \sim 1100\ M^{-1}\ cm^{-1}$) rapidly accumulates and then more slowly decays to give the ring-cleaved product ($\varepsilon_{380\ nm} \sim 38{,}000\ M^{-1}\ cm^{-1}$). The absorption maximum for product is shifted to 325 nm ($\varepsilon_{325\ nm} \sim 23{,}600\ M^{-1}\ cm^{-1}$) when the reaction is conducted at pH 5.5, allowing a second maximum in the spectrum of $H200N_{Int1}^{HPCA}$ to be observed near 395 nm ($\varepsilon_{395\ nm} \sim 3200\ M^{-1}\ cm^{-1}$) (Figure 1B). These same features plus an additional feature at 310 nm are revealed by subtracting the 3 ms spectrum from the 32 ms spectrum for the reaction at pH 7.5 (Figure 1A, inset). When the reaction is conducted at pseudo first-order concentrations of O_2 at pH 7.5 (Figure S1), the time course can be fit well by a two-summed exponential equation with reciprocal relaxation times of $1/\tau_1 = 230 \pm 20\ s^{-1}$ and $1/\tau_2 = 1.60 \pm 0.15\ s^{-1}$ showing that the reaction consists of at least two steps. The spectroscopic data reported

below shows that the intermediate builds to nearly stoichiometric yield. The observed value of $1/\tau_1$ is linearly dependent on O_2 concentration with a zero intercept,[18] suggesting that the reaction is irreversible O_2 binding with a $1/\tau_1 = k_{form} = k_1$. The formation of the alkylperoxo intermediate and the ring-cleaving reaction are also likely to be irreversible so that $1/\tau_2 = k_{decay} = k_2$ for $H200N_{Int1}^{HPCA}$. At pH 5.5, the reaction is slightly slower due to a decrease in k_2 ($k_1 = 235 \pm 20\ s^{-1}$ and $k_2 = 1.1 \pm 0.1\ s^{-1}$). The two reciprocal relaxation times derived from the fits of the time course at this pH are found to be independent of wavelength when monitored at 310, 395, or 610 nm, suggesting that all features result from $H200N_{Int1}^{HPCA}$. The spectra of the intermediate change very little in the range between pH 5.5 and 9 (Figure 1B, inset). The reaction could not be monitored at pH values significantly above pH 9 due to structural alterations of the enzyme.

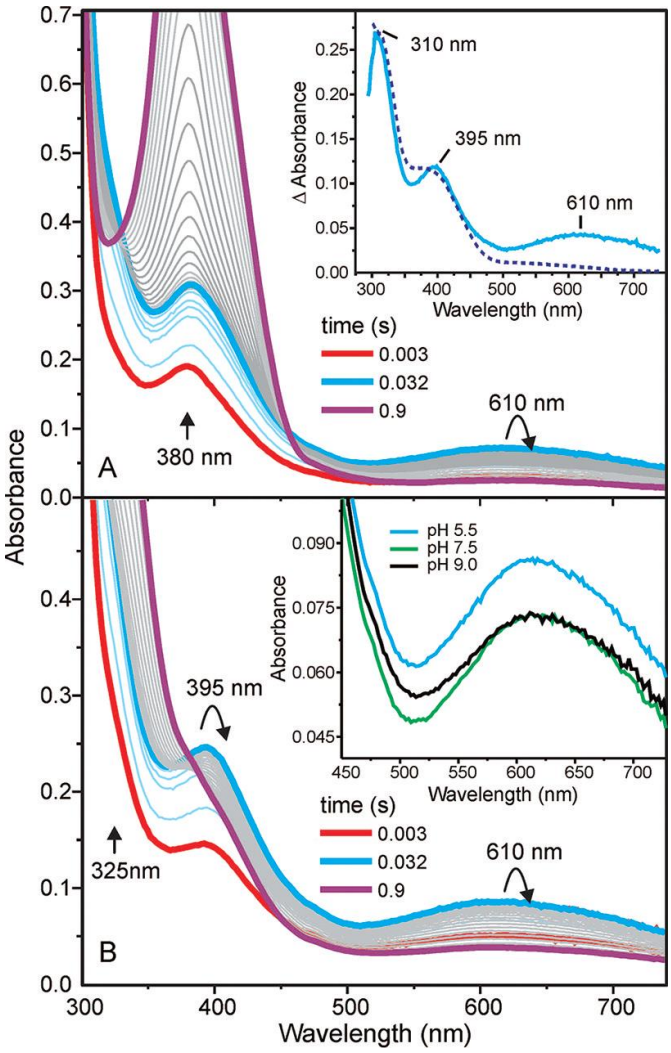

Figure 1. H200N-HPCA + O_2 reaction monitored by stopped-flow. Panel A shows diode array spectra recorded between 3 ms and 2 s after mixing stoichiometric 640 µM (sites) H200N-HPCA anaerobic complex with O_2-saturated buffer (~ 1.8 mM) (1:1) at 4 °C in 200 mM MOPS pH 7.5 (2 mm pathlength). The thick line spectra are for the specific times shown. Thin line cyan, 3 – 32 ms; gray, 32 ms – 2 s. The *inset* shows spectrum that results from subtracting the spectrum at 3 ms from that at 32 ms (cyan) and the spectrum of HPCA quinone produced by treatment of HPCA with mushroom tyrosinase (blue, dashed). Panel B shows the time course of the same reaction as in Panel A, but in 200 mM MES buffer pH 5.5. Inset: Comparison of the spectra of the 610 nm feature formed at pH 5.5, 7.5, and 9.0.

RFQ EPR and Mössbauer Studies Show that H200N$_{Int1}^{HPCA}$ has an S_1=5/2 Fe^{III} Site Coupled to an S_R =½ Radical. The anaerobic H200N-HPCA complexes (see below) contain a high-spin Fe^{II} that is EPR-silent in both perpendicular (not shown) and parallel modes (Figure 2, top). The parallel mode EPR spectra of RFQ samples frozen at times between 20 ms and 2 s during the time course of the reaction of this complex with O_2 are shown in Figure 2. At 20 ms, an EPR resonance near g = 8.2 is observed in parallel mode (Figure 2). This feature maximizes at approximately 40 ms and then decays over the course of 2 s.

A superposition of the fit of the 610 nm stopped-flow data from Figure S1 and the g = 8.2 EPR time course is shown in Figure 2, inset. The congruence of these data indicates that the g = 8.2 EPR feature originates from H200N$_{Int1}^{HPCA}$. Furthermore, the observation of this signal in parallel mode and its absence in perpendicular mode demonstrates that it belongs to a species with integer electronic spin.

The EPR spectrum of H200N$_{Int1}^{HPCA}$ quenched at 40 ms is shown in more detail in Figure 3. The spectrum has contributions from two species, namely, H200N$_{Int1}^{HPCA}$ (g = 8.2) and a broader resonance from an Fe^{II} species. At 2 K, the g = 8.2 signal intensity is small relative to that of the Fe^{II} species. The g = 8.2 feature is significantly larger at 10 K, indicating that it originates from an *excited* spin doublet. The Mössbauer spectra discussed below reveal that the iron of H200N$_{Int1}^{HPCA}$ is high-spin (S_1 = 5/2) Fe^{III} that resides in a complex with integer spin. The Mössbauer and EPR data are readily

reconciled by assuming that $H200N_{Int1}{}^{HPCA}$ has an $S_1 = 5/2$ site that is antiferromagnetically (AF, $J > 0$) coupled to an $S_R = ½$ radical. The exchange coupling separates the electric levels into a ground multiplet with $S = 2$ and an excited state with $S = 3$. The $g = 8.2$ signal originates from the $M_S = \pm 2$ doublet, at energy $E \approx 5.4$ cm^{-1}, of the $S = 2$ multiplet; this doublet is indicated in the level diagram in Figure 3. The electronic levels of the system can be described by the spin

Hamiltonian (this is the uncoupled representation):

$$H_e = JS_1 \bullet S_R + D_1[S^2_{1z} - 35/12 + (E/D)_1 (S^2_{1x} - S^2_{1y})] + \beta(S_1 \bullet g_1 + S_R \bullet g_R) \bullet B \quad (1)$$

where the subscripts 1 and R refer to the Fe^{III} and the radical, respectively. The exchange coupling (J), the zero-field splitting (D, E) of the ferric ion, and electronic Zeeman terms have their common definitions.

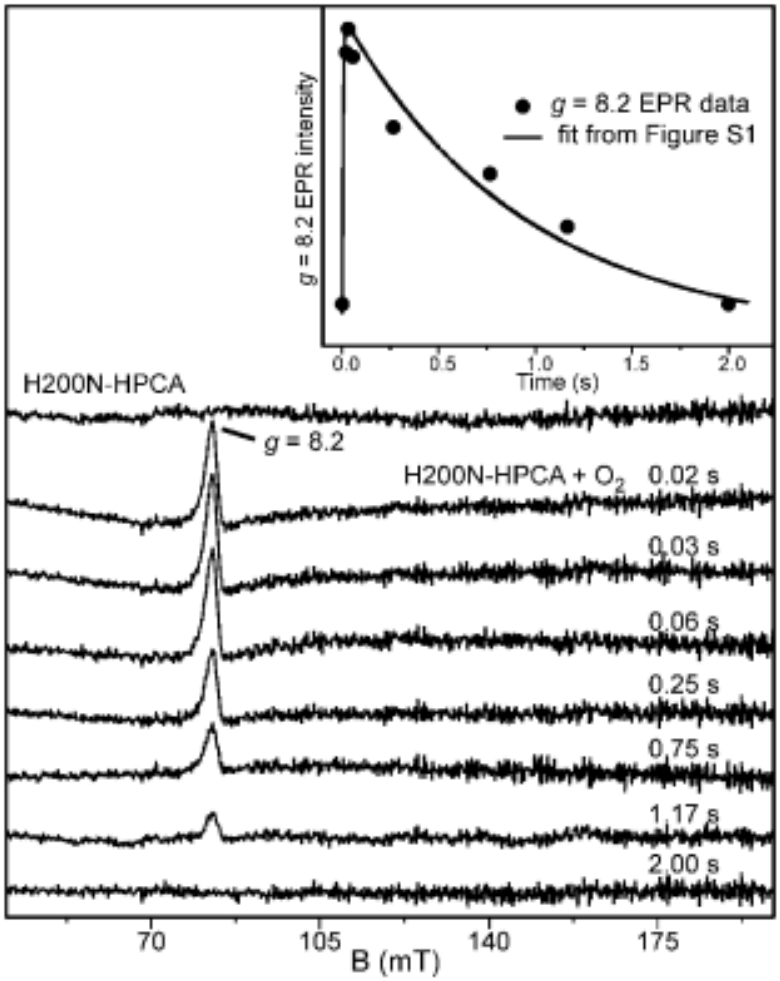

Figure 2. Time dependent parallel mode EPR spectra from the H200N-HPCA + O_2 reaction. Parallel mode EPR spectra in the g = 8 region of RFQ samples frozen between 0 (top, unreacted) and 2 s after mixing 1.65 mM anaerobic H200N-HPCA complex with O_2-saturated buffer (1:1) at 4 °C in 200 mM MOPS buffer, pH 7.5 are shown. EPR conditions: Frequency 9.35 GHz; microwave power, 50.4 mW; modulation amplitude, 1 mT, and temperature 50 K. Inset: Time course of the g = 8.2 signal intensity (•). The solid line is the fit to the optically monitored time course at 610 nm from Figure S1.

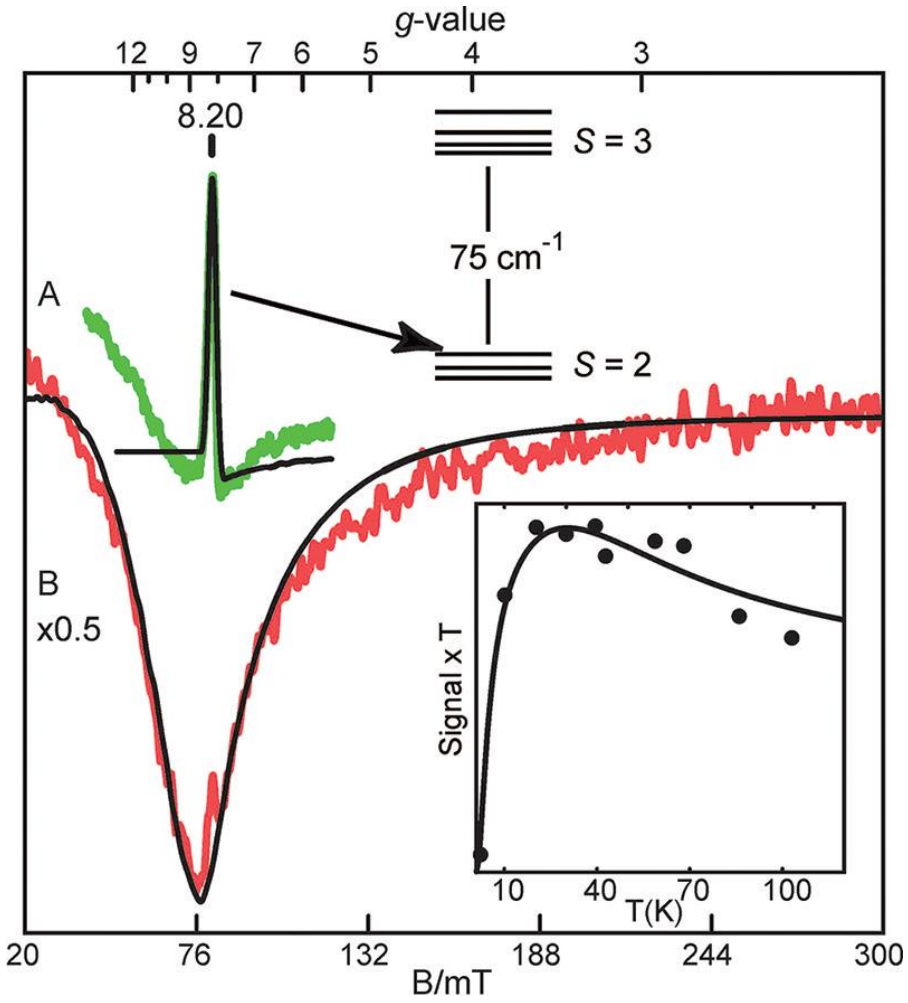

Figure 3. Parallel-mode EPR spectra (colored) and simulations (black) for H200N-HPCA frozen 40 ms after reaction with O_2 at temperatures of (A) 10 K and (B) 2 K. Prior to mixing with O_2-saturated buffer: 1.5 mM H200N-HPCA, 200 mM MOPS buffer pH 7.5. Simulation parameters: A: $S_1 = 5/2$, $S_R=1/2$, $J = +25$ cm^{-1}, $D_1 = 1$ cm^{-1}, $E/D_1 = 0.12$, $g_{1z} = 2.015$, $g_{Rz} = 2.00$. B: $S = 2$, $D = -4$ cm^{-1}, $E/D = 0.15$, $g_z = 2.00$. EPR conditions: microwaves, 20 mW (A), 0.2 mW (B) at 9.29 GHz; modulation, 1.0 mT. The intensity of B has been reduced by a factor of 2. The inset shows a plot of signal times temperature for the $g = 8.2$ feature and a theoretical fit to this intensity.

Throughout this manuscript we will use isotropic $g_1 = 2.015$ and $g_R = 2.00$ (our data are sensitive only to the z-component of the tensors). For describing the broadening of the $g = 8.2$ resonance for ^{17}O enriched samples is advisable (reason given below) to use the $S = 2$ Hamiltonian (the coupled representation).

$$H_{S=2} = D\,[S^2_z - 2 + (E/D)\,(S^2_x - S^2_y)] + \beta B_z g_z S_z + S_z A_z^{O,c} I_z^{O} \qquad \textbf{(2)}$$

The parameters of eq 2 are related to those of eq 1 by: $D = (4/3)D_1$, $E/D = (E/D)_1$ and $g_z = (7/6)g_{1z} - (1/6)g_{Rz} \approx 2.00$. The third term in eq 2 describes the hyperfine interaction of the ^{17}O nucleus with its electronic environment; where $A_z^{O,c}$ is expressed in the coupled representation. For the $^{17}O_2$ enriched sample, depending on the bonding, there could be one or two ^{17}O nuclei contributing to the broadening. The spectra are only broadened by the nuclear interaction and do not show resolved splittings, thus the derived value of $A_z^{O,c}$ assumes one ^{17}O interaction and is an upper limit (two equivalent ^{17}O nuclei would reduce $A_z^{O,c}$ by 25%). The temperature dependence of the $g = 8.2$ $H200N_{Int1}{}^{HPCA}$ signal in Figure 3 is plotted as signal times temperature versus temperature. Signal times temperature is proportional to the population of the EPR active doublet, and a fit to the points based on eq. 1 gives the exchange coupling constant $J = +25$ cm^{-1}. The rise of the signal at low temperature is due to the increasing population of the $M_S = \pm 2$ level within the $S = 2$ multiplet, whereas its decline at higher temperature reflects population of the $S = 3$ multiplet. The solid line in Figure 3A shows a SpinCount simulation of the $H200N_{Int1}{}^{HPCA}$ spectrum using the parameters given in the caption and in Table 1.

For $J/D_1 \approx 25$, the system is in the strong coupling limit and consists of two well-separated $S = 2$ and $S = 3$ multiplets. The intensity of the EPR signal (accounting for ≈ 80 % of the iron in the sample) is in approximate agreement with the concentration of the sample; however, due to somewhat variable packing density of the RFQ sample, this

concentration has a 10 % uncertainty. Figure 3B shows a simulation of the Fe^{II} species with parameters given in the figure caption. This species account for ≈ 20 % of the iron in the sample, and it is not present in the starting Fe^{II} enzyme prior to mixing with substrate and oxygen. Further details of this species are given below.

Figures 4A-D show selected Mössbauer spectra from the time course of the H200N-HPCA reaction with O_2; these spectra were collected at 4.2 K in the absence of an applied magnetic field (B = 0). As reported previously, the iron site of H200N exhibits *one* doublet with quadrupole splitting ΔE_Q = 3.01 mm/s and isomer shift δ = 1.24 mm/s; these parameters are typical of high-spin Fe^{II} with octahedral O/N coordination.[19] The anaerobically prepared, stoichiometric H200N-HPCA sample of Figure 4A exhibits two high-spin ferrous species, namely $H200N_{ES1}{}^{HPCA}$ (green, 60% of Fe) with ΔE_Q = 3.45 mm/s, δ = 1.16 mm/s and $H200N_{ES2}{}^{HPCA}$ (blue, 40%) with ΔE_Q = 2.32 mm/s, δ = 1.20 mm/s (see also Table 2). Samples prepared with a 2-fold excess of substrate or at pH 6 displayed the same species in the same ratio (footnote2).

Table 1. Spin-Hamiltonian parameters for exchange coupled intermediates from EPR (italics) and Mössbauer spectroscopy of the H200N HPCD variant.

Species	δ **(mm/s)**	ΔE_Q **(mm/s)**	η	J **(cm^{-1})**	D_1 **(cm^{-1})**	$(E/D)_1$	$A_0/g_n\beta_n$ **(T)**	A^O **(MHz)**		**Ref**
								$^{17}O_2$	**^{17}O-HPCA**	
H200N$_{Int1}^{4NC}$	0.5	-0.33	-3[a]	*+6(2)*[a]	-0.59 *-0.48*	0.20 *0.20*	-21.4(2)	*180*	N/A	[19]
H200N$_{Int2}^{4NC}$	0.49	0.87	-7.2	*+40(10)*	+0.67 *+0.50*	0.11 *0.13*	-21.5(2)	*<5*	N/A	[19]
H200N$_{Int1}^{HPCA}$	0.48(1)	0.95(2)	+3[a]	*+25(5)*	+1.1[b] *+1.1*	0.12 *0.12*	-21.5(2)			This work
H200N$_{Int1}^{HPCA}$ *S* = 2 Hamiltonian[b]	0.48	0.95	+3		1.5	0.12	-25.1	*17*	*17*	This work

[a] η = +3 and η =-3 imply that the EFG is axial around the x and y axis, respectively.

[b] The last row lists the parameters as evaluated for S = 2 multiplet of the coupled system. The full Hamiltonian is given in eq 2. This representation must be used for analysis of the ^{17}O data (an explanation is given in the text). If the radical were on the O_2 moiety, the coupling in the uncoupled representation would be 6×17=102 MHz which can be compared with the 180 MHz reported for H200N$_{Int1}^{4NC}$.

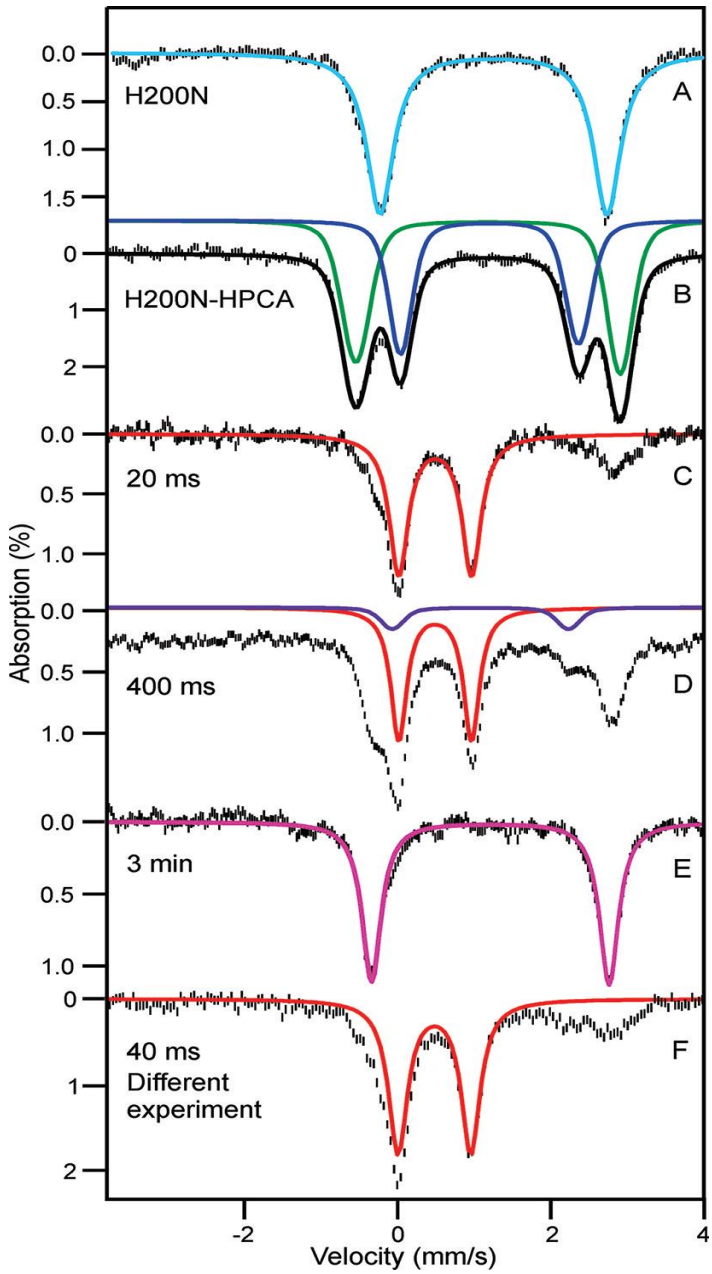

Figure 4. 4.2 K zero field Mössbauer spectra of H200N-HPCA complexes. **(A)** Stoichiometric (sites) H200N-HPCA complex, 1.54 mM, at pH 7.5 in 200 mM MOPS buffer. Simulations of the doublets of the two enzyme-substrate complexes, $H200N_{ES1}^{HPCA}$ (green) and $H200N_{ES2}^{HPCA}$ (blue), are depicted by the colored lines. The black line represents the sum of the two species. (B-E) Reaction of 1.48 mM H200N-HPCA with O_2-saturated buffer (1:1). For the RFQ samples quenched at **(B)** 20 ms and **(C)** 400 ms, we have outlined in red the spectrum of the intermediate, $H200N_{Int1}^{HPCA}$. **(D)** Sample frozen (not by RFQ) at 3 min representing the end of the reaction. The colored line is a simulation of the spectrum. **(E)** B = 0 spectrum of the RFQ sample of Figure 5 prepared in a different experiment under the same conditions.

Table 2. Comparison of quadrupole splitting and isomer shift parameters for the Mössbauer spectra of FeHPCD and its variants and complexes.

Species	ΔE_Q (mm/s)	δ (mm/s)	% present in sample at maximum
FeHPCD	2.97(3)	1.23(2)	>90
H200N	3.01(3)	1.24(2)	>90
H200N-4NC[a]	3.57	1.12	>90
$FeHPCD_{ES1}^{HPCA}$ **$FeHPCD_{ES2}^{HPCA}$**	3.29(3) 2.18(3)	1.14(2) 1.18(2)	55 45
$H200N_{ES1}^{HPCA}$ **$H200N_{ES2}^{HPCA}$**	3.45(3) 2.32(3)	1.16(2) 1.20(2)	60 40
$FeHPCD_{Int1}^{HPCA}$	2.33(3)	1.08(2)	~ 95[b]
$H200N_{Int1}^{HPCA}$	0.95(2)	0.48(1)	~ 95[b]
$H200N_{Int2}^{HPCA}$	≈2.30	≈1.10	~ 10

[a] From Ref. [19]

[b] After correction for material splashed from the rapid freezing surface at high ram velocities

Within 20 ms after mixing the H200N-HPCA complex(es) with stoichiometric amounts of O_2, both doublets have disappeared. The 20 ms spectrum is dominated by a new species (representing ~ 75% of the Fe) with $\Delta E_Q = 0.95$ mm/s and $\delta = 0.48$ mm/s. This species, called $H200N_{Int1}^{HPCA}$, has a δ value typical of high-spin Fe^{III} ($S_1 = 5/2$). The observation of a quadrupole doublet at 4.2 K in zero field, rather than a spectrum exhibiting paramagnetic hyperfine structure as is usual for isolated Fe^{III}, suggests that $H200N_{Int1}^{HPCA}$ has an overall zero or integer spin. This is consistent with the formulation of $H200N_{Int1}^{HPCA}$ that emerged from our EPR studies. Ca 20-25% of the iron in 20 ms the sample belongs to an Fe^{II} species, perhaps multiple species, with $\Delta E_Q \approx 3.10$ mm/s and $\delta \approx 1.20$ mm/s (this species may give rise to the broad integer spin EPR spectrum of Figure

3B). As pointed out in Methods, at high mixing speeds some of the material bounces off the aluminum wheel of the quencher and cools more slowly, leading to the appearance of later species in earlier time point samples. Our kinetic data indicate that the reaction has not progressed appreciably beyond $H200N_{Int1}^{HPCA}$ at 40 ms under the experimental conditions (Figure S2), suggesting that the ferrous species in the 20 ms sample, which differ(s) from the substrate complexes, arises from this "splashed" material. A spectrum recorded for a sample quenched at 40 ms (not shown) was identical to the one obtained at 20 ms, showing that the amount of material attributed to splash is constant, as expected. At 400 ms, the fraction of iron in $H200N_{Int1}^{HPCA}$ has decreased to 50% of the Fe in the sample (Figure 4D). In this sample, approximately 10% of the Fe belongs to a doublet with $\Delta E_Q \approx 2.30$ mm/s and $\delta \approx 1.10$ mm/s (blue line in Figure 4C); this ferrous species is possibly another intermediate (tentative $H200N_{Int2}^{HPCA}$, Table 2). Figure 4E shows a spectrum of a sample frozen (not by RFQ) at 180 s, a time where solution kinetics predict product will have formed and dissociated (Figure S2). However, the parameters of the observed doublet are $\Delta E_Q = 3.10$ mm/s and $\delta = 1.20$ mm/s (> 90% of Fe), which are slightly different than those of the substrate-free enzyme. It is possible that the high concentration of product present in the Mössbauer sample prevents net product dissociation or leads to a mixture of product bound and free enzyme in this sample. Accordingly, this species is also present in the 400 ms sample (representing roughly 20% of Fe over and above the splashed material), a time at which approximately 25 % of the

enzyme is expected to be present in the product complex (Figure S2). The product proved to be insufficiently stable to make an enzyme-product complex by adding purified product to resting enzyme.

Figure 4E shows a zero field spectrum from a different set of experiments for a sample quenched at 40 ms. The sample contains ca. 70 % of the Fe in $H200N_{Int1}{}^{HPCA}$ (red line). Figure 5 shows spectra of this sample taken in parallel-applied fields of 4.0 T and 8.0 T. The features observed are typical of high-spin Fe^{III} sites (the middle section of the spectra is contaminated by the unknown spectral features of the "splashed" ferrous species). We have analyzed the spectra of $H200N_{Int1}{}^{HPCA}$ with the spin Hamiltonian $H = H_e + H_{hf}$ (omitting the dipole-dipole term in H_e of eq 1) where H_{hf} describes the ^{57}Fe hyperfine interactions.

$$H_{hf} = A_0\mathbf{S}_1\bullet\mathbf{I}_1 + (eQV_{zz}/12)[3I^2_{1z} - 15/4 + \eta(I^2_{1x} - I^2_{1y})] - g_n\beta_n\mathrm{B}\bullet\mathbf{I}_1 \qquad \textbf{(3)}$$

In eq 3 all symbols have their conventional meanings. For the ^{57}Fe magnetic hyperfine coupling constant of the ferric ion, we obtained $A_0/g_n\beta_n = -21.5 \pm 0.2$ T, which compares well with A_0 values reported for octahedral Fe^{III} sites with N/O coordination.[25] This observation, together with the observation that the δ value of $H200N_{Int1}{}^{HPCA}$ falls squarely into the center of high-spin ferric δ values, indicates that the iron is Fe^{III} with little delocalization between the radical and the ferric ion. From the field dependence of the Mössbauer spectra, we were able to constrain the zero field splitting parameter, D_1, as follows. The observation of the resonance at $g = 8.2$ implies that the EPR active doublet

is split in zero field by $\Delta = (4/3)\ 3D_1(E_1/D_1)^2 \approx 0.065\ cm^{-1}$; (4/3 is a spin projection factor that enters through consideration of exchange coupling when the EPR data are described by eq 2). The high field Mössbauer spectra then constrain D_1 and $(E/D)_1$ to the reasonably narrow ranges $1.1\ cm^{-1} \leq D_1 <\leq 1.4\ cm^{-1}$ and $0.12 \leq (E/D)_1 \leq 0.14$. The red lines in Figure 5 are spectral simulations of $H200N_{Int1}^{HPCA}$ using the parameters listed in Table 1.

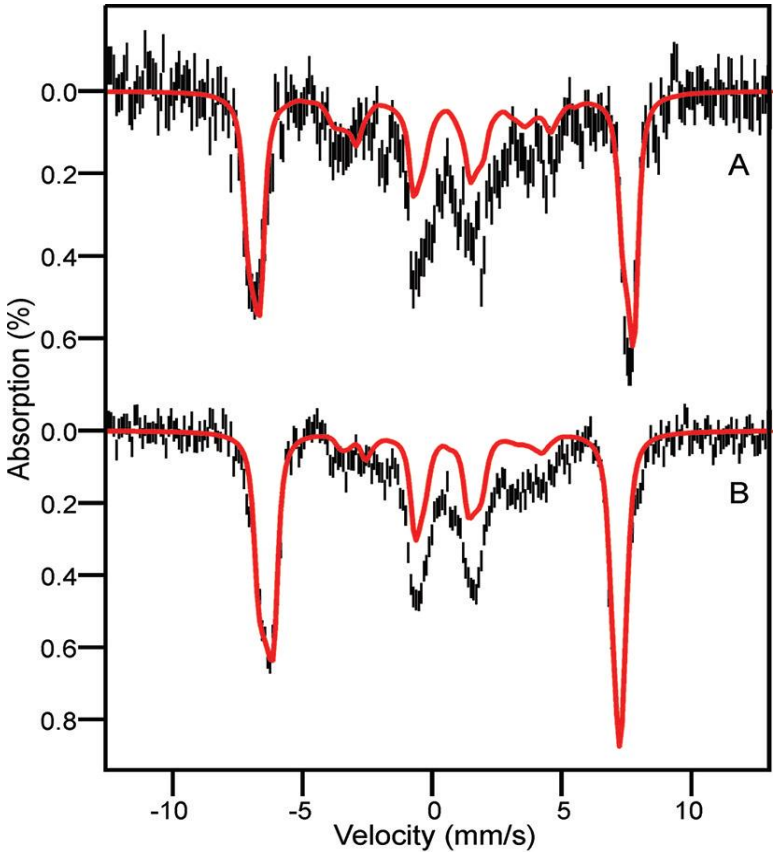

Figure 5. 4.2 K Mössbauer spectra of $H200N_{Int1}^{HPCA}$ recorded in parallel applied magnetic fields of (A) 4.0 T, and (B) 8.0 T. The central features of the spectra have unresolved contributions from the "splashed" ferrous contaminant. The red lines, drawn to represent 70 % of total Fe, are WMOSS spectral simulations based on eq 1 using the parameters listed in Table 1. This is the sample from Figure 4E.

^{17}O-Hyperfine Coupling Suggests that H200N$_{Int1}^{HPCA}$ Contains an Fe-Peroxo and a Substrate Radical Moiety. To further probe the nature of the S_R = 1/2 species in H200N$_{Int1}^{HPCA}$, we have prepared samples enriched with ^{17}O in either $^{17}O_2$ or in ^{17}O-C3-HPCA (^{17}O, I_{17O} = 5/2). Parallel-mode EPR spectra of H200N$_{Int1}^{HPCA}$ prepared with $^{16}O_2$ (red), 70% enriched $^{17}O_2$ (blue), and 68% enriched ^{17}O-C_3-HPCA (green) are shown in Figure 6. The g = 8.2 resonance of both enriched samples is broadened relative to its ^{16}O counterpart. For the two samples, the broadening is the same within the experimental uncertainty.

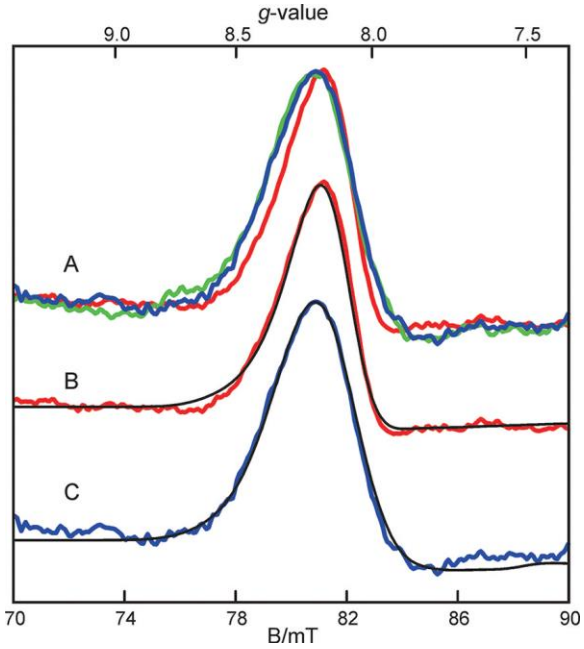

Figure 6. (A) EPR spectra of isotopically enriched H200N$_{Int1}^{HPCA}$ prepared with (red) natural abundance isotopes, (blue) 70% enriched $^{17}O_2$, (green) HPCA enriched to 68% with ^{17}O at the C3 OH functional group. Samples were prepared as described in Figure 2. Conditions before mixing: 1.65 mM H200N-HPCA complex, saturated O_2-containing buffer, 200 mM MOPS pH 7.5 and 4 °C. EPR conditions: Frequency 9.29 GHz; microwave power, 20 mW; modulation, 1.0 mT, temperature, 10 K. The simulations of natural abundance **(B)** and 70% enriched $^{17}O_2$ **(C)** samples are for S = 2, D = 1.3 cm^{-1}, E/D = 0.12, with $A_z^{O,c}$ of 0 (B) or 17 MHz (C).

For our analysis of the ^{17}O broadenings, we used the $S = 2$ Hamiltonian of eq 2. As will emerge shortly, the uncoupled representation of eq 1 is less suitable for this analysis. Using eq 2, SpinCount analysis yielded $|A_z^{O,c}| = 17$ MHz for both the $^{17}O_2$ and ^{17}O-C_3-HPCA enriched samples. As mentioned above, the $^{17}O_2$ analysis assumes that only one ^{17}O nucleus contributes to the signal. The $g = 8.2$ resonance is observed when the applied field, B, is along the molecular z-direction defined by the zero-field splitting term of eq 2. Therefore, the spectra are only sensitive to A_z^O. We have considered whether the ^{17}O is part of the radical moiety (such as a superoxo radical) or whether it is part of a non-radical bearing ligand coordinated to the iron. In the former case, the ^{17}O *A*-tensor of the coupled representation is related to the intrinsic (uncoupled) hyperfine tensor by $\mathbf{A}^{O,c} = (-1/6)\mathbf{A}^O$, which yields $A_z^O = 102$ MHz. In previous work, we have characterized a related intermediate species from a the same mutant HPCD using 4NC as a substrate, identified as an Fe(III)-superoxo species.[19] The superoxo-based radical had a substantially larger $A_z^O = 180$ MHz, resulting in a profound broadening of the EPR signal, and different values of J, D_1 and $(E/D)_1$ (see Table 1). One might suspect that the reduced A_z^O reflects a superoxo radical that has donated significant negative spin density to the iron. However, if this were the case, we would have observed a larger Mössbauer isomer shift and the ^{57}Fe *A*-tensor would exhibit substantial anisotropy due to a spin-dipolar term that would reflect the ferrous admixture to the site. This consideration is in marked contrast to what is observed here. We thus conclude that $H200N_{Int1}^{HPCA}$ does not

contain a superoxo radical, but instead contains a radical which resides on the HPCA moiety, presumably as an aromatic radical. Indeed, none of the other iron ligands are likely radical sites. The broadening from $^{17}O_2$ enrichment is therefore likely due to a peroxo species bound to the iron in a HPCA$^{\bullet}$-Fe^{III}-(hydro)peroxo complex. If the radical is located on the HPCA, the observed ^{17}O hyperfine coupling would be due to covalent spin polarization delocalization of the peroxo moiety by the ferric ion. In this case, the ^{17}O *A*-tensor in the coupled representation is related to the intrinsic (uncoupled) hyperfine tensor by $\mathbf{A}^{O,c} = (7/6)\mathbf{A}^{O}$, from which we obtain $|A_z^{O}| = 15$ MHz.

The labeling of the ^{17}O-C3-HPCA results in a broadening of the spectrum comparable to that of the $^{17}O_2$ sample. The interpretation of the broadening for ^{17}O-C3-HPCA is significantly more complex, because the C3 oxygen may have spin density contributions not only from coordination to the Fe^{III} but also from the HPCA radical. A covalent spin polarization contribution to the ^{17}O hyperfine interaction induced by the Fe^{III} has a favorable spin projection factor (+7/6), compared to the (-1/6) factor for the case in which the radical resides on the HPCA moiety (N.B. The use of eq 1, rather than eq 2, would bias the primary analysis of the EPR spectra.). Thus, for comparable spin density contributions to the labeled O (Fe *vs*. HPCA•) the *A*-value would be dominated by the contribution from the Fe^{III}. In the absence of quantitative insight about the source of the spin density at the C3 oxygen by quantum chemical calculations it seems prudent

to reserve judgment as to the precise origin of the broadening by ^{17}O-C3-HPCA. (footnote 3)

Stopped-flow Spectroscopy of the FeHPCA + O_2 Reaction Reveals No Evidence for an Intermediate Similar to H200N$_{Int1}^{HPCA}$. Figure 7 shows diode spectra from the single-turnover reaction in which pre-formed, anaerobic, stoichiometric FeHPCD-HPCA substrate complex is rapidly mixed with O_2-containing buffer at 4 °C. The spectra show only formation of the ring-cleaved product with λ_{max} near 380 nm with no detectable chromophore in the lower energy region from 500 - 700 nm; reaction of a 1 mM FeHPCD-HPCA sample also failed to show a long wavelength band. However, kinetic analysis of product formation using a single wavelength trace at 380 nm has previously revealed that product formation proceeds in several phases, including a fast phase that decays with $k_1 \sim 38$ s^{-1} and a slower phase with $k_2 \sim 3.8$ s^{-1}.[20]

In our current preparations, both rates are slightly faster ($k_1 = 59 \pm 4$ s^{-1} and with $k_2 = 6.0 \pm 0.5$ s^{-1}). The fast phase is associated with a lag in product formation as shown in Figure 7, *inset*, and precedes formation of the product chromophore. Consequently, while there are discrete intermediates in the oxygen activation and insertion processes, none of the detectible intermediates have optical features like H200N$_{Int1}^{HPCA}$. Following mixing of the FeHPCD-HPCA complex with O_2, single wavelength data at 380 nm (Figure 7, *inset*) show that the lag phase persists to ~ 30 ms, providing an opportunity to

use the RFQ approach for trapping reaction intermediates that precede product formation in the FeHPCD + O_2 reaction.

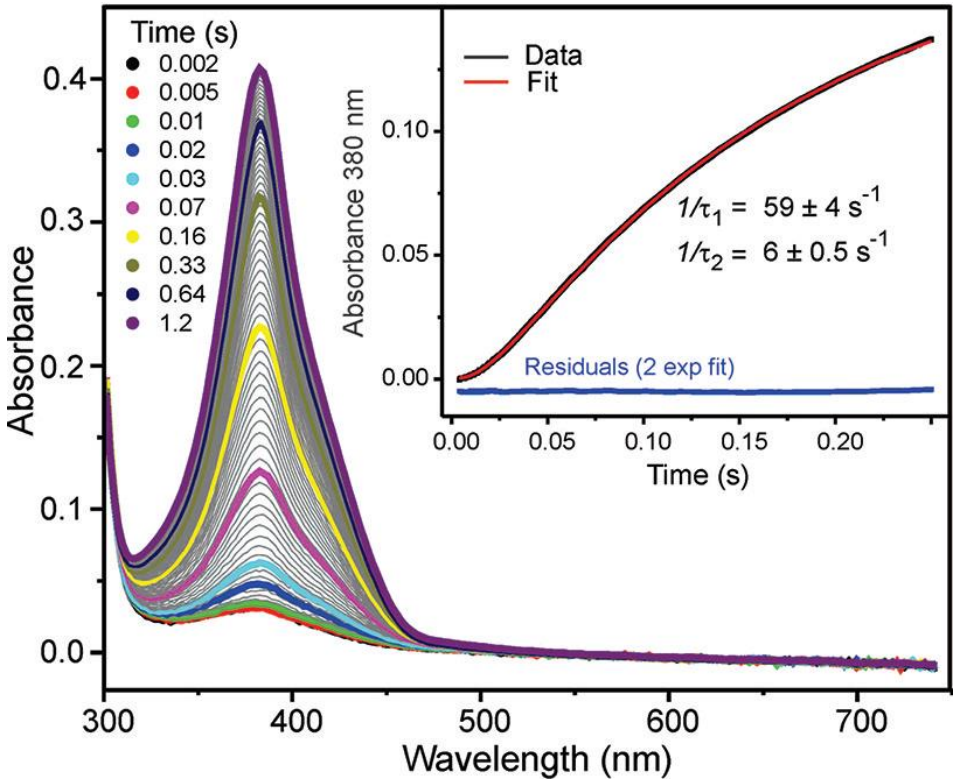

Figure 7. FeHPCD-HPCA + O_2 reaction monitored by stopped-flow. Diode array spectra recorded between 4 ms and 2 s after mixing 100 µM (based on active sites) stoichiometric, anaerobic FeHPCD-HPCA complex with O_2 saturated buffer (~1.8 mM) at 4 °C in 200 mM MOPS pH 7.5 (2 mm pathlength). Inset: Reaction monitored by single wave stopped-flow spectroscopy at 380 nm. In the time range shown, the data (black line) can be fit to a sum of two exponential terms (red line) with the reciprocal relaxation times shown.

RFQ Samples from the FeHPCD + O_2 Reaction Reveal an Fe^{II} Reaction Intermediate.

Because both the H200N-4NC + O_2 and H200N-HPCA + O_2 reactions have revealed high yields of oxygenated intermediates at times < 1 s (Figure 1-6[19]), we have prepared RFQ samples from the wild type FeHPCD-HPCA + O_2 reaction in order to

look for reaction intermediates associated with the lag phase in the kinetic time course before product formation.

The Mössbauer spectrum of the resting state WT enzyme consists of one doublet with $\Delta E_Q = 2.97$ mm/s and $\delta = 1.23$ mm/s, consistent with a 6-coordinate high-spin Fe^{II} species (Figure 8A). [2,23] Anaerobic addition of HPCA to the resting state WT enzyme yields a Mössbauer spectrum consisting of two ferrous doublets (Figure 8B). One doublet accounts for 55% of the iron with parameters $\Delta E_Q = 3.29$ mm/s and $\delta = 1.14$ mm/s ($FeHPCD_{ES1}^{HPCA}$, Table 2) while the other species has 45% of the iron giving a doublet with parameters $\Delta E_Q = 2.18$ mm/s and $\delta = 1.18$ mm/s ($FeHPCD_{ES2}^{HPCA}$, Table 2) (footnote 2). Note that these parameters differ from those observed for the H200N-HPCA complex. The spectrum of a sample frozen at 15 ms, which is within the lag phase of the FeHPCD-HPCA + O_2 reaction, is shown in Figure 8C. It reveals two new species exhibiting quadrupole doublets from ferrous ions. One doublet has $\Delta E_Q = 2.33$ mm/s, $\delta =$ 1.08 mm/s ($FeHPCD_{Int1}^{HPCA}$, Table 2) and accounts for ~ 70% of the iron. This species appears to decay to the second species which has parameters similar to those of the resting state enzyme ($\Delta E_Q = 3.03$ mm/s, $\delta = 1.24$ mm/s) which amounts to ~95% of the signal shown at the end of the reaction (Figure 8E). It is not clear whether this is the product-free resting enzyme or enzyme with product still bound due to its relatively high concentration in the Mössbauer sample. Its presence in the 15 ms sample may again be due to splash from the freezing wheels at high ram velocity. Our combined stopped-flow

and RFQ/Mössbauer data suggest that $FeHPCD_{Int1}^{HPCA}$ is a ferrous reaction intermediate that accumulates to nearly quantitative yields in the reaction cycle of the wildtype enzyme.

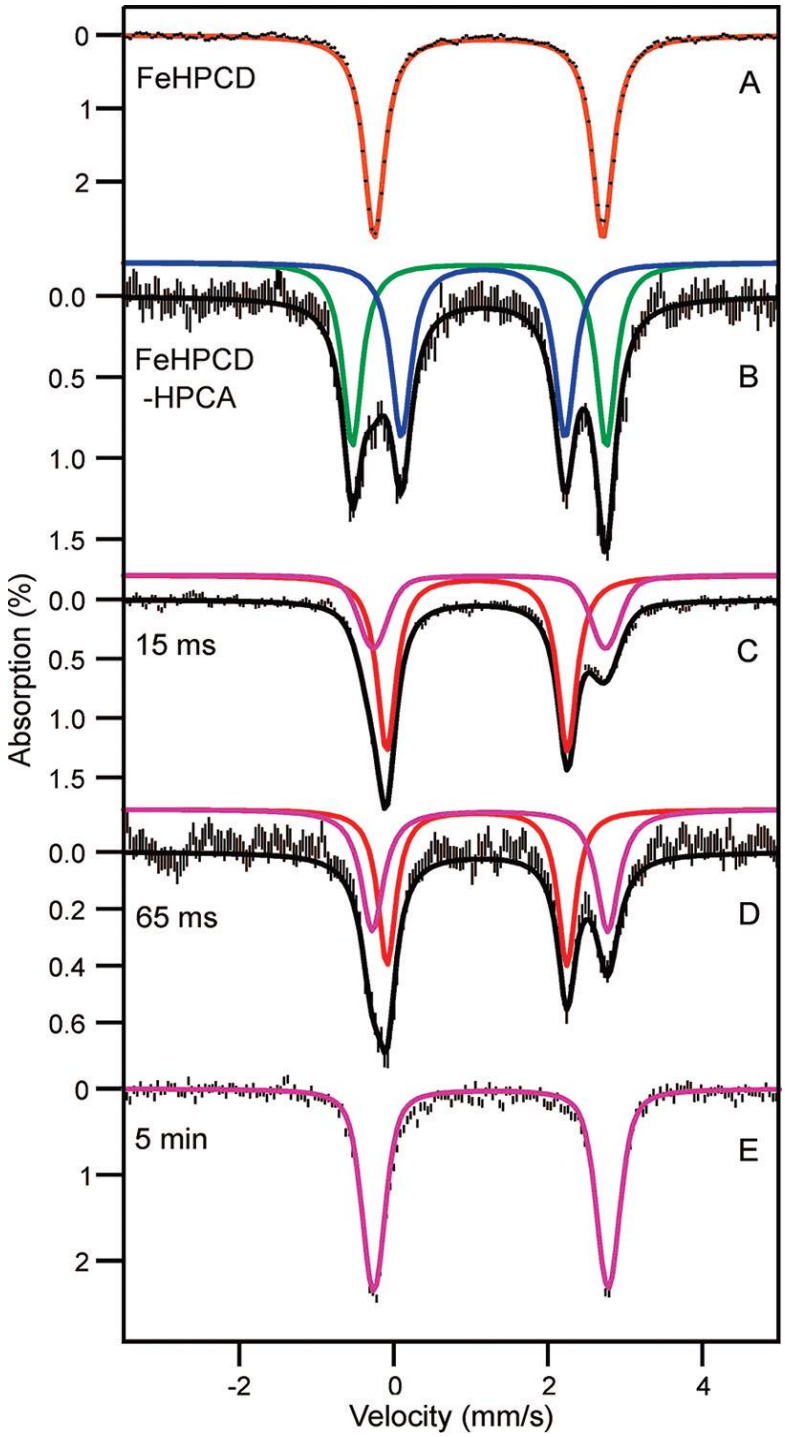

Figure 8. Mössbauer spectra from the FeHPCD-HPCA + O_2 reaction recorded at 4.2K for B = 0. **(A)** FeHPCD, **(B)** The anaerobic FeHPCD-HPCA complex, **(C)** FeHPCD-HPCA + O_2 at 15 ms after mixing with O_2, **(D)** FeHPCD-HPCA + O_2 at 65 ms after mixing with O_2, **(E)** 5 min after mixing. Conditions before mixing: ~ 1.8 mM enzyme-substrate complex, 200 mM MOPS, pH 7.5, and 4 °C all reactions. For (A) the sample concentration was ~ 0.9 mM.

Discussion

The isolation and characterization of the intermediates that follow binding of O_2 in the reaction cycle of Fe^{II}-containing catechol dioxygenases such as FeHPCD has been an elusive goal. Our recent characterization of the relatively long-lived intermediates in the reaction of H200N-4NC with O_2 was informative; however, the reaction leads to ring oxidation rather than ring cleavage.[18,19] The short lifetimes of intermediates in the reaction cycles of WT and mutant enzymes catalyzing ring cleavage reactions present a greater challenge. Here, the intermediates formed after oxygen binding in the H200N- and FeHPCD-catalyzed ring cleavage of HPCA have been trapped for spectroscopic characterization and comparison. The results show that the first intermediates trapped after O_2 addition in each of these systems differ fundamentally from each other as well as from the 4NC-Fe^{III}-superoxo intermediate trapped in the non-ring cleaving H200N-4NC + O_2 system. The structural insights gained from the evaluation of the spectra of these intermediates and the relevance to the mechanism of O_2 activation for aromatic ring cleavage are discussed here.

Identity of $H200N_{Int1}^{HPCA}$. The studies described here show that $H200N_{Int1}{}^{HPCA}$ contains a high-spin Fe^{III} (S_1 = 5/2) site that is antiferromagnetically coupled to a radical (S_R = 1/2) to yield a ground multiplet with S = 2. The ^{57}Fe magnetic hyperfine coupling of $H200N_{Int1}{}^{HPCA}$ ($A_0/g_n\beta_n$ = -21.5 T) compares well to those observed for mononuclear Fe^{III} sites and the isomer shift, δ = 0.48 mm/s, is characteristic of octahedral high-spin Fe^{III}

sites with N/O ligands (Table 1).[2,19,23,26] As judged by the values of A_0 and δ one electron has been transferred from the Fe^{II}. A radical species that couples to the resulting Fe^{III} must have been formed either directly or indirectly as a result of this transfer.

The most likely candidates for the $S_R = 1/2$ species bound to the Fe^{III} are suggested by the two intermediates discovered during our previous study of the H200N-4NC + O_2 reaction; namely, $H200N_{Int1}{}^{4NC}$ formulated as 4NC-Fe^{III}- $O_2^{\bullet-}$ and $H200N_{Int2}{}^{4NC}$ formulated as 4NC$^{\bullet}$-Fe^{III}- (hydro)peroxo. The spectroscopic data for $H200N_{Int1}{}^{HPCA}$ are overall quite similar to those of the latter, $H200N_{Int2}{}^{4NC}$, and differ significantly from the former. Specific similarities include: Mössbauer parameters, EPR spectra, substantial positive J values (antiferromagnetic) with $D_1 > 0$, and small ^{17}O hyperfine constants. In contrast, the 4NC-Fe^{III}- $O_2^{\bullet-}$ complex has much smaller J value (6 cm^{-1}), $D_1 < 0$, and its EPR signal is significantly more broadened when $^{17}O_2$ is used. Thus, we propose that $H200N_{Int1}{}^{HPCA}$ is formulated as HPCA$^{\bullet}$-Fe^{III}-(hydro)peroxo. (footnote 3)

The HPCA-SQ$^{\bullet}$ as the site of the radical is in accord with the crystallographic structure of the oxy-intermediate formed in the reaction of FeHPCD-4NC with O_2, which revealed substantial ring deformation at the carbon where oxygen subsequently attacks to form the alkylperoxo intermediate. This suggests that a localized radical forms at this carbon of the ring.[12] However, the 2.4 Å bond lengths of the metal ligands to the bound dioxygen species which we see in this intermediate suggest that the iron is in the Fe^{II}

state. This would mean that the bound oxygen is likely to be superoxo rather than peroxo.

The UV-vis spectrum of $H200N_{Int1}^{HPCA}$ shows three main features; namely, a high-energy shoulder at ~310 nm ($\varepsilon_{310\ nm} \sim 7000\ M^{-1}\ cm^{-1}$), a maximum at 395 nm ($\varepsilon_{395\ nm} \sim 3200\ M^{-1}\ cm^{-1}$) and a lower energy feature near 610 nm ($\varepsilon_{610\ nm} \sim 1100\ M^{-1}\ cm^{-1}$). This spectrum is inconsistent with HPCA bound in the catecholic form.[27-29] The two higher energy features are similar to those observed for unbound catechol quinones and semiquinones, which themselves have similar spectra (Table S2).[30,31] Indeed, the spectrum of $H200N_{Int1}^{HPCA}$ in the 300-500 nm region is very similar to that of HPCA quinone (Figure 1A, *inset*, blue dashed spectrum). Binding of these molecules to oxidized metals causes little change in the band positions or intensities. However, the semiquinone complexes can give rise to additional charge transfer bands in the 600 - 800 nm region with widely ranging extinction coefficients (300 - 3000 $M^{-1}\ cm^{-1}$) (Table S2).[32,33] Very few ligand-Fe^{III}-$SQ^{\bullet}$ model complexes with $S = 2$ have been spectroscopically characterized, but those available show similar optical characteristics (Table S2).[33-35] When considered in light of the EPR and Mössbauer analysis, the optical spectrum of $H200N_{Int1}^{HPCA}$ is most consistent with a HPCA-$SQ^{\bullet}$ radical and peroxo ligands bound to Fe^{III}.

While the 610 nm chromophore may derive from an HPCA $SQ^{\bullet}$-Fe^{III} interaction, another possibility is a (hydro)peroxo-to-Fe^{III} LMCT band, given the structure of

$H200N_{Int1}^{HPCA}$ proposed here. A band in this region might also arise from a Fe^{III}-OOR complex, but in the current case, this would be the alkylperoxo intermediate of the reaction cycle which is expected to contain Fe^{II} based on computational studies.[36,37] Many end-on Fe^{III}-OOH and side-on bound Fe^{III}-O_2^{2-} complexes from non-heme mononuclear model complexes have been characterized (Table S2).[38,39] The Fe^{III}-OOH complexes are often low-spin when the iron is coordinated by nitrogen ligands, but incorporation of at least one carboxylate ligand can result in a high spin Fe^{III}-OOH complex as would pertain to the intermediates of FeHPCD. In comparison to the 610 nm species observed here, the high spin Fe^{III}-OOH model complexes generally have a UV-vis transition with comparable intensity (ε = 450 - 2000 M^{-1} cm^{-1}) but shorter λ_{max} (440 - 570 nm) (Table S2).[38,39]

In model compounds, it has been shown that the Fe^{III}-OOH complexes can be deprotonated to form the conjugate base side-on bound Fe^{III}-O_2^{2-} complex for pH > 10.[38,39] In such a case, the resultant complex is often high spin, exhibiting a λ_{max} shift into the range of the 610 nm species (λ_{max} ~ 525 – 750 nm), but the ε values (ε = 450 - 600 M^{-1} cm^{-1}) are lower. Many of these side-on peroxo species have an EPR spectrum originating from an excited state like $H200N_{Int1}^{HPCA}$, but the Mössbauer isomer shift is somewhat larger (0.66 mm/s vs 0.48 mm/s). A third possibility is suggested by the high spin Fe^{III}-(hydro)peroxo intermediate in benzoate 1,2-dioxygenase, which we know from the crystal structure of the equivalent intermediate found in naphthalene 1,2-dioxygenase

to be a side-on bound Fe^{III} species.[40] Our spectroscopic analysis of the species from benzoate 1,2 dioxygenase shows that the Mössbauer isomer shift is 0.5 mm/s, as found for $H200N_{Int1}{}^{HPCA}$. We have proposed that this is due to protonation of the side-on bound peroxo moiety.[41] If this is the case, a pH dependence might be expected for the low energy band of the $H200N_{Int1}{}^{HPCA}$ spectrum, but none is observed in the range between pH 5.5 and 9.0 (Figure 1B, *inset*). One possible explanation for this is that the pK_a for this type of species is relatively high, as observed for the end-on hydroperoxo complexes, such that it remains protonated throughout the range of stability for the enzyme.

Based on this analysis, it is not currently possible to definitively assign the origin of the 610 nm species, and it could, in fact, result from the sum of both Fe^{III}-HPCA $SQ^{\bullet}$ and Fe^{III}-(hydro)peroxo interactions. Resonance Raman data may provide an assignment, but attempts to obtain spectra to date have been unsuccessful due to experimental difficulties arising from the ice lattice of frozen RFQ samples.

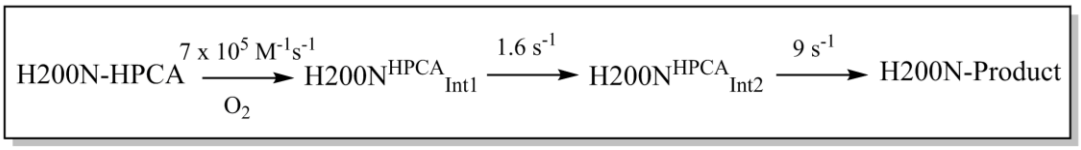

Scheme 2. Kinetic Model from Stopped-flow Studies of the H200N-HPCA + O_2 Reaction.

Identity of $H200N_{Int2}^{HPCA}$. Analysis of transient kinetic data from the time course of the 610 nm intermediate as well as product formation in the H200N-HPCA + O_2 reaction (values from the current preparation are shown in Figure S1, S2 and Scheme 2) [18] suggests that $H200N_{Int1}^{HPCA}$ accumulates to near stoichiometric yield. This is in accord with the Mössbauer and EPR spectra of this reaction intermediate shown here. On the other hand, the kinetic model predicts $H200N_{Int2}^{HPCA}$ would accumulate to only ~12 % at 400 ms due to the rapid decay of the species (Figure S2). Analysis of the Mössbauer reaction time-course does show that $H200N_{Int2}^{HPCA}$ accumulates to only ~10 % at 400 ms (Figure 6C). Due to low yields of $H200N_{Int2}^{HPCA}$, we were unable to obtain precise Mössbauer parameters of this species. However, it is clear that $H200N_{Int2}^{HPCA}$ is ferrous with $\Delta E_Q \approx 2.33$ mm/s and $\delta \approx 1.1$-1.2 mm/s. It is possible that this species is either the predicted (Scheme 1D) $HPCA^{\bullet}$-Fe^{II}-$O_2^{\bullet-}$, or perhaps more likely, the Fe^{II}-alkylperoxo or lactone intermediates, which derive from $H200N_{Int1}^{HPCA}$ prior to formation of the yellow ring cleaved product.

Identity of $FeHPCD_{Int1}^{HPCA}$. The Mössbauer parameters for $FeHPCD_{Int1}^{HPCA}$ show that this reaction intermediate contains a high-spin Fe^{II} site, in sharp contrast to the Fe^{III} containing initial intermediates described here and in our earlier study.[19] Unlike $H200N_{Int1}^{HPCA}$, no optical spectrum of this intermediate could be detected even in the first few milliseconds of the reaction. Consequently, our stopped-flow studies of the FeHPCD-HPCA + O_2 reaction were limited to monitoring product formation, which is

clearly at least a two step process.[20] The largest reciprocal relaxation time from this process makes the largest contribution to the observed lag phase and shows no O_2 concentration dependence. Thus, it is dominated by the rate constants for a step separated from the initial O_2 binding by at least one irreversible step. $FeHPCD_{Int1}{}^{HPCA}$ is temporally associated with this initial lag in product formation, suggesting that it occurs after the effectively irreversible step in the reaction. The lack of an optical spectrum from a semiquinone or quinone for $FeHPCD_{Int1}{}^{HPCA}$ is consistent with this hypothesis and also argues against a HPCA $SQ^{\bullet}$-Fe^{II}-$O_2{}^{\bullet-}$ or HPCA quinone-Fe^{II}-(hydro)peroxo structure. $FeHPCD_{Int1}{}^{HPCA}$ cannot be a product complex, which would be intensely yellow even before dissociation from the enzyme; the true product complex builds on a much longer time scale. Taken together, these observations suggest $FeHPCD_{Int1}{}^{HPCA}$ is one of the intermediates that results after oxygen attacks the substrate, but before ring cleavage, such as the alkylperoxo or lactone intermediates of the proposed reaction cycle. Accordingly, the Mössbauer parameters for this species are very similar to those of $H200N_{Int2}{}^{HPCA}$, which is postulated above to be such a species.

Mechanistic Implications of the Observed Intermediates. Our studies of the intermediates of the O_2 activation and insertion portion of the extradiol dioxygenase reaction cycle have shown that the nature and reactivity of the intermediates are functions of both the electronic characteristics of the substrate and the amino acid residues present in the second sphere of the active site. Scheme 3 illustrates the intermediates that have

been trapped and characterized by various means. Studies thus far have focused on substrates with progressively more electron withdrawing *para*-substituents and mutation of the key acid/base catalyst, His200. It is found that when a shorter Asn residue is substituted for His200, two types of intermediates can rapidly form in nearly 100% yield, both of which contain Fe^{III} spin-coupled to a radical. More specifically, an end-on bound Fe^{III}-$O_2^{\bullet-}$ adduct is formed when the substrate has a strongly electron withdrawing *p*-nitro substituent (Scheme 3B),[19] whereas a substrate $SQ^{\bullet}$-Fe^{III}-(hydro)peroxo species (peroxo orientation is not definitively determined) is formed when HPCA with its electron donating substituent is used (Scheme 3C). These two intermediates differ substantially not only in their respective lifetimes, but also in the eventual outcomes of catalysis.

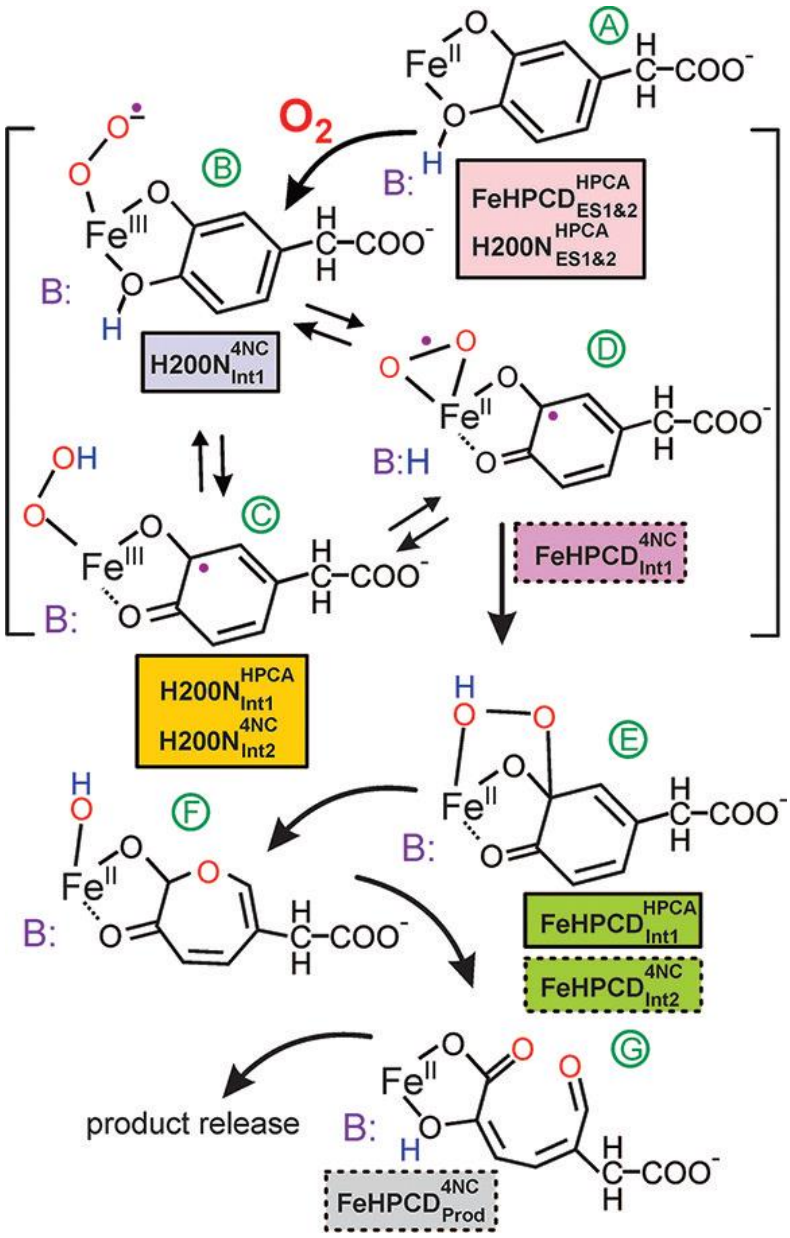

Scheme 3. Intermediates from the FeHPCD and H200N Turnover Cycles. The intermediates identified in boxes with solid borders are from solution RFQ studies reported here and in a previous study.[19] The intermediates identified in boxes with dashed borders are from crystal structures reported previously.[12]

The 4NC-Fe^{III}-$O_2^{\bullet-}$ intermediate persists for many minutes and eventually yields 4NC-quinone and H_2O_2, whereas the HPCA $SQ^{\bullet}$-Fe^{III}-(hydro)peroxo intermediate disappears in 2 s at 4 °C and yields the normal ring cleaved product. The ability of O_2 to

bind to the enzyme is also affected by the *para*-substituent of the substrate in the H200N mutant such that the binding rate constant is 4-fold slower and the reaction becomes reversible when 4NC is bound in place of HPCA.[18] These observations suggest that the effects of either electron withdrawal or donation in the substrate ring are transmitted through the iron to affect its ability to share electrons with the O_2 during binding. We have proposed that this transmission of electron density from the substrate through the iron to the bound O_2 is a fundamental aspect of oxygen activation in this enzyme family.[10,12,13]

The reaction of the native enzyme with 4NC and HPCA reveals other aspects of the mechanism. When His200 is present, substrates with either electron withdrawing or donating substituents are converted into ring-cleaved products, albeit at 25-fold different rates. The crystallographically characterized intermediate in the reaction of FeHPCD-4NC with O_2 ($FeHPCD_{Int1}{}^{4NC}$) (Scheme 3D)[12] and the spectroscopically characterized $FeHPCD_{Int1}{}^{HPCA}$ intermediate (Scheme 3E) described here both have Fe^{II} in the active site rather than Fe^{III}. However, the former appears to be a species with radical character on both the substrate and the bound O_2, while it is argued above that the latter is likely to be a state after oxygen attack on the substrate. If this is the case, then the formation and reaction of the reactive oxygen intermediate(s) must be very fast such that there is no evidence for any of the types of spin-coupled Fe^{III} intermediates described here or in our previous study. This may mean that an Fe^{III} species of some sort forms, but its lifetime is

too short to be detected even on the millisecond time scale. Alternatively, the iron may serve purely as a conduit for electron density that does not change oxidation state as an electron is transferred from the catechol to O_2. The final alternative, namely that there is no transfer of electron density between the substrates is unlikely because the reaction of unactivated oxygen with catechols is slow and does not result in ring cleavage.

Conclusion

The oxy-intermediates that have been trapped thus far using FeHPCD and its variants with HPCA and alternative substrates show that a radical species can reside on either the substrate or the oxygen and that an electron can be transferred from the iron, the substrate, or both to the oxygen. Based on the *in crystallo* studies published previously,[12] it is possible for an electron to be transferred in either a stepwise or a concerted fashion from the iron to the oxygen and from the substrate to the iron to yield a diradical pair. All of these observations support the most fundamental aspect of catalysis established for this enzyme class, which envisions oxygen activation by coordinating oxygen reduction with substrate oxidation to form a reactive pair. The results reported in our previous study show that simple formation of an Fe^{III}- $O_2^{\bullet-}$ species alone is not sufficient for high reactivity or ring cleaving chemistry. The current study suggests that, following electron transfer from the substrate, either a substrate $SQ^{\bullet}$-Fe^{II}-$O_2^{\bullet-}$ or a substrate $SQ^{\bullet}$-Fe^{III}-peroxo intermediate might serve as the reactive species. However, the high reactivity of the enzyme containing Fe^{II}, Mn^{II}, or Co^{II} [15,16] favors the substrate $SQ^{\bullet}$-Fe^{II}-$O_2^{\bullet-}$ species, for which there is no net change in oxidation state between the enzyme-substrate complex and the reactive species. Although the current study suggests for the first time that a substrate $SQ^{\bullet}$-Fe^{III}-peroxo intermediate can lead to ring cleavage, its low rate of reaction suggests that it is not the species that carries out this reaction in the reaction cycle of the WT enzyme.

Acknowledgements

This work is supported by the NIH grant GM 24689 (to J. D. L.), grant EB-001475 (to E. M.), grant GM77387 (to M. P. H.) and graduate traineeship GM08700 (to M. M. M.). We would like to thank Dr. David Ballou for the generous gift of the C1 and C2 enzymes used for synthesis of 17O-labeled HPCA.

References

1. Lipscomb, J. D., and Orville, A. M. (1992) Mechanistic aspects of dihydroxybenzoate dioxygenases. *Metal Ions Biol. Syst. 28*, 243-298.

2. Arciero, D. M., Lipscomb, J. D., Huynh, B. H., Kent, T. A., and Münck, E. (1983) EPR and Mössbauer studies of protocatechuate 4,5-dioxygenase. Characterization of a new Fe^{2+} environment. *J. Biol. Chem. 258*, 14981-14991.

3. Boldt, Y. R., Sadowsky, M. J., Ellis, L. B. M., Que, L., and Wackett, L. P. (1995) A manganese-dependent dioxygenase From *Arthrobacter globiformis* CM-2 belongs to the major extradiol dioxygenase family. *J. Bacteriol. 177*, 1225-1232.

4. Vaillancourt, F. H., Bolin, J. T., and Eltis, L. D. (2006) The ins and outs of ring-cleaving dioxygenases. *Crit. Rev. Biochem. Mol. Biol. 41*, 241-267.

5. Kovaleva, E. G., Neibergall, M. B., Chakrabarty, S., and Lipscomb, J. D. (2007) Finding intermediates in the O_2 activation pathways of non-heme iron oxygenases. *Acc. Chem. Res. 40*, 475-483.

6. Dagley, S. (1978) Microbial catabolism, the carbon cycle and environmental pollution. *Die Naturwissenschaften 65*, 85-95.

7. Bugg, T. D. H., and Winfield, C. J. (1998) Enzymic cleavage of aromatic rings: mechanistic aspects of the catechol dioxygenases and later enzymes of bacterial oxidative cleavage pathways. *Nat. Prod. Rep. 15*, 513-530.

8. Hegg, E. L., and Que, L. (1997) The 2-His-1-carboxylate facial triad: An emerging structural motif in mononuclear non-heme iron(II) enzymes. *Eur. J. Biochem. 250*, 625-629.

9. Arciero, D. M., Orville, A. M., and Lipscomb, J. D. (1985) [^{17}O]Water and nitric oxide binding by protocatechuate 4,5-dioxygenase and catechol 2,3-dioxygenase. Evidence for binding of exogenous ligands to the active site Fe^{2+} of extradiol dioxygenases. *J. Biol. Chem. 260*, 14035-14044.

10. Arciero, D. M., and Lipscomb, J. D. (1986) Binding of ^{17}O-labeled substrate and inhibitors to protocatechuate 4,5-dioxygenase-nitrosyl complex. Evidence for direct

substrate binding to the active site Fe^{2+} of extradiol dioxygenases. *J. Biol. Chem. 261*, 2170-2178.

11. Kovaleva, E. G., and Lipscomb, J. D. (2008) Versatility of biological non-heme Fe(II) centers in oxygen activation reactions. *Nat. Chem. Biol. 4*, 186-193.

12. Kovaleva, E. G., and Lipscomb, J. D. (2007) Crystal structures of Fe^{2+} dioxygenase superoxo, alkylperoxo, and bound product intermediates. *Science 316*, 453-457.

13. Shu, L., Chiou, Y. M., Orville, A. M., Miller, M. A., Lipscomb, J. D., and Que, L., Jr. (1995) X-ray absorption spectroscopic studies of the Fe(II) active site of catechol 2,3-dioxygenase. Implications for the extradiol cleavage mechanism. *Biochemistry 34*, 6649-6659.

14. Spence, E. L., Langley, G. J., and Bugg, T. D. H. (1996) Cis-trans isomerization of a cyclopropyl radical trap catalyzed by extradiol catechol dioxygenases: Evidence for a semiquinone intermediate. *J. Am. Chem. Soc. 118*, 8336-8343.

15. Emerson, J. P., Kovaleva, E. G., Farquhar, E. R., Lipscomb, J. D., and Que, L., Jr. (2008) Swapping metals in Fe- and Mn-dependent dioxygenases: Evidence for oxygen activation without a change in metal redox state. *Proc. Natl. Acad. Sci. U. S. A. 105*, 7347-7352.

16. Fielding, A. J., Kovaleva, E. G., Farquhar, E. R., Lipscomb, J. D., and Que, L., Jr. (2011) A hyperactive cobalt-substituted extradiol-cleaving catechol dioxygenase. *JBIC, Journal of Biological Inorganic Chemistry 16*, 341-355.

17. Gunderson, W. A., Zatsman, A. I., Emerson, J. P., Farquhar, E. R., Que, L., Lipscomb, J. D., and Hendrich, M. P. (2008) Electron paramagnetic resonance detection of intermediates in the enzymatic cycle of an extradiol dioxygenase. *J. Am. Chem. Soc. 130*, 14465-14467.

18. Groce, S. L., and Lipscomb, J. D. (2005) Aromatic ring cleavage by homoprotocatechuate 2,3-dioxygenase: Role of His200 in the kinetics of interconversion of reaction cycle intermediates. *Biochemistry 44*, 7175-7188.

19. Mbughuni, M. M., Chakrabarti, M., Hayden, J. A., Bominaar, E. L., Hendrich, M. P., Münck, E., and Lipscomb, J. D. (2010) Trapping and spectroscopic characterization of an FeIII-superoxo intermediate from a nonheme mononuclear iron-containing enzyme. *Proc Natl Acad Sci U S A 107*, 16788-16793.

20. Groce, S. L., Miller-Rodeberg, M. A., and Lipscomb, J. D. (2004) Single-turnover kinetics of homoprotocatechuate 2,3-dioxygenase. *Biochemistry 43*, 15141-15153.

21. Jollie, D. R., and Lipscomb, J. D. (1990) Formate dehydrogenase from *Methylosinus trichosporium* OB3b. *Methods Enzymol. 188*, 331-334.

22. Miller, M. A., and Lipscomb, J. D. (1996) Homoprotocatechuate 2,3-dioxygenase from *Brevibacterium fuscum* - A dioxygenase with catalase activity. *J. Biol. Chem. 271*, 5524-5535.

23. Münck, E. (2000) Aspects of ^{57}Fe Mössbauer spectroscopy, In *Physical Methods in Bioinorganic Chemistry* (Que, L., Jr, Ed.), pp 287-319, University Science Books, Sausalito, CA.

24. Sucharitakul, J., Chaiyen, P., Entsch, B., and Ballou, D. P. (2005) The reductase of p-hydroxyphenylacetate 3-hydroxylase from *Acinetobacter baumannii* requires p-hydroxyphenylacetate for effective catalysis. *Biochemistry 44*, 10434-10442.

25. Whittaker, J. W., Lipscomb, J. D., Kent, T. A., and Münck, E. (1984) *Brevibacterium fuscum* protocatechuate 3,4-dioxygenase. Purification, crystallization, and characterization. *J. Biol. Chem. 259*, 4466-4475.

26. Wolgel, S. A., Dege, J. E., Perkins-Olson, P. E., Jaurez-Garcia, C. H., Crawford, R. L., Münck, E., and Lipscomb, J. D. (1993) Purification and characterization of protocatechuate 2,3-dioxygenase from *Bacillus macerans*: A new extradiol catecholic dioxygenase. *J. Bacteriol. 175*, 4414-4426.

27. Costas, M., Mehn, M., P., Jensen, M., P., and Que, L., Jr. (2004) Dioxygen activation at mononuclear nonheme iron active sites: enzymes, models, and intermediates. *Chem. Rev. 104*, 939-986.

28. Cox, D. D., Benkovic, S. J., Bloom, L. M., Bradley, F. C., Nelson, M. J., Que, L., Jr., and Wallick, D. E. (1988) Catecholate LMCT bands as probes for the active sites of nonheme iron oxygenases. *J. Am. Chem. Soc. 110*, 2026-2032.

29. Anitha, N., and Palaniandavar, M. (2011) Mononuclear iron(III) complexes of 3N ligands in organized assemblies: spectral and redox properties and attainment of regioselective extradiol dioxygenase activity. *Dalton Trans. 40*, 1888-1901.

30. Stallings, M. D., Morrison, M. M., and Sawyer, D. T. (1981) Redox chemistry of metal-catechol complexes in aprotic media. 1. Electrochemistry of substituted catechols and their oxidation products. *Inorg. Chem. 20*, 2655-2660.

31. Chedekel, M. R., Land, E. J., Thompson, A., and Truscott, T. G. (1984) Early steps in the free radical polymerization of 3,4-dihydroxyphenylalanine (dopa) into melanin. *J. Chem. Soc., Chem. Commun.*, 1170-1172.

32. Hartl, F., Stufkens, D. J., and Vlcek, A., Jr. (1992) Nature of the manganese(I)-dioxolene bonding as a function of the ligand oxidation state: UV-visible, IR, and resonance Raman spectroelectrochemical study of [Mn(CO)3Ln(Diox)]z (n = 0, 1; z = -2, -1, 0, +1) and [Mn(CO)2{P(OEt)3}m(Diox)]z (m = 1, 2; z = -1, 0, +1) complexes. *Inorg. Chem. 31*, 1687-1695.

33. Mialane, P., Anxolabeheremallart, E., Blondin, G., Nivorojkine, A., Guilhem, J., Tchertanova, L., Cesario, M., Ravi, N., Bominaar, E., Girerd, J. J., and Münck, E. (1997) Structure and Electronic Properties of (N,N'-Bis(4-Methyl-6-Tert-Butyl-2-Methyl-Phenolate)-N,N'-Bismethyl-1,2-Di Aminoethane)Fe-Iii (Dbsq) - Spectroelectrochemical Study of the Red-Ox Properties - Relevance to Intradiol Catechol Dioxygenases. *Inorg. Chim. Acta 263*, 367-378.

34. Kessel, S. L., Emberson, R. M., Debrunner, P. G., and Hendrickson, D. N. (1980) Iron(III), manganese(III), and cobalt(III) complexes with single chelating o-semiquinone ligands. *Inorg. Chem. 19*, 1170-1178.

35. Lynch, M. W., Valentine, M., and Hendrickson, D. N. (1982) Mixed-valence semi-quinone catecholate iron complexes. *J. Am. Chem. Soc. 104*, 6982-6989.

36. Siegbahn, P. E. M., and Haeffner, F. (2004) Mechanism for catechol ring-cleavage by non-heme iron extradiol dioxygenases. *J. Am. Chem. Soc. 126*, 8919-8932.

37. Deeth, R. J., and Bugg, T. D. H. (2003) A density functional investigation of the extradiol cleavage mechanism in non-heme iron catechol dioxygenases. *J. Biol. Inorg. Chem. 8*, 409-418.

38. Girerd, J.-J., Banse, F., and Simaan, A. J. (2000) Characterization and properties of non-heme iron peroxo complexes. *Struct. Bonding 97*, 145-177.

39. Roelfes, G., Vrajmasu, V., Chen, K., Ho, R., Y. N., Rohde, J.-U., Zondervan, C., La Crois, R., M., Schudde, E., P., Lutz, M., Spek, A., L., Hage, R., Feringa, B., L., Münck, E., and Que, L., Jr. (2003) End-on and side-on peroxo derivatives of non-

heme iron complexes with pentadentate ligands: models for putative intermediates in biological iron/dioxygen chemistry. *Inorg. Chem. 42*, 2639-2653.

40. Karlsson, A., Parales, J. V., Parales, R. E., Gibson, D. T., Eklund, H., and Ramaswamy, S. (2003) Crystal structure of naphthalene dioxygenase: Side-on binding of dioxygen to iron. *Science 299*, 1039-1042.

41. Neibergall, M. B., Stubna, A., Mekmouche, Y., Münck, E., and Lipscomb, J. D. (2007) Hydrogen peroxide dependent cis-dihydroxylation of benzoate by fully oxidized benzoate 1,2-dioxygenase. *Biochemistry 46*, 8004-8016.

Supporting Information

Liquid Chromatography/Electrospray Ionization-Tandem Mass Spectrometry of ^{17}OH-C3-HPCA. LC/MS/MS determinations of 3-^{17}OH-HPCA were performed using a Waters Acquity UPLC coupled to a Waters TQD mass spectrometer. Separation was achieved with a Waters Acquity UPLC HSS T3 column (100 mm x 2.1 mm, 1.8 μm) C_{18} column heated to 35 °C employing a flow rate of 0.4 mL/min and mobile phase A and B, 0.1% aqueous formic acid and 0.1% formic acid in acetonitrile, respectively, and with the following gradient: 3% B, 0 to 2 min, 3% B to 97% B, 2 to 6 min, 97% B, 6 to 8 min, 97% B to 3% B, 8 to 9 min. Total run time was 12 min. Electrospray ionization tandem mass spectrometric methods (ESI-MS–MS) were created for the 3-^{17}OH-HPCA using selected reaction monitoring (SRM) optimized by direct infusion. Parameters of the ESI-MS–MS system were selected based on in-source generation of the deprotonated ions of each reactant and product (monoisotopic and isotopically labeled) as well as production of compound-specific fragment ions. The following negative ionization mode parameters were used for determination of these compounds: capillary, 3.20 kV; cone, 21 V; extractor, 3 V; rf lens, 0.3 V; source temperature, 150 ºC; desolvation temperature, 350 ºC; desolvation gas flow, 800 L/h; cone gas flow, 20 L/h; low-mass resolution (Q1), 12 V; high-mass resolution (Q1), 12 V; ion energy (Q1), 0.3 V; entrance, -5 V; collision energy, 8 V; exit, 1 V; low-mass resolution (Q2), 15 V; high-mass resolution (Q2), 15 V; ion energy (Q2), 3.5 V; gain, 1.0.

SRM transitions monitored for each analyte were as follows: HPCA: 167.2>123.1; HPCA first isotope (for calculation of natural first isotope abundance, accounted for in calculation of percent enrichment ^{17}O in corresponding products): 168.2>124.1; Product: 199.2>155.1 (loss of CO_2); $^{17}O_1$ Product: 200.2>155.1 (loss of $^{17}O_1$-CO_2); 200.2>156.1 (loss of CO_2); $^{17}O_2$ Product: 201.2 >156.1 loss of $^{17}O_1$-CO_2); 201.2>157.1 (loss of CO_2). The mass spec results are summarized in Table S1.

Table S1. Mass Spec Analysis of ^{17}O-C3-HPCA.

Compound	SRM Transition (MS/MS)	Intensity	%	Corrected %
HPCA	167.2 > 123.1	22902	92.8	
HPCA	168.2 > 124.1	1801	7.2	
^{17}O(C3)-HPCA	167.2 > 123.1	6372	30.3	32.6
^{17}O(C3)-HPCA	168.2 > 124.1	14648	69.7	67.3

Table S2. Electronic parameters for quinone, semiquinone and peroxo model complexes.

Complex	λ_{max} nm (ε_M)	Ref
Fe(III)-η^1-OOR		
[Fe(6-MeTPA)H_2O(OO*t*-Bu)]	598 (2000[a])	[1]
[Fe(6-Me_2TPA)H_2O(OO*t*-Bu)]	552 (2000 [a])	[1]
[Fe(6-Me_3TPA)H_2O(OO*t*-Bu)]	562 (2000[a])	[1,2]
[Fe(6-Me_3TPA)OBz(OO*t*-Bu)]	510 (2300[b])	[3]
[Fe(6-Me_3TPA)OBz(OOcumyl)]	506 (2300[b])	[3]
[Fe(BBPA)(OO*t*-Bu)]	613 (2000[a])	[4]
[Fe(BBPA)(OOcumyl)]	585 (2200[a])	[4]
[Fe(Me_4(15)aneN_4)SPh(OO*t*-Bu)]	630 (2300[b])	[5]
[Fe(Me_4(15)aneN_4)OTf(OO*t*-Bu)]	600 (1080[b])	[5]
[Fe(L_3Py_2)OTf(OO*t*-Bu)]	580 (2500[b])	[6]
[Fe(L_3Py_2)OBz(OO*t*-Bu)]	545(2700[b])	[6]
[Fe(L_3Py_2)SAr(OO*t*-Bu)]	510(2200[b])	[6]
[Fe(L_3Py_2)pyO (OO*t*-Bu)]	510(2450[b])	[6]
[Fe(L_4)(OO*t*-Bu)]	550 (700[c])	[7]
SLO-1 + 13-HPDO	590 (1400)[e]	[8]
15-RLO + 13-HPDO	580 (2400)[e]	[9]
Fe(III)-η^1-OOH		

[(TMC)Fe(η^1-OOH)]	500 (450)[a]	[10]
[Fe(H_2bppa)(OOH)]	568 (1200[d])	[11]
Fe(III)-η^2-OO^{2-}		
[(EDTA)Fe(η^2-O_2)]	520 (520)	[12]
[(trispicMeen)Fe(η^2-O_2)]	740 (500[f])	[13,14]
[(ettpen)Fe(η^2-O_2)]	747 (500[f])	[15]
[(bztpen)Fe(η^2-O_2)]	748 (500[f])	[16]
[(N4Py)FeIII((η^2-O_2)]	685 (520[f])	[17]
[(Rtpen)FeIII((η^2-O_2)]	716-771 (NA)	[18]
[(OEP)Fe(η^2-O_2)]-		[19]
[(Me-tpen)FeIII((η^2-O_2)]	780 (>350[f])	[20]
[(N4Py-tpen)FeIII((η^2-O_2)]	721 (521[f])	[20]
SOR-E47A-η^2-OO^{2-}	560 (400)	[21]
[(cydta)FeIII(η^2-O_2)]	545	[22,23]
Fe(III)-SQ		
[L_1-Fe(III)-DBSQ]	560 (6000)[h] 350 (8500)[h] 290 (20000)[h]	[24]
L_2-Fe(III)-NPSQ	463 (NR)[g] 430 (NR)[g] 298 (NR)[g]	[25]
L_2-Fe(III)-PheSQ	463 (NR)[g] 402 (NR)[g] 299 (NR)[g]	[25]
L_2-Fe(III)-DBSQ	613 (NR)[g] 489 (NR)[g] 452 (NR)[g] 425 (NR)[g] 357 (NR)[g] 302 (NR)[g]	[25]
Semiquinone		
3,5-di-tert-butyl-o-benzosemiquinone	~ 650 (~500)[i] 350-400 (~ 2900)[i] ~ 300 (~8000)[i]	[26]
Norepinephrine SQ	~ 310 (~5500)[e] ~ 350 (~ 2100)[e]	[27]
D L β-3,4-dihydroxyphenylalanine SQ	~ 310 (~6000) ~ 350 (~ 2100)	[27]
2,5-dihydroxyphenylacetate SQ	~ 310 (~11000) ~ 350 - 425 (~ 6000)	[27]
6-hydroxydopamine SQ	~ 350 (~8000) ~ 450 (~ 3900)	[27]
Quinone		
4-Nitro-catechol Q	380 (8500)[e]	[28]

3, 4-Dihydroxyphenylalanine Q	305 (9332)[e] 475 (3467)[e]	[29]
Rubreserin	300 (9332)[e] 480 (2754)[e]	[30]
Adrenochrome	300 (NR)[e] 480 (NR)[e]	[30]
3,5-di-tert-butylquinone	~ 400 (~ 1900)[i]	[31]
Catechol Q	300 (NR)[e] 390 (1834)[e] 420 (2040)[e]	[29, 28]
4-Thiocyanato- catechol Q	395 (1330)[e]	[28]
4-Acetyl-catechol Q	410 (1090)[e]	[28]
4-methyl catechol Q	300 (NR)[e] 400 (NR)[e]	[32]
4-Formyl-catechol Q	410 (1470)[e]	[28]
4-*tert*-butylcatechol Q	420 (NR)	[33]
Dopa quinone	278 (NR) 395 (1250)[e]	[33]
Dopamine quinone	303 (NR) 394 (NR)	[33]
Norepinephrine Q	296 (NR) 384 (NR)	[33]
Epinephrine	302 (NR) 387 (NR)	[33]
N-Acetyldopamine	392 (NR)	[33]

Abbreviations: Solvent are denoted by the superscript: a = acetonitrile, b = dichloromethane, c = diethylether, d = acetone, e = aqueous, f = methanol, g = benzene, h = THF, i = dimethylformamide. NR = not reported, L_1 = N,N'-bis(4-methyl-6-tert-butyl-2-methyl-phenolato)-N,N'-bismethyl- 1,2 diaminoethane, L_2 = N,N'-ethylenebis(salicylidenimine), L_3 = N,N'-bis(2-pyridylmethyl)-1,5-diazacyclooctane, L_4 = hydrotris(3-tert-butyl-5-isopropyl-1-pyrazolyl)borate. TPA = tris(2-pyridylmethyl)amine, BBPA = bis(6-pivalamido-2-pyridylmethyl)(2-pyridylmethyl)amine, Me_4(15)aneN_4 = 1,4,8,12-tetraazacyclopentadecane 1,4,8,12-Tetramethyl-1,4,8,12-tetraazocyclopentadecane, OTf = ortho-triflated, OBz = ortho-Benzoate, SAr = 4-methylbenzenethiolate, pyO = pyridine N-oxide.

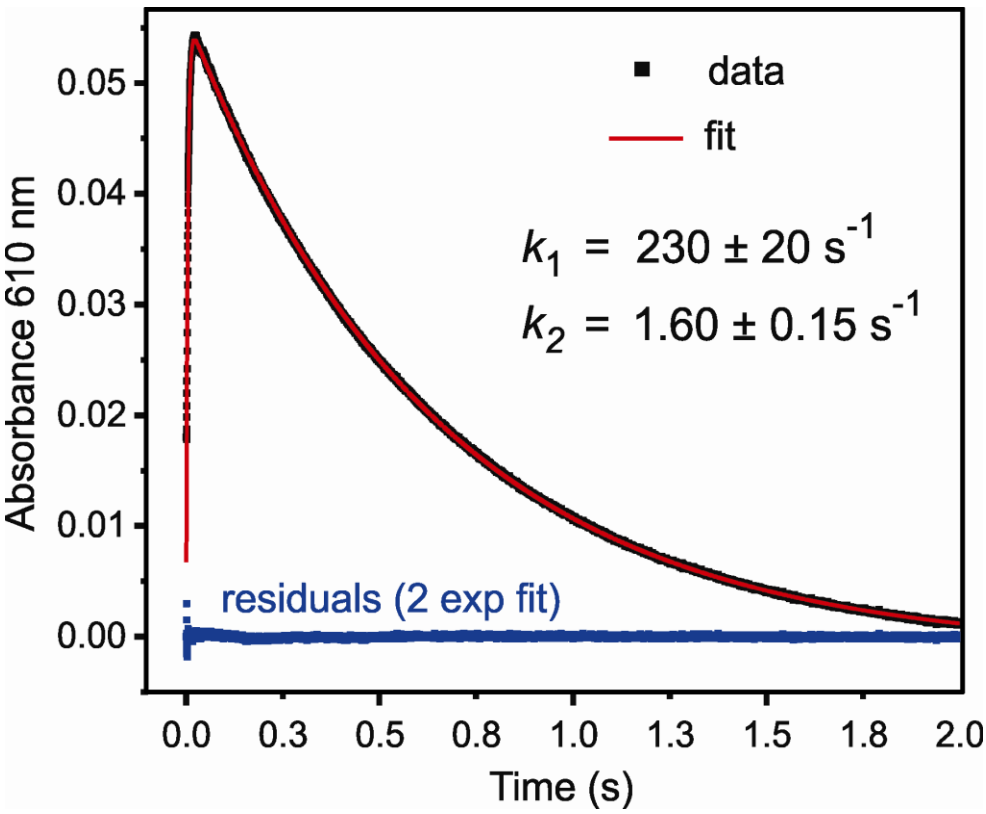

Figure S1. The time course of the reaction of H200N-HPCA + O_2 monitored at 610 nm using a single wavelength detector after mixing 100 µM anaerobic stoichiometric (sites) H200N-HPCA 1:1 with 600 µM O_2-containing 200 mM MOPS buffer at pH 7.5 (1 cm pathlength) (black line). The 610 nm data can be fit to a sum of two exponentials (red line).

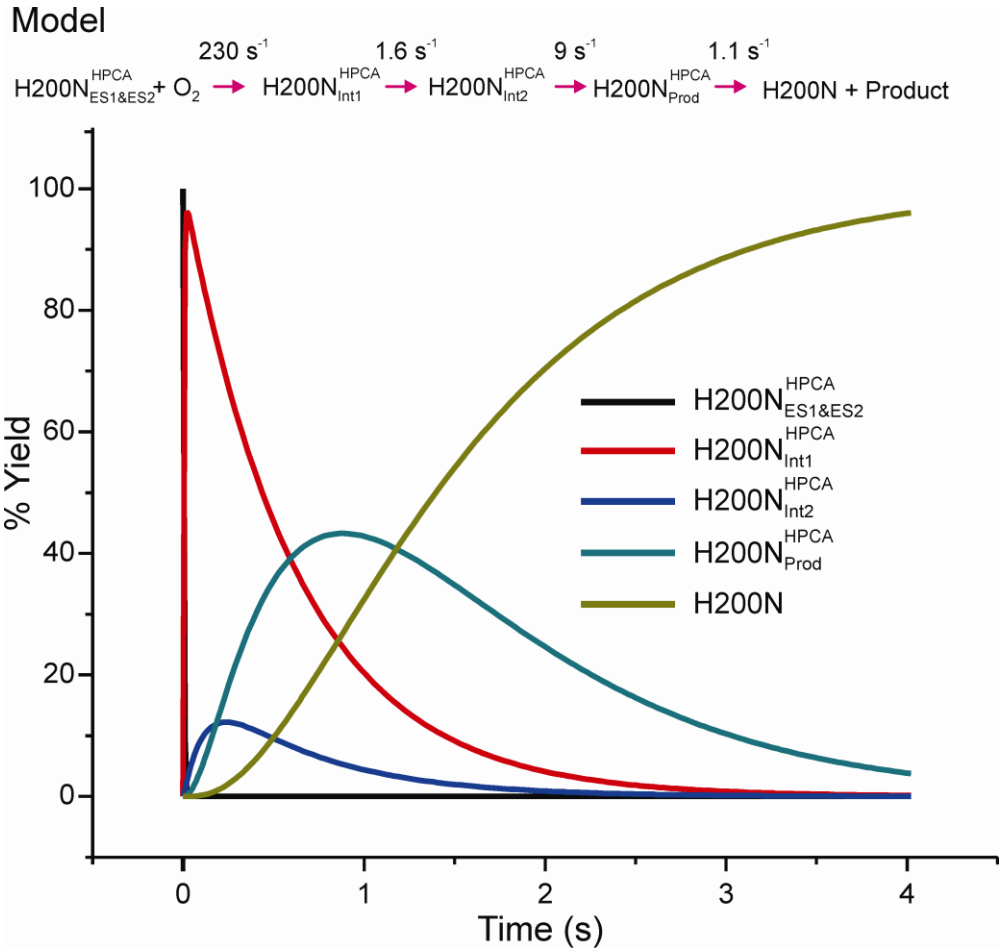

Figure S2. Numerical integration simulation of the time course of the reaction of H200N-HPCA + O_2 using the model shown on the figure.

References

1. Zang, Y., Kim, J., Dong, Y. H., Wilkinson, E. C., Appelman, E. H., and Que, L. (1997) Models for nonheme iron intermediates: Structural basis for tuning the spin states of Fe(TPA) complexes. *J. Am. Chem. Soc. 119*, 4197-4205.

2. Lehnert, N., Ho, R. Y. N., Que, L., Jr., and Solomon, E. I. (2001) Electronic structure of high-spin Iron(III)-alkylperoxo complexes and its relation to low-spin analogues: Reaction coordinate of O-O bond homolysis. *J. Am. Chem. Soc. 123*, 12802-12816.

3. Zang, Y., Elgren, T. E., Dong, Y., and Que, L., Jr. (1993) A high-potential ferrous complex and its conversion to an alkylperoxoiron(III) intermediate. A lipoxygenase model. *J. Am. Chem. Soc. 115*, 811-813.

4. Wada, A., Ogo, S., Watanabe, Y., Mukai, M., Kitagawa, T., Jitsukawa, K., Masuda, H., and Einaga, H. (1999) Synthesis and characterization of novel alkylperoxo mononuclear iron(III) complexes with a tripodal pyridylamine ligand: A model for peroxo intermediates in reactions catalyzed by non-heme iron enzymes. *Inorg. Chem. 38*, 3592-3593.

5. Namuswe, F., Hayashi, T., Jiang, Y., Kasper, G. D., Sarjeant, A. A. N., Moenne-Loccoz, P., and Goldberg, D. P. (2010) Influence of the nitrogen donors on nonheme iron models of superoxide reductase: High-spin FeIII-OOR complexes. *J. Am. Chem. Soc. 132*, 157-167.

6. Bukowski, M. R., Halfen, H. L., van den Berg, T. A., Halfen, J. A., and Que, L., Jr. (2005) Spin-state rationale for the peroxo-stabilizing role of the thiolate ligand in superoxide reductase. *Angew. Chem. Int. Ed. 44*, 584-587.

7. Lehnert, N., Fujisawa, K., and Solomon, E. I. (2003) Electronic structure and reactivity of high-spin iron-alkyl- and -pterinperoxo complexes. *Inorg. Chem. 42*, 469-481.

8. Skrzypczak-Jankun, E., Bross, R. A., Carroll, R. T., Dunham, W. R., and Funk, M. O. Jr. (2001) Three-dimensional structure of a purple lipoxygenase. *J. Am. Chem. Soc. 123,* 10814-10820.

9. Zhang, Y., Gan, Q.-F., Pavel, E. G., Sigal, E., and Solomon, E. I. (1995) EPR Definition of the non-heme ferric active sites of mammalian 15-lipoxygenases: Major spectral differences relative to human 5-lipoxygenases and plant lipoxygenases and their ligand field origin. *J. Am. Chem. Soc. 117*, 7422-7427.

10. Li, F. F., Meier, K. K., Cranswick, M. A., Chakrabarti, M., Van Heuvelen, K. M., Münck, E., and Que, L. (2011) Characterization of a high-spin non-heme Fe-III-O intermediate and its quantitative conversion to an Fe-IV = O complex. *J. Am. Chem. Soc. 133*, 7256-7259.

11. Wada, A., Ogo, S., Nagatomo, S., Kitagawa, T., Watanabe, Y., Jitsukawa, K., and Masuda, H. (2002) Reactivity of hydroperoxide bound to a mononuclear non-heme iron site. *Inorg. Chem., 41,* 616-618.

12. Horner, O., Jeandey, C., Oddou, J. L., Bonville, P., and Latour, J. M. (2002) A Mössbauer study of [Fe(EDTA)(O-2)](3-) agrees with a high-spin Fe-III peroxo complex. *Eur. J. Inorg. Chem. 2002*, 1186-1189.

13. Simaan, A. J., Banse, F., Mialane, P., Boussac, A., Un, S., Kargar-Grisel, T., Bouchoux, G., and Girerd, J. J. (1999) Characterization of a nonheme mononuclear peroxoiron(III) intermediate by UV Vis and EPR spectroscopy and mass spectrometry. *Eur. J. Inorg. Chem. 1999*, 993-996.

14. Simaan, A. J., Banse, F., Girerd, J. J., Wieghardt, K., and Bill, E. (2001) The electronic structure of non-heme iron(III)-hydroperoxo and iron(III)-peroxo model complexes studied by Mössbauer and electron paramagnetic resonance spectroscopies. *Inorg. Chem. 40*, 6538-6540.

15. Jensen, K. B., McKenzie, C. J., Nielsen, L. P., Pedersen, J. Z., and Svendsen, H. M. (1999) Deprotonation of low-spin mononuclear iron(III)-hydroperoxide complexes give transient blue species assigned to high-spin iron(III)-peroxide complexes. *Chem. Commun. 1999*, 1313-1314.

16. Horner, O., Jeandey, C., Oddou, J. L., Bonville, P., McKenzie, C. J., and Latour, J. M. (2002) Hydrogenperoxo-[(bztpen)Fe(OOH)](2+) and its deprotonation product peroxo-[(bztpen)Fe(O-2)](+), studied by EPR and Mössbauer spectroscopy - Implications for the electronic structures of peroxo model complexes. *Eur. J. Inorg. Chem. 2002*, 3278-3283.

17. Roelfes, G., Vrajmasu, V., Chen, K., Ho, R., Y. N., Rohde, J.-U., Zondervan, C., La Crois, R., M., Schudde, E., P., Lutz, M., Spek, A., L., Hage, R., Feringa, B., L., Münck, E., and Que, L., Jr. (2003) End-on and side-on peroxo derivatives of non-heme iron complexes with pentadentate ligands: Models for putative intermediates in biological iron/dioxygen chemistry. *Inorg. Chem. 42*, 2639-2653.

18. Hazell, A., McKenzie, C. J., Nielsen, L. P., Schindler, S., and Weitzer, M. (2002) Mononuclear non-heme iron(III) peroxide complexes: Syntheses, characterization, mass spectrometric and kinetic studies. *J. Chem. Soc.-Dalton Trans.* 310-317.

19. Burstyn, J. N., Roe, J. A., Miksztal, A. R., Shaevitz, B. A., Lang, G., and Valentine, J. S. (1988) Magnetic and spectroscopic characterization of an iron porphyrin peroxide complex. Peroxoferrioctaethylporphyrin(1-). *J. Am. Chem. Soc. 110*, 1382-1388.

20. Bukowski, M. R., Comba, P., Limberg, C., Merz, M., Que, L., Jr., and Wistuba, T. (2004) Bispidine ligand effects on iron/hydrogen peroxide chemistry. *Angew. Chem. Int. Ed. 43*, 1283-1287.

21. Horner, O., Mouesca, J. M., Oddou, J. L., Jeandey, C., Niviere, V., Mattioli, T. A., Mathe, C., Fontecave, M., Maldivi, P., Bonville, P., Halfen, J. A., and Latour, J. M. (2004) Mössbauer characterization of an unusual high-spin side-on peroxo-Fe^{3+} species in the active site of superoxide reductase from *Desulfoarculus baarsii*. Density functional calculations on related models. *Biochemistry 43*, 8815-8825.

22. Brausam, A., Maigut, J., Meier, R., Szilagyi, P. A., Buschmann, H. J., Massa, W., Homonnay, Z., and van Eldik, R. (2009) Detailed spectroscopic, thermodynamic, and kinetic studies on the protolytic equilibria of Fe(III)CYDTA and the activation of hydrogen peroxide. *Inorg. Chem. 48*, 7864-7884.

23. Homonnay, Z., Szilagyi, P. A., Vertes, A., Kuzmann, E., Sharma, V. K., Molnar, G., Bousseksou, A., Greneche, J. M., Brausam, A., Meier, R., and Eldik, R. (2008) Iron chelates: A challenge to chemists and Mössbauer spectroscopists. *Hyperfine Interact. 182*, 77-86.

24. Mialane, P., Anxolabeheremallart, E., Blondin, G., Nivorojkine, A., Guilhem, J., Tchertanova, L., Cesario, M., Ravi, N., Bominaar, E., Girerd, J. J., and Münck, E. (1997) Structure and electronic properties of (N,N'-bis(4-methyl-6-tert-butyl-2-methyl-phenolate)-N,N'-bismethyl-1,2-di aminoethane)Fe-III (DBSQ) - Spectroelectrochemical study of the red-ox properties - Relevance to intradiol catechol dioxygenases. *Inorg. Chim. Acta 263*, 367-378.

25. Kessel, S. L., Emberson, R. M., Debrunner, P. G., and Hendrickson, D. N. (1980) Iron(III), manganese(III), and cobalt(III) complexes with single chelating o-semiquinone ligands. *Inorg. Chem. 19*, 1170-1178.

26. Stallings, M. D., Morrison, M. M., and Sawyer, D. T. (1981) Redox chemistry of metal-catechol complexes in aprotic media .1. Electrochemistry of substituted catechols and their oxidation-products. *Inorg. Chem. 20*, 2655-2660.

27. Steenken, S., and Neta, P. (1982) One-electron redox potentials of phenols. Hydroxy- and aminophenols and related compounds of biological interest. *J. Phys. Chem. 86*, 3661-3667.

28. Duckworth, H. W., and Coleman, J. E. (1970) Physicochemical and kinetic properties of mushroom tyrosinase. *J. Biol. Chem. 245*, 1613-1625.

29. Mason, H. S. (1948) The chemistry of melanin; mechanism of the oxidation of dihydroxyphenylalanine by tyrosinase. *J. Biol. Chem. 172*, 83-99.

30. Ellis, S. (1943) Physostigmine and related substances. IV. Chemical studies on physostigmine breakdown products and related adrenaline derivatives. *J. Pharmacol. 79*, 364-372.

31. Stallings, M. D., Morrison, M. M., and Sawyer, D. T. (1981) Redox chemistry of metal-catechol complexes in aprotic media. 1. Electrochemistry of substituted catechols and their oxidation products. *Inorg. Chem. 20*, 2655-2660.

32. Mason, H. S., and Peterson, E. W. (1965) Melanoproteins. I. Reactions between enzyme-generated quinones and amino acids. *Biochim. Biophys. Acta, Gen. Subj. 111*, 134-146.

33. Kalyanaraman, B., Felix, C. C., and Sealy, R. C. (1985) Semiquinone anion radicals of catechol(amine)s, catechol estrogens, and their metal ion complexes. *EHP, Environ. Health Perspect. 64*, 185-198.

Chapter II – Substrate-mediated Oxygen Activation by Homoprotocatechuate 2,3-dioxygenase: Intermediates Formed by a Tyrosine 257 Variant

Published: Mbughuni, M.M.; **Meier, K.K.**; Münck, E.; Lipscomb, J.D. "Substrate-Mediated Oxygen Activation by Homoprotocatechuate 2,3-Dioxygenase: Intermediates Formed by a Tyrosine 257 Variant." *Biochemistry*. 2012, 51, pp 8743-8754.

Author Contributions: M.M.M., K.K.M., E.M., and J.D.L. conceived and designed the experiments. M.M.M. and K.K.M., (Mössbauer, EPR) performed the experiments. M.M.M., K.K.M., E.M., J.D.L. analyzed the data. All authors participated in the writing of the paper.

Abstract

Homoprotocatechuate (HPCA; 3,4-dihydroxyphenylacetate or 4-carboxymethyl catechol) and O_2 bind in adjacent ligand sites of the active site Fe^{II} of Homoprotocatechuate 2,3-Dioxygenase (FeHPCD). We have proposed that electron transfer from the chelated aromatic substrate through the Fe^{II} to O_2 gives both substrates radical character. This would promote reaction between the substrates to form an alkylperoxo intermediate as the first step in aromatic ring cleavage. Several active site amino acids are thought to promote these reactions through acid/base chemistry, hydrogen bonding, and electrostatic interactions. Here the role of Tyr257 is explored by using the Tyr257Phe (Y257F) variant, which decreases k_{cat} by about 75%. The crystal structure of the FeHPCD-HPCA complex has shown that Tyr257 hydrogen bonds to the

deprotonated C2-hydroxyl of HPCA. Stopped-flow studies show that at least two reaction intermediates, termed $Y257F_{Int1}^{HPCA}$ and $Y257F_{Int2}^{HPCA}$, accumulate during the Y257F-HPCA + O_2 reaction prior to formation of the ring-cleaved product. $Y257F_{Int1}^{HPCA}$ is colorless and is formed as O_2 binds reversibly to the HPCA-enzyme complex. $Y257F_{Int2}^{HPCA}$ forms spontaneously from $Y257F_{Int1}^{HPCA}$ and displays a chromophore at 425 nm (ε_{425} = 10,500 M^{-1} cm^{-1}). Mössbauer spectra of the intermediates trapped by rapid freeze quench show that both intermediates contain Fe^{II}. The lack of a chromophore characteristic of a quinone or semiquinone form of HPCA, the presence of Fe^{II}, and the low O_2 affinity suggests that $Y257F_{Int1}^{HPCA}$ is an HPCA-Fe^{II}-O_2 complex with little electron delocalization onto the O_2. In contrast, the intense spectrum of $Y257F_{Int2}^{HPCA}$ suggests the intermediate is most likely an HPCA quinone-Fe^{II}-(hydro)peroxo species. Steady state and transient kinetic analyses show that steps of the catalytic cycle are slowed by as much as 100-fold by the mutation. These effects can be rationalized by a failure of Y257F to facilitate the observed distortion of the bound HPCA that is proposed to promote transfer of one electron to O_2.

Introduction

Homoprotocatechuate 2,3-dioxygenase (FeHPCD) from *Brevibacterium fuscum* catalyzes the insertion of both atoms from O_2 into the aromatic ring of homoprotocatechuate (HPCA, 3,4-dihydroxybenzoate) resulting in ring opening as shown in Scheme 1.[1,2]

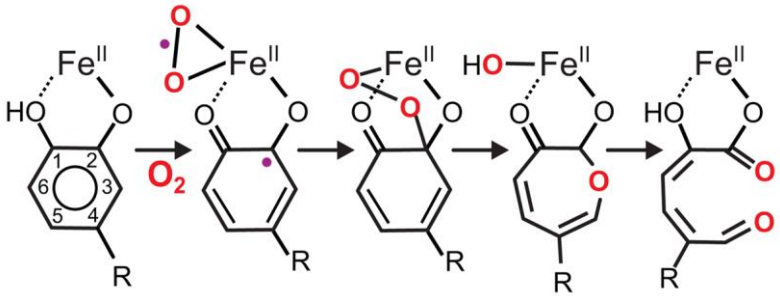

Scheme 1. Proposed reaction sequence for extradiol dioxygenases. For the studies described here, R = CH_2COO^-. The numbering system shown is adopted for consistency with studies described in the accompanying report.[2] The endogenous Fe^{II} ligands are omitted for clarity.

The enzyme utilizes an Fe^{II}, which is bound in the active site by two histidine and one glutamic acid side chains in a 2-His-1-carboxylate facial triad motif shown in Figure 1A.[3-7] Substrates bind in multistep processes to displace solvents from the Fe^{II} and form a chelate complex.[8] For catecholic substrates such as HPCA with relative high p*K*a values for the hydroxyl substituents, only the C2-hydroxyl group deprotonates upon binding, so that the overall charge of the metal center is neutral.[3-5,9] Crystallographic studies have shown that small molecules such as O_2 and the O_2 surrogate NO bind in the open ligand site of the Fe^{II} adjacent to the substrate.[5,6] We and others have proposed the mechanism summarized in Scheme 1 in which an electron is transferred from the aromatic substrate

through the iron to the oxygen, giving both substrates radical character ($SQ^{\bullet}$-Fe^{II}-$O_2^{\bullet-}$). [8,10-14] Recombination of the radicals would yield an alkylperoxo intermediate. A subsequent Criegee-type rearrangement would result in O-O bond cleavage to yield a substrate lactone intermediate with the second atom of oxygen retained on the iron. Hydrolysis of the lactone by this oxygen would yield the bound product ready for release.

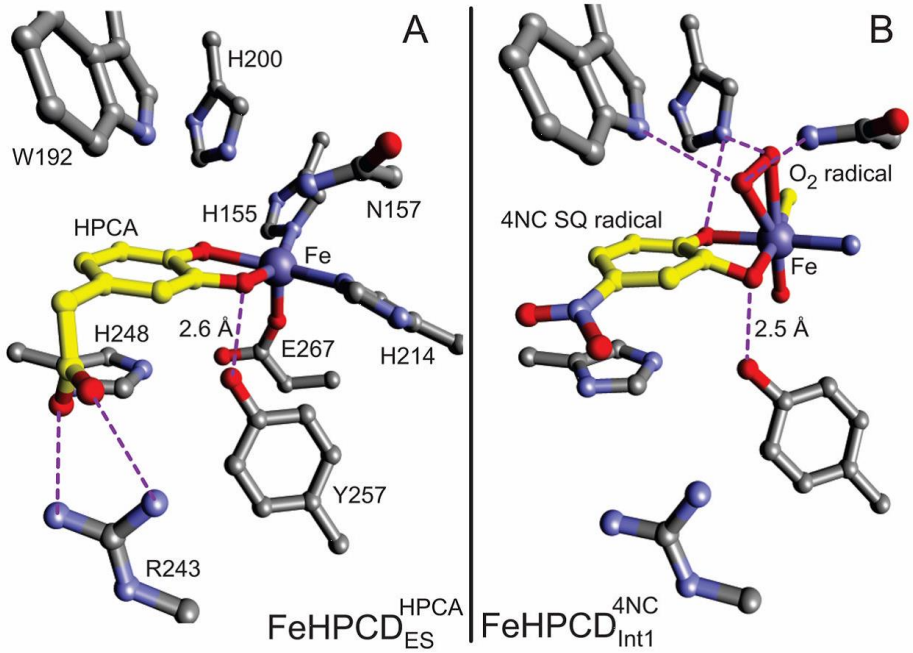

Figure 1. Second sphere residues proposed to participate in catalysis. A) $FeHPCD_{ES}^{HPCA}$, structure of the anaerobic FeHPCD-HPCA substrate complex (PDBID: 1Q0C).[3] B) $FeHPCD_{Int1}^{4NC}$, structure of the oxy complex from the FeHPCD-4NC + O_2 reaction (PDBID: 2IGA, subunit C). [6] This reaction intermediate is proposed to have a $SQ^{\bullet}$-Fe^{II}-$O_2^{\bullet-}$ electronic structure. The endogenous iron ligands are omitted for clarity.

Crystallographic studies in which the slow alternative substrate 4-nitrocatechol (4NC) was diffused anaerobically into the crystal and the reaction initiated by exposure

to low concentrations of O_2, have allowed the $SQ^{\bullet}$-Fe^{II}-$O_2^{\bullet-}$ (Figure 1B), alkylperoxo, and the product complexes to be structurally characterized.[6] A gem-diol intermediate (or stabilized form), which presumably occurs between the alkylperoxo and lactone intermediates, was trapped in a crystal and structurally characterized using a similar approach.[15] These studies and earlier structural studies of the FeHPCD-HPCA complex[3] have revealed several residues in the active site that are likely to facilitate catalysis (Figure 1A). In particular, residue His200 is positioned to interact with both the substrate C4-OH substituent and the bound oxygen. Mutation of this residue indicates that it plays many roles including that of an acid-base catalyst to promote the Criegee rearrangement chemistry.[12] It may also serve to sterically promote the side-on binding orientation of the oxygen in the $SQ^{\bullet}$-Fe^{II}-$O_2^{\bullet-}$ complex revealed by the crystal structure and to stabilize the oxy complex by a combination of hydrogen bonding and charge interaction with the bound superoxo anion (Figure 1B). Substitution of His200 by shorter residues that cannot effectively hydrogen bond or catalyze acid-base chemistry and/or the use of alternative substrates greatly slow catalysis, allowing several intermediates to be trapped by rapid freeze quench (RFQ) techniques for spectroscopic characterization.[16,17]

Another active site residue, Tyr257, also appears to be important for catalysis based on its interaction with the HPCA C2-O^-. This residue is located on the opposite side of the substrate from His200 and forms a hydrogen bond with the deprotonated substrate hydroxyl (Figure 1A). We postulate that Tyr257 promotes oxygen activation,

ring attack, and ring cleaving chemistry in several ways related to favoring a tetrahedral geometry at the carbon bearing this hydroxyl. This proposal is based on the observation that the structurally characterized intermediates exhibit an increasingly tetrahedral substrate C2 as they progress toward product formation (see for example Figure 1B).[6,15] Consequently, active site structural elements that favor sp^3 hybridization at substrate C2 should promote each step of the reaction.

Here we explore the roles of Tyr257 in catalysis by mutating it to a Phe (Y257F), which preserves the spatial characteristics of Tyr, but not the ability to hydrogen bond or sterically interact with the substrate via the Tyr hydroxyl substituent. It is found that, in accord with the postulated role for Tyr257, the Y257F-HPCA + O_2 reaction forms a ring-cleaved product with kinetics that are slow in comparison to those of the wild-type reaction. The slow internal steps of the Y257F reaction cycle allow new intermediates to be detected, trapped, and characterized. The new intermediates support the proposed requirement for electron transfer to the oxygen from the substrate without a net change in metal oxidation state prior to O_2 attack in order to sustain efficient catalysis. The structural bases for the roles of Tyr257 are explored in the accompanying report.[2]

Experimental Methods

Reagents and Enzymes. All chemicals were purchased from Sigma-Aldrich and were used without purification except for HPCA which was recrystallized from water at 4 °C to remove minor contaminants. Anaerobic conditions were achieved by repeated cycling of solutions between argon gas and vacuum. Trace contaminating O_2 was removed from the Ar gas by passage through an Agilent GC-1 POP O_2 scrubbing cartridge, then through an Agilent GC-4 POP O_2 indicating cartridge. Mushroom tyrosinase was purchased from Sigma-Aldrich.

Y257F Variant. Y257F mutant of FeHPCD was prepared using the Stratagene QuickChange kit. The following mutagenesis primer was used along with its reverse complement:

GCGTCTCCAACGCGTTCTACCTG**TTC**ATCC.

The mutant codon is shown in bold highlight. The mutation was confirmed via sequencing at the University of Minnesota MicroChemical Facility.

Recombinant WT FeHPCD and Y257F were purified as previously described[1,12] with a few modifications. No cysteine or Fe was added to the purification buffers, but all buffers used in the purification were continually sparged with 1 psi of N_2 to remove O_2. After loading FeHPCD onto the DEAE Sepharose column, the column was gravity washed with 10 column volumes of buffer (50 mM MOPS pH 6.8 + 190 mM NaCl). The wash buffer is sparged with 1 psi of N_2 during this process. After the wash, a salt gradient

totaling 10 column volumes was run from 190 - 350 mM NaCl using a gravity dependent gradient maker sparged with 1 psi N_2 in the mixing chamber (chamber with low salt buffer). The pooled fractions from the DEAE Sepharose column were found to be sufficiently pure for kinetic and spectroscopic studies. Purified Y257F yielded the correct ring cleaved product from HPCA.

The isotope ^{57}Fe was incorporated into the enzyme by growth on ^{57}Fe-enriched media as previously described except that the media contained 4 g/L yeast extract and 4 ml/L of filter sterilized glycerol.[16] Mössbauer analysis of the purified Y257F mutant revealed ~1 eq of $^{57}Fe^{II}$/site enrichment as previously described for the wild type enzyme and the H200N mutant.[16,17]

Iron Quantification using ICP-OES. The ICP-OES samples are digested in 20% nitric acid at 37 °C for at least 24 h. Insoluble materials were removed by centrifugation at 10,000 × g at 4 °C. The supernatant was analyzed for transition metals using ICP-OES at the Aqueous Geochemistry Lab (University of Minnesota, Department of Earth Science).

Stopped-Flow Kinetics and Spectroscopy. All stopped-flow experiments were performed using an Applied Photophysics model SX.18MV stopped-flow device. The reaction procedures were as previously described.[8] All stopped-flow experiments were conducted at 4 °C in 50 mM MOPS buffer at pH 7.5 or 50 mM MES buffer at pH 5.5, as previously described. [17] Solutions varying in O_2 concentrations were prepared by diluting

a stock saturated O_2 buffer solution with anaerobic buffer in a gas-tight 5 ml Hamilton syringe equilibrated on ice. The kinetic data were analyzed to extract reciprocal relaxation times using the Applied Photophysics Pro-Data Viewer version 4.0.17. In general, the reaction time courses were fit to summed exponential expressions, which are appropriate for series of first order or pseudo first order reactions.[18] EPR spectra were collected using a Bruker Elexsys E-500 spectrometer equipped with a Bruker dual mode cavity and an Oxford ESR 910 liquid helium cryostat. Mössbauer spectroscopy was performed as previously described.[16,19] Spectra were analyzed using the software WMOSS (SEE Co, Edina, MN, USA).

Steady-State Kinetic Experiments. Steady-state kinetic parameters for the ring-cleaving reaction of FeHPCD and the Y257F variant were monitored using UV-vis detection. The initial velocity of product formation was observed at 380 nm using a stopped-flow device. The linear portion of the trace was fit using the Pro Data Viewer software package. The enzyme concentration was 1 μM for FeHPCD and 3 – 6 μM for Y257F after mixing with varying HPCA substrate concentrations. Experiments were done at either 4 °C or 22 °C in 200 mM MES or MOPS buffer at pH 5.5 or pH 7.5, respectively, in air saturated buffer as noted in the figure legends. Initial velocities were fit as a hyperbolic function of substrate concentration to determine K_m and V_{max} using the data analysis software in Origin.

Rapid Freeze Quench (RFQ) Methods. Y257F-HPCA anaerobic complex (1.6 mM) was prepared in the glove box by mixing 1 eq of Y257F with 1 eq of HPCA. RFQ syringes were loaded inside the Coy anaerobic glove box and then transferred to an Update Instrument model 1019 RFQ apparatus and allowed to equilibrate for 30 min at 4 °C. The RFQ samples were mixed with O_2 buffer as previously described.[17] Previously, we observed a splash artifact when the shortest time reaction mixtures were frozen on the counter-rotating aluminum wheels maintained at Liq N_2 temperature.[17] To avoid this artifact, the instrument was redesigned to rotate the wheels at a higher velocity and plastic scrapers were placed to remove the frozen solution from the wheels each cycle. This allowed the reaction mixture to always contact the metal surface rather than frozen solution on the wheel. Samples at times > 1 s were frozen as previously described.[17]

Preparation of HPCA Semiquinone and HPCA Quinone. HPCA was oxidized to a quinone using mushroom tyrosinase (Sigma) in 100 mM MOPS buffer pH 7.5 and 4 °C. A solution of 2 mM HPCA was mixed with 10 mg/ml mushroom tyrosinase. The quinone formed during the first 4 min of the reaction. It is photo-labile and decays to an unidentified secondary species over the next 10 min. HPCA was oxidized to a transient semiquinone by oxidation with 3,4,5,6-tetrachloro-1,2-benzoquinone (O-chloranil, Sigma-Aldrich) in ethanol at 20 °C. [20,21] The reaction was initiated and monitored using the stopped-flow spectrometer with diode-array detection (2 mm path). A solution of 2

mM HPCA was mixed with 2 mM of O-chloranil. The semiquinone formed during the first 150 s of the reaction and then slowly decayed to an unidentified species.

Results

The Y257F Variant of FeHPCD Reacts Slowly. The steady-state parameters for Y257F with the HPCA substrate were determined at 4 and 22 °C and at pH 7.5 and pH 5.5 by monitoring the initial velocity of product formation using stopped-flow spectroscopy as summarized in Table 1. An example of the Michaelis-Menten plot for HPCA varied at pH 7.5 and 4 °C is shown in Figure S1. The results show that the k_{cat} value decreases to about 27% of that of the WT enzyme at pH 7.5, 22 °C. The K_m^{HPCA} is increased by about 16 fold by the mutation, whereas K_m^{O2} is increased only slightly.

Substrate Binds Tightly to Y257F. Direct determination of the K_d for HPCA is complicated by the lack of a visible or fluorescence change upon binding. However, the K_d can be approximated by comparison to 4NC binding. The K_d for 4NC for WT enzyme has been previously determined to be 5 μM based on the spectroscopic change that occurs as monoanionic 4NC in solution converts to the dianionic form bound to the enzyme.[8] The fraction of 4NC bound upon addition of a fixed concentration to Y257F is the same as that observed for the WT enzyme, showing that the K_d does not change significantly (Figure 2, blue and black traces). When HPCA and 4NC are added in equal concentrations to either FeHPCD or Y257F, only the spectrum of free 4NC is observed, showing that HPCA binds much tighter than 4NC (K_d > 5 μM) in each case (Figure 2, red trace). This is not the case when a weak binding substrate 4-chlorocatechol (4CC) is added instead of HPCA (Figure 2, green and black traces). These results suggest that the

relatively high K_m^{HPCA} value observed for Y257F must be attributed to reaction cycle steps other than those associated with formation of the final substrate complex. The low K_d value facilitates transient kinetic experiments as described below.

Table 1. Steady state parameters for FeHPCD-HPCA and Y257F-HPCA reaction with O_2.

Kinetic parameter	**Wild type 22 °C pH 7.5**	**Y257F 22 °C pH 7.5**	**Y257F 4 °C pH 7.5**	**Y257F 22 °C pH 5.5**
k_{cat} **(s^{-1})**	10.0 ± 1.5	2.70 ± 0.13	0.38 ± 0.07	0.4 ± 0.1
K_m^{HPCA} **(mM)**	0.016[b]	0.26 ± 0.05	0.25 ± 0.05	0.13 ± 0.02
k_{cat}/K_m^{HPCA} **($mM^{-1}s^{-1}$)**	625	10.4	1.5	3.1
K_m^{O2} **(mM)**	0.015 ± 0.007	0.08 ± 0.03	0.02 ± 0.01	0.01 ± 0.005
k_{cat}/K_m^{O2} **($mM^{-1}s^{-1}$)**	667	34	19	40

[a] Reactions were conducted in 200 mM MES or MOPS at pH 5.5 or 7.5, respectively. The buffer is air saturated at either 4 °C or 22 °C. At this O_2 concentration, the reaction is saturated. [b] From ref. [1]

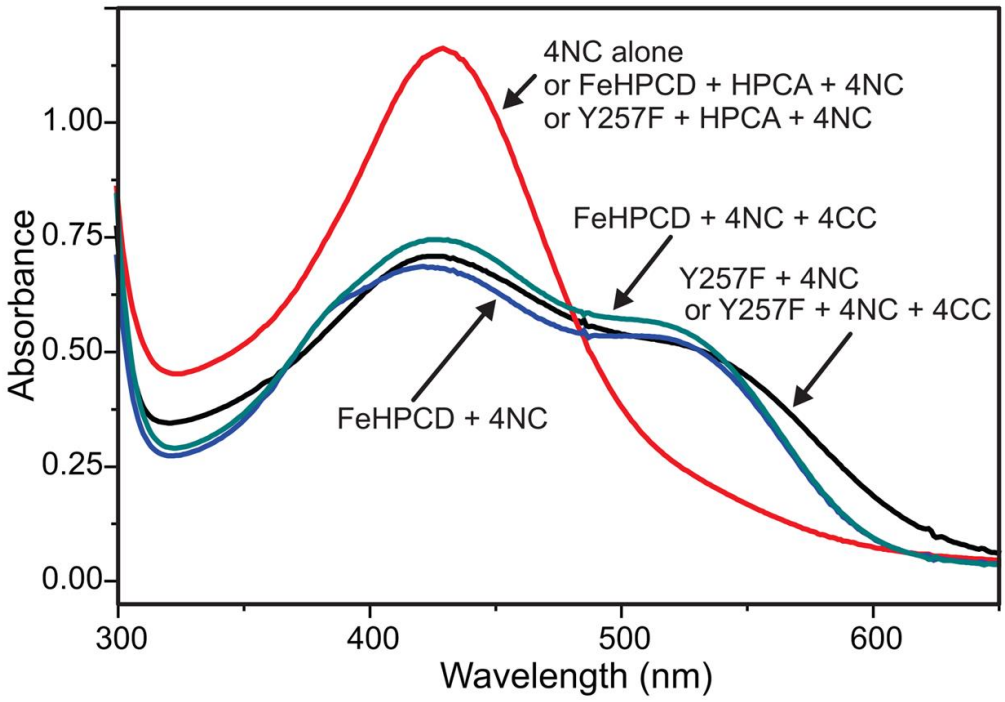

Figure 2. Estimation of K_d for HPCA binding to Y257F. The anaerobic substrate complexes were prepared in 200 mM MOPS buffer pH 7.5, 22 °C. 4CC is a weak-binding catechol, 4-chlorocatechol. Concentrations: Y257F and FeHPCA, 40 µM; HPCA, 4NC, and 4CC, 80 µM when present.

Single-Turnover Studies of the Y257F-HPCA + O_2 Reaction Reveal Two Reaction Intermediates. The diode-array stopped-flow spectra from an experiment wherein anaerobic, stoichiometric Y257F-HPCA complex reacts with a large excess O_2 at 4 °C at pH 7.5 or pH 5.5 are shown in Figures 3A and B, respectively. There is little change in the spectra in the first 30 ms at either pH value. Indeed, single wavelength data at 450 nm from pH 7.5 and pH 5.5 diode-array time courses clearly reveal a lag-phase during this period (Figure 3A and B insets). This suggests that there is at least one

colorless intermediate formed at the outset of the reaction before formation of a chromophoric species.

At slightly longer times, a transient species with a chromophore in the 400 - 470 nm range is observed. At pH 7.5, the chromophore begins to appear after 30 ms and maximizes at ~ 250 ms before it decays over the course of several seconds to yield the extradiol ring-cleaved product (λ_{max} = 380 nm). The spectrum of the transient species has an isosbestic point with that of the ring-cleaved product, so it may be the direct precursor of product formation in the reaction cycle. However, it is possible that other short-lived intermediates may intervene.

It was previously shown that λ_{max} for the ring-cleaved product shifts to shorter wavelength at low pH.[17] Accordingly, when the Y257F-HPCA + O_2 reaction is conducted at pH 5.5, λ_{max} for the ring-cleaved product shifts to 325 nm, revealing the chromophore associated with the new intermediate at 425 nm (Figure 3B). The pH 5.5 data shows that the new intermediate maximizes at ~ 700 ms, suggesting one or both rate constants for formation and decay of this species have changed at low pH. We will term the first and second new intermediates $Y257F_{Int1}^{HPCA}$ and $Y257F_{Int2}^{HPCA}$, respectively.

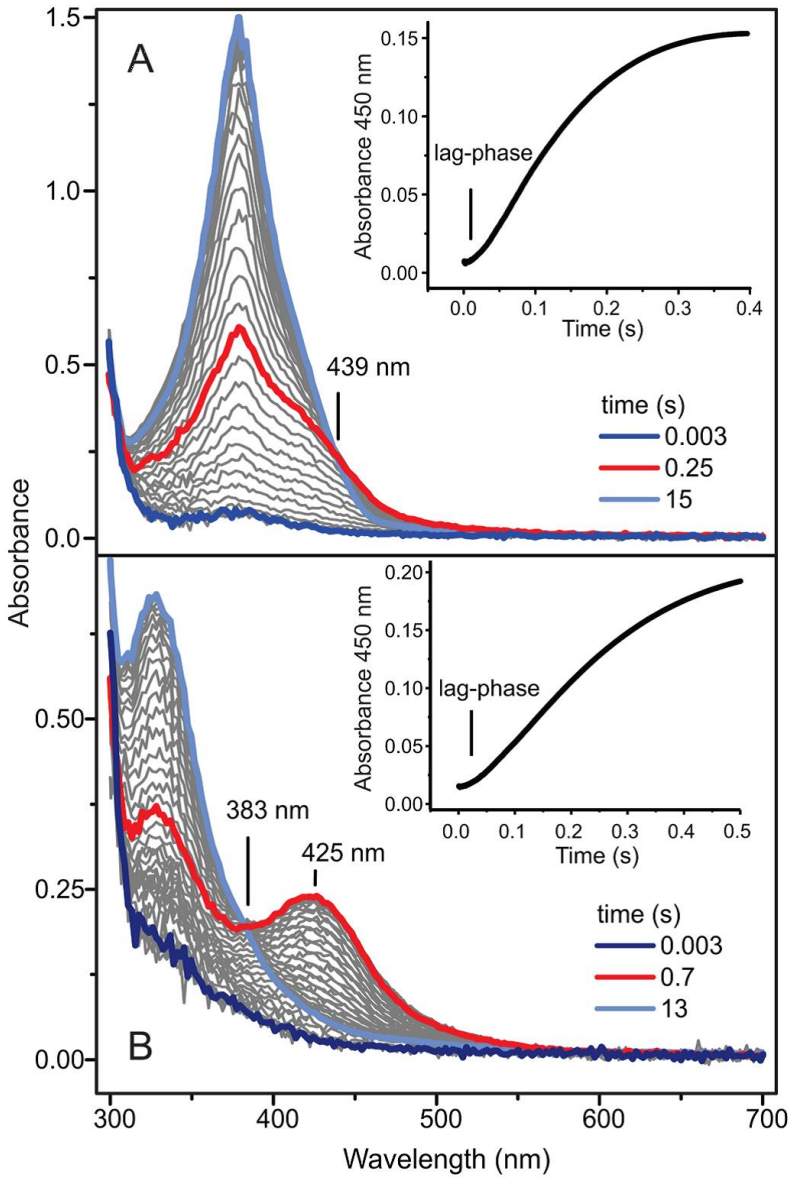

Figure 3. The Y257F-HPCA + O_2 reaction time-course followed using diode-array detection. Approximately 80 µM Y257F-HPCA complex was mixed with ~ 500 µM O_2 at 4 °C and pH 7.5 **(A)** and pH 5.5 **(B)** (1 cm pathlength). **Inset:** The reaction time-course monitored with single-wavelength detection at 450 nm.

Table 2. Reciprocal relaxation times and amplitudes obtained from fitting single wavelength data from the Y257F-HPCA + O_2 reaction at one O_2 concentration.[a]

Reciprocal relaxation time number	450 nm pH 5.5 s^{-1} (amp)	350 nm pH 5.5 s^{-1} (amp)	450 nm pH 7.5 s^{-1} (amp)	350 nm pH 7.5 s^{-1} (amp)
1	13 (0.09)	10 (-0.1)	21[b] (0.07)[c]	21 (0.017)
2	2.9 (-0.41)	2.9 (0.12)	5.5 (-0.40)	5.0 (0.18)
3	0.75 (0.30)	0.65 (-0.41)	1.8 (0.27)	2.2 (-0.91)
4	0.002 (-0.08)	0.002 (-0.08)	0.03 (-0.18)	0.03 (-0.25)

[a] Fitting to a 4 summed exponential equation by nonlinear regression using Pro Data viewer software available with Applied Photophysics SX series stopped-flow. 80 µM Y257F-HPCA complex was mixed with 500µM O_2 at 4 °C and pH 7.5, (1 cm pathlength, 2 mm slit width).
[b] The fitting error for all data in a single experimental run with at least 5 repeated trials is less than ± 3 %. For the experiment repeated using different enzyme batches over multiple days, the error is approximately ± 10%.
[c] The sign of an amplitude from exponential fitting is the opposite of the observed direction of change.

Rate Constants for the Formation and Decay of the Intermediates. Single-wavelength kinetic time courses were analyzed using regression methods to obtain reciprocal relaxation times ($1/\tau$ values) associated with the reaction. Figure 4 shows the single wavelength time course monitored under pseudo first order conditions at 450 nm or 350 nm for the first 15 s of the Y257F-HPCA + O_2 reaction at pH 7.5 or 5.5, 4 °C. Each of the time courses requires four summed exponential phases to achieve a satisfactory fit (summarized in Table 2). The slowest phase is not kinetically competent

and arises from a photochemical side reaction of the product bound to the enzyme as described in *Supporting Information* (Figure S2).

Observation of at least three competent phases in product formation at pH 5.5 and pH 7.5 shows that the Y257F-HPCA + O_2 single turnover reaction entails at least three distinct steps under both low and high pH conditions (Table 2). For a given pH, pairs of reciprocal relaxation times are similar at the two wavelengths monitored in all cases, suggesting that three phases are sufficient to describe the product formation time courses. The slower reciprocal relaxation times decrease with decreasing pH, albeit not proportionally, consistent with the slower formation and longer lifetime observed for the chromophoric intermediate $Y257F_{Int2}^{HPCA}$ at pH 5.5 (Figures 3A and B).

The reciprocal relaxation times for the reaction monitored at 425 nm are plotted vs the O_2 concentration in Figure 5. For the reaction at pH 5.5, it is seen that only $1/\tau_1$ is dependent on O_2 concentration and that the dependence is linear passing through zero (Figure 5A). The linear dependence suggests that $1/\tau_1$ is at least dominated by the rate constant for the O_2 binding step and the zero intercept suggests that this step is effectively irreversible. If the binding reaction occurs first in the reaction sequence and is irreversible, then $1/\tau_1 = k_1 = 4.0 \times 10^4 \pm 0.2\ M^{-1}\ s^{-1}$.

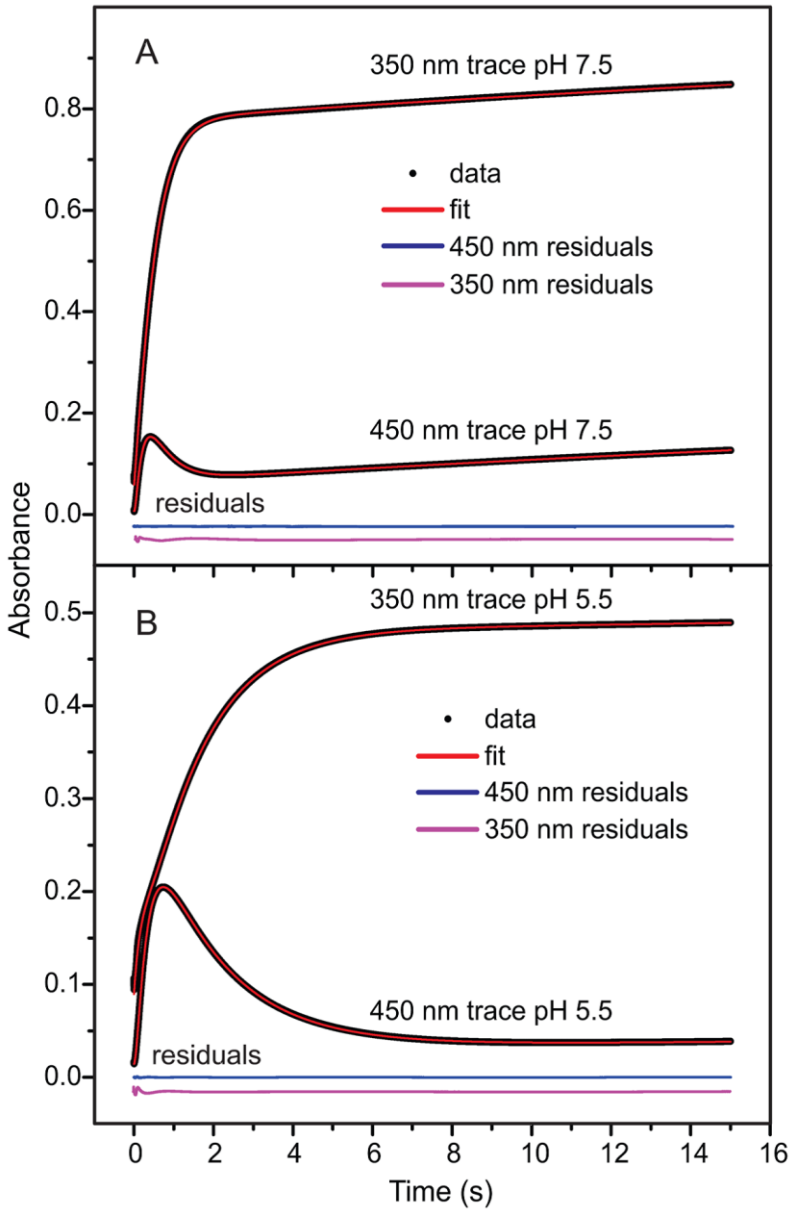

Figure 4. The Y257F-HPCA + O_2 reaction time course followed using single-wavelength detection at 450 nm and 350 nm. Approximately 80 µM Y257F-HPCA complex was mixed with ~ 500 µM O_2 at 4 °C and **(A)** pH 7.5 or **(B)** pH 5.5 (1 cm pathlength). The residuals from the fit are plotted on the same absorbance scale as the transient data but displaced for clarity.

At pH 7.5, the fastest reciprocal relaxation time is again linearly dependent on O_2 concentration, but the intercept of the plot is not zero (Figure 5D). This is the expected

result if the O_2 binding reaction occurs first and is reversible at this pH value. The forward and reverse rate constants are given by the slope and intercept of the plot respectively (k_1 = 2.7 x 10^4 ± 0.2 M^{-1} s^{-1}, k_{-1} = 11.0 ± 0.1 s^{-1}, $K_d^{O2} = k_{-1}/k_1 \approx$ 400 μM). The consequence of a fast reversible first step in the reaction is expected to be a hyperbolic plot for another of the $1/\tau$ vs O_2 plots, as observed in Figure 5E. The y-intercept of this plot is the reverse rate constant k_{-2} for the step following O_2 binding (zero in this case). The plot asymptotically approaches the sum of $k_2 + k_{-2}$, while the K_{app} for the plot is the K_d for the O_2 binding reaction (non-linear fitting gives k_2 = 15.0 ± 0.6 s^{-1} and K_d^{O2} = 500 ± 40 μM). The irreversible nature of this step would uncouple the third reciprocal relaxation time from the others, so it would be expected to be independent of O_2 concentration and equal to the sum of the forward and reverse rate constants for the third step in the reaction, as observed ($k_3 + k_{-3}$ = 2 ± 0.1 s^{-1}) (Figure 5F). The amplitude for this uncoupled third phase monitored at 350 nm is much larger than those of the others, suggesting that the third step in the reaction is ring-cleavage. If this is the case, then the reaction is irreversible and $k_{-3} = 0$. The irreversible steps following O_2 association are presumably the explanation for the low observed K_m value for O_2 (Table 1) despite that rather high K_d^{O2} value for complex formation.

Returning to the pH 5.5 data, the occurrence of an initial irreversible O_2 binding step would uncouple $1/\tau_2$ and $1/\tau_3$ from O_2 concentration dependence, as observed in Figures 5 B and C). This does not indicate *a priori* that $1/\tau_2$ and $1/\tau_3$ are uncoupled from

each other, and they may not be if the second reaction step is reversible. However, our previous studies of intermediates in extradiol dioxygenase cycles have shown that the steps in their formation are generally well described as irreversible; attack of an activated oxygen intermediate on substrate to form a covalent alkylperoxo species or subsequent breaking of the O-O bond are unlikely to be reversible processes.[8,12] Thus, it is likely that $1/\tau_2$ and $1/\tau_3$ are equal to rate constants of unique steps. This analysis does not indicate which rate constant is associated with which step, although it is likely that the order established by the pH 7.5 data is maintained ($k_2 = 2.6 \pm 0.2\ s^{-1}$ and $k_3 = 0.70 \pm 0.06\ s^{-1}$). The assignment can be directly probed by analysis of the extinction coefficient of the chromophoric intermediate (see *Discussion*) or by directly trapping the intermediate for quantification using a technique such as Mössbauer spectroscopy, as described below.

Rate-Limiting Step. The rate constants for the reaction cycle steps that can be directly observed are all significantly greater than the k_{cat} value at both pH 7.5 and 5.5. These steps apparently encompass O_2 binding through formation of the product. Consequently, the rate-limiting step must be either product release or a step in the substrate binding sequence or both.

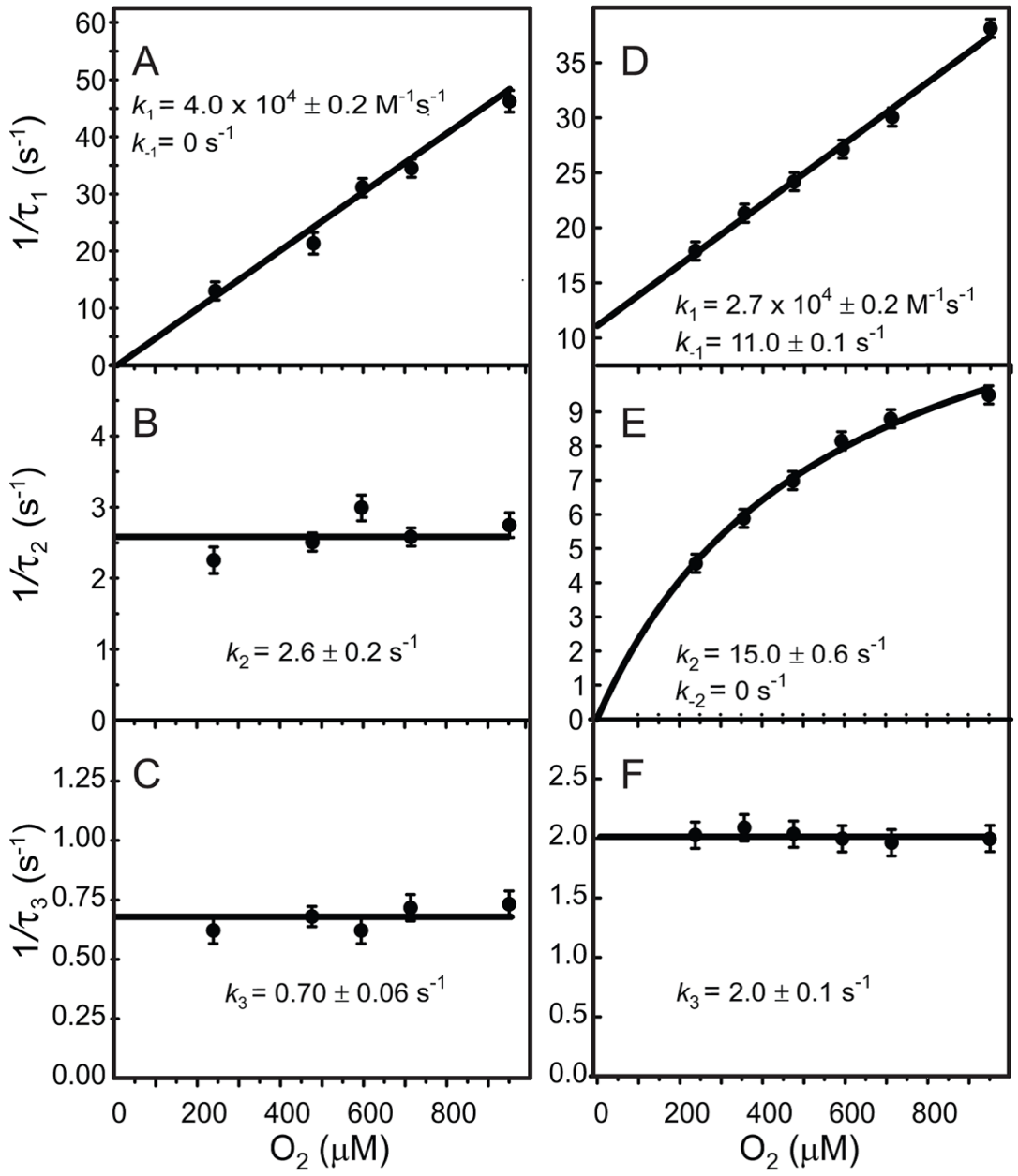

Figure 5. O_2 dependence of the three kinetically competent reciprocal relaxation times from the Y257F-HPCA + O_2 reaction. The data were collected using single wavelength detection at 425 nm following the reaction of ~ 60 - 80 μM Y257F-HPCA complex with varying amounts of O_2 at 4 °C and pH 5.5 (left) or pH 7.5 (right).

Mössbauer Study of the Anaerobic Y257F-HPCA Complex. The anaerobic Y257F-HPCA complex ($Y257F_{ES}^{HPCA}$) exhibits well-resolved Mössbauer spectra in strong applied magnetic fields, B, a rather rare occurrence for the type of ligand environments afforded by ferrous sites with a 2-His-1-carboxylate facial triad ligand motif. Therefore, it is useful to extract zero field splitting (ZFS), magnetic hyperfine (^{57}Fe *A*-tensor) and electric field gradient (EFG) parameters from the data. Figures 6 and 7 show variable field, variable temperature Mössbauer spectra of $Y257F_{ES}^{HPCA}$. The zero field spectrum of Figure 6A exhibits a doublet with quadrupole splitting ΔE_Q = 3.19 mm/s and isomer shift δ = 1.12 mm/s, parameters typical of high-spin Fe^{II}. $Y257F_{ES}^{HPCA}$ exhibits a single doublet, in contrast to the HPCA complexes formed with H200N and FeHPCD,[17] which exhibited, for reasons not yet understood, two species. The variable field spectra of $Y257F_{ES}^{HPCA}$ observed at 4.2 K reflect an S = 2 spin system for which the two lowest levels form a quasi-doublet with expectation values of the electronic spin, <**S**>, that are large in one particular direction (here z) and small in directions perpendicular to z. <**S**>, together with the ^{57}Fe magnetic hyperfine tensor, **A**, determines the internal magnetic field at the nucleus, $\mathbf{B}_{int} = -\langle\mathbf{S}\rangle \bullet \mathbf{A}/g_n\beta_n$, which in turn determines the observed magnetic splitting.

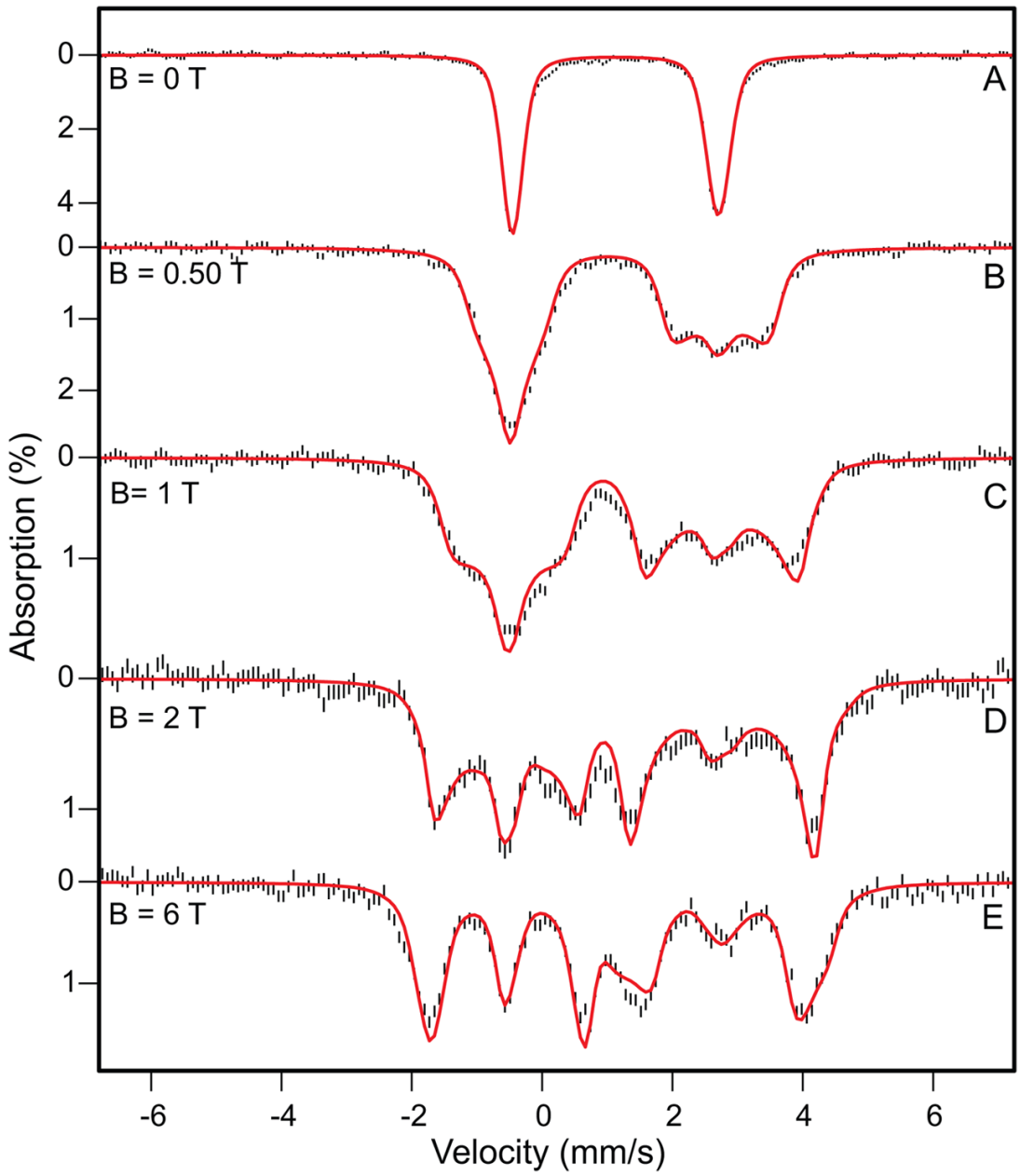

Figure 6. 4.2 K Mössbauer spectra of Y257F$_{ES}^{HPCA}$ recorded in parallel-applied magnetic fields as indicated. The red curves are spectral simulations, in the slow relaxation limit of the electronic spin, based on the S = 2 Hamiltonian of eq 1 using the parameters listed in Table 3.

Table 3. $S = 2$ Spin Hamiltonian parameters of Y257F-HPCA evaluated using eq 1.

D (cm^{-1}) = -11.2 cm^{-1}	$A_x/g_g\beta_n$ = -22 T	ΔE_Q = +3.19 mm/s
E/D = 0.32	$A_y/g_g\beta_n$ ~ -29 T	η = 0.20
g_x = 2.00[a]	$A_z/g_g\beta_n$ = -6.3 T	$(\alpha\beta\gamma)_{EFG}$[b] = (160, 27, 0)°
g_y = 2.00		$(\alpha\beta\gamma)_A$[b] = (98, 6.5,76)°
g_z = 2.00	δ = 1.12 mm/s	

[a]g-values were fixed to $g = 2.00$. [b]$(\alpha\beta\gamma)_{EFG}$ and $(\alpha\beta\gamma)_A$ are the Euler angles that rotate the EFG- and A- tensor into (x,y,z). The simulations are more sensitive to β than to α and γ.

We have analyzed the spectra of Figures 6 and 7 in the framework of the commonly used $S = 2$ spin Hamiltonian:

$$\mathcal{H} = D\left[S_z^2 - 2 + \left(\frac{E}{D}\right)\left(S_x^2 - S_y^2\right)\right] + \beta\vec{S}\cdot\hat{g}\cdot\vec{B} + \vec{S}\cdot\hat{A}\cdot\vec{I}$$
$$-g_n\beta_n\vec{B}\cdot\vec{I} + \frac{eQV_{z'z'}}{12}\left[3I_{z'}^2 - \frac{15}{4} + \eta\left(I_{x'}^2 - I_{y'}^2\right)\right] \quad \textbf{(1)}$$

The traceless ZFS tensor (parameters D and E) defines the main molecular frame, (x, y, z). The quadrupole interaction (the last term in eq 1) is written in its conventional form in the frame (x', y', z'). The method of analyzing the spectra follows that described by Zimmermann et al. for protocatechuate 3,4 dioxygenase. [22] Our major conclusions are summarized in the following. The ZFS tensor of Y257F-HPCA is nearly rhombic, E/D = 0.32. For perfect rhombicity, namely E/D = 1/3, the three t_{2g}-derived orbital states would be equally spaced with respect to each other (provided they have the same covalency).[23] The two lowest spin levels of $Y257F_{ES}^{HPCA}$ have $M_S = \pm 2$ heritage (i.e., they would have the exact $M_S = \pm 2$ label in the limit $E/D = 0$). In moderate applied fields, the induced magnetic hyperfine interactions of the spectra of Figures 6B–D depend on the

splitting Δ of the "$M_S = \pm 2$" doublet and not on D and E/D separately; where Δ is given by: [22]

$$\Delta = 2D\,[(1 + 3(E/D)^2)^{1/2} - 1] \qquad \textbf{(2)}$$

Analysis of the spectra in Figures 6B–D showed that $Y257F_{ES}^{HPCA}$ has $\Delta \cong 3.2$ cm^{-1}. This Δ value is much too large for observation of integer spin EPR signals at either X- or Q- band ($h\upsilon = 0.3$ cm^{-1} at X-band). Further analysis revealed that the EFG tensor of $Y257F_{ES}^{HPCA}$ is quite axial ($\eta = (V_{x'x'} - V_{y'y'})/V_{z'z'} = 0.20$), that its largest component, $V_{z'z'}$, is positive (hence $\Delta E_Q > 0$), and that z' makes an angle $\beta_{EFG} \approx 27°$ relative to z. The stated properties are readily extracted from the spectra of Figures 6B–D. The high-energy (right) features of the spectra of Figures 6B and C depend on g_zA_z. However, the right hand features of Figure 6D depend only on A_z (for the quoted value of Δ the expectation value $\langle S_z \rangle$ saturates at $\langle S_z \rangle = -2$ independent of g_z), which allowed us to determine $A_z/g_n\beta_n = -6.3$ T. Above 20 K the electronic spin system is in the fast relaxation regime. The 25 K spectrum shown in Figure 7A is reasonably sensitive to D but depends only weakly on E/D. This behavior allowed for fitting of the 25 K spectrum to obtain $D = -11.2$ cm^{-1} which, using the expression for Δ, yielded $E/D = 0.32$.

The simulations shown in Figures 6 and 7 represent the data very well. The spin Hamiltonian parameters of Table 3 will be a useful spectroscopic benchmark for density functional calculations based on the X-ray structure of $Y257F_{ES}^{HPCA}$ (see accompanying report). The solution presented in Table 3 is not unique. We have made many attempts to

fit the spectra and have found that all reasonable solutions share the following features: D is confined to (9–11) cm^{-1} and, roughly, $0.31 < E/D < 0.36$. β_{EFG} may vary between 20 and 35°, and β_A is between 3 and 10° ($\beta_A = 0$ did not produce good fits). The observation that the EFG and *A*-tensors have different principal axis systems suggests that the *A*-tensor has substantial orbital contributions; as the latter are proportional to $(g_i - 2)$, it follows that the *g*-values cannot be 2.00, as we have arbitrarily assumed. The orbital contributions to **A** are expected to be diagonal in (x, y, z), whereas the spin-dipolar contribution to **A** is expected to be diagonal in (x', y', z'), the principal axis system of the EFG tensor. The combination of the orbital and spin dipolar parts determines the principal axis frame of the *A*-tensor. The software package WMOSS allows group fits to *theoretical* spectra. Thus, if quantum chemical calculations suggest different solutions, researchers can use the solution given here to explore whether particular parameter sets are compatible with the data.

Density functional calculations, combined with a ligand field approach, will relate the spin Hamiltonian parameters to molecular coordinates and delineate the orbitals available for interaction with O_2; such studies are in progress. While these calculations are beyond the scope of the present work, the spectra collected here are useful in judging the Mössbauer spectra of $Y257F_{Int1}^{HPCA}$ and $Y257F_{Int2}^{HPCA}$, presented next.

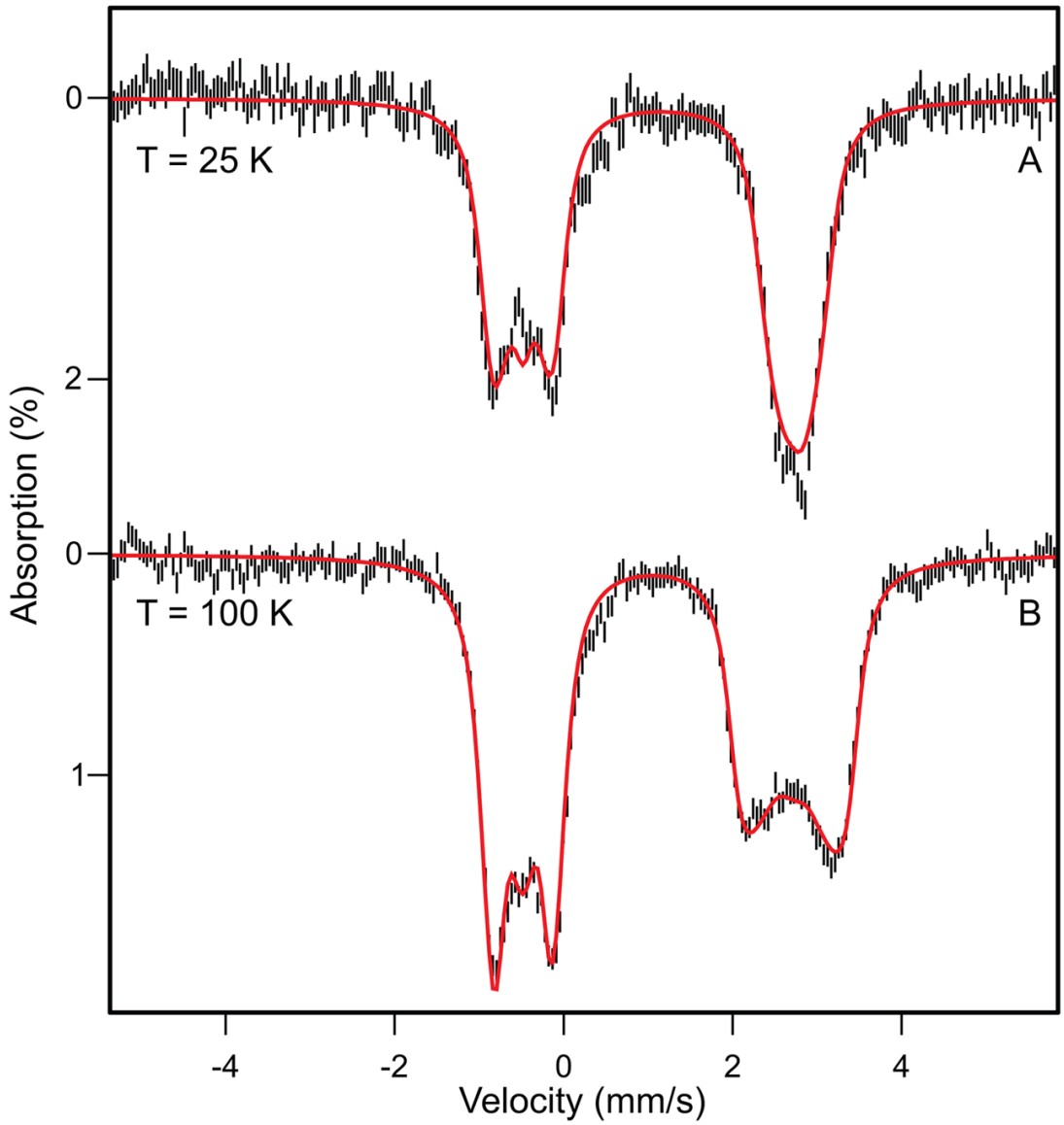

Figure 7. 6.0 T Mössbauer spectra of Y257F_{ES}^{HPCA} recorded at the temperatures indicated on the left side of the figure. The red curves are spectral simulations, performed in the fast relaxation limit of the electronic spin, using the parameters of Table 3.

Mössbauer Spectra of Y257F$_{Int1}^{HPCA}$ and Y257F$_{Int2}^{HPCA}$. Figure 8 shows 4.2 K Mössbauer spectra recorded for B = 0 of Y257F$_{Int1}^{HPCA}$ and Y257F$_{Int2}^{HPCA}$ formed at pH 6.0. The sample for Y257F$_{Int1}^{HPCA}$ was rapidly quenched 100 ms after mixing with O_2. The kinetic data suggests that this sample should contain 60% Y257F$_{Int1}^{HPCA}$, 20% Y257F$_{Int2}^{HPCA}$ and 20% Y257F$_{ES}^{HPCA}$ (see *Discussion*). The sample for Y257F$_{Int2}^{HPCA}$ was quenched at 500 ms and, according to the kinetic data, should contain 60% Y257F$_{Int2}^{HPCA}$, 20% Y257F$_{Int1}^{HPCA}$ and 20% Y257F-product (Y257F$_{Prod}^{HPCA}$). Neither sample exhibited an EPR spectrum in either perpendicular or parallel mode. It can be seen that the spectra of the two samples are essentially the same and, moreover, the spectra are close to those seen for the Y257F$_{ES}^{HPCA}$ and Y257F$_{Prod}^{HPCA}$; zero field spectra for Y257F$_{ES}^{HPCA}$ and Y257F$_{Prod}^{HPCA}$, Y257F$_{Int1}^{HPCA}$ and Y257F$_{Int2}^{HPCA}$ are shown in Figure S3. Clearly, the iron sites of Y257F$_{Int1}^{HPCA}$ and Y257F$_{Int2}^{HPCA}$ are high-spin ferrous, in stark contrast to the Fe^{III} – radical intermediates observed for the early oxy-intermediates of the H200N variant.[16,17] In order to get the best possible ΔE_Q and δ values for Y257F$_{Int1}^{HPCA}$ and Y257F$_{Int2}^{HPCA}$ the contributions of Y257F$_{ES}^{HPCA}$ and Y257F$_{Prod}^{HPCA}$ were subtracted from the spectra and then the remaining spectra were combined such that the contribution of either Y257F$_{Int1}^{HPCA}$ or Y257F$_{Int2}^{HPCA}$ canceled. In this way, we found ΔE_Q = 3.02(3) mm/s and δ =1.15(2) mm/s for Y257F$_{Int1}^{HPCA}$ and ΔE_Q = 3.08(3) mm/s and δ =1.18(2) mm/s for Y257F$_{Int2}^{HPCA}$.

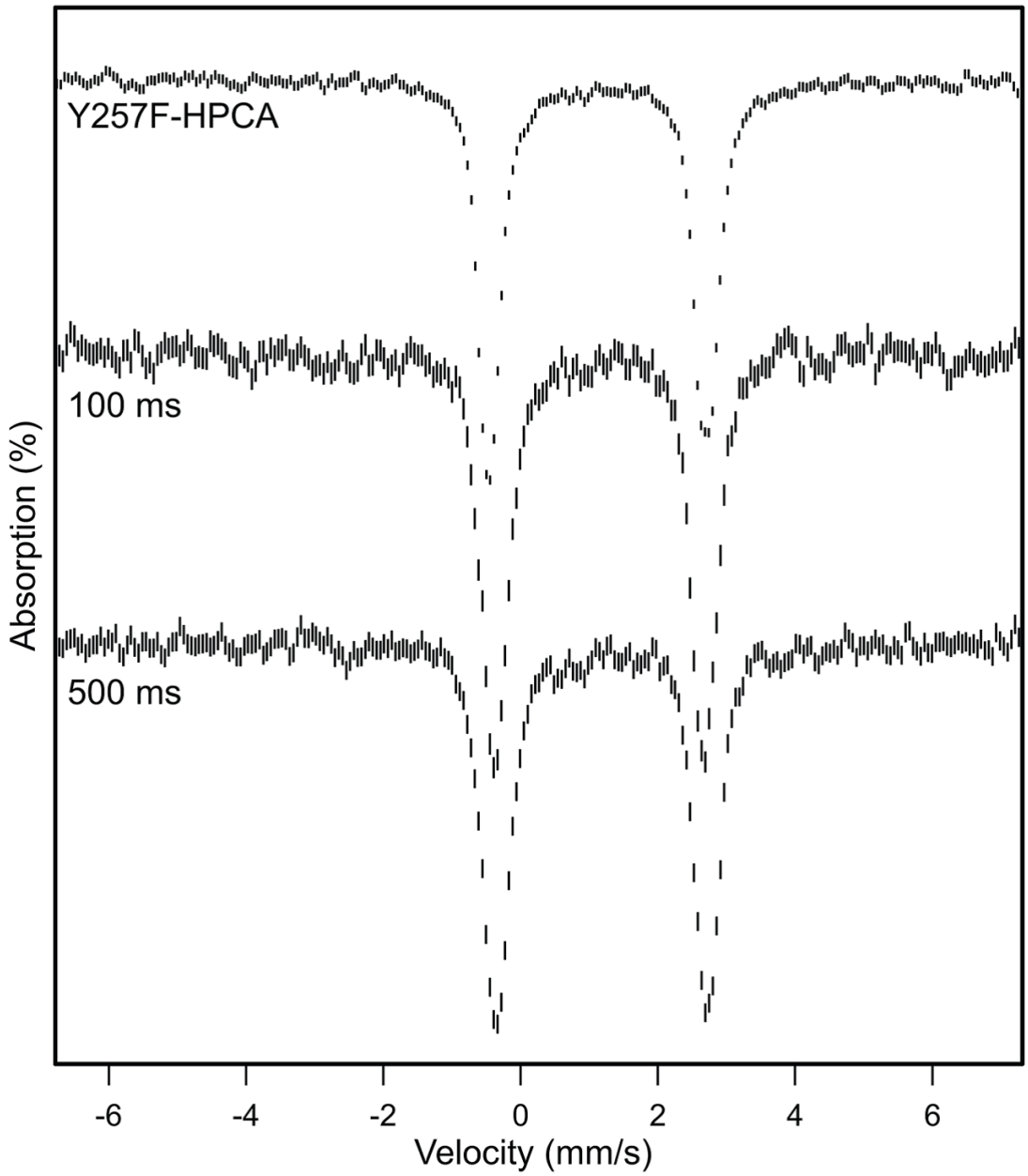

Figure 8. Zero field 4.2 K Mössbauer spectra of $Y257F_{ES}^{HPCA}$, $Y257F_{Int1}^{HPCA}$ (100 ms sample) and $Y257F_{Int2}^{HPCA}$ (500 ms sample). Quadrupole splittings and isomer shifts are ΔE_Q = 3.02(3) mm/s and δ =1.15(2) mm/s for $Y257F_{Int1}^{HPCA}$ and ΔE_Q = 3.08(3) mm/s and δ =1.18(2) mm/s for $Y257F_{Int2}^{HPCA}$ (see text).

Figure 9 shows 2.0 T spectra of $Y257F_{Int1}^{HPCA}$ (black hash marks) and $Y257F_{Int2}^{HPCA}$ (blue) samples recorded at 4.2 K. For comparison, we show the theoretical curve (red) of the $Y257F_{ES}^{HPCA}$ complex. It can be seen that the 2T spectra of $Y257F_{Int1}^{HPCA}$ and

$Y257F_{Int2}^{HPCA}$ are indistinguishable within the noise, and that both differ from the spectrum of $Y257F_{ES}^{HPCA}$. Subtraction of the spectrum represented by the red curve from the 2T spectrum of $Y257F_{Int1}^{HPCA}$ showed that the 100 ms sample could have no more than 15% contribution to the total iron from $Y257F_{ES}^{HPCA}$. Likewise, subtraction of the zero field spectrum of $Y257F_{Prod}^{HPCA}$ from the corresponding spectrum of the 500 ms sample showed the end complex can account for no more than 20% of total iron in the 500 ms sample.

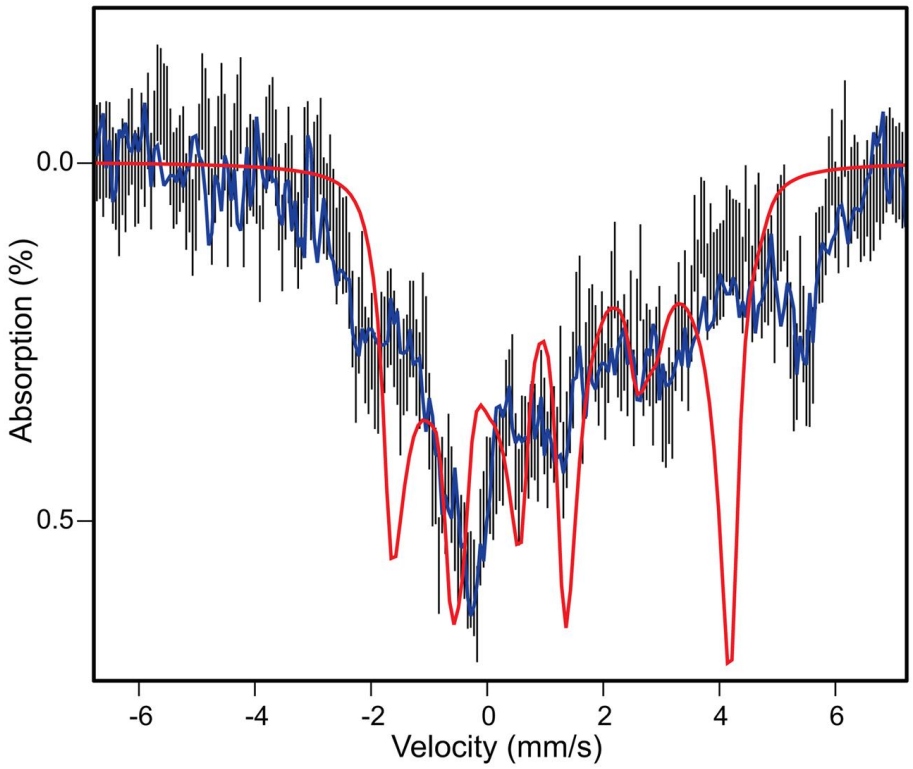

Figure 9. 2.0 T Mössbauer spectra of $Y257F_{Int1}^{HPCA}$ (black hashed) and $Y257F_{Int2}^{HPCA}$ (blue) recorded at 4.2 K. For comparison is shown the spectral simulation for the enzyme substrate complex, Y257F-HPCA (red, same curve as in Figure 6D).

The reader may wonder why the ΔE_Q values of Y257F, $Y257F_{ES}^{HPCA}$, $Y257F_{Int1}^{HPCA}$ $Y257F_{Int2}^{HPCA}$ and $Y257F_{Prod}^{HPCA}$ are the same within 6%. The present complexes have a distorted octahedral symmetry for which the three lowest states are combinations of mainly d_{xy}, d_{yz}, and d_{xz} orbitals. It has been shown that any linear combination of these three orbitals (the $^5T_2$ approximation) yields the same ΔE_Q at 4.2 K as long as there are no major changes in covalency.[24] As the states observed here present us with various FeO_5N coordinations, the small variability in ΔE_Q is not surprising.

Discussion

The results described here show that Tyr257 plays an important role in efficient catalysis at several points in the catalytic cycle of FeHPCD. Structural studies indicate that it has two different types of interactions with the substrate.[2,3,6] First, there is a van der Waals interaction between the Tyr-OH and the C2 carbon of the substrate forcing a slight global deformation to the aromatic ring. Second, the Tyr-OH forms a hydrogen bond to the deprotonated substrate C2-O^- in both the anaerobic enzyme substrate complex and the $FeHPCD^{4NC}_{Int1}$ intermediate (Figure 1). The second interaction causes a substantial localized distortion in the normally planar ring. This work complements earlier studies in which the roles of His200 and the nature of its interaction with the second iron-bound substrate, O_2, were examined.[12,16,17,25] These studies support the hypothesis that the two substrates are connected electronically through the iron and that the transfer of electron density from the catecholic substrate to O_2 is the basis for oxygen activation in this system. The current studies show that the second sphere residues of the iron, specifically His200 and Tyr257, must also work in concert to make the O_2 activation process efficient and specific. Newly recognized aspects of this complex collaboration for catalysis are discussed here.

Kinetic Model for Catalysis. The rate constants assigned for the single turnover reactions at pH 7.5 and 5.5 are shown in Scheme 2A and B, respectively. Figure 10 shows a numerical integration simulation of the single turnover reaction of Y257F-

HPCA + O_2 at pH 5.5 for the model shown in Scheme 2B. The simulation predicts that $Y257F_{Int1}^{HPCA}$ will accumulate to ~ 64% at 90 ms, and $Y257F_{Int2}^{HPCA}$ will build to ~ 63% at 700 ms. The simulation for the reaction at pH 7.5 predicts an accumulation of $Y257F_{Int1}^{HPCA}$ of ~ 30% at 50 ms while that of $Y257F_{Int2}^{HPCA}$ is computed to be ~ 55% at 250 ms (simulation not shown). These values together with the known total enzyme concentration can be used to predict the extinction coefficient of $Y257F_{Int2}^{HPCA}$ of ε_{425} =10,500 M^{-1} cm^{-1} at each pH value. The values predicted by Model B at pH 5.5 for the intermediate concentrations are similar to those observed in RFQ/Mössbauer samples from a reaction time course at pH 6.0 (Figure 8), supporting the order for the rate constants associated with the second and third steps shown in Scheme 2 (enzyme precipitation at high concentration prevented making pH 5.5 Mössbauer samples).

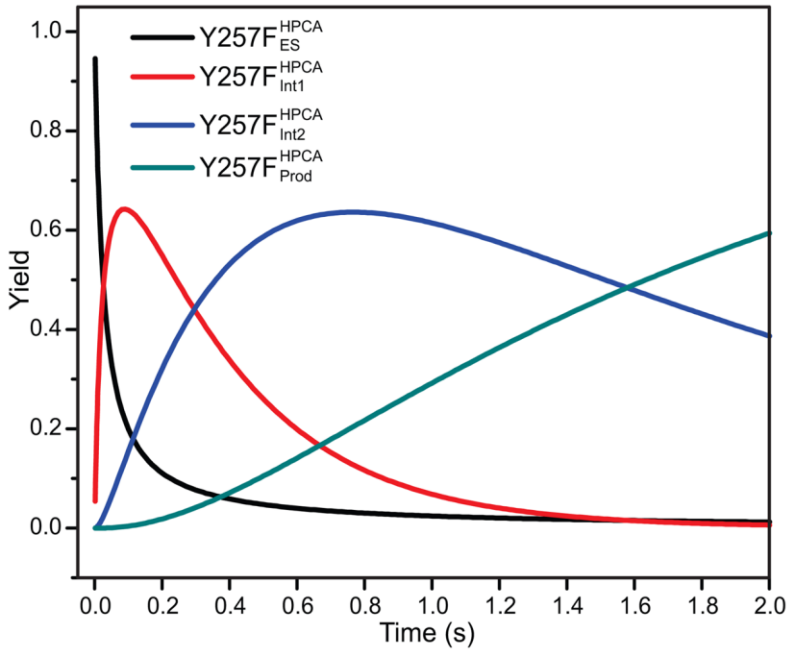

Figure 10. Simulation of expected time-dependent relative yields for reaction intermediates from the Y257F-HPCA + O_2 reaction at pH 5.5 for the model shown in Scheme 2B.

Model A - pH 7.5

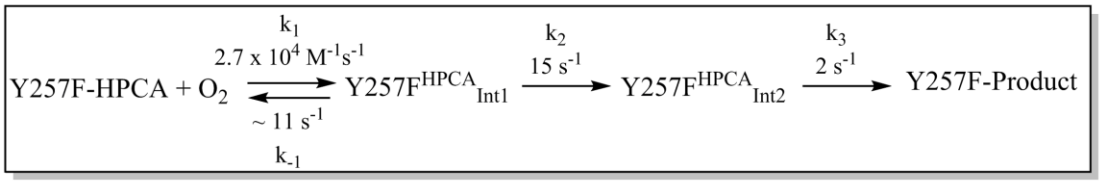

Model B - pH 5.5

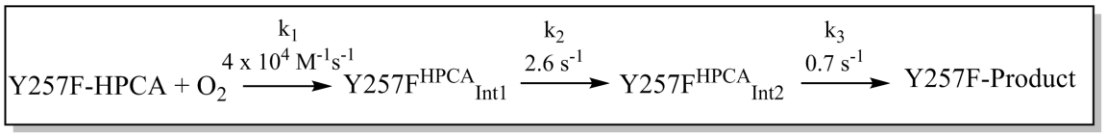

Scheme 2. Kinetic models for species occurring in the Y257F-HPCA + O_2 single-turnover reaction. Rate constant are as determined from kinetic analysis of the Y257F-HPCA + O_2 reaction at pH 7.5 (Model A) and pH 5.5 (Model B).

Chemical Nature of $Y257F^{HPCA}_{Int1}$. $Y257F^{HPCA}_{Int1}$ forms in a second-order reaction between Y257F-HPCA and O_2, so it is an oxygen complex of some sort. However, it differs from each of the oxygen complexes found thus far for FeHPCD and its variants as summarized in Table 4. For example, $Y257F^{HPCA}_{Int1}$ closely resembles $FeHPCD^{HPCA}_{Int1}$ in most of its characteristics, but these intermediates are clearly quite different because only $Y257F^{HPCA}_{Int1}$ exhibits an O_2 concentration dependence for its formation rate constant. Consequently, $Y257F^{HPCA}_{Int1}$ must represent a species occurring as O_2 binds, while we have proposed that $FeHPCD^{HPCA}_{Int1}$ is a species occurring after irreversible oxygen attack on the substrate.[17] $Y257F^{HPCA}_{Int1}$ could, in principle, be the $SQ^{\bullet}$-Fe^{II}-$O_2^{\bullet-}$ species postulated to be the reactive oxygen-activated species and observed *in cystallo* when a crystal of FeHPCD-4NC is exposed to O_2.[6] However, it is illustrated below that the electronic transitions which give rise to the $SQ^{\bullet}$ chromophore are easily detected and not greatly

perturbed when the $SQ^{\bullet}$ ligand is exchange coupled to a high-spin Fe^{III}-(H)peroxo site. This is likely to also be the case for a $SQ^{\bullet}$ ligand bound to an Fe^{II}-$O_2^{\bullet-}$ site, but there is no precedent in solution for this state to the best of our knowledge. Consequently, the lack of a strong chromophore from $Y257F_{Int1}^{HPCA}$ suggests that this intermediate does not contain a semiquinone or quinone form of the substrate. Since Mössbauer data show that $Y257F_{Int1}^{HPCA}$ contains only Fe^{II}, the lack of a bound $SQ^{\bullet}$ or quinone suggests that the bound oxygen must remain close to the O_2 oxidation state. This would not be expected to be a strong bond, which is in accord with the weak affinity observed here for the complex at pH 7.5 (see below for a discussion of the complex at pH 5.5). It is also possible that O_2 is bound in the active site, but not to the iron (In this case, however, there must be some adjustment in the iron coordination as the Mössbauer spectra of $Y257F_{Int1}^{HPCA}$ differ from those of Y257F-HPCA as shown in Figure 9). This type of complex appears to be an intermediate in the O_2 binding process in FeHPCD and other dioxygenases based on previous transient kinetic studies.[8,26,27] We propose that $Y257F_{Int1}^{HPCA}$ is most likely an HPCA-Fe^{II}-O_2 complex with minor electron transfer or spin delocalization to the oxygen. The relevance of this conclusion to the role of Tyr257 is discussed below.

Chemical Nature of $Y257F_{Int2}^{HPCA}$. In contrast to $Y257F_{Int1}^{HPCA}$, $Y257F_{Int2}^{HPCA}$ exhibits a relatively intense chromophore at 425 nm and possibly a weak feature near 325 nm. The λ_{max} and intensity of this chromophore is consistent with the spectra observed in the UV-vis region from unbound quinones or semiquinones, albeit with a slightly larger

extinction coefficient.[17] In the absence of FeHPCD, incubation of HPCA with a high potential quinone results in an unbound HPCA-SQ$^{\bullet}$ exhibiting a very similar long wavelength spectrum to that observed for H200N$^{HPCA}_{Int1}$ (Figure 11, λ_{max} near 610 for H200N$^{HPCA}_{Int1}$ and 645 nm for HPCA-SQ$^{\bullet}$),[17] suggesting that the electronic transitions which give rise to the SQ$^{\bullet}$ chromophore are retained when the SQ$^{\bullet}$ ligand is exchange coupled to a high-spin Fe^{III}-(H)peroxo site. This is likely to also be true for a SQ$^{\bullet}$-Fe^{II}-$O_2^{\bullet-}$ site, since the origin of the semiquinone chromophore is not charge transfer to the iron.

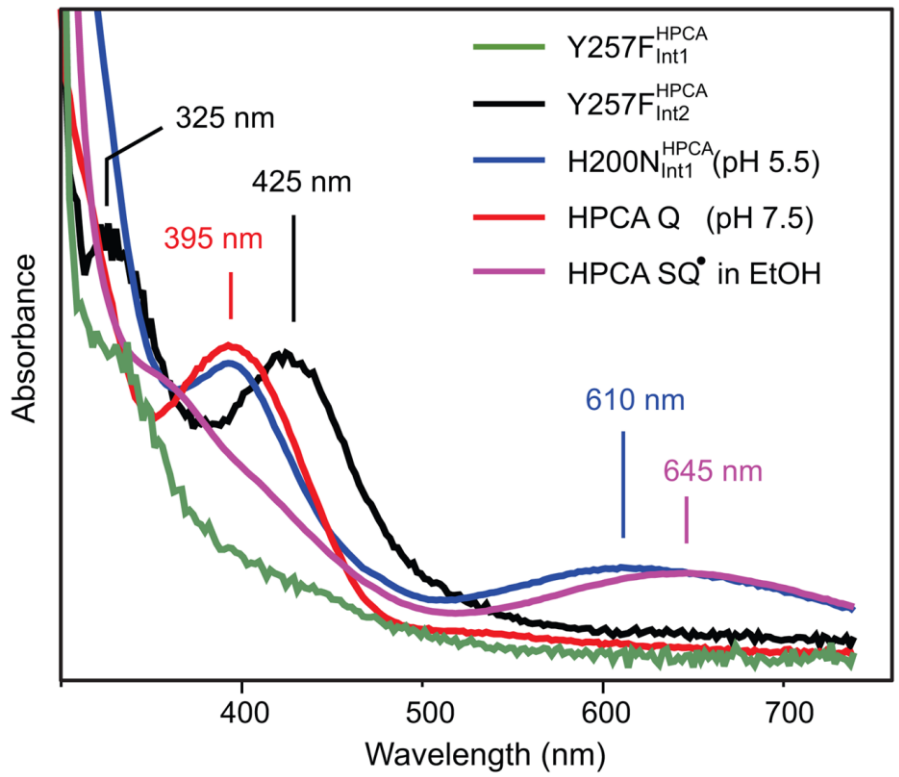

Figure 11. Comparison of UV-vis spectra of unbound HPCA quinone and HPCA semiquinone to those of Y257F$^{HPCA}_{Int1}$, Y257F$^{HPCA}_{Int2}$ and H200N$^{HPCA}_{Int1}$. The spectra of Y257F$^{HPCA}_{Int1}$ and Y257F$^{HPCA}_{Int2}$ are derived from the time course of Figure 3. HPCA quinone and HPCA semiquinone were synthesized as described in *Experimental Procedures*. The spectra are scaled arbitrarily to facilitate comparison of UV-vis features.

Table 4. Intermediates Formed by FeHPCD and Its Variants with HPCA and Alternative Substrates.

Intermediate[a]	**Fe ox state (Mössbauer)**	**Optical spectrum ε M^{-1} cm^{-1}**	**EPR spectrum**	**Reversible O_2 binding**	**Assignment**	**Ref**
$FeHPCD_{Int1}^{HPCA}$	Fe^{II}	No	No	No	Fe^{II}-alkylperoxo	17
$H200N_{Int1}^{HPCA}$	Fe^{III} Spin-coupled	Yes HPCA-SQ $\varepsilon_{395} \cong 3200$ $\varepsilon_{610} \cong 1100$	Yes $S = 2$ ES[b]	No	HPCA SQ-Fe^{III}-(H)peroxo	17
$H200N_{Int2}^{HPCA}$	Fe^{II}	No	No	No	Fe^{II}-alkylperoxo	17
$H200N_{Int1}^{4NC}$	Fe^{III} Spin-coupled	Yes 4NC $\varepsilon_{506} \cong 10{,}000$ $\varepsilon_{630} \cong 1{,}200$	Yes $S = 2$ GS[b]	Yes	4NC-Fe^{III}-$O_2^{\bullet-}$	16
$H200N_{Int2}^{4NC}$	Fe^{III} Spin-coupled	Yes 4NC-SQ $\varepsilon_{405} \cong 15{,}000$ $\varepsilon_{675} \cong 1{,}000$	Yes $S = 2$ ES	N/A[b]	4NC SQ-Fe^{III}-(H)peroxo	16
$Y257F_{Int1}^{HPCA}$	Fe^{II}	No	No	Yes	HPCA-Fe^{II}-O_2	This work
$Y257F_{Int2}^{HPCA}$	Fe^{II}	Yes $\varepsilon_{425} \cong 10{,}500$	No	N/A[b]	HPCA Q-Fe^{II}-(H)peroxo	This work

[a] $FeHPCD_{Int1}^{HPCA}$, first intermediate observed after mixing FeHPCD-HPCA with O_2; $H200N_{Int1}^{HPCA}$ and $H200N_{Int2}^{HPCA}$, first and second intermediates observed after mixing H200N-HPCA with O_2; $H200N_{Int1}^{4NC}$ and $H200N_{Int2}^{4NC}$ first and second intermediates observed after mixing H200N-4NC with O_2

[b] Abbreviations: ES = Excited state; GS = Ground state; N/A = not applicable

The UV-vis spectrum of $Y257F_{Int2}^{HPCA}$ is missing the low energy UV-vis feature associated with the HPCA-$SQ^{\bullet}$, but it does have a feature similar to that observed for the unbound HPCA-Q (Figure 11, λ_{max} near 425 nm for $Y257F_{Int2}^{HPCA}$ and 395 nm for unbound HPCA-Q). Based on this spectrum, $Y257F_{Int2}^{HPCA}$ is unlikely to contain a HPCA $SQ^{\bullet}$. Mössbauer spectra from a sample expected to contain > 60% $Y257F_{Int2}^{HPCA}$ shows that only Fe^{II} species are present. The absence of Fe^{III} species, the lack of a low-energy band, and the presence of an intense feature near 425 nm suggest that $Y257F_{Int2}^{HPCA}$ is most likely a HPCA-Q-Fe^{II}-(H)peroxo complex.

Origin of Rate Constant Decreases in Reaction Cycle Steps – Mechanistic Significance. The rate constants for intermediate conversion in the catalytic cycle are affected in similar ways by the Y257F mutation as by the use of 4NC as the substrate. We have proposed that 4NC slows the reaction because the electron withdrawing nitro substituent makes electron transfer through the Fe^{II} to the O_2 less favorable.[8,11,12] This is dramatically observed in the H200N-4NC reaction with O_2 where the 4NC-Fe^{III}-$O_2^{\bullet-}$ species persists for hundreds of seconds without attacking the 4NC.[16] In the case of HPCA, the electron donating inductive effects of the para substituent will make it much more favorable to donate an electron through the iron to the O_2, leading to rapid, nearly irreversible binding. The effect of this putative electron transfer will be to give the substrate semiquinone character that would facilitate subsequent attack by the superoxo species formed in the process. However, a radical semiquinone will normally form by delocalizing the unpaired spin on the ring, which would cause the ring to remain essentially planar. Moreover, no position would be preferentially activated for attack by the superoxide, so specificity would result solely from orientation of the superoxo

moiety. Stabilization of the HPCA C2-O^- below the plane of the ring by interaction with Tyr257 would serve to not only promote the formation of the semiquinone, and thus electron transfer, but also to localize the radical on HPCA C2. This would activate this position for superoxide attack, thereby accelerating the reaction. It is possible that without this additional stabilization, electron transfer between the substrates does not readily occur, leading to slow kinetics for the same reasons just described for the 4NC reaction.

The natures of $Y257F_{Int1}^{HPCA}$ and $Y257F_{Int2}^{HPCA}$ appear to support the proposal that the rate of electron transfer between substrates is slowed. The discussion above suggests that no electron has transferred from the substrate in $Y257F_{Int1}^{HPCA}$ while in $Y257F_{Int2}^{HPCA}$ most likely two electrons have transferred without attack on the substrate by a putative intermediate superoxo species as occurs in the reaction cycle of the WT enzyme. It may be that without the localized radical and ring distortion caused by Tyr257, attack on the ring is much less favorable. It remains unclear whether the attacking species is superoxo or (hydro)peroxo in the wild type enzyme with HPCA as the substrate. While it appears from the current results that the (hydro)peroxo intermediate can go forward to attack the quinone form of the aromatic substrate, this reaction is slow relative to the normal rate of formation of the alkylperoxo intermediate. One possibility is that the electrons from substrate are transferred one at a time, normally leading to a reactive substrate and oxygen radical pair after the first electron is transferred. If the reactivity of this pair is decreased due to lack of stabilization by Tyr257, then there is time for transfer of the second electron to form the quinone and (hydro)peroxo pair bound to the Fe^{II}.

Basis for pH Effects on O_2 Binding. The binding of O_2 to the iron of FeHPCD is a complex process that is carefully regulated to assure specificity. The current and several past studies show that substrate must bind first to provide the electrons needed to stabilize the Fe-O_2 bond and perhaps to facilitate the release of solvent that blocks the O_2 binding site in the resting enzyme.[28-31] In the absence of Tyr257, we hypothesize that the supply of electrons to stabilize the Fe-O_2 bond will be compromised, causing the binding process to be slow and reversible. One way the enzyme can counter the reversibility is to protonate His200 that is in hydrogen bonding and charge interaction range of the bound O_2 (Figure 1). In particular, the new positive charge gained by protonating His200 at low pH would stabilize $O_2^{\bullet-}$ character as O_2 binds to the iron. This would not necessarily make the binding process more rapid, but it might serve to slow oxygen release leading to the observed high O_2 affinity.

Roles of Tyr257 in Other Reaction Cycle Steps. The results indicate that the slowest step in the reaction of Y257F is shifted from product formation to either product release or substrate binding. This suggests that Tyr257 may play a role in one or both of these processes. In another branch of the extradiol dioxygenase family typified by *Sphingomonas paucimobilis* SYK-6 protocatechuate 4,5-dioxygenase (LigAB) or *E. coli* 2,3-dihydroxyphenylpropionate1,2-dioxygenase (MhpB), a histidine is sometimes present in place of Tyr257.[32] Mutagenesis and kinetic studies of MhpB indicate that this histidine may play a role as a base catalyst by promoting deprotonation of the substrate during binding with transfer back to the lactone intermediate during ring opening.[33] The structural studies presented in the accompanying report suggest that Tyr257 is not involved in active site interactions that would stabilize a deprotonated form, and thus it is

unlikely to act as an active site base.[2] However, it does participate in key hydrogen bonding and van der Waals interactions with substrate that would favor the anionic form of the substrate C2-hydroxyl. Thus, it may accomplish some of the mechanistically relevant roles attributed to the MhpB histidine through a different strategy. These interactions are absent in Y257F, and this may account for the decreased rate of steps in the substrate binding and/or product release processes.

Conclusions

For the reaction of the WT FeHPCD, the oxygen binding, activation, and reaction steps to form the alkylperoxo intermediate of the reaction cycle are complete within the dead time of the stopped flow instrument at 4 °C (~1 ms). In contrast, these steps in the Y257F variant require well over 100 ms to complete. The > 100-fold decrease in observed rate (and rate constants) shows that Tyr257 plays a key role in aiding the ring attack/oxygen insertion steps. The catalytic process does proceed in the absence of Tyr257, encompassing the putative HPCA-FeII-O2 and HPCA quinone-FeII-(H)peroxo intermediates described here, but the decreased rates suggest that these intermediates are not optimized for the most efficient catalytic process.

Acknowledements

Funding Sources: This work is supported by National Institutes of Health Grant GM 24689 (to J. D. L.), NSF Grant CHE-1012485 (to E.M.) and graduate traineeship GM08700 (to M. M. M.)

References

1. Miller, M. A., and Lipscomb, J. D. (1996) Homoprotocatechuate 2,3-dioxygenase from *Brevibacterium fuscum* - A dioxygenase with catalase activity. *J. Biol. Chem. 271*, 5524-5535.

2. Kovaleva, E. G., and Lipscomb, J. D. (2012) Structural basis for the role of tyrosine 257 of homoprotocatechuate 2,3-dioxygenase in substrate and oxygen activation. *Biochemistry 51*, 8755-8763.

3. Vetting, M. W., Wackett, L. P., Que, L., Jr., Lipscomb, J. D., and Ohlendorf, D. H. (2004) Crystallographic comparison of manganese- and iron-dependent homoprotocatechuate 2,3-dioxygenases. *J. Bacteriol. 186*, 1945-1958.

4. Han, S., Eltis, L. D., Timmis, K. N., Muchmore, S. W., and Bolin, J. T. (1995) Crystal structure of the biphenyl-cleaving extradiol dioxygenase from a PCB-degrading pseudomonad. *Science 270*, 976-980.

5. Senda, T., Sugiyama, K., Narita, H., Yamamoto, T., Kimbara, K., Fukuda, M., Sato, M., Yano, K., and Mitsui, Y. (1996) Three-dimensional structures of free form and two substrate complexes of an extradiol ring-cleavage type dioxygenase, the BphC enzyme from *Pseudomonas sp*. strain KKS102. *J. Mol. Biol. 255*, 735-752.

6. Kovaleva, E. G., and Lipscomb, J. D. (2007) Crystal structures of Fe^{2+} dioxygenase superoxo, alkylperoxo, and bound product intermediates. *Science 316*, 453-457.

7. Hegg, E. L., and Que, L. (1997) The 2-His-1-carboxylate facial triad: An emerging structural motif in mononuclear non-heme iron(II) enzymes. *Eur. J. Biochem. 250*, 625-629.

8. Groce, S. L., Miller-Rodeberg, M. A., and Lipscomb, J. D. (2004) Single-turnover kinetics of homoprotocatechuate 2,3-dioxygenase. *Biochemistry 43*, 15141-15153.

9. Vaillancourt, F. H., Barbosa, C. J., Spiro, T. G., Bolin, J. T., Blades, M. W., Turner, R. F. B., and Eltis, L. D. (2002) Definitive evidence for monoanionic binding of 2,3-dihydroxybiphenyl to 2,3-dihydroxybiphenyl 1,2-dioxygenase from UV resonance Raman spectroscopy, UV/vis absorption spectroscopy, and crystallography. *J. Am. Chem. Soc. 124*, 2485-2496.

10. Arciero, D. M., and Lipscomb, J. D. (1986) Binding of ^{17}O-labeled substrate and inhibitors to protocatechuate 4,5-dioxygenase-nitrosyl complex. Evidence for direct substrate binding to the active site Fe^{2+} of extradiol dioxygenases. *J. Biol. Chem. 261*, 2170-2178.

11. Lipscomb, J. D. (2008) Mechanism of extradiol aromatic ring-cleaving dioxygenases. *Curr. Opin. Struct. Biol. 18*, 644-649.

12. Groce, S. L., and Lipscomb, J. D. (2005) Aromatic ring cleavage by homoprotocatechuate 2,3-dioxygenase: Role of His200 in the kinetics of interconversion of reaction cycle intermediates. *Biochemistry 44*, 7175-7188.

13. Vaillancourt, F. H., Bolin, J. T., and Eltis, L. D. (2006) The ins and outs of ring-cleaving dioxygenases. *Crit. Rev. Biochem. Mol. Biol. 41*, 241-267.

14. Bugg, T. D. H. (2011) Non-heme iron-dependent dioxygenases: Mechanism and structure, In *Iron-containing enzymes: Versatile catalysts of hydroxylation reactions in nature* (de Visser, S. P., and Kumar, D., Eds.), pp 42-66, The Royal Society of Chemistry, Cambridge, UK.

15. Kovaleva, E. G., and Lipscomb, J. D. (2008) Intermediate in the O-O bond cleavage reaction of an extradiol dioxygenase. *Biochemistry 47*, 11168-11170.

16. Mbughuni, M. M., Chakrabarti, M., Hayden, J. A., Bominaar, E. L., Hendrich, M. P., Münck, E., and Lipscomb, J. D. (2010) Trapping and spectroscopic characterization of an Fe^{III}-superoxo intermediate from a nonheme mononuclear iron-containing enzyme. *Proc Natl Acad Sci U S A 107*, 16788-16793.

17. Mbughuni, M. M., Chakrabarti, M., Hayden, J. A., Meier, K. K., Dalluge, J. J., Hendrich, M. P., Münck, E., and Lipscomb, J. D. (2011) Oxy-intermediates of homoprotocatechuate 2,3-dioxygenase: Facile electron transfer between substrates. *Biochemistry 50*, 10262-10274.

18. Lee, S. K., Nesheim, J. C., and Lipscomb, J. D. (1993) Transient intermediates of the methane monooxygenase catalytic cycle. *J. Biol. Chem. 268*, 21569-21577.

19. Münck, E. (2000) Aspects of ^{57}Fe Mössbauer spectroscopy, In *Physical Methods in Bioinorganic Chemistry* (Que, L., Jr, Ed.), pp 287-319, University Science Books, Sausalito, CA.

20. Omote, Y., Hirama, T., and Komatsu, T. (1974) Dopaquinone and related compounds. Reactions with o-phenylenediamine. *Bull. Chem. Soc. Jpn. 47*, 1957-1959.

21. Kessel, S. L., Emberson, R. M., Debrunner, P. G., and Hendrickson, D. N. (1980) Iron(III), manganese(III), and cobalt(III) complexes with single chelating o-semiquinone ligands. *Inorg. Chem. 19*, 1170-1178.

22. Zimmermann, R., Huynh, B. H., Münck, E., and Lipscomb, J. D. (1978) High field Mössbauer studies of reduced protocatechuate 3,4 dioxygenase. *J. Chem. Phys. 69*, 5463-5467.

23. Neidig, M. L., Kavana, M., Moran, G. R., and Solomon, E. I. (2004) CD and MCD studies of the non-heme ferrous active site in (4-hydroxyphenyl)pyruvate dioxygenase: Correlation between oxygen activation in the extradiol and alpha -KG-dependent dioxygenases. *J. Am. Chem. Soc. 126*, 4486-4487.

24. Zimmermann, R., and Spiering, H. (1975) Properties of a 5T2 in iron (II) under the action of arbitrary-symmetry ligand fields and spin-orbit coupling I. On the quadrupole splitting. *Phys. Stat. Sol. 67*, 487-494.

25. Groce, S. L., and Lipscomb, J. D. (2003) Conversion of extradiol aromatic ring-cleaving homoprotocatechuate 2,3-dioxygenase into an intradiol cleaving enzyme. *J. Am. Chem. Soc. 125*, 11780-11781.

26. Frazee, R. W., Orville, A. M., Dolbeare, K. B., Yu, H., Ohlendorf, D. H., and Lipscomb, J. D. (1998) The axial tyrosinate Fe^{3+} ligand in protocatechuate 3,4-dioxygenase influences substrate binding and product release: evidence for new reaction cycle intermediates. *Biochemistry 37*, 2131-2144.

27. Valley, M. P., Brown, C. K., Burk, D. L., Vetting, M. W., Ohlendorf, D. H., and Lipscomb, J. D. (2005) Roles of the equatorial tyrosyl iron ligand of protocatechuate 3,4-dioxygenase in catalysis. *Biochemistry 44*, 11024-11039.

28. Arciero, D. M., Orville, A. M., and Lipscomb, J. D. (1985) [^{17}O]Water and nitric oxide binding by protocatechuate 4,5-dioxygenase and catechol 2,3-dioxygenase. Evidence for binding of exogenous ligands to the active site Fe^{2+} of extradiol dioxygenases. *J. Biol. Chem. 260*, 14035-14044.

29. Mabrouk, P. A., Orville, A. M., Lipscomb, J. D., and Solomon, E. I. (1991) Variable-temperature variable-field magnetic circular dichroism studies of the iron(II) active site in metapyrocatechase: implications for the molecular mechanism of extradiol dioxygenases. *J. Am. Chem. Soc. 113*, 4053-4061.

30. Zhou, J., Kelly, W. L., Bachmann, B. O., Gunsior, M., Townsend, C. A., and Solomon, E. I. (2001) Spectroscopic studies of substrate interactions with clavaminate synthase 2, a multifunctional a-KG-dependent non-heme iron enzyme: Correlation with mechanisms and reactivities. *J. Am. Chem. Soc. 123*, 7388-7398.

31. Solomon, E. I. (2001) Geometric and electronic structure contributions to function in bioinorganic chemistry: Active sites in non-heme iron enzymes. *Inorg. Chem. 40*, 3656-3669.

32. Sugimoto, K., Senda, T., Aoshima, H., Masai, E., Fukuda, M., and Mitsui, Y. (1999) Crystal structure of an aromatic ring opening dioxygenase LigAB, a protocatechuate 4,5-dioxygenase, under aerobic conditions. *Structure (London) 7*, 953-965.

33. Mendel, S., Arndt, A., and Bugg, T. D. H. (2004) Acid-base catalysis in the extradiol catechol dioxygenase reaction mechanism: Site-directed mutagenesis of His-115 and His-179 in *Escherichia coli* 2,3-dihydroxyphenylpropionate 1,2-dioxygenase (MhpB). *Biochemistry 43*, 13390-13396.

Supporting Information

Steady-State Turnover of HPCA by Y257F.

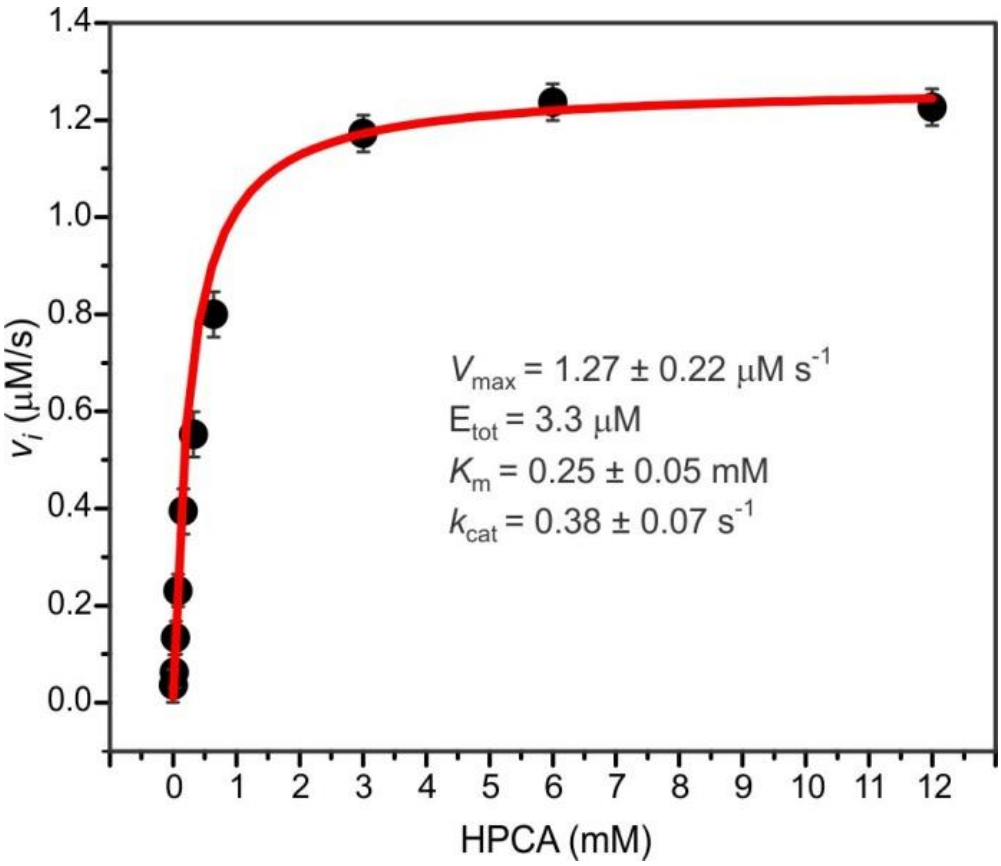

Figure S1. Michaelis-Menten plot from the reaction of Y257F with HPCA and O2 at 4°C. Reaction was conducted in 200 mM MOPS buffer pH 7.5 in air saturated buffer. Initial velocities were measured by stopped-flow spectroscopy as described in the main text.

Experimental Procedures

Photochemical Conversion of the Enzyme-Product Complex. When the reaction is followed over a long time period using diode-array detection at pH 7.5 and 4 °C, the time course reveals a slow change in the UV-vis spectrum of the product, resulting in a decrease of absorption near 380 nm and an increase at 470 nm (Figure S2 A). The slow product transformation can also be observed for reactions catalyzed by the WT enzyme

(Figure S2 B) and H200N mutant (data not shown). However, it occurs faster with the Y257F mutant. The reaction is also much faster for enzyme that has been reduced anaerobically with dithionite before removal of excess reductant and byproducts by gel filtration. The reaction rate is dependent on the intensity of the white light source, and thus, it appears to involve photochemistry of the product. Surprisingly, it is not observed in the absence of enzyme, suggesting that it occurs in the enzyme-product complex. The 470 nm species can be separated from the enzyme (Figure S2 C) by gel filtration, showing that it is not a modified form of the enzyme. The photochemical reaction occurs when enzyme is added stoichiometrically to isolated product, suggesting that product may rebind to the enzyme at high concentrations to allow the reaction. The rate of this product transformation under all conditions is much less than kcat for enzyme turnover. Consequently, it is unlikely to be relevant to normal enzyme catalysis.

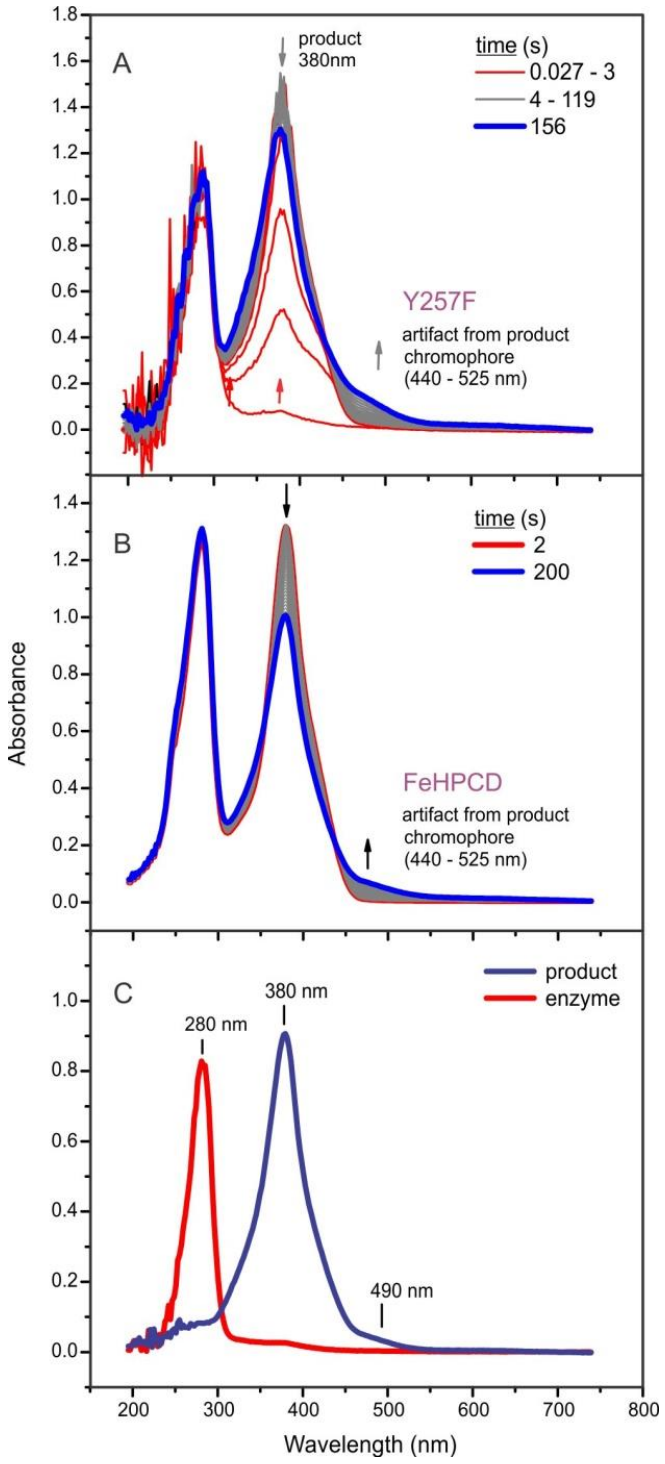

Figure S2. Photochemistry of the ring-cleavage product. **A)** ~ 80 μM Y257F-HPCA complex is mixed with ~ 500 μM O2 at 4°C and pH 7.5, (1 cm pathlength, 2 mm slit width). **B)** Approximately 80 μM FeHPCD-HPCA complex is mixed with ~ 500 μM O2 at 4°C and pH 7.5 (1 cm pathlength, 10 mm slit width). **C)** UV-vis spectrum of 2,3-HPCD and ring-cleaved product separated using a Sephadex PD10 column following a single turnover reaction.

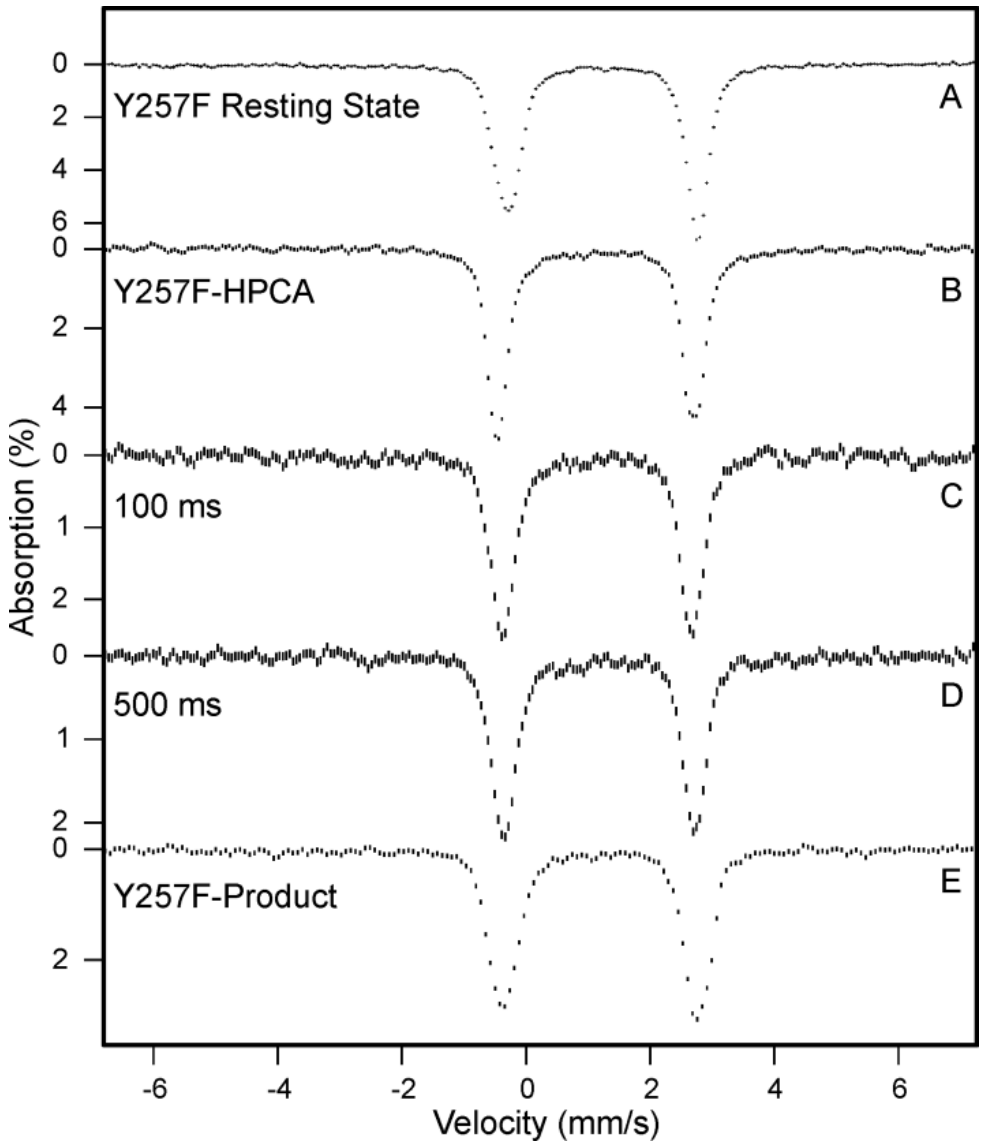

Figure S3. Zero-field Mössbauer spectra collected at 4.2 K for A) Y257F, B) $Y257F_{ES}^{HPCA}$ C) $Y257F_{Int1}^{HPCA}$, D) $Y257F_{Int2}^{HPCA}$, and (E) $Y257F_{Prod}^{HPCA}$.

Chapter III – Characterization of a new, long-lived intermediate in the H200C mutant of homoprotocatechuate 2,3-dioxygenase by Mössbauer, EPR, and DFT methods

Near submission: Meier, K. K.*; Rogers, M.; Kovaleva, E. G.; Bominaar, E. L.; Lipscomb, J. D.; Münck, E.* (to be submited to Inorganic Chemistry).

Author Contributions: K.K.M., M.R., E.G.K., E.M., and J.D.L. conceived and designed the experiments. K.K.M., (Mössbauer, EPR), M.R., E.G.K. (crystal) performed the experiments. K.K.M., M.R., E.G.K., E.M., J.D.L. analyzed the data. K.K.M. and E.L.B. carried out calculations. All authors participated in the writing of the paper.

Abstract

The extradiol-cleaving dioxygenase homoprotocatechuate 2,3-dioxygenase (FeHPCD) is known to bind substrate homoprotocatechuate (HPCA; 3,4-dihydroxyphenylacetate) and O_2 at adjacent ligand sites in a multistep process. The resting enzyme contains a high-spin Fe(II) active site that binds substrate and subsequently activates dioxygen via an internal electron transfer from the substrate through the Fe(II) center to dioxygen. Crystallographic and spectroscopic studies combined with site-directed mutagenesis techniques have allowed for characterization of several oxygen-activated intermediates along the catalytic pathway and have contributed to our understanding of the roles of active site amino acids in catalysis. The present study of the HPCD variant where residue His200 was mutated to Cys (H200C) revealed that the reaction proceeds to completion and yields the correct ring-cleaved product, albeit with significantly reduced k_{cat} values. Stopped-flow studies provided evidence for formation of a yellow, long-lived intermediate, H200C-HPCA-Int1 (*Int1*). Mössbauer and integer-

spin EPR studies of a sample frozen approximately 34s after reaction of the ES complex with O_2 show that *Int1* contains a high-spin Fe(III) center anti-ferromagnetically coupled to a S=1/2 radical. Comparison of DFT calculated properties for several computational models with experimental data suggests that (a) *Int1* is not a superoxo intermediate (H200C-HPCA-superoxo computational model favored a septet ground state (S = 3)), (b) the substrate O_{C1} is deprotonated, and (c) the distal O (not the proximal O) of O_2 is protonated. Using DFT calculations and well-resolved Mössbauer and integer spin EPR data, we have established relationships for the angular dependence between the molecular frame of Int1, the frame of the EFG, and the easy axis of magnetization that can be used to predict experimentally observable ^{17}O hyperfine splittings. Scans along the intrinsic reaction coordinate for the proton-coupled-electron-transfer (PCET) process revealed that the electron transfer step lags behind the proton transfer process, and that that crystallographic waters such as H_2O-1061 are integral components of the hydrogen-bonding network and must be included in our calculations. In summary, our optical, spectroscopic, and computational analyses suggest that *Int1* is a distal-protonated S = 2 semiquinone radical-Fe^{III}-O_2(H) species.

Introduction

The recovery of carbon from stable aromatic compounds by bacteria in the environment under aerobic conditions generally involves ring activation by the introduction of hydroxyl functional groups followed by oxidative ring cleavage. The latter process is catalyzed by dioxygenase enzymes that utilize an active site mononuclear iron, or in rare cases other metals, to activate O_2 and to direct the incorporation of both atoms of oxygen into the substrate, opening the ring. Many examples of aromatic ring cleaving dioxygenases have been reported, but the enzymes that catalyze the cleavage of catechols and catechol derivatives are among the most extensively studied.[1,4,6,8,10,13,15,33] These studies have shown that there are two families of catechol dioxygenases. The Fe^{III}-containing *intradiol* dioxygenases open the aromatic ring of catechol substrates between the hydroxyl moieties to yield muconic acid derivatives. In contrast, the Fe^{II}-containing *extradiol* dioxygenases cleave the ring at a position adjacent to the vicinal hydroxyl groups to yield beta-hydroxy muconic semialdehyde adducts. The extradiol mechanism has been most thoroughly studied using the enzyme homoprotocatechuate 2,3-dioxygenase (HPCD). Use of active site mutants and alternative chromophoric substrates have allowed detection of eight intermediates in the substrate binding, activation, ring-opening, and product dissociation steps.[1,4,5,12,13] Moreover, by carrying out the reaction in an enzyme crystal, the O_2 complex, the alkyl peroxo intermediate, and the product complex were trapped and structurally characterized using x-ray crystallography.[13] A detailed mechanism has emerged from the observation that the substrate binds to the iron as an asymmetric chelate complex with O_2 occupying an adjacent ligand site. Asymmetric substrate binding suggests that only one of the two catecholic hydroxyl

functional groups is deprotonated upon binding. Furthermore, slight distortion of the normally planar aromatic ring of the substrate in the oxygen complex is consistent with electron transfer from the substrate to the bound O_2 via the iron.[15] The resulting radical character in both the substrate and the oxygen would facilitate their reaction to form the observed alkylperoxo intermediate.[9,13] Subsequent Criegee rearrangement of the alkylperoxo intermediate would yield a 7-membered ring lactone which could be hydrolyzed by the second oxygen derived from O_2 to give the ring-opened product.

The central aspect of the proposed extradiol mechanism is the rapid transfer of an electron between the substrate and dioxygen to provide mutual activation without a net change in the iron oxidation state. This concept was tested in solution studies using active site mutations, many of which involved replacing the histidine residue at position 200 (H200). H200 is proposed to be involved in: (i) transfer of the second hydroxyl proton from the substrate to an alkylperoxo oxygen to promote O-O bond cleavage, (ii) stabilization of a superoxo species after electron transfer from the substrate, and (iii) steric alignment of the two substrates to facilitate rapid radical recombination. When H200 was replaced by asparagine (H200N), the proposed electron transfer and radical recombination reactions appeared to slow down, occurring in a stepwise fashion so that new intermediate species could be observed and trapped.[1,4]

The nature of the substrate also determined the types of intermediates observed. When the slow substrate 4-nitrocatechol (4NC) was used in single turnover reactions of H200N, an Fe^{III}-superoxo intermediate (H200N-4NC $_{Int1}$) was observed, trapped and characterized by EPR and Mössbauer spectroscopies.[1] The ground state of H200N-$4NC_{Int1}$ is an S = 2 multiplet resulting from antiferromagnetic coupling of a high-spin

Fe^{III} to a superoxo radical. Parallel mode X-band EPR studies of a sample of H200N-$4NC_{Int1}$ prepared by reacting the ES complex with ^{17}O-labeled O_2 led to the observation of an ^{17}O hyperfine coupling ($A_z(^{17}O) \approx 30$ MHz , quoted for an S = 2 spin Hamiltonian) comparable to those observed for superoxo radicals, thereby confirming the single electron transfer from Fe^{II} to O_2. For H200N-4NC only the transfer of an electron from Fe^{II} to the O_2 appeared to occur rapidly. The accompanying electron transfer from 4NC to the resulting Fe^{III} was inhibited by the electron withdrawing nitro substituent on the 4NC substrate. A second intermediate was also observed for the H200N-4NC mutant (H200N-$4NC_{Int2}$), and was identified as a quasi-stable (H)peroxo-Fe^{III}-4NC quinone radical species. When the native substrate HPCA was used in the H200N reaction, a different Fe^{III} intermediate (H200N-$HPCA_{Int1}$) was observed. It was proposed that the S = 2 integer spin EPR signal for the new intermediate results from a substrate radical coupled to the Fe^{III}, so that electrons from both the substrate and the iron had been transferred to the O_2. Mbughuni and coworkers reported $A_z(^{17}O) \approx 17$ MHz for both the proximal oxygen of the hydroperoxo ligand and O_{C2} of coordinated oxygen of the substrate.[1] They speculated that in the absence of H200, the reaction between substrate and oxygen radicals is slow, allowing time for transfer of the second electron to the oxygen to form a (hydro)peroxo intermediate.

The putative peroxo intermediate formed by reaction of the H200N variant with HPCA substrate is significant for two reasons. First, its formation demonstrates the facile electron transfer between the substrate and O_2 that is at the heart of the proposed extradiol dioxygenase mechanism. However, the slow rate of HPCA ring cleavage exhibited by this mutant also shows that either the resulting H200N-$HPCA_{Int1}$ is not the

actual reactive species or H200 is critical for rapid reaction due to the steric and other effects described above. Therefore, in the absence of rapid formation of the alkylperoxo intermediate, there may be sufficient time to form the more stable peroxo species. Second, if an Fe^{III}-hydroperoxo species has been formed in H200N-$HPCA_{Int1}$, its characterization will impact the study of enzymes throughout the mononuclear non-heme iron oxygenase/oxidase family. While similar intermediates have been proposed in the mechanisms of these enzymes, spectroscopic characterization and reactivity analyses of reported intermediates have been limited.

A difficulty in using H200N-$HPCA_{Int1}$ to carry out the detailed characterizations of the spectroscopic properties and reactivity of an Fe^{III}-peroxo intermediate is that the species has a rather short lifetime. Thus, it must be made and trapped using rapid freeze quench techniques that yield non-uniform and low concentration samples. Here we describe the use of the cysteine variant, H200C, of HPCD. This variant yields the correct ring-cleaved product and is found to have an intermediate, H200C-$HPCA_{Int1}$ (for short *Int1*) that is spectroscopically similar to H200N-$HPCA_{Int1}$ but has a lifetime of many seconds. As a result, samples that contain a 10-fold higher concentration of the intermediate can be prepared using a simple mixing and freezing procedure. Like H200N-$HPCA_{int1}$, *Int1* is found to have an Fe^{III} site that is antiferromagnetically coupled to a substrate semiquinone radical to yield an S = 2 multiplet. *Int1* samples produced well-resolved Mössbauer spectra and a sharp parallel mode EPR resonance at g = 8.04. The latter is associated with an $M_S = \pm 2$ non-Kramers doublet. Such a doublet has uniaxial magnetic properties[25,26] that define an easy axis of magnetization along the z-axis of the zero-field splitting (ZFS) tensor. Analysis of the Mössbauer spectra locates the

electric field gradient (EFG) tensor at the ^{57}Fe nucleus relative to this axis. The EFG tensor can be calculated and related to the molecular structure of the active site by DFT. Knowledge of the easy axis is important for the interpretation of ^{17}O magnetic hyperfine interactions measured by EPR. We have analyzed by DFT a number of *Int1* models, considered many OOH orientations, and calculated exchange coupling constants, isomer shifts and quadrupole interactions. These calculations strongly support an Fe^{III}-hydroperoxo-substrate-radical formulation for *Int1*. We also present a mechanistic study addressing the conversion of an Fe^{III}-superoxo to an Fe^{III}-hydroperoxo species by proton-coupled electron transfer (PCET), which shows that the iron may act as a conduit for passing an electron from the substrate to the dioxygen.

Experimental Procedures and Computational Methods

Sample Preparation

Reagents. Biochemicals and chemicals were purchased from Sigma-Aldrich or Fisher Scientific and ^{57}Fe metal (96.8 %) and $^{17}O_2$ gas were obtained from Cambridge Isotopes (MA).

Production of H200C HPCD Expression Plasmid. The H200C HPCD expression plasmid was produced via site-directed mutagenesis from a plasmid containing the *Brevibacterium fuscum* 2,3-homoprotocatechuate dioxygenase *hpcd* gene in pTrc99a [32, 6]. The H200C mutation was verified by gene DNA sequence analysis (University of Minnesota Genomics Center) using the oligonucleotide primer 5'-GCACATGCGCTACGACCTGTACTC-3'**.**

Over-expression of H200C HPCD. H200C HPCD was over-expressed in *Escherichia coli* BL21 (DE3). A 10 L culture was grown in a BioFlo 110 (37 °C, 400-800 rpm, 5 % oxygen) to OD_{600} of ~ 7, cooled to 28 °C, and induced with 260 μM IPTG for 4 hours. Cell paste was collected via centrifugation (3635 g_{aver}, 30 min, 4 °C).

^{56}Fe H200C HPCD was purified from cells grown using Terrific broth-glycerol media supplemented with 40 μM ferrous ammonium sulfate and 50 μg/ml carbenicillin. ^{57}Fe H200C HPCD was purified from cells grown using Bacto casamino acids, yeast extract, NaCl, phosphate salts media supplemented with carbenicillin, Mg, Ca. Iron was added as ^{57}Fe metal (100 mg) dissolved in 3 M sulfuric acid and diluted with water to <0.5 M before step-wise addition into the 10 L culture.

Purification of H200C HPCD. All steps were conducted at 4 °C unless stated. A suspension of H200C HPCD-containing *E. coli* in 50 mM MOPS, pH 6.8 (3 ml /g cells)

was sonicated for a total of 15 min while maintaining the solution temperature below 10 °C. The lysed solution was clarified via centrifugation (28969 g_{aver}, 60 min, 4 °C). The cell-free extract was treated with by the addition of acetone to 55 % followed by centrifugation (28969 g_{aver}, 60 m, 4 °C). The clarified extract was applied to a DEAE Sepharose FF column equilibrated with N_2-gas sparged 50 % cold acetone in 50 mM MOPS, pH 6.8. The column was washed with 50 mM MOPS, pH 6.8, 180 mM NaCl and eluted using a gradient of 180 mM to 350 mM NaCl. Selected fractions containing HPCD, screened via SDS-PAGE and activity assay, were pooled and concentrated using Ar-gas driven ultrafiltration (10 kDa molecular weight cutoff).

Iron quantitation via ICP-MS. The total iron occupancy and % percent ^{57}Fe enrichment were determined from centrifuged protein samples (17.8 μM) following digestion with nitric acid (2.7 mM) at 60 °C for 17 h via ICP-MS using a Thermo Scientific XSERIES 2 ICP-MS (Department of Earth Sciences, University of Minnesota).

Preparation of fully-reduced H200C HPCD. H200C was deoxygenated by flowing argon gas over a gently stirring solution of enzyme on ice. Buffers were deoxygenated by sparging with argon gas at room temperature. Anaerobic enzyme manipulations were performed in a Coy glove bag. Residual active site ferric iron, present following protein purification, was reduced using 0.5 equivalents of sodium dithionite added to the enzyme under anaerobic conditions. Sodium dithionite was removed from the solution using a 10 ml Sephadex G-25 column (PD-10, GE Healthcare Life Sciences).

Oxygen generating system. Millimolar concentrations of dissolved oxygen were produced using *Dechloromonas aromatica* strain RCB chlorite dismutase (Cld)(generous gift of Prof. Jennifer Dubois, Montana State University, Bozeman, MT) and sodium chlorite[34]. Cld (30 μM) was added to the H200C solution and sodium chlorite was added to the O_2-saturated (4 °C) buffer solution to provide a total of 1.2 equivalents O_2 over enzyme.

Preparation of EPR samples. The intermediate was produced during reaction of pre-formed 2.296 mM H200C - 2.8 mM HPCA (1.22 eq), Cld (28 μM) with sodium chlorite (9 mM) in a Reacti-vial with rapid stirring at 4 °C. The buffer was 200 mM MOPS, pH 7.5. An aliquot of the reaction mix was transferred to an EPR tube, aged to 31s and frozen in a dry-ice bath.

EPR samples of the intermediate using $^{17}O_2$, or $^{16}O_2$ for direct comparison, were produced in a similar manner. Pre-formed 2.194 mM H200C- 2 mM HPCA reacted with an equal volume of either $^{17}O_2$ (70 %, Cambridge Isotope Laboratories, Tewkesbury, MA) or $^{16}O_2$ saturated (1800 μM) buffer solution in a Reacti-vial with rapid stirring at 4 °C. A reaction aliquot was transferred into an EPR tube, aged and frozen in a methanol-dry ice mix.

Preparation of Mössbauer samples. Resting H200C (4.18 mM) was produced from dithionite-reduced enzyme and the E.S complex, H200C-HPCA at 1.2 eq substrate, resulted following the addition of anaerobic HPCA (5.016 mM) to reduced enzyme (4.18 mM). Mössbauer samples were prepared in 200 mM MOPS, pH 7.5.

The H200C$^{HPCA}_{Int1}$ Mössbauer sample was produced via reaction of 4.2 mM H200C, 5.57 mM HPCA, 30 μM Cld, following addition of 9.5 mM sodium chlorite dissolved in O_2-saturated (4 °C buffer) in 200 mM MOPS. pH 7.5 at 4 °C. The reaction was performed in a Reacti-vial with rapid stirring at 4 °C. An aliquot was transferred to a Mössbauer cup which was frozen at 34 s in liquid nitrogen.

Steady state kinetics. Steady state kinetic parameters were measured by monitoring ring-cleaved product formation at 380 nm (36 000 $M^{-1}cm^{-1}$) during the reaction of H200C HPCD (16 μM) with HPCA (0.019 mM to 4.86 mM) in 50 mM MOPS, pH 7.5 at 4 °C using a stopped-flow spectrophotometer (Applied Photophysics, Leatherhead, U.K.). The experiment was performed under aerobic conditions, using air-saturated buffer (4 °C, ~ 400 μM O_2).

Pre-steady state kinetics and spectroscopy. The formation and decay of the intermediate was monitored by mixing preformed anaerobic H200C-HPCA with oxygen-saturated buffer (4 °C, ~ 1.8 mM) using a stopped-flow spectrophotometer (Applied Photophysics, Leatherhead, U.K.) using either photodiode array detection or photomuliplier detection at 610 nm in 50 mM MOPS, pH 7.5 at 4 °C.

Spectroscopy

EPR spectroscopy. X-band EPR spectra were recorded on a Bruker ELEXYS-II E500 spectrometer equipped with an Oxford ESR910 cryostat for low temperature measurements and a bimodal cavity (Bruker ER4116DM) for generation of microwave fields parallel and perpendicular to the static field. All experimental data were collected under non-saturating microwave conditions. The microwave frequency was calibrated

with a frequency counter, and the magnetic field was calibrated with an NMR gaussmeter. The temperature was calibrated with resistors (CGR-1-1,000) from LakeShore. A modulation frequency of 100 kHz and amplitude 1 mT pp was used for all spectra unless otherwise noted. SpinCount, a Windows software package (available from www.chem.cmu.edu/groups/hendrich/facilities/index.html), was used to analyze and simulate the spectra. Spin quantification was determined from double integration, relative to a CuEDTA standard for which the copper concentration was accurately determined from plasma emission spectroscopy.

Mössbauer spectroscopy. Mössbauer spectra were recorded using Janis Research Super-Varitemp dewars that allowed studies in applied magnetic fields up to 8.0 T. Mössbauer spectral simulations were performed using the WMOSS software package (SEE Co), and EPR spectra were simulated with SpinCount, a program developed by Prof. M. P. Hendrich of Carnegie Mellon University. Isomer shifts are quoted relative to Fe metal at 298 K.

X-ray Crystallography. H200C 2,3-HPCD was crystallized by the hanging-drop method at 20 °C in 13 – 15 % PEG6000, 0.1 M calcium chloride, 0.1 M Tris-HCl, pH 6.5. Crystals were briefly transferred into a mother liquor solution containing 25% PEG400 as a cryoprotectant before cryo-cooling in liquid nitrogen and data collection at 100 K.

Anaerobic substrate complex was formed by first incubating all solutions and crystals of H200C 2,3-HPCD in an anaerobic glove box for at least 18h. Then a crystal was incubated with 2 mM anaerobic HPCA for 30 min before being transferred briefly

into a mother liquor containing 25% PEG400 as a cryoprotectant. The crystal was then cryo-cooled in liquid nitrogen inside the glovebox and stored for later diffraction experiments.

The XDS package [27] was used to process diffraction data. The 2,3-HPCD (PDB 3OJT) coordinates were used as an initial rigid body refinement model followed by cycles of restrained refinement with Refmac5[28], which is part of the CCP4 program suite [29,30]. Model building was done using Coot. [31] The 4 subunits of the single enzyme molecule present in the asymmetric unit were refined independently. Ligand refinement protocols were essentially the same as those described previously.[12,13] X-ray data processing and refinement statistics are summarized in Table S1. All structure figures were produced using Pymol (The PyMOL Molecular Graphics System, Version 1.5.0.4 Schrödinger, LLC).

Computational Methods. The DFT calculations presented in Tables 2-7 were performed using Guassian ’09, Revision B.01, M. J. Frisch, G. W. Trucks, H. B. Schlegel, G. E. Scuseria, M. A. Robb, J. R. Cheeseman, G. Scalmani, V. Barone, B. Mennucci, G. A. Petersson, H. Nakatsuji, M. Caricato, X. Li, H. P. Hratchian, A. F. Izmaylov, J. Bloino, G. Zheng, J. L. Sonnenberg, M. Hada, M. Ehara, K. Toyota, R. Fukuda, J. Hasegawa, M. Ishida, T. Nakajima, Y. Honda, O. Kitao, H. Nakai, T. Vreven, J. A. Montgomery, Jr., J. E. Peralta, F. Ogliaro, M. Bearpark, J. J. Heyd, E. Brothers, K. N. Kudin, V. N. Staroverov, T. Keith, R. Kobayashi, J. Normand, K. Raghavachari, A. Rendell, J. C. Burant, S. S. Iyengar, J. Tomasi, M. Cossi, N. Rega, J. M. Millam, M. Klene, J. E. Knox, J. B. Cross, V. Bakken, C. Adamo, J. Jaramillo, R. Gomperts, R. E. Stratmann, O. Yazyev, A. J. Austin, R. Cammi, C. Pomelli, J. W. Ochterski, R. L.

Martin, K. Morokuma, V. G. Zakrzewski, G. A. Voth, P. Salvador, J. J. Dannenberg, S. Dapprich, A. D. Daniels, O. Farkas, J. B. Foresman, J. V. Ortiz, J. Cioslowski, D. J. Fox, Gaussian, Inc., Wallingford CT, 2010.

Unless otherwise noted, calculations were performed using Becke's three-parameter hybrid functional (B3LYP) and basis set 6-311G. ^{57}Fe Mössbauer isomer shifts, δ, were calculated from the DFT charge density at the iron nucleus using the calibration from Vrajmasu et al.[36] The ^{57}Fe hyperfine parameters were calculated using the properties keyword, prop, of the Gaussian code.

Results and Discussion

X-ray crystal structure of H20C Variant. The crystal structure of the H200C variant with HPCA substrate (yellow) is shown in Figure 1. The light gray sticks correspond to the carbon atoms in the H200C mutant. The darker gray sticks represent the wild-type FeHPCD system with HPCA substrate. Inspection of the overlay of these two structures reveals very little change in the ligands that directly coordinate to the iron active site. However, there is a dramatic shift in the distance from the iron to the closest atom of the residue at position 200. In the wild-type enzyme, His200 is approximately 2.9-3.0 Å away from the iron center. In the H200C variant, however, the distance is significantly larger, as we would expect since Cys is shorter than His by at least 2 bonds. Here we present a discussion of the implications that mutation of His200 to Cys has on the structure, mechanism and reactivity of the H200C variant. We will report elsewhere detailed Mössbauer and quantum-chemical studies for the resting enzyme and the H200C-HPCA complex, as well as for the ΔE_Q = 2.32 mm/s species.

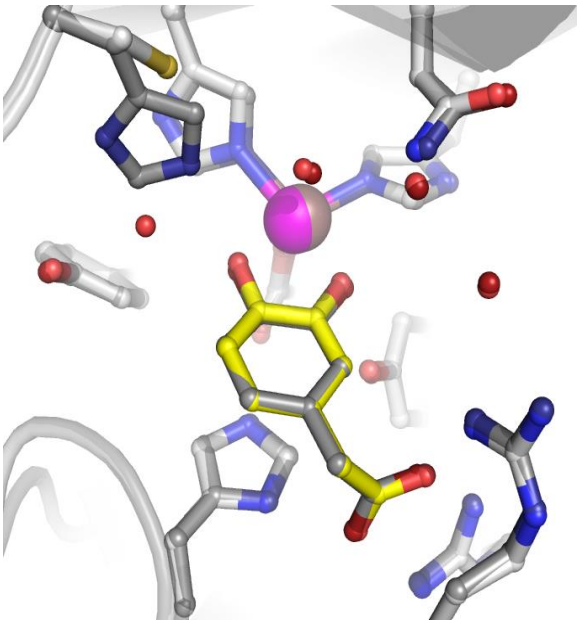

Figure 1. Overlay of the WT-FeHPCD: HPCA enzyme substrate crystal structure (PDB ID: 4GHG; shown in darker colors) with the crystal structure of the H200C: HPCA enzyme substrate crystal structure (lighter colors). Carbon atoms of the HPCA substrate are shown in yellow. Iron is shown in purple in the H200C structure.

Kinetic profile of *Int1*. Stopped-flow spectroscopy revealed the appearance of a feature at 610 nm, attributed to formation of an intermediate, *Int1*, following reaction of the H200C-HPCA complex (Figure 2, red curve) with O_2 (Figure 2, blue curve). An HPCA substrate titration measuring the initial velocity of the H200C-catalysed product formation (pH 7.5, 4 °C, 380 nm) provided the following steady-state parameters: k_{cat} = 0.007 s^{-1} (WT HPCD k_{cat} 3.2 s^{-1}) [33] and K_M = 18 μM (WT HPCD K_M 25 μM, 22 °C [33]). The accuracy of these measurements is impacted by the low rates of reaction and a high substrate affinity. The k_{cat} for the overall reaction is comparable to the decay rate of the 610 nm intermediate. This suggests that the rate-limiting step is shifted from product release to oxygen activation in this mutational variant.

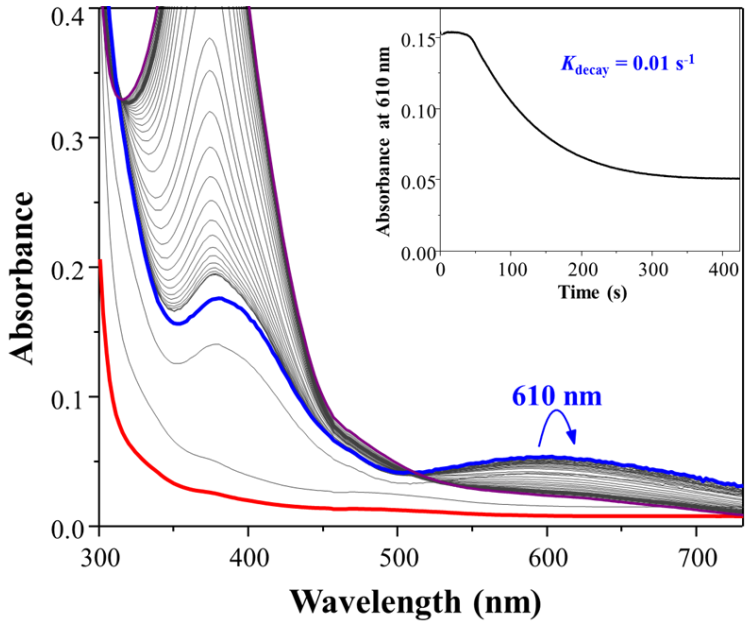

Figure 2. H200C-HPCA + O_2 reaction monitored by stopped-flow spectroscopy. Pre-formed H200C-HPCA complex (220 μM) reacted with O_2 (900 μM) in 200 MOPS, pH 7.5 at 4 °C in a cuvette with path length of 2 mm. Spectra were recorded between 1.26 ms and 100 s. Spectra in bold are as follows: H200C-HPCA complex, red; 610 nm intermediate, blue; final species, magenta. **Inset:** Absorbance decrease at 610 nm resulting from decay of the intermediate. Preformed H200C-HPCA complex (100 μM) reacted with O_2 (900 μM) in 200 mM MOPS, pH 7.5 at 4 °C with path length 10 mm. The rate of decay of the 610 nm species was determined by fitting the data to a single exponential. The initial plateau region results from a slight excess of HPCA leading to steady state turnover.

Mössbauer characterization of H200C-HPCA$_{Int1}$. Figure 3A shows a 4.2 K zero applied field Mössbauer spectrum of the enzyme-substrate complex of the H200C-HPCA variant system. The spectrum exhibits a well-defined quadrupole doublet having parameters typical of high-spin Fe^{II}, namely quadrupole splitting ΔE_Q = 3.55 mm/s and isomer shift δ = 1.14 mm/s. The spectrum also reveals a minority Fe^{II} species (6% of Fe, magenta line) with ΔE_Q = 2.32 mm/s and δ = 1.20 mm/s. Figure 3B shows a spectrum of a H200C-HPCA sample frozen 34 s after incubation with O_2. It should be noted that exposure to O_2 leads to the complete disappearance of the ΔE_Q = 3.55 mm/s H200C-HPCA complex, as well as the ΔE_Q = 2.32 mm/s component, in favor of a new species with ΔE_Q = 0.97 mm/s and δ = 0.48 mm/s. This new species is designated H200C-HPCA$_{Int1}$; for brevity we will refer to this intermediate simply as *Int1*.

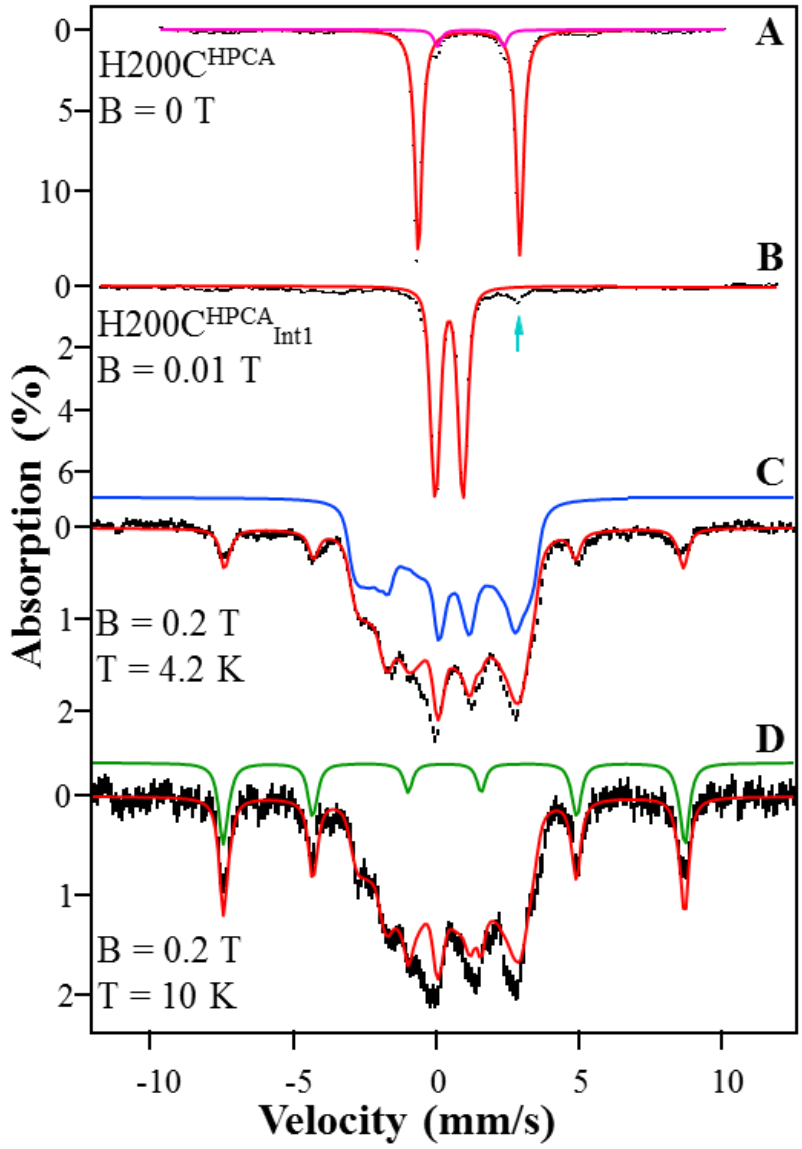

Figure 3. (A) Zero-field, 4.2 K Mössbauer spectrum (black) of H200C-HPCA (simulation, red curve) and the minority species with ΔE_Q = 2.32 mm/s and δ = 1.20 mm/s (magenta curve). The spectra shown in panels **A** and **B** are raw data, and do not have the high-spin ferric contaminants subtracted. Spectra shown in panels **C** and **D** were obtained by removing the high-spin ferric and high-spin ferrous impurities. (**B, C)** Spectra of the oxygenated intermediate, H200C-HPCA$_{Int1}$ = *Int1*, recorded at 4.2 K in parallel applied magnetic fields as indicated. **(D)** B = 0.2 T spectrum recorded at 10 K. The spectra in (C) and (D) contain a 6-line pattern (green curve) associated with the excited $M_S = \pm 2$ doublet of the S = 2 multiplet. The absorption of this feature increases with increasing temperature, showing that D > 0. The dominant contributions of the central feature, blue in (C), are from the $M_S = 0$ and $M_s = \pm 1$ doublets.

The isomer shift of *Int1* is characteristic of high-spin ($S_1 = 5/2$) Fe^{III}, and as this species yields for B = 0 a quadrupole doublet rather than a spectrum exhibiting paramagnetic hyperfine structure, the Fe^{III} must reside in a complex with integer (or zero) electronic spin. The oxygen-exposed sample also contains a minority (6% of Fe) high-spin Fe^{II} species with parameters essentially the same as those observed for resting H200C, namely $\Delta E_Q = 3.25$ mm/s and $\delta = 1.22$ mm/s. It is possible that this minority component is also present, but not resolved, in the H200C-HPCA complex of Figure 3A. If this doublet indeed represents the resting enzyme, it should be present (as it is) in the spectrum of Figure 3B too, because the resting enzyme does not react with oxygen. The sample of Figure 3B also contains, although barely discernible, a monomeric high-spin Fe^{III} contaminant (ca. 8%, broad features near +5 mm/s and -4 mm/s); we can simulate the spectra of this species reasonably well and have subtracted its contribution from the raw data of Figure 4 (see Figure S1 for simulated spectra of the high-spin ferric contaminant along with parameters listed in the figure caption).

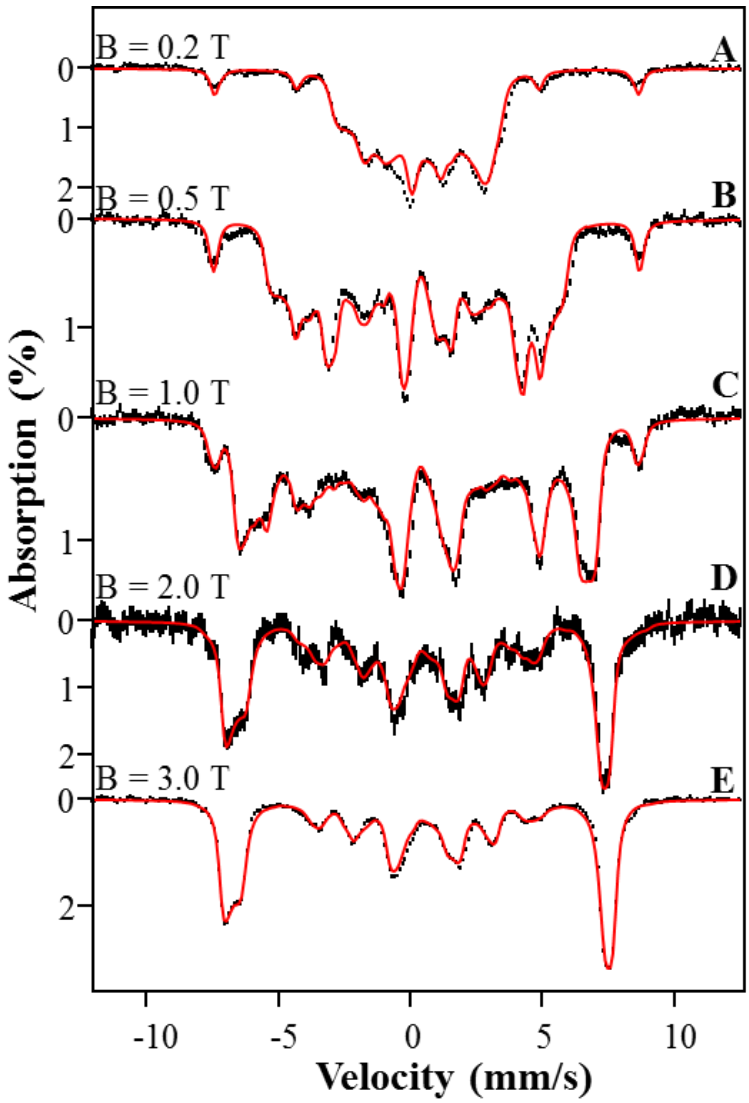

Figure 4. 4.2 K Mössbauer spectra of *Int1* recorded in variable, parallel applied magnetic fields as indicated. The black hash-mark curves are the spectra that result after subtraction of the minority high-spin ferrous (6%) and high-spin ferric (8%) contaminants from the raw data. The high-spin ferric contaminant was simulated with parameters given in the caption of Figure S1. Red lines are spin Hamiltonian simulations using the parameters listed in Table 1.

Table 1. Comparison of the parameters of Fe species obtained for H200C with those reported for intermediates of H200N evaluated with eq 1.

	D_1 (cm^{-1})	$(E/D)_1$	J (cm^{-1})	ΔE_Q (mm/s)	η	α,β,γ	A_1[x,y,z] (T)	δ (mm/s)	Ref.
$H200C^{HPCA}_{Int1}$ (H)OO-Fe^{III}-HPCA$^{\bullet}$	+1.2	0.05(3)	> +50	-0.97	0.55	58,70,51	-21.0, -21.5, -21.6(1)	0.48	This work
$H200N^{HPCA}_{Int1}$ (H)OO-Fe^{III}-HPCA$^{\bullet}$	+1.1	0.12	+25(5)	-0.95(2)	0	-, 90,-	-21.5(2), -21.5(2), -21.5(2)	0.48(1)	4
$H200N^{4NC}_{Int2}$ (H)OO-Fe^{III}-4NC-SQ$^{\bullet}$	+0.67	0.11	+40(10)	-0.87	0.8	-	-21.5, -21.5, -21.5	0.49	1
$H200N^{4NC}_{Int1}$ $^{-\bullet}O_2$-Fe^{III}-4NC	-0.59	0.20	+6(2)	-0.33	-3	-	-21.4, -21.4, -21.4	0.50	1
$H200C^{HPCA}_{Int1}$ (S=2 representation)	+1.6	0.05(3)	-	-0.97	0	55,70,0	-24.5, -25.0, -25.2(1)	0.48	This work

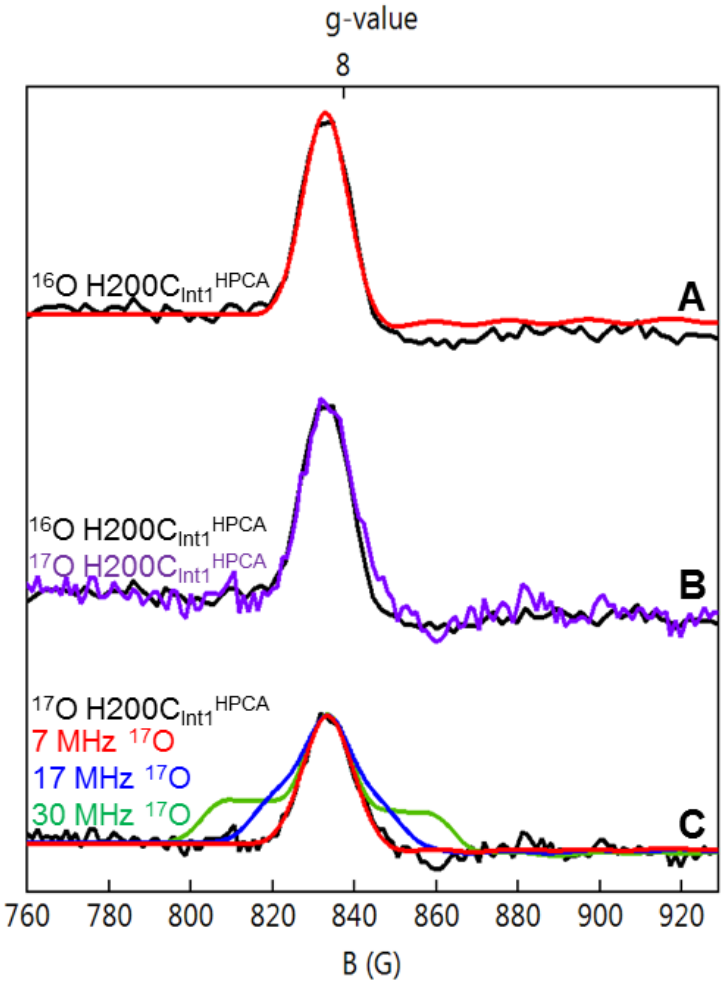

Figure 5. Parallel mode X-band EPR spectra of H200C-HPCA $_{Int1}$ recorded at 21 K. **(A)** ^{16}O *Int1*, black curve. The red line is an S = 2 SpinCount simulation based on eq 4 using D = +1.6 cm^{-1}, E/D = 0.055, g_z = 2.01, σ(E/D) = 0.005 and 0.57 mT packet line width. (**B**) Comparison of spectra of the ^{16}O sample of (A) (black) with a sample of *Int1* enriched with ~ 70% $^{17}O_2$ (purple curve). The purple curve has been scaled to match the peak amplitude of the g = 8.04 feature of the ^{16}O sample. **(C)** Experimental spectrum of the $^{17}O_2$ enriched sample (black) with simulations for $A_{z,eff}$ (^{17}O) = 7 MHz (red), 17 MHz (blue) and 30 MHz (green). Conditions: 9.37 GHz frequency, 20 mW microwave power, 1 mT modulation, T = 21 K.

The nature of the applied field spectra of Figures 2 and 3 suggested to us that *Int1* should yield a parallel mode X-band EPR signal. Indeed, *Int1* exhibits a sharp feature (Figure 5) with a peak at g = 8.04 (where the italicized *g* is defined by g = hν/βB). Such a

feature typically results from the $M_S = \pm 2$ doublet of an S = 2 multiplet for which $g \approx 2g_zS$. These observations suggest that the iron center of *Int1* is a system for which the high-spin Fe^{III} is exchange coupled to a radical ($S_R = 1/2$). We describe this interaction by the Hamiltonian of equation 1.

$$\widehat{\mathcal{H}} = J\hat{\mathbf{S}}_1 \cdot \hat{\mathbf{S}}_R + D_1\left[\hat{S}_{1z}^2 - \frac{35}{12} + \left(\frac{E}{D}\right)_1\left(\hat{S}_{1x}^2 - \hat{S}_{1y}^2\right)\right] + \beta\left(\hat{\mathbf{S}}_1 \cdot \mathbf{g}_1 + \hat{\mathbf{S}}_R \cdot \mathbf{g}_R\right) \cdot \mathbf{B} + \widehat{\mathcal{H}}_{hf} \quad (1)$$

where $\widehat{\mathcal{H}}_{hf}$ describes the hyperfine interactions of the ^{57}Fe nucleus,

$$\widehat{\mathcal{H}}_{hf} = \hat{\mathbf{S}}_1 \cdot \mathbf{a_1} \cdot \hat{\mathbf{I}} + \frac{eQV_{z'z'}}{12}\left[3\hat{I}_{1z'}^2 - \frac{15}{4} + \eta\left(\hat{I}_{1x'}^2 - \hat{I}_{1y'}^2\right)\right] - g_n\beta_n\mathbf{B} \cdot \hat{\mathbf{I}} \quad (2)$$

In eq 1, D_1 and E_1 are the axial and rhombic zero-field splitting (ZFS) parameters of the Fe^{III} ion, and $\mathbf{g_1}$ and $\mathbf{g_R}$ are the g-tensors of the Fe^{III} and the radical, respectively. For the present type of ligand coordination, namely high-spin Fe^{III} with nitrogen and oxygen ligands, $|D_1|$ is typically ≈ 1 cm^{-1} (below we find $D_1 = +1.2$ cm^{-1}). In the following we assume that $\mathbf{g}_1$ and $\mathbf{g}_R$ are isotropic and that $g_1 \approx g_R \approx 2.00$. $\mathbf{A}_1$ is the ^{57}Fe magnetic hyperfine tensor; for a high-spin Fe^{III}, $\mathbf{A}_1$ is isotropic to within a few percent. The electric quadrupole interaction, the second term in eq 2, is written in the principal axis frame (x',y',z') of the electric field gradient (EFG) tensor. Mössbauer spectroscopists generally choose (x',y',z') such that $|V_{z'z'}| \geq |V_{y'y'}| \geq |V_{x'x'}|$. This choice confines the asymmetry parameter, $\eta = (V_{x'x'} - V_{y'y'})/V_{z'z'}$, to the range $0 \leq \eta \leq 1$. The Euler angles α, β, and γ relate the principal axis frames of the EFG and ZFS tensors; the polar angles α and β position z' in (x,y,z) and γ rotates the EFG around z'. These angles are called $(\alpha\beta\gamma)_{EFG}$ in the WMOSS software.

For *Int1* we found that the exchange coupling constant, J, is positive (antiferromagnetic coupling) and large (> 30 cm^{-1}) compared to the ZFS of the ferric ion, $J >> D_1$. Under these conditions it is useful to treat the system as an isolated S = 2 ground multiplet and to describe it in the *coupled* representation using eq 3.

$$\widehat{\mathcal{H}}_{S=2} = \mathrm{D} \quad \left[\hat{\mathrm{S}}_{\mathrm{z}}^2 - 2 + \left(\frac{\mathrm{E}}{\mathrm{D}}\right) \quad \left(\hat{\mathrm{S}}_{\mathrm{x}}^2 - \hat{\mathrm{S}}_{\mathrm{y}}^2\right)\right] + \beta\, \hat{\mathbf{S}} \cdot \mathbf{g} \quad \mathbf{B} + \widehat{\mathcal{H}}_{hf} \qquad (3)$$

The quantities of equation 3 are related to those of the uncoupled representation of eq 1 by $D = (4/3)\, D_1$, $(E/D) = (E/D)_1$, and $\mathbf{g} = (7/6)\mathbf{g}_1 - (1/6)\mathbf{g}_R$ (throughout this chapter, we take $g_x = g_y = 2.0$; below we find that $g_z = 2.01$). For the hyperfine interactions of the S = 2 multiplet, we can use equation 2 by replacing $\hat{\mathbf{S}}_1 \cdot \mathbf{a_1} \cdot \hat{\mathbf{I}}$ by $\hat{\mathbf{S}}_1 \cdot \mathbf{A^c} \cdot \hat{\mathbf{I}}$; the expression $\mathbf{A}^c = (7/6)\, \mathbf{a}_1$ relates the A-tensor of the local Fe^{III} site to the A-tensor of the coupled system, $\mathbf{A}^c$.

The red lines in Figures 2C, D and 3 A-E are spectral simulations based on eqs 1 and 2 using the parameters listed in Table 1. Although the spectra depend on many parameters, we do not have to rely on multi-parameter fits because most of the critical unknowns can be isolated and determined with good precision by identifying the behavior of key features of the spectra under conditions of variable temperature and/or variable field. At 4.2 K, the relaxation rate of the electronic spin is slow compared to the nuclear precession frequencies. Consequently, the spectra of *Int1* are a superposition of five sub-spectra, one for each of the five M_S levels of the S=2 multiplet. The spectra of Figures 1C and D contain a 6-line pattern (green line) whose intensity increases as the temperature is raised from 4.2 K to 10 K. The behavior of this 6-line pattern suggests that it originates from molecules in the $M_S = \pm 2$ levels (for B = 0.2 T both $M_S = \pm 2$ levels

yield essentially the same spectrum). Since the $M_S = \pm 2$ levels are excited states, it follows that $D > 0$, as shown in the diagram of Figure 6A. The intensity of this feature is determined by the Boltzmann factor that governs the population of the sublevels of the S = 2 state. From the experimentally determined intensities, we were able to extract the ZFS parameter, $D \approx +1.6\ cm^{-1}$ ($D_1 = 1.2\ cm^{-1}$).

Figure 3C shows that the central features of the Mössbauer spectra reflect to a large extent the $M_S = 0$ ground state that is mixed with the $M_S = \pm 1$ levels by the x and y components of the applied magnetic field. "Magnetization" curves, i.e. plots of $\langle S_i \rangle$ versus B, for the "$M_S = 0$" state are shown in Figure 6B. The magnetic splitting of the Mössbauer spectra is governed by the internal magnetic field $\mathbf{B}_{int} = -\langle \mathbf{S} \rangle \cdot \mathbf{A}^c / g_n \beta_n$. The shapes of the magnetization curves depend mainly on D and E/D; $|\langle S_x \rangle| < |\langle S_y \rangle|$ for $E/D \neq 0$. Fitting the field dependence of the spectra requires $D = +1.6\ cm^{-1}$, in good agreement with the value obtained from the Boltzmann populations at 4.2 K and 10 K. As shown in Figure 7, we obtained the same value for D by fitting the temperature dependence of the g = 8.04 parallel mode X-band EPR feature.

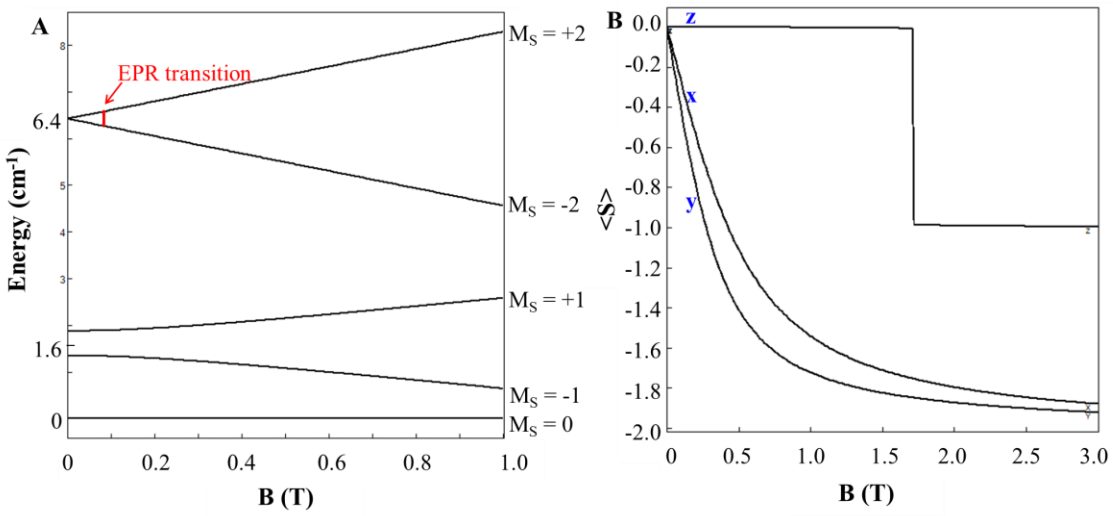

Figure 6. (A) Schematic energy levels of the S = 2 system for B = 0. For simplicity the levels are labeled by M_S quantum numbers rather than by non-magnetic states ϕ^0, ϕ^{1s}, ϕ^{1a}, ϕ^{2s}, and ϕ^{2a}. For instance, $|\phi_{1s,1a}\rangle = (|M_S = +1\rangle \pm |M_S = -1\rangle)/\sqrt{2}$; see Hendrich Debrunner.[22] **(B)** Spin expectation values for the lowest spin level of H200C-HPCA$_{Int1}$. $\langle S_{x,y,z}\rangle$ are the expectation values of the electronic spin when B is applied along x, y, or z. The jump of $\langle S_z\rangle$ near B = 1.8 T is due to level crossing as the M_S = -1 state becomes the ground state for molecules for which B is along z.

E/D can be determined in different ways. First, the intensity of the g = 8.04 EPR feature is proportional to $(\Delta_{\pm 2})^2$, where $(\Delta_{\pm 2})$ refers to the splitting of the $M_S = \pm 2$ levels in zero field. $\Delta_{\pm 2}$ is defined as $3D(E/D)^2$, and is related to the EPR intensity which, with known D, is proportional to $(E/D)^4$. Therefore, a quantitative analysis of the EPR signal intensity using the known concentration of *Int1* provides a sensitive measure of E/D. From this analysis (see below) we obtained E/D = 0.055.

E/D can also be obtained from the Mössbauer spectra. Given that the A-tensor for high-spin Fe^{III} is quite isotropic, the anisotropy of B_{int} in the x-y plane is determined by E/D. Our EPR derived result was confirmed by analysis of the variable Mössbauer

spectra of Figures 1C and 2A which favor a value of E/D < 0.08. Moreover, the Mössbauer spectra establish that E/D > 0.03. The latter inequality follows from consideration of the magnetization behavior of the $M_S = \pm 1$ states which, together, are ≈ 48% populated at 4.2 K. For E/D ≤ 0.03 the internal field associated with the $M_S = \pm 1$ states, $B_{int,z}(\pm 1)$, would rise steeply at low field, giving rise to a Mössbauer spectrum associated with the $M_S = -1$ level that would contribute sharp features outside those associated with the $M_S = 0$ state, in contrast to the experimental observation.

Next we consider again the spectra associated with the $M_S = \pm 2$ levels (green curve in Figure 3D). For these two levels, $\langle \mathbf{S} \rangle$ is such that $\langle S_z \rangle = \pm 2$, $\langle S_{x,y} \rangle \approx 0$ for $0 < B < 0.2$ T (we will refer to z as the "easy" axis). Hence, B_{int} is locked along the z axis of the ZFS tensor for essentially all molecular orientations. This describes a situation for which B_{int} is fixed relative to the EFG tensor too. In the principal frame x', y', z', with the largest EFG component along z', the EFG tensor is diagonal. We readily obtained the magnetic splitting $A_{1z}/g_n\beta_n = -21.6 \pm 0.1$ T (A_{1x} and A_{1y} were obtained from the 3.0 T spectrum using the known D and E/D values; we know $|\Delta E_Q| = (eQV_{zz}/2)(1+ \eta^2/3)^{1/2} =$ 0.97 mm/s is known from the spectrum of Figure 3B). The experimental splitting of the 6-line pattern requires a small positive component of the EFG along z. This can be achieved for positive as well as negative ΔE_Q. As will become clear below, knowledge of the orientation of the "easy" axis in the EFG frame allows one to relate Mössbauer, EPR-determined ^{17}O hyperfine structure and DFT results, and thus correlate spectroscopic information with a geometric structure. Determination of α and β turned out to be a rather arduous task (requiring a few hundred spectral simulations). With $B_{int,z}$ known the line positions of the 6-line pattern depend on angles β and γ through the effective

quadrupole interaction along the direction of B_{int}, namely $(eQV_{z'z'}/12)(3\cos^2\beta - 1 + p \sin^2\beta)/2$, where $p = \eta \cos 2\gamma$ (there are small off-diagonal terms); as the electronic system is essentially uniaxial at B = 0.2 T the expression does not depend on α.

If the spin relaxation rate of *Int1* would be fast compared to the nuclear precession frequencies at 150 K, one could determine the sign of the quadrupole splitting from a high field spectrum (although the Fe^{III} impurity might be bothersome). Unfortunately, this option is not available as *Int1* displayed broad and unresolved spectra at 150 K, indicating intermediate relaxation rates. Therefore, we have started our analysis with the B = 0.2 T spectra of Figures 3C and D, where the green curve indicates the contribution of the $M_S = \pm 2$ electronic doublet. The six lines of this doublet are reasonably well known (the two inner lines can be located after subtracting the approximate contribution of the $M_S = 0$ and ±1 levels). Analysis of the 6-line spectrum confines the polar angle β to $55° < \beta < 70°$; the line positions are not sufficiently well known to determine β and p with accuracy as the effective component of the EFG along z is quite small. Next we least-square fitted groups of four 4.2 K spectra which brings the magnetization behavior of the $M_S = 0$ and ± 1 levels into the problem (before attempting these fits we understood the origin of all lines in the spectra of Figures 1C and 2A and B). These fits converged to a solution for which the polar angles were $\alpha \approx 55\text{-}60°$ and $\beta \approx 70°$. This result is significant as it locates the z-axis of the ZFS tensor in the (x', y', z') frame of the EFG tensor (we show below that the z'-axis is roughly along the direction defined by the O_{OOH}-Fe-O_{E267}) bond.

The sensitivity of the data to α can be understood by inspection of Figure 6 which shows that, despite the small value of E/D, there is considerable anisotropy of <**S**> in the

x-y plane for B = 0.2 and 0.5 T. The solution with $\beta = 70°$ assures that the EFG frame is tilted such that the quadrupole interaction has a small positive component along z. The best fits to the experimental spectra were obtained for $\Delta E_Q < 0$, i.e. $\Delta E_Q = -0.97$ mm/s. The asymmetry parameter η was found to be quite soft, with acceptable fits for values of η approaching 1.0. In the limit $\eta = 1$, the EFG components are $V_{z'z'} = -V_{y'y'}$ and $V_{x'x'} = 0$, and the sign(ΔE_Q) depends on whether we choose the largest EFG component to be along z' or y'. Thus our analysis admits a solution for $\Delta E_Q > 0$ provided $\eta \approx 1$.

EPR Studies of *Int1*. Next we turn to the parallel-mode EPR spectra of H200C-HPCA$_{Int1}$, which reveal a fairly sharp feature at g = 8.04. An expanded view of a spectrum recorded at 21 K is shown in Figure 5. We have recorded spectra under non-saturating conditions (20 mW) between 10 K and 60 K; a set of 9 spectra were collected and wider scans are shown in Figure S2. The g = 8.04 feature results from the excited $M_S = \pm 2$ doublet at energy $\varepsilon = 4D \approx 6.4$ cm^{-1} above the $M_S = 0$ ground state. At temperatures above 60 K the g = 8.04 feature broadened and became difficult to analyze; below 10 K the signal amplitude declined sharply due to depopulation of the $M_S = \pm 2$ doublet. The red solid line in Figure 5A is a SpinCount simulation generated using the parameters listed in the figure caption. The peak of the resonance is positioned at g = 8.04 rather than g = 8.00. From the resonance condition $h\nu = \{(4g_z\beta B)^2 + \Delta_{\pm 2}^2\}^{1/2}$ we infer that that the shift of the resonance from g = 8.00 to g = 8.04 is mainly due to g_z (= 2.01); $\Delta_{\pm 2} = 0.014$ cm^{-1} shifts the resonance by a mere 0.006 (g_z is defined by eq 3). The intensity of the resonance is proportional to $(E/D)^4$ and, since we know the concentration of *Int1*, we can

use this relationship as a sensitive measure of E/D, yielding E/D = 0.055 in good agreement with the $0.03 < \eta < 0.08$ obtained from the Mössbauer analysis.

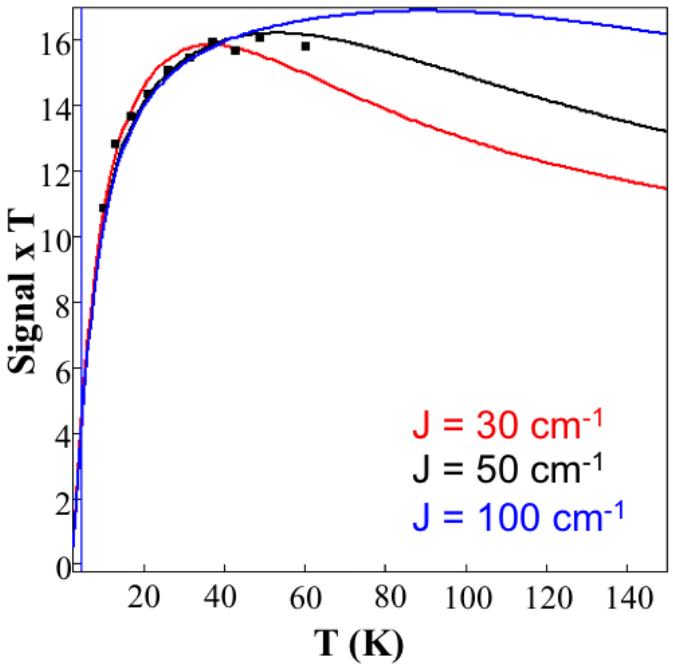

Figure 7. (Signal × T) versus T plot of $H200C^{HPCA}_{Int1}$ obtained from analysis of the variable temperature EPR spectra shown in Figure S2 (see SI).

Using the SpinCount software developed by Michael Hendrich of Carnegie Mellon University, we have analyzed and simulated the entire set of spectra (Figure 5). Figure 7 shows a plot of signal × T versus T for the g = 8.04 resonance, where signal × T is proportional to the population of the $M_S = \pm 2$ doublet. The solid lines in Figure 7 are calculations for different values of J according to eq 1; the rise of the curve depends mainly on the zero-field splitting parameter D_1 and is well represented by choosing $D_1 = +1.2\ cm^{-1}$, in good agreement with the Mössbauer results. For *Int1* of the H200N mutant we were able to track the g = 8.20 resonance of the S = 2 multiplet at temperatures up to

100 K. Again, using the relationship between E/D and signal intensity it is readily seen that for the case of the H200N variant with E/D = 0.12, the signal intensity increases accounting for its higher intensity as compared to its H200C analog with E/D = 0.055. The data of Figure 7 indicate that the exchange coupling constant J must be larger than 30 cm^{-1}.

It is worth noting that the g = 8.04 feature of *Int1* is three time narrower than the corresponding parallel-mode EPR signal of H200N-HPCA$_{Int1}$. This would suggest that we should be able to probe the state of the dioxygen in H200C-HPCA$_{Int1}$ by using ^{17}O enriched O_2. Below we calculate ^{17}O hyperfine interactions for the two oxygens of the hydroperoxo and for O_{C1} and O_{C2}. Prior to a discussion of our data, we want to make a few remarks regarding the EPR properties of the $M_S = \pm 2$ non-Kramers doublet of *Int1*.[25,26] The g = 8.04 resonance is observed for a transition within a non-Kramers doublet with uniaxial magnetic properties. At X-band we have $4g_z\beta B/\Delta_{\pm 2} \approx 20$ at resonance, which implies that the eigenstates of the doublet are predominantly $M_S = +2$ and $M_S = -2$ rather than zero field states ϕ^{2s}, and ϕ^{2a}. For describing ^{17}O hyperfine splittings we add the term $\hat{\mathbf{S}}_1 \cdot \mathbf{A}(^{17}O) \cdot \hat{\mathbf{I}}_O$ to eq. 3 where $\hat{\mathbf{I}}_O$ is the spin operator of the ^{17}O nucleus ($I_O = 5/2$). Additionally, in the limit where $\beta B << D$, mixing with $M_S = 0$ and ± 1 states can be neglected and only terms containing S_z are relevant. Replacing S_z by its expectation value $\langle S_z \rangle = \pm 2$, we obtain for each of the two spin levels a nuclear Hamiltonian:

$$\mathcal{H}_{^{17}O} = \pm 2\left(A_{xz}I_x + A_{yz}I_y + A_{zz}I_z\right), \qquad (4)$$

where the A_{iz} are elements of the ^{17}O hyperfine tensor in the (x,y,z) frame; there is no reason to assume that any $\mathbf{A}(^{17}O)$ of *Int 1* is diagonal in (x,y,z). Eq 4 can be written as:

$$\mathcal{H}_{^{17}O} = \pm 2A_{eff}\left(\frac{A_{xz}I_x + A_{yz}I_y + A_{zz}I_z}{A_{eff}}\right) \quad (5)$$

where $A_{eff} = (A_{xz}^2 + A_{yz}^2 + A_{zz}^2)^{1/2}$ is a normalization factor (we have momentarily dropped the ^{17}O label). The coefficients $A_{iz}/A_{eff} = \cos\varphi_i$ can be viewed as direction cosines so that $\hat{\mathcal{H}}_{^{17}O} = \pm 2A_{eff}\hat{I}_n$ with $I_n = \cos\varphi_x I_x + \cos\varphi_y I_y + \cos\varphi_z I_z$. Quantizing along $\hat{I}_n$ then yields for the hyperfine splitting:

$$E_{\pm 2}(m_I) = \pm 2A_{eff}\, m_I = \pm 2(A_{xz}^2 + A_{yz}^2 + A_{zz}^2)^{1/2}\, m_I \quad (6)$$

In an EPR experiment tuned to the g = 8.04 resonance, one measures the quantity A_{eff} . In our S = 2 SpinCount simulations, we can assume that $\mathbf{A}(^{17}O)$ is diagonal in (x,y,z) and use $\mathcal{H}_{^{17}O} = A_{eff}\hat{S}_z\hat{I}_z$, which also yields $E_{\pm 2}(m_I) = \pm 2A_{eff}\, m_I$. In the following section, we develop expressions for the ^{17}O hyperfine tensor for the cases where the oxygen is either an iron ligand (covalent delocalization for the hydroperoxo ligand) or a coordinating ligand with radical character (radical contribution plus covalent delocalization as would apply for the oxygens of O_{C1} and O_{C2}). Using the $\mathbf{A}(^{17}O)$ calculated by DFT in combination with information about the orientation of the easy axis, z, as determined by Mössbauer spectroscopy, we evaluate (in Figures 7 and 9, below) the A-value of eq 6 for four oxygen atoms of *Int1*.

Figure 5B shows parallel mode X-band EPR spectra of *Int1* recorded at 21 K for samples prepared using $^{16}O_2$ (black) and 70% enriched $^{17}O_2$ (purple curve; scaled to match the intensity of the ^{16}O spectrum). Within the noise, both resonances have nearly

the same linewidth (the shoulder on the high field side of the ^{17}O spectrum is probably noise from the background as there is not a corresponding feature on the low field slope of the line). Figure 5C shows the resonance of the ^{17}O enriched sample together with three SpinCount simulations generated using the parameters of Figure 6A and adding the $A_{z,eff}\hat{S}_z\hat{I}_{z,O}$ term in the S = 2 Hamiltonian of eq 3. The green line assumes an obviously too large $A_{z,eff}(^{17}O)$ = 30 MHz (the value of the superoxo species of H200N-4NC$_{Int1}$), the blue line assumes $A_{z,eff}(^{17}O)$ = 17 MHz (the value found for H200N-HPCA$_{Int1}$), and the red line shows a simulation for $A_{z,eff}(^{17}O)$ = 7 MHz which we may take as an upper limit for $A_{z,eff}$ (^{17}O) of *Int1*.

Inspection of Table 1 reveals that the spin Hamiltonian parameters of H200C-HPCA$_{Int1}$ are very similar to those of the HPCA-SQ$^{\bullet}$-Fe(III)-(hydro)peroxo complex, H200N-HPCA$_{Int1}$. For the latter we observed $A_{z,eff}(^{17}O)$ = 17 MHz for the proximal oxygen of the hydroperoxo ligand. The same ^{17}O splitting was observed when the O_{C1} was enriched with ^{17}O.[1] The lack of observable $A_{z,eff}(^{17}O)$ splitting in H200C-HPCA$_{Int1}$ does not imply that the H200C intermediate is not a semiquinone complex. In fact, such an assignment is supported by our DFT and ^{17}O hyperfine analysis. The following is a brief comment on why our result for $A_{eff}(^{17}O)$, without a detailed DFT analysis, does not rule out the possibility that *Int1* is a high-spin ferric superoxo complex.

There are two studies of superoxo radicals for which precise ^{17}O A-tensors have been reported. Chiesa et al.[23] studied an (η^2-O_2^-)/MgO system and determined **a**(^{17}O) = (-213, +20.2, +23.2) MHz, and Pietrzyk et al.[24] reported a comparable **a**(^{17}O) = (-166, +28.9, +29.4) MHz for an (η^2-O_2)/Ni ZSM-5 zeolite. In these two examples the large

negative component of the a-tensor component results from an unpaired electron in a 2p π^x_g orbital for which the (negative) spin-dipolar contribution of the ^{17}O a-tensor is large along x. This component also has a negative contribution from the Fermi contact term; the quoted $\mathbf{a}(^{17}O)$ is the intrinsic magnetic hyperfine tensor in the $S_R = ½$, $\mathbf{S}_R \bullet \mathbf{a}(^{17}O) \bullet \mathbf{I}_O$ term. For the superoxo complex of H200N-4NC $_{Int1}$ we found $a_{eff}(^{17}O) \approx 180$ MHz (in ref. 1 the large component was along the easy axis, z, hence we used the index z). Since the value of $a_{eff}(^{17}O)$ is comparable to the largest component of the above cited superoxo radicals we may assume that that the largest component of the ^{17}O hyperfine tensor is (approximately) along the "easy" axis the exchange coupled Fe^{III}-superoxo complex, allowing us to use $a_{eff}(^{17}O) = a_z(^{17}O)$. Owing to the antiferromagnetic exchange, the ^{17}O hyperfine interaction appears in the S = 2 representation as $A_z(^{17}O) = (-1/6)a_z(^{17}O)$, i.e. the interaction is scaled by the (-1/6) spin projection factor. The absence of observable ^{17}O broadening for *Int1* could be interpreted in two ways. Either *Int1* does not contain a superoxo radical (as suggested by the DFT results discussed below) or the easy axis, z, of H200C-HPCA$_{Int1}$ is essentially perpendicular to the direction of the largest component of $\mathbf{a}(^{17}O)$. (NB: Note that the zero-field splitting parameters of the H200N-4NC$_{Int1}$ superoxo complex and H200C-HPCA$_{Int1}$ have opposite signs ($D_1 = -0.6$ cm^{-1} vs $+1.2$ cm^{-1}). This suggests, but does not prove, that the easy axes in the two complexes might be orthogonal).

On the other hand, if H200C$^{HPCA}_{Int1}$, like H200N$^{HPCA}_{Int1}$, were an Fe^{III}(hydro)peroxo complex coupled to a substrate radical moiety, the experiment of Figure 5 would yield ^{17}O hyperfine splitting from the enriched peroxo ligand. This hyperfine structure would reflect covalent delocalization of α-spin density from the iron

to the proximal oxygen, described by the transferred hyperfine term $S_{1z}\, a_{eff}(^{17}O)\, I^{O}_{z}$. When referring to the S = 2 state, this term is modified by the spin projection factor (+7/6) to give $S_z\, A_z(^{17}O)$, with $A_z(^{17}O) = (+7/6)a_{eff}\,(^{17}O)$ to be used in eq 4. In the following section we give detailed expressions, and provide an explanation for our observations as well as our conclusions.

DFT analysis of *Int1*. A number of equi-electronic structures have been analyzed by DFT to determine their suitability as formulations of *Int1*. The models investigated include hydroperoxo and superoxo species in two substrate protonation states (i.e. protonated versus deprotonated). Among the OOH species, we have considered models in which either the proximal or distal oxygens are protonated.

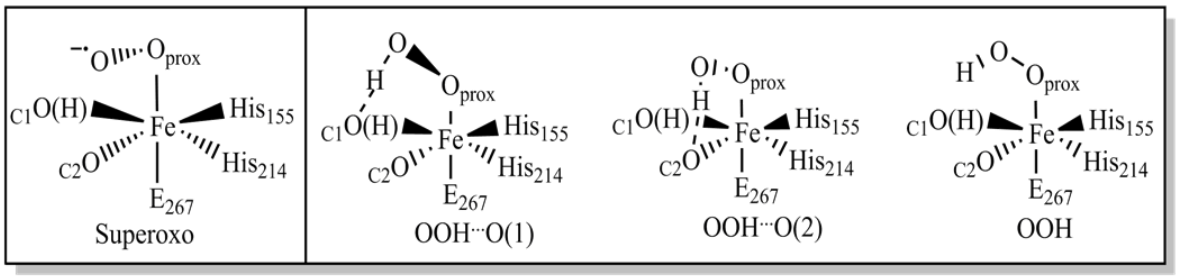

Figure 8. Cartoon representations of the various conformers considered as potential models for *Int* 1. Additional discussions on models varying in size are summarized in Figure 9.

Distal hydroperoxo models for Int 1. Three computational models for *Int* 1 were studied (Models I, II, III of Figure 9). The models were derived from the crystal structure of the ES complex and consisted of the Fe and its facial triad (His155, His214, Glu267) with terminal atoms frozen, as well as HPCA substrate and a hydroperoxo ligand. Also included were several second sphere residues whose positions were fixed as in the ES structure, and water 1061 of which the oxygen was fixed while the hydrogens were

allowed to optimize freely to account for hydrogen bonding interactions with the substrate. Herein we refer to the various models as Model I, II, and III, which are distinguished by the number of atoms included in the calculations. The models are depicted in Figures 7 and 8.

Model I includes Arg243, Arg293, Asn157 (with flexible NH_2 protons), Cys200, Trp192, His248, Tyr257, two additional crystallographic waters, and HPCA substrate. It is worth noting that in this model, the carboxylate group of HPCA is deprotonated and forms a salt bridge to one of the Arg residues. Two protonation states were considered for the coordinating oxygen atoms of the substrate, O_{C1} (closest to Cys200) and O_{C2} (hydrogen bonded to Tyr257); one in which both oxygens were both deprotonated and one in which only O_{C1} was protonated. Interestingly, DFT calculations and spin distribution analysis of Model I Fe^{III}–radical states revealed that the majority of unpaired spin density was delocalized out of the catechol ring with the radical predominantly located on the salt-bridge-forming residue, Arg243. This finding raises serious concerns regarding effects on reactivity for this model. After thorough analysis, we have concluded that this discrepancy may be a consequence of an incomplete description of the second coordination sphere (i.e. due to the absence of hydrogen bonding partners in the vicinity of Arg243 that were not included in the calculation. To address this concern, a second model was introduced (Model II).

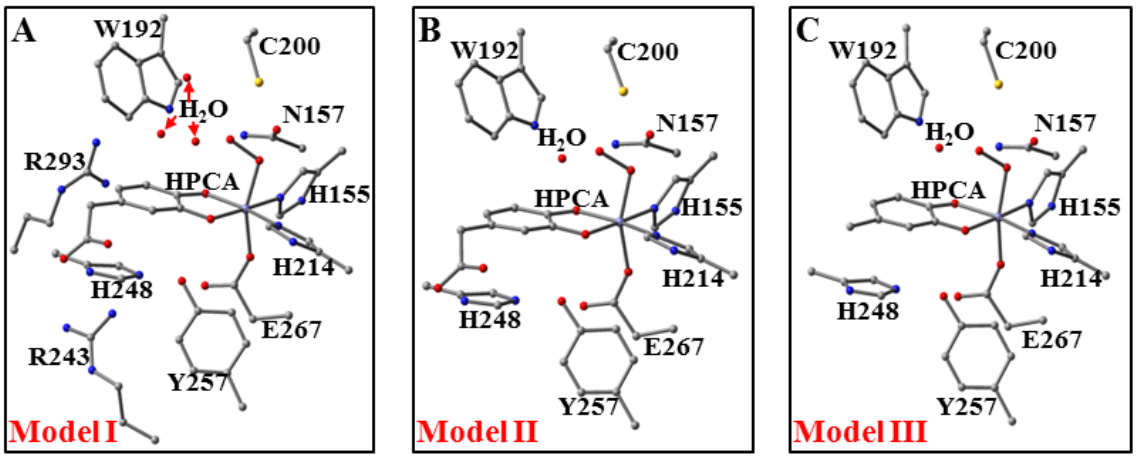

Figure 9. The active site of DFT models for *Int* 1, shown in ball-and-stick representation. Panel **(A)** shows the full OOH model including second- and third-coordination sphere residues Y257, H248, N157, C200, W192, R243, R293, and three crystallographic waters (from the ES crystal structure) adjacent to the active site; referred to as Model I in the text. Panel **(B)** shows the OOH model for *Int* 1 where residues R243, R293, and two of the crystallographic waters have been removed; referred to as Model II in the text. Panel **(C)** shows the same model as in **(A)** and **(B)**, but the substrate carboxylate tail has been truncated and replaced by a methyl group.

Model II was constructed to force the spin density back onto the substrate by removing the two Arg residues (and two nearby waters) from Model I. The oxygen atoms of the carboxylate tail of the HPCA substrate were fixed from the geometry optimized structure of Model I to mimic the steric and electrostatic constraints of the salt bridge and second-to-third coordination sphere of the enzyme while removing the potential for extended delocalization of the spin density onto the arginines. Property calculations for Model II systems yielded solutions for which the spin density was predominantly localized on the oxygen atoms of the HPCA carboxylate tail rather than delocalized across the atoms of the substrate ring. Efforts to force the radical onto the substrate ring required a third model, Model III.

The primary difference between Models II and III is that the latter contained a truncated substrate, with the carboxylate tail replaced by a methyl group. Optimizations

of the system of Model III had the added constraint that one of the hydrogen atoms of the methyl-modified HPCA tail was frozen in space to model the preferred orientation of the ring and tail based on calculations of Models I and II. Indeed, calculations for Model III resulted in a solution with substrate-radical character localized on the catechol ring and the iron coordinating atoms. We have analyzed key features of each model to distinguish between potential conformations of *Int1*. Of particular interest are the spin densities on the substrate O_{C1} and O_{C2} atoms, as they may give rise to ^{17}O magnetic hyperfine broadening observable in parallel mode EPR spectra of a sample of *Int1* prepared with ^{17}O-enriched substrate. The spin populations of the oxygen atoms in the broken symmetry calculations, as obtained in Models I and II, have the same (by definition *positive*) sign as the spin populations of the iron and belong to the spin system of the iron. In calculations of Model III, however, the oxygen atoms have a large *negative* spin density in the π lobes that are part of the substrate radical orbital while retaining some *positive*, albeit smaller, spin densities in the σ lobes. This latter observation is indicative of a fractional (iron-radical) heritage of the spin densities at O_{C1} and O_{C2}, suggesting that a description of the magnetic hyperfine interactions of the ^{17}O nuclei requires a spin Hamiltonian that includes terms for the couplings of the I(^{17}O) nuclear spin with the electronic spins of both the iron and the radical (*cf.* Methods and Materials).

Energies, J values, and electric hyperfine parameters for distal hydroperoxo models. Tables 2-4 list the DFT results obtained for Models I-III for the relative energies, exchange-coupling constants, and ^{57}Fe electric hyperfine parameters, respectively. For all Model–Protonation combinations, three conformations were identified with the axial hydroperoxo being hydrogen bonded to (a) O_{C1} in the first conformation, (b) O_{C2} in the

second conformation, and (c) neither O_{C1} or O_{C2} in the third conformation (dihedral angle H-O-O-Fe ≈ 150°). The relative energies of the conformations are given in Table 2 for each protonation state.

Table 2. Relative energies for distal hydroperoxo conformations [a]

Substrate	Conformer	Model I	Model II	Model III
Deprot. [c]	$OOH\cdots O_{C1}$	0	0/0 [b]	0
	$OOH\cdots O_{C2}$	2737	2792/1329 [b]	2593
	OOH	2819	2537/502 [b]	1169
Prot. [d]	$OOH\cdots O_{C1}$	678	1108	1501
	$OOH\cdots O_{C2}$	2198	2415	2275
	OOH	0	0	0

[a] Relative energies of broken symmetry states in wavenumbers using B3LYP/6-311G.
[b] Results obtained with TZVP for 6-311G optimized structure.
[c] O_{C1} and O_{C2} of substrate are deprotonated.
[d] O_{C1} is protonated, O_{C2} is deprotonated.

Table 2 shows that one conformation is consistently lowest in energy for all three models. The lowest conformations are $OOH\cdots O_{C1}$ and OOH for the deprotonated and protonated substrates, respectively (first and sixth row). On this criterion alone, these conformers appear to be the best candidates for *Int1*. However, both energy order and energies of the higher-lying conformations display a significant dependence on the model. As an example, the middle column (Model II) of Table 2 shows the results obtained with a basis set that includes polarization functions, TZVP. These calculations resulted in lower excitation energies for both excited conformations (Model II, upper half). In addition to the basis set dependence, there is the distinct possibility that the hydroperoxo-H in the OOH conformation is engaged in interactions with parts of the

structure not considered in our models. Given these uncertainties, it seems prudent at this juncture not to dismiss any of the conformations at higher energy as potential formulations of *Int1*. In particular, the OOH conformation for Model II presents a plausible alternative.

Comparison of exchange-coupling constants. The ligands of paramagnetic transition-metal ions are known to acquire spin density by covalent delocalization of the ligand electrons into the metal 3d orbitals. In the case of the metal–ligand interactions of a high-spin Fe^{III}, which has a half-filled 3d shell containing 5 spin-up electrons, the spin polarization of a ligand can only be due to the transfer of spin-down density into the vacant spin-down orbitals of the metal. This transfer would then lead to a ligand spin density with the same sign as that of the metal; transfer of spin-up density is obviously forbidden as the spin-up orbitals of high-spin Fe^{III} are occupied. Thus, if a spin-down electron is removed from a ligand orbital to obtain a ligand radical that is ferromagnetically coupled to the metal spin, this orbital will no longer contribute to the ligand-to-metal transfer. Alternatively, if a spin-up electron is removed to obtain an antiferromagnetic (actually, a broken symmetry) state, the transfer is still allowed. As transfer lowers energy, the energy of the antiferromagnetic state becomes lower than the energy of the ferromagnetic state, effectively leading to an antiferromagnetic coupling of the ligand and metal spins that is expressed by $J > 0$ in the convention $J\widehat{\boldsymbol{S}}_1\widehat{\boldsymbol{S}}_2$. This narrative provides a simple explanation for the trends in the J values listed in Table 3.

Table 3. Exchange-coupling constants for distal hydroperoxo conformations [a]

Substrate	Conformer	Model I	Model II	Model III
Deprot. [d]	OOH···O_{C1}	2.3	13.4/18.1 [b]	4.3
	OOH···O_{C2}	32.6	63.5/78.4 [b]	12.9
	OOH	103.6 (175.4)[b]	147.0/174.7 [b]	167.6
Prot. [e]	OOH···O_{C1}	–0.5	–2.8	–16.0[f]
	OOH···O_{C2}	–0.8	–2.5	–4.9[f]
	OOH	–0.7	–2.8	–124.8

[a] J in wavenumbers in $J\widehat{\boldsymbol{S}}_{\boldsymbol{1}}\widehat{\boldsymbol{S}}_{\boldsymbol{2}}$ convention evaluated from the vertical S = 3 excitation energy at the optimized BS structure obtained with B3LYP/6-311g.
[b] Without Elena's water.
[c] Numbers obtained with B3LYP/TZVP.
[d] O_{C1} and O_{C2} of substrate are deprotonated.
[e] O_{C1} is protonated, O_{C2} is deprotonated.
[f] Solutions with large spin densities on His248.

Addition of a positive charge, perhaps by protonation of the substrate, suppresses delocalization and consistently results in small and/or ferromagnetic J values (lower half of Table 3). Despite weaker sequestration of electron density than that from covalent O-H bonds (lower half of the Table 3), hydrogen bonds formed between the hydroperoxo and the coordinating oxygen atoms of the substrate (listed in the first two rows of Table 3) lead to J values that are smaller than those obtained when these hydrogen bonds are absent (third row). Table 3 shows that this reasoning holds for all three models. Our calculations suggest that antiferromagetic coupling is further enhanced by removal of crystallographic water 1061 and its hydrogen bonding interaction with O_{C1} (see J value in parentheses in Table 3).

Similarly, the presence of the salt bridge in Model I explains the smaller calculated J values as compared to those calculated for Model II (see rows 1-3).

Furthermore, the observation that calculated J values for Model III are smaller than those of Model II (first and second rows of Table 3) is readily explained by the electron donating capacities of the deprotonated substrate radicals in Model I versus Models II/III which retain monoanionic and dianionic character, respectively. The third row appears to be a marginal exception, and required a more detailed analysis. Interestingly, the $OOH\cdots O_{C1}$ conformation yielded consistently lower J values than the $OOH\cdots O_{C2}$ conformation (compare first and second row of Table 3), which suggests that the hydrogen bond between the hydroperoxo and O_{C1} has a larger effect on the redox active orbital of the substrate than a hydrogen bond to O_{C2}. The explanations presented here focus on the antiferromagnetic term J_{AF} in the expression $J = J_F + J_{AF}$, as well as the effects of protonation and hydrogen bonding on the denominator, U, in the second-order expression $J_{AF} \sim \langle h \rangle^2/U$. The J_F term appears to be particularly prominent in the last row for Model III and is likely due to the spin delocalization of the substrate and metal into orthogonal p-orbitals of the coordinating O atoms.

The experimental lower bound, $J > 30\ cm^{-1}$, clearly excludes the structures listed in the lower half of Table 3 as formulations of *Int1*. Therefore, if *Int1* were a distal hydroperoxo species, the substrate must be deprotonated. Among the conformations in the upper half of Table 3, only those in the second and third rows appear to be admissible as candidates for *Int1*. This finding, along with the energy analysis that suggests the third row is energetically favored over the second in Table 2, is consistent with a conformation for *Int1* that is closest to the OOH conformer.

Table 4 lists the ^{57}Fe electric hyperfine parameters for the six distal-protonated hydroperoxo models. The isomer shifts listed in the table are typical for high spin Fe^{III}

and are all in good agreement with experiment. Therefore, with differences in the calculated δ values being so small, it is not possible to select or exclude potential models of *Int1* on this property alone. However, the quadrupole splittings in Table 4 appear to be more discerning than the isomer shifts, with the values in the lower half of the table being consistently larger than the experimental value for $|\Delta E_Q|$ (0.97 mm/s). This observation further corroborates the conclusion drawn from analysis of the J values, namely that the substrate bound in *Int1* must be deprotonated. The ΔE_Q values in the second and third rows of Table 4 show a satisfactory agreement with the experimental value, especially for Models I and II. For Model II, Table 4 also lists ΔE_Q and η values obtained with the basis set TZVP that includes polarization functions. The dependence of these parameters on the choice of basis set appears to be rather small.

Table 4. ^{57}Fe electric hyperfine parameters from DFT for distal hydroperoxo conformations [a]

Substrate	Conformer	Model I			Model II			Model III		
		δ	ΔE_Q	η	δ	ΔE_Q	η	δ	ΔE_Q	η
Deprot [c]	OOH···O_{C1}	0.53	1.075	0.358	0.53	1.117 1.064[b]	0.379 0.567[b]	0.51	−1.487	0.906
	OOH···O_{C2}	0.54	0.801	0.872	0.54	−0.831 −0.826[b]	0.977 0.741[b]	0.51	−1.249	0.236
	OOH	0.54	0.854	0.809	0.55	0.873 −0.866[b]	0.811 0.929[b]	0.51	−1.126	0.284
Prot [d]	OOH···O_{C1}	0.50	1.548	0.168	0.49	1.532	0.288	0.48	1.536	0.592
	OOH···O_{C2}	0.51	1.699	0.896	0.50	−1.713	0.919	0.49	−1.756	0.699
	OOH	0.51	1.359	0.134	0.50	1.347	0.061	0.49	1.418	0.674

[a] δ and ΔE_Q in mm/s; obtained for the BS state with B3LYP/6-311G.
[b] Values obtained with basis TZVP by single point calculations for the 6-311G optimized geometry in the BS state.
[c] O_{C1} and O_{C2} of substrate are deprotonated.
[d] O_{C1} is protonated, O_{C2} is deprotonated.

The ΔE_Q and η values of Table 4 are quoted in a 'proper' coordinate frame for which z is along the largest component of the EFG. Use of a proper coordinate frame can be quite misleading for large η values ($\eta \approx 1$) in the limit ($V_{zz} \approx -V_{yy}$), where subtle changes render either the negative ($\Delta E_Q < 0$) or positive ($\Delta E_Q > 0$) largest in magnitude. For example, in Table 4, row 3, Model II the sign of ΔE_Q changes from positive to negative upon switching to the TZVP basis set. In either case, as in all cases of Table 4, the largest component of the EFG is roughly along the O-Fe-O_{E267} direction. Comparing the values (TZVP in italics) for $eQV_{xx}/2$; $eQV_{yy}/2$; $eQV_{zz}/2$ = {*+0.024*, -0.075*; +0.649,* +0.790; *-0.672*, -0.716} shows that the differences in the individual components are rather small. In this limit, a change in the sign of ΔE_Q can be brought about by minor changes in the principal values of the EFG that render either the positive or negative component to be largest in magnitude.

Proximal hydroperoxo models for *Int1*. Calculations for the proximally protonated hydroperoxo species were performed for Model I with the proton now on the proximal oxygen. The geometry optimizations converged to one conformation with a dihedral angle H-O-O-Fe $\approx 140°$. The results for the ^{57}Fe electric hyperfine parameters and the exchange-coupling constant, J, between the substrate radical and the high-spin iron(III) are listed in Table 5 for both the deprotonated substrate ($HPCA^{3-}$) and the O_{C1}-protonated form. The protonated form has a small ferromagnetic J, similar to the distal-protonated conformer. This observation leaves only the deprotonated form, which has admissible J and ΔE_Q values (see Table 5), as a viable candidate for *Int1*. However, the value $\delta = 0.60$ mm/s for the deprotonated species appreciably exceeds the experimental value for the isomer shift (0.48 mm/s). Together, the large value for the relative energy

and the 0.12 mm/s difference in calculated versus experimental isomer shifts excludes the formulation of *Int1* as a proximally protonated hydroperoxo.

Table 5. Parameters from DFT for proximal hydroperoxo species [a]

Substrate	δ	ΔE_Q	η	J [b]	E [c]
Deprot.	0.60	0.894	0.731	65.5	5199
Prot.	0.58	1.644	0.319	–1.1	3863

[a] δ and ΔE_Q in mm/s; obtained for the BS state with B3LYP/6-311G.
[b] J in wavenumbers in $J\widehat{\boldsymbol{S}}_{\boldsymbol{1}}\widehat{\boldsymbol{S}}_{\boldsymbol{2}}$ convention evaluated from the vertical S = 3 excitation energy at the optimized BS structure obtained with B3LYP/6-311g.
[c] Energy in wavenumbers relative to the energy of the corresponding lowest deprotonated/protonated substrate conformation for Model I in Table 2.

Superoxo models for *Int1*. Our experimental data do not rule out the possibility that *Int1* is a superoxo complex as the easy axis could be along a minor component of $\mathbf{A}(^{17}O)_{superoxo}$. DFT calculations for the superoxo species were performed for a model similar to Model I, but with an O_2 moiety instead of a hydroperoxo functional group at the position *trans* to E267. The results for the ^{57}Fe electric hyperfine parameters and the exchange-coupling constant, J, between the superoxo radical and the high-spin Fe^{III} are listed in Table 6 for both the deprotonated substrate ($HPCA^{3-}$) and the O_{C1}-protonated forms.

The calculations resulted in an unpaired electron of the superoxo moiety in the out-of-plane (Fe-O-O) orbital π^*_{out}, and the electron reducing O_2 to $O_2^{-,\bullet}$ in the in-plane orbital π^*_{in}. This electronic configuration provides a favorable condition for overlap of the L–M resonance of the spin-down π^*_{in} electron in the ferromagnetic state, which leads to a strong ferromagnetic coupling between the iron and the superoxo radical (last column of Table 6). The strongly favored S = 3 ground state for the superoxo model

predicted by the calculations disagrees with the S = 2 ground state observed for *Int1*. This result, along with the fact that both the calculated ^{57}Fe isomer shifts and quadrupole splittings for the superoxo models (see Table 6) are significantly larger than the experimentally observed values for *Int1*, implies that we can exclude a formulation of *Int1* as a superoxo species. This conclusion is consistent with the absence of observable hyperfine broadening in the parallel mode EPR spectra of *Int1* for samples prepared using ^{17}O enriched O_2 (see discussion below).

Table 6. Parameters from DFT for superoxo species [a]

Substrate	δ	ΔE_Q	η	J [b]	E
Deprot.	0.63	−1.338	0.711	−158.2	–
Prot.	0.70	2.022	0.731	−131.5	7068 [c]

[a] δ and ΔE_Q in mm/s; obtained for the BS state with B3LYP/6-311G.
[b] J in wavenumbers in $J\widehat{\boldsymbol{S}}_{\boldsymbol{1}}\widehat{\boldsymbol{S}}_{\boldsymbol{2}}$ convention evaluated from the vertical S = 3 excitation energy at the optimized BS structure obtained with B3LYP/6-311g.
[c] Energy in wavenumbers relative to the energy of the corresponding lowest deprotonated substrate conformation for Model I in Table 2.

If a ferromagnetic superoxo state can be trapped for the H200C variant one would look for a parallel mode EPR feature characteristic of an S = 3 system. Possible signals might arise from the $M_S = \pm 3$ non-Kramers doublet near g = 12 (difficult if E/D is small) or the $M_S = \pm 2$ doublet near g = 8. However, this state would most profitably be explored by Mössbauer spectroscopy.

Evaluation of ^{17}O hyperfine interactions. In this section we assemble the expressions required to obtain $A_{eff}(^{17}O)$, the effective component of the ^{17}O magnetic hyperfine interactions. Although line broadening was not observed in our experiment, the data are quite valuable once they are analyzed with the results of the DFT calculations.

The magnetic hyperfine interactions of the ^{17}O nuclei of oxygen atoms that are part of a ligand radical (R, here superoxo or a semiquinone) have been described by the Hamiltonian

$$\widehat{\mathcal{H}}_{\mathrm{hf}} = \hat{\mathbf{I}}_{\mathrm{O}} \cdot \left(\mathbf{a}_{\mathrm{R}} \cdot \hat{\mathbf{S}}_{\mathrm{R}} + \mathbf{a}_{\mathrm{Fe}} \cdot \hat{\mathbf{S}}_{\mathrm{Fe}}\right). \tag{7}$$

The first term, involving the radical spin S_R = ½ represents the coupling of the unpaired radical electron to the ^{17}O nucleus. The second term describes the interaction of the ^{17}O nucleus with spin density induced by covalent delocalization of unpaired electrons of the iron onto the oxygen. If only the Fermi contact interaction is considered, the coupling tensors are isotropic, a_R and a_{Fe}, and the internal magnetic field at the ^{17}O nucleus can be expressed as

$$g_n \beta_n B_{\mathrm{int}}^{\mathrm{F}} = (a_{\mathrm{R}} + 5a_{\mathrm{Fe}})/2 \tag{8}$$

in the ferromagnetically (F) coupled state (S = 3, spins of radical and iron are parallel) and as

$$g_n \beta_n B_{\mathrm{int}}^{\mathrm{BS}} = (-a_{\mathrm{R}} + 5a_{\mathrm{Fe}})/2 \tag{9}$$

in the broken symmetry state (BS) in which the radical spin has been flipped. Substituting for $B_{\mathrm{int}}^{\mathrm{F}}$ and $B_{\mathrm{int}}^{\mathrm{BS}}$ the DFT values for the Fermi contact field in the two states yields two equations from which one obtains the DFT values for a_{R} and a_{Fe}, respectively. In an analogous manner one can extract the spin-dipolar (SD) tensors $\mathbf{a}_{\mathrm{R}}^{\mathrm{SD}}$ and $\mathbf{a}_{\mathrm{Fe}}^{\mathrm{SD}}$ provided the principal axes of the SD tensors obtained for the two states are collinear, an assumption supported by the DFT calculations of the systems considered here. From this analysis one obtains the calculated ^{17}O magnetic hyperfine tensors in the uncoupled representations $\hat{\mathbf{S}}_{\mathrm{Fe}} \cdot \mathbf{a}_{\mathbf{Fe}} \cdot \hat{\mathbf{I}}_{\mathbf{O}}$ and $\hat{\mathbf{S}}_{\mathrm{R}} \cdot \mathbf{a}_{\mathbf{R}} \cdot \hat{\mathbf{I}}_{\mathbf{O}}$. Since the data were analyzed using the S = 2 Hamiltonian

(eq 3) of the coupled system one has to multiply the local tensors with the appropriate spin projection factors to obtain $\mathbf{S} \cdot \mathbf{A}(^{17}\mathrm{O}) \cdot \mathbf{I_O}$ where

$$\mathbf{A(^{17}O)} = -(1/6)\mathbf{a_R} + (7/6)\mathbf{a_{Fe}} \qquad (10)$$

As indicated above, the calculated J, ΔE_Q and η allowed us to narrow the choice for a viable *Int1* model, namely the models (OOH) listed in rows 3 of Tables 3 and 4. For these models we have calculated A(^{17}O) for the two oxygens of the hydroperoxo ligand, which were enriched with ^{17}O in the experiment of Figure 5. For future reference the calculated A(^{17}O) for the coordinated O_{C1} and O_{C2} of the substrate radical was added. Gaussian was used to calculate the components of A(^{17}O) in the principal axis frame (x′y′z′) of the EFG tensor for Models I, II and III (row 3 of Table 4). Given that the Mössbauer analysis relates the principal axis frames of the EFG and ZFS tensors (α = 50°, β = 70° of Table 1), one can calculate the Cartesian components of $A_{DFT}(^{17}O)$ in (xyz) and then determine the splitting constant A_{eff} by using eq 6. It will be quite instructive to fix β at 70° and plot A_{eff} along the azimuth α.

Figure 10 shows the spin densities for Model III, the model that best describes our data. For this model Figure 11 shows a plot of A_{eff} for O_{prox} and O_{distal} of the hydroperoxo ligand and for O_{C1} and O_{C2} of the HPCA ligand. There is a narrow range of α values, namely α ≈ 35° - 65°, for which A_{eff} of O_{prox} assumes values that are compatible with our experimental data, namely $A_{eff} \leq 7$ MHz, and interestingly the Mössbauer result α ≈ 50° falls into this range. Note also that for α ≈ 150° one would observe A_{eff} values for O_{C1} near 17 MHz. The calculated A_{eff} values for O_{C1} and O_{C2} are quite similar, but the two curves in the A_{eff} vs α plot are displaced by Δα ≈ 90° (the O_{C1}-Fe-O_{C2} angle is near 90°). (NB or footnote: For H200N-$HPCA_{int1}$ the value A_{eff} ≈ 17 MHz for both O_{prox} and O_{C1}

was obtained;[4] the quality of the *Int1* Mössbauer spectra for the H200N mutant is inferior to those reported here, so we do not have good values for angles α and β are not available). As expected, $A_{eff} < 4$ MHz for O_{distal} would be too small to cause measurable broadening of the g = 8.04 resonance. The corresponding A_{eff} plots of Models I and II are quite similar to that of Model III except that the minima for O_{prox} occur near $\alpha = 20°$ (see Figures 9 and S3).

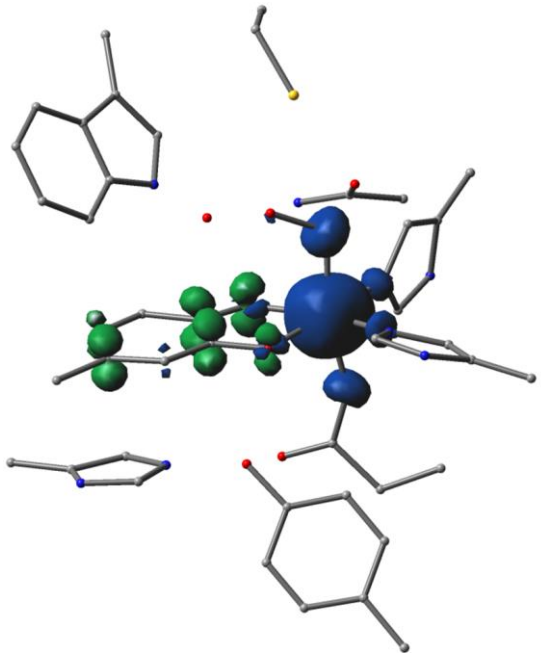

Figure 10. Spin density plot for conformer OOH of Model III. Regions of blue correspond to spin-up density, and regions of green correspond to spin-down density.

Mechanistic considerations. The HPCA substrate binds the Fe^{II} center of HPCD as a monoanion that is protonated at O_{C1}, with both the O_{C2} and carboxylate deprotonated to form the enzyme substrate (ES) complex. We may assume that the ES complex is converted to a superoxo–Fe^{III} complex upon binding molecular oxygen. The putative superoxo complex, perhaps too short-lived to be trapped on the millisecond time scale, is the precursor to *Int1*, which was established here to be a hydroperoxo species in which

the HPCA is coordinated to the iron in the deprotonated form, $HPCA^{3-}$. Assuming that the substrate has retained the O_{C1}-proton in the formation of the superoxo species, the transformation from the superoxo species to *Int1* is most elegantly described by transfer of a proton and an electron from the substrate to the superoxo ligand (proton-coupled electron transfer, PCET). Although a somewhat contrived scenario in which deprotonation of the substrate and protonation of the superoxo ligand involve different protons cannot be ruled out, the present analysis will focus on the PCET process between the substrate and superoxo moiety. For the sake of simplicity, we limit the present discussion to a model in which the second sphere residues Asn157 and Tryp192 have been removed from Model III. The results of the DFT calculations are summarized in Figure 12.

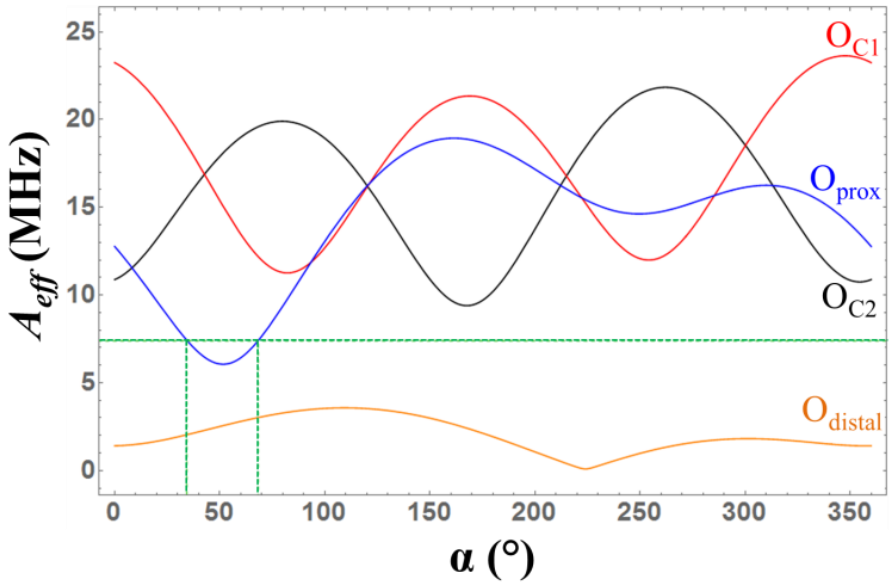

Figure 11. Plot of A_{eff} calculated for O_{C1} and O_{C2} of the HPCA substrate, and O_{prox} (proximal to the iron) and O_{distal} of the hydroperoxo ligand. The green dashed line indicates the experimentally determined upper limit for A_{eff} for the proximal hydroperoxo oxygen. The plot was prepared using β = 70°. The DFT-calculated principal axis components of $\mathbf{A}(^{17}O_{prox})$ are [-5.8, -16.2, -21.0] MHz.

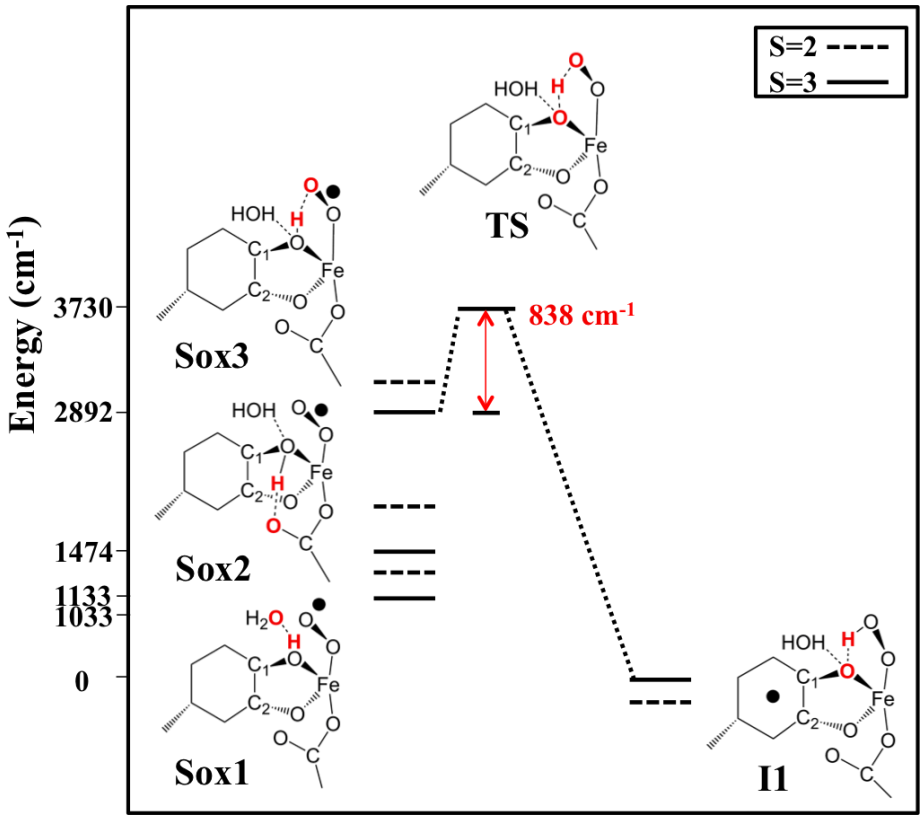

Figure 12. Diagram depicting the DFT calculated transformation from the superoxo species to *Int1* as described by transfer of a proton and an electron from the substrate to the superoxo ligand (proton-coupled electron transfer, PCET). Solid lines indicate the septet ground state and dashed lines indicate the quintet ground state. Atoms highlighted in red are involved in hydrogen bonding interactions that facilitate this transfer.

The figure shows the energies (solid lines) for the S = 3 state (ferromagnetically coupled iron–radical states) of the superoxo–Fe^{III} complex (left) and the HOO–Fe^{III}–substrate radical complex, *Int1* (right). Also shown are energies (dashed) for the antiferromagnetic states (S = 2) obtained for the J values determined from broken-symmetry calculations. Just as shown above for *Int1*, the superoxo species has three conformations distinguished by different hydrogen-bonding (HB) patterns. The O_{C1}-H donates a HB to water 1061 in the ground conformation $\mathbf{S_{ox1}}$, to the distal O of Glu267 in the next higher-energy conformation $\mathbf{S_{ox2}}$, and to the distal O of superoxo in the highest

energy conformation $\mathbf{S_{ox3}}$ (see Figure 12). $\mathbf{S_{ox3}}$ is of special interest as it places the O_{C1}-proton in an ideal position for making the transfer to the superoxo and is highest in energy due to the elastic strain associated with the deformations required to bring the proton donor (O_{C1}) and acceptor (distal O of superoxo) atoms together to form the hydrogen bond; we will refer to the atoms as O_D and O_A, where the subscripts D and A refer to donor and acceptor, respectively. A brief discussion of both the ET and PT aspects of the PCET process and their relationship follows. The transition state (**TS**) for S = 3 was determined to be about 800 cm^{-1} above the initial state of the transfer (i.e., the O_{C1}-H···O_{sox} conformation) and has a structure in which O_D-H > H-O_A (see Table 6). In moving from O_D to O_A, the proton raises the energy of the redox active π-type donor orbital on the substrate and lowers the out-of-plane π^*_{out} acceptor orbital on the superoxo (see Figure 12A). This alteration leads to a level crossing and results in transfer of the electron. Ideally, the proton coordinate at the crossing depends on the initial energy difference and the difference of the slopes. The path of the transferring proton places it into the lobe of the donor π orbital and in the nodal plane of the π^*_{out} acceptor orbital, creating a configuration that favors coupling of the proton to an electron in the π lobe of the donor orbital. A number of observations can be made from the Mulliken spin densities (SD) listed in Table 7. (1) The Mulliken spin density of iron at the TS is nearly equal to those of iron at the initial and final states of the process. The electron transfer process is thus best described as a direct transfer between the donor and acceptor that does not proceed sequentially as in the step-wise process donor → Fe → acceptor. (2) The ^{57}Fe isomer shift (see Table 4) calculated at the TS is only marginally higher than at the terminal points, confirming that the iron remains in the ferric state during the transfer.

(3) The process involves a net population of 1.15 – 0.35 ≈ 1.17 – 0.38 ≈ 0.8 electrons; the complementary 0.2 electrons remain on the iron. (4) At the TS, 1.15 – 0.96 ≈ 0.61 – 0.38 ≈ 0.2 electrons have been transferred, with the major part of the charge, 0.8 – 0.2 = 0.6, still to go, showing that the electron transfer lags the proton transfer. (5) The same conclusion can be drawn from the distribution of the orbital containing the transferring β electron (spin-down-HOMO – 1, shown in Figure 13B) over the substrate donor, the iron intermediary, and the O_2 acceptor (see last row of Table 7). In general, the transition states of the ET and PT parts of a PCET process do not coincide. In the present case, the crossing of the donor and acceptor levels (Figure 13A), where the populations of the donor and acceptor orbitals are about equal, occurs *after* the TS of the overall process, suggesting that the TS of the ET is located after the TS (level crossing) of the PT on the internal reaction coordinate (IRC) (*cf.* discussion below). The contour plot of the transfer orbital at the TS (shown in Figure 13B) reveals a linear combination of the π_z donor orbital of the substrate, the d_{xz} iron orbital, and the π^*_x acceptor orbital of the superoxo. The plot nicely illustrates the role of the iron orbital in connecting the orthogonally oriented, and therefore poorly interacting, π_z donor and π^*_x acceptor orbitals by forming bonding combinations with both these redox active ligand orbitals.

Table 7. Spin population analysis of PCET between substrate and superoxo ligands.

State	**Configuration**	**Substrate**	**Fe**	**O_2**	**Rest**	**Sum**	**δ (mm/s)**	**O_D-H[a]**	**H-O_A[a]**
Initial	H-Sub Fe^{III} $O_2^{\bullet}$	0.38	4.22	1.15	0.29	6	0.56	1.037	1.507
TS		0.61	4.18	0.96	0.26	6	0.58	1.273	1.163
Final	$Sub^{\bullet}$ Fe^{III} OOH	1.17	4.22	0.35	0.25	6	0.53	1.930	0.989
β HOMO – 1 at TS		–0.59	–0.22	–0.12	–0.07	–1	–		

[a] in Å.

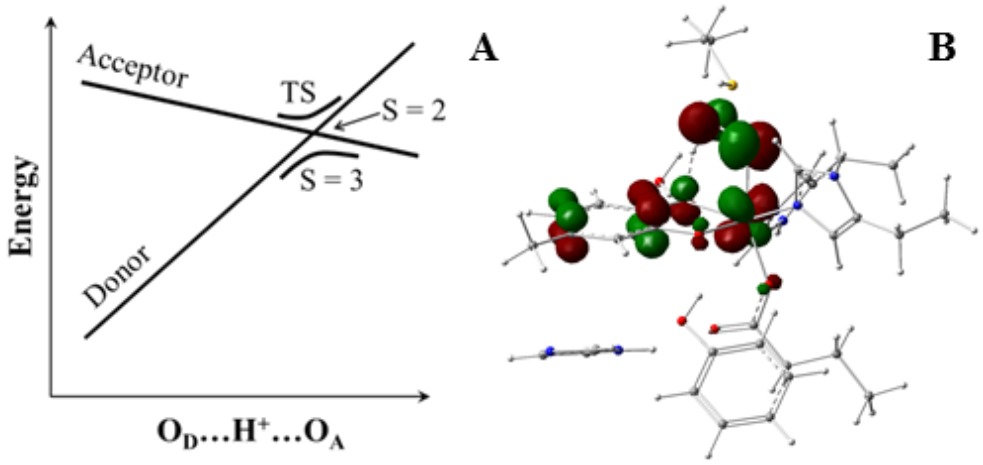

Figure 13. (Left) Schematic depicting the crossing of the donor and acceptor levels. (Right) Diagram depicting the spin down HOMO of transfer orbital.

Another important factor in the electron-transfer process is the system spin. In the S = 3 state the transferred electron is spin-down and can pass through the empty down-spin 3d orbitals of the Fe^{III} ion. In the S = 2 state, however, the transfer essentially concerns a spin-up electron, as can be understood by approximating the antiferromagnetically coupled state by the broken-symmetry configuration. In this case, the spin-up electron cannot pass through the 3d shell because the spin-up orbitals are occupied. As also evidenced in the section about J, the down-spin orbitals of the ligands can delocalize onto the iron, leading to a significant overlap between the donor and acceptor orbitals at the metal. The large overlap gives rise to a strong electronic coupling between the donor and acceptor orbitals in the S = 3 case, and did not result in a crossing phenomenon, as illustrated in Figure 13A. The up-spin orbitals on the other hand lack this delocalization, resulting in weaker electronic coupling in the S = 2 case (see Figure 13A). The stronger coupling for S = 3 leads to a lower TS energy for the ET and a larger transmission coefficient than in the S = 2 case. (*Comment:* For the case when the transmission coefficient < 1, the system needs to pass the crossing multiple times before

transfer occurs.) However, the situation is rather complex as the resonance lowering of the barrier may be veiled by the energetics of the O-H bond breaking and formation. Instead, the spin-state effect described here stems from the spin dependence of the electronic matrix element connecting donor and acceptor. This differs from the proposed spin effects on the hydrogen atom abstraction by Fe^{IV}=O species, which originate from energy differences between the spin terms of the electron-accepting metal ion. Although the ferromagnetic coupling prevailing in the superoxo intermediates yield the ground state with the most reactive spin (S = 3), the spin state energetics play only a minor role in the PCET reaction considered here.

Figure 14 shows the results of the intrinsic reaction coordinate (IRC) calculations of the PCET process. Figure 14A shows the correlation between the distances of the transferring proton to the donor and acceptor atoms, O_D and O_A, along the IRC. The plot displays the typical hyperbolic shape where the increase of the $O_D\cdots H$ distance is correlated with a shortening of the $H\cdots O_A$ distance. Figure 14B displays the system energy along the correlation path of Figure 14A, using as coordinate x the normalized distance traversed by the proton along the curved path. As mentioned above, the TS lies about 800 cm^{-1} above the initial state of the process. After reaching the TS, the energy curve steeply decays to reach the final state. To obtain a better understanding of this behavior, Figure 14C shows the energy curve along the IRC plotted as a function of the O-H bond "breaking and making" coordinate which is a measure of the $O_D\cdots H$ distance before the TS and of the $H\cdots O_A$ distance after the TS. This coordinate has been illustrated by dotted lines in Figure 14A. More precisely, the coordinate y has been defined as $y = \frac{(O_D\cdots H) - (O_D{-}H)_{init}}{(O_D\cdots H)_{TS} - (O_D{-}H)_{init} + (H\cdots O_A)_{TS} - (H{-}O_A)_{fin}}$ before the TS and

$y = \frac{(O_D \cdots H)_{TS} - (O_D - H)_{init} + (H \cdots O_A)_{TS} - (H \cdots O_A)}{(O_D \cdots H)_{TS} - (O_D - H)_{init} + (H \cdots O_A)_{TS} - (H - O_A)_{fin}}$ after the TS; the denominators were introduced to normalize y to the range [0, 1]. The energy is confined to a narrow range for y < 0.9 (see Figure 14C). At y = 0.9, where 90% of the bond breaking and making has been accomplished, the energy is approximately equal to the initial energy. Thus, 90% of the bond breaking and making takes place in an energy range of about 800 cm^{-1}. The potential energy drops steeply for y > 0.9 (Figure 14C) which may reflect the transformation of the system from a rather strained $O_{C1}H\cdots O_{sox}$ conformation to a more relaxed hydroperoxo conformation. The black dots in Figure 14C mark (a) the point where the spin populations of the substrate and O_2 moiety are equal (labeled "cross 1") and (b) the point where the populations of the transfer orbital at the substrate and the O_2 moiety are equal (labeled "cross 2"). As expected from the nature of the ET process, the two points nearly coincide. Cross 2 can be interpreted as the point where the electron donor and acceptor levels cross; the contour of the transfer orbital (down-spin-HOMO – 1) at this crossing point is shown in Figure 13B. The level crossing is located after the TS state of the overall PCET process, confirming that the ET process lags the PT (see above). The energy drop for y > 0.9 may reflect the transformation of the system from a rather strained $O_{C1}H\cdots O_{superoxo}$ conformation to a more relaxed hydroperoxo conformation as well as energy contributions associated with the completion of the ET process.

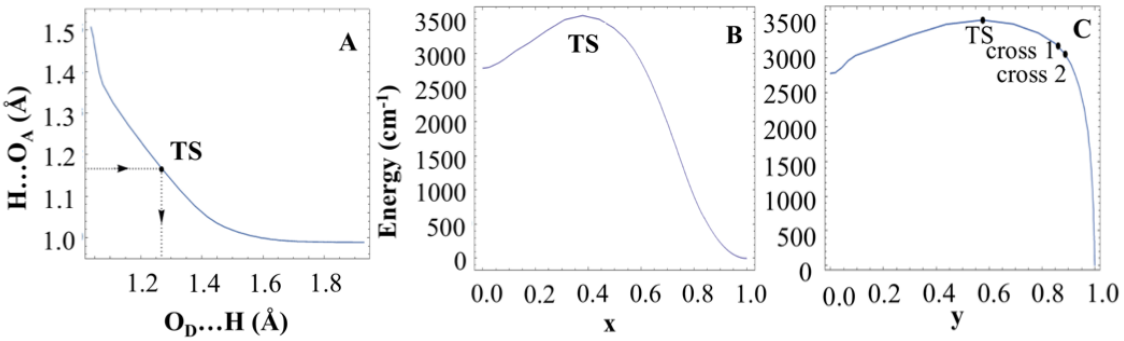

Figure 14. (A) Plot displaying the correlation between the distances of the transferring proton to the donor and acceptor atoms, O_D and O_A, along the IRC. **(B)** Plot of the system energy along the correlation path of (A), using as coordinate x the normalized distance traversed by the proton along the curved path. **(C)** Energy curve along the IRC plotted as a function of the O-H bond "breaking and making" coordinate.

Since water 1061 continues to act as a hydrogen bond donor to O_{C1} during the PCET and the transferring proton remains hydrogen bonded, initially to O_A and finally to O_D, the number of hydrogen bonds appears to be conserved in the process. However, the number of HBs increases by one in passing from the lowest superoxo conformation to the highest one (see Figure 12) due to the conversion of water 1061 from HB acceptor to HB donor. As the catalytic cycle is likely to pass through the lowest superoxo conformation, water 1061 is expected to be one of the factors responsible for determining the kinetics and thermodynamics of the reaction. Furthermore, if water 1061 were absent, the middle $O_{C1}H\cdots O_{Glu}$ conformation would assume the role of lowest superoxo conformation. In that case, the barrier to reach the reactive superoxo conformation, $O_{C1}H\cdots O_{superoxo}$, would likely increase dramatically, suggesting that water 1061 plays an essential role in the reaction mechanism. In contrast, residue 200 appears to play only a minor role in the PCET process in the H200C variant where the cysteine sulfur acts as an acceptor of a weak HB to one of the protons of water 1061.

Conclusions

The studies described here allow us to draw some conclusions regarding the mechanism of the H200C variant. It is important to recall that this mutant is active, albeit 400-600 times slower than WT HPCD. Our data suggest that *Int1*, identified as a (distal-hydroperoxo)-Fe^{III}-(semiquinone) species, is on the catalytic pathway and is formed/consumed in the rate-limiting step. Most likely, the oxygen activation reaction passes through a ferromagnetically coupled S = 3 Fe^{III}-superoxo complex of the variety listed in Table 2. High-spin Fe^{III}-superoxo complexes have recently been observed for the H200N mutant when the slow (difficult to oxidize) substrate 4NC is used, H200N-$4NC_{Int1}$,[1] and for a model complex involving the BDPP (BDPP=(2,6-bis((((S)-2-(diphenylhydroxymethyl)-1-pyrrolidinyl)methyl)pyridine)) ligand.[35] Mössbauer and EPR data show that the BDPP complex is ferromagnetically coupled to yield an S = 3 ground state whereas H200N-$4NC_{Int1}$ is a weakly coupled antiferromagnetic state. One might have expected that in the absence of His200 the system would be trapped at the superoxo level. However, we now know that the system gets trapped in a hydroperoxo state (*Int1*).

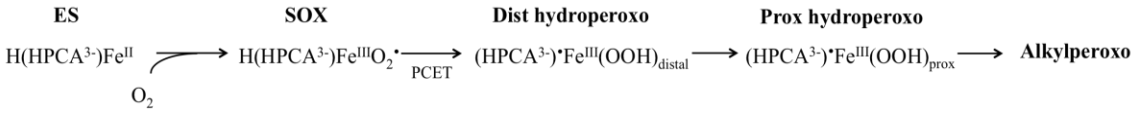

Scheme 1. Schematic of the proposed pathway for the H200C-HPCD variant that involves conversion of a ferric superoxo intermediate to a distal-protonated hydroperoxo, semiquinone radical intermediate via PCET.

As a potential way to attain *Int1*, we identified an inner-sphere PCET process, involving the O_{C1} proton that converts the superoxo species into a *distal* hydroperoxo species as shown in Scheme 1. The work of Neese suggests that a *proximal* hydroperoxo

species would be able to attack the C2 carbon of the substrate to yield the alkylperoxo intermediate. The proximal hydroperoxo intermediate can be formed from the distal hydroperoxo intermediate by a second proton transfer (Scheme 1). The importance of the O_{C1} proton for the dioxygenase reaction is supported by studies in which HPCA was replaced by the nitrocatechol, 4NC: the latter substrate, which binds in the *deprotonated* form, does not yield a ring-opened product. It is important to note that in the pathway of Scheme 1, the proton remains covalently bound to the (HPCA)FeO_2 fragment due to the absence of a viable proton acceptor. However, in the WT enzyme, the proton can be (temporarily) stored at the vicinal H200 residue, allowing formation of a deprotonated form of the (HPCA)FeO_2 fragment that could initiate an alternative pathway to the alkylperoxo intermediate. Fast kinetics of the latter pathway could preempt the pathway shown in Scheme 1. In summary, we conclude the following: (i) Starting from the ES complex the distal ferric hydroperoxo species of H200C (*Int1*) has been attained without the intervention of an outer-sphere proton shuttle agent (like His200 in WT), most likely by an inner-sphere PCET process. (ii) The distal hydroperoxo intermediate is located *on* the catalytic cycle of H200C, and not on a side track as proposed for the WT.[14]

Acknowledgements

This work is supported by National Institutes of Health Grant GM024689 (to J.D.L.), and by the National Science Foundation Grant CHE-1305111 (to E.M.). We also acknowledge support from the National Science Foundation via grant (NSF CHE-1126268) to Dr. Michael Hendrich.

References

1. Mbughuni, M. M.; Chakrabarti, M.; Hayden, J. A.; Bominaar, E. L.; Hendrich, M. P.; Münck, E.; Lipscomb, J. D. (2010) Trapping and spectroscopic characterization of an FeIII-superoxo intermediate from a nonheme mononuclear iron-containing enzyme. *PNAS 107,* 16788-16793.

2. Wallar, B. J.; Lipscomb, J. D. (1996) Dioxygen Activation by Enzymes Containing Binuclear Non-Heme Iron Clusters. *Chem. Rev. 96,* 2625-2657.

3. Que Jr., L.; Ho, R. Y. N. (1996) Dioxygen Activation by Enzymes with Mononuclear Non-Heme Iron Active Sites. *Chem. Rev. 96,* 2607-2624.

4. Mbughuni, M. M.; Chakrabarti, M.; Hayden, J. A.; Meier, K. K.; Dalluge, J. J.; Hendrich, M. P.; Münck, E.; Lipscomb, J. D. (2011) Oxy intermediates of homoprotocatechuate 2,3-dioxygenase: facile electron transfer between substrates. *Biochem. 50,* 10262-10274.

5. Mbughuni, M. M.; Meier, K. K.; Münck, E.; Lipscomb, J. D. (2012) Substrate-mediated oxygen activation by homoprotocatechuate 2,3-dioxygenase: intermediates formed by a tyrosine 257 variant. *Biochem. 51,* 8743-8754.

6. Groce, S. L.; Lipscomb, J. D. (2005) Aromatic Ring Cleavage by Homoprotocatechuate 2,3-Dioxygenase: Role of His200 in the Kinetics of Interconversion of Reaction Cycle Intermediates. *Biochem. 44,* 7175-7188.

7. Dong, G.; Lai, W. (2014) Reaction Mechanism of Homoprotocatechuate 2,3-Dioxygenase with 4-Nitrocatechol: Implications for the Role of Substrate. *J. Phys. Chem. B. 118,* 1791-1798.

8. Miller, M. A.; Lipscomb, J. D. (1996) Homoprotocatechuate 2,3-Dioxygenase from *Brevibacterium fuscum* A DIOXYGENASE WITH CATALASE ACTIVITY. *J. Biol. Chem. 271,* 5524-5535.

9. Dong, G.; Shaik, S.; Lai, W. (2013) Oxygen activation by homoprotocatechuate 2,3-dioxygenase: a QM/MM study reveals the key intermediates in the activation cycle. *Chem. Sci. 4,* 3624.

10. Groce, S. L.; Lipscomb, J. D. (2003) Conversion of extradiol aromatic ring-cleaving homoprotocatechuate 2,3-dioxygenase into an intradiol cleaving enzyme. *J. Am. Chem. Soc. 125,* 11780.

11. Henderson, K. L.; Le, V. H.; Lewis, E. A.; Emerson, J. P. (2012) Exploring substrate binding in homoprotocatechuate 2,3-dioxygenase using isothermal titration calorimetry. *J. Biol. Inorg. Chem. 17,* 991-994.

12. Kovaleva, E. G.; Lipscomb, J. D. (2012) Structural Basis for the Role of Tyrosine 257 of Homoprotocatechuate 2,3-Dioxygenase in Substrate and Oxygen Activation. *Biochem. 51,* 8755-8763.

13. Kovaleva, E. G.; Lipscomb, J. D. (2007) Crystal Structures of Fe2+ Dioxygenase Superoxo, Alkylperoxo, and Bound Product Intermediates. *Science 316,* 453-457.

14. Christian, G. J.; Ye, S.; Neese, F. (2012) Oxygen activation in extradiol catecholate dioxygenases – a density functional study. *Chem. Sci. 3,* 1600-1611.

15. Kovaleva, E. G.; Lipscomb, J. D. (2008) Intermediate in the O-O Bond Cleavage Reaction of an Extradiol Dioxygenase. *Biochem. 47,* 11168-11170.

16. McLaughlin, M. P.; Retegan, M.; Bill, E.; Payne, T. M.; Shafaat, H. S.; Pena, S.; Sudhamsu, J.; Ensign, A. A.; Crane, B. R.; Neese, F.; Holland, P. L. (2012) Azurin as a protein scaffold for a low-coordinate non-heme iron site with a small-molecule binding pocket. *J. Am. Chem. Soc. 134,* 19746-19757.

17. Lu, L. L.; Zhu, Y. C.; Wang, X. F.; Zuo, G. F.; Guo, F.; Zhao, S. R.; Wang, Y. C. (2013) Spin-orbit coupling and zero-field splitting of the high-spin ferric enzyme substrate complex: Protocatechuate 3,4-dioxygenase complexed with 3,4-dihydroxyphenylacetate. *Chinese Science Bulletin 58,* 627-633.

18. Shaanan, B. (1982) The iron-oxygen bond in human oxyhaemoglobin. *Nature 296,* 683-684.

19. Sharrock, M.; Debrunner, P.G.; Schulz, C.; Lipscomb, J.D.; Marshall, V.; Gunsalus, I.C. (1976) Cytochrom P450cam and its complexes. Mössbauer parameters of the heme iron. *Biochim. Biophys. Acta. 420,* 8-26.

20. Schlichting, I.; Berendzen, J.; Chu, K.; Stock, A.M.; Maves, S.A.; Bensen, D.E.; Sweet, R.M.; Ringe, D.; Petsko, G.A.; Sligar, S.G. (2000) The catalytic pathway of cytochrome p450cam at atomic resolution. *Science 287,* 1615-1622.

21. Davydov, R.; Makris, T.M.; Kofman, V.; Werst, D.E.; Sligar, S.G.; Hoffman, B.M. (2001) Hydroxylation of camphor by reduced oxy-cytochrome P450cam: mechanistic implications of EPR and ENDOR studies of catalytic intermediates in native and mutant enzymes. *J. Am. Chem. Soc. 123,* 1403-1415.

22. Hendrich, M. P.; Debrunner, P. G. (1989) Integer Spin Electron Paramagnetic Resonance of Iron Proteins. *BioPhys. J. 56,* 490-506.

23. Chiesa, M.; Giamello, E.; Paganini, M. C. (2002) Continuous wave electron paramagnetic resonance investigation of the hyperfine structure of 17O2- adsorbed on the MgO surface. *J. Chem. Phys. 116,* 4266-4274.

24. Pietrzyk, P.; Podolska, K.; Mazur, T.; Sojka, Z. (2011) Heterogeneous binding of dioxygen: EPR and DFT evidence for side-on nickel(II)-superoxo adduct with unprecedented magnetic structure hosted in MFI zeolite. *J. Am. Chem. Soc. 133,* 19931-19943.

25. Hoffman, B. M. (1994) ENDOR and ESEEM of a Non-Kramers Doublet in an Integer-Spin System. *J. Phys. Chem. 98,* 11657-11665.

26. Griffith, J. S. (1963) Spin Hamiltonian for even-electron systems having even multiplicity. *Phys. Rev. 132,* 316-319.

27. Kabsch, W. (2010) XDS, Acta Crystallogr D Biol Crystallogr. 66, 125-132.

28. Murshudov, G. N., Skubak, P., Lebedev, A. A., Pannu, N. S., Steiner, R. A., Nicholls, R. A., Winn, M. D., Longa, F., and Vagin, A. A. (2011) REFMAC5 for the refinement of macromolecular crystal structures, Acta Cryst. D67 355-367.

29. Bailey, S. (1994) The CCP4 Suite - Programs for Protein Crystallography, Acta Crystallogr. 50, 760-763.

30. Winn, M. D., Ballard, C. C., Cowtan, K. D., Dodson, E. J., Emsley, P., and Evans, P. R. (2011) Overview of the CCP4 suite and current developments, Acta Crystallogr D 67, 235-242.

31. Emsley, P., and Cowtan, K. (2004) Coot: model-building tools for molecular graphics. *Acta Crystallogr.* E60, 2126-2132.

32. Wang, Y.Z.; Lipscomb, J.D. (1997) Cloning, overexpression, and mutagenesis of the gene for homoprotocatechuate 2,3-dioxygenase from *Brevibacterium fuscum*. *Protein Expr Purif. 10*, 1-9.

33. Groce, S. L.; Miller-Rodeberg, M. A.; Lipscomb, J. D. (2004) Single-Turnover Kinetics of Homoprotocatechuate 2,3-Dioxygenase. *Biochem. 43,* 15141-15153.

34. Krebs C, Dassama LM, Matthews ML, Jiang W, Price JC, Korboukh V, Li N, Bollinger JM Jr. (2013) Novel Approaches for the Accumulation of Oxygenated Intermediates to Multi-Millimolar Concentrations. *Coord Chem Rev. 257,* 234-243.

35. Chiang, C.-W.; Kleespies, S. T.; Stout, H. D.; Meier, K. K.; Li, P.-Y.; Bominaar, E. L.; Que Jr., L.; Münck; Lee, W.-Z. (2014) Characterization of a Paramagnetic Mononuclear Nonheme Iron-Superoxo Complex. *J. Am. Chem. Soc. 136,* 10846-10849.

36. Vrajmasu, V.; Münck, E.; Bominaar, E.L. (2003) Density functional study of the electric hyperfine interactions and the redox-structural correlations in the cofactor of nitrogenase. Analysis of general trends in (57)Fe isomer shifts. *Inorg. Chem. 42,* 5974-5988.

Supporting Information

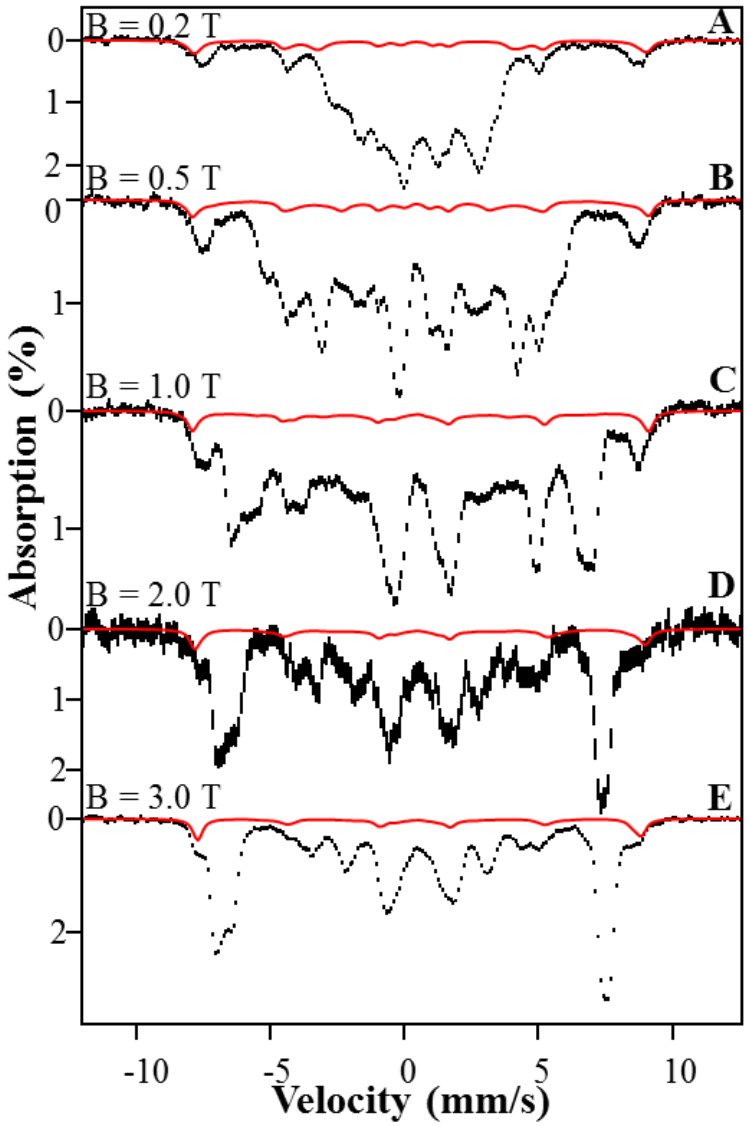

Figure S1. 4.2 K Mössbauer spectra of *Int1* recorded in variable, parallel applied magnetic fields as indicated. The black hash-mark curves are the raw experimental spectra. The solid red curves represent the 8% high-spin ferric contaminant, and was generated using the parameters: D = -0.50 mm/s, E/D = 0.33 , ΔE_Q = 0.30 mm/s, A_0 = -21.9 T, δ = 0.45 mm/s.

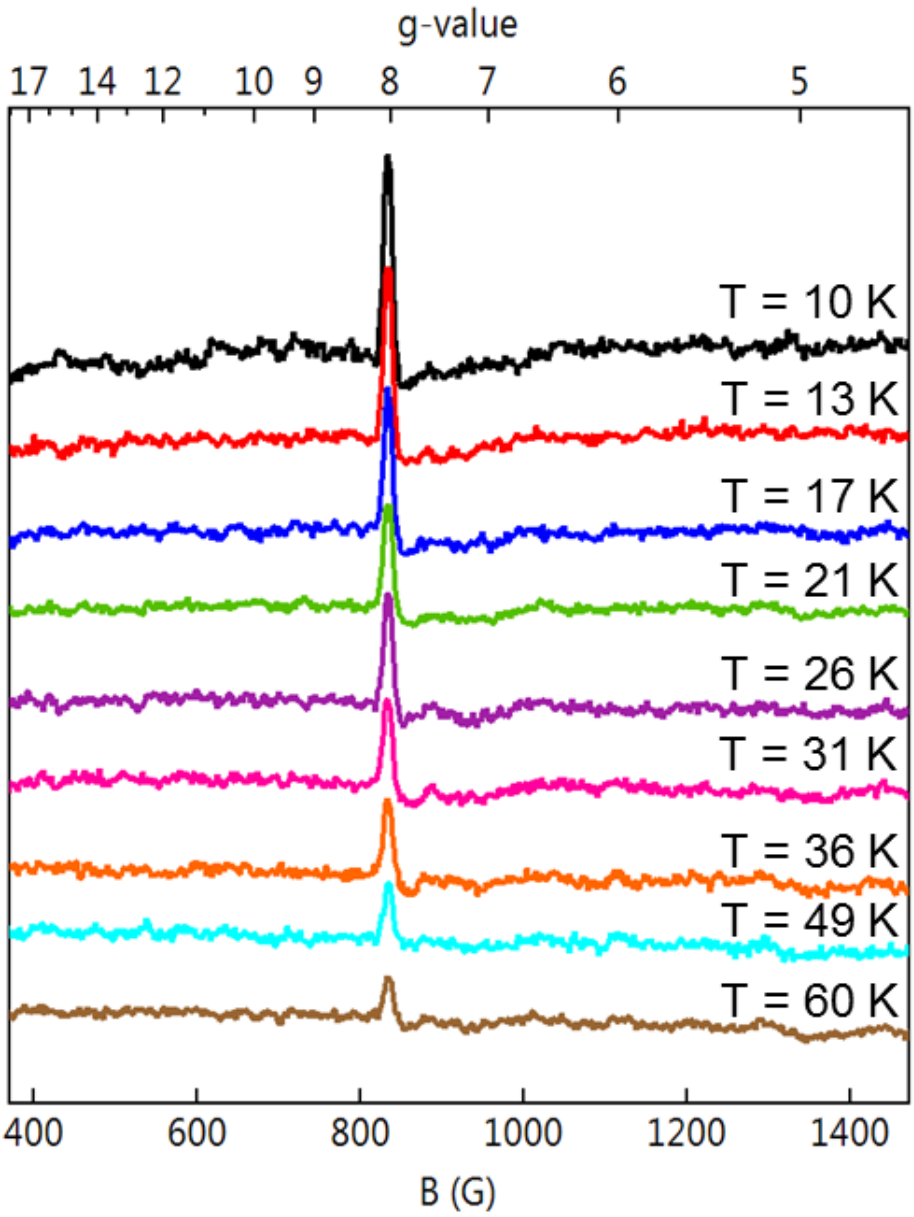

Figure S2. Parallel mode X-band EPR spectra of the g = 8.04 resonance of *Int1*. Spectra were collected for temperatures ranging from 10 K to 60 K. Conditions: 9.37 GHz frequency, 20 mW microwave power, 1 mT modulation, T = 21 K. These data were used to generate the signal x T analysis shown in Figure 6 of the main text.

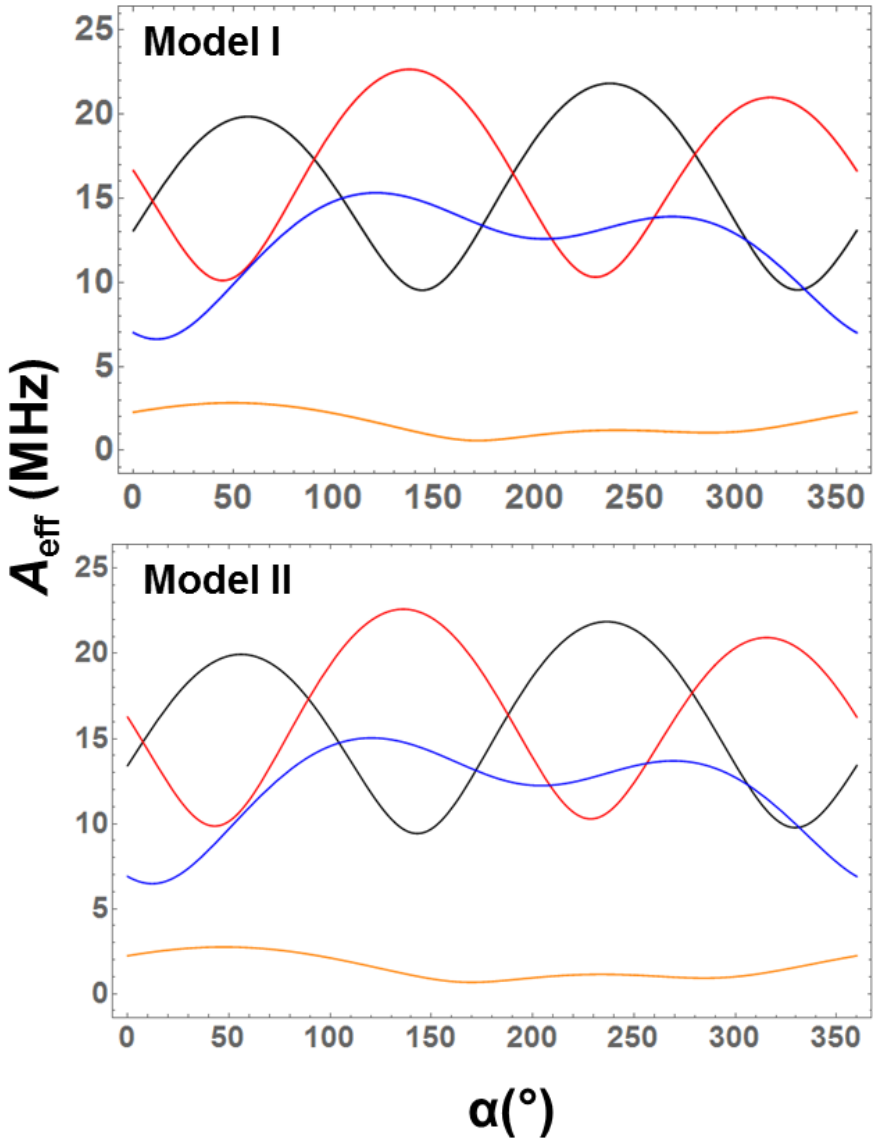

Figure S3. Plot of A_{eff} calculated for O_{C1} and O_{C2} of the HPCA substrate, and O_{prox} (proximal to the iron) and O_{distal} of the hydroperoxo ligand. The plot was prepared using β = 70°. (Top = Model I; Bottom = Model II).

Table S1. DFT coordinates for the geometry optimized structure of conformation OOH in Model 3. Geometry optimization was performed using the 6-311g basis set and B3LYP functional.

C	5.34859500	1.30628700	-1.94196900	N	-2.34228300	3.55434000	0.27609100
C	4.15045200	0.94493700	-1.12590300	C	-2.12751000	2.24624000	-0.04489100
C	2.80820200	0.86747800	-1.40195900	N	-0.84360600	1.94979600	0.15055400
N	4.26408900	0.56022600	0.21707700	C	-2.28453000	-7.31072800	3.00399100
C	3.02554000	0.27391100	0.70424700	C	-2.24332100	-5.81131400	3.15354300
N	2.11539900	0.45188500	-0.25535100	C	-1.16048100	-4.93909300	3.12051400
C	-1.71034300	3.10667300	-3.26294000	N	-3.36473100	-5.03383200	3.16461600
C	-2.96857700	2.39440800	-3.69243300	C	-3.00620900	-3.74723900	3.20234200
N	-3.01202500	1.07859200	-3.49217500	N	-1.64816000	-3.68625200	3.17934300
O	-3.89901100	3.02198300	-4.20001900	C	-3.92077100	3.05851500	6.78680300
C	-0.53737900	-4.64531300	-6.71144700	C	-3.76620400	2.07030200	5.66494900
C	-1.31794000	-4.15653000	-5.50318200	C	-3.07950400	2.40879100	4.49444300
C	-0.82465900	-3.44305200	-4.42226600	C	-4.27096100	0.79265800	5.78266500
C	-2.75183000	-4.33306600	-5.21957500	C	-2.94362000	1.48899300	3.46197300
C	-3.00195700	-3.67622700	-3.94144900	C	-4.14979700	-0.11886200	4.75657800
C	-3.80864600	-4.94627000	-5.88013700	C	-3.48111700	0.22273500	3.61332300
N	-1.82706600	-3.15886500	-3.52841200	O	-3.39912500	-0.73831400	2.63284600
C	-4.25378500	-3.66141500	-3.35977100	C	0.86294100	2.03824800	3.84266300
C	-5.07565900	-4.92580700	-5.28593800	C	0.54028300	0.61057600	4.27664800
C	-5.29758300	-4.28583400	-4.05917100	C	0.33145300	-0.37983800	3.14061000
C	4.38872700	-3.08874700	-5.99010400	O	0.43193300	0.09647400	1.91280400
C	2.94665200	-2.56792600	-5.92836200	O	0.08086400	-1.57715400	3.40804600
S	2.54332500	-1.56720200	-4.49439600	Fe	0.00000000	0.00000000	0.00000000
C	-1.00978400	5.53615900	1.14488400	O	0.05682700	0.17717800	-1.97221400
C	-1.13452200	4.12250800	0.69539100	O	1.55795000	-3.60639400	-1.81820500
C	-0.21505900	3.11041000	0.60049700	C	-3.62058100	-3.88341600	0.11571800

C	-3.50099600	-2.49890600	0.19354200	H	-2.64478100	-7.56208400	2.02831700
C	-2.23550400	-1.89812000	0.10350600	H	-1.30015400	-7.70935700	3.13437100
O	-1.98854200	-0.60015800	0.27162000	H	-0.12820600	-5.21402300	3.05950500
C	-1.05406000	-2.71543400	-0.12245500	H	-1.10202700	-2.84887800	3.20224800
O	0.08502300	-2.05771600	-0.16390900	H	-3.67195500	-2.91058600	3.24350200
C	-1.19470100	-4.11921300	-0.27891300	H	-4.04689100	4.04089100	6.38191900
C	-2.44592700	-4.67370200	-0.15433800	H	-4.77829000	2.80150100	7.37289600
C	-4.95010000	-4.57437100	0.28920500	H	-2.65467100	3.38559500	4.39310200
H	5.96226200	0.42949700	-2.16516100	H	-4.76538300	0.50398300	6.68660800
H	5.98112400	2.03205900	-1.42394400	H	-2.43029500	1.75609100	2.56194200
H	2.28296100	1.04660500	-2.31838700	H	-4.57889800	-1.09418800	4.85410600
H	2.81171600	-0.04541700	1.70335100	H	-2.84856200	-0.41696200	1.91518600
H	-1.00154800	2.39185300	-2.90033300	H	0.14943900	2.37899300	3.09791900
H	-1.94306500	3.80269700	-2.48336000	H	1.86008800	2.11535400	3.40442600
H	-0.85103600	-5.63729200	-6.96137200	H	-0.37815200	0.59231800	4.86846600
H	0.50798100	-4.64861000	-6.48319800	H	1.31671200	0.20148900	4.92883500
H	0.19834700	-3.15295200	-4.30156500	O	-0.96731700	-0.69427900	-2.65928400
H	-1.70758900	-2.65384000	-2.67364500	H	1.24426200	-2.96351400	-1.14701800
H	-3.65705600	-5.42502300	-6.82497400	H	2.13837600	-3.17191500	-2.46437800
H	-5.89279700	-5.40943000	-5.77918700	H	-4.35784400	-1.88079500	0.41508600
H	-4.42160400	-3.19238800	-2.41276600	H	-0.31849900	-4.70801800	-0.50299000
H	-6.28483100	-4.27309500	-3.64677000	H	-2.56515800	-5.74363600	-0.24729800
H	2.84324700	-1.91471900	-6.76954000	H	-5.52394300	-4.55188500	-0.64331100
H	2.33170700	-3.44007100	-5.84963800	H	-4.80738100	-5.61499400	0.57144400
H	1.25771700	-1.31548700	-4.48621800	H	-1.22137700	6.23019000	0.33333000
H	4.45368300	-3.87398200	-6.71404400	H	-3.04716900	3.03667000	7.40425200
H	-1.68857500	5.76552200	1.96983300	H	-2.93790700	-7.72506400	3.74312900
H	0.00457600	5.73058900	1.48928600	H	0.80667900	2.71920200	4.68743200
H	0.83151400	3.12555500	0.83033400	H	5.06179500	1.75090200	-2.89334900
H	-2.87569300	1.55963300	-0.38821600	H	-1.29465100	3.63168100	-4.09684400

H	-0.71929900	-3.99412800	-7.54079300
H	4.67359300	-3.46465300	-5.02965800
H	5.04446700	-2.29077700	-6.26963200
H	-3.22771700	4.02734000	0.21905000
H	5.12416400	0.49005700	0.73230500
H	-0.52079100	-0.90657300	-3.50226300
H	-2.24799900	0.51584800	-3.14244500
H	-3.78368300	0.55989400	-3.88649800
H	-5.55747500	-4.11827600	1.07477300

Chapter IV – Intermediate P* from Soluble Methane Monooxygenase Contains a Diferrous Cluster

Published: Banerjee, R.; **Meier, K.K.**; Münck, E.; Lipscomb, J.D. "Intermediate P* from Soluble Methane Monooxygenase Contains a Diferrous Cluster." *Biochemistry.* 2013, 52, pp 4331-4342.

Author Contributions: R.B., K.K.M., E.M., and J.D.L. conceived and designed the experiments. R.B. and K.K.M. (Mössbauer, EPR) performed the experiments. R.B., K.K.M., E.M., J.D.L. analyzed the data. All authors participated in the writing of the paper.

Abstract

During a single turnover of the hydroxylase component (MMOH) of soluble methane monooxygenase from *Methylosinus trichosporium* OB3b, several discrete intermediates are formed. The diiron cluster of MMOH is first reduced to the $Fe^{II}Fe^{II}$ state (**H**^{red}). O_2 binds rapidly at a site away from the cluster to form the $Fe^{II}Fe^{II}$ intermediate **O**, which converts to an $Fe^{III}Fe^{III}$-peroxo intermediate **P** and finally to the $Fe^{IV}Fe^{IV}$ intermediate **Q**. **Q** binds and reacts with methane to yield methanol and water. The rate constants for these steps are increased by a regulatory protein, MMOB. Previously reported transient kinetic studies have suggested that an intermediate **P*** forms between **O** and **P** in which the g = 16 EPR signal characteristic of the reduced diiron cluster of **H**^{red} and **O** is lost. This was interpreted as signaling oxidation of the cluster, but low accumulation of **P*** prevented further characterization. In this study,

three methods to directly detect and trap **P*** are applied together to allow its spectroscopic and kinetic characterization. First, the MMOB mutant His33Ala is used to specifically slow the decay of **P*** without affecting its formation rate, leading to its nearly quantitative accumulation. Second, spectra-kinetic data collection is used to provide a sensitive measure of the formation and decay rate constants of intermediates as well as their optical spectra. Finally, the substrate furan is included to react with **Q** and quench its strong chromophore. The optical spectrum of **P*** closely mimics those of $\mathbf{H^{red}}$ and **O**, but it is distinctly different from that of **P**. The reaction cycle rate constants allowed prediction of the times for maximal accumulation of the intermediates. Mössbauer spectra of rapid freeze quench samples at these times show that the intermediates are formed at almost exactly the predicted levels. The Mössbauer spectra show that the diiron cluster of **P***, quite unexpectedly, is in the $Fe^{II}Fe^{II}$ state. Thus, the loss of the $g = 16$ EPR results from a change of the electronic structure of the $Fe^{II}Fe^{II}$ center rather than oxidation. The similarity of the optical and Mössbauer spectra of $\mathbf{H^{red}}$, **O**, and **P*** suggest that only subtle changes occur in the electronic and physical structure of the diiron cluster as **P*** forms. Nevertheless, the changes that do occur are necessary for O_2 to be activated for hydrocarbon oxidation.

Introduction

The soluble form of methane monooxygenase (sMMO) found in many methanotrophs catalyzes the oxidation of methane to methanol as part of the metabolic pathway that allows these microorganisms to use methane as the sole carbon and energy source.[1] This demanding reaction (methane bond dissociation energy equals 105 kcal mole^{-1}) [2] is catalyzed only by sMMO and particulate MMO (and to a lesser extent, pMMO-like ammonia monooxygenase in autotrophic ammonia-oxidizing bacteria). [3,4] sMMO is an enzyme system comprised of three protein components: i) a hydroxylase (MMOH) containing a diiron metal cluster in the active site, ii) a [2Fe-2S] cluster and FAD containing reductase (MMOR) that mediates electron transfer between NADH and the diiron cluster, and iii) a regulatory protein MMOB that is devoid of any cofactors. [5-7] The unique reactivity of sMMO has spurred research into its chemical mechanism and led to extensive efforts to mimic the chemistry using synthetic model compounds. [6-12]We have studied the mechanism of sMMO using the enzyme from the Type II methanotroph *Methylosinus trichosporium* OB3b (*M. t.* OB3b), while others have used the enzyme from the Type X methanotroph *Methylococcus capsulatus* Bath (*M. c.* Bath) with similar results.[6-8,13]

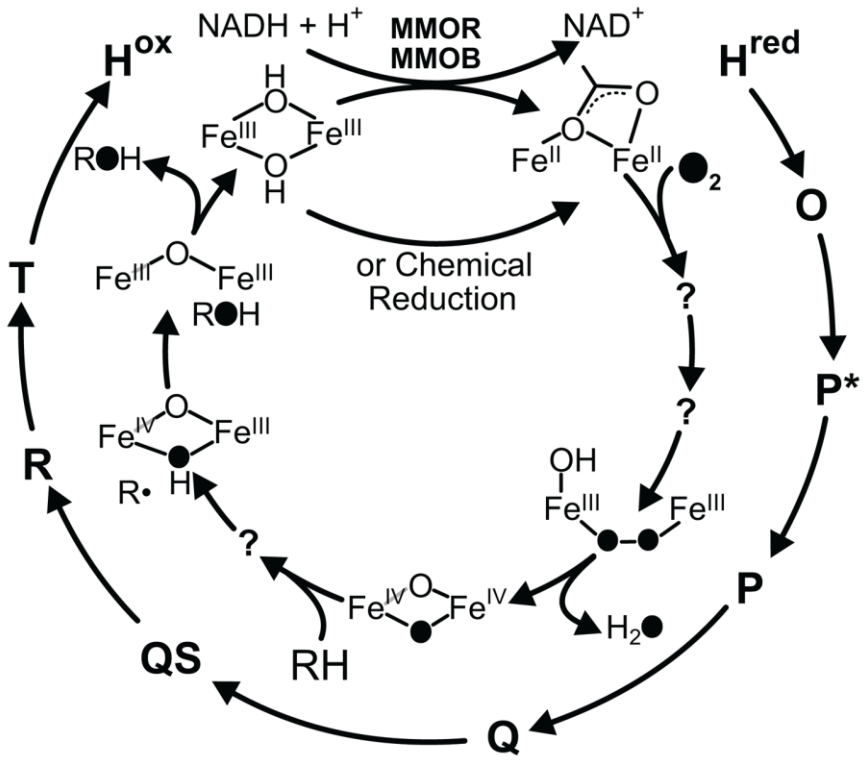

Scheme 1. Reaction cycle intermediates of MMOH.

Single turnover transient kinetic studies in the presence of MMOB have been used to map the reaction cycle intermediates as shown in Scheme 1. [6,7,14-16] Table S1 summarizes the experimental evidence for the various intermediates of the reaction cycle. The resting diferric MMOH (**H^{ox}**) can be reduced by two electrons from either MMOR or chemical reductants to form diferrous MMOH (**H^{red}**).[5] This form of the enzyme reacts with O_2 to form intermediate **O** which has oxygen bound to the enzyme, but perhaps not to the diiron cluster.[17] Intermediate **O** decays to form intermediate **P**; the latter exhibits a weak optical band at 700 nm and Mössbauer parameters diagnostic of a diferric cluster with a peroxo moiety bound to the iron atoms.[18-20] The precise nature of the cluster in **P** is

unknown, but comparison with model complexes and peroxo intermediates in related diiron enzymes suggests that it is a μ-1,2-peroxo dinuclear Fe^{III} complex.[8] Intermediate **P** decays to form intermediate **Q**, which has been shown by Mössbauer and X-ray absorption studies to contain a unique bis- μ -oxo Fe^{IV}_2 diamond core cluster.[14,20,21] **Q** exhibits a relatively intense optical spectrum with maxima at 330 and 430 nm (η_{430} = 7500 M^{-1} cm^{-1}). This spectrum has allowed extensive studies of the mechanism of the reaction with methane and adventitious substrates.[14,15,18,22-25] It is likely that the reaction occurs by hydrogen atom abstraction with a substantial tunneling component to form intermediate **R**.[7,22,24,26-28] In contrast to intermediates **O**, **P**, and **Q**, intermediate **R** does not live long enough to be directly observed, but it is postulated to occur based on racemization during chiral ^1H, ^2H, ^3H-ethane oxygenation and computational studies showing that a substrate radical is transiently formed.[26,29-31] Rebound of the cluster-bound hydroxyl group onto the substrate radical would yield the product complex, termed **T**, which dissociates to complete the cycle.[14]

Our transient kinetic studies of the **O** to **P** conversion have indicated the presence of an intervening intermediate termed **P***.[19] Two experimental observations led to this mechanistic proposal. The first evidence is that the rate constant of formation of **P** (10 s^{-1} at 4 °C, pH 7.0) is slower than the rate constant for the decay of **O** (26 s^{-1} at 4 °C, pH 7.0), indicating that there must be an intermediate in between. The second line of evidence arises from the observation that the decay rate constant of **O** is pH independent,

in contrast to the pH dependent rate constant for the formation of **P,** showing that the reactions cannot be the same. To date, transient kinetic single turnover studies on MMOH from *M. t.* OB3b have failed to reveal any spectral features that can be attributed to **P***. However, the fact that the g = 16 signal of diferrous cluster disappears as **P*** is formed was interpreted to indicate that either one or both cluster irons are oxidized due to formation of a metal-ligated superoxo or peroxo complex.[19]

Recent studies using the *M. c.* Bath enzyme provide kinetic evidence for the presence of an intermediate before $\mathbf{H_{peroxo}}$ (equivalent to **P**) in the MMOH catalytic cycle. [16] A global fitting of the kinetic time traces at 420 nm and 720 nm of a single turnover reaction of reduced *M. c.* Bath MMOH with O_2 in the presence of methane is consistent with an intermediate with an electronic absorption spectrum similar to that of $\mathbf{H_{peroxo}}$, which is known to have an $Fe^{III}Fe^{III}$ cluster. Accordingly, it was reasoned that the intermediate (also named **P***) and $\mathbf{H_{peroxo}}$ both have $Fe^{III}Fe^{III}$ clusters in similar electronic environments.

One particularly relevant aspect of the MMOH reaction cycle for the present study is the dramatic effect of MMOB on the rate of catalysis. [6,28,32] The overall rate constant for the conversion of intermediate $\mathbf{H^{red}}$ to **P** in the *M. t.* OB3b enzyme system is accelerated 1000 fold by the presence of MMOB. [17] For adventitious substrates, the regiospecificity of hydroxylation usually changes quite markedly when MMOB is added, and spectroscopic studies indicate that the diiron cluster environment of MMOH is

altered in the MMOH-MMOB complex. [33-35] The residues that form the interface between MMOH and MMOB have been identified by spectroscopic studies. [36,37] A set of MMOB variants made by introducing site-specific mutations at these residues has been shown to alter the rate constants for interconversion between MMOH reaction cycle intermediates. [28,32] One of the variants, MMOB His33Ala (H33A), specifically decreases one or more of the rate constants for the steps in the conversion of $\mathbf{H^{red}}$ to **P**, potentially allowing the reactions in this sequence to be studied in detail.

Here, we show that MMOB H33A decreases the rate constant for the specific step of **P** formation from **P*** by about 30 fold without a significant decrease in the rate constant for **O** decay, resulting in nearly quantitative accumulation of **P***. This permits the observation of the electronic absorption and Mössbauer spectra of **P***. It is shown that **P*** has a different oxidation state than previously proposed, suggesting a new approach to formation of the peroxo complex in diiron cluster containing oxygenases.

Experimental Procedures

Chemicals. 3-(N-morpholino)-propanesulfonic acid, glycerol, ferrous ammonium sulfate, cysteine, urea, furan, sodium hydrosulfite and methyl viologen were purchased from Sigma-Aldrich.

Biological Materials. MMOH was purified from *M. trichosporium* OB3b with the following modifications to the published protocol. [38] All purification buffers contained 0.2 mM ferrous ammonium sulfate and 2.0 mM cysteine as a stabilizer for the active site iron of MMOH. These were added to the cold buffers at least 3 h before use and nitrogen purged for 1 h before and during use. The chromatography columns were also equilibrated with nitrogen-purged buffers before loading the iron/cysteine stabilizer containing buffers. The second high-resolution ion-exchange chromatography column was additionally scrubbed free of oxygen with 20 ml of 5.0 mM sodium hydrosulfite solution. The *M. t.* OB3b cell free extract was applied to the initial DEAE ion-exchange column in a batch-binding manner. The protein fractions containing MMOH were subsequently collected in sealed argon-purged glass vials. The MMOH containing protein fractions were pooled and concentrated. This concentrated eluent pool was desalted through a Sephadex G-25 column (22 × 2.8 cm) equilibrated in 25 mM MOPS, pH 6.8. The desalted protein pool was subsequently applied to a high-resolution Q-Sepharose column (12 × 2.8 cm) equilibrated in 25 mM MOPS, pH 6.8. MMOH is eluted with a 900 ml gradient from 0 M to 0.08 M NaCl in the same buffer at a linear flow rate of 23 cm/h.

The MMOH containing protein fractions were collected in argon-purged sealed glass vials, pooled and concentrated via ultrafiltration. Glycerol was added to a final concentration of 5% (v/v) to the protein pool. Recombinantly expressed H33A MMOB mutant was purified according to the protocol previously described.[39]

Transient Kinetic Experiments. Transient kinetic single turnover experiments were performed on an Applied Photophysics stopped-flow instrument (Model SX.18MV with SX Pro-Data upgrade). The sample preparation for MMOH involved making MMOH anaerobic under argon at 4 °C followed by a transfer into an anaerobic glove bag (Coy). The protein was reduced with a stoichiometric excess of sodium hydrosulfite and methyl viologen (10 % of the MMOH active site concentration) at room temperature for 20 minutes. The chemical reductants were separated from MMOH by passage through a Sephadex G-25 PD-10 desalting column (GE Healthcare) equilibrated in 100 mM MOPS buffer at the chosen pH point containing 0.2 mM ferrous ammonium sulfate and 2.0 mM cysteine. The iron/cysteine-containing buffer was incubated for 1.5 h at 4 °C before being made anaerobic. The reduced protein was loaded into one of the drive syringes on the stopped flow instrument using a Hamilton gas-tight syringe. The other drive syringe was loaded with a stoichiometric equivalent amount of H33A MMOB in oxygen-saturated buffer. If an sMMO substrate was utilized in the single turnover experiment, it is also added to this drive syringe. For both these experiments and the rapid freeze quench (RFQ) experiments described below, the results are not affected by pre-mixing MMOH

and MMOB in one syringe or mixing them during the transient kinetic experiment. MMOH is much more soluble when mixed with MMOB so that pre-mixing facilitates sample handling when using very high enzyme concentrations in the RFQ experiments. On the other hand, reduced MMOH reacts much slower with O_2 in the absence of MMOB, facilitating handling for lower concentration samples. The single-wavelength transient kinetic data was analyzed with the Pro-Data Viewer software from Applied Photophysics and fit to a summed exponential expression.[15] Singular value decomposition of spectra-kinetic multiple-wavelength data was performed using the Pro-Kineticist global analysis software (Applied Photophysics). The protein concentration of MMOH used in the transient kinetic experiments is described in terms of reactive MMOH active sites. This description arises from the presence of two populations of MMOH active sites: i) a population that undergoes turnover with previously observed kinetic rates and forms catalytic intermediates,[14] ii) a population that undergoes a slow reaction with O_2 and therefore does not accumulate catalytic intermediates during turnover. The presence of two populations of MMOH with only one population displaying intermediates in the single turnover catalytic cycle, is also observed in MMOH from *M. c.* Bath.[16] The reactive population of MMOH active sites comprises 40% of the total MMOH active sites in the MMOH protein used in most of the experiments described in this study, although preparations with as high as 60% have been obtained. The active fraction was determined from a comparison of the observed specific activity to

the specific activity of a fully active preparation (1200 nmoles/min/mg).[38] The active fraction can also be determined from the maximum observed yield of **Q** by optical detection and the known rate constants for the reaction cycle. The two methods give good agreement.

RFQ Mössbauer and EPR Experiments. For the preparation of rapid freeze-quench Mössbauer and EPR samples, MMOH was reduced with a stoichiometric amount of sodium hydrosulfite in the presence of methyl viologen (10 % of the MMOH active site concentration). A stoichiometric amount (per active site) of H33A MMOB was then added to reduced MMOH under anaerobic conditions and the mixture loaded in an RFQ syringe. The RFQ syringe was loaded on an Update Instrument Model 1019 RFQ apparatus. A low-temperature bath circulator (Neslab LT-50) maintained the reactants in the RFQ assembly at a temperature of 4 °C. The RFQ samples were produced by mixing the reduced MMOH enzyme with oxygen-saturated buffer and freezing the reaction at specified time points on counter-rotating aluminum wheels at liquid nitrogen temperature. [40] The frozen sample was then packed in RFQ Mössbauer cups or EPR tubes under liquid nitrogen. EPR spectra were collected using a Bruker Elexsys E-500 or Bruker ESP 300 spectrometer each equipped with a Bruker dual mode cavity and an Oxford ESR 910 liquid helium cryostat. Mössbauer spectroscopy was performed as previously described.[40,41] Spectra were analyzed using the software WMOSS (SEE Co, Edina, MN, USA).

Results

Single Turnover Reaction Using H33A MMOB in the Absence of Substrate Slows the P* to P Conversion Step. The photodiode-array traces for the single-turnover reaction of $\mathbf{H^{red}}$ in the presence of H33A MMOB but absence of substrate are shown in Figure 1. While the formation and decay of intermediate **Q** are readily seen in the 400 – 450 nm region, there is no evidence of the spectrum of intermediate **P**, normally seen in the 700 nm region. [15,16,18,28] Extraction of the rate constants for the reaction by multiple exponential fitting of the time course shown in the inset of Figure 1, indicates that the apparent formation rate constant of **Q** at 4 °C is decreased from 2.7 s^{-1} (observed with wild-type MMOB) to 0.38 s^{-1}, similar to our previous findings. [28] When considered together, these results indicate that the use of MMOB H33A greatly slows formation of **Q** by slowing a step prior to the **P** to **Q** conversion.

The slow step in the **O** to **P** sequence can be determined by monitoring the disappearance of intermediate **O** using rapid freeze quench techniques and EPR spectroscopy. As shown in Figure 2, the rate constant of decay of the parallel mode g = 16 EPR signal of **O** is nearly unchanged when using H33A MMOB in place of WT MMOB (k = 28 s^{-1} and 26 s^{-1}, respectively). Together the kinetic data show that it is the **P*** to **P** step which is greatly slowed by the mutation.

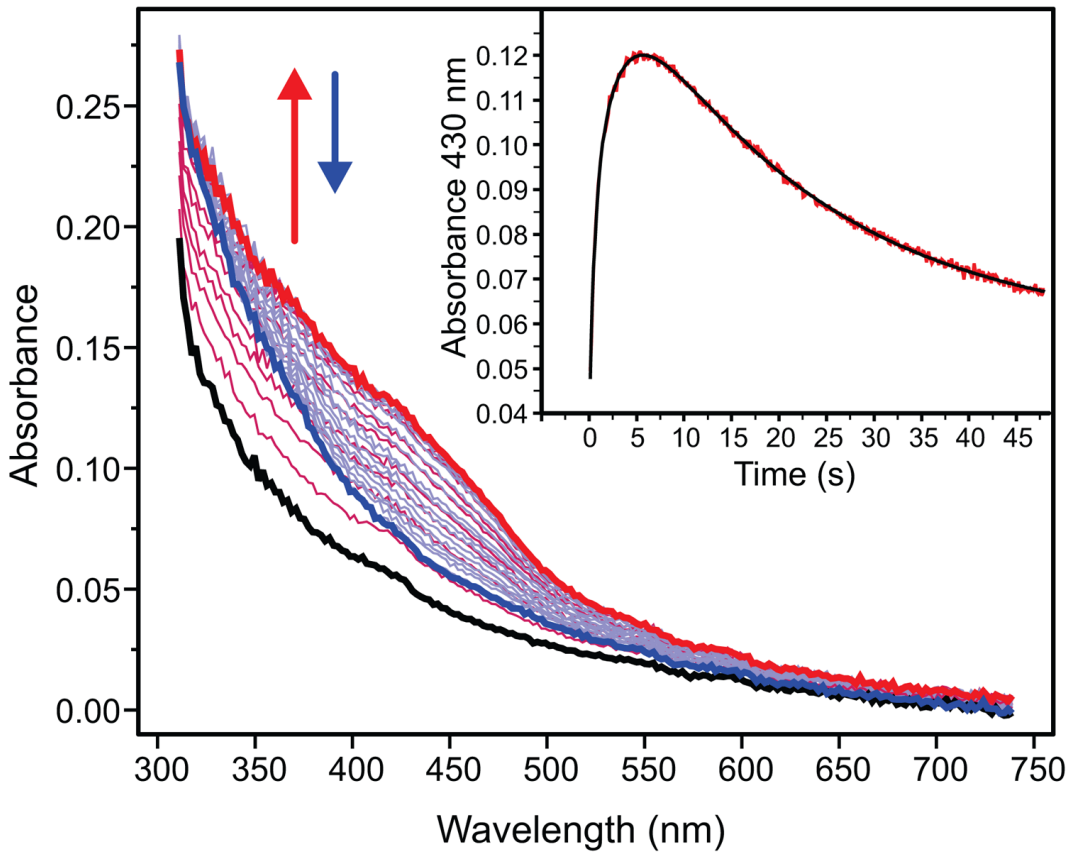

Figure 1. Photo-diode array spectra of a single-turnover reaction of MMOH with H33A MMOB (12 μM reactive MMOH active sites) in the absence of substrate, pH 7.0, 4 °C. The diferrous form of the enzyme H^{red} (black trace) oxidizes to form Q (red trace). Q subsequently decays to the resting diferric state H^{ox} of the enzyme (blue trace). There is no optical evidence for the formation any other intermediate apart from Q in this reaction. Inset: Kinetic time course at 430 nm (red) extracted from the diode array data. The 2-exponential fit (black) shows that Q forms with a rate constant of 0.38 s^{-1}.

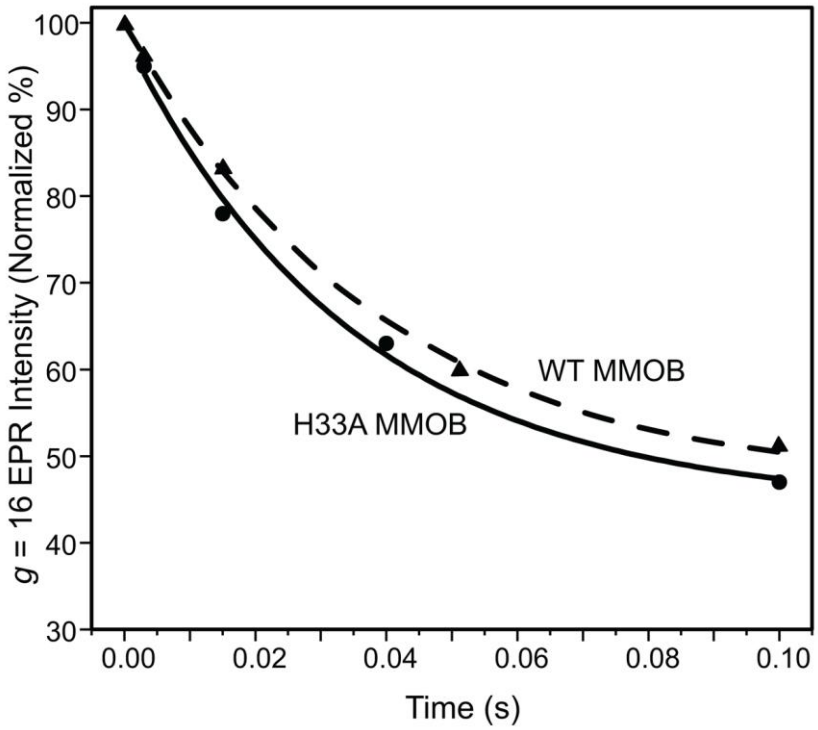

Figure 2. Decay of the parallel mode g = 16 integer-spin signal of compound O with WT MMOB (▲) or H33A MMOB (●) at pH 7.0, 4 °C. A single exponential fit to the data yields rate constants of 26 s^{-1} or 28 s^{-1}, respectively. The signal is normalized to that of a sample mixed with anaerobic buffer. EPR measurement conditions: T = 2.0 K, microwave power = 0.5 mW, microwave frequency = 9.405 GHz. The residual g =16 EPR intensity at 0.1 s arises from the slow-reacting fraction of reduced MMOH that reacts very slowly with oxygen. This represents approximately 45 % of the active sites in the particularly active MMOH sample utilized for EPR studies.

Single Turnover Reaction Using H33A MMOB in the Presence of a Substrate Facilitates Direct Detection of P*. The broad electronic absorption spectrum of **Q** with large extinction coefficients (Figure 1) masks the spectra of other intermediates with weaker optical absorbance. In order to circumvent this problem, we have added furan as a substrate to rapidly react with **Q**, and therefore quench its optical spectrum.[15] Since this substrate does not change the rate constants of the catalytic cycle prior to the decay of

Q,[14,15]the accumulation of intermediates preceding **Q** should not be altered.[14,15] We have also used methane instead of furan to quench **Q** with no change in the results. However, since methane is a gas, it limits the amount of O_2 that can be dissolved in the buffer, thereby restricting the concentration range available for the kinetic experiments.

A search for the optical features of **P*** using the commonly employed diode array detector as in Figure 1 proved unsuccessful. This is due to the relative insensitivity of the diode array detector. As an alternative, a spectra-kinetic data accumulation method was used to observe the single turnover reaction of MMOH with H33A MMOB and furan. In this technique, a series of single wavelength time courses are monitored at 15 nm intervals between 325 nm and 685 nm. These traces are then used to reconstruct the electronic absorption spectra of **O** and the other intermediates in the catalytic cycle. While this requires much more enzyme than a single diode-array measurement, the input light intensity is greatly attenuated (avoiding potential photochemical bleaching), and much finer temporal resolution is obtained due to the shorter integration time, leading to substantially higher signal to noise ratios. Moreover, the higher dynamic range of the photomultiplier detector allows the 300-380 nm region to be accurately monitored at the protein concentrations used in the experiment. The latter was critical for the characterization of **P***.

In the single turnover reaction of $\mathbf{H^{red}}$ with H33A MMOB and furan, we can observe the rapid formation of an intermediate species maximizing at 250 ms, which

subsequently decays over 10 seconds to the resting diferric form of the enzyme, $\mathbf{H^{ox}}$ (Figure 3). While the formation of this transient intermediate can be observed across the whole wavelength region scanned, the decay can be only seen at long wavelengths between 535 nm and 685 nm. The absence of this decay phase at shorter wavelengths occurs because the formation of diferric $\mathbf{H^{ox}}$ has a comparable rate constant as the decay of the intermediate and because $\mathbf{H^{ox}}$ possesses an electronic absorption band with a large extinction coefficient in the near-UV region (Figure 1), which masks the decay of the intermediate.

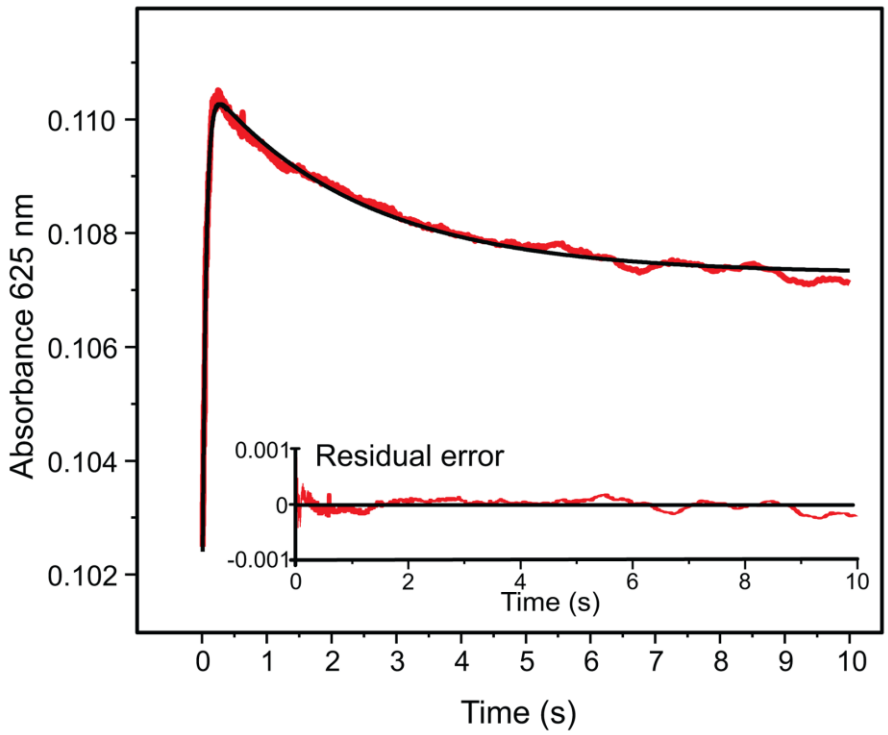

Figure 3. Single wavelength kinetic trace at 625 nm for the single turnover reaction of H^{red} and stoichiometric (to total diiron cluster concentration) H33A MMOB (83 µM reactive MMOH active sites) and 6 mM furan with 0.9 mM O_2 at pH 7.0 and 4 °C, indicates the rapid formation and decay of a transient species. The fit to the kinetic data (black trace) was obtained from a global fit to the multiple wavelength data (325 nm - 685 nm range).

In order to obtain accurate rate constants and estimates for the relative accumulation of the intermediates, a global analysis was performed using the large data set accumulated over a range of wavelengths. This technique utilizes the entire data set and adds the additional constraint of accommodating the kinetic model at multiple wavelengths. The global fitting analysis of the spectra-kinetic data supports the following kinetic model for the single turnover reaction: **O** → **P*** → **P** → $\mathbf{H^{ox}}$. The rate constants determined for the steps in the reaction in the order shown are: $k_1 = 21.9 \pm 0.5\ s^{-1}$, $k_2 = 0.33 \pm 0.03\ s^{-1}$, $k_3 = 1.76 \pm 0.05\ s^{-1}$. The result of this fit is shown as an overlay of the time course at 625 nm in Figure 3. The formation rate constant of 21.9 s^{-1} for the first intermediate is similar to the decay rate constant of compound **O**, as measured by following the decay of its characteristic integer spin $g = 16$ EPR signal (Figure 2). [17] The decay rate constant for this intermediate (0.33 s^{-1}) is also similar to the formation rate constant of 0.38 s^{-1} for **Q** (in actuality **P)** in the single turnover reaction monitored by diode array (Figure 1). [28] This confirms the identity of the observed intermediate as compound **P***. It also implies that the observation of the single turnover reaction starts with compound **O**. The formation of **O** is not observed here as it likely occurs in the dead time of the stopped flow instrument and has spectral properties indistinguishable from those of $\mathbf{H^{red}}$.

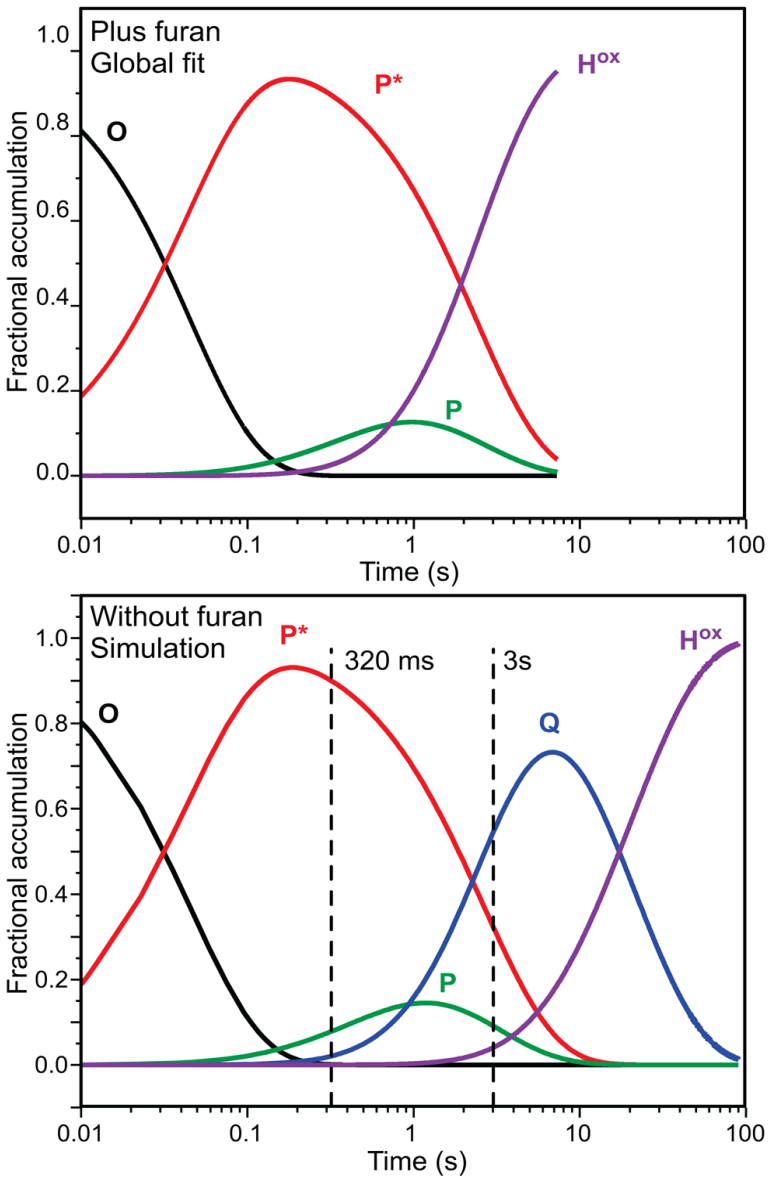

Figure 4. Speciation plots based on the global fitting analysis to the spectra-kinetic data of the single turnover reaction of MMOH in the presence of H33A MMOB. **Top:** in the presence of furan. **Bottom:** in the absence of a substrate. The top plot shows time courses for each species obtained directly from a global fit of the spectra-kinetic data from 325 nm – 685 nm collected over a 10 s interval. For the simulation in the bottom panel, a numerical integration method using the rate constants determined here and the previously determined value for the rate constant for Q decay when using MMOB H33A in the absence of substrate was used to compute the time courses shown.[28] The dashed vertical lines indicate the times at which rapid freeze quench samples were obtained for Mössbauer spectroscopy. In both top and bottom panels, the fractional accumulation refers to the reactive fraction of MMOH.

The global fit allows estimation of the time dependent accumulation of each intermediate as shown in Figure 4, *top*. **P*** is predicted to accumulate to approximately 90 % of the total active site concentration after 250 ms. Later, a small accumulation of intermediate **P** is also predicted as **P*** decays. The observed decay rate constant of **P** (1.7 s^{-1}) is slightly smaller than is observed in a single-turnover reaction in the presence of wild type MMOB (2.7 s^{-1}). [28] This is not unexpected because the functionally related MMOB H5A variant has been shown to decrease this rate constant to 1.71 s^{-1}. [28] The global fit to the MMOH reaction does not require the accumulation of compound **Q** between the decay of **P** and the formation of $\mathbf{H^{ox}}$. This is expected because the presence of 6 mM furan will completely quench **Q** (k_{form} = 1.7 s^{-1}, k_{decay} ~ 72 s^{-1} as calculated from the second order rate constant of **Q** decay with furan). [14,28] Compound **P*** is a catalytically competent intermediate because its rate constant for decay exceeds the turnover number for furan as a substrate at 4 °C (k_{cat} = 0.12 s^{-1}). [14,28]

UV-Vis Spectrum of P*. Multicomponent analysis of the entire multi-wavelength data set from which the time course shown in Figure 3 was extracted allows the electronic absorption spectrum of **P*** to be approximated (Figure 5). It has a maximal absorption in the near-UV region (ε_{325} = 12000 M^{-1} cm^{-1}) which is very similar to that observed for **O** (and $\mathbf{H^{red}}$) (ε_{325} = 11100 M^{-1} cm^{-1}). In fact, the entire UV-vis spectrum of **P*** is remarkably similar to, albeit distinguishable from, those of **O** and $\mathbf{H^{red}}$ (Figure 5,

inset). This suggests that they are similar species and markedly different than the more strongly absorbing intermediate **P**.

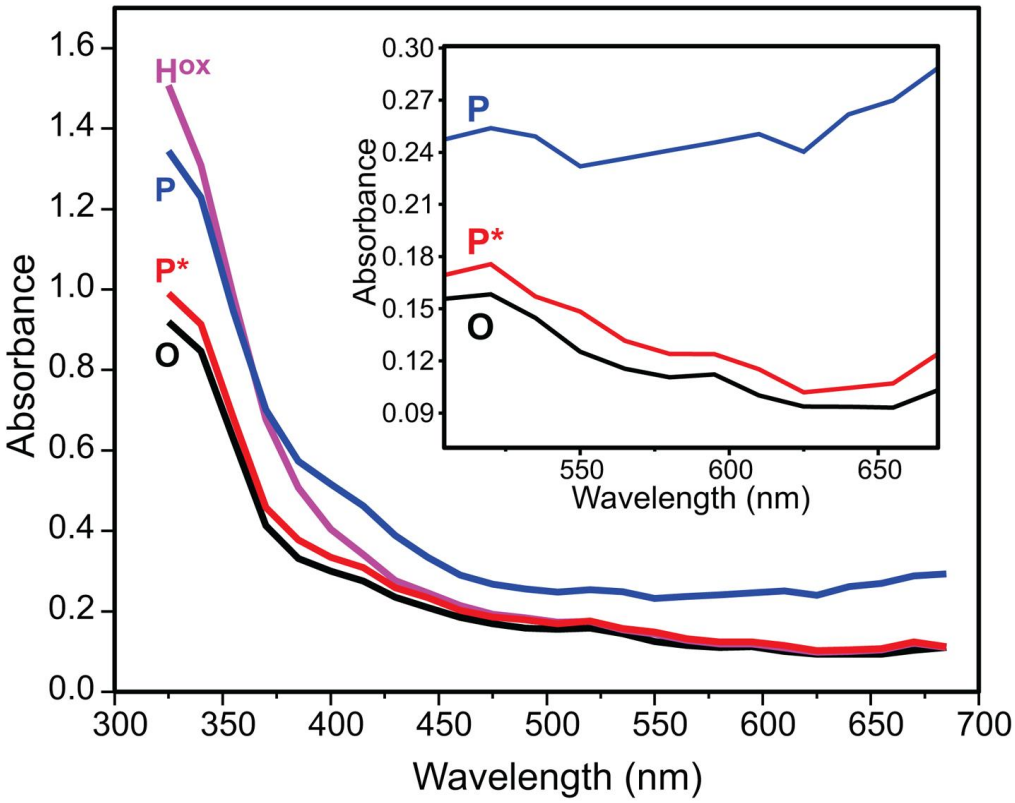

Figure 5. The pure component spectra of compound P* (red) as obtained by global fitting of spectra-kinetic data compared to those of compound O/H^{red} (black) and H^{ox} (magenta). The pure component spectrum of P (blue) (from a H^{red} single turnover reaction using WT-MMOB) has been overlaid for a comparison with P*. Experimental conditions as in Figure 3. Inset: Expanded spectra showing the difference in absorbance for intermediates P*, O, and P the long wavelength region.

Mössbauer Characterization of Compound P* Reveals a Diferrous Center.

Using ^{57}Fe enriched $\mathbf{H^{red}}$ and H33A MMOB in the absence of a substrate, we have prepared three samples for Mössbauer characterization of **P*** (Figure 7A, B, and C). Of the three samples, the first is the fully reduced sMMO, while the latter two were rapid-freeze quenched at 320 ms and 3 s, respectively, after mixing with O_2 at the times for which **P*** and **Q** are predicted to be near maximum levels (see Figure 4, *bottom*). Analyses of the Mössbauer spectra were complicated by the presence of a large fraction of slow-reacting diferrous MMOH ($\mathbf{H_{sl}^{red}}$**,** ca. 60% in the Mössbauer samples, 45% in the EPR samples) that is always encountered for MMOH from both *M. t.* OB3b and *M. c.* Bath.[18,20] In the absence of substrates, $\mathbf{H_{sl}^{red}}$ decays into an oxidized state $\mathbf{H_{sl}^{ox}}$ with an overall rate constant of 0.023 s^{-1} at 4 °C, pH 7.[17]

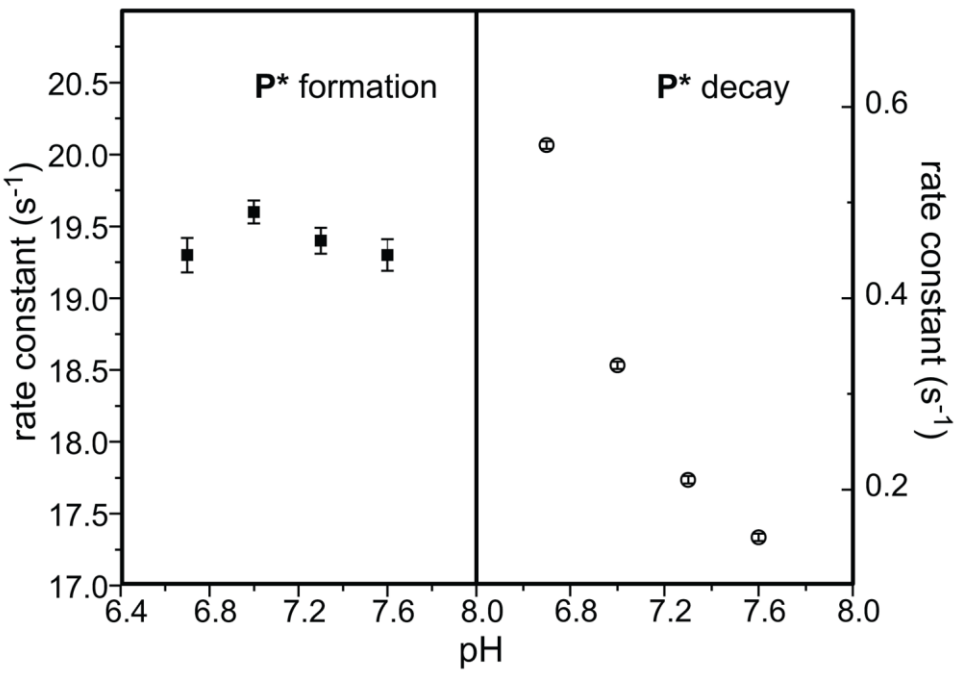

Figure 6. pH dependence profile of the kinetic steps of P* formation and decay. The rate constants were obtained from a global fit of H^{red} single turnover reaction using H33A MMOB in the presence of furan at each pH point. The experimental error for the data in the right panel falls within the symbols used to indicate the data.

Mössbauer Characterization of Compound P* Reveals a Diferrous Center.

Using ^{57}Fe enriched $\mathbf{H^{red}}$ and H33A MMOB in the absence of a substrate, we have prepared three samples for Mössbauer characterization of **P*** (Figure 7A, B, and C). Of the three samples, the first is the fully reduced sMMO, while the latter two were rapid-freeze quenched at 320 ms and 3 s, respectively, after mixing with O_2 at the times for which **P*** and **Q** are predicted to be near maximum levels (see Figure 4, *bottom*). Analyses of the Mössbauer spectra were complicated by the presence of a large fraction of slow-reacting diferrous MMOH ($\mathbf{H_{sl}^{red}}$**,** ca. 60% in the Mössbauer samples, 45% in the EPR samples) that is always encountered for MMOH from both *M. t.* OB3b and *M. c.*

Bath.[18,20] In the absence of substrates, $\mathbf{H_{sl}^{red}}$ decays into an oxidized state $\mathbf{H_{sl}^{ox}}$ with an overall rate constant of 0.023 s^{-1} at 4 °C, pH 7.[17]

Measurements of MMOH samples exhibiting a range of activities have shown that the reactive and slow-reacting fractions exhibit indistinguishable Mössbauer spectra for both the diferric and diferrous states.[42,43] Previous studies have established that the yield of product is >80% from a single turnover reaction in the presence of MMOB allowed to proceed until all of the diferrous MMOH has been oxidized independent of the fraction of slow-reactive MMOH present.[17] We hypothesize that $\mathbf{H_{sl}^{red}}$ fails to form the proper complex with MMOB, thereby making O_2 binding a rather slow and rate limiting step and masking intermediate formation. The diiron cluster itself is likely to remain in a uniform, active conformation.

The two iron sites of H^{red} are inequivalent and display distinct Mössbauer spectra.[43] In the absence of an applied magnetic field each site yields a quadrupole doublet. The quadrupole splitting, $\Delta E_Q(1)$, of site 1 is essentially the same for all molecules in the sample, i. e. the two lines of the doublet are sharp. $\Delta E_Q(2)$, however, is substantially distributed about its mean value, resulting in the observation of broad absorption lines (such broadening is frequently observed for high-spin Fe^{II} complexes). We wondered whether these lines were truly broadened or whether they

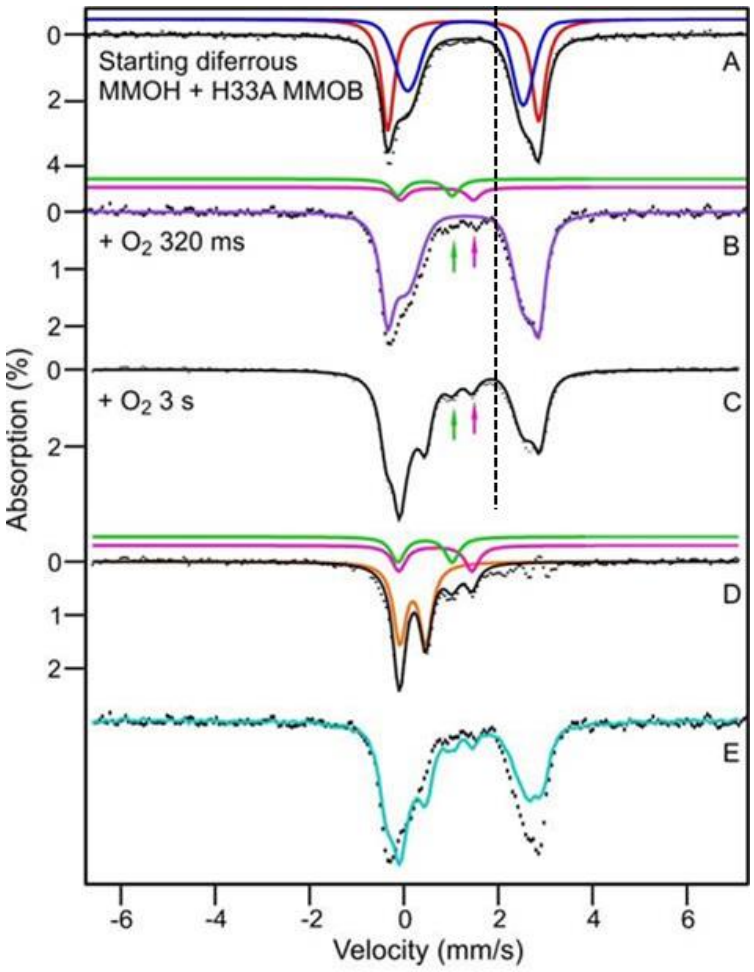

Figure 7. RFQ Mössbauer spectra from the time course of the reaction of $\mathbf{H}^{red}$ in the presence of stoichiometric H33A MMOB with a saturated solution of O_2. Spectra were recorded at 4.2 K in zero magnetic field. **(A)** Spectrum of $\mathbf{H}^{red}$. The black line is a representation of $\mathbf{H}^{red}$ drawn to represent 95% of the Fe in the sample. Contributions of the individual sites (47.5% each) are shown in red and blue. Red: ΔE_Q = 3.22 mm/s, δ = 1.26 mm/s; Lorentzian lines with 0.35 mm/s FWHM. Blue: ΔE_Q = 2.37 mm/s, δ = 1.35 mm/s; Voigt lines with -0.6 mm/s FWHM. The remainder of the sample (5%) is comprised of unidentified non-diferrous species. **(B)** Sample quenched at 320 ms. Purple line (86% of total Fe) represents all ferrous species in the sample. Magenta line shows contribution of **P** (3% of Fe); magenta arrow points at the high energy line of **P**. The sample also contains ~ 5% $\mathbf{H}^{ox}$ (green line and green arrow) and ~5% unchanging non-diferrous species. **(C)** Sample quenched at 3 s. Black line is the sum of simulations for diferrous species (58%), intermediate **Q** (23%), intermediate **P** (magenta arrow, 7%) and $\mathbf{H}^{ox}$ (green arrow, 7%). ~5% unchanging non-diferrous species are also present. **(D)** Spectrum obtained by subtracting the contributions of $\mathbf{H}^{red}$ from Figure 7C. The solid black line is the sum of the colored curves, which correspond to **Q** (orange), **P** (ΔE_Q = 1.55 mm/s, δ = 0.69 mm/s, magenta) and $\mathbf{H}^{ox}$ (green). **(E)** Superposition of the raw data of the samples of (B, black hashed) and (C, cyan).

masked the presence of two doublets representing site 2 (as the latter case, for instance, might occur if a binding site for water is partially occupied). To address this point and to enhance the spectral resolution, we have removed the line width contribution of the ^{57}Co Mössbauer source (~ 0.12 mm/s) using a Fourier transform procedure described by Dibar-Ure and Flinn and others.[44,45] The resolution-enhanced spectra, shown and described in SI, suggest that the line positions of all doublets present have been identified and that site 2 produces *one*, albeit broadened, doublet rather than two. The sharp doublet of site 1 has quadrupole splitting ΔE_Q = 3.22 mm/s and isomer shift δ = 1.26 mm/s (red line in Figure 7A). We have simulated the broadened doublet of site 2 (blue line in Figure 7A) by using Voigt line shapes, convoluting a Lorentzian of 0.15 mm/s full width into a Gaussian with full width 0.65 mm/s (this is accomplished by using a negative line width in WMOSS).

For this study, we were interested in modeling the shape of the high-energy lines of sites 1 and 2 such that a good value is obtained for the total amount of diferrous cluster in the sample (the spectral area to the right of the dashed line, which represents half of the ferrous absorption, is not contaminated by contributions from other species). The blue and red lines were obtained by simulating the ferrous high-energy feature, assuming a 1:1 site ratio (a 1:1 site ratio is strongly indicated by the 8.0 Tesla spectrum of Figure 13 of ref [43]). We are not claiming that the black solid line in Figure 7A (sum of red and blue curves) is a unique representation for $\mathbf{H^{red}}$ (both reactive and slow-reacting), but the

decomposition will serve well for the present purpose. The parameters used are quoted in the caption of Figure 7.

The black curve of Figure 7A suggests that ca. 95% of the iron in the sample prior to mixing with O_2 is high-spin ferrous. The remaining 5% of the iron is probably originates from unreduced diferric species that remains constant in all samples. The high energy lines of this species would appear in the central part of the spectrum (see green arrows in Figure 7). In the following, all Fe percentages quoted refer to percentage of *total* Fe in a sample.

Figure 7B shows a Mössbauer spectrum of a sample freeze-quenched at 320 ms (**P*** sample). It can be seen that the spectra of Figures 7A and B are exceedingly alike. Fitting the rightmost feature as described above shows that ~ 86% of the iron of the **P*** sample is diferrous. Yet, nearly all of the g = 16 EPR feature belonging to the *active* fraction of MMOH, $\mathbf{H^{red}}$ and **O,** has disappeared at this time (Figure 2). If the disappearing fraction of the signal were to indicate *oxidation* of the cluster, we would expect to observe at most 55% of the diferrous cluster (the remaining $\mathbf{H_{sl}^{red}}$) in the Mössbauer spectrum, suggesting that **P*** is diferrous (we will strengthen this argument shortly). The ~8 % Fe that disappeared from the ferrous pool accumulates in the spectral region where diferric intermediates **P**, $\mathbf{H^{ox}}$ and $\mathbf{H_{sl}^{ox}}$ absorb (Figure 7B arrows). We note that a **P*** sample of a second enzyme preparation produced a spectrum identical to that of Figure 7B.

Figure 7C shows a Mössbauer spectrum quenched 3 s after adding O_2. The most conspicuous change between the spectra of the 320 ms and 3 s samples is a pronounced decline of the diferrous species. This change is readily appreciated by plotting (Figure 7E) the spectra of Figures 7 B (hashed) and 7C (cyan) such that their spectral area represents the same amount of total iron. Analysis of the spectrum in Figure 7C shows that the ferrous pool now contains 58% of the total Fe. Hence between 320 ms and 3 s about 28 % of the iron in the sample is converted from the ferrous state into a higher oxidation state. By removing the remaining 58 % of the ferrous Fe from the spectrum of Figure 7C (this fraction is due to residual $\mathbf{H_{sl}^{red}}$ plus presumably some **P***), we obtained the spectrum of Figure 7D, which shows the spectra of the species that result from the iron that vanished from the ferrous pool. The majority component in Figure 7D, representing 23 % of total Fe (57 % of the active iron), is a species (orange line) with ΔE_Q = 0.53 mm/s and δ = 0.18 mm/s. Within the uncertainties (±0.02 mm/s for ΔE_Q and ±0.01 mm/s for δ) these values agree with those previously reported for the $Fe^{IV}Fe^{IV}$ intermediate **Q**.[20,21] An additional ~7 % of the iron can be attributed to a doublet with parameters (ΔE_Q = ~1.55 mm/s, δ = ~0.69 mm/s) indicative of the diferric peroxo intermediate **P**; its contribution is outlined by the magenta line in Figure 7D. Approximately 6 % of the total iron (over and above the original unreduced fraction) is diferric at 3 s (green curve).

Table 1. Predicted and observed distribution of intermediates in RFQ experiments

***t* = 0 s**		***t* = 320 ms**		***t* = 3 s**	
Prediction (At start)	Observation (Mössbauer)	Prediction (Kinetics)	Observation (Mössbauer)	Prediction (Kinetics)	Observation (Mössbauer)
100 % $\mathbf{H^{red}}$	95 % diferrous	55 % $\mathbf{H_{sl}^{red}}$	86 % diferrous	50 % $\mathbf{H_{sl}^{red}}$	58 % diferrous
		33 % **P***		10 % **P***	
		3.4 % **P**	3 % **P**	4 % **P**	7 % **P**
		3.6 % (**Q** + $\mathbf{H^{ox}}$)		22 % **Q**	23 % **Q**
			5 % $\mathbf{H^{ox}}$	2 % $\mathbf{H^{ox}}$	7 % $\mathbf{H^{ox}}$+ $\mathbf{H_{sl}^{ox}}$
				6 % $\mathbf{H_{sl}^{ox}}$	
	5 % unidentified[a]	5 % unidentitied[b]	5 % unidentified[a]	5 % unidentified [b]	5 % unidentified[a]

[a] In all samples, approximately 5 % of the Mössbauer absorption could not be positively identified as it competes with the noise. This absorption is probably associated with diferric species (not a single one). It is certainly not originating from ferrous MMOH and may derive in part from unreduced enzyme.

[b]Assumed from the Mössbauer spectrum of the t = 0 sample.

As summarized in Table 1, the distribution of species revealed by the Mössbauer spectra correlates very well with the kinetics-derived speciation plot of Figure 4, *bottom*. At 3 s, the kinetics predict that the sample will be composed of 50 % $\mathbf{H_{sl}^{red}}$, 10% **P***, 4 % **P**, 22 % **Q**, 2 % $\mathbf{H^{ox}}$, 6 % $\mathbf{H_{sl}^{ox}}$ and 5 % unidentified species that may include $\mathbf{H^{ox}}$ that was never reduced. The observed fractions are 58 % diferrous ($\mathbf{H_{sl}^{red}}$ plus presumably **P***), 7 % **P**, 23 % **Q**, 7 % diferric ($\mathbf{H^{ox}}$ plus $\mathbf{H_{sl}^{ox}}$), and 5 % other unidentified non-diferrous species. The excellent agreement at this time point, particularly the correct prediction of the amount of **Q** observed, suggests that the speciation plot is accurate and can be used to predict the distribution of species at 320 ms. The 28 % loss of diferrous material observed between the 320 ms to 3 s time points is accounted for as a 6 % loss of $\mathbf{H_{sl}^{red}}$ and a 22 % loss of **P***. **P*** is partially converted into **P** and then **Q,** while the small fraction of **P** present at 320 ms also flows into **Q**. Since the speciation plot and the Mössbauer spectra show that approximately the same amount of **P** is present at both time points, the net loss in diferrous **P*** (22%, Figure 7C) should approximately equal the net gain in **Q** (23%), as observed. The speciation plot predicts that **P*** declined by 67 % between 320 ms and 3 s, suggesting that 35% of the total iron was in the **P*** state when it had its maximum concentration near 0.3 s after reaction with O_2. This value is also consistent with kinetic predictions and the observed Mössbauer total of 86 % diferrous cluster at 320 ms (predicted 55% $\mathbf{H_{sl}^{red}}$ plus 33% **P***). Together these findings strongly support the assignment of **P*** as a diferrous species.

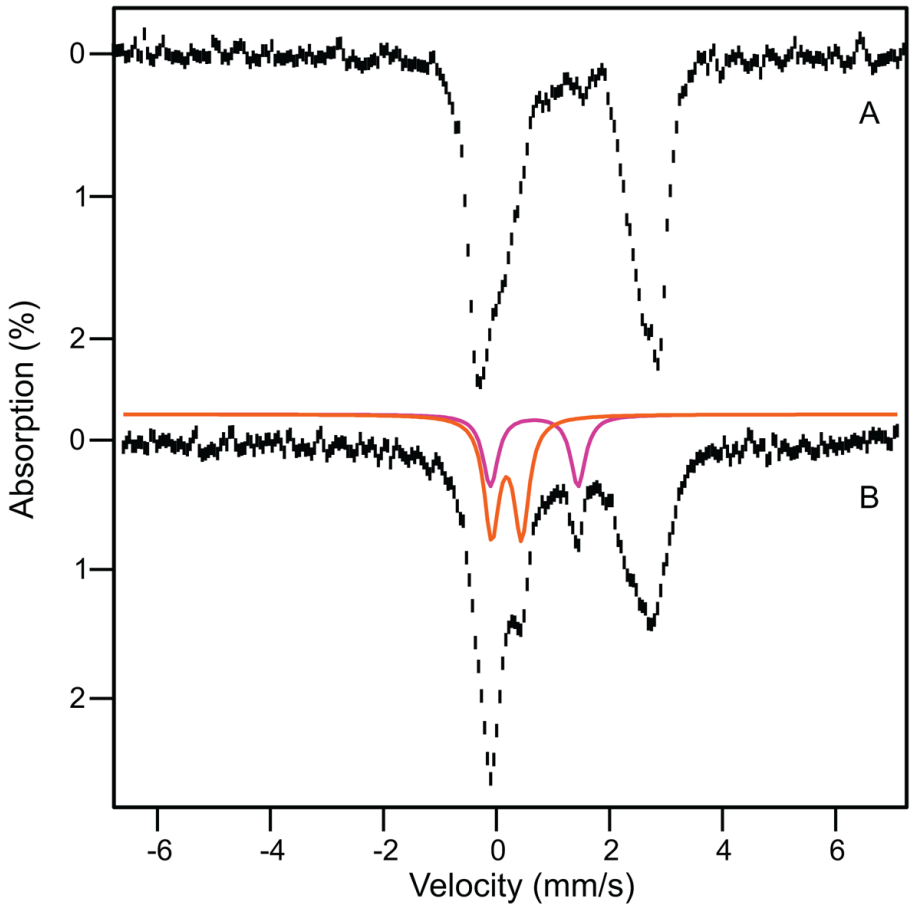

Figure 8. 4.2 K Mössbauer spectra of rapid freeze quenched samples of the H^{red} single turnover reaction at 320 ms. The reaction for spectrum A uses H33A MMOB while the reaction for spectrum B uses WT MMOB. Here spectrum A is the same as that shown in Figure 7B. Spectrum B exhibits considerable accumulation of intermediates P (15% of Fe, magenta) and Q (20%, orange).

The line shape of the ferrous pool has small variations throughout the series of experiments, but these variations are so minor that we were not able to extract a unique spectrum for **P*** by examining difference spectra. Obviously, the Mössbauer spectrum of **P*** is very similar to that of $\mathbf{H^{red}}$. As pointed out above, we explored the possibility that the distribution of the ΔE_Q values at site 2 arises from the superposition of two or more distinct species (more than one form of $\mathbf{H^{red}}$ or $\mathbf{H^{red}}$ plus **O** or **P***). However, the Fourier

transform treated spectra shown in SI Figure S1 provide no evidence that site 2 contributes two different doublets which would indicate, across the molecular population, two ligand geometries for site 2.

As described above, the use of H33A MMOB shifts the kinetics such that **P*** can be trapped effectively in a 0.3 - 3 s time window. As a control, a sample was prepared at 0.3 s using WT MMOB. A 4.2 K, zero field Mössbauer spectrum is shown in Figure 8B. The spectrum of the H33A MMOB sample of Figure 7B is shown in Figure 8A for comparison. In spectrum 8B, ca. 15% of the iron belongs to intermediate **P** (magenta line) and 20 % is associated with intermediate **Q** (orange line), which is in excellent agreement with the expected amounts of these species based on the rate constants for intermediate conversion reported previously.[15,19] We note that the amount of iron in **P** and **Q** represents essentially all iron belonging to the reactive MMOH fraction, and thus the formation of these species is significantly accelerated when using WT MMOB. The Mössbauer parameters of **P** are not readily obtained because the low-energy line of the doublet is invariably masked by the contribution of other species. Currently, our best estimate, obtained from analysis of the spectrum of Figure 8 B is $\Delta E_Q = 1.53 \pm 0.06$ mm/s and $\delta = 0.66 \pm 0.03$ mm/s. These values using WT MMOB agree well with ΔE_Q =1.51 mm/s and δ = 0.66 mm/s reported for **P** (termed $\mathbf{H_{peroxo}}$) for the *M. c.* Bath enzyme.[18]

Discussion

The combined use of H33A MMOB to provide a constriction in the flow of the reaction cycle, inclusion of substrate to eliminate the strong background chromophore from compound **Q**, and the use of sensitive spectra kinetic data collection has allowed the observation of the transient intermediate **P*** in the single turnover reaction of MMOH. Our early transient kinetic studies strongly suggested that a reaction cycle intermediate occurs after **O** and before **P**, and that it should accumulate to observable levels (maximum ~45 %).[17,19,28] Nevertheless, direct detection has proven difficult. The current results show that this was the case because intermediates $\mathbf{H^{red}}$, **O**, and **P*** have very similar optical spectra and also because the kinetics of intermediate interconversion dictate that a high background from the more strongly absorbing **P** and **Q** are always present when wild type MMOB is utilized in the reaction. Based on the observation that the decay of **O** results in the loss of the g = 16 EPR signal characteristic of the diferrous cluster, we originally proposed that **P*** would contain one or two Fe^{III} ions in some sort of oxygen-bound cluster [17,19] The current study shows that this is not the case, suggesting that the critical step in the preparation of the cluster to bind and activate O_2 occurs by a novel mechanism. This aspect of the MMOH reaction cycle is discussed here.

The Loss of the g = 16 EPR Signal in the Transformation from O to P* is Caused by a Structural Change of the Diferrous Cluster, not the Result of Oxidation. The view that any form of MMOH containing a diferrous cluster must exhibit

a g = 16 EPR is too restrictive as is apparent from a consideration of its origin. As shown previously, the two high-spin ferrous sites of $\mathbf{H}^{\mathbf{red}}$ are weakly coupled by ferromagnetic exchange, with J-values around -0.75 cm^{-1} in the $\mathbf{H}_{exch} = J\,\boldsymbol{S_1 \bullet S_2}$ convention ($S_1 = S_2 = 2$) **.** Evaluated in the weak coupling scheme (see Figure 4 of ref [34]) the g_{eff} = 16 resonance results from a particular combination of J and the zero-field splitting parameters D_1, E_1/D_1 , D_2 and E_2/D_2 of the two sites. Spin concentration and line shapes of the g_{eff} = 16 signal are well described by choosing J = -0.75 cm^{-1}, $D_1 = D_2$ = -5 ± 1 cm^{-1} , $E_1/D_1 = E_2/D_2$ = 0.27 together with $\sigma_{E/D}$= 0.05 ($\sigma_{E/D}$ describes a Gaussian distribution of E/D values, assumed to be the same for both sites). The assumption of equal D and E/D values for both sites is convenient but not crucial (see ref[34]) The g = 16 feature at X-band results from $\Delta m_i = 0$ transitions between the members of a (quasi) doublet of $m_1, m_2 = \pm 2$ heritage which is split by $\Delta \approx 9(E_1/D_1)^4\, D_1^2/8J \approx 0.2$ cm^{-1}. [34] The expression for Δ reveals that a minor structural change at the active site could change one of the relevant parameters such that Δ exceedes ≈ 0.3 cm^{-1}, the energy of the microwave quantum at X-band, essentially abolishing the resonance. Given that J is already very small, a *decline* of J, for instance, by a mere 0.3 cm^{-1} would be sufficient to explain the disappearance of the EPR signal for **P***. In principle, these changes could be probed at Q-band, but the interpretation of such experiments might be difficult as the signals from $\mathbf{H}^{\mathbf{red}}$ and **P*** may overlap. Of course, in the transition from **O** to **P***, the exchange coupling constant J may

change sign to render an antiferromagnetically coupled system, with the consequence that the ground quasi doublet is EPR silent.

The Diferrous Nature of P* is not Consistent with a Superoxo or Peroxo Cluster. The analysis of the transient kinetics of the single turnover reaction of $\mathbf{H^{red}}$ in the presence of H33A MMOB and either presence or absence of furan allows prediction of the relative concentrations of **O**, **P***, **P**, and **Q** at any point during the time course (Figure 4). Mössbauer spectra of samples taken at diagnostic points during the time course show that the concentrations of the previously characterized intermediates **P** and **Q** are predicted very accurately. This strongly suggests that **P*** is also present at the predicted concentrations. This being the case, the Mössbauer spectrum of the 320 ms sample shows that the only species present in sufficient concentration to be **P*** must have a diferrous cluster with parameters similar to those of $\mathbf{H^{red}}$ and **O**. Thus, **P*** can be neither an $Fe^{II}Fe^{III}$-superoxo intermediate nor an $Fe^{III}Fe^{III}$-peroxo intermediate distinct from **P**. Considering that the spectroscopic characterization of **P** indicates that it is an $Fe^{III}Fe^{III}$-peroxo intermediate of some sort, [18,20] the current spectroscopic and kinetic data suggest that the diiron cluster in MMOH proceeds directly from a diferrous state in **P*** to a bridged peroxo-bound diferric state in **P** without an intervening $Fe^{II}Fe^{III}$ intermediate detectable on the millisecond time scale. This experimental conclusion is supported by density functional theory studies, which indicate that the binding of oxygen to *one* of the

two iron atoms to form a $Fe^{II}Fe^{III}$ -superoxo intermediate is thermodynamically unfavorable.[46,47]

The Mössbauer Spectrum of P* Suggests that it is Structurally Similar to H^{red}. H^{red} from *M. t.* and *M. c.* have a characteristic Mössbauer spectrum in which one iron site exhibits a sharp quadrupole doublet while the spectrum of the second site has a distributed ΔE_Q resulting in a broad quadrupole doublet. The distribution of ΔE_Q must entail some form of a structural heterogeneity at site 2. However, as demonstrated by Stoian et al.,[48]a broadly distributed hyperfine parameter may possibly reflect a "soft" coordinate that vastly amplifies a minute structural heterogeneity, rather than a molecular structure with pronounced disorder. The distributed ΔE_Q of site 2, while not yet understood, is valuable for the current study in that it becomes a sensitive monitor of the structure of the diferrous MMOH diiron cluster.

It is noteworthy that the zero field Mössbauer spectra of $\mathbf{H^{red}}$ and **P*** are essentially identical. There are very minor changes, but these changes are too small to be analyzed, and they may reflect subtle changes between preparations or even freezing effects. In particular, both $\mathbf{H^{red}}$ and **P*** seem to have a similar, if not identical, distributed ΔE_Q for site 2. This suggests that the changes that occur during formation of **P*** and attendent loss of the $g = 16$ EPR signal have only small effects on the cluster structure and ligation.

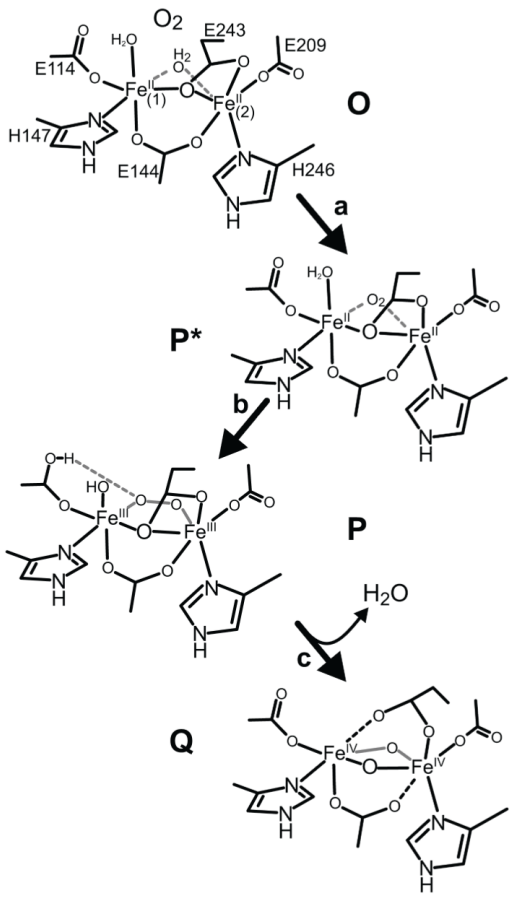

Scheme 2. Proposed structures of MMOH single turnover cycle intermediates. The introduction of O_2 in place of water in the cluster coordination sphere of intermediate O is speculative. However, the water must be displaced and O_2 bound at some point during process of formation of intermediate P.

Potential Structures of P*. The data available are not sufficient to determine the precise nature of the change occuring as **O** is converted to **P***. These changes, however, result in the loss of the $g = 16$ signal without a change in oxidation state or major change in the cluster structure. One possibility, illustrated in Scheme 2, step a, is that O_2 binds nearby or directly to the cluster, displacing the solvent water molecule that has been shown to bridge the iron atoms in the crystal structure of diferrous MMOH from the nearly identical $\mathbf{H}^{\mathbf{red}}$ from *M. c.* Bath. [49] VTVH MCD and CD studies indicate that the

iron atoms of the diferrous cluster are both primarily 5-coordinate, indicating that the solvent seen in the crystal structure is likely to be weakly bound and displaceable.[46,50] The preceding intermediate **O** requires O_2 for its formation but its decay rate monitored by the loss of the g = 16 EPR signal shows no O_2 concentration dependence, suggesting that O_2 binds essentially irreversibly in the active site. The formation of **P*** may involve the next step in O_2 activation as solvent is released from the cluster to allow O_2 to bind. If the conversion of **O** to **P*** involves actual association of O_2 with the cluster, then O_2 must bind with little electron transfer from the cluster iron atoms. While there is no precedent for this in O_2 reactions with *diiron* clusters, we have recently shown that a weak Fe^{II}-O_2 complex can form in the active site of a mononuclear Fe^{II} dioxygenase when an active site mutation prevents efficient electron transfer to the oxygen. [51] Computational studies for both nonheme and heme systems have shown that O_2 binding to Fe^{II} is comparatively weak, a useful property in systems where modulation of O_2 affinity is important. [52-55] Transfer of electron density from the Fe^{II} to the O_2 is often far from complete, and it is strongly dependent on factors such as the state of hydrogen bonding or charge interactions in the active site, as well as the nature of the ligand *trans* to the metal bound O_2.[56,57] In the current case, displacing solvent and/or replacing it with weakly bound O_2 in the coordination sphere would be consistent with the minor increase in the intensity of the optical spectrum of **P*** compared with that of **O** as well as the minor changes observed in the Mössbauer spectrum.

Steps in O_2 Activation. Three facts are known about intermediates **P** and/or **Q** that must be reconciled in considering the models for **P*** that arise from the discussion here and from DFT studies. [29-31,58-61] First, Mössbauer spectra reported here and elsewhere show that the two iron atoms in intermediate **P** are in very similar electronic environments, and the same is true of the two iron atoms in **Q**.[18,20,21] Second, pH studies reported here and in previous studies of both *M. t.* and *M. c.* MMOH single turnover kinetics show that the **O** to **P*** transition does not require a proton transfer, whereas both the **P*** to **P** and **P** to **Q** transitions are pH dependent.[16,19] A proton inventory study suggests that each of the pH dependent steps involve a single proton hop, although one essential and one nonessential proton translocation are predicted based on fitting the pH dependency for the **P** to **Q** transition in *M. c.* MMOH.[16,18,19] Third, the Mössbauer spectrum of **P** exhibits an isomer shift of about 0.66 mm/s which is similar to that observed for deprotonated peroxo ligands. [62-65] This suggests that a proton is transferred to some moiety other than the bridging peroxo group as **P** is formed. It is also relevant to note here that metal centers in enzymes tend to maintain a constant net local charge, and this appears to be a net charge of zero for the structurally characterized states of MMOH. [66-68] For this to be true in the case of **P** formation from **P***, the proton transfer must occur between groups bound to the diiron cluster, and charge balance at each iron requires that the donor and acceptor groups be associated with the same iron atom.

The intermediates shown in Scheme 2 steps a-c satisfy all of the experimental observations and maintain a neutral overall net charge for the cluster. Glu114 is proposed to play the role of accepting a proton from Fe1-bound solvent and eventually donating it to the peroxo moiety to promote O-O bond cleavage. [19] This maintains the local charge on Fe1 and satisfies the required one hop proton transfer process. The protonation of the carboxylate residue and its hydrogen bonding interaction with the bridging peroxide moeity is supported by information obtained from synthetic diiron model compound mimics of **P** and DFT studies of oxygen activation in RNR.[69,70] This pathway also requires the minimum structural reorganizations in the **O** to **P*** to **P** sequence, consistent with the Mössbauer results reported here.

Comparison with Intermediate P* from *M. capsulatus* Bath. An intermediate occuring before $\mathbf{H_{peroxo}}$ in the *M. c.* Bath MMOH single turnover cycle (*M. c*. **P***) has been observed that differs from the **P*** reported here in its reported oxidation state.[16] An $Fe^{III}Fe^{III}$ oxidation state assignment in the case of *M. c*. **P*** was based on the observation of an electronic absorption spectrum similar to that of $\mathbf{H_{peroxo}}$. This was obtained by a global fit of the single turnover absorption data at two diagnostic wavelengths for a reaction of *M. c.* $\mathbf{H^{red}}$ with O_2 in the presence of wild type *M. c.* MMOB and methane. While the presence of a substrate in both studies quenches the large absorption background arising from **Q**, the use of H33A MMOB in our study provides the additional advantages of increasing the yield of **P*** and reducing the background absorption from **P**.

In our case, the oxidation state of **P*** was directly determined using Mössbauer spectroscopy, making it clear that there is insufficient $Fe^{III}Fe^{III}$ species present to account for **P*** at the time it maximizes. The kinetics of intermediate conversion also differ significantly in the *M. t.* OB3b and *M. c.* Bath enzymes. The **P*** formation rate constants at 4 °C and pH 7.0 are 26 s^{-1} and 6.7 s^{-1}, for the *M. t.* and *M. c.* enzymes, respectively, in the presence of their specific WT MMOBs. Similarly, the **P** formation rate constants are reported to be 10 s^{-1} and 0.75 s^{-1} using wild type MMOB for *M. t.* and *M. c.* enzymes, respectively. The similarity of the formation rate constants of *M. c.* **P*** and *M. t.* **P** raises the possibility that *M. c.* **P*** is another form of *M. c.* **P**, accounting for its similar optical spectrum. Thus far, we have not observed evidence for this species in the *M. t.* system.

Conclusion

In summary, this study has elucidated the electronic absorption and Mössbauer spectra of intermediate **P*** in the single turnover cycle of *M. t.* MMOH. We should note that we were pleasantly surprised to find that the spectra-kinetic and Mössbauer data correlate exceedingly well, implying that either approach is likely to yield further useful results for eludidating the catalytic cycle of MMOH. Our results show that **P*** is a diferrous intermediate that is EPR silent at X-band (studies at Q-band might recover the $g = 16$ signal). One possibility for the formation of **P*** requiring minimal overall structural reorganization assumes association of O_2 with the diferrous cluster as the first step in a multiphase binding process that follows an effectively irreversible O_2 binding in the hydrophobic enzyme active site during the formation of intermediate **O**. A comparatively slow displacement of solvent from the metal center, and possibly formation of a weak Fe^{II}-oxygen complex, would overcome the most difficult steps in metal-O_2 complex formation and facilitate formation of the strong peroxo complex needed for O-O bond cleavage in the next step.

Acknowledgements

This work is supported by the NIH grants GM40466 and GM100943 (to J. D. L.) and NSF Grant CHE-1012485 (to E.M.).

References

(1) Hanson, R. S., and Hanson, T. E. (1996) Methanotrophic bacteria. *Microbiol. Rev. 60*, 439-447.

(2) Ruscic, B., Litorja, M., and Asher, R. L. (1999) Ionization energy of methylene revisited: Improved values for the enthalpy of formation of CH_2 and the bond dissociation energy of CH_3 via simultaneous solution of the local thermochemical network. *J. Phys. Chem. A 103*, 8625-8633.

(3) Hakemian, A. S., and Rosenzweig, A. C. (2007) The biochemistry of methane oxidation. *Annu. Rev. Biochem. 76*, 223-241.

(4) Hyman, M. R., Murton, I. B., and Arp, D. J. (1988) Interaction of ammonia monooxygenase from *Nitrosomonas europaea* with alkanes, alkenes, and alkynes. *Appl. Environ. Microbiol. 54*, 3187-3190.

(5) Fox, B. G., Froland, W. A., Dege, J. E., and Lipscomb, J. D. (1989) Methane monooxygenase from *Methylosinus trichosporium* OB3b. Purification and properties of a three-component system with high specific activity from a type II methanotroph. *J. Biol. Chem. 264*, 10023-10033.

(6) Wallar, B. J., and Lipscomb, J. D. (1996) Dioxygen activation by enzymes containing binuclear non-heme iron clusters. *Chem. Rev. 96*, 2625-2657.

(7) Baik, M.-H., Newcomb, M., Friesner, R. A., and Lippard, S. J. (2003) Mechanistic studies on the hydroxylation of methane by methane monooxygenase. *Chem. Rev. 103*, 2385-2419.

(8) Tinberg, C. E., and Lippard, S. J. (2011) Dioxygen activation in soluble methane monooxygenase. *Acc. Chem. Res. 44*, 280-288.

(9) Lipscomb, J. D. (2006) Catalysis and regulation in the soluble methane monooxygenase system: Applications of isotopes and isotope effects, in *Isotope Effects in Chemistry and Biology* (Kohen, A., and Limbach, H.-H., Eds.), pp 931-953, CRC Press, Boca Raton, FL.

(10) Que, L., Jr., and Tolman, W. B. (2002) Bis(m-oxo)dimetal "diamond" cores in copper and iron complexes relevant to biocatalysis. *Angew. Chem. Int. Edit. 41*, 1114-1137.

(11) Wang, D., Farquhar, E. R., Stubna, A., Münck, E., and Que, L., Jr. (2009) A diiron(IV) complex that cleaves strong C-H and O-H bonds. *Nature Chem. 1*, 145-150.

(12) Do, L. H., and Lippard, S. J. (2011) Evolution of strategies to prepare synthetic mimics of carboxylate-bridged diiron protein active sites. *J. Inorg. Biochem. 105*, 1774-1785.

(13) Kovaleva, E. G., Neibergall, M. B., Chakrabarty, S., and Lipscomb, J. D. (2007) Finding intermediates in the O_2 activation pathways of non-heme iron oxygenases. *Acc. Chem. Res. 40*, 475-483.

(14) Lee, S.-K., Nesheim, J. C., and Lipscomb, J. D. (1993) Transient intermediates of the methane monooxygenase catalytic cycle. *J. Biol. Chem. 268*, 21569-21577.

(15) Brazeau, B. J., and Lipscomb, J. D. (2000) Kinetics and activation thermodynamics of methane monooxygenase compound Q formation and reaction with substrates. *Biochemistry 39*, 13503-13515.

(16) Tinberg, C. E., and Lippard, S. J. (2009) Revisiting the mechanism of dioxygen activation in soluble methane monooxygenase from *M. capsulatus* (Bath): Evidence for a multi-step, proton-dependent reaction pathway. *Biochemistry 48*, 12145-12158.

(17) Liu, Y., Nesheim, J. C., Lee, S.-K., and Lipscomb, J. D. (1995) Gating effects of component B on oxygen activation by the methane monooxygenase hydroxylase component. *J. Biol. Chem. 270*, 24662-24665.

(18) Liu, K. E., Valentine, A. M., Wang, D. L., Huynh, B. H., Edmondson, D. E., Salifoglou, A., and Lippard, S. J. (1995) Kinetic and spectroscopic characterization of intermediates and component interactions in reactions of methane monooxygenase from *Methylococcus capsulatus* (Bath). *J. Am. Chem. Soc. 117*, 10174-10185.

(19) Lee, S.-K., and Lipscomb, J. D. (1999) Oxygen activation catalyzed by methane monooxygenase hydroxylase component: proton delivery during the O-O bond cleavage steps. *Biochemistry 38*, 4423-4432.

(20) Shu, L., Nesheim, J. C., Kauffmann, K., Münck, E., Lipscomb, J. D., and Que, L., Jr. (1997) An $Fe(IV)_2O_2$ diamond core structure for the key intermediate Q of methane monooxygenase. *Science 275*, 515-518.

(21) Lee, S. K., Fox, B. G., Froland, W. A., Lipscomb, J. D., and Münck, E. (1993) A transient intermediate of the methane monooxygenase catalytic cycle containing an Fe(IV)Fe(IV) cluster. *J. Am. Chem. Soc. 115*, 6450-6451.

(22) Nesheim, J. C., and Lipscomb, J. D. (1996) Large isotope effects in methane oxidation catalyzed by methane monooxygenase: evidence for C-H bond cleavage in a reaction cycle intermediate. *Biochemistry 35*, 10240-10247.

(23) Brazeau, B. J., Austin, R. N., Tarr, C., Groves, J. T., and Lipscomb, J. D. (2001) Intermediate Q from soluble methane monooxygenase hydroxylates the mechanistic substrate probe norcarane: Evidence for a stepwise reaction. *J. Am. Chem. Soc. 123*, 11831-11837.

(24) Zheng, H., and Lipscomb, J. D. (2006) Regulation of methane monooxygenase catalysis based on size exclusion and quantum tunneling. *Biochemistry 45*, 1685-1692.

(25) Valentine, A. M., Stahl, S. S., and Lippard, S. J. (1999) Mechanistic studies of the reaction of reduced methane monooxygenase hydroxylase with dioxygen and substrates. *J. Am. Chem. Soc. 121*, 3876-3887.

(26) Priestley, N. D., Floss, H. G., Froland, W. A., Lipscomb, J. D., Williams, P. G., and Morimoto, H. (1992) Cryptic stereospecificity of methane monooxygenase. *J. Am. Chem. Soc. 114*, 7561-7562.

(27) Brazeau, B. J., Wallar, B. J., and Lipscomb, J. D. (2001) Unmasking of deuterium kinetic isotope effects on the methane monooxygenase compound Q reaction by site-directed mutagenesis of component B. *J. Am. Chem. Soc. 123*, 10421-10422.

(28) Wallar, B. J., and Lipscomb, J. D. (2001) Methane monooxygenase component B mutants alter the kinetics of steps throughout the catalytic cycle. *Biochemistry 40*, 2220-2233.

(29) Basch, H., Musaev, D. G., Mogi, K., and Morokima, K. (2001) Theoretical studies on the mechanism of the methane -> methanol conversion reaction catalyzed by methane monooxygenase (MMO): The O-side vs N-side mechanisms. *J. Chem. Phys. A 105*, 3615-3622.

(30) Siegbahn, P. E. M., Crabtree, R. H., and Nordlund, P. (1998) Mechanism of methane monooxygenase - a structural and quantum chemical perspective. *J. Biol. Inorg. Chem. 3*, 314-317.

(31) Gherman, B. F., Baik, M.-H., Lippard, S. J., and Friesner, R. A. (2004) Dioxygen activation in methane monooxygenase: a theoretical study. *J. Am. Chem. Soc. 126*, 2978-2990.

(32) Brazeau, B. J., and Lipscomb, J. D. (2003) Key amino acid residues in the regulation of soluble methane monooxygenase catalysis by component B. *Biochemistry 42*, 5618-5631.

(33) Froland, W. A., Andersson, K. K., Lee, S.-K., Liu, Y., and Lipscomb, J. D. (1992) Methane monooxygenase component B and reductase alter the regioselectivity of the hydroxylase component-catalyzed reactions. A novel role for protein-protein interactions in an oxygenase mechanism. *J. Biol. Chem. 267*, 17588-17597.

(34) Hendrich, M. P., Münck, E., Fox, B. G., and Lipscomb, J. D. (1990) Integer-spin EPR studies of the fully reduced methane monooxygenase hydroxylase component. *J. Am. Chem. Soc. 112*, 5861-5865.

(35) Mitić, N., Schwartz, J. K., Brazeau, B. J., Lipscomb, J. D., and Solomon, E. I. (2008) CD and MCD studies of the effects of component B variant binding on the biferrous active site of methane monooxygenase. *Biochemistry 47*, 8386–8397.

(36) Chang, S. L., Wallar, B. J., Lipscomb, J. D., and Mayo, K. H. (2001) Residues in *Methylosinus trichosporium* OB3b methane monooxygenase component B involved in molecular interactions with reduced- and oxidized-hydroxylase component: a role for the N-terminus. *Biochemistry 40*, 9539-9551.

(37) Zhang, J., Wallar, B. J., Popescu, C. V., Renner, D. B., Thomas, D. D., and Lipscomb, J. D. (2006) Methane monooxygenase hydroxylase and B component interactions. *Biochemistry 45*, 2913-2926.

(38) Fox, B. G., Froland, W. A., Jollie, D. R., and Lipscomb, J. D. (1990) Methane monooxygenase from *Methylosinus trichosporium* OB3b. *Methods Enzymol. 188*, 191-202.

(39) Zhang, J., and Lipscomb, J. D. (2006) Role of the C-terminal region of the B component of *Methylosinus trichosporium* OB3b methane monooxygenase in the regulation of oxygen activation. *Biochemistry 45*, 1459-1469.

(40) Mbughuni, M. M., Chakrabarti, M., Hayden, J. A., Bominaar, E. L., Hendrich, M. P., Münck, E., and Lipscomb, J. D. (2010) Trapping and spectroscopic characterization of an FeIII-superoxo intermediate from a nonheme mononuclear iron-containing enzyme. *Proc. Natl. Acad. Sci. U. S. A. 107*, 16788-16793.

(41) Münck, E. (2000) Aspects of ^{57}Fe Mössbauer spectroscopy, in *Physical Methods in Bioinorganic Chemistry* (Que, L., Jr, Ed.), pp 287-319, University Science Books, Sausalito, CA.

(42) Fox, B. G., Surerus, K. K., Münck, E., and Lipscomb, J. D. (1988) Evidence for a μ-oxo-bridged binuclear iron cluster in the hydroxylase component of methane monooxygenase. Mössbauer and EPR studies. *J. Biol. Chem. 263*, 10553-10556.

(43) Fox, B. G., Hendrich, M. P., Surerus, K. K., Andersson, K. K., Froland, W. A., Lipscomb, J. D., and Münck, E. (1993) Mössbauer, EPR, and ENDOR studies of the

hydroxylase and reductase components of methane monooxygenase from *Methylosinus trichosporium* OB3b. *J. Am. Chem. Soc. 115*, 3688-3701.

(44) Dibar-Ure, M. C., and Flinn, P. A. (1971) A technique for the removal of the" blackness" distortion of Mössbauer spectra, in *Mössbauer Effect Methodology* (Gruverman, I. G., Ed.), pp 245-262, Plenum Press, New York, N.Y.

(45) Dunham, W. R., Harding, L. J., and Sands, R. H. (1993) Mössbauer spectroscopy of metalloproteins and the use of Fourier transforms. *Eur. J. Biochem. 214*, 1-8.

(46) Schwartz, J. K., Wei, P.-p., Mitchell, K. H., Fox, B. G., and Solomon, E. I. (2008) Geometric and electronic structure studies of the binuclear nonheme ferrous active site of toluene-4-monooxygenase: Parallels with methane monooxygenase and insight into the role of the effector proteins in O_2 activation. *J. Am. Chem. Soc. 130*, 7098-7109.

(47) Wei, P. P., Skulan, A. J., Wade, H., DeGrado, W. F., and Solomon, E. I. (2005) Spectroscopic and computational studies of the de novo designed protein DF2t: correlation to the biferrous active site of ribonucleotide reductase and factors that affect O_2 reactivity. *J. Am. Chem. Soc. 127*, 16098-16106.

(48) Stoian, S. A., Smith, J. M., Holland, P. L., Münck, E., and Bominaar, E. L. (2008) Mössbauer, electron paramagnetic resonance, and theoretical study of a high-spin, four-coordinate Fe(II) diketiminate complex. *Inorg Chem 47*, 8687-8695.

(49) Whittington, D. A., and Lippard, S. J. (2001) Crystal structures of the soluble methane monooxygenase hydroxylase from *Methylococcus capsulatus* (Bath) demonstrating geometrical variability at the dinuclear iron active site. *J. Am. Chem. Soc. 123*, 827-838.

(50) Pulver, S., Froland, W. A., Fox, B. G., Lipscomb, J. D., and Solomon, E. I. (1993) Spectroscopic studies of the coupled binuclear non-heme iron active site in the fully reduced hydroxylase component of methane monooxygenase: Comparison to deoxy and deoxy-azide hemerythrin. *J. Am. Chem. Soc. 115*, 12409-12422.

(51) Mbughuni, M. M., Meier, K. K., Münck, E., and Lipscomb, J. D. (2012) Substrate-mediated oxygen activation by homoprotocatechuate 2,3-dioxygenase: intermediates formed by a tyrosine 257 variant. *Biochemistry 51*, 8743-8754.

(52) Marti, M. A., Crespo, A., Capece, L., Boechi, L., Bikiel, D. E., Scherlis, D. A., and Estrin, D. A. (2006) Dioxygen affinity in heme proteins investigated by computer simulation. *J. Inorg. Biochem. 100*, 761-770.

(53) Capece, L., Marti, M. A., Crespo, A., Doctorovich, F., and Estrin, D. A. (2006) Heme protein oxygen affinity regulation exerted by proximal effects. *J. Am. Chem. Soc. 128*, 12455-12461.

(54) Shibata, T., Nagao, S., Fukaya, M., Tai, H., Nagatomo, S., Morihashi, K., Matsuo, T., Hirota, S., Suzuki, A., Imai, K., and Yamamoto, Y. (2010) Effect of heme modification on oxygen affinity of myoglobin and equilibrium of the acid-alkaline transition in metmyoglobin. *J. Am. Chem. Soc. 132*, 6091-6098.

(55) Olea, C., Boon, E. M., Pellicena, P., Kuriyan, J., and Marletta, M. A. (2008) Probing the function of heme distortion in the H-NOX family. *ACS Chemical Biology 3*, 703-710.

(56) Chen, H., Ikeda-Saito, M., and Shaik, S. (2008) Nature of the Fe-O_2 bonding in oxy-myoglobin: effect of the protein. *J. Am. Chem. Soc. 130*, 14778-14790.

(57) Jensen, K. P., and Ryde, U. (2004) How O_2 binds to heme: reasons for rapid binding and spin inversion. *J. Biol. Chem. 279*, 14561-14569.

(58) Siegbahn, P. E. M. (2001) O-O bond cleavage and alkane hydroxylation in methane monooxygenase. *J. Biol. Inorg. Chem. 6*, 27-45.

(59) Torrent, M., Musaev Djamaladdin, G., Basch, H., and Morokuma, K. (2002) Computational studies of reaction mechanisms of methane monooxygenase and ribonucleotide reductase. *J. Comput. Chem. 23*, 59-76.

(60) Rinaldo, D., Philipp, D. M., Lippard, S. J., and Friesner, R. A. (2007) Intermediates in dioxygen activation by methane monooxygenase: A QM/MM study. *J. Am. Chem. Soc. 129*, 3135-3147.

(61) Han, W. G., and Noodleman, L. (2008) Structural model studies for the high-valent intermediate Q of methane monooxygenase from broken-symmetry density functional calculations. *Inorg. Chim. Acta 361*, 973-986.

(62) Neibergall, M. B., Stubna, A., Mekmouche, Y., Münck, E., and Lipscomb, J. D. (2007) Hydrogen peroxide dependent cis-dihydroxylation of benzoate by fully oxidized benzoate 1,2-dioxygenase. *Biochemistry 46*, 8004-8016.

(63) Li, F. F., Meier, K. K., Cranswick, M. A., Chakrabarti, M., Van Heuvelen, K. M., Münck, E., and Que, L. (2011) Characterization of a high-spin non-heme Fe^{III}-O intermediate and its quantitative conversion to an Fe^{IV} = O complex. *J. Am. Chem. Soc. 133*, 7256-7259.

(64) Kim, K., and Lippard, S. J. (1996) Structure and Mössbauer spectrum of a (□-1,2-peroxo)bis(□-carboxylato)diiron(III) model for the peroxo intermediate in the methane monooxygenase hydroxylase reaction cycle. *J. Am. Chem. Soc. 118*, 4914-4915.

(65) Roelfes, G., Vrajmasu, V., Chen, K., Ho, R. Y. N., Rohde, J.-U., Zondervan, C., la Crois, R. M., Schudde, E. P., Lutz, M., Spek, A. L., Hage, R., Feringa, B. L., Münck, E.,

and Que, L., Jr. (2003) End-on and side-on peroxo derivatives of non-heme iron complexes with pentadentate ligands: models for putative intermediates in biological iron/dioxygen chemistry. *Inorg. Chem. 42*, 2639-2653.

(66) Orville, A. M., Elango, N., Lipscomb, J. D., and Ohlendorf, D. H. (1997) Structures of competitive inhibitor complexes of protocatechuate 3,4-dioxygenase: Multiple exogenous ligand binding orientations within the active site. *Biochemistry 36*, 10039-10051.

(67) Orville, A. M., Lipscomb, J. D., and Ohlendorf, D. H. (1997) Crystal structures of substrate and substrate analog complexes of protocatechuate 3,4-dioxygenase: Endogenous Fe^{3+} ligand displacement in response to substrate binding. *Biochemistry 36*, 10052-10066.

(68) Dong, Y., Yan, S., Young, J., V. G., and Que, L., Jr. (1996) The crystal structure of a synthetic nonheme diiron-O_2 adduct: insight into oxygen activation. *Angew. Chem. Int. Edit. 35*, 618-620.

(69) Do, L. H., Hayashi, T., Moenne-Loccoz, P., and Lippard, S. J. (2010) Carboxylate as the protonation site in (peroxo)diiron(III) model complexes of soluble methane monooxygenase and related diiron proteins. *J. Am. Chem. Soc. 132*, 1273-1275.

(70) Jensen, K. P., Bell, C. B., III, Clay, M. D., and Solomon, E. I. (2009) Peroxo-type intermediates in class I ribonucleotide reductase and related binuclear non-heme iron enzymes. *J. Am. Chem. Soc. 131*, 12155-12171.

Supporting Information

Table S1. Characteristics of the reaction cycle intermediates of the *M. trichosporium* diferrous MMOH-MMOB single turnover cycle.[a,b]

Intermediate	Nature of the diiron cluster	Evidence
H^{red}	$Fe^{II}Fe^{II}$ cluster, ferromagnetically coupled	Characteristic EPR signal at $g = 16$ Mössbauer spectrum in a strong applied magnetic field shows two sites with 1:1 site ratio
O	$Fe^{II}Fe^{II}$ cluster, ferromagnetically coupled with O_2 bond in the active site	Same spectral features as **H^{red}**. The apparent rate constant for decay of the $g = 16$ signal is independent of the O_2 concentration, implying that an irreversibly formed intermediate occurs between **H^{red}** and **P*** or **P**.
P*	Shown here to be an $Fe^{II}Fe^{II}$ cluster, but distinct from **O**	Mössbauer spectra demonstrate that the cluster is diferrous; it lacks, however, the $g = 16$ EPR signal. A small change in the exchange coupling between **P*** and **H^{red}** or **O** may account for the disappearance of the $g = 16$ signal. The decay rate constant for **O** is much faster than the formation rate constant for **P**, indicating that there must be an intermediate between **O** and **P**.
P	Cis μ-peroxo $Fe^{III}Fe^{III}$ cluster with the antiferromagnetically coupled irons	The optical spectrum of **P** at 700 nm can be observed. It has much faster formation than decay rate constants, and it breaks down to yield **Q**. The Mössbauer spectrum of **P** shows that the irons are ferric and antiferromagnetically coupled. The isomer shift of **P** is larger than that of **H^{ox}**.
Q	Bis-μ-oxo $Fe^{IV}Fe^{IV}$ cluster, antiferromagnetically coupled	Mössbauer spectra reveal an antiferromagnetically coupled Fe^{IV} Fe^{IV} cluster comprising high-spin Fe^{IV} sites. EXAFS analysis reveals a short Fe-Fe distance, consistent with a diamond core structure. The kinetics of the reaction can be monitored using the intense yellow color of **Q**. **Q** forms with the same rate constant as **P** decays. The rate

		constant for **Q** decay depends on the concentration of added substrate, suggesting that it is the reactive intermediate of the cycle. The **Q** reaction with methane shows a deuterium kinetic isotope effect of ~50 suggesting that a tunneling reaction mechanism dominates.
R	Too short-lived to be trapped. Thought to be an $Fe^{III}Fe^{IV}$-OH cluster with a substrate radical bound nearby	$^{1}H,^{2}H,^{3}H$-Chiral ethane shows ~70 % racemization during reaction with **Q** to form ethanol, requiring a radical intermediate with a very short lifetime. Similar results were obtained using radical clock substrates and by observing the desaturation chemistry.
T	$Fe^{III}Fe^{III}$ cluster with product bound to the cluster or nearby	Substrates that form chromophoric products show that product formation is faster than product release, thereby requiring a discrete product complex. All rate constants for the formation and decay of intermediates between $\mathbf{H^{red}}$ and **R** exceed the turnover number for methane and other substrates, implying a product complex with rate limiting product release.

[a] Compiled from references[1-12]

[b] Comparable intermediates have been described for the *Methylococcus capsulatus Bath* soluble methane monooxygenase system.[13]

Fourier Transform Treated Spectra of Figure 7. Briefly, a Mössbauer spectrum is the convolution of a source line shape [a Lorentzian of ~0.12 mm/s full width with our current ^{57}Co(Rh) source] with the spectrum of the absorber. By the convolution theorem, the Fourier transform of a Mössbauer spectrum is the product of the transforms of the source (known) and the absorber (the desired quantity). By removing the source contribution in the time-domain and back transforming we obtain, in the ideal case, the spectrum of the absorber as it would appear if the source would not contribute to the line

width. In practice, experimental noise requires filtering the data in the time domain, which yields some distortion of the lines; for details see references.[14,15] The Fourier transform treated spectra presented here (Figure S1) yield rather precise line positions. A line that is substantially broadened by heterogeneities (e.g. a distribution in ΔE_Q) will narrow very little by this treatment. The colored arrows indicate the positions of the two lines belonging to each identified species; this analysis shows that all species present have been identified.

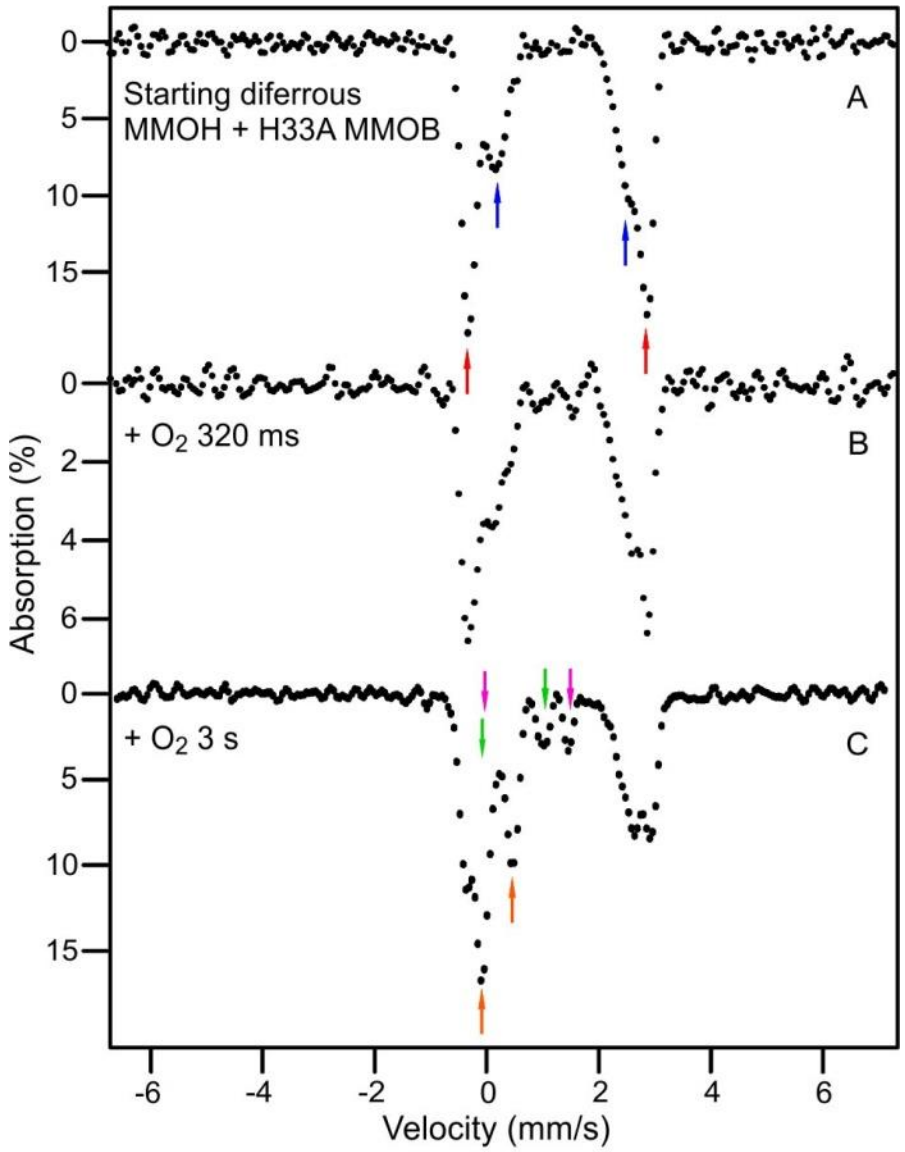

Figure S1. Fourier transform treated data of the spectra shown in Figure 7 (panels A, B, and C) of the main text. The colored arrows mark the two lines of each assigned quadrupole doublet. Sites 1 and 2 of $\mathbf{H}^{\mathbf{red}}$ (red and blue, respectively); intermediates **P** (magenta) and **Q** (orange) and $\mathbf{H}^{\mathbf{ox}}$ (green). Intensities are obtained from fitting the original spectra of Figure 7 using the constrained line positions. The spectrum of (A) shows that site 2 (blue arrows) is heterogeneously broadened and contributes a single (broadened) doublet rather than two doublets with sharp lines and different quadrupole splittings.

References

1. Fox, B. G., Froland, W. A., Dege, J. E., and Lipscomb, J. D. (1989) Methane monooxygenase from *Methylosinus trichosporium* OB3b. Purification and properties of a three-component system with high specific activity from a type II methanotroph. *J. Biol. Chem. 264*, 10023-10033.

2. Fox, B. G., Hendrich, M. P., Surerus, K. K., Andersson, K. K., Froland, W. A., Lipscomb, J. D., and Münck, E. (1993) Mössbauer, EPR, and ENDOR studies of the hydroxylase and reductase components of methane monooxygenase from *Methylosinus trichosporium* OB3b. *J. Am. Chem. Soc. 115*, 3688-3701.

3. Hendrich, M. P., Münck, E., Fox, B. G., and Lipscomb, J. D. (1990) Integer-spin EPR studies of the fully reduced methane monooxygenase hydroxylase component. *J. Am. Chem. Soc. 112*, 5861-5865.

4. Lee, S. K., Fox, B. G., Froland, W. A., Lipscomb, J. D., and Münck, E. (1993) A transient intermediate of the methane monooxygenase catalytic cycle containing an Fe(IV)Fe(IV) cluster. *J. Am. Chem. Soc. 115*, 6450-6451.

5. Lee, S.-K., Nesheim, J. C., and Lipscomb, J. D. (1993) Transient intermediates of the methane monooxygenase catalytic cycle. *J. Biol. Chem. 268*, 21569-21577.

6. Lee, S.-K., and Lipscomb, J. D. (1999) Oxygen activation catalyzed by methane monooxygenase hydroxylase component: proton delivery during the O-O bond cleavage steps. *Biochemistry 38*, 4423-4432.

7. Nesheim, J. C., and Lipscomb, J. D. (1996) Large isotope effects in methane oxidation catalyzed by methane monooxygenase: evidence for C-H bond cleavage in a reaction cycle intermediate. *Biochemistry 35*, 10240-10247.

8. Wallar, B. J., and Lipscomb, J. D. (1996) Dioxygen activation by enzymes containing binuclear non-heme iron clusters. *Chem. Rev. 96*, 2625-2657.

9. Jin, Y., and Lipscomb, J. D. (2000) Mechanistic insights into C-H activation from radical clock chemistry: Oxidation of substituted methylcyclopropanes catalyzed by soluble methane monooxygenase from *Methylosinus trichosporium* OB3b. *Biochim. Biophys. Acta 1543*, 47-59.

10. Brazeau, B. J., Wallar, B. J., and Lipscomb, J. D. (2001) Unmasking of deuterium kinetic isotope effects on the methane monooxygenase compound Q reaction by site-directed mutagenesis of component B. *J. Am. Chem. Soc. 123*, 10421-10422.

11. Wallar, B. J., and Lipscomb, J. D. (2001) Methane monooxygenase component B mutants alter the kinetics of steps throughout the catalytic cycle. *Biochemistry 40*, 2220-2233.

12. Zhang, J., Wallar, B. J., Popescu, C. V., Renner, D. B., Thomas, D. D., and Lipscomb, J. D. (2006) Methane monooxygenase hydroxylase and B component interactions. *Biochemistry 45*, 2913-2926.

13. Tinberg, C. E., and Lippard, S. J. (2011) Dioxygen activation in soluble methane monooxygenase. *Acc. Chem. Res. 44*, 280-288.

14. Dibar-Ure, M. C., and Flinn, P. A. (1971) A technique for the removal of the" blackness" distortion of Mössbauer spectra, in *Mössbauer Effect Methodology* (Gruverman, I. G., Ed.), pp 245-262, Plenum Press, New York, N.Y.

15. Dunham, W. R., Harding, L. J., and Sands, R. H. (1993) Mössbauer spectroscopy of metalloproteins and the use of Fourier transforms. *Eur. J. Biochem. 214*, 1-8.

Chapter V – Redesigning the Blue Copper Azurin into a Redox-Active Mononuclear Nonheme Iron Protein: Preparation and Study of Fe(II)-M121E Azurin

Published: Liu, J.; **Meier, K.**; Tian, S.; Zhang, J.; Guo, H.; Schulz, C. E.; Robinson, H.; Nilges, M. J.; Münck, E.; Lu, Y. "Redesigning the Blue Copper Azurin into a Redox-Active Mononuclear Nonheme Iron Protein: Preparation and Study of Fe(II)-M121E Azurin." *J. Am. Chem. Soc.* 2014, 136, pp 12337-12344.

Author Contributions: J.L., K.K.M., C.E.S., H.R., M.J.N., J.L., E.M., Y.L. conceived and designed the experiments. J.L. prepared samples, J.L., K.K.M., S.T., J.-L.Z., H.G., C.E.S., H.R., M.J.N. performed the experiments. J.L., K.K.M., M.J.N., E.M., Y.L. analyzed the data. All authors participated in the writing of the paper.

Abstract

Much progress has been made in designing heme and dinuclear nonheme iron enzymes. In contrast, engineering mononuclear nonheme iron enzymes is lagging, even though these enzymes belong to a large class that catalyzes quite diverse reactions. Herein we report spectroscopic and X-ray crystallographic studies of Fe(II)-M121E azurin (Az), by replacing the axial Met121 and Cu(II) in wild-type azurin (wtAz) with Glu and Fe(II), respectively. In contrast to the redox inactive Fe(II)-wtAz, the Fe(II)-M121EAz mutant can be readily oxidized by Na_2IrCl_6, and interestingly, the protein exhibits superoxide scavenging activity. Mössbauer and EPR spectroscopies, along with X-ray structural comparisons, revealed similarities and differences between Fe(II)-

M121EAz, Fe(II)-wtAz, and superoxide reductase (SOR) and allowed design of the second generation mutant, Fe(II)-M121EM44KAz, that exhibits increased superoxide scavenging activity by 2 orders of magnitude. This finding demonstrates the importance of noncovalent secondary coordination sphere interactions in fine-tuning enzymatic activity.

Introduction

Rational design of metalloproteins is an exciting field where our understanding of native proteins can not only be tested and expanded, but also applied toward engineering less expensive and more robust biocatalysts for many applications.[1−8] While much progress has been made in designing metalloproteins that structurally mimic native enzymes, the design of proteins with new and desired functions is still largely limited to heme enzymes or proteins containing small inorganic catalysts.[1,2,7−19] Recent successes in the de novo design of enzymes based on helix bundles bearing diiron[20,21]or dirhodium centers[22,23] have been reported. In contrast, limited success has been achieved in the design of mononuclear nonheme iron enzymes,[24,25] even though they belong to a large and important family of enzymes that are active in oxidative stress defenses, oxidation, and oxygenation reactions.[26−28] Such diversity in reaction, combined with the relative abundance of iron and its wide range of accessible oxidation states, has made these enzymes attractive targets for biophysical investigations and synthetic modeling, with the aim of understanding them and developing efficient biomimetic catalysts with earth-abundant metal ions.[26,29−38]

To complement the study of native enzymes and synthetic models, we have chosen the classic electron transfer (ET) protein azurin (Az), from Pseudomonas aeruginosa, as a scaffold for biosynthetic modeling. Azurin can easily be purified from Escherichia coli in high yields, and the protein is very stable at room temperature. Thus, Az is among the

most extensively studied cupredoxins.[39–41] As an ET protein, Az provides a rigid scaffold to position the metal-binding sites as well as to fine-tune its surrounding environment, allowing use of a bottom-up approach to test structural features important for enzymatic activity. The ligand environment in Az comprises His46, His117, and Cys112 in the trigonal plane as well as Met121 and the backbone carbonyl oxygen of Gly45 in the axial positions (Figure 1A).[42]

As the first step to transform this ET protein into a mononuclear nonheme iron enzyme, McLaughlin et al. substituted the native Cu(II) with Fe(II) in wtAz and obtained its crystal structure (Figure 1B).[43] However, the iron occupancy in the crystal was low (35% in two of four chains, with the other two sites being empty), perhaps because Met121 could not bind sufficiently strongly to the iron. No redox or enzymatic activity was observed at the Fe(II) center. We hypothesized that replacing the Met121 with Glu, which is not only one carbon atom closer to the metal center than Met, but is also a more common ligand in nonheme iron enzymes, would increase the affinity for iron. Moreover, we expected that the M121E mutation would lower the reduction potential of the iron center through its negative carboxylate charge and would thus convert the redox-inactive Fe(II)-wtAz into a redox-active protein displaying enzymatic activity. Herein we report the design of a nonheme iron binding site in Az and show that the glutamate residue at position 121 plays important roles in conferring higher Fe(II) binding affinity and new redox and superoxide scavenging activity. Furthermore, mutation of the secondary

coordination sphere residue Met44 to Lys (M44K) increased the superoxide scavenging activity even further.

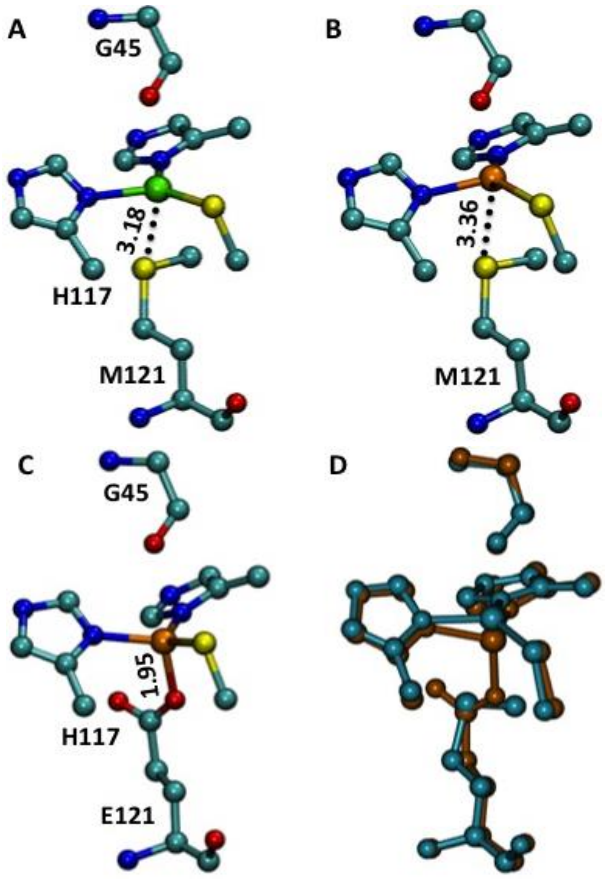

Figure 1. Crystal structures of (A) Chain A of Cu(II)-wtAz. PDB ID: 4AZU. (B) Chain B of Fe(II)-wtAz. PDB ID: 4HZ1. (C) Chain B of Fe(II)-M121EAz. PDB ID: 4QLW. Resolution: 2.0 Å. Distance unit: Å. Color code: C, cyan; S, yellow; N, blue; O, red; Cu, green; Fe, orange. (D) Overlay of chain B of Fe(II)-wtAz (cyan) and Fe(II)-M121EAz (orange).

Results and Discussion

M121EAz was expressed and purified from E. coli in metal-free apo form following reported procedures.[44] Upon addition of $(NH_4)_2Fe(SO_4)_2$ to apo-M121EAz under anaerobic conditions, development of an absorption at ~315 nm was observed (Figure 2). After passing the protein through a desalting column (PD-10 from GE) to remove free iron, inductively coupled plasma (ICP) analysis confirmed iron incorporation with <1% Zn and <0.1% Cu present in the sample (Table S1).

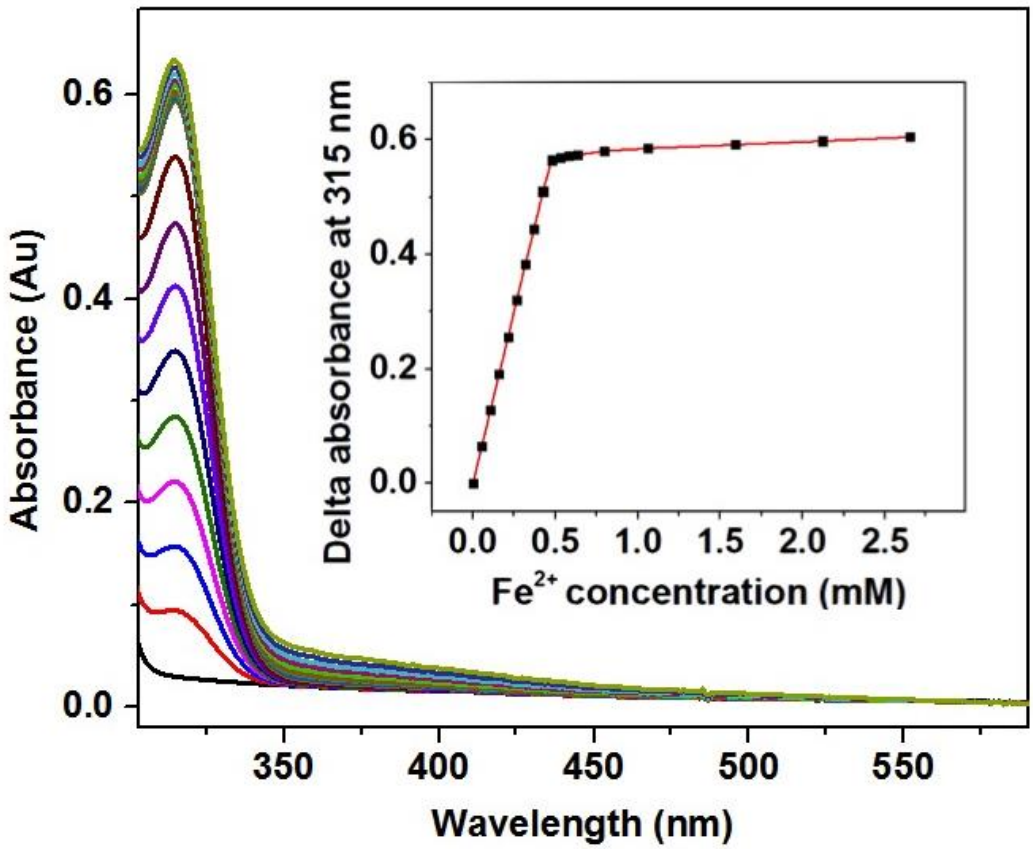

Figure 2. UV−vis absorption spectral increase after successive addition of 0.1−5 equiv of Fe^{2+} to apo-M121EAz (0.48 mM). (Inset) Titration curve monitored by the absorbance maxima at 315 nm.

Based on these results, an extinction coefficient of 1610 $M^{-1}cm^{-1}$was determined for the absorption at 315 nm. Both the position and extinction coefficient of the absorption band are similar to those observed in cysteinyl coordinated mononuclear nonheme iron enzymes such as Fe(II)-wtAz,[43] superoxide reductase (SOR),[45] and corresponding sulfur-containing small molecular models.[46,47] The features were assigned as sulfur→Fe(II) ligand to metal charge transfer (LMCT) bands. Our results support the successful iron incorporation as well as cysteinyl coordination in M121EAz. The iron incorporation ratio was determined to be 0.9 by titration using ε_{280}= 8800$M^{-1}cm^{-1}$ [48] for apo M121EAz with K_d stronger than 1μM (Figure 2). Electrospray ionization mass spectrometry (ESI MS) of the protein after iron incorporation displayed a major peak with mass of 14000.0 Da (Figure S2b, calculated mass of Fe + M121EAz: 13999.6 Da), further supporting the monoiron incorporation into the protein.

The purified Fe(II)-M121EAz was successfully crystallized. Its structure, solved at 2.0 Å resolution, showed that the protein is a tetramer consisting of two heterodimers. Subunits A and C are in conformation 1 (Figure S3a) with no observable metal occupancy, similar to the result reported for Fe(II)-wtAz.[43] Subunits B and D are in conformation 2 (Figure S3b) with 100% occupancy, much higher than the 35% occupancy of the corresponding site in Fe(II)-wtAz.[43] This observation demonstrates that the extended carboxylate ligand from Glu121increases iron binding as designed. While this mutant binds Fe(II) more effectively than Fe(II)-wtAz, the observed sample

heterogeneity in Fe(II)-M121EAz may be due to thermodynamic or kinetic effects of Fe(II)−protein or Fe(II)−buffer interactions or some combination of both effects, depending on the mutant.

The major difference between the two conformations is that His117 of subunit A (conformation 1) is shifted away from the active site by 1.6 Å, with slight movement of His46 and Glu121(Figure S3c). It has been noted that His117, located in the loop region near the protein surface, is highly flexible as shown in the crystal structures of two of the four subunits of apo-wtAz[49] and Fe(II)-wtAz.[43] In wtAz, this movement has been proposed to be responsible for transferring external metal ions into the binding site during metal incorporation.[49] Thus, under the acidic crystallization condition at pH 5.3, the flexibility of His117 in combination with high concentrations of coordinating acetate anions in crystallization buffers would lead to removal of iron in subunits A and C as well as to a decrease in metal/protein ratio in the crystallized form (0.5) compared to that in solution (0.9). To confirm that the acetate buffer played a role in the observed sample heterogeneity, we investigated the effect of adding 100 mM OAc− to freshly prepared Fe(II)-M121EAz. As shown in Figure S4, at pH 5.3, the 315 nm absorption band decreased with time. On the other hand, this band remained stable at pH 7.8. Therefore, the acetate can remove Fe(II) at low pH, but not high pH, probably because it can compete with the His ligands for the Fe(II) at a low pH where the His can be protonated,

while acetate remains deprotonated. No other metal-binding site was observed in any other part of the protein.

In conformation 2 of Fe(II)-M121EAz, for which the iron occupancy is 100%, the primary coordination sphere consists of His117, His46, Cys112, Glu121, and the backbone carbonyl of Gly45 (Figure 1C). Interestingly, the Fe(II)-S(Cys112) bonds in Fe(II)-M121EAz (2.38−2.40 Å) are distinctly longer than the corresponding bonds in Fe(II)-wtAz (2.26−2.29 Å)[43,50] but are similar to those of SOR (2.38−2.45 Å).[51] The Fe(II)-N(His) bond lengths (2.05−2.08 Å) in Fe(II)-M121EAz suggest tight binding. Glu121 coordinates to the Fe(II) in a monodentate mode, similar to that in Cu(II)-M121EAz.[50] The Fe-O(Glu121) distances are 1.95−2.02 Å, which are much shorter than the Fe-S(Met121) distance of 3.36 Å for Fe(II)-wtAz (Figure 1D).[43] These results confirm that the stronger bond between Fe-O(Glu121), as opposed to the Fe-S(Met121) bond in wtAz, is responsible for the more effective binding of Fe(II) by Fe(II)-M121EAz.

Except for cryoreduction by γ-radiation, Fe(II)-wtAz was reported to be inert to most oxidation and reduction attempts.[18,43] In contrast, Fe(II)-M121EAz is readily oxidized by the one-electron oxidant Na_2IrCl_6, as demonstrated by the development of absorption features centered around 600 and 410 nm (Figure 3). This result indicates that the introduction of the negatively charged carboxylate ligand of Glu121 lowers the reduction potential of Fe(II)-M121EAz relative to that of Fe(II)-wtAz, making it oxidizable by Na_2IrCl_6. To determine the redox properties of the Fe(II)-M121EAz mutant

quantitatively, we have measured the reduction potential of the iron site using cyclic voltammetry (CV) and obtained +327±9 mV (Figure S5).[52] This value is ~100 mV higher than that of native SOR (+238±10 mV).[53] Furthermore, in addition to using Na_2IrCl_6 (E_m= +0.87 V), we have measured oxidation of the Fe(II)-M121EAz using 1 equiv of $K_3Fe(CN)_6$ (E_m= +0.358V) and *N,N,N′,N′*-tetramethyl-p-phenylenediamine (TMPD) (E_m= +0.276 V) respectively. Based on UV−vis spectroscopy (see Figure S6), oxidation by $K_3Fe(CN)_6$ was observed, while no oxidation was observed by TMPD, consistent with the reduction potentials measured by CV.

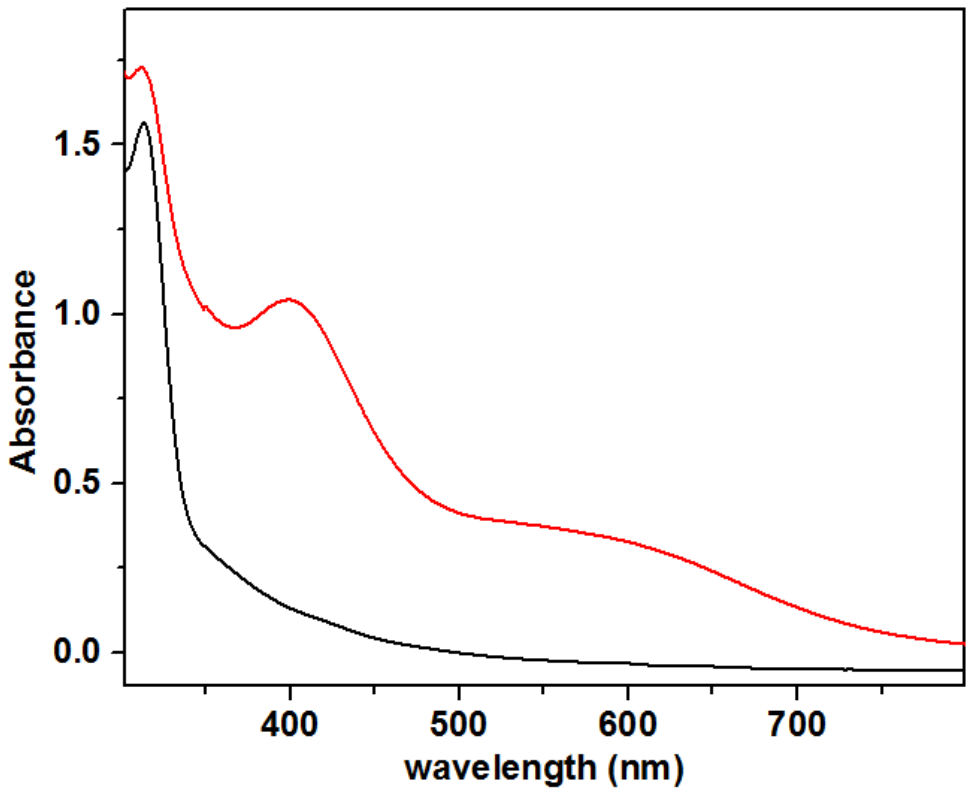

Figure 3. UV−vis spectra of Fe(II)-M121EAz (0.86 mM, black line) and after its oxidation with 1 equiv of Na_2IrCl_6 at room temperature for 10 min (red line).

The observation of the new redox activity conferred by the M121E mutation raised the question of whether the Fe(II)-M121EAz displayed any enzymatic activity. Considering that one prominent member of Cys-containing nonheme iron enzymes is SOR, we investigated the superoxide scavenging activity of Fe(II)-M121EAz using the Fridovich method.[54] Reactions of nitrotetrazolium blue chloride (NBT) with superoxide flux generated by xanthine/xanthine oxidase were followed in the presence of catalase and different amounts of Fe(II)-M121EAz. As shown in Figure 4, the reaction rate decreased upon addition of Fe(II)-M121EAz as competitor, with a second-order rate constant of $\sim 1.8\times10^{4}\,M^{-1}s^{-1}$ at pH 7.8 and 25°C. This rate is comparable to that reported for the superoxide scavenging reagent NBT ($5.94\times10^{4}M^{-1}s^{-1}$).[55] These results indicate that by replacing Met121 with Glu we have succeeded in converting Fe(II)-wtAz into a nonheme iron protein with superoxide scavenging activity. To elucidate the electronic structure of Fe-M121EAz, we have recorded a series of Mössbauer spectra at 4.2 K in zero-field (B= 0 T) and in applied fields up to B= 9.0 T.

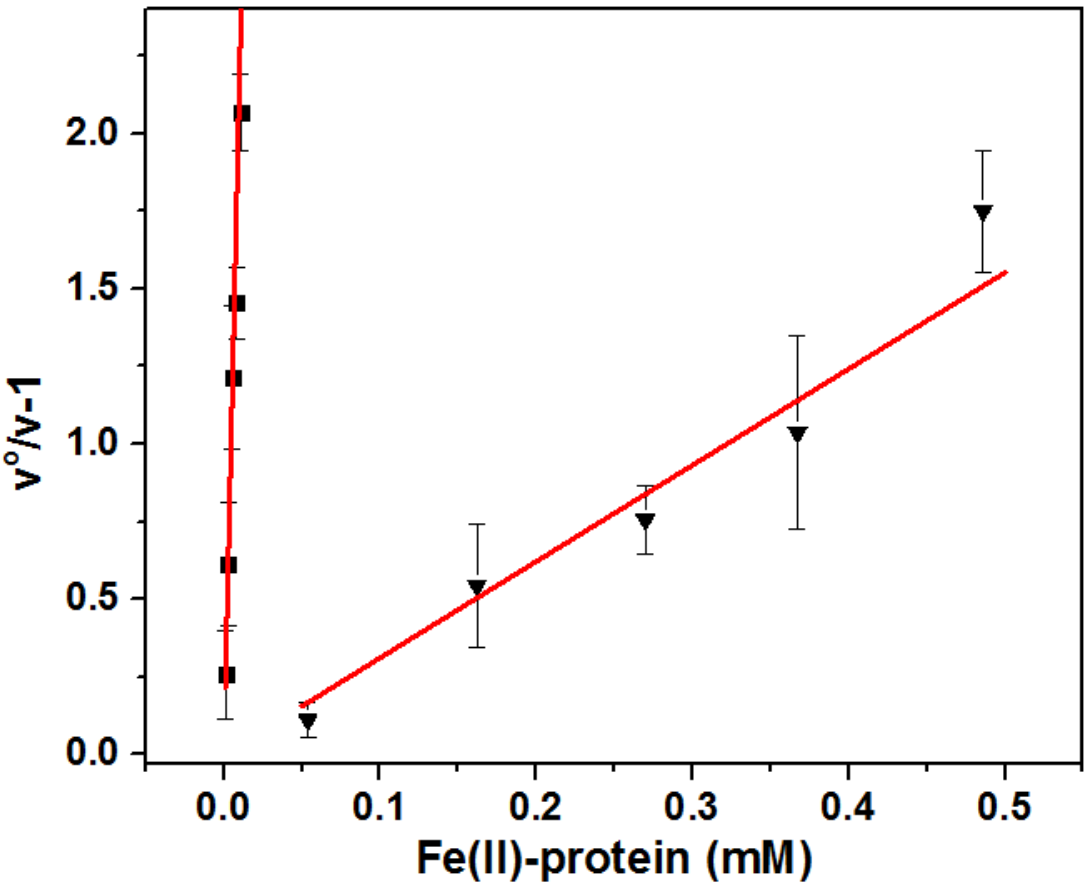

Figure 4. Reactivity toward superoxide by Fridovich test. Triangle: Fe(II)-M121EAz and square: Fe(II)-M121EM44KAz; v^o:$\Delta A_{535\ nm}$/min without protein and v:$\Delta A_{535\ nm}$/min with protein.

The data have been analyzed in the framework of the commonly used spin Hamiltonian:

$$H = D\left[S_z^2 - \frac{S(S+1)}{3} + \left(\frac{E}{D}\right)\left(S_x^2 - S_y^2\right)\right] + \beta\vec{S}\cdot\hat{g}\cdot\vec{B} + \vec{S}\cdot\hat{A}\cdot\vec{I} - g_n\beta_n\vec{B}\cdot\vec{I} + H_Q \quad \textbf{(1)}$$

$$H_Q = \frac{eQV_{z'z'}}{12}\left[3I_{z'}^2 - \frac{15}{4} + \eta\left(I_{x'}^2 - I_{y'}^2\right)\right]$$

In eq 1 we used S= 5/2 for Fe(III)-M121EAz and S= 2 for Fe(II)-M121EAz. D and E/D are zero-field splitting (ZFS) parameters, g is the electronic g-tensor (we use g = 2.00 below), A is the 57Fe magnetic hyperfine tensor, and HQ describes the interaction of the

electric field gradient (EFG) with the nuclear quadrupole moment Q; $\eta=(V_{x'x'}-V_{y'y'})/V_{z'z'}$ is the asymmetry parameter of the EFG tensor. The principal axis system of the EFG tensor, x′y′z′, is related to xyz by the rotation $(\alpha\beta\gamma)_{EFG}$, where (αβγ) are Euler angles as used in WMOSS.

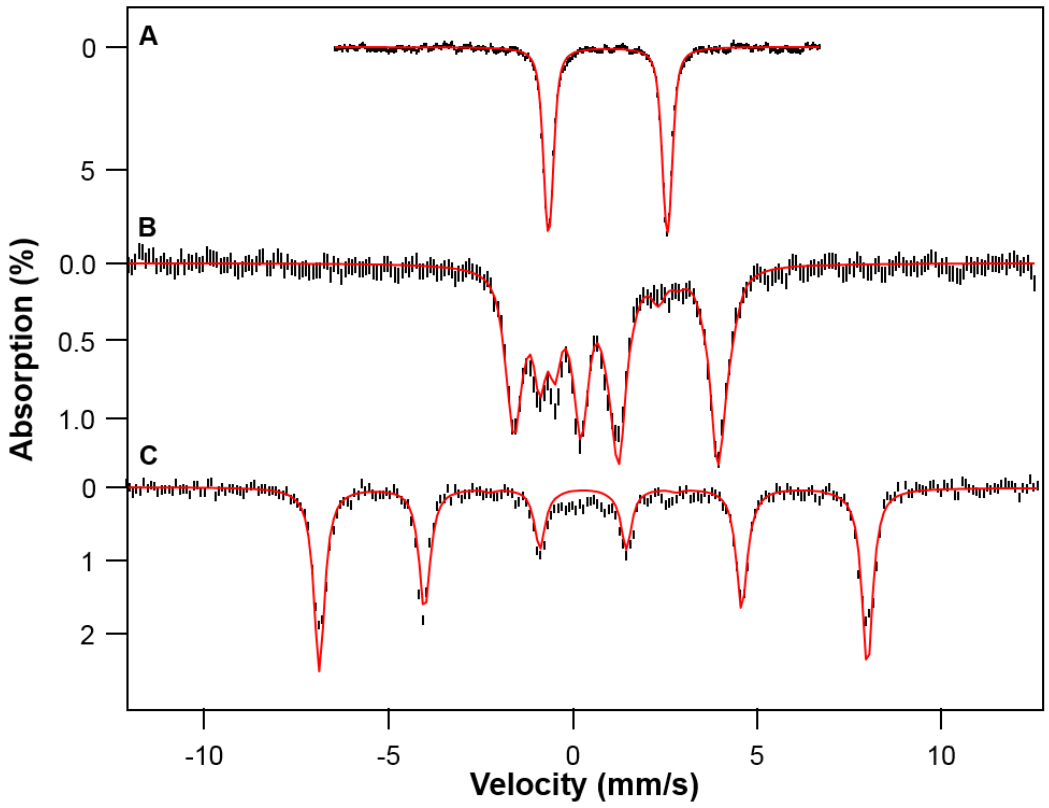

Figure 5. Mössbauer spectra of Fe-M121EAz recorded at 4.2 K in variable magnetic fields applied parallel to the observed γ-radiation. (A) Spectrum of Fe(II)-M121EAz recorded in zero field. The red line is a simulation for ΔE_Q= 3.22 mm/s and δ= 0.94 mm/s. (B) Spectrum of Fe(II)-M121EAz recorded in a 2.0 T field. The red line is a theoretical curve (using WMOSS software) based on the S= 2 spin Hamiltonian of eq 1 using the parameters listed in Table 1. (Please note footnote (a) of Table 1.) (C) Zero-field spectrum of Fe(III)-M121EAz obtained by treating an aliquot of the sample of (A) with Na_2IrCl_6. The red line is a spectral simulation of Fe(III)-M121EAz, using an S= 5/2 spin Hamiltonian with the parameters listed in Table 1; see also variable field spectra in Figure S8.

Table 1. Mössbauer Parameters of Fe-(II)-M121EAz and Fe(III)-M121EAz

	D (cm^{-1})	E/D	δ (mm/s)	ΔE_Q (mm/s)	η	$\frac{A_x}{g_n\beta_n}$ (T)	$\frac{A_y}{g_n\beta_n}$ (T)	$\frac{A_z}{g_n\beta_n}$ (T)
Fe(II)-M121EAz	{ [a] }	{ [a] }	0.94 (1)	+3.22 (2) [b]	0.7(2)	-20(10)	-12(3)	-5.3 (2)
Fe(III)-M121EAz	-3.0 (5)	0.05	0.41 (2)	[c]	[c]	-20.0 (5)	-20.0 (5)	-18.4 (1)

[a]The ZFS parameters are constrained from EPR by $\Delta = 3|D|(E/D)^2 = 0.33$ cm^{-1}. Determination of D and E/D requires extensive variable field/variable temperature Mössbauer studies; however, D < 0. [b]In the WMOSS simulation the EFG tensor is rotated relative to the ZFS frame by Euler angles $(\alpha\beta\gamma)_{EFG}$ = (0, 23±2, 0) degrees. [c]Only the projection of the EFG onto the electronic z axis is well determined. The spectrum of Figure 5C yields $eQV_{zz}/2$ = +0.30(3) mm/s. However, ΔE_Q is confined to +0.2 mm/s < ΔE_Q < +0.8mm/s.

The zero-field, 4.2 K Mössbauer spectrum of Fe(II)-M121EAz shown in Figure 5A consists of a doublet with quadrupole splitting ΔE_Q= 3.22 mm/s and isomer shift δ=0.94 mm/s. These parameters are indicative of a high-spin (S=2) Fe(II) site. A spectrum collected at 4.2 K in a parallel-applied magnetic field of 45 mT (not shown) revealed significant magnetic hyperfine broadening of the high-energy feature. This observation indicates that the two lowest spin levels of the S= 2 multiplet are narrowly spaced (energy gap $\Delta \leq 0.4$ cm^{-1}) and that an electron paramagnetic resonance (EPR) transition might be observable at X-band in both parallel and perpendicular modes. Figure 6A shows an EPR spectrum of Fe(II)-M121EAz recorded in parallel mode (a transverse mode spectrum is shown in Figure S7). This spectrum can be assigned to the "M_S=±2" levels of an S= 2 system, implying D < 0. As discussed in refs 56 and 57, the observed EPR signal depends on $\Delta=3|D|(E/D)^2$ and g_z (fixed at 2.00 here). Simulations using the software SpinCount58 yielded the theoretical curve (red) of Figure 6A for Δ =

0.328 cm^{-1}. The shape of the EPR signal depends on Δ, not on D and E separately, and on a parameter describing the distribution of Δ, here σE/D.

Treatment of Fe(II)-M121EAz with 2 equiv of Na_2IrCl_6 yields complete conversion to Fe(III)-M121EAz. The 4.2 K, zero-field Mössbauer spectrum of the oxidized sample (Figure 5C) reveals a high-spin (S= 5/2) ferric component (red line). The observation of a 6-line spectrum with a 3:2:1:1:2:3 intensity pattern indicates that this spectrum is associated with a Kramers doublet for which $g_z \gg g_x, g_y$, a property fitting to the M_S=±5/2 doublet. The Mössbauer spectrum is associated with the electronic ground state, and thus the ZFS parameter D is negative. This assignment is confirmed by EPR (see Figures 6B and S9) which revealed two similar species in roughly equal proportions, with D< 0 and E/D= 0.04 and E/D= 0.06. The features between g = 5 and 7 originate from the M_S=±3/2 and ±1/2 excited Kramers doublets. We have recorded variable magnetic field Mössbauer spectra to determine the magnitude of D, thereby avoiding temperature uncertainties inherent in the use of continuous flow EPR cryostats. Analysis of the Mössbauer spectra of Figure S8 yielded D = −3.0(5) cm^{-1}. The spectrum of Figure 5C is not sensitive enough to E/D to distinguish between E/D= 0.04 and 0.06, so it was simulated for E/D= 0.05.

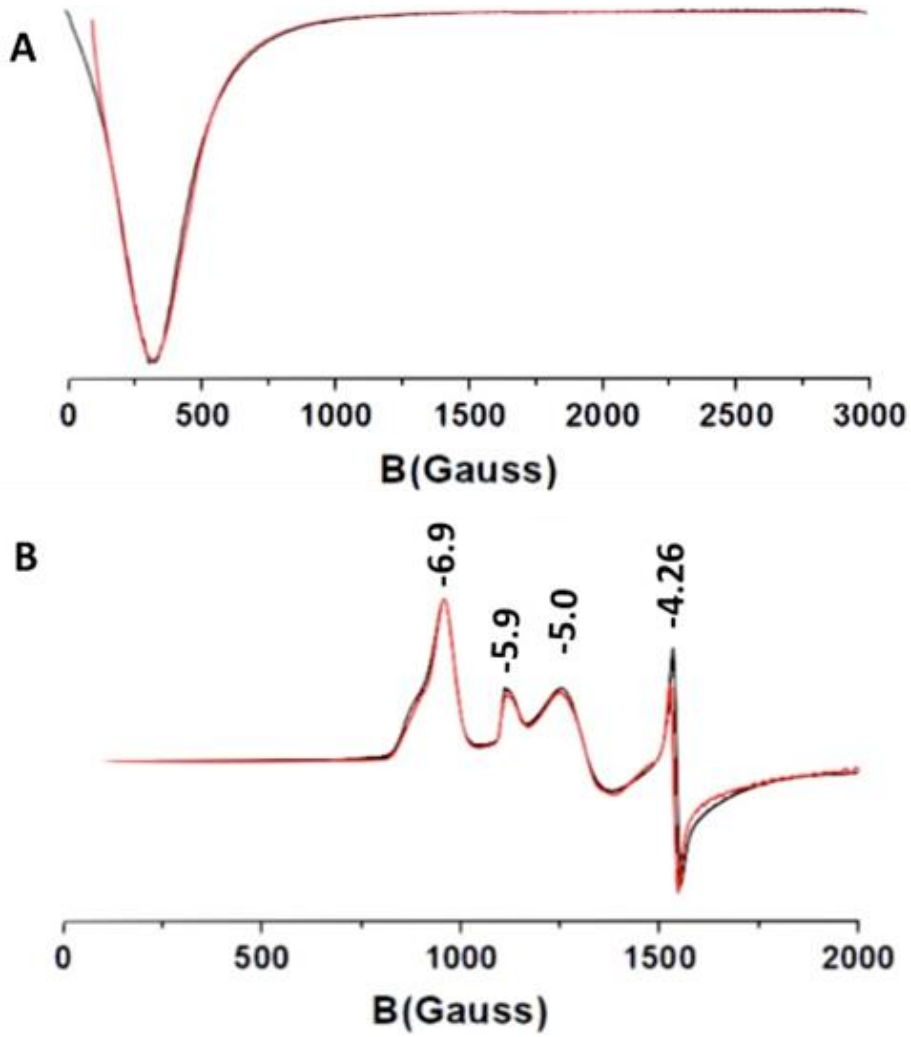

Figure 6. (A) Parallel mode X-band EPR spectrum of Fe(II)-M121EAz recorded at 9 K. The black curve is the experimental spectrum, and the red curve is a simulation generated using the software SpinCount[58] with the parameters listed in Table 1; the parameter E/D(= 0.177) was assumed to have a Gaussian distribution with $\sigma_{E/D}$= 0.0055 (this entails a distribution in Δ). Conditions: microwave power: 2 mW (nonsaturated), microwave frequency: 9.375 GHz, modulation amplitude: 1 mT. **(B)** Perpendicular mode X-band EPR spectrum of Fe(III)-M121EAz recorded at 10 K. The feature at g= 4.26 is a minor contaminant, representing <5% of Fe^{III} present. Conditions: 4 mW, 9.21 GHz, 1 mT. The spectrum was obtained after removing a substantial contribution from Fe(II)-M121EAz.

Recently, McLaughlin et al.[43] reported $\Delta E_Q = -3.19$ mm/s and δ= 0.93 mm/s for Fe(II)-wtAz. The negative ΔE_Q value indicates a low-lying orbital with ~d_{z2} symmetry,

consistent with a coordination tetrahedron flattened along the z-axis (d_{z2} isdoubly occupied, containing the β electron). As Fe(II)- M121EAz has a tetrahedral coordination as well, we were curious to know whether the M121E mutant also has a d_{z2} ground state. The 4.2 K, 2.0 T Mössbauer spectrum of Figure 5B reveals a splitting pattern that is left−right reversed compared to that reported for Fe(II)-wtAz,[43] implying that Fe(II)-M121EAz has $\Delta E_Q > 0$, suggesting an $\sim d_{x2-y2}$ ground state. In Fe(II)-wtAz, the d_{z2} and d_{x2-y2} orbitals were found to be very close in energy (643 cm^{-1} energy gap), so the reversal observed here is not too surprising.

It is also instructive to compare the Mössbauer parameters of Fe(II)-M121EAz with those reported by Horner et al.[59] for center II of Fe(II)-SOR, namely ΔE_Q= 2.82 mm/s and δ=1.06 mm/s. While ΔE_Q values of high-spin Fe(II) sites are not very site-specific, isomer shifts are quite sensitive to the coordination geometry. Comparison of the δ values (0.94 vs 1.06 mm/s) indicates substantial differences between the Fe(II)-M121EAz and SOR sites. Inspection of the two structures, shown side by side in Figure 7A,B (for detailed metrics, see Figure S10), shows that Fe(II)-SOR has a square pyramidal geometry, while Fe(II)-M121EAz has a distorted tetrahedral ligand environment. Perhaps most significantly, both centers have a cysteinate ligand coordinated trans to the putative O_2^- binding site, a feature which may explain why Fe(II)-M121EAz displays superoxide scavenge activity.

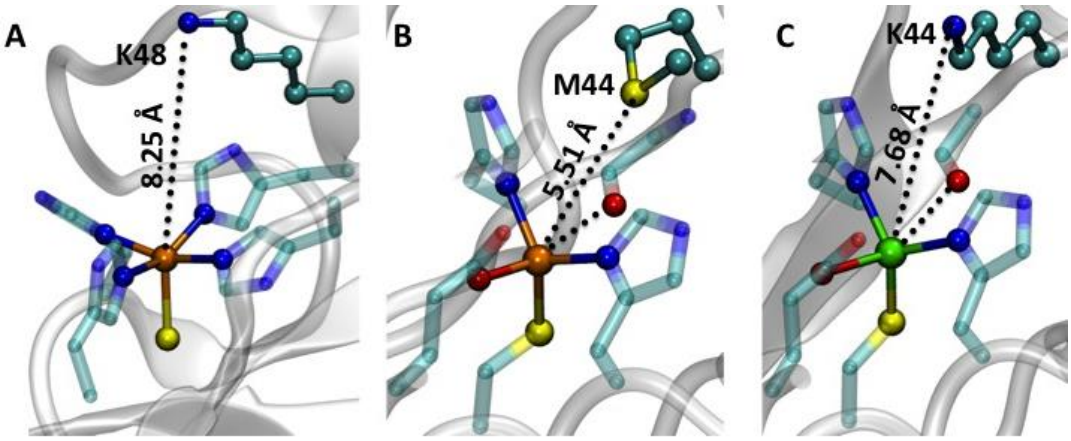

Figure 7. Structure comparison of (A) SOR, PDB ID: 2JI1. (B) Fe(II)-M121EAz, PDB ID: 4QLW. Resolution: 2.0 Å. (C) Cu(II)-M121EM44KAz PDB ID: 4QKT. Resolution: 1.64 Å. Color code: C, cyan; S, yellow; N, blue; O, red; Cu, green; Fe, orange.

Even though we have converted a redox-inactive Fe(II)-wtAz into a redox-active Fe(III)-M121EAz with superoxide scavenging capability, the activity is still substantially lower than that of native SOR ($8\times10^{8}M^{-1}s^{-1}$).[60] Therefore, we set out to improve the activity of this mutant, directing our attention to the secondary coordination sphere. It has been reported[60] that a Lys residue (Lys48) near the axial position of the iron center in SOR is critical for the reaction with superoxide (Figure 7A), as it may guide the binding superoxide to the iron center.[61] Mutation of Lys48 to Ile resulted in ~20-fold decrease in activity compared to that of wtSOR.[60] The crystal structure of Fe(II)-M121EAz reveals that Met44 is 5.51 Å away from the iron center (Figure 7B). Therefore, an additional M44K mutant was designed based on structural comparison with SOR. Mutation of Met44 to Lys resulted in Fe(II)-M121EM44KAz that displayed a LMCT band at 319 nm with Kd stronger than 1μM, similar to that of Fe(II)-M121EAz (Figure S11). The crystal

structure of Cu(II)-M121EM44KAz shows that the newly introduced Lys is 7.7−8.0 Å from the metal center, analogous to the Lys residue in SOR (Figures 7C and S13). The reduction potential of Fe(II)-M121EM44KAz was measured by CV to be +320±10 mV,52 within the error range comparable to that of Fe(II)-M121EAz (Figure S14). Oxidation experiments with Na_2IrCl_6, $K_3Fe(CN)_6$ and TMPD gave results similar to those of Fe(II)-M121EAz (Figure S15).

Interestingly, the rate constant of Fe(II)-M121EM44KAz with superoxide was determined to be $\sim 1.1\times10^6 M^{-1}s^{-1}$, which is 2 orders of magnitude higher than that observed for Fe(II)M121EAz (Figure 4). Since the reduction potential of this mutant is about the same as the one without the M44K mutation, ruling out reduction potential as a factor responsible for the difference in activity, one explanation for the enhanced activity is that the side chain of the positively charged Lys residue assists in guiding the negatively charged superoxide anions toward the Fe(II) center in Fe(II)-M121EM44KAz. Another possible explanation is that Lys may potentially form a hydrogen bond to the superoxo substrate that is bound to the Fe center, thus promoting activity. To determine the stability of both Fe(II)-M121EAz and Fe(II)-M121EM44KAz within the time frame of the activity assay, we measured the UV−vis spectra of both mutants in the assay buffer of 50 mM potassium phosphate (pH 7.8) containing 0.1 mM EDTA and found that the LMCT bands of both mutants remained stable throughout the NBT test time frame

(Figure S4), indicating that the superoxide scavenging activity is associated with the protein metallo-cofactor, not with leaked free iron.

Conclusions

In summary, by replacing Met121 with Glu and native Cu(II) with Fe(II), we have Engineered a nonheme iron-binding site in the ET protein Az producing a 2N(His)-1O(Glu)-1S(Cys) coordination sphere. The resulting M121EAz mutant has a higher affinity for Fe(II) than wtAz. In contrast to the redox-inactive Fe(II)-wtAz, Fe(II)-M121EAz is readily oxidized by Na_2IrCl_6 and, more interestingly, displays superoxide scavenging activity. Mössbauer and EPR spectroscopies, along with comparisons of X-ray structures, have been used to elucidate the similarities and differences between these two proteins. While the spectroscopic data reported here are part of an ongoing study, it should be noted that the EPR spectrum of Fe(II)-M121EAz is readily observed in both parallel and perpendicular modes, making it a convenient monitor for reactivity studies. Additionally, the secondary sphere mutation M44K, which was inspired by structural comparison with SOR, yielded a rate constant toward superoxide that was increased by 2 orders of magnitude. This finding demonstrates the importance of noncovalent second sphere interactions for fine-tuning enzymatic activity. While these initial findings are interesting, comprehensive studies, involving several spectroscopic techniques in conjunction with quantum chemical computations, are required to provide a correlation between the electronic structures of both mutants and their superoxide scavenging activity. Such studies as well as a search for intermediates have been initiated in our laboratories.

Experimental Methods

Materials. Nirotetrazolium blue chloride (NBT), xanthine, Fe-$(NH_4)_2(SO_4)_2 \cdot 6H_2O$, FeNa(EDTA), Na_2IrCl_6,$K_3Fe(CN)_6$, TMPD, chelex-100 sodium form, and catalase from Bovine liver (3809 units/mg) were purchased from Sigma-Aldrich Chemical Co. Xanthine oxidase from buffer milk (20 mg/mL) was purchased from EMD Chemicals, Inc. The water used in all experiments was purified by a Milli-Q system (Millipore, Bedford, MA, USA). All buffers were cleaned by chelex-100 sodium form. All other chemical reagents were obtained from Fisher Scientific Inc. and used without further purification.

Protein Purification. M121EAz and M121EM44KAz were expressed and purified as reported previously.[44] Homogeneity of the apo protein was achieved by passing through a size exclusion column at the last step.

Fe(II) incorporation. Fe(II) incorporation was carried out under anaerobic conditions. Apo Az mutant in Tris·HCl (25 mM, pH 7.8) was degassed with N_2 and transferred into a glovebag. Concentrations of the protein were measured based on the absorption at 280 nm (extinction coefficient of 8800 $M \cdot cm^{-1}$was used),[48] and 0.9−1 equiv of $Fe(NH_4)_2(SO_4)_2 \cdot 6H_2O$ was added slowly to the protein solution during stirring. The mixture was stirred at 5°C under N_2 atmosphere for 2 h to ensure complete incorporation of Fe(II). Excess iron salt was removed by a desalting PD-10 column in the glovebag to afford the ferrous holo-protein. The resulting Fe(II)-M121EAz was characterized by

UV−vis spectrometry, syringe-pump electrospray ionization mass spectrometry, and inductively coupled plasma analysis (ICP). The Fe(II)-M121EAz concentrations were calculated based on ε_{315} nm of 1610 $M^{-1}cm^{-1}$ determined by ICP, and the same extinction coefficient was used for the 319 nm peak of the Fe(II)-M121EM44KAz mutant.

Electron Spray Ionization Mass Spectrometry (ESI MS). Mass spectra of proteins were measured with a Waters Quattro II spectrometer operating in positive-ion mode. Protein samples were exchanged into acidic ammonium acetate buffer to make the final concentration between 10 and 20μM. The injection syringe was prewashed with 20% formic acid (20% v/v aqueous solution), and 10μL protein was injected into 50% CH_3CN/H_2O mobile phase with 50μL/min flow rate. The resulting spectra were integrated over the first minute of detection. The mass spectra were collected from 500 to 2000 m/z and were deconvoluted using the MassLinx software package with a 1 Da resolution and a 10,000−20,000 Da calculation window. Syringe pump mass spectra were used to detect interactions weaker than covalent bonding, such as metal cofactors coordinated by the protein scaffold. Protein samples were exchanged into ammonium acetate buffer (pH 5.1−6.3, 10 mM) to make the final concentration between 0.1 and 0.2 mM. The injection syringe was prewashed with MeOH. The protein sample was loaded into the syringe and was directly injected into the spectrometer by syringe pump at a rate of 5 μL/min. The mass spectra were collected from 500 to 2050 m/z and were

deconvoluted using the MassLinx software package with a 1 Da resolution and a 10,000-20,000 Da calculation window.

EPR Spectroscopy. The EPR spectra were collected and analyzed, throughout the development of the project, in two different laboratories. The EPR spectra of Figures 6B and S9 were recorded at the University of Illinois and those of Figures 6A and S7 at Carnegie Mellon University. Fe(II)-M121EAz Sample Preparation and EPR Data Collection. A 200μL of Fe(II)-M121EAz (2 mM) in in Mes (50 mM, pH 5.5) was mixed thoroughly with 50μL of glycerol, transferred to EPR tube, and frozen in liquid N_2 for data collection. The perpendicular (9.66 GHz) and parallel (9.38 GHz) mode X-band EPR spectra of Fe(II)-M12EAz shown in Figures 6A and S7 were recorded at Carnegie Mellon University on a Bruker E500 spectrometer equipped with an Oxford ESR910 liquid helium cryostat for low-temperature measurements and a bimodal cavity (Bruker ER4116DM) for generation of microwave fields parallel and perpendicular to the static field. The SpinCount software[58] used for EPR analysis was provided by Dr. Michael P. Hendrich of Carnegie Mellon University. Weak signals in the g = 2 region were observed in the Fe(II)-M121EAz spectrum (Figure S7) and are attributed to ~1μM Cu(II) contamination from the protein preparation. Fe(III)-M121EAz Sample Preparation and EPR Data Collection. An 1 equiv of Na_2IrCl_6 (10.6μL, 100 mM) was added slowly to Fe(II)-M121EAz (5.6 mM, 189.4μL) in Mes (50 mM, pH 5.5) under stirring. The resulting mixture was reacted at room temperature for 8.5 min before mixing with 50 μL

glycerol (which took~0.5 min) and freezing in liquid N_2. The final concentration of total Fe was 4.24 mM. Three Fe(II)-M121EAz samples were prepared similarly without Na_2IrCl_6, containing 0.42 mM (10%) and 0.85 mM (20%) ferrous protein, respectively. Five Fe(III)Na(ETDA) samples were prepared by diluting 50 mM stock solution in Mes (50 mM, pH 5.5) with the same buffer and mixing with 20% glycerol, and the final concentrations of Fe(III) were 1, 2, 3, 4, and 5 mM, respectively. X-band EPR was recorded at 10 K on a Varian E-line Century Series EPR spectrometer (E102 Microwave Bridge) fitted with a liquid He coldfinger. Double integration of the Fe(III)Na(EDTA) sample after gain correction gave a standard plot for area and spin concentration.[62] The total spin density of the Na_2IrCl_6 oxidized sample was calculated to be 82% of the starting ferrous sample by double integration of the spectra. Fitting of spectra was done with the simulation program SIMPIPM.[63] The remaining ferrous concentration was estimated by comparison with the two Fe(II)-M121EAz samples (Figure S9). A control sample of excess $Na_2IrCl_6$was scanned for comparison with the g = 2 region of the Fe(III)-M121EAz spectrum (Figure S9).

Mössbauer Spectroscopy. ^{57}Fe2+incorporation was carried out with $^{57}FeCl_2$ following procedures described above. The ^{57}Fe(II)-M121EAz was buffered in 50 mM MES at pH 5.5. Mössbauer spectra shown in Figure 5 of the main text were recorded at Carnegie Mellon University with two spectrometers, using Janis Research (Wilmington, MA) SuperVaritemp dewars that allow studies in applied magnetic fields up to 8.0 T in

the temperature range from 1.5 to 200 K. Mössbauer spectral simulations were performed using the WMOSS software package (SEE Co, Edina, MN). Isomer shifts are quoted relative to Fe metal at 298 K. Mössbauer spectra shown in Figure S8 were recorded at Knox College at 4.2 K in applied fields of 0, 1, 5, and 9 T. Mössbauer spectral simulations were performed using a proprietary nonlinear least-squares fitting program.

X-ray Crystallography. The Fe(II)-M121EAz was crystallized based on apo-Az crystallization condition.[49] The Fe(II)-M121EAz (2mM) was mixed with crystallization buffer containing $(NH_4)_2SO_4$ (3.25 M), $LiNO_3$ (0.1 M), NaOAc (0.1 M) at pH 5.3 in 3:3, 3:2, and 3:1 ratio, respectively, on a silica slide and equilibrate over 500 μL well buffer using hanging drop method at 5°C. Colorless block crystals were obtained after 2−3 weeks. The crystals were dipped in cryo-buffer containing 70% of well buffer and 30% of glycerol before mounting and frozen in liquid N_2 for diffraction data collection and analysis. Crystallographic parameters are shown in Table S2. Diffraction data were collected using 1.0750 Å as wavelengths of data collection at the Brookhaven National Synchrotron Light Source X29 beamline. All data were integrated using the program HKL2000.[64] The crystal structure was solved by the molecular replacement method using MOLREP in the CCP4 Suite.[65] Refinement was performed using Refmac[66] in the CCP4 Suite and Coot.[67] The Cu(II)-M121EM44KAz was crystallized following literature conditions.[44] 3 uL of approximately 20 mg/mL apo-M121EM44KAz in NaOAc (100 mM, pH 5.6) were mixed with a well buffer containing PEG 4000 (25%), $LiNO_3$ (100

mM), $CuSO_4$ (10 mM), and Tris (100 mM, pH 8.0) in 3:3, 3:2 and 3:1 ratio, respectively, on a silica slide and allowed to equilibrate over 300 μL well buffer using hanging drop method at 5°C. Light-gray block crystals were grown within 3 days. The crystals were dipped in cryo-buffer containing 70% of well buffer and 30% of glycerol before mounting and frozen in liquid N_2 for diffraction data collection and analysis. Crystallographic parameters are shown in Table S3. Diffraction data were collected using 1.0750 Å as wavelengths of data collection at the Brookhaven National Synchrotron Light Source X29 beamline. All data were integrated using the program HKL2000.[64] The crystal structure was solved by the molecular replacement method using PhaserMR in the PHENIX Suite.[68] Refinement was performed using phenix.refine in the PHENIX Suite[68] and Coot.[67]

Superoxide Activity Assay. Superoxide scavenging activity was determined by the Fridovich method using nirotetrazolium blue chloride (NBT) reduction.[54] Superoxide was generated enzymatically by the xanthine−xanthine oxidase system and spectrophotometrically detected by monitoring the formation of the NBT reduction at 535 nm. All measurements were carried out in 1 cm cuvettes at 25°C controlled by a NESLAB Digital Plus RTE 7 water bath circulator and monitored by an Agilent 8453 UV−vis spectrometer. The reaction system was in phosphate buffer KPi (pH 7.8, 50 mM) containing 0.1 mM EDTA to stabilize xanthine oxidase. 7 μL xanthine oxidase was diluted by 193 μL KPi (50 mM, pH 7.8) containing 0.1 mM EDTA as stock solution. The

reaction mixture was composed of xanthine (0.5 mM, 60 μL), catalase (2 μL, 5×10^4 units/mL, to decompose possible H_2O in the reaction system and avoid side reactions with Az mutants), NBT (10 μL, 1.5 mM), and reaction buffer with or without investigated Az mutants to make 140 μL solution. 10 μL xanthine oxidase stock solution was added to the reaction mixture and mixed thoroughly with 200μL Pipetman to initiate the reaction. The NBT reduction rate was measured both in the presence and absence of the ferrous Az mutants for 250s for each concentration. The rate without ferrous Az is defined as v^o, and the one with Az is v. Five concentrations were tested for each mutant for three times, and $[(v^o/v)-1]$ values were plotted against protein concentration to estimate the concentration which causes 50% of inhibition of NBT reduction ($(v^o/v)-1 = 1$). The reaction rate with superoxide was estimated by $[Az]^{50}*rate = [NBT]*rate^{NBT}$, [NBT] = 0.1 mM, $rate^{NBT}= 5.94\times10^4 M^{-1}s^{-1}$,[55] $[Az]^{50}$ is the concentration when $(v^o/v)-1=1$.

Electrochemical Measurements. The reduction potential of each mutant was determined by CV using a CH Instruments 617A potentiostat equipped with a picoamp booster and a Faraday cage. A pyrolytic graphite edge electrode was polished, and 2−3 μL of protein solution was applied directly to the electrode following previously described methods.[52] After a short incubation time, the electrode was immersed in MOPS (pH 7.0, 50 mM) with 100 mM $NaNO_3$ on ice before data collection. Each protein was then sampled on two different electrodes with or without coabsorbent

didecyldimethylammonium bromide (DDAB) between −200 mV and 500 mV. The reduction potentials were measured against Ag/AgCl and converted to SHE.

Acknowledgements

We wish to thank Ms. Rebecca L. Keller, Professor Carsten Krebs, Professor J. Martin Bollinger, Jr. from The Pennsylvania State University for initial investigations of the protein using Mössbauer spectroscopy, Mr. Yi-Gui Gao from University of Illinois at Urbana-Champaign for initial investigations of the protein crystal structure, and Ms. Parisa Hosseinzadeh from University of Illinois at Urbana-Champaign for help with the CV data collection and analysis. This work was supported by the National Science Foundation under awards CHE1413328 (Y.L.) and CHE1305111 (E.M.)

References

1. Lu, Y.; Yeung, N.; Sieracki, N.; Marshall, N. M. Nature 2009, 460, 855.

2. Lu, Y.; Berry, S. M.; Pfister, T. D. Chem. Rev. 2001, 101, 3047.

3. Goodman, C. M.; Choi, S.; Shandler, S.; DeGrado, W. F. Nat. Chem. Biol. 2007, 3, 252.

4. Ghosh, D.; Pecoraro, V. L. Curr. Opin. Chem. Biol. 2005, 9, 97.

5. Schueler-Furman, O.; Wang, C.; Bradley, P.; Misura, K.; Baker, D. Science 2005, 310, 638.

6. Gibney, B. R. Protein Folding Met. Ions 2011, 227.

7. Abe, S.; Ueno, T.; Watanabe, Y. Top. Organomet. Chem. 2009, 25, 25.

8. Kohler, V.; Wilson, Y. M.; Lo, C.; Sardo, A.; Ward, T. R. Curr.Opin. Biotechnol. 2010, 21, 744.

9. Yeung, N.; Lin, Y.-W.; Gao, Y.-G.; Zhao, X.; Russell, B. S.; Lei, L.; Miner, K. D.; Robinson, H.; Lu, Y. Nature 2009, 462, 1079.

10. Lu, Y.; Valentine, J. S. Curr. Opin. Struct. Biol. 1997, 7, 495.

11. Lu, Y. Curr. Opin. Chem. Biol. 2005, 9, 118.

12. Lu, Y. Angew. Chem., Int. Ed. 2006, 45, 5588.

13. Lu, Y. Inorg. Chem. 2006, 45, 9930.

14. Kurtz, D. M., Jr. Dalton Trans. 2007, 4115.

15. Clark, K. M.; van der Donk, W. A.; Lu, Y. Methods Enzymol. 2009, 462, 97.

16. Lu, Y.; Garner, D. K.; Zhang, J.-l. Wiley Encycl. Chem. Biol. 2009, 1, 124.

17. Marshall, N. M.; Garner, D. K.; Wilson, T. D.; Gao, Y.-G.; Robinson, H.; Nilges, M. J.; Lu, Y. Nature 2009, 462, 113.

18. Davydov, R. M.; McLaughlin, M. P.; Bill, E.; Hoffman, B. M.; Holland, P. L. Inorg. Chem. 2013, 52, 7323.

19. Petrik, I. D.; Liu, J.; Lu, Y. Curr. Opin. Chem. Biol. 2014, 19, 67.

20. Reig, A. J.; Pires, M. M.; Snyder, R. A.; Wu, Y.; Jo, H.; Kulp, D. W.; Butch, S. E.; Calhoun, J.R.; Szyperski, T. G.; Solomon, E. I.; DeGrado, W. F. Nat. Chem. 2012, 4, 900.

21. Calhoun, J. R.; Nastri, F.; Maglio, O.; Pavone, V.; Lombardi, A.; DeGrado, W. F. Biopolymers 2005, 80, 264.

22. Popp, B. V.; Ball, Z. T. J. Am. Chem. Soc. 2010, 132, 6660.

23. Chen, Z.; Vohidov, F.; Coughlin, J. M.; Stagg, L. J.; Arold, S. T.; Ladbury, J. E.; Ball, Z. T. J. Am. Chem. Soc. 2012, 134, 10138.

24. Farinas, E.; Regan, L. Protein Sci. 1998, 7, 1939.

25. Pinto, A. L.; Hellinga, H. W.; Caradonna, J. P. Proc. Natl. Acad. Sci. U. S. A. 1997, 94, 5562.

26. Costas, M.; Mehn, M. P.; Jensen, M. P.; Que, L., Jr. Chem. Rev. 2004, 104, 939.

27. Solomon, E. I.; Brunold, T. C.; Davis, M. I.; Kemsley, J. N.; Lee, S.-K.; Lehnert, N.; Neese, F.; Skulan, A. J.; Yang, Y.-S.; Zhou, J. Chem. Rev. 2000, 100, 235.

28. van der Donk, W. A.; Krebs, C.; Bollinger, J. M., Jr. urr. Opin. Struct. Biol. 2010, 20, 673.

29. Tshuva, E. Y.; Lippard, S. J. Chem. Rev. 2004, 104, 987.

30. Girerd, J.-J.; Banse, F.; Simaan, A. J. Struct. Bonding (Berlin, Ger.) 2000, 97, 145.

31. Que, L. Acc. Chem. Res. 2007, 40, 493.

32. Cho, J.; Sarangi, R.; Nam, W. Acc. Chem. Res. 2012, 45, 1321.

33. Kovacs, J. A.; Brines, L. M. Acc. Chem. Res. 2007, 40, 501.

34. McQuilken, A. C.; Goldberg, D. P. Dalton Trans. 2012, 41, 10883.

35. Berry, J. F.; Bill, E.; Bothe, E.; DeBeer George, S.; Mienert, B.;Neese, F.; Wieghardt, K. Science 2006, 312, 1937.

36. Ye, S.; Neese, F. Curr. Opin. Chem. Biol. 2009, 13, 89.

37. MacBeth, C. E.; Golombek, A. P.; Young, V. G., Jr.; Yang, C.; Kuczera, K.; Hendrich, M. P.; Borovik, A. S. Science 2000, 289, 938.

38. Braymer, J. J.; O'Neill, K. P.; Rohde, J.-U.; Lim, M. H. Angew. Chem., Int. Ed. 2012, 51, 5376.

39. Fernandez, C. O.; Vila, A. J. ACS Symp. Ser. 2003, 858, 287.

40. Messerschmidt, A. Struct. Bonding (Berlin, Ger.) 1998, 90, 37.

41. Kolczak, U.; Dennison, C.; Messerschmidt, A.; Canters, G. W. Handb. Metalloproteins 2001, 2, 1170.

42. Nar, H.; Messerschmidt, A.; Huber, R.; Van de Kamp, M.; Canters, G. W. J. Mol. Biol. 1991, 221, 765.

43. McLaughlin, M. P.; Retegan, M.; Bill, E.; Payne, T. M.; Shafaat, H. S.; Pena, S.; Sudhamsu, J.; Ensign, A. A.; Crane, B. R.; Neese, F.; Holland, P. L. J. Am. Chem. Soc. 2012, 134, 19746.

44. Lancaster, K. M.; George, S. D.; Yokoyama, K.; Richards, J. H.; Gray, H. B. Nat. Chem. 2009, 1, 711.

45. Jovanovic, T.; Ascenso, C.; Hazlett, K. R. O.; Sikkink, R.; Krebs, C.; Litwiller, R.; Benson, L. M.; Moura, I.; Moura, J. J. G.; Radolf, J. D.; Huynh, B. H.; Naylor, S.; Rusnak, F. J. Biol. Chem. 2000, 275, 28439.

46. McDonald, A. R.; Van Heuvelen, K. M.; Guo, Y.; Li, F.; Bominaar, E. L.; Münck, E.; Que, L. Angew. Chem., Int. Ed. 2012, 51, 9132.

47. Namuswe, F.; Kasper, G. D.; Narducci Sarjeant, A. A.; Hayashi, T.; Krest, C. M.; Green, M. T.; Moenne-Loccoz, P.; Goldberg, D. P. J.Am. Chem. Soc. 2008, 130, 14189.

48. Tennent, D. L.; McMillin, D. R. J. Am. Chem. Soc. 1979, 101, 2307.

49. Nar, H.; Messerschmidt, A.; Huber, R.; Van de Kamp, M.; Canters, G. W. FEBS Lett. 1992, 306, 119.

50. Karlsson, B. G.; Tsai, L.-C.; Nar, H.; Sanders-Loehr, J.; Bonander, N.; Langer, V.; Sjolin, L. Biochemistry 1997, 36, 4089.

51. Katona, G.; Carpentier, P.; Niviere, V.; Amara, P.; Adam, V.; Ohana, J.; Tsanov, N.; Bourgeois, D. Science 2007, 316, 449.

52. Jeuken, L. J. C.; Armstrong, F. A. J. Phys. Chem. B 2001, 105, 5271.

53. Clay, M. D.; Jenney, F. E., Jr.; Hagedoorn, P. L.; George, G. N.; Adams, M. W. W.; Johnson, M. K. J. Am. Chem. Soc. 2002, 124, 788.

54. Beauchamp, C.; Fridovich, I. Anal. Biochem. 1971, 44, 276.

55. Liao, Z. R.; Zheng, X. F.; Luo, B. S.; Shen, L. R.; Li, D. F.; Liu, H. L.; Zhao, W. Polyhedron 2001, 20, 2813.

56. Hendrich, M. P.; Debrunner, P. G. Biophys. J. 1989, 56, 489.

57. Gupta, R.; Lacy, D. C.; Bominaar, E. L.; Borovik, A. S.; Hendrich, M. P. J. Am. Chem. Soc. 2012, 134, 9775.

58. Golombek, A. P.; Hendrich, M. P. J. Magn. Reson. 2003, 165, 33.

59. Horner, O.; Mouesca, J.-M.; Oddou, J.-L.; Jeandey, C.; Niviere, V.; Mattioli, T. A.; Mathe, C.; Fontecave, M.; Maldivi, P.; Bonville, P.; Halfen, J. A.; Latour, J.-M. Biochemistry 2004, 43, 8815.

60. Lombard, M.; Houee-Levin, C.; Touati, D.; Fontecave, M.; Niviere, V. Biochemistry 2001, 40, 5032.

61. Adams, M. W. W.; Jenney, F. E., Jr.; Clay, M. D.; Johnson, M. K. JBIC, J. Biol. Inorg. Chem. 2002, 7, 647.

62. Bou-Abdallah, F.; Chasteen, N. D. JBIC, J. Biol. Inorg. Chem. 2008, 13, 15.

63. Nilges, M. J. SIMPIPM; University of Illinois: Urbana−Champaign, IL, 2002.

64. Otwinowski, Z.; Minor, W. Methods Enzymol. 1997, 276, 307.

65. Vagin, A.; Teplyakov, A. J. Appl. Crystallogr. 1997, 30, 1022.

66. Murshudov, G. N.; Vagin, A. A.; Dodson, E. J. Acta Crystallogr., Sect. D: Biol. Crystallogr. 1997, D53, 240.

67. Emsley, P.; Cowtan, K. Acta Crystallogr., Sect. D: Biol. Crystallogr. 2004, D60, 2126.

68. Adams, P. D.; Afonine, P. V.; Bunkoczi, G.; Chen, V. B.; Davis, I. W.; Echols, N.; Headd, J. J.; Hung, L. W.; Kapral, G. J.; Grosse-Kunstleve, R. W.; McCoy, A. J.; Moriarty, N. W.; Oeffner, R.; Read, R.J.; Richardson, D. C.; Richardson, J. S.; Terwilliger, T. C.; Zwart, P. H. Acta Crystallogr., Sect. D: Biol. Crystallogr. 2010, 66, 213.

Supporting Information

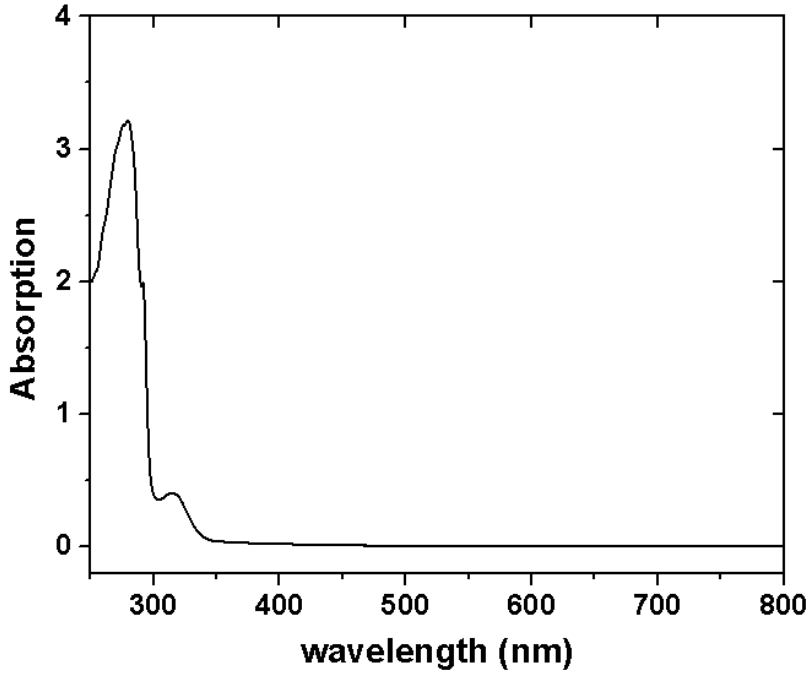

Figure S1. UV-Vis absorption spectra of Fe(II)-M121EAz monitored by Cary 5000.

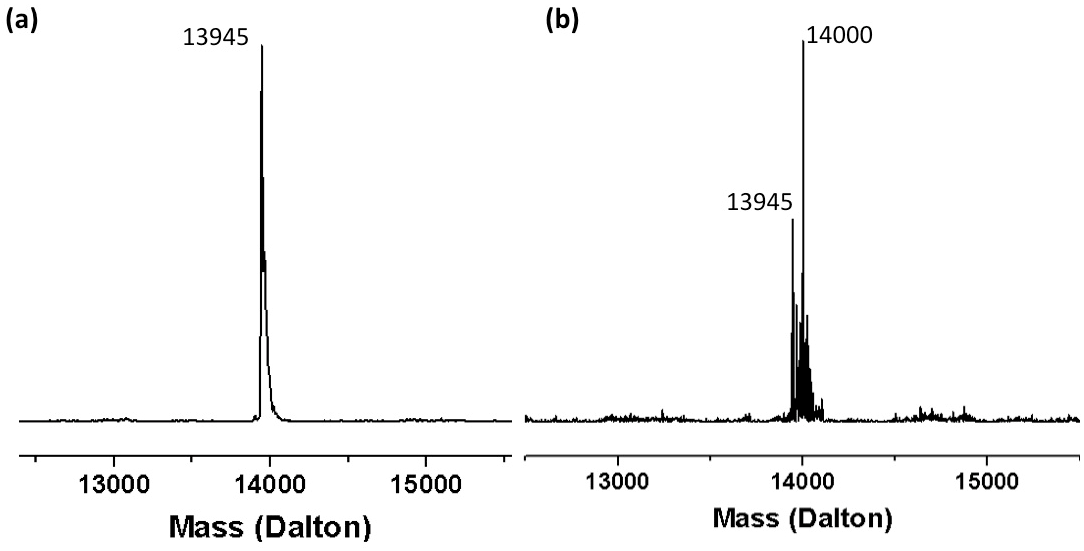

Figure S2 (a) ESI MS spectrum of apo M121EAz. (Calculated mass: 13943.7 Da); (b) Syringe-pump ESI MS spectrum of Fe(II)-M121EAz (Calculated mass: 13999.6 Da).

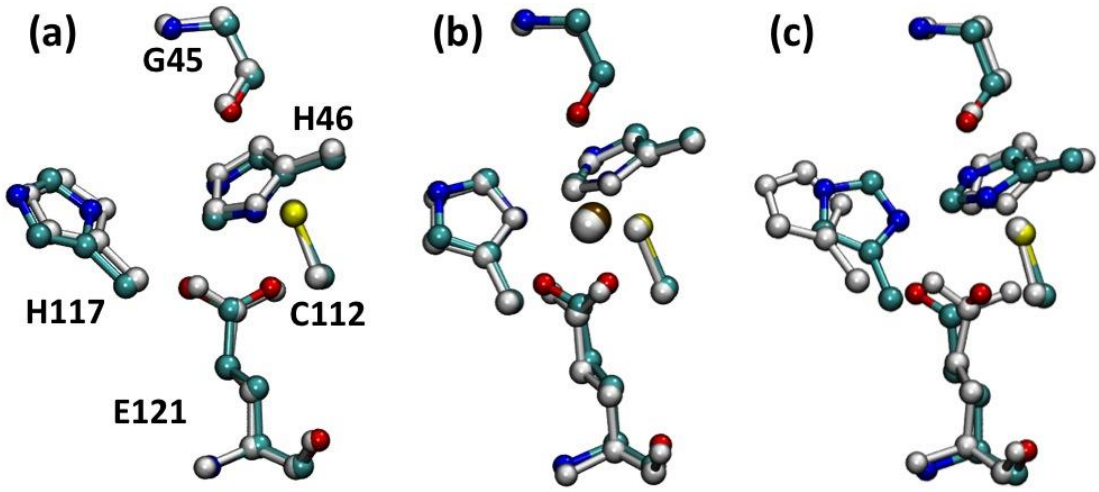

Figure S3. Subunit structure comparison of Fe(II)-M121EAz. Resolution: 2.0 Å. (a) Chain A (white) and chain C (colored). (b) Chain D (white) and chain B (colored). (c) Chain A (white) and chain B (colored).

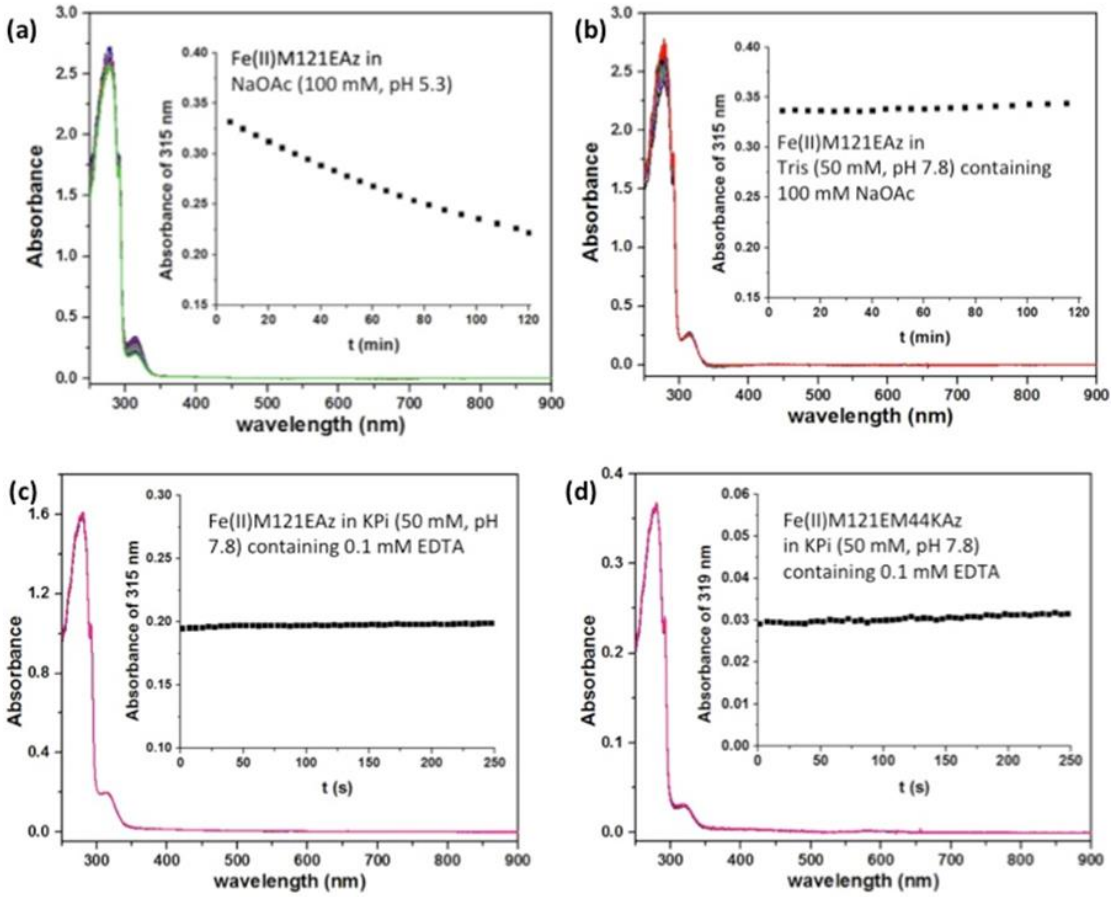

Figure S4. Stability test of Fe(II)-M121EAz and Fe(II)-M121EM44KAz.

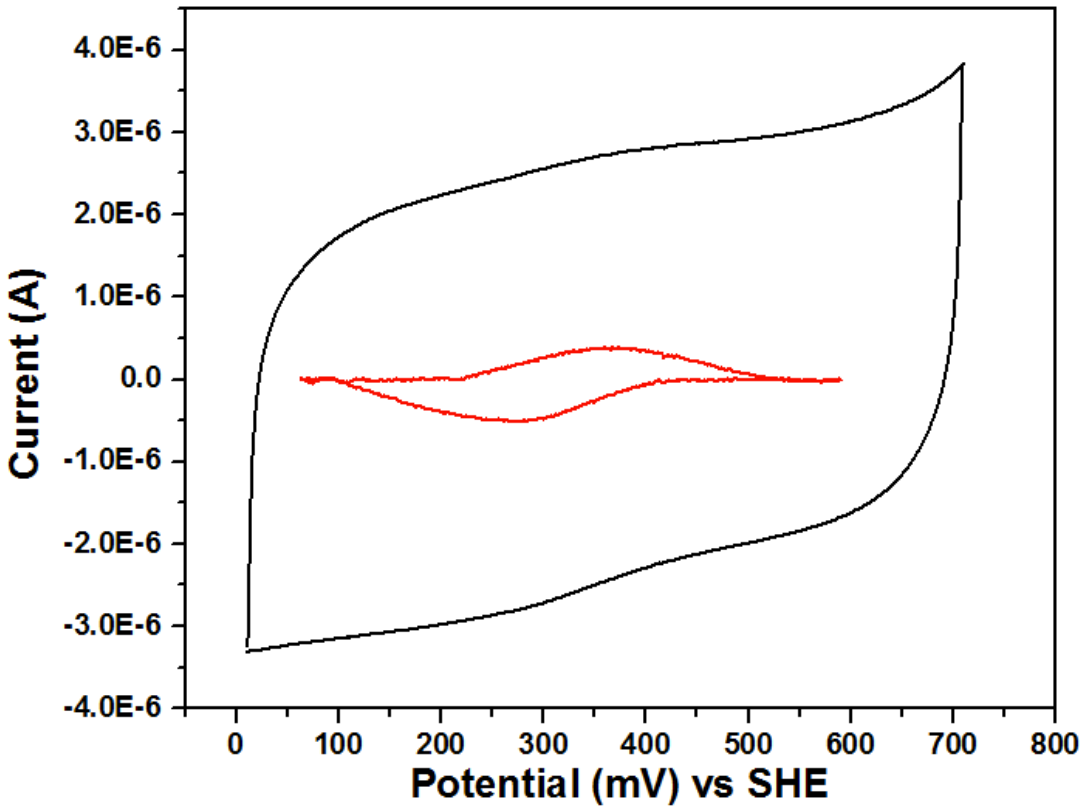

Figure S5. Cyclic voltammogram of Fe-M121EAz at pH 7.0 on a pyrolytic graphite edge (PGE) electrode.

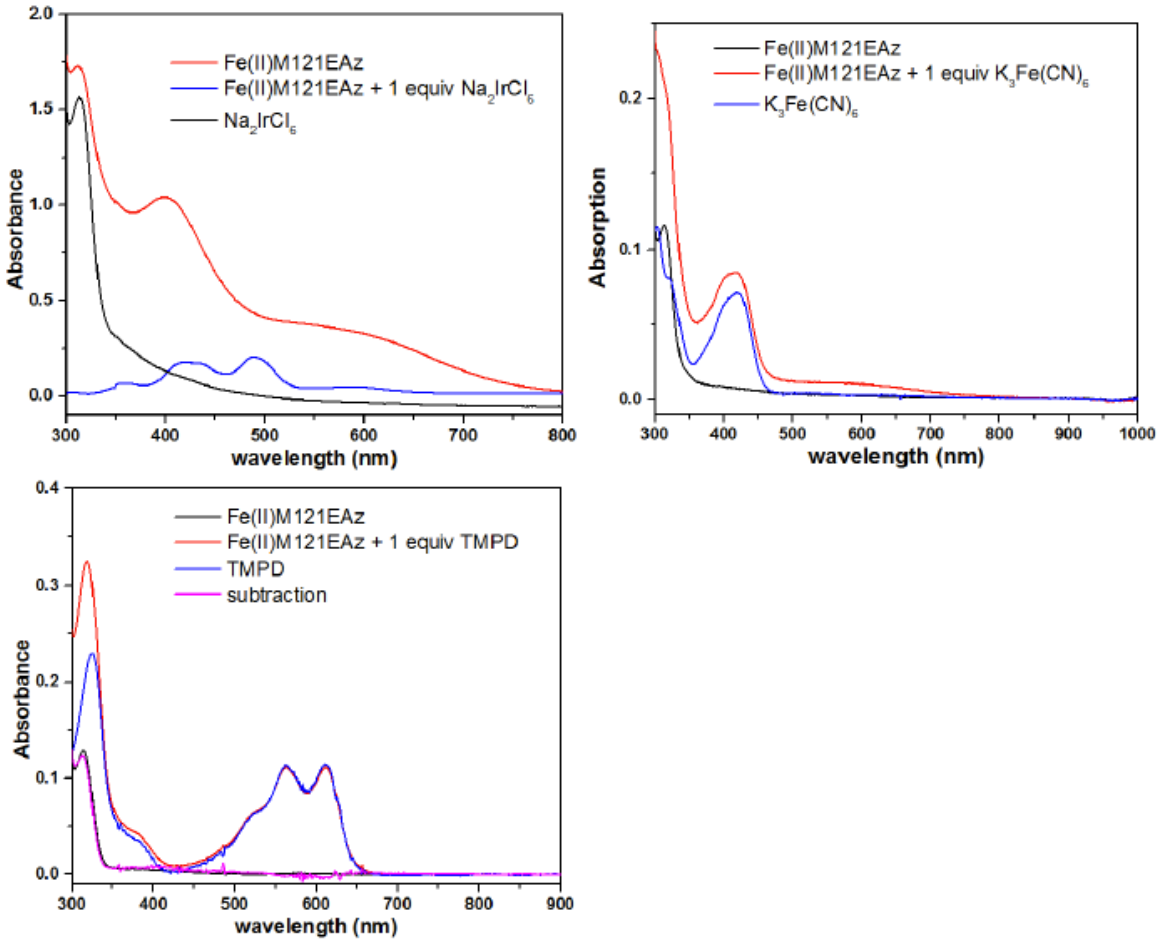

Figure S6. Reaction mixture (red line) of Fe(II)-M121EAz (black line) with Na_2IrCl_6, $K_3Fe(CN)_6$ or TMPD (blue line in each graph) in MES (50 mM, pH 5.5) at room temperature.

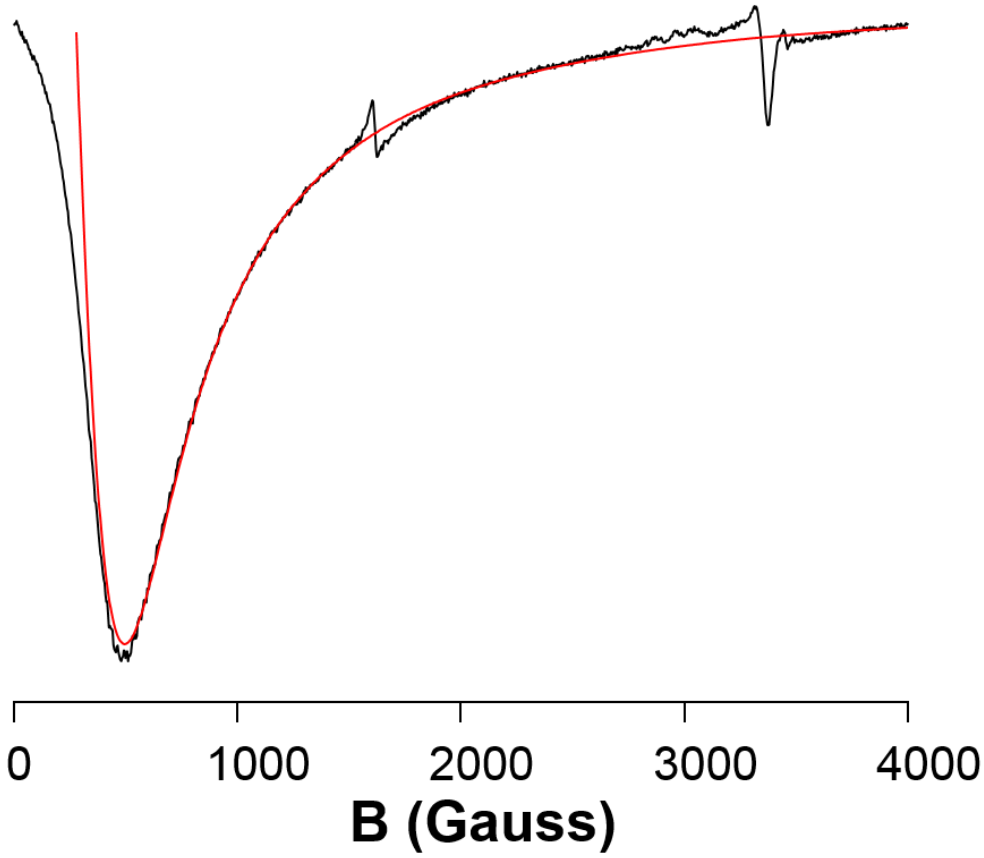

Figure S7. Perpendicular mode X-band EPR spectrum of Fe(II)-M121EAz recorded at 11.2 K. The black curve is the experimental spectrum, and the red curve is a simulation generated using the software SpinCount[1] for D = -3.47 cm^{-1} and E/D = 0.177; the parameter E/D was assumed to have a Gaussian distribution with $\sigma_{E/D}$ = 0.002 Conditions: microwave power; 2 mW, microwave frequency; 9.663 GHz, modulation amplitude; 1 mT.

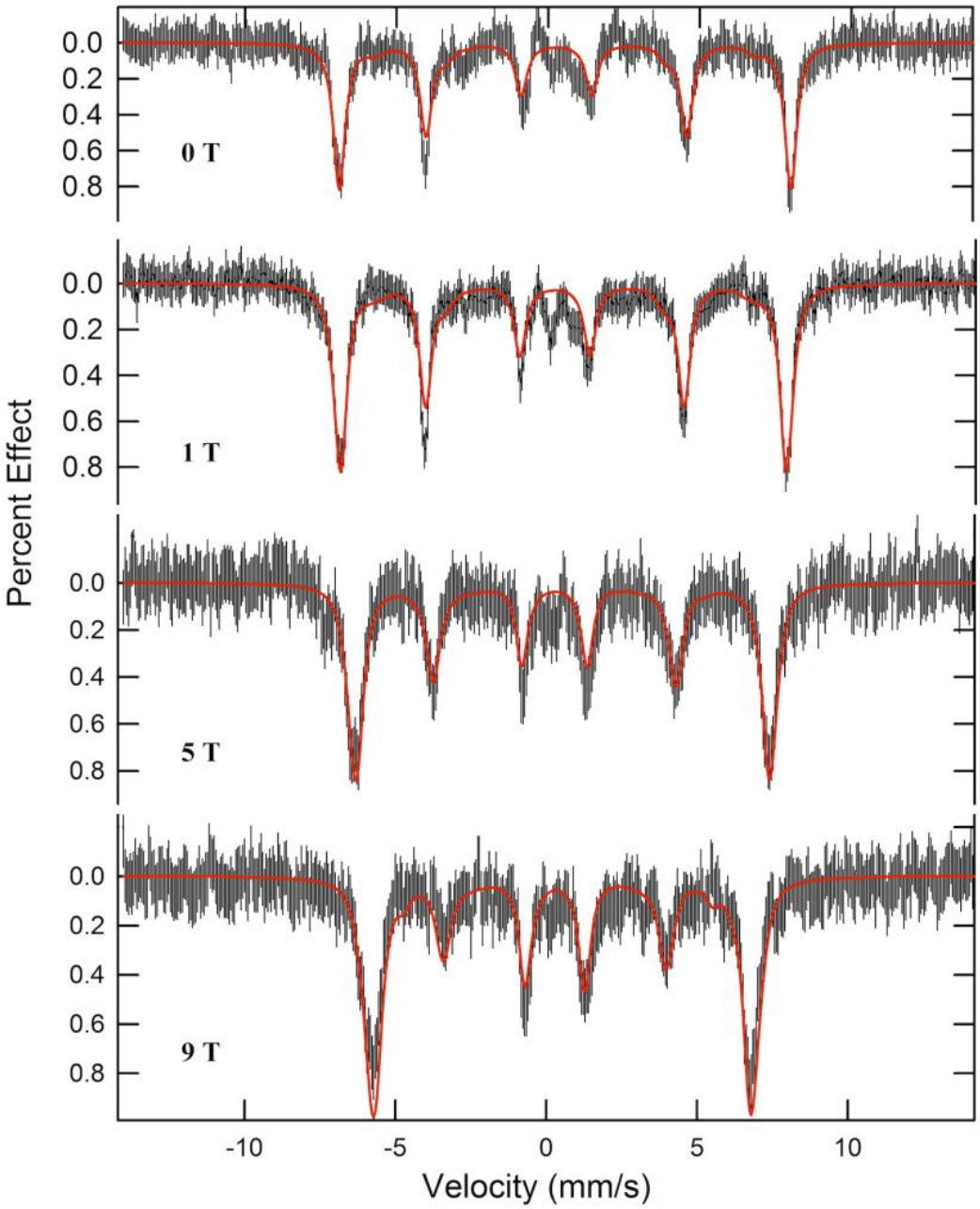

Figure S8. Variable field Mössbauer spectra of Fe(III)-M121EAz recorded at 4.2 K at fields indicated. The black hash-marked curves are the experimental spectra. Simulations, using the parameters of Table 1 in the main text, are shown as the solid red curves.

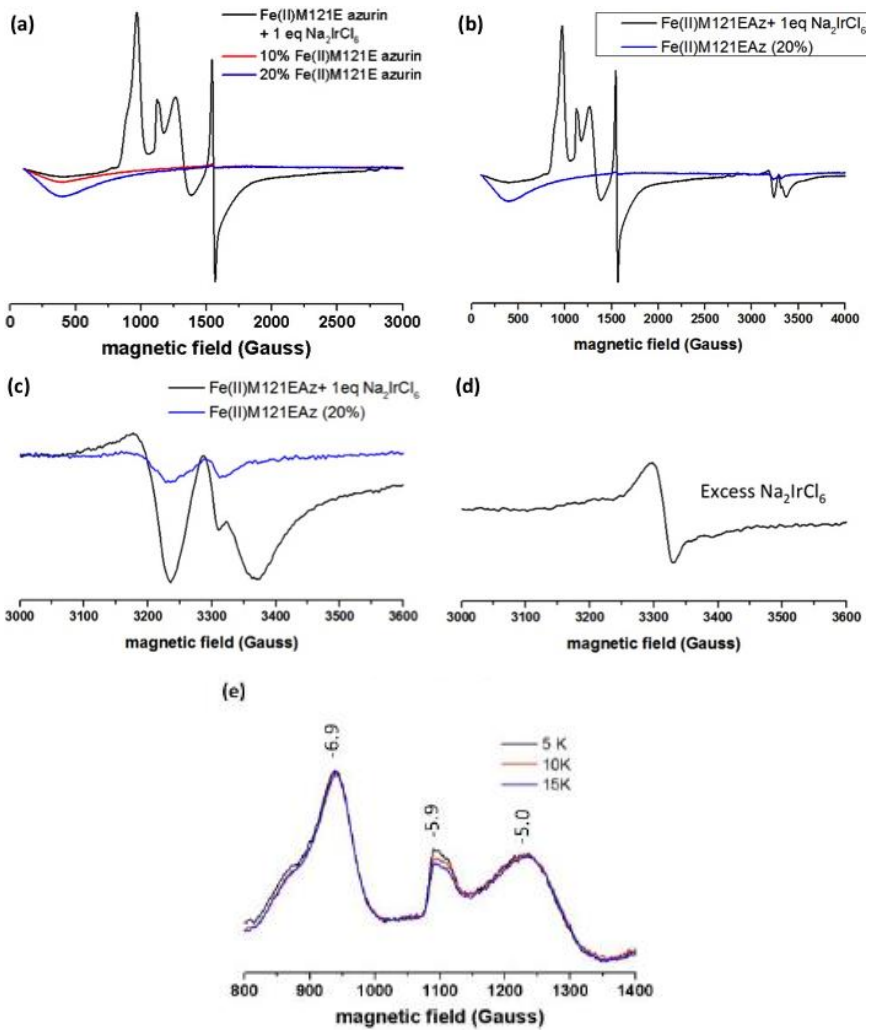

Figure S9. (a) Comparison of EPR spectra in MES (50 mM, pH 5.5) containing 20 % glycerol. *Black line*: reaction mixture of 4.2 mM Fe(II)-M121EAz with 1 equiv of Na2IrCl6 without PD-10 column.; *red line*: Fe(II)-M121EAz (0.42 mM); *blue line*: Fe(II)-M121EAz (0.85 mM). (Shapes of blue and red spectra were used to subtract Fe(II)M121EAz from raw data and estimate the amount of remaining ferrous protein after oxidation). **(b)** Full spectra of Fe(II)-M121EAz with 1 equiv of Na_2IrCl_6 in comparison to Fe(II)M121EAz**. (c)** g = 2 region of Fe(II)-M121EAz with 1 equiv of Na_2IrCl_6 in comparison to Fe(II)-M121EAz and **(d)** g = 2 region of Na_2IrCl_6. **(e)** EPR spectra of the reaction mixture of Fe(II)-M121EAz with 1 equiv of Na_2IrCl_6 after PD-10 column in MES (50 mM, pH 5.5) containing 20 % glycerol. Spectra collected from 5 K to 15 K, after subtraction of ferrous signal and rescaling. The change of the 5.9 signals indicates a negative D value.[2] Parameters: microwave power: 4 mW, microwave frequency: 9.21 GHz; modulation amplitude: 10 G.

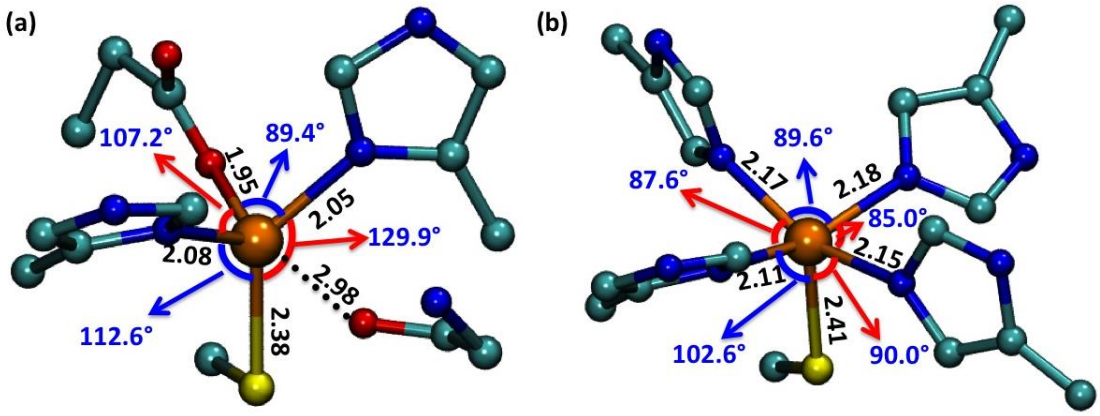

Figure S10. Structural comparison of **(a)** chain B of Fe(II)-M121EAz and **(b)** superoxide reductase (PDB ID: 2JI1). Distances (in Å) are shown in black fonts, and angles are shown in blue fonts. Color code: C, cyan; S, yellow; N, blue; O, red; Fe, orange.

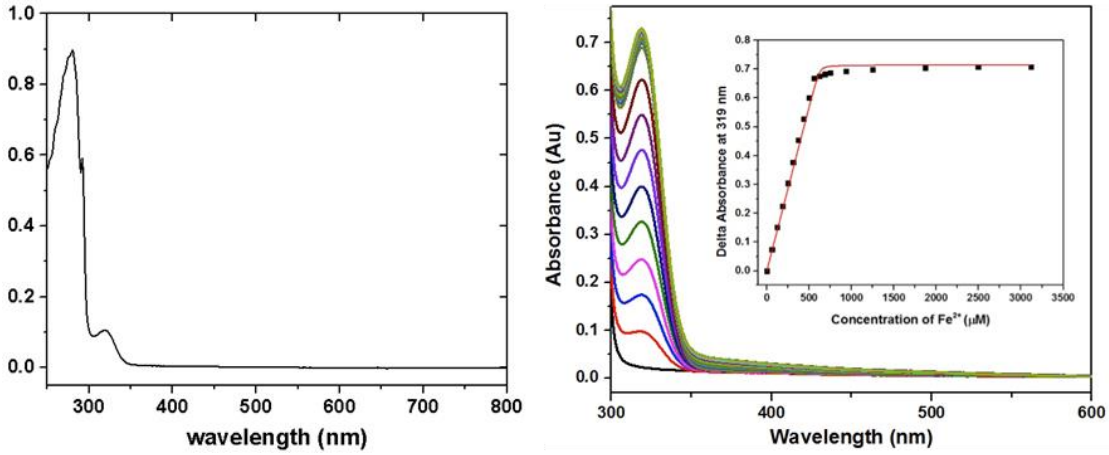

Figure S11. (a) UV-Vis absorption of Fe(II)-M121EM44KAz spectrum. (b) Development of absorbance at 319 nm after successive addition of 0.1-5 equiv of Fe^{2+} to apo-M121EM44KAz. (Inset) Titration curve of the absorbance maxima at 319 nm.

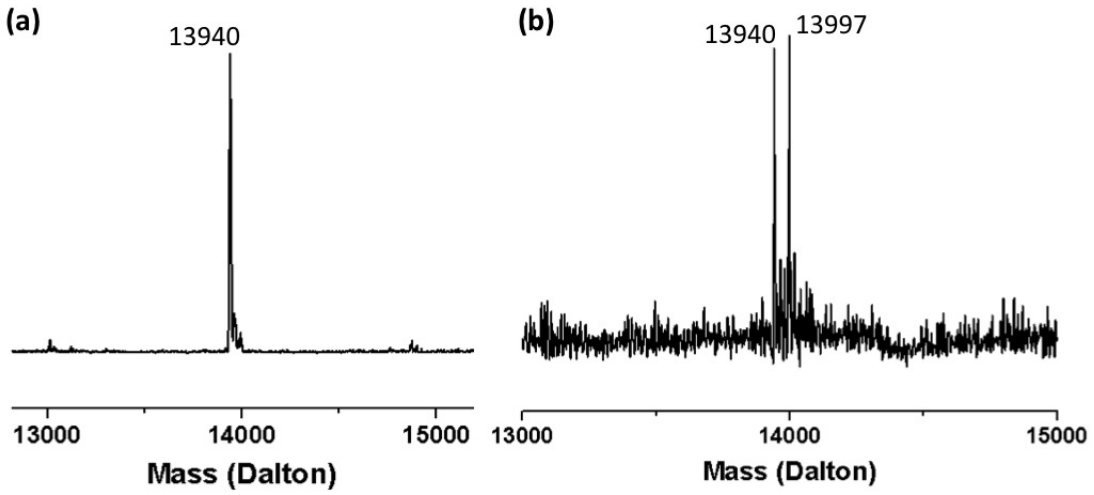

Figure S12. (a) ESI MS spectrum of apo-M121EM44KAz (calculated mass: 13940.7 Da); (b) Syringe-pump ESI MS spectrum of Fe(II)-M121EM44KAz (calculated mass: 13996.6 Da).

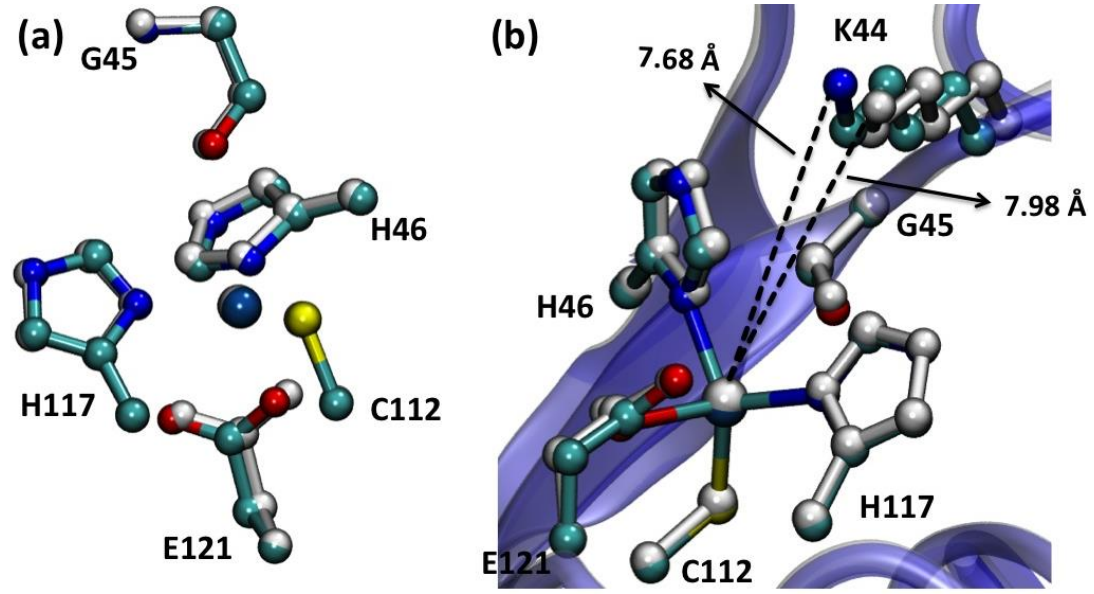

Figure S13. Subunit structure comparison of Cu(II)-M121EM44KAz. Resolution: 1.64 Å. (a) metal binding sites of Chain A (white) and chain B (colored). (b) K44 position in Chain A (white) and chain B (colored). Color code: C, cyan; S, yellow; N, blue; O, red; Cu, gray blue.

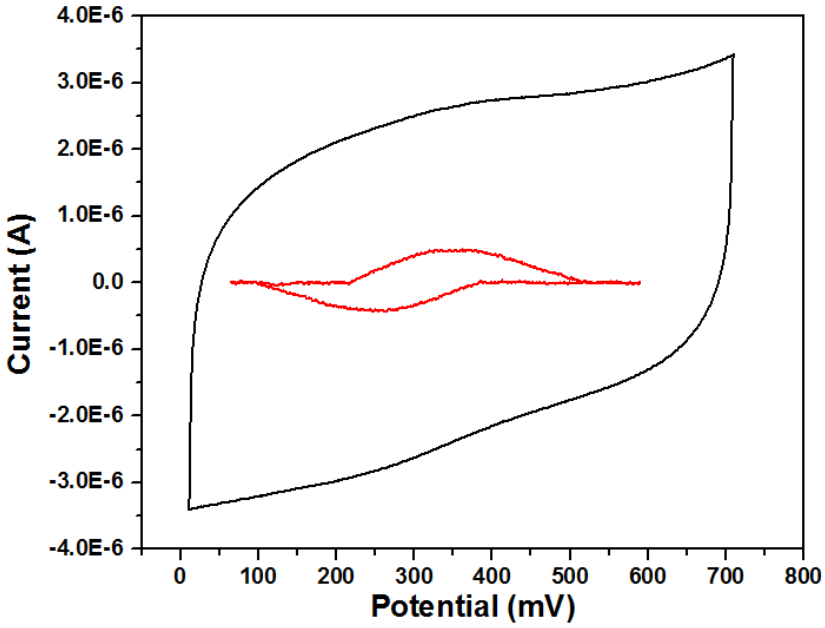

Figure S14. Cyclic voltammogram of Fe(II)-M121EM44KAz at pH 7.0 on a pyrolytic graphite edge (PGE) electrode.

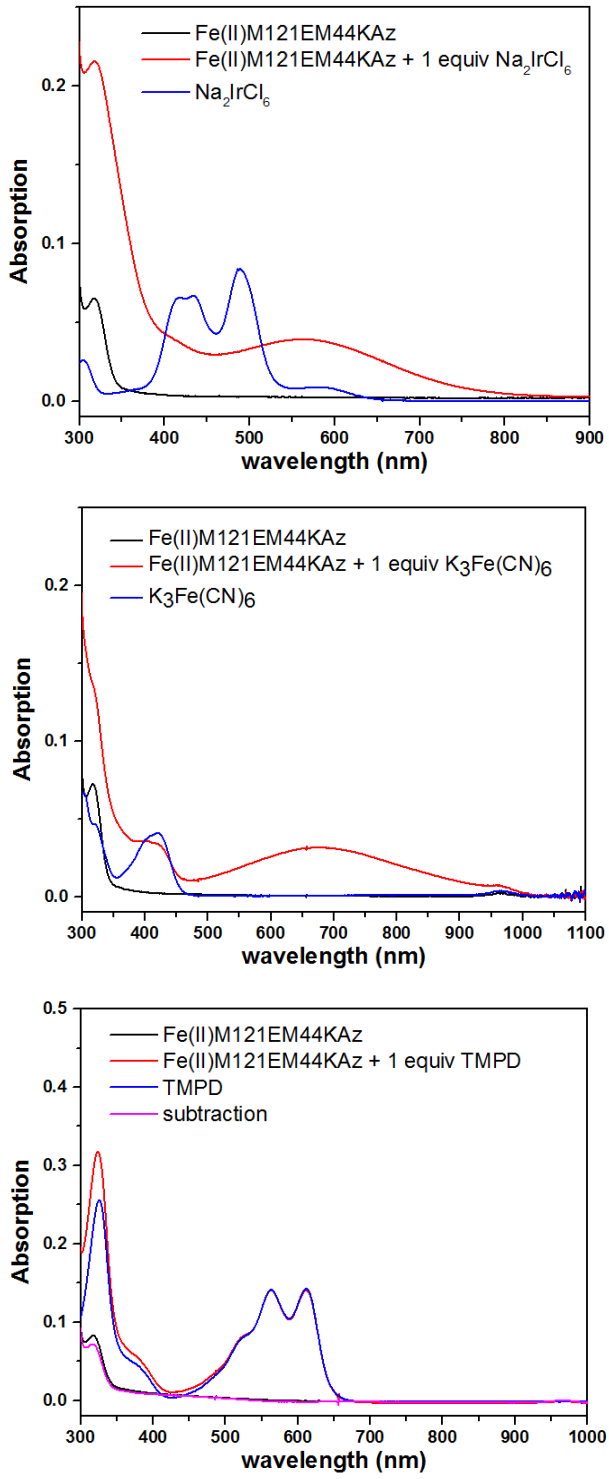

Figure S15. Reaction mixture (red line) of Fe(II)-M121EM44KAz (black line) with Na_2IrCl_6, $K_3Fe(CN)_6$ or TMPD (blue line in each graph) in MES (50 mM, pH 5.5) at room temperature.

Table S1. Inductively Coupled Plasma (ICP) analysis of metals in Fe(II)-M121EAz*

Element	Found	Protein incorporation ratio
Cu	0.21ppm	0.09%
Fe	140.7ppm	70%
Zn	1.43ppm	0.62

* ε_{280nm}=8800 $M^{-1}cm^{-1}$ was used to determine the protein concentration.[3]
* Measured by inductively coupled plasma mass spectrometry (ICP-MS) using PerkinElmer-SCIEX ELAN DRCe ICP-MS.

Table S2. Crystallographic parameters for Fe(II)-M121EAz.[4]

Data Collection Statistics	
Space Group	$P2_12_12_1$
Unit Cell	a = 56.853, b = 80.208, c = 109.04 α = 90°, β = 90°, γ = 90°
Wavelength (Å)	1.0750
Resolution (Å)	2.0
R_{sym} (%)	19.1
$\langle I/\sigma I \rangle$	13.3
Completeness (%)	99.6
Redundancy	13.2
Refinement Statistics	
Resolution (Å)	2.00 (46.38-2.00)
R-Factor (%)	20.46
R_{free} (%)	26.19
Protein atoms	3905
Water Molecules	373
Fe	2
Unique Reflections	32211
R.m.s.d.	
Bonds (Å)	0.0176
Angles (˚)	1.9399

Table S3. Crystallographic parameters for Cu(II)-M121EM44KAz.[4]

Data Collection Statistics	
Space Group	C121
Unit Cell	a = 55.285, b = 48.695, c = 95.068 α = 90°, β = 94.65°, γ = 90°
Wavelength (Å)	1.0750
Resolution (Å)	1.64
R_{sym} (%)	8.5
$\langle I/\sigma I \rangle$	14.7
Completeness (%)	98.4
Redundancy	13.2
Refinement Statistics	
Resolution (Å)	1.64 (47.38-1.64)
R-Factor (%)	18.12
R_{free} (%)	21.56
Protein atoms	1910
Water Molecules	205
Cu	6
Unique Reflections	30508
R.m.s.d.	
Bonds (Å)	0.007
Angles (˚)	0.98

References

1. Golombek, A. P.; Hendrich, M. P. *J. Magn. Reson.* 2003, *165*, 33.

2. Clay, M. D.; Jenney, F. E., Jr.; Hagedoorn, P. L.; George, G. N.; Adams, M. W. W.; Johnson, M. K. *J. Am. Chem. Soc.* 2002, *124*, 788.

3. Tennent, D. L.; McMillin, D. R. *J. Am. Chem. Soc.* 1979, *101*, 2307.

4. Winn, M. D.; Ballard, C. C.; Cowtan, K. D.; Dodson, E. J.; Emsley, P.; Evans, P. R.; Keegan, R. M.; Krissinel, E. B.; Leslie, A. G. W.; McCoy, A.; McNicholas, S. J.; Murshudov, G. N.; Pannu, N. S.; Potterton, E. A.; Powell, H. R.; Read, R. J.; Vagin, A.; Wilson, K. S. *Acta Crystallogr., Sect. D Biol. Crystallogr.* 2011, *D67*, 235.

Chapter VI – Nature of the Key Oxidant in Hydrocarbon Oxidations by Bio-Inspired Non-heme Iron Catalysts and H_2O_2/AcO.

Published: Oloo, W.N.; **Meier, K.K.**, Wang, Y.; Shaik, S.; Münck, E., Que Jr., L. "Identification of a low-spin acylperoxoiron(III) intermediate in bio-inspired nonheme iron-catalysed oxidations." *Nature Commun.* 2013, 5, pp 3046-3054

Author Contributions: W.N.O., K.K.M.,E.M., and L.Q. conceived and designed the experiments. W.N.O. and K.K.M. performed the experiments. W.N.O., K.K.M., E.M., L.Q. analyzed the data. K.K.M., Y.W. and S.S. performed DFT calculations. All authors participated in the writing of the paper.

Abstract

Synthetically useful hydrocarbon oxidations that employ bio-inspired nonheme iron catalysts and H_2O_2 have recently been reported, where AcOH has been found to increase both the selectivity and catalytic efficiency. While studying the effect of AcOH, Talsi discovered a low-intensity g = 2.7 EPR signal and assigned it to a putative (OAc)Fe^{V}=O oxidant. We have generated this species at -40°C in 50% yield with Fe^{II}(TPA*) (TPA* = tris(3,5-dimethyl-4-methoxypyridyl-2-methyl)amine) and found by UV-vis, EPR, Mössbauer, and ESIMS methods that it is actually a low-spin acylperoxoiron(III) complex (**4**). Kinetic studies show that **4** decays exponentially in a rate-determining step that unmasks the oxidant responsible for substrate oxidation. DFT calculations show that O–O bond cleavage of **4** generates a highly reactive oxoiron(V)

species that can rapidly oxidize the substrate. This mechanistic scheme serves as the prototype for rationalizing the high selectivity exhibited by these nonheme iron catalysts.

Introduction

Nonheme iron complexes have recently emerged as potentially useful oxidation catalysts for the regio- and/or stereoselective functionalization of C–H and C=C bonds in complex organic molecules with H_2O_2 as the oxidant. These catalysts are inspired by the large and versatile family of oxygen activating enzymes that carry out oxidative transformations involving C–H and C=C bonds in metabolically important molecules.[1-3] The bio-inspired complexes belonging to this class are typically supported by tetradentate N4 ligands (Chart 1) and have an iron center with two *cis*-labile coordination sites at which to activate the H_2O_2 for reactions that exhibit high retention of configuration.[4-6] Their catalytic activity and selectivity are further enhanced by the addition of acetic acid to the reaction mixture, leading to predictable regio- and stereoselectivity in the oxidation of particular aliphatic C–H bonds in complex organic molecules, as demonstrated by White for (+)-artemisinin and (-)-dihydropleuromutilone.[7, 8] Highly enantioselective olefin epoxidation reactions can also be achieved.[9-11]

The selectivity exhibited by these reactions strongly implicates a metal-based species, rather than HO•, as the oxidant generated by the reaction of the iron complex with H_2O_2.[12] In early studies, Que and co-workers observed the generation of a

(TPA)Fe^{III}–OOH intermediate upon reaction of the [(TPA)Fe^{II}] catalyst (**1a**) with excess H_2O_2 at -40 °C in CH_3CN solvent, as well as label incorporation from $H_2{}^{18}O$ into the oxidation products.[13, 14] These results led to postulation of a mechanism that involves heterolytic cleavage of the O–O bond in the Fe^{III}–OOH intermediate that was promoted by bound water to form a Fe^{V}(O)(OH) oxidant (Scheme 1). This hypothesis has received recent support from kinetic studies demonstrating both an accelerative effect of added water and a significant H_2O/D_2O kinetic isotope effect on both the decay rate of the Fe^{III}–OOH intermediate and the rate of product formation.[15] Direct spectroscopic evidence for the putative Fe^{V}(O)(OH) oxidant was obtained by Costas and Cronin from variable temperature electrospray mass spectrometric experiments in studies of their [(PyTACN)$Fe^{II}(OTf)_2$] catalyst.[16]

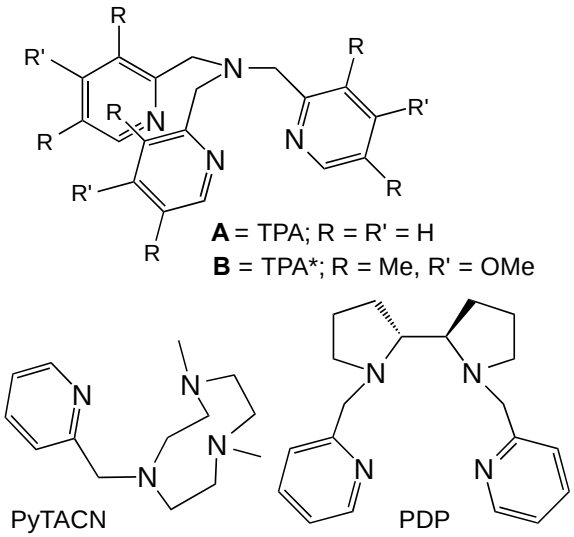

Chart 1. Tetradentate ligands for bioinspired nonheme iron catalysts.

To account for the effect of the acetic acid additive first observed by White,[17] Mas-Balleste and Que modified the proposed water-assisted mechanism into a carboxylic-acid-assisted version that generates an $Fe^{V}(O)(OAc)$ oxidant (Scheme 1).[18] Such an oxidant would be consistent with the observed increase in epoxide selectivity at the expense of *cis*-diol formation in the oxidation of olefins. The involvement of the $Fe^{V}(O)(OAc)$ oxidant was also supported by the formation of a minor *cis*-hydroxyacetoxylated product in olefin oxidation by Fe(TPA) in the presence of acetic acid[19] as well as the observed decay of the Fe^{III}–OOH intermediate in the presence of a carboxylic acid to the corresponding $Fe^{IV}(O)$ species **3** and a carboxyl radical, which was found to occur in competition with the formation of olefin oxidation products when olefin substrate was present.[18]

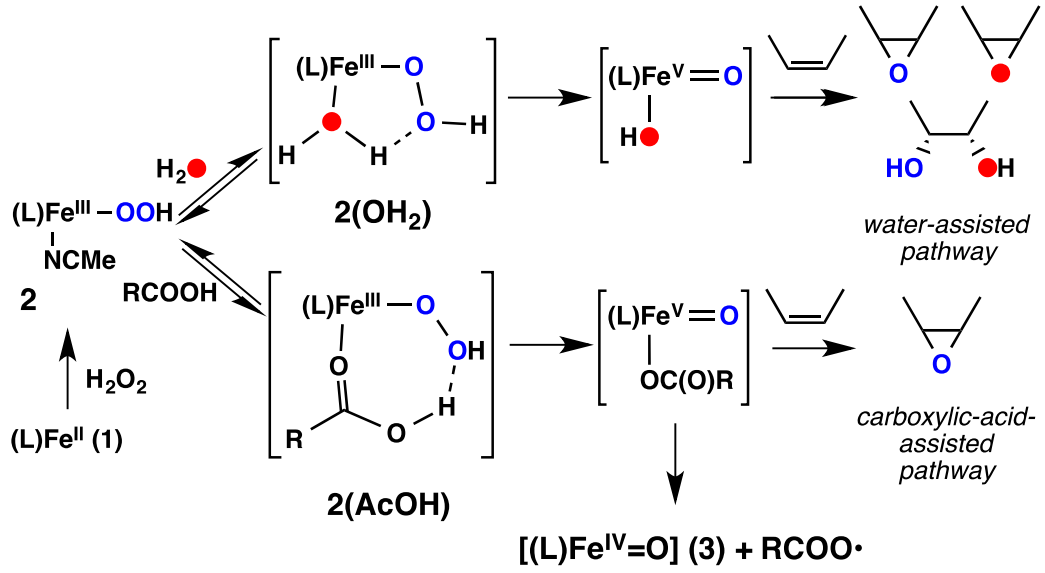

Scheme 1. Proposed mechanisms for nonheme iron oxidation catalysts.

A claim for the putative $Fe^{V}(O)(O_2CR)$ oxidant was reported by Talsi and co-workers,[20, 21] who observed a novel $S = ½$ EPR signal at g = 2.71, 2.42, and 1.53 upon mixing a 40-mM solution of Fe(TPA) **1a** in 1:1.7 CH_3CN/CH_2Cl_2 with either 30% H_2O_2/AcOH, peracetic acid or *m*-CPBA at -60 °C. Similar EPR features have also been observed for related nonheme iron catalysts.[9, 21, 22] The observation that the self-decay rate of $1.6(2) \times 10^{-3}$ s^{-1} at -70 ^{o}C of the $S = ½$ species increased 5-fold upon addition of 12 equiv. cyclohexene with concomitant formation of cyclohexene oxide led Talsi to postulate the g = 2.7 species to be the $Fe^{V}(O)$ oxidant. However, EPR quantification showed that the $g = 2.7$ species was formed only in 7% yield, and no additional spectroscopic characterization to support the claimed Fe^{V} oxidation state assignment was reported. In this paper, we report reaction conditions that increase the yield of the $g = 2.7$ intermediate to 50%, paving the way for its characterization by UV-visible, Mössbauer, and electrospray mass spectrometric methods. Taken together, our data show that the intermediate is in fact a low-spin Fe(III) complex, most probably acylperoxoiron(III), that undergoes rate determining O–O bond cleavage to unmask the oxidant that carries out substrate oxidation.

Results and Discussion

Our attempts to characterize the g = 2.7 species started with the introduction of excess H_2O_2 (70%) to a CH_3CN solution of the Fe(TPA) complex **1a** in the presence of excess AcOH at -40 ^oC. This reaction afforded a species that exhibits an absorbance maximum at 460 nm (Fig. S1), a brown chromophore that is distinct from the purple chromophore obtained in the absence of AcOH and associated with Fe^{III}–OOH intermediate **2a** (λ_{max} 540 nm).[23] The brown intermediate, designated as **4a**, has a lifetime of only 5 minutes at -40 ^oC and decays to the corresponding (TPA)Fe^{IV}(O) species **3a** (λ_{max} = 720 nm) in about 70% yield, while **2a** persists for up to 3 hours under similar conditions,[14, 15] indicating that **4a** is significantly more reactive than the Fe^{III}-OOH complex **2a**. Even more importantly, the EPR features obtained for a frozen CH_3CN solution of **4a** are identical to those reported by Talsi and assigned to an Fe^{V}(O) species (Fig. S2).[20, 21] Simulation of the EPR signals of **4a** using the SpinCount software[24] shows that this species is formed in ~20 % yield, an amount that is higher than that reported by Talsi, but still not high enough for Mössbauer characterization to determine its oxidation state reliably.

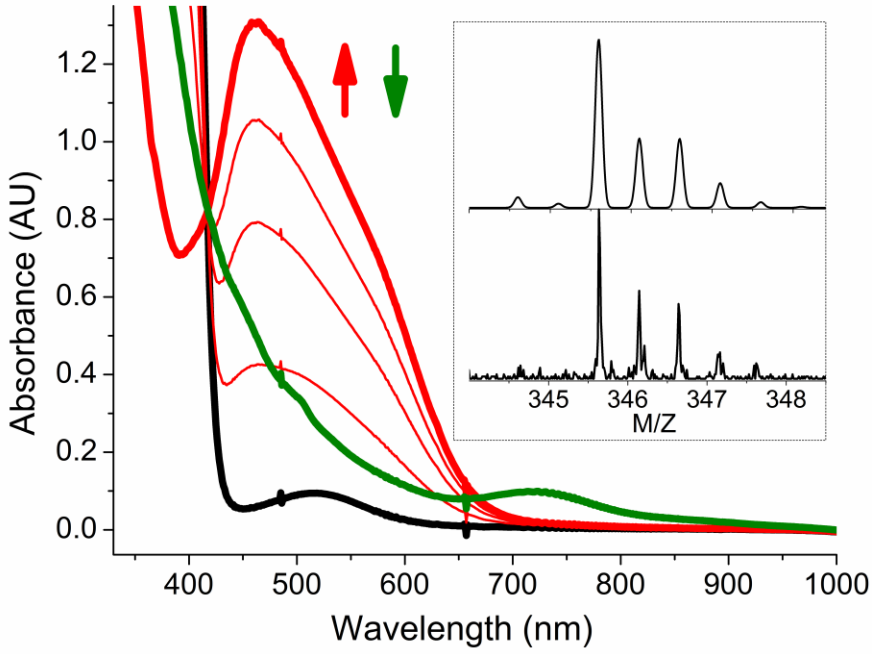

Figure 1. UV−vis evolution of the 460-nm intermediate (red trace) upon addition of 10 equiv. 70% HOOH at -40 ^{o}C to 0.5-mM 1b (black trace) in CH_3CN in the presence of 200 equiv. AcOH. Inset: isotope distribution pattern for the peak at m/z 345.6167 observed by ESI-MS for a mixture of 1b and excess *m*CPBA in CH_3CN at -40 ^{o}C.

To increase the fraction of the g = 2.7 intermediate in our samples required extending the lifetime of the intermediate. This goal was achieved by replacing TPA with its more electron donating variant TPA*, an approach that previously enabled us to generate highly reactive (μ-oxo)diiron complexes.[25, 26] As shown in Figure 1, the addition of 10 equiv. 70% H_2O_2 to a 0.5-mM solution of the Fe^{II}(TPA*) complex **1b** in CH_3CN in the presence of 200 equiv. AcOH at -40 ^{o}C also produces a 460-nm chromophore, designated **4b**, which has at least twice the intensity of that produced from **1a** and is distinct from the purple Fe^{III}–OOH chromophore **2b(OH$_2$)** (λ_{max} 510 nm) generated in the absence of AcOH (Fig. S3). In this case, the 460-nm intermediate persisted in a steady

state phase before undergoing rapid exponential decay (k_{obs} = 0.018 s^{-1}), and gave rise to the Fe^{IV}=O complex **3b** (λ_{max} 720 nm) in ~ 70 % yield.

The 460-nm chromophore was also generated in comparable yield from the reactions of **1b** with peracids in CH_3CN at -40 ^oC (Figure S4). In the case of peracetic acid, **4b** decayed to **3b** as observed for the H_2O_2/AcOH combination. However for *m*-chloroperbenzoic acid (*m*CPBA), the intermediate analogous to **4b** evolved into a different chromophore with a λ_{max} at 560 nm. Insight into the nature of the 460-nm and 560-nm intermediates in the latter experiment was obtained from high resolution electrospray ionization mass spectrometric analysis, which revealed two predominant mass envelopes at m/z = 345.6167 and 690.1944 (Figures 1 and S5). The latter peak arises from $[(TPA^*)Fe^{III}(5\text{-Cl-salicylate})]^+$ (calcd for $C_{34}H_{39}ClFeN_4O_6$ = 690.1908), which is a byproduct resulting from self-hydroxylation of the *m*CPBA ligand, as previously observed in the reaction of **1a** with *m*CPBA.[27] The m/z = 345.6167 peak has a value and isotope distribution pattern corresponding to the $[C_{34}H_{40}ClFeN_4O_6]^{2+}$ ion (calcd. 345.5988). Since this species could be formulated either as $[(TPA^*)Fe^{III}(O_3CC_6H_4Cl)]^{2+}$ or $[(TPA^*)Fe^{V}(O)(O_2CC_6H_4Cl)]^{2+}$, experiments are needed to assign the oxidation state of the iron.

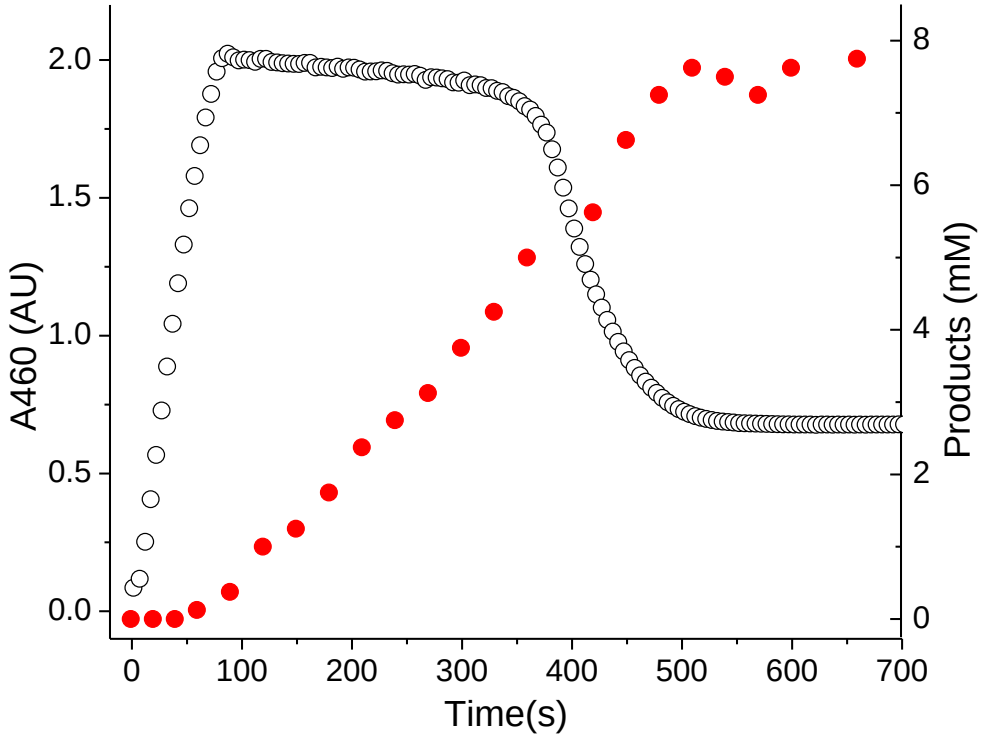

Figure 2. Catalytic oxidation of 1-octene (250 eq) with Fe(TPA*) complex 1b (1.0 mM) and 20 eq 70% H_2O_2 at -40 ^oC, as followed by GC analysis of the reaction aliquots quenched at -40 ^oC (red filled circles). The A460 value corresponding to intermediate 4b (black open circles) was monitored in a parallel experiment.

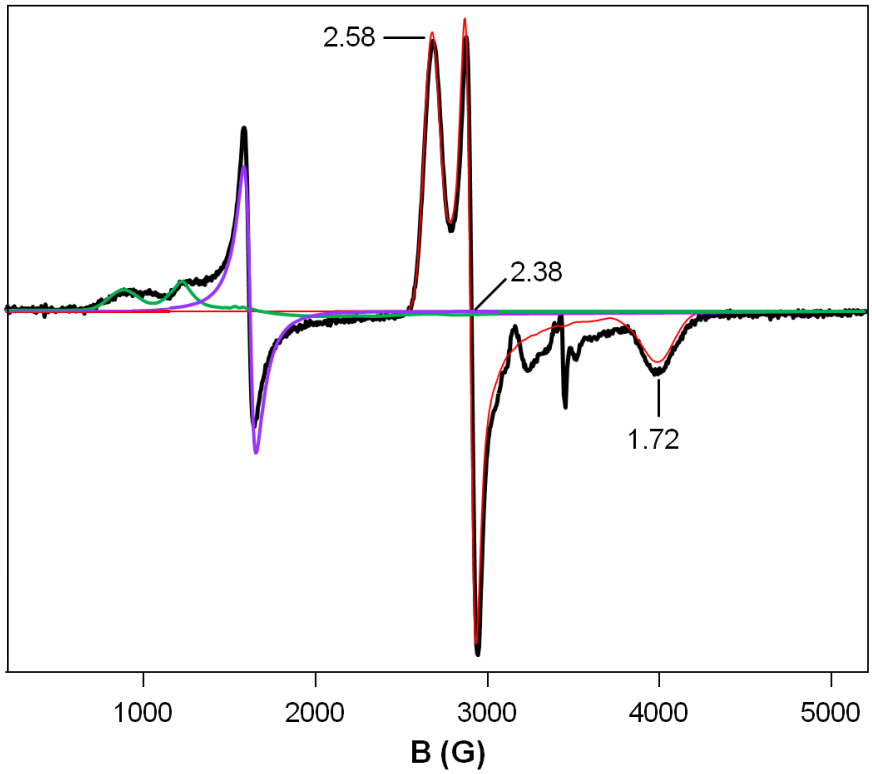

Figure 3. X-band EPR spectrum (black line) of the 460-nm intermediate in MeCN, recorded at T = 10 K. The red line shows an *S* = 1/2 spectral simulation for the 460-nm intermediate using g_x = 1.72, g_y = 2.38 and g_z = 2.58; the line width was modeled by assuming a Gaussian distribution of g-values with σ ($g_{x,y,z}$) = (0.045; 0.02; 0.04). The simulation represents 47 % of the Fe in the sample. The sample contains also two high-spin (S = 5/2) ferric species, which together represent ca. 35% of the total Fe; details can be found in the Supporting Information. Conditions: 9.64 GHz frequency, 20 μW microwave power, 1 mT modulation.

The 460-nm intermediate, **4b**, exhibits an EPR spectrum with g-values at *g* = 2.58, 2.38 and 1.72 that represents 47% of the Fe in the sample, based on a SpinCount simulation[24] indicated by the red line in Figure 3. The fraction of Fe represented by this species is 3-7 times higher than that reported for the g = 2.7 species by Lyakin et al.[20, 21] There are also two additional *S* = 5/2 signals that arise from high-spin (S = 5/2) iron(III): a major component (green curve, ≈ 30% of Fe) that originates from the upper Kramers

doublet of a species with D ≈ -0.8 cm^{-1} and E/D ≈ 0.10 and a minor fraction (purple curve, ~5 % of Fe) with E/D ≈ 1/3 that gives rise to the resonance at g = 4.3. The S = 1/2 EPR signals of the 460-nm intermediates generated from the reaction of **1b** with peracids have g values and intensities comparable to those in Fig. 3 (Fig. S4).[28]

Figure 4 shows Mössbauer spectra of the same sample as used for the EPR spectrum of Figure 3. Additional spectra recorded in variable applied magnetic fields, B, are shown and discussed in Fig. S6. The green line in the 8.0 T spectrum of Figure 4, top panel, is a spectral simulation (normalized to represent 35% of Fe) for the two high-spin Fe^{III} species; we comment in SI why these species are indistinguishable at 8.0 T. Subtracting the simulated spectrum from the raw data yields the spectrum in the middle panel of Figure 4 that, except for a small diamagnetic contaminant (12% of Fe, blue line, see SI), represents the *S* = 1/2 species **4b** observed in a parallel applied field of 8.0 T. At 4.2 K the spin system of the *S* = 1/2 species is in the slow relaxation regime and its spectra exhibit paramagnetic hyperfine structure. At T = 160 K, however, the electronic spin relaxes fast so that the magnetic hyperfine interactions are averaged out, yielding a quadrupole doublet for the *S* = 1/2 species (Figure 4 bottom panel, red line) with splitting ΔE_Q = 2.60 ± 0.05 mm/s and isomer shift δ = +0.17 ± 0.03 mm/s. (After a correction for the second-order Doppler shift, the latter value translates to δ ≈ +0.23 mm/s at 4.2 K.) The value of δ falls squarely into the range of low-spin Fe^{III} complexes[29] and is about 0.2 mm/s higher than that found for the ferryl complex $[Fe^{IV}(O)(TPA)(NCCH_3)]^{2+}$ [30]. For

comparison, the δ value for $[Fe^{V}(O)(TAML)]^{-}$, the bona fide S = 1/2 Fe^{V}=O complex reported by Tiago Oliveira et al. has δ = -0.42 ± 0.03 mm/s[31] (the δ value of the other established Fe^{V}=O complex, $[(TMC)Fe^{V}(O)(NR)]^{+}$, has a more positive δ value, due to the presence of a *trans* O=Fe=NR unit)[32].

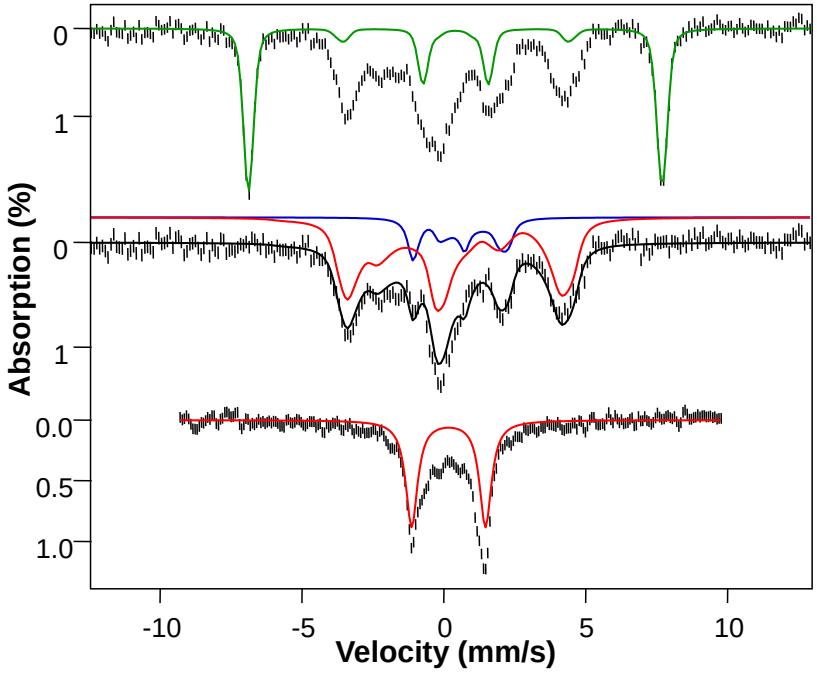

Figure 4. Mössbauer spectra of a sample of **4b** (0.8 mM Fe) in MeCN. **(Top panel)** Spectrum recorded at 4.2 K in a parallel applied field of 8.0 T. The green line is a theoretical curve representing 35% of the Fe belonging to a high-spin Fe^{III} species with D = - 0.8 cm^{-1} and E/D = 0.10 (see SI). **(Middle panel)** 8.0 T spectrum of the 460-nm intermediate **4b** obtained from (top panel) by subtracting the contribution of the high-spin Fe^{III} species. The red curve, representing 50% of Fe, is a simulation for **4b** using eq 1 and the parameters: $g_{x,y,z,}$ = (1.72, 2.38, 2.58), $A_{x,y,z}/g_n\beta_n$ = (-45, +19, +31) T, ΔE_Q = +2.6 mm/s, η = -6, δ = 0.23 mm/s. The blue curve is attributed to a diiron(III) contaminant (≈12% of Fe, see SI). The black line is the sum of the red and blue curves. Additional 4.2 K spectra recorded at 0.1 T, 2.0 T and 5.0 T are shown in SI. **(Bottom panel).** Zero field spectrum recorded at 160 K. The doublet outlined in red is attributed to **4b**. The absorption in the center belongs to the diferric species (blue line in the middle panel) and in part to mononuclear high-spin Fe^{III} undergoing intermediate relaxation. Spectra were simulated using the software WMOSS.

We have analyzed the 4.2 K spectra of **4b** using the S = 1/2 spin Hamiltonian

$$H = \beta \boldsymbol{S} \cdot \boldsymbol{g} \cdot \boldsymbol{B} + \boldsymbol{S} \cdot \boldsymbol{A} \cdot \boldsymbol{I} - g_n \beta_n \boldsymbol{B} \cdot \boldsymbol{I} + H_Q \quad \textbf{(1)}$$

$$H_Q = \frac{eQV_{zz}}{12}\left[3\boldsymbol{I}_z^2 - I(I+1) + \eta\left(\boldsymbol{I}_x^2 - \boldsymbol{I}_y^2\right)\right] \quad (2)$$

where **g** is the electronic g-tensor and $\boldsymbol{A}$ the magnetic hyperfine tensor. $\boldsymbol{H}_{\mathrm{Q}}$ describes the interaction of the nuclear quadrupole moment Q with the electric field gradient (EFG) tensor (principal components $\mathrm{V_{ii}}$); $\eta = \frac{V_{xx}-V_{yy}}{V_{zz}}$ is the asymmetry parameter. For the analysis we have assumed that all tensors share a common principal axis system, defined by the principal g-values of the S = 1/2 species, $\mathrm{g_{x,y,z}}$ = 1.72, 2.38, 2.58. The best match to the intensities is obtained by assuming that **4b** represents 50% of the total Fe, a value in excellent agreement with the EPR quantification (47%). The solid red lines in Figure 4 and Figure S6 are theoretical curves generated from eq 1 for the parameters listed in the caption of Figure 4.

We wish to comment on a few points. The magnetic splittings of the S = 1/2 species are controlled by the internal magnetic field $\boldsymbol{B}_{int} = -\frac{\langle \boldsymbol{S} \rangle \cdot \boldsymbol{A}}{g_n \beta_n}$, where $\langle \boldsymbol{S} \rangle$ is the expectation value of the electronic spin. The anisotropy of **g** imposes a directional preference (the z direction) on $\langle \boldsymbol{S} \rangle$, a fact which allowed us to establish a spatial correlation between the g-, A- and EFG-tensors. The analysis establishes clearly the signs of the three A-tensor components, and these signs are readily rationalized by analyzing the data in the framework of the $(t_{2g})^5$ hole model for low-spin Fe^{III} introduced by Griffith[33] and amended for Mössbauer analysis by Oosterhuis and Lang[34]. Analysis of the

g-values in this model reveals that the ground state of the S = 1/2 species is predominantly a d_{yz} hole (orbital displayed in Figure 5 below). For this state the largest EFG component would be negative and along x, just as observed. (Note: the quoted experimental ΔE_Q = + 2.6 mm/s, η = -6 corresponds to ΔE_Q =-2.6 mm/s, η = 0.43 when the EFG is quoted in the conventional frame of the Mössbauer literature, x', y', z', for which $|V_{z'z'}| \geq |V_{y'y'}| \geq |V_{x'x'}|$). The Fermi contact term (scaling factor κ), the spin dipolar term and the orbital term (which is roughly proportional to g_x - 2) all have a negative contribution to A_x, rationalizing why A_x is negative and large. In contrast, the spin-dipolar and (large) orbital contributions along z are positive, yielding a positive A_z. Using the model of Oosterhuis and Lang[35] implemented in SpinCount[24], we obtained Δ = 1,015 cm^{-1} and V = 1,157 for the tetragonal and rhombic crystal field splittings, respectively (using $\lambda \approx 380$ cm^{-1} for the spin-orbit coupling constant). Using the scaling factors $P = 2g_n\beta_n\langle r^{-3}\rangle = 85\ MHz$ and κ = 0.35 (see eq 10 in ref. [34]), we obtained for the A-tensor components $A_{x,y,z}/g_n\beta_n$ = (-44, +20, +31) T, which in sign and magnitude are in excellent agreement with the experimental data ($A_{x,y,z}/g_n\beta_n$ = (-45, +19, +31) T).

In order to gain further insight into the structure of the acylperoxo complex **4b** we have performed a DFT study and obtained the geometry optimized structure (Table S1) shown in Figure 5. This structure, for which the peroxo group is *trans* to the tertiary amine, yields a calculated ΔE_Q = -2.48 mm/s, η = 0.20, and δ = 0.20 mm/s, in excellent agreement with the experimental ΔE_Q = -2.6 mm/s, η = 0.43 (quoted in the conventional

frame of the EFG tensor), and $\delta = 0.23$ mm/s. Recall that we found that the largest (and negative) component of the EFG is V_{xx}. The calculated EFG allows us to correlate the axes of the spin Hamiltonian of eqs 1 and 2 to the calculated structure. Thus, V_{xx}, and consequently $g_x = 1.72$, are along the acyl oxygen-Fe-N_{pyr} axis. The orientation of the y and z axes are probably correct as indicated in Figure 5, but a more reliable assignment of these two axes in the calculated structure would require a DFT program that incorporates spin-orbit coupling for calculations of the g-values.

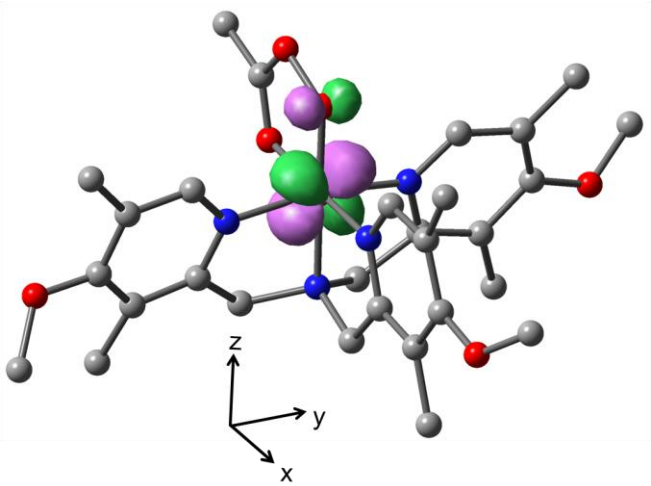

Figure 5. DFT geometry optimization of the proposed structure of low-spin Fe(III) complex 4b, using the Gaussian 09 software and 6-311G/B3LYP. Hydrogen atoms have been omitted for clarity. Element colors are: red = oxygen, blue = nitrogen, gray = carbon, pink = iron. Shown in magenta/green is the LUMO $d_{yz}(\beta)$ molecular orbital (representing the hole in the Griffith model). The indicated coordinate axes are the same as those of Table S1; however, x and y were interchanged so that V_{xx} of eqs 1 and 2 correspond to V_{xx} of the calculated EFG, correlating the DFT structure with the spin Hamiltonian.

Given that our Mössbauer analysis shows that the *S* = 1/2 iron center for the 460-nm intermediate does not have an iron(V) oxidation state but is instead low-spin iron(III),

we therefore formulate **4b** as the low-spin (κ^2-acylperoxo)iron(III) species shown in Figure 5. The progressive blue shift of the λ_{max} observed for the Fe^{III}(TPA)(OOR) series (R = ^{t}Bu (600 nm)[35], H (540 nm)[23], and CH_3CO (460 nm) reflects the decreasing basicity of the peroxo ligand (pKa = 8.2 for peracetic acid vs 11.8 for H_2O_2 and 12.3 for ^{t}BuOOH)[36]. Based on EPR and Mössbauer quantifications of the spectra shown in Figures 3 and 4, the molar extinction coefficient of **4b** is deduced to be ≈ 4000 $M^{-1}cm^{-1}$, a value that is about two- to four-fold larger than those associated with related low-spin Fe^{III}-peroxo complexes such as $[Fe(TPA)(OOH)(NCMe)]^{2+}$ (ε_M 2200 $M^{-1}cm^{-1}$), $[Fe(TPA)(OO^tBu)(NCMe)]^{2+}$ (ε_M 2200 $M^{-1}cm^{-1}$), $[Fe(N4Py)(OOH)]^{2+}$ (ε_M 1300 $M^{-1}cm^{-1}$), and $[Fe(Me\text{-}TPEN)(OOH)]^{2+}$ (ε_M 1000 $M^{-1}cm^{-1}$) (N4Py = bis(2-pyridylmethyl)bis(2-pyridyl)methylamine, Me-TPEN = N-methyl-N,N',N'-tris(2-pyridylmethyl)-1,2-diaminoethane).[1] Precedents for (κ^2-acylperoxo)iron(III) complexes have been reported by Furutachi and Suzuki, who provided crystallographic evidence for the formation of iron(III)-κ^2-peroxocarbonate and iron(III)-κ^2-peracetate complexes[37-39]. Like **4b**, these complexes exhibit intense UV-Vis bands near 400 nm (λ_{max} 440 nm (ε 1450 $M^{-1}cm^{-1}$) for the peroxocarbonate complex and ($\lambda_{shoulder}$ 367 nm (ε 2260 $M^{-1}cm^{-1}$) for the peracetate complex). However, these complexes have high-spin iron(III) centers, which may account for their greater stability and their lower molar extinction coefficients.

Our ability to generate **4b** in high yield presents a unique opportunity to study its involvement in **1b**-catalyzed oxidation**.** Like **1a**, **1b** is an efficient catalyst at 25 °C in the

oxidation of alkanes and olefins using H_2O_2 both in the presence and absence of AcOH (Table S2). In the oxidation of cyclohexane, the alcohol product is obtained nearly exclusively, while hydroxylation of the tertiary C–H bonds of *cis*-1,2-dimethylcyclohexane occurs with >99% retention of configuration. Oxidations of olefins also result in the formation of epoxide and *cis*-diol with nearly complete retention of configuration, and the use of acetic acid changes the selectivity of the catalyst from favoring *cis*-diol to favoring epoxide formation. These results exclude the involvement of hydroxyl radicals and strongly argue for a metal-based oxidant.

The acylperoxoiron(III) intermediate **4b** can be generated at -40 ^{o}C even in the presence of 250 equiv. 1-octene (Figure 2). Its characteristic band at 460 nm formed rapidly, persisted in a steady state for ~300 s, and, after exhaustion of H_2O_2, underwent exponential decay with a first order rate constant of 0.018(3) s^{-1}. In a parallel experiment, GC product analysis was carried out on aliquots of the reaction mixture quenched at -40 °C, and the formation of 1,2-epoxyoctane was monitored as a function of time. Notably, formation of epoxide occurred only after the 460-nm species was generated and ceased upon complete decay of **4b**. The product was formed linearly versus time at a rate of 0.017(3) mM/s, which upon division by the catalyst concentration gives a rate constant of 0.017(3) s^{-1} for product formation, in excellent agreement with the rate constant for **4b** decay. Furthermore, the rate of **4b** decay was found to be independent of the amount of substrate present (0 – 1000 equiv) as well as the nature of the substrate (1-octene or *t*-

butyl acrylate) (Table S3), implicating **4b** decay as the rate-determining step in the olefin oxidation reaction. For comparison, corresponding rate constants for the decay of the **2a(OH$_2$)** intermediate and the formation of olefin oxidation products in the parallel **1a**-catalyzed olefin oxidation in the absence of acetic acid at -40 °C were found to be an order of magnitude smaller (~0.002 s^{-1})[15], demonstrating that the added carboxylic acid accelerates the rate of substrate oxidation.

To gain insight into how the rate-determining step in the presence of acetic acid differs from that in the absence of acetic acid, additional kinetic data were obtained. The decay of the closely related **2a(OH$_2$)** intermediate in the corresponding **1a**-catalyzed oxidation of olefin in the absence of acetic acid was found to be accelerated with increasing water concentration and to exhibit a kinetic isotope effect (KIE) value of 2.5 when H_2O is substituted with D_2O.[15] These observations support the proposed water-assisted mechanism where rate determining heterolytic O–O bond cleavage is facilitated by the adjacent water ligand (Scheme 1). In contrast for the catalytic oxidation in the presence of acetic acid, the decay rate of the 460-nm intermediate **4b** was not affected by AcOH concentration, nor was a KIE observed when AcOH was replaced by AcOD (Table S3). Analysis of the temperature dependence of **4b** decay (Fig. S7) gave Eyring activation parameters of $\Delta H^{\ddagger}$ = 16.0(5) kcal/mol and $\Delta S^{\ddagger}$ = 3(5) cal/K•mol, which are quite distinct from those for the decay of **2a(OH$_2$)**. While **4b** decay has an activation enthalpy 5 kcal/mol higher than that for **2a(OH$_2$)** decay, it exhibits a much smaller

activation entropy when compared to a value of -23(5) cal K^{-1}-mol^{-1} for **2a(OH_2)** decay. These values correspond to a free energy of activation of 15.5 kcal mol^{-1} at 233 K for **4b** decay, which is 0.7 kcal mol^{-1} smaller than that for **2a(OH_2)** decay, accounting for the 10-fold faster decay rate of **4b**. The rate of **4b** decay extrapolated from the Eyring plot to -70 ^{o}C of 0.00067 s^{-1} is in reasonable agreement to the rate of 0.0017 s^{-1} obtained by Talsi for the decay of the EPR signal of **4a**; the latter would be expected to be somewhat faster due to the lower basicity of TPA. However, unlike Talsi, we do not observe an accelerative effect of the addition of substrate on **4b** decay (Table S3).

DFT calculations on the Fe^{II}(TPA)/H_2O_2/AcOH reaction support the notion of acylperoxoiron(III) species **4b** as a relatively stable intermediate and shed light on the nature of the high-valent species formed upon rate determining O–O bond cleavage. The results from these calculations are in general agreement with those previously reported for the Fe^{II}(PDP)/H_2O_2/AcOH system, but there are some differences (for details see SI). Figure 6a shows the free energy profiles for the high-valent species that may be involved in cyclooctene epoxidation. The acylperoxoiron(III) species **4** has a doublet ground state and is hereafter designated as ^{2}**4**. Our calculations show that direct reaction of ^{2}**4** with cyclooctene has a barrier of roughly 20 kcal/mol, making it unlikely that it is the actual oxidant. Instead, ^{2}**4** undergoes O–O bond cleavage to afford either [(TPA)Fe^{IV}(O)(•OC(O)CH_3)] (**5**) or [(TPA)Fe^{V}(O)(OC(O)CH_3)] (**5'**), which lie at higher energy by 9.1 and 11.5 kcal/mol and have doublet and quartet spin states, respectively;

hence they are designated as ^{2}**5** and ^{4}**5'**, respectively. Although ^{2}**5** is slightly more stable than ^{4}**5'**, the former can also be excluded as the oxidant because it encounters a substantial barrier for cyclooctene epoxidation and readily reverts to ^{2}**4** without a barrier. In contrast, the perferryl species ^{4}**5'** epoxidizes cyclooctene without any barrier, thus making it a very powerful oxidant. The free energy barrier for the formation of ^{4}**5** from ^{2}**4** should consist of the barrier (~9 kcal/mol) for O–O bond cleavage from ^{2}**4** to ^{2}**5** and the energy associated with the spin crossover from ^{2}**5** -> ^{4}**5'**, which can be estimated from the spin crossover energy diagram shown in Figure 6 (box), along with the vertical energy gaps between the species. Assuming that the spin crossover probability is unity, then the incremental barrier for this step would simply be the height of the crossing point (CP) for the ^{2}**5'** -> ^{4}**5** crossover, which depends on the nature of the two curves. If we assume the two curves behave like parabola as in Marcus electron transfer theory, then the height of the crossing point will be about 4 kcal/mol relative to ^{2}**5'**, thus making 13 kcal/mol the total free energy barrier for epoxidation. This calculated value is in reasonably good agreement with the experimental value of 16 kcal/mol.

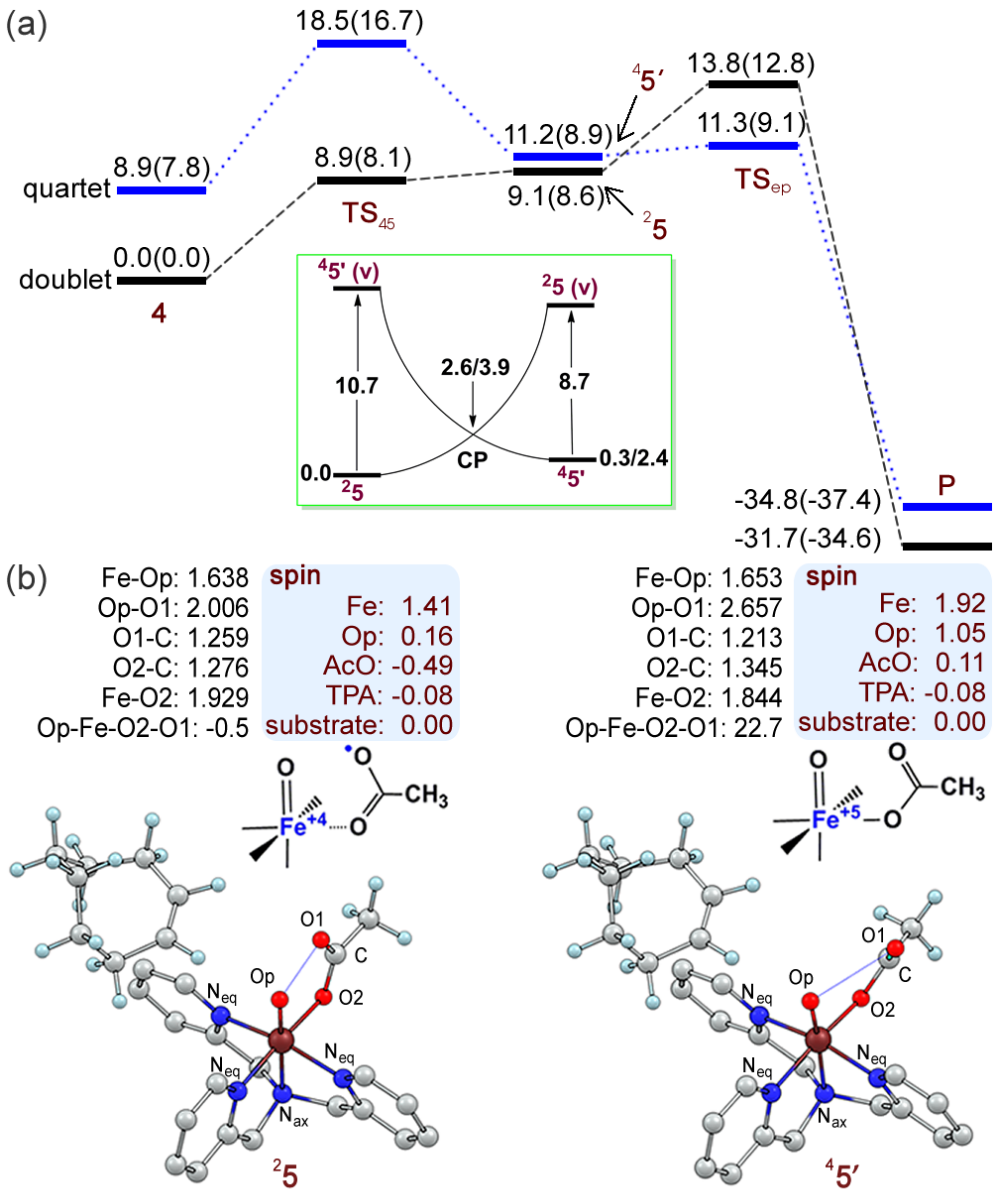

Figure 6. DFT calculated results for the Fe(TPA)/H_2O_2/HOAc system. (a) Energy profiles (in kcal mol^{-1}) for cyclooctene epoxidation with energies calculated at the B3LYP/def2-TZVPP//B3LYP*/TZVP(Fe,N,O)-6-31G**(H,C) level. (b) Geometric and electronic information of ^{2}5 and ^{4}5', Bond lengths are in Å. Hydrogen atoms on the TPA skeleton are omitted for clarity. Box: schematic plot of the crossing point (CP) between ^{2}5', ^{4}5 and their vertical transition species ^{2}5(v) and ^{4}5'(v).

Conclusions

In this report, we have demonstrated the trapping of an intermediate in the Fe^{II}(TPA*)/H_2O_2/AcOH system and characterized it by EPR, Mössbauer, and ESIMS methods to be a low-spin acylperoxoiron(III) species (**4b**), and not an oxoiron(V) complex as proposed by Talsi.[20] Intermediate **4b** forms at -40 °C and persists in a steady state phase, during which catalytic epoxidation is observed (Figure 2). Upon depletion of H_2O_2, **4b** decays exponentially at a rate that is unaffected by the nature and the concentration of substrate, strongly implicating **4b** decay as the rate determining step for the epoxidation. Computational results show that ^{2}**4** undergoes O–O bond homolysis to form the computational species ^{2}**5**, a unimolecular decomposition pathway corroborated by the near zero activation entropy and the absence of an AcOH/AcOD KIE experimentally associated with **4b** decay. However as our DFT results further show, ^{2}**5** cannot readily epoxidize olefins and easily reverts to ^{2}**4**; therefore ^{2}**5** must isomerize to ^{4}**5'** to move forward along the reaction coordinate towards substrate oxidation. Here again emerges a two-state reactivity that has been found for other iron oxidation systems.[40] We suggest that these mechanistic notions apply to other nonheme iron catalysts. Postulating ^{4}**5'** as the oxidant is fully consistent with the reactivity associated with the Fe(*S,S*-PDP)/H_2O_2/RCO_2H combination, particularly with Talsi's observation that the enantioselectivity of epoxidation can be tuned by the R group on the carboxylic acid additive[9] and White's beautiful results in the regio- and stereoselective

transformations of C–H bonds in complex natural products.[7, 8] Lastly, the O–O bond activation by a nonheme iron center postulated here proceeds via the formation of an Fe^{IV}=O/ligand radical species, not unlike those associated with cytochrome P450 and related heme systems[41], thereby emphasizing a mechanistic commonality among iron oxidation catalysts in biology.

Acknowledgements

This work was supported by the US Department of Energy (grant DE-FG02-03ER15455 to L.Q.), the US National Science Foundation (grants CHE-1012485 and CHE-1305111 to E.M.), the National Science Foundation of China (grant no. 21003116 and 21173211 to Y.W.), and the Israel Science Foundation (S.S.). K.K.M. wishes to thank Dr. E.L. Bominaar for providing valuable insight into the DFT calculations of the ferric acylperoxo complexes.

References

1. Costas, M., Mehn, M.P., Jensen, M.P. & Que, L. Dioxygen activation at mononuclear nonheme iron active sites: Enzymes, models, and intermediates. *Chem. Rev.* **104**, 939-986 (2004).

2. Abu-Omar, M.M., Loaiza, A. & Hontzeas, N. Reaction mechanisms of mononuclear non-heme iron oxygenases. *Chem. Rev.* **105**, 2227-2252 (2005).

3. Tinberg, C.E. & Lippard, S.J. Dioxygen Activation in Soluble Methane Monooxygenase. *Acc. Chem. Res.* **44**, 280-288 (2011).

4. Que, L. & Tolman, W.B. Biologically inspired oxidation catalysis. *Nature* **455**, 333-340 (2008).

5. Sun, C.L., Li, B.J. & Shi, Z.J. Direct C-H Transformation via Iron Catalysis. *Chem. Rev.* **111**, 1293-1314 (2011).

6. White, M.C. Adding Aliphatic C-H Bond Oxidations to Synthesis. *Science* **335**, 807-809 (2012).

7. Chen, M.S. & White, M.C. Combined Effects on Selectivity in Fe-Catalyzed Methylene Oxidation. *Science* **327**, 566-571 (2010).

8. Chen, M.S. & White, M.C. A predictably selective aliphatic C-H oxidation reaction for complex molecule synthesis. *Science* **318**, 783-787 (2007).

9. Lyakin, O.Y., Ottenbacher, R.V., Bryliakov, K.P. & Talsi, E.P. Asymmetric Epoxidations with H2O2 on Fe and Mn Aminopyridine Catalysts: Probing the Nature of Active Species by Combined Electron Paramagnetic Resonance and Enantioselectivity Study. *ACS Catal.* **2**, 1196-1202 (2012).

10. Wang, B., Wang, S., Xia, C. & Sun, W. Cover Picture: Highly Enantioselective Epoxidation of Multisubstituted Enones Catalyzed by Non-Heme Iron Catalysts (Chem. Eur. J. 24/2012). *Chem. Eur. J.* **18**, 7313 (2012).

11. Wu, M. et al. Chiral Bioinspired Non-Heme Iron Complexes for Enantioselective Epoxidation of a,ss-Unsaturated Ketones. *Adv. Synth. Catal.* **353**, 3014-3022 (2011).

12. Costas, M., Chen, K. & Que, L. Biomimetic nonheme iron catalysts for alkane hydroxylation. *Coord. Chem. Rev.* **200**, 517-544 (2000).

13. Chen, K. & Que, L. Stereospecific alkane hydroxylation by non-heme iron catalysts: Mechanistic evidence for an Fe-V = O active species. *J. Am. Chem. Soc.* **123**, 6327-6337 (2001).

14. Chen, K., Costas, M., Kim, J.H., Tipton, A.K. & Que, L. Olefin cis-dihydroxylation versus epoxidation by non-heme iron catalysts: Two faces of an FeIII-OOH coin. *J. Am. Chem. Soc.* **124**, 3026-3035 (2002).

15. Oloo, W.N., Fielding, A.J. & Que, L. Rate-Determining Water-Assisted O-O Bond Cleavage of an FeIII-OOH Intermediate in a Bio-inspired Nonheme Iron-Catalyzed Oxidation. *J. Am. Chem. Soc.* **135**, 6438-6441 (2013).

16. Prat, I. et al. Observation of Fe(v)=O using variable-temperature mass spectrometry and its enzyme-like C-H and C=C oxidation reactions. *Nat. Chem.* **3**, 788-793 (2011).

17. White, M.C., Doyle, A.G. & Jacobsen, E.N. A synthetically useful, self-assembling MMO mimic system for catalytic alkene epoxidation with aqueous H2O2. *J. Am. Chem. Soc.* **123**, 7194-7195 (2001).

18. Mas-Balleste, R. & Que, L. Iron-catalyzed olefin epoxidation in the presence of acetic acid: Insights into the nature of the metal-based oxidant. *J. Am. Chem. Soc.* **129**, 15964-15972 (2007).

19. Mas-Balleste, R., Fujita, M. & Que, L. High-valent iron-mediated cis-hydroxyacetoxylation of olefins. *Dalton Trans.* 1828-1830 (2008).

20. Lyakin, O.Y., Bryliakov, K.P., Britovsek, G.J.P. & Talsi, E.P. EPR Spectroscopic Trapping of the Active Species of Nonheme Iron-Catalyzed Oxidation. *J. Am. Chem. Soc.* **131**, 10798-+ (2009).

21. Lyakin, O.Y., Bryliakov, K.P. & Talsi, E.P. EPR, H-1 and H-2 NMR, and Reactivity Studies of the Iron-Oxygen Intermediates in Bioinspired Catalyst Systems. *Inorg. Chem.* **50**, 5526-5538 (2011).

22. Talsi, E.P. & Bryliakov, K.P. Chemo- and stereoselective C-H oxidations and epoxidations/cis-dihydroxylations with H2O2, catalyzed by non-heme iron and manganese complexes. *Coord. Chem. Rev.* **256**, 1418-1434 (2012).

23. Mairata i Payeras, A., Ho, R.Y.N., Fujita, M. & Que, L. The reaction of Fe-II(tpa) with H2O2 in acetonitrile and acetone-distinct intermediates and yet similar catalysis. *Chem. Eur. J.* **10**, 4944-4953 (2004).

24. Golombek, A.P. & Hendrich, M.P. Quantitative analysis of dinuclear manganese(II) EPR spectra. *J. Magn. Reson.* **165**, 33-48 (2003).

25. Xue, G.Q., Fiedler, A.T., Martinho, M., Münck, E. & Que, L. Insights into the P-to-Q conversion in the catalytic cycle of methane monooxygenase from a synthetic model system. *Proc. Natl. Acad. Sci. USA.* **105**, 20615-20620 (2008).

26. Xue, G.Q., De Hont, R., Münck, E. & Que, L. Million-fold activation of the Fe-2(mu-O)(2) diamond core for C-H bond cleavage. *Nature Chemistry* **2**, 400-405 (2010).

27. Oh, N.Y. et al. Self-hydroxylation of perbenzoic acids at a nonheme iron(II) center. *Chem. Commun.*, 5644-5646 (2005).

28. Richens and co-workers also reported similar EPR signals in the reaction of **1a** with *m*CPBA, but they represented only ~10% of the Fe in the sample. Guisado-Barrios, G., Zhang, Y.T., Harkins, A.M. & Richens, D.T. Low temperature reaction of Fe(TPA)(CH3CN)(2) (2+) with excess 3-chloroperoxybenzoic acid in semi-frozen acetonitrile; EPR detection of an acylperoxo iron(III) adduct. *Inorg. Chem. Commun.* **20**, 81-85 (2012).

29. Roelfes, G. et al. End-on and side-on peroxo derivatives of non-heme iron complexes with pentadentate ligands: Models for putative intermediates in biological iron/dioxygen chemistry. *Inorg. Chem.* **42**, 2639-2653 (2003).

30. Lim, M.H. et al. An Fe-IV = O complex of a tetradentate tripodal nonheme ligand. *Proc. Natl. Acad. Sci. USA.* **100**, 3665-3670 (2003).

31. de Oliveira, F.T. et al. Chemical and spectroscopic evidence for an Fe-V-Oxo complex. *Science* **315**, 835-838 (2007).

32. Van Heuvelen, K.M. et al. One-electron oxidation of an oxoiron(IV) complex to form an O=Fe-V=NR (+) center. *Proc. Natl. Acad. Sci. USA.* **109**, 11933-11938 (2012).

33. Griffith, J.S. Theory of electron resonance in ferrihemoglobin azide. *Nature (London, U. K.)* **180**, 30-1 (1957).

34. Oosterhuis, W.T. & Lang, G. Moessbauer effect in potassium hexacyanoferrate(III). *Phys. Rev.* **178**, 439-56 (1969).

35. Zang, Y. et al. Models for nonheme iron intermediates: Structural basis for tuning the spin states of Fe(TPA) complexes. *J. Am. Chem. Soc.* **119**, 4197-4205 (1997).

36. Strukul, G. (ed.) Catalytic Oxidations with Hydrogen Peroxide as Oxidant (Kluwer Academic Publishers, Dordrecht, the Netherlands, 1992).

37. Furutachi, H. et al. Reversible O-O bond cleavage and formation of a peroxo moiety of a peroxocarbonate ligand mediated by an iron(III) complex.*J. Am. Chem. Soc.* **127**, 4550-4551 (2005).

38. Hashimoto, K. et al. A new mononuclear iron(III) complex containing a peroxocarbonate ligand.
39. *Angew. Chem. Intl. Ed.* **41**, 1202-+ (2002).

40. Zhang, X. et al. A Mononuclear Peracetatoiron(III) Complex: Structural and Spectroscopic Characterization, and Oxidation Reactivity. *Chem. Lett.* **40**, 515-517 (2011).

41. Shaik, S., Hirao, H. & Kumar, D. Reactivity of high-valent iron-oxo species in enzymes and synthetic reagents: A tale of many states. *Acc. Chem. Res.* **40**, 532-542 (2007).

42. Denisov, I.G., Makris, T.M., Sligar, S.G. & Schlichting, I. Structure and chemistry of cytochrome P450. *Chem. Rev.* **105**, 2253-2277 (2005).

Supporting Information

Materials. All reagents were purchased from Aldrich and used as received unless otherwise indicated. Preparation and handling of air-sensitive materials were carried out under an inert atmosphere by using either standard Schlenk and vacuum line techniques or a glove box. The organic substrates were purified either by passing through silical gel or by vacuum distillation before use. The Fe^{II}(TPA) complex[1] was prepared according to published literature procedures.

Preparation of Fe^{II}(TPA):* The Fe^{II}(TPA*) complex was prepared by a procedure similar to that for Fe^{II}(TPA), where an equimolar mixture of $Fe^{II}(CH_3CN)_2(OTf)_2$ (OTf = trifluoromethanesulfonate) and TPA* ligand in THF were stirred for 3 hours (TPA* = tris(3,5-dimethyl-4-methoxypyridylmethyl)amine). Slow vapor diffusion of diethyl ether into the reaction mixture afforded white crystals of the target product in analytically pure form. This complex was characterized via ^{1}H NMR and ESI-MS, while its purity was established via elemental analysis perfomed by Atlantic Microlab (Norcross, GA).

Anal. Calcd (Found) for $C_{31}H_{41}F_6FeN_4O_{9.5}S_2$ 0.5 diethyl ether; C, 43.57(43.51); H, 4.64(4.83); N, 6.67(6.55)

^{1}H NMR (CD_3CN, 22^{o}C), δ: 2.10 (br, 3H), 2.19 (br, 3H), 3.76 (br, 3H), 5.75 (br, 2H), 10.01 (br, 1H).

ESI-MS of solution of Fe(TPA*) in CH_3CN, positive mode, m/z = 669.1611, Calculated for $C_{28}H_{36}F_3FeN_4O_6S$, 669.1651.

Physical Methods. UV-visible spectra were recorded on a Hewlett–Packard 8453A diode array spectrometer with samples maintained at low temperature by using a cryostat from Unisoku Scientific Instruments, Osaka. Electrospray mass spectrometry was performed on a Finnigan-MAT (San Jose, CA) LCQ ion trap instrument. The spectra of the reactive species were obtained by direct introduction of the solution of the intermediate generated at either -78^{o}C into the injector port of the spectrometer. The capillary heater on the instrument was turned off and the flow of the atomizing gas was increased to minimize thermal decomposition of the unstable intermediate. Product analyses were performed on a Perkin-Elmer Sigma 3 gas chromatograph (AT-1701 column, 30 m) with a flame ionization detector.

EPR and Mössbauer Methods. EPR spectra were measured using a Bruker Elexsys E-500 spectrometer equipped with a Bruker dual mode cavity and Oxford ESR 910 liquid helium cryostat. The software package SpinCount (M.P. Hendrich, Carnegie Mellon University) was used to analyze the spectra. Mössbauer spectroscopy was performed as described in reference S3, except that we used a Cernox temperature sensor from Lakeshore Cryotronix. Spectra were analyzed using the WMOSS (SEE Co, Edina, MN, USA) software package.

Reactivity Studies. Reactivity studies for the reactive intermediates were conducted under nitrogen atmosphere and were monitored via UV-visible spectroscopy at -40 ^{o}C. In a typical experiment, a 1.0 mM solution of the (L)Fe^{II} complex in CH_3CN (with or without AcOH) was treated with the oxidant. Upon maximum formation of the intermediate, a CH_3CN solution of the organic substrate was added and the UV visible chromophore of interest was monitored. In other sets of experiments, the oxidant was added to a CH_3CN of the (L)Fe^{II} complex in the presence of the substrate at -40^{o}C.

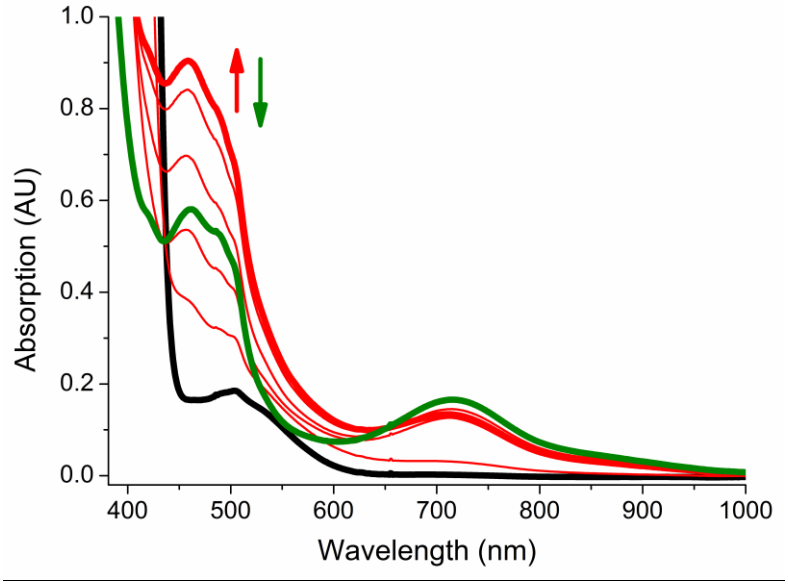

Figure S1. Addition of 10 equiv. H_2O_2 (70%) to 1.0 mM 1a in CH_3CN (black trace) and 200 equiv. AcOH at -40^{o}C resulting in the evolution of a new chromophore at 460 nm (4a, red trace) and its subsequent decay to form the Fe^{IV}(O) complex 3a with λ_{max} at 720 nm (green trace). Inset: X-band EPR spectrum recorded at T = 10 K (black line) of a solution frozen when the 460-nm intermediate was formed maximally. The red line is an *S* = 1/2 spectral simulation using g_x = 1.56, g_y = 2.42 and g_z = 2.75, representing 22 % of the Fe in the sample.

Catalytic Oxidations. In a typical reaction carried out at 25 °C, 2 mL of a CH_3CN solution of 1.0 mM **1b** and 1.0 M of the organic substrate was prepared under aerobic conditions. The reaction was initiated by the addition of 10 eq. H_2O_2 via syringe pump over a period of 30 minutes. In reactions conducted in the presence of AcOH, the additive was added prior to the addition of H_2O_2. At the end of the reaction, the reaction mixture was stirred for an additional 30 minutes after which it was worked up analyzed by gas chromatography according to published procedures.[14]

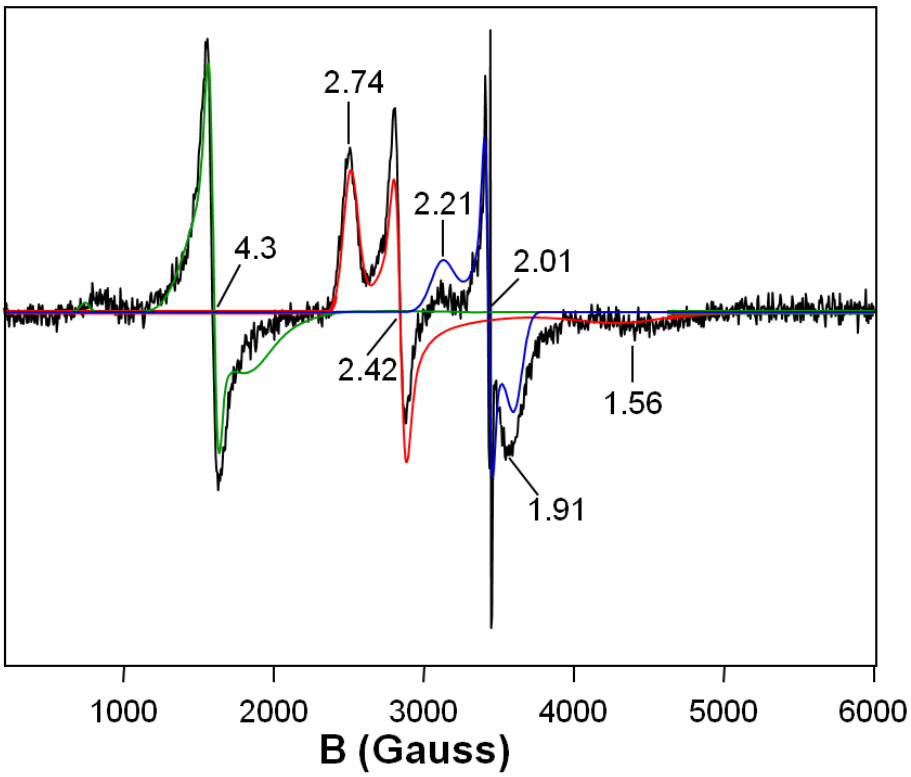

Figure S2. (X-band EPR spectrum (black line) of the 460-nm intermediate **4a** prepared by adding 10 equiv. H_2O_2 (70%) to a 1.0 mM CH_3CN solution of **1a** and 200 equiv. AcOH at -40°C. in MeCN recorded at T = 20 K. The red line is an *S* = 1/2 spectral simulation for the 460-nm intermediate using g_x = 1.56, g_y = 2.42 and g_z = 2.75 representing 21.5% of the Fe in the sample. The line width was modeled assuming a Gaussian distribution of g-values with σ ($g_{x,y,z}$) = (0.096; 0.026; 0.052). The sample also contains two additional species. The first is a high-spin (S = 5/2) ferric species (green curve), which represents ca. 16% of the total Fe. The second is a low-spin ferric peroxo species (blue curve; S=1/2) which has g-values g_x = 1.91, g_y = 2.02 and g_z = 2.21 with corresponding distribution of g-values σ ($g_{x,y,z}$) = (0.058; 0.010; 0.026), D = -0.50 cm^{-1}, E/D = 0.23, σE/D = 0.06 and accounts for ~7% of total iron in the sample. The black curve is the experimental spectrum, which was recorded at 9.645 GHz frequency, 200 μW microwave power, and 1 mT modulation.

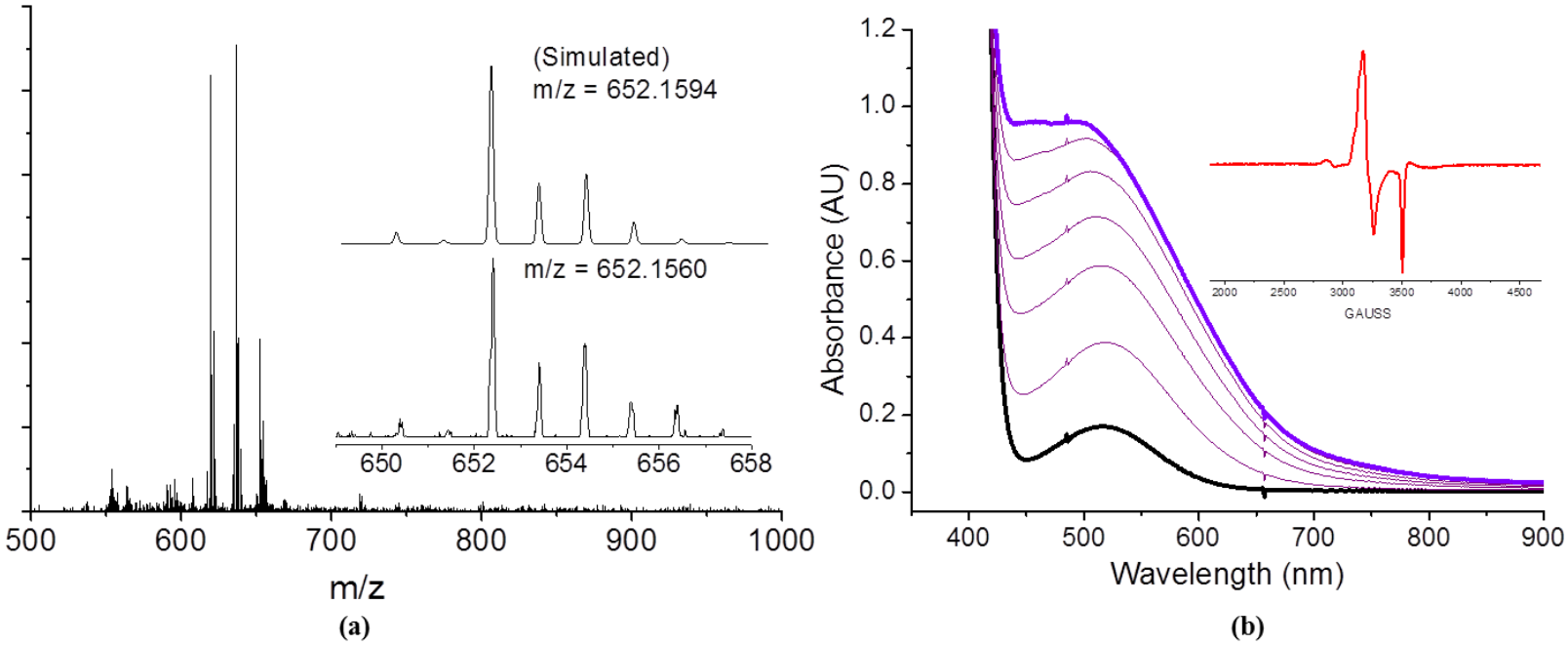

Figure S3. (a) ESI-MS spectrum of a CH_3CN solution of 2b at -40 ^oC showing its signature signal at m/z = 652.1560 (Calcd = 652.1594).**(b)** UV−vis spectral evolution of the reaction between 1b and H_2O_2 (10 equiv.) in CH_3CN at -40^oC showing the formation of (TPA*)Fe^{III}-OOH species 2b at λ_{max} = 510nm. (Inset) X-band EPR spectrum of a 1mM frozen solution of 2b at 10K.

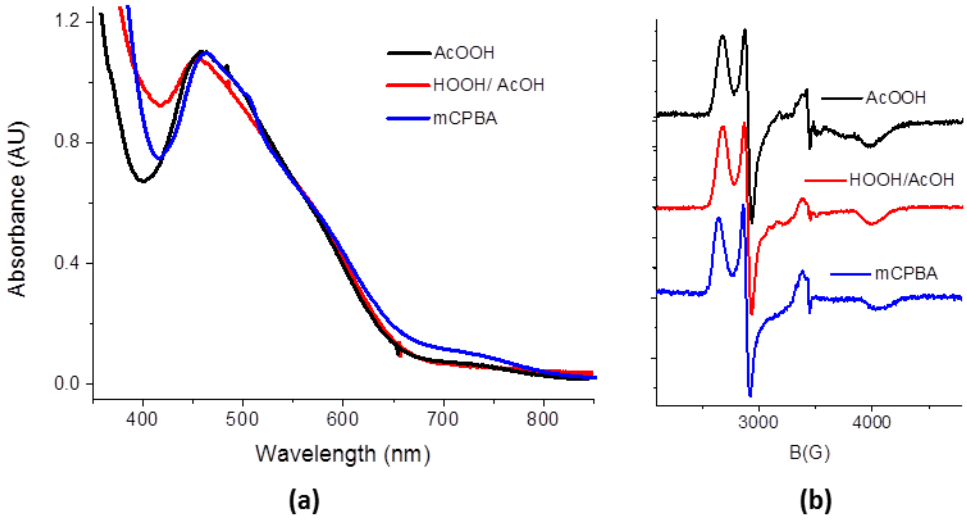

Figure S4. (a) Visible spectra obtained for a 0.5 mM solution of 1a in CH_3CN at -40^{o}C upon addition of 10 eq. of 70% HOOH in the presence of 160 eq. AcOH (red line), 5 equiv of mCPBA (blue line), or 5 equiv AcOOH (black line). (b) EPR spectra of the solutions shown in (a) with 30db power at 10K. EPR integrations relative to an external copper standard afforded the target complex in 43% (blue), 45% (red), and 42% (black) yields.

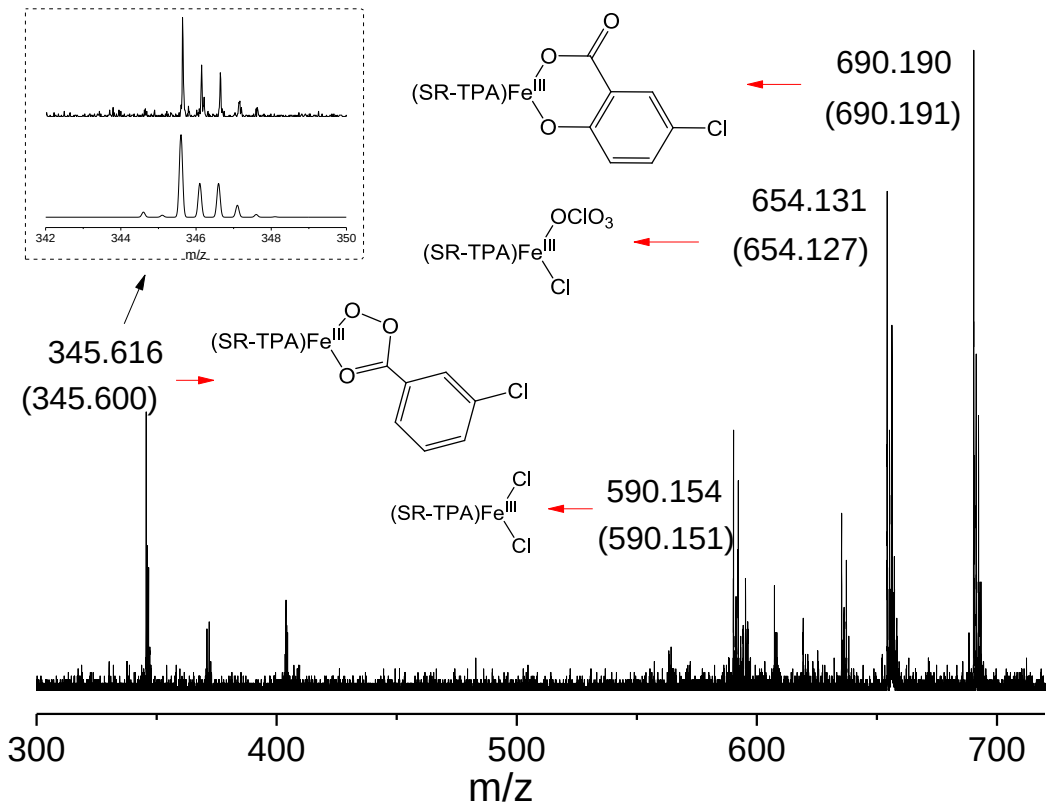

Figure S5. ESI-MS spectrum of a mixture of 1b and excess *m*CPBA in CH_3CN at -40 ^{o}C. The peak at m/z 345.6167 has a mass and isotope distribution pattern consistent with **4b** (calcd for $[C_{34}H_{40}ClFeN_4O_6]^{2+}$ = 345.5988). The peak at m/z = 690.190 can be assigned to $[(TPA^*)Fe^{III}$(5-Cl-salicylate)$]^+$ (calcd for $C_{34}H_{39}ClFeN_4O_6$ = 690.1908). The other signals at 590.154 and 654.131 arise from the interaction of Fe(III) in the solution with chloride and perchlorate anions.

Mössbauer Spectroscopy. In the following we provide some details about the Mössbauer and EPR analyses of species **4b**. The samples used for EPR and Mössbauer were drawn from the same batch at - 40 °C and were immediately frozen in liquid nitrogen. Thus, the two samples have the same distribution of species. Figure S6 shows a series of 4.2 K Mössbauer spectra. We first focus on the high-spin (S = 5/2) Fe^{III} species with E/D = 0.10 displayed as the green curve in the 0.1 T spectrum of Figure S1 (A). The

well-defined six-line pattern, which originates from the *ground* state, must be associated with a Kramers doublet having uniaxial magnetic properties, e. g. g_x, $g_y << g_z$. Such doublets are virtually EPR silent (the signal intensity is proportional $g_x^2 + g_y^2$) or, at best, produce a very weak signal between g = 9.7 and 10. For high-spin Fe^{III} this situation occurs when the zero-field splitting parameter D is negative. For a negative D we may expect to observe an EPR signal from the *upper* Kramers doublet, the $M_S = \pm 1/2$ state, which for E/D = 0.10 would have effective g-values $g_{x,y,z}$ = 3.6, 8.04, 1.70. In fact, the D < 0 species contributes such a signal (green curve Figure 3, main text); the signal declined when the temperature was lowered to 2 K showing that it indeed originates from an excited state. In Figure S1 (A), lines 2 and 5 of the 0.1 T spectrum are nuclear $m_{excited} - m_{ground} = \Delta m = 0$ transitions whose intensities will diminish with increasing applied field (as the Zeeman term overwhelms the zero-field splitting). This field dependence allowed us to determine that $D \approx -0.80$ cm^{-1}. Using this value for D together with E/D = 0.10 we were able to simulate the shape of the EPR spectrum and at the same time determine a spin concentration corresponding to ≈ 0.30 spins/Fe, in close agreement with that obtained from Mössbauer spectroscopy. For the simulations of the Mössbauer spectrum of this species we used the parameters listed in the caption of Figure S1.

In the Mössbauer spectra we did not see evidence for the presence of the high-spin Fe^{III} with g = 4.3 (estimated from EPR to represent ≈ 5% of total Fe). We are not surprised by this "observation" because the Mössbauer spectrum associated with the

ground Kramers doublet of this species is expected to have a magnetic splitting very close to that of the majority E/D = 0.10 species, for the following reason. For the ground doublets of both Fe^{III} species, the expectation values of the electronic spin, $\langle S_i \rangle = g_i/4$, will be the same within 3% and the A-values are not expected to differ by more than 5%, if at all. Hence, the internal magnetic fields at the nucleus will essentially be the same. By using $A_0/g_n\beta_n$ = - 21.5 T (1% percent larger than the value used for the E/D = 0.10 component) for the E/D = 1/3 species and keeping ΔE_Q near zero, the spectra of the two species match.

The reader's attention is now directed to Fig S6 (B), which shows the 0.1 T spectrum after subtraction of the (green) Fe^{III} species. The red curve shows the final simulation of species **4b**. The center part of the experimental spectrum contains a feature that appears to be a quadrupole doublet with $\Delta E_Q \approx 1.1$ mm/s and $\delta = 0.55$ mm/s (possibly two doublets with similar ΔE_Q and δ values). We have considered whether these lines could be part of paramagnetic species **4b**, but we found that it is impossible to simulate in one spectrum the two central lines together while still capturing the outer features of **4b**, with the given constraints of $\Delta E_Q \approx 2.6$ mm/s and $\delta \approx 0.23$ mm/s. For these reasons the two inner lines most likely belong to a *diamagnetic* diferric species formed during the course of the preparation (diferric species are frequently encountered in TPA chemistry). In fact, the simulations (B)-(E) show that a diamagnetic species accounting for ca. 12% of total Fe fits the field dependence of the spectra well.

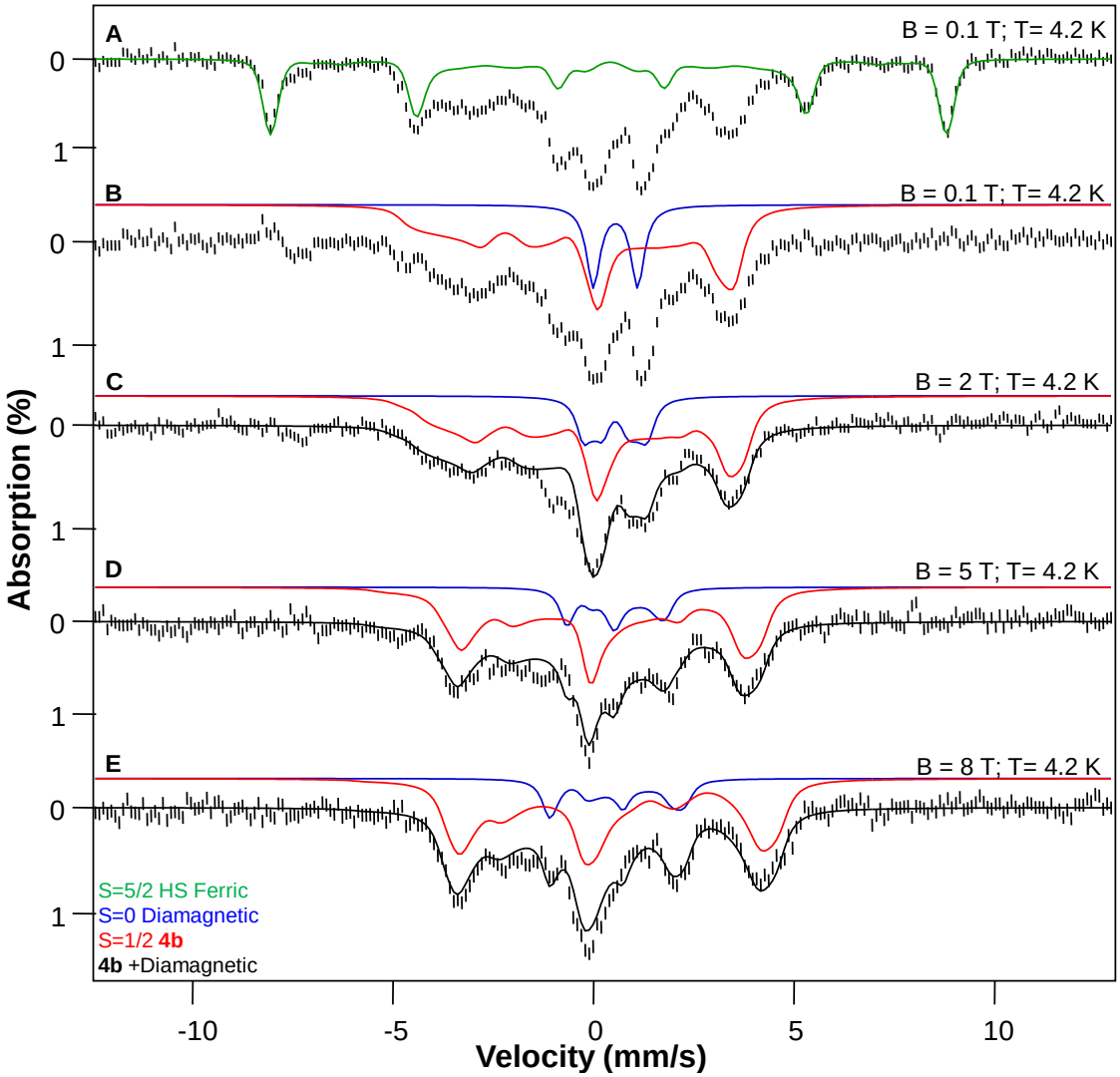

Figure S6. 4.2 K Mössbauer spectra of 4b recorded in variable parallel-applied magnetic fields. (A) 0.1 T spectrum, raw data are shown as the black-hashed line. The green line in A is a simulation (representing 35% of the Fe in the sample) for the majority high-spin ferric species using an S = 5/2 spin Hamiltonian with D = -0.8 cm^{-1}, E/D = 0.10, isotropic g_0 = 2.00, isotropic $A_0/g_n\beta_n$ = - 21.5 T, ΔE_Q = -0.07 mm/s, EFG asymmetry parameter η = 0 and isomer shift δ = 0.40 mm/s. For the spectra shown in (B) to (E) we have removed the contribution of this species. The red lines represent species 4b. Blue lines indicate the contribution of an indicated diferric species with $\Delta E_Q \approx 1.10$ mm/s and $\delta \approx 0.55$ mm/s.

In the T = 160 K spectrum of Figure 4C (main text) the electron spin of **4b** approaches the fast relaxation limit and **4b** produces a doublet for which the left line is already quite sharp, while the right line exhibits some relaxation broadening. At 160 K the spins of the high-spin Fe^{III} species, as frequently observed, are not yet in the fast relaxation limit. Some absorption in the center of the spectrum may be due to the high-spin ferric components with the remainder attributable to the diferric species. Roughly 50% of the Fe in the sample can be assigned to the doublet of **4b**, in good agreement with the results obtained at T= 4.2 K.

Once the spectral features of the contaminants were well understood, obtaining an accurate spectral simulation for **4b** was a straightforward task. Based on the observed g-values, the Griffith model predicts a large positive orbital contribution to A_z and a large negative contribution to A_x. Moreover, since the spin-dipolar contribution to the A-tensor is proportional to the valence part of the EFG tensor, the large negative value for eQV_{xx} suggests that there is a large negative A_x(spin-dipolar) and two smaller positive components along y and z. With this information in hand, we used WMOSS to simulate spectra of **4a**. The red lines in Figure S1 were obtained using eq 1 with the parameters listed in the caption of Figure 4.

For calculating the quadrupole splitting of **4b** given in the main text we used the keyword“prop” of the Gaussian code and Q(^{57}Fe) = 0.17 barn. Finally, Shaik and

coworkers[2] have performed DFT calculations of the $Fe^{V}(O)(OH)$ complex postulated by Talsi et al. These calculations indicate that such a complex, with the OH π donor *cis* to the oxo group, would be *high-spin* (S = 3/2).

Table S1. Cartesian coordinates for the optimized structure of 4b (Figure 5). Gaussian09, 6-311G/B3LYP

Fe	-0.01637783	-0.73558034	-0.44553470	H	-1.63699821	-1.17711569	2.98394036
O	0.06541354	-0.76285226	-2.25675546	H	-1.13386762	-2.48264304	1.90966843
N	-0.10493368	-0.66718050	1.56802518	O	-0.01729041	-2.72722086	-0.60991810
N	-0.01517981	1.20936130	-0.35556866	H	2.52607405	-0.30734937	-2.04078779
N	1.94065029	-0.78505300	-0.11808978	C	7.06399668	-1.41167291	0.27301957
N	-1.99225211	-0.79506807	-0.27690332	H	7.75813821	-1.73627099	1.03940122
C	0.03028710	2.01800775	-1.43876322	H	6.76184234	-2.25483173	-0.34476204
C	0.03559889	3.40896133	-1.36146972	H	7.52074189	-0.62988295	-0.32454990
C	0.04445460	3.97251068	-0.06289377	H	5.61513731	-1.01472631	-2.37224875
C	-0.05591115	3.13439914	1.08192419	H	4.72060596	0.47730862	-2.60872822
C	-0.07285678	1.75760239	0.88835551	H	6.06360159	0.42723402	-1.47695090
C	-0.15266851	0.78016603	2.03537051	H	5.00429760	-0.82252334	3.20541602
C	2.88504119	-0.52483293	-1.04644433	H	3.33191015	-1.05342976	3.71852335
C	4.24964397	-0.51027279	-0.75961056	H	4.27757096	-2.41019773	3.11157933
C	4.62582446	-0.82293703	0.56551704	H	-3.62810265	-2.36516939	3.04908600
C	3.63930042	-1.04505196	1.56859673	H	-4.48968775	-0.84868155	3.29436765
C	2.30493147	-1.02812623	1.17791402	H	-5.26760063	-2.19264581	2.47139189
C	1.13944658	-1.37620019	2.06824643	C	-6.81146371	-0.19595082	1.39380294
C	-2.86023651	-0.56992033	-1.29280183	H	-6.25681891	0.68664065	1.70882411
C	-4.23717696	-0.60965559	-1.11389810	H	-7.75106941	0.09474901	0.93805987
C	-4.71664317	-0.87749931	0.18916267	H	-7.00047868	-0.85756655	2.23351005
C	-3.82405346	-1.18396846	1.24483846	H	-4.75176713	-0.64030383	-3.20654870
C	-2.45722379	-1.09544860	0.96797196	H	-6.12760478	-0.83990171	-2.10557669
C	-1.36351252	-1.41788130	1.95742918	H	-5.40133261	0.73799073	-2.32039275
H	0.04100298	1.52244991	-2.39852442	H	1.03230614	4.38381675	-3.02695322
C	0.02241426	4.18891950	-2.65838170	H	-0.49969340	3.62604267	-3.43070274
O	0.09926248	5.29961199	0.24996091	H	-0.47601099	5.14761925	-2.56112717
C	-0.09396091	3.74577869	2.45992737	C	0.68035350	6.37416090	-0.57644694
H	-1.07817376	0.93060328	2.59244021	H	-0.06502180	6.77627464	-1.25572505
H	0.66564548	0.94756652	2.73620462	H	0.96263961	7.13530209	0.14184401
C	5.21670760	-0.13682594	-1.85895988	H	1.55653503	6.01970019	-1.11372514
O	5.90823366	-0.88802992	1.03185248	H	0.91515897	3.86117903	2.86706585
C	4.07796962	-1.34301260	2.98035260	H	-0.53073985	4.73903437	2.42242836
H	0.94806618	-2.44753862	2.00309008	H	-0.66969071	3.14461928	3.16320578
H	1.31334405	-1.13150837	3.11457381	H	-2.42341695	-0.35625903	-2.25589971
C	-5.17935809	-0.33094692	-2.25378255	O	0.05716072	-2.21073909	-2.81224272
O	-6.08004360	-0.91005191	0.32285991	C	0.01722715	-3.10950026	-1.82086610
C	-4.32355933	-1.66590318	2.58796909	C	0.02372753	-4.52943318	-2.25592601

H	-0.06160275	-4.61313946	-3.33486835
H	0.95169927	-5.00452962	-1.93256719
H	-0.80050054	-5.05978432	-1.77930170

Experimental Reactivity Section

Table S2. **Oxidation of hydrocarbons by the** 1b/ H_2O_2/ AcOH **system**

Entry	Substrate	AcOH (eq)	Alcohol (TON)	Ketone (TON)
1	Cyclohexane	0	4.0(2)	0.2(1)
2	Cyclohexane	200	3.9(2)	0.2(1)
3	Cyclooctane	0	5.2(1)	1.2(1)
4	Cyclooctane	200	5.1(1)	1.2(1)
5	1,2-DMC	0	2.2(2) %RC >99	-
6	1,2-DMC	200	1.7(2) %RC >99	-
	Diol (TON)	Epoxide (TON)		
7	Cyclooctene	0	4.4(2) %RC >99	3.6(2)
8	Cyclooctene	200	0.4(1) %RC >99	6.2(2)
9	1-octene	0	7.3(2)	1.6(2)
10	1-octene	200	1.0(1)	4.5(2)

Reaction conditions applied: **1b**/ H_2O_2/ Substrate = 1:10:1000. The H_2O_2 was added via syringe pump over a period of 30 minutes. For the cis-1,2-dimethylcyclohexane (1,2-DMC), only the (1S,1S)-1,2-dimethylcyclohexanol product was observed by GC. The other isomer, (*1R,2S*)-1,2-dimethylcyclohexanol, was not observed.

Table S3. Decay rate of complex **1b** as a function of the nature and concentration of the substrate.

Substrate	**Concentration (mM)**	**k_{obs} (s^{-1})**	**Yield (mM)**
None	0	0.019	-
1-octene	125	0.015	-
1-octene	250	0.017	7.8(2)
t-butyl acrylate	250	0.018	
cyclooctene	250	0.015	10.1(2)
Additive	Concentration (mM)	k_{obs} (s^{-1})	
AcOH	50	0.021	
AcOH	100	0.021	
AcOH	200	0.019	
AcOH	340	0.018	
AcOD	200	0.019	

Reaction conditions: 1 mM solution of Fe(TPA*) in CH_3CN with 200 equiv. AcOH and 20 equiv. H_2O_2 (70%) at -40°C. The observed first order rate of decay of complex **1b** in the presence of various substrates is given.

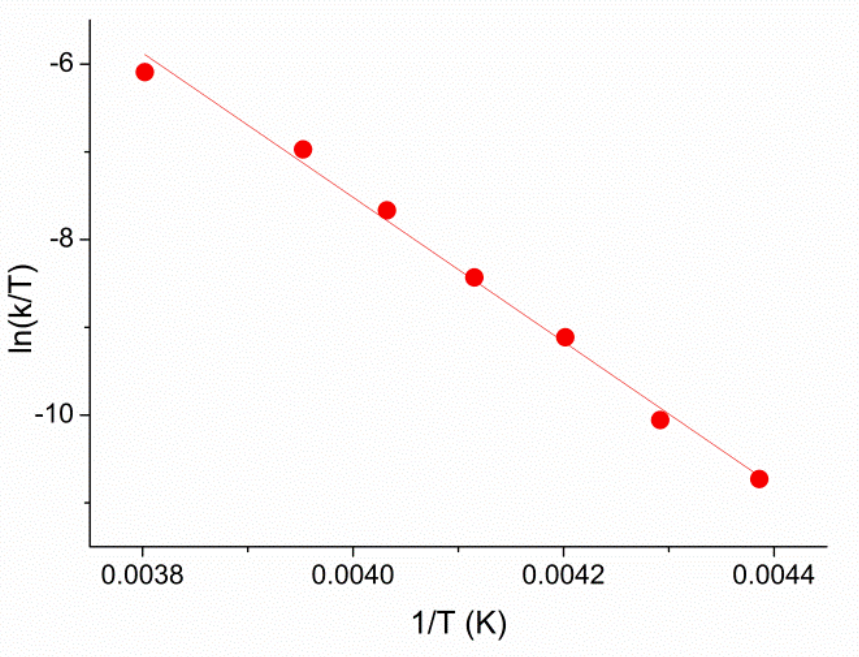

Figure S7. Eyring plot for the decay of 4b. Activation parameters: $\Delta H^{\ddagger}$ = 67 kJ/mol and $\Delta S^{\ddagger}$ = 13 J/mol.K, or 16 kcal/mol and 3 cal/mol, respectively.

Density Functional Theoretical (DFT) Calculations on the Reaction Mechanism. The spin-unrestricted B3LYP functional was employed with two basis sets: (a) TZVP basis set for iron, electron-rich N and O atoms, and 6-31G** basis set for the rest C and H atoms. This basis set is denoted as B1, and was used to optimize transition states and minima; (b) The Def2-TZVPP basis set for all atoms, denoted as B2, was used for single point energy corrections. Transition states were ascertained by vibrational frequency analysis to possess a single mode along the reaction path with only one imaginary frequency. Intrinsic reaction coordinate (IRC) searching was performed to confirm transition states linking right intermediates in the **4→5/5'** conversion and cyclooctene epoxidation. All optimizations and single point calculations were performed with solvation included using the self-consistent reaction field (SCRF) calculations, in the polarizable continuum model (PCM); the experimental solvent acetonitrile ($\varepsilon = 35.688$) was used. DFT calculations were performed with Gaussian 09 suite of quantum chemical packages.

Figure 1 demonstrates that acylperoxo intermediate **4** in the Fe(TPA) system behaves differently from the corresponding species in the Fe(PDP) system. Very large activation barriers (31.8 kcal/mol for the quartet and 21.2 kcal/mol for the doublet) are found for the homolysis of the O-O bond of **4** of Fe(TPA) in the course of direct C=C bond attack. This occurs before epoxidation ($r_{C\text{-}Op} = 2.25$ Å). In the case of C-H hydroxylation by **4** of the Fe(PDP) system, homolysis of O-O bond is concerted with C-H

cleavage and has relative low activation energies (12.3/14.9 kcal/mol for the doublet/quartet states). As shown in Figure 6 in the main text, for cyclooctene epoxidation by **4** of Fe(TPA), the stepwise O-O homolysis/epoxidation mechanism has a much lower activation barrier compared to the concerted mechanism shown in the above figure. Thus, for the Fe(TPA) system, **4** needs to convert to **5**/**5**', which then carries out the epoxidation.

DFT calculations revealed that O-O homolysis of **4** occurs quite differently on the doublet and quartet states. On the doublet spin state, O-O homolysis generates an $O=Fe^{IV}(AcO\cdot)$ species ^{2}**5** while on the quartet spin state, an $O=Fe^{V}(AcO)$ species ^{4}**5'** is formed.

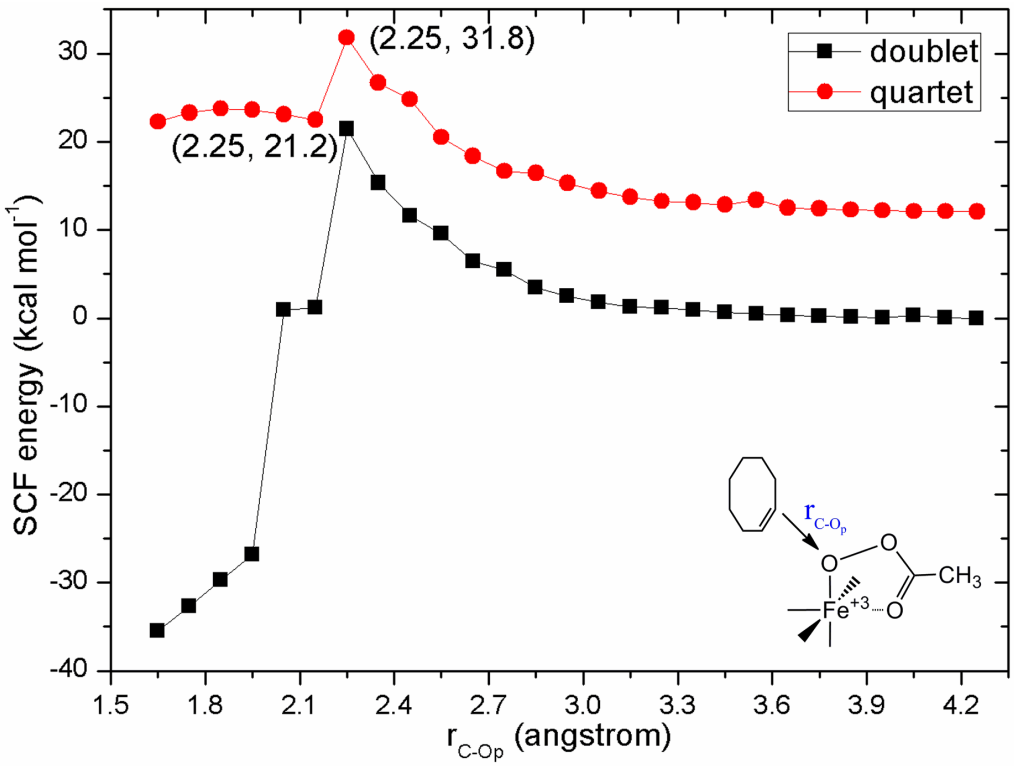

Figure S8. Relaxed-scan energy points for cyclooctene epoxidation as the C=C bond approaches the O_p atom of **4**. Calculations were performed at the B3LYP*/B1 level in solvent.

Scheme S1. The mechanism of cyclooctene epoxidation by 4 via the 4→3/3’ conversion revealed by DFT study

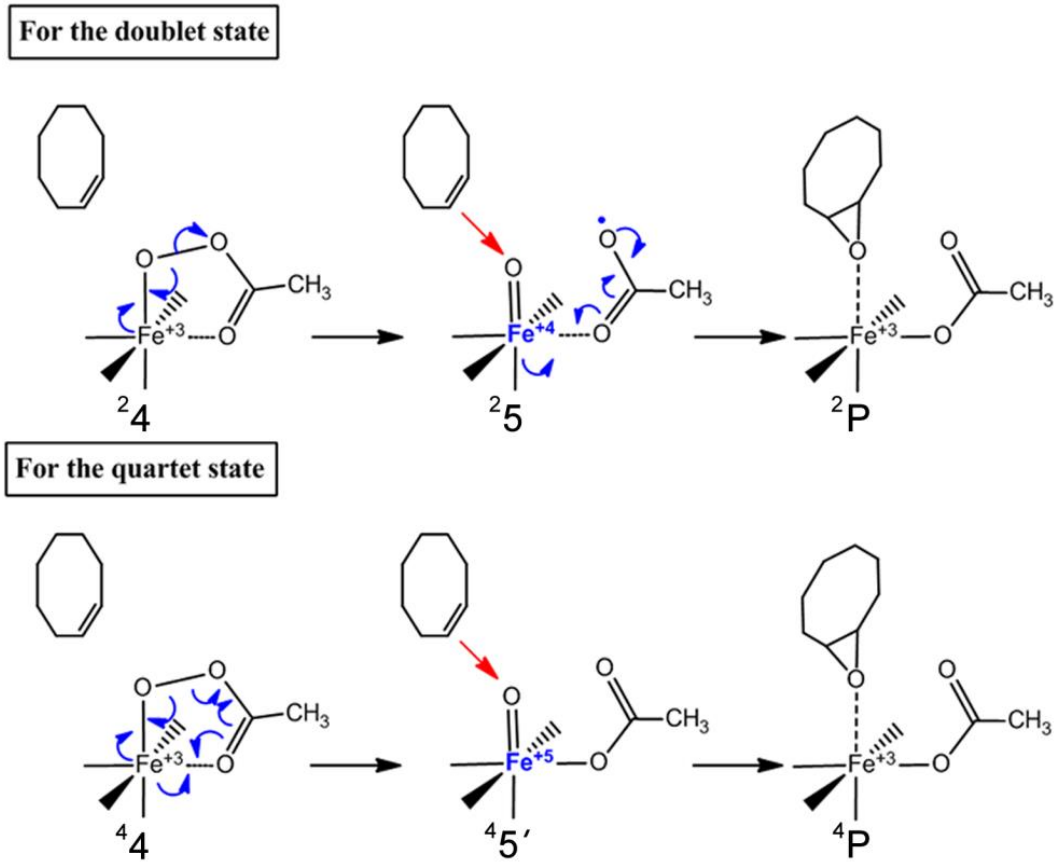

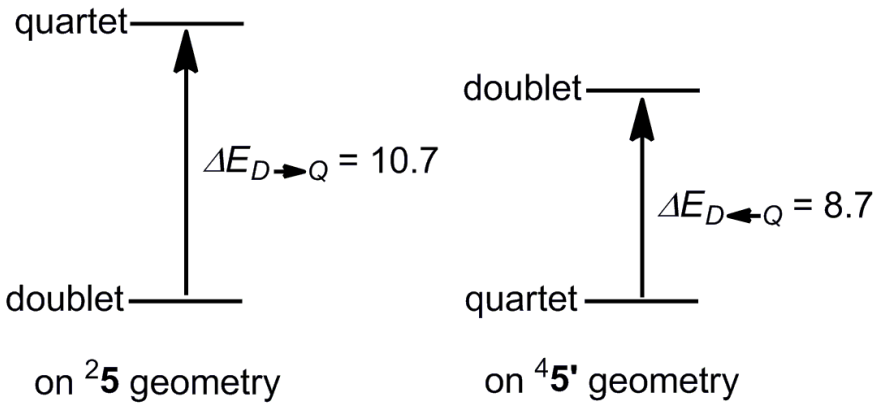

Figure S9. Vertical transition gaps $\Delta E_{D\rightarrow Q}$ and $\Delta E_{D\leftarrow Q}$ (in kcal mol^{-1}) between doublet and quartet spin states of 5(5'). Calculations were done on ^{2}5 and ^{4}5' geometries at the B3LYP/B2 level. Figure S9 presents data required for estimating the crossing point (CP) energy shown in Figure 6 in the text.

Table S4. Various SCRF and free energies (calculated at 233.15 K) of key intermediates in cyclooctene epoxidation by 4 via the 4→5/5' conversion. Calculations were done in solvent.

	B3LYP*/B2//B1 +ZPE(B1)		B3LYP/B2//B3LYP*/B1 +ZPE(1)		Free Energy(B1)	
	E	*ΔE*	*E*	*ΔE*	*G*	*ΔG*
^{2}**4**	-2795.805522	**0.0**	-2796.201127	**0.0**	-2795.854206	**0.0**
^{4}**4**	-2795.791783	**8.6**	-2796.187001	**8.9**	-2795.841717	**7.8**
^{2}**TS$_{45}$**	-2795.792376	**8.2**	-2796.186877	**8.9**	-2795.841362	**8.1**
^{4}**TS$_{45}$**	-2795.777653	**17.5**	-2796.171718	**18.5**	-2795.827633	**16.7**
^{2}**5**	-2795.792085	**8.4**	-2796.186636	**9.1**	-2795.840544	**8.6**
^{4}**5'**	-2795.790080	**9.7**	-2796.183221	**11.2**	-2795.839962	**8.9**
^{2}**TS$_{ep}$**	-2795.787677	**11.2**	-2796.179097	**13.8**	-2795.833798	**12.8**
^{4}**TS$_{ep}$**	-2795.793521	**7.5**	-2796.183165	**11.3**	-2795.839681	**9.1**
^{2}**P**	-2795.869195	**-40.0**	-2796.256595	**-34.8**	-2795.913151	**-37.0**
^{4}**P**	-2795.863789	**-36.6**	-2796.251633	**-31.7**	-2795.909408	**-34.6**

[a] Absolute energies are in a.u. units and the relative ones are in kcal mol^{-1} units.

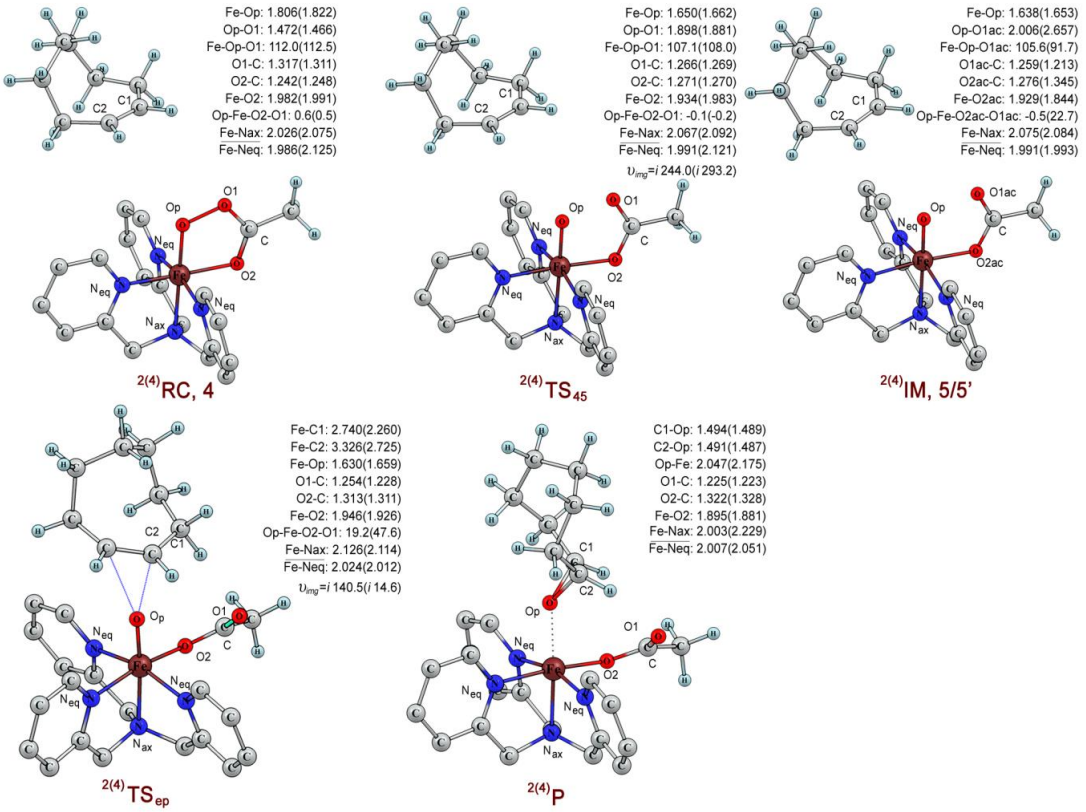

Figure S10. Geometric information of the key intermediates in cyclooctene epoxidation by **4** via the **4→5/5'** conversion. Calculations were done at the UB3LYP/B1 level in solvent. Bond lengths are in Å. Hydrogen atoms on the TPA skeleton are omitted for clarity. Values outside parentheses are for the doublet state, those inside parentheses are for the quartet state.

Table S5. Mulliken charges and spin densities of key intermediates in cyclooctene epoxidation by 4 via the 4→5/5' conversion. Calculations were done at the UB3LYP/B1 level in solvent.

	spin density						**charge**					
	Fe	TPA	O_p	O_{ac}	OCMe	Sub	Fe	TPA	O_p	O_{ac}	OCMe	Sub
^{2}**4**	0.96	-0.06	0.11	-0.01	-0.01	0.00	0.12	1.89	-0.24	-0.05	0.27	0.03
^{4}**4**	2.78	0.15	0.06	-0.01	0.01	0.00	0.42	1.57	-0.24	-0.04	0.26	0.03
^{2}**TS$_{43}$**	1.29	-0.08	0.20	-0.36	-0.05	0.00	0.09	2.02	-0.23	-0.17	0.26	0.03
^{4}**TS$_{43}$**	3.06	0.20	0.13	-0.40	0.00	0.00	0.40	1.70	-0.22	-0.14	0.24	0.03
^{2}**3'**	1.41	-0.09	0.16	-0.43	-0.06	0.00	0.10	2.06	-0.24	-0.19	0.25	0.03
^{4}**3**	1.92	-0.08	1.05	0.08	0.03	0.00	0.06	2.26	-0.17	-0.38	0.19	0.04
^{2}**TS$_{ep}$**	1.35	-0.08	0.39	-0.16	-0.04	-0.46	0.14	1.87	-0.26	-0.35	0.13	0.47
^{4}**TS$_{ep}$**	1.43	-0.05	0.75	0.01	-0.03	0.88	0.23	1.76	-0.38	-0.48	0.05	0.82
^{2}**P**	1.06	-0.08	-0.01	0.02	0.01	0.00	0.33	1.84	-0.35	-0.47	0.04	0.61
^{4}**P**	2.92	0.03	0.04	0.02	-0.02	0.02	0.55	1.63	-0.39	-0.46	0.08	0.59

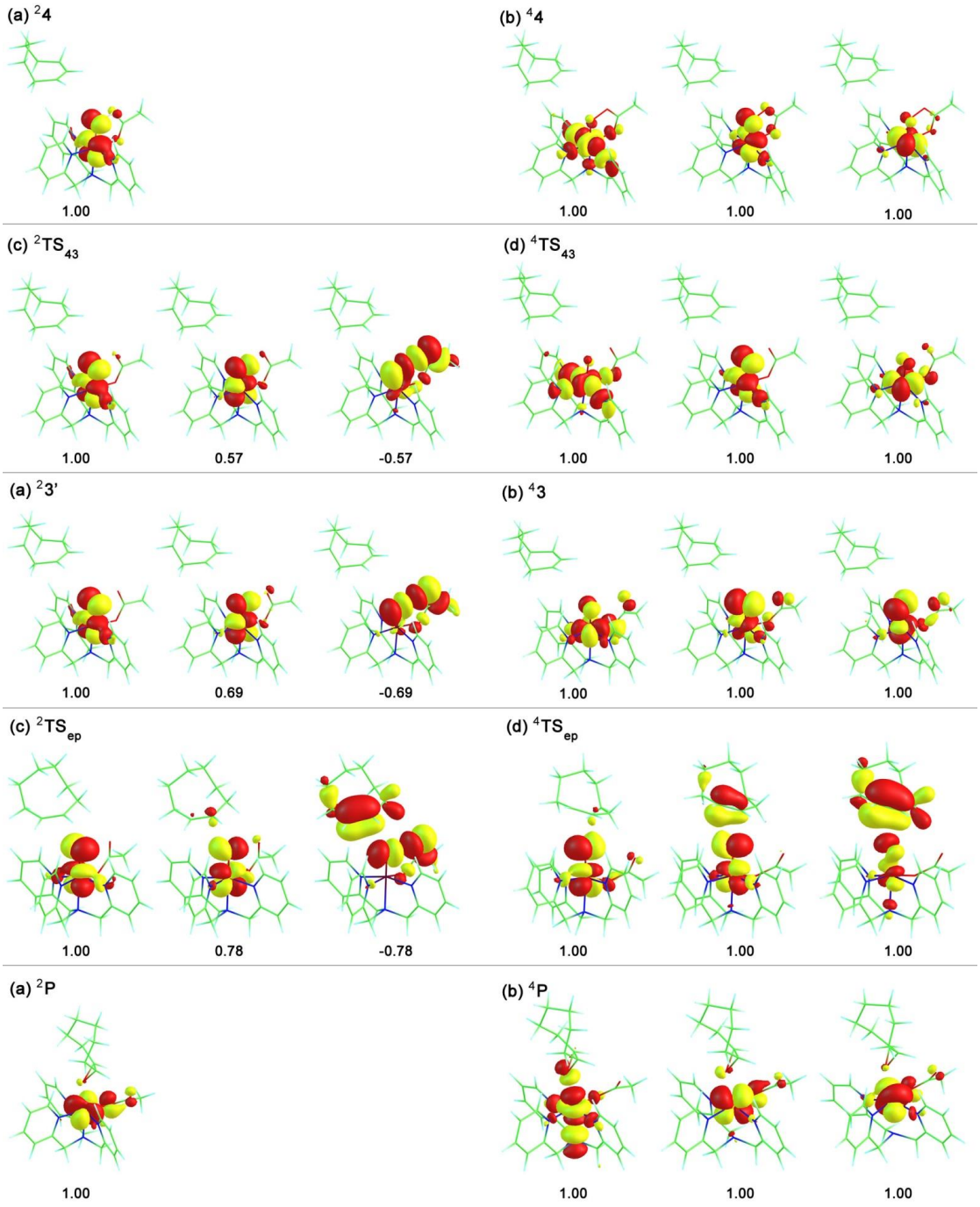

Figure S11. Singly occupied natural orbitals (SNOs) of key intermediates in cyclooctene epoxidation by 4 via 5/5'.

Table S6. DFT-calculated Cartesian coordinates of key intermediates in cyclooctene epoxidation by 4.

^{2}**4**

Fe	-0.173517000	-0.452488000	0.459189000
N	0.084211000	-0.042331000	2.427047000
N	1.779540000	-0.629341000	0.398614000
N	-0.005139000	1.532323000	0.293403000
N	-0.326373000	-2.322919000	1.142405000
C	2.483530000	-0.935629000	-0.707862000
C	3.865635000	-1.050560000	-0.682383000
C	4.534680000	-0.841967000	0.525066000
C	3.800021000	-0.526809000	1.664458000
C	2.413286000	-0.427758000	1.567427000
C	0.260296000	2.203423000	-0.839854000
C	0.406321000	3.586315000	-0.842261000
C	0.286812000	4.281369000	0.360077000
C	0.019876000	3.575570000	1.533378000
C	-0.128382000	2.195596000	1.464790000
C	-0.210413000	-3.435134000	0.398608000
C	-0.286851000	-4.699907000	0.970116000
C	-0.473287000	-4.806164000	2.347719000
C	-0.582768000	-3.646107000	3.115008000
C	-0.512403000	-2.412880000	2.478033000
C	1.555120000	-0.090996000	2.761525000
C	-0.486640000	1.327687000	2.640864000
C	-0.687897000	-1.089390000	3.172808000
H	1.910760000	-1.085481000	-1.615541000
H	4.399629000	-1.298253000	1.591829000
H	5.614899000	-0.923954000	0.578133000
H	4.286989000	-0.358884000	2.618612000
H	0.351639000	1.616692000	-1.747759000
H	0.616425000	4.098599000	-1.773259000
H	0.405464000	5.359122000	0.387726000
H	-0.073002000	4.081769000	2.487372000
H	-0.194080000	-5.576934000	0.341069000
H	-0.526615000	-5.779868000	2.822527000
H	-0.720829000	-3.692819000	4.188945000
H	-0.057205000	-3.289269000	0.66399600
H	1.718000000	-0.829807000	3.550542000
H	1.859846000	0.875602000	3.171112000
H	-1.574590000	1.231617000	2.690331000
H	-0.144679000	1.750208000	3.589357000
H	-1.744983000	-0.811790000	3.139070000
H	-0.384532000	-1.124096000	4.222455000
O	-0.397374000	-0.824014000	-1.29470200
O	-2.149893000	-0.294108000	0.457894000
C	-2.610280000	-0.524730000	-0.673410000
C	-4.064179000	-0.487012000	-1.010256000
H	-4.600616000	-1.134110000	-0.31218200
H	-4.422785000	0.537112000	-0.873101000
H	-4.242012000	-0.806978000	-2.03587800
O	-1.817569000	-0.821064000	-1.68263000
C	1.241963000	1.065189000	-4.555868000
C	0.048068000	1.655608000	-4.726587000
C	-0.325136000	3.082484000	-5.064620000
C	0.781468000	4.134951000	-5.250617000
C	1.579895000	4.051129000	-6.571094000
C	2.053620000	2.661841000	-7.033620000
C	3.072612000	1.936230000	-6.142810000
C	2.623602000	1.672167000	-4.683395000
H	1.221162000	-0.003322000	-4.340551000
H	-0.826099000	1.011646000	-4.613100000
H	-1.006310000	3.432476000	-4.274563000
H	-0.951953000	3.057036000	-5.969986000
H	0.303674000	5.122286000	-5.221218000
H	1.454161000	4.116999000	-4.388268000
H	0.947209000	4.458542000	-7.371274000
H	2.443159000	4.726835000	-6.498950000
H	2.501895000	2.776529000	-8.029255000
H	1.180258000	2.014393000	-7.174853000
H	4.011386000	2.505669000	-6.113381000
H	3.312132000	0.975821000	-6.617652000
H	2.689761000	2.602221000	-4.113844000
H	3.348912000	0.992715000	-4.221399000

^{4}**4**

Fe	-0.205236000	-0.545876000	0.329926000
N	0.058999000	-0.072964000	2.333780000

N	1.779107000	-0.705914000	0.292177000
N	-0.003819000	1.636453000	0.216498000
N	-0.389550000	-2.517080000	1.269494000
C	2.494385000	-0.996548000	-0.812459000
C	3.878984000	-1.049580000	-0.784903000
C	4.534558000	-0.787195000	0.420435000
C	3.787983000	-0.486129000	1.556880000
C	2.398466000	-0.455535000	1.463557000
C	0.276253000	2.365633000	-0.874848000
C	0.511570000	3.734938000	-0.797012000
C	0.467256000	4.353197000	0.452321000
C	0.184424000	3.588851000	1.585193000
C	-0.053805000	2.227655000	1.424136000
C	-0.274778000	-3.712017000	0.670795000
C	-0.330296000	-4.900589000	1.391315000
C	-0.498993000	-4.836313000	2.774594000
C	-0.609065000	-3.590921000	3.394812000
C	-0.555706000	-2.448340000	2.602816000
C	1.530878000	-0.177236000	2.663666000
C	-0.457712000	1.317827000	2.556347000
C	-0.738215000	-1.052650000	3.143142000
H	1.926027000	-1.182088000	-1.716881000
H	4.426381000	-1.287713000	-1.688766000
H	5.617506000	-0.816204000	0.474118000
H	4.269549000	-0.279165000	2.505916000
H	0.317610000	1.834231000	-1.821139000
H	0.731683000	4.296277000	-1.697314000
H	0.656893000	5.417173000	0.546914000
H	0.148038000	4.036748000	2.571783000
H	-0.237093000	-5.849335000	0.876238000
H	-0.537859000	-5.744359000	3.366851000
H	-0.734523000	-3.505641000	4.468256000
H	-0.134294000	-3.700762000	-0.40478600
H	1.669600000	-0.981860000	3.391041000
H	1.856371000	0.744118000	3.153059000
H	-1.549548000	1.259303000	2.584383000
H	-0.121849000	1.695387000	3.526280000
H	-1.791830000	-0.773430000	3.053649000
H	-0.463281000	-0.982340000	4.199654000
O	-0.393640000	-0.978040000	-1.43018000
O	-2.188953000	-0.394055000	0.253235000
C	-2.617532000	-0.664039000	-0.888401000
C	-4.061080000	-0.642900000	-1.261638000
H	-4.604676000	-1.298796000	-0.57689800
H	-4.434581000	0.376245000	-1.127434000
H	-4.210275000	-0.962824000	-2.29162800
O	-1.796431000	-0.987744000	-1.85880100
C	1.194850000	1.112072000	-4.600155000
C	0.014724000	1.738956000	-4.731700000
C	-0.325030000	3.186716000	-5.011576000
C	0.805449000	4.215320000	-5.186736000
C	1.577748000	4.152316000	-6.523652000
C	2.010866000	2.767223000	-7.036076000
C	3.024563000	1.989836000	-6.183863000
C	2.589255000	1.688880000	-4.727337000
H	1.149830000	0.037527000	-4.421674000
H	-0.874646000	1.114463000	-4.627681000
H	-0.977655000	3.527002000	-4.193587000
H	-0.972650000	3.210230000	-5.902223000
H	0.353959000	5.213099000	-5.118593000
H	1.493105000	4.154102000	-4.338187000
H	0.940875000	4.598027000	-7.299744000
H	2.457852000	4.805526000	-6.447413000
H	2.447567000	2.902666000	-8.034252000
H	1.120123000	2.145551000	-7.184458000
H	3.976807000	2.536140000	-6.149632000
H	3.234965000	1.040084000	-6.692755000
H	2.685186000	2.597934000	-4.128929000
H	3.303884000	0.977379000	-4.298069000

^{2}**TS**$_{43}$

Fe	-0.190749000	-0.410251000	0.388020000
N	0.092680000	-0.034272000	2.400861000
N	1.781311000	-0.572546000	0.352360000
N	-0.018523000	1.576985000	0.277451000
N	-0.327032000	-2.288816000	1.052282000
C	2.485525000	-0.845329000	-0.764577000
C	3.867522000	-0.948108000	-0.743619000
C	4.537604000	-0.762203000	0.467123000
C	3.802474000	-0.481133000	1.614318000
C	2.414325000	-0.392616000	1.525067000
C	0.223683000	2.267393000	-0.849238000

C	0.359222000	3.650879000	-0.829016000
C	0.250555000	4.323877000	0.386866000
C	0.004981000	3.596261000	1.551179000
C	-0.133033000	2.216044000	1.463404000
C	-0.222920000	-3.382707000	0.280590000
C	-0.300264000	-4.659363000	0.823977000
C	-0.478137000	-4.795543000	2.200054000
C	-0.579094000	-3.652992000	2.994052000
C	-0.507566000	-2.404537000	2.387076000
C	1.560885000	-0.096601000	2.730466000
C	-0.472554000	1.333300000	2.634940000
C	-0.677960000	-1.099637000	3.119253000
H	1.911844000	-0.976391000	-1.674113000
H	4.400498000	-1.168698000	-1.660556000
H	5.618591000	-0.834984000	0.516032000
H	4.288817000	-0.330779000	2.571615000
H	0.306729000	1.695734000	-1.767382000
H	0.551930000	4.180580000	-1.753984000
H	0.360671000	5.401939000	0.431560000
H	-0.079879000	4.085169000	2.514878000
H	-0.216086000	-5.522098000	0.174370000
H	-0.532333000	-5.779414000	2.653206000
H	-0.711618000	-3.723675000	4.067297000
H	-0.080725000	-3.211994000	-0.77952700
H	1.725293000	-0.865060000	3.490263000
H	1.870619000	0.852559000	3.175391000
H	-1.559390000	1.238639000	2.699057000
H	-0.115005000	1.749141000	3.580553000
H	-1.734443000	-0.820671000	3.096850000
H	-0.369731000	-1.167126000	4.165858000
O	-0.382429000	-0.723905000	-1.22100000
O	-2.104540000	-0.215105000	0.596168000
C	-2.775532000	-0.377677000	-0.472145000
C	-4.276649000	-0.249530000	-0.422939000
H	-4.660173000	-0.991585000	0.282220000
H	-4.523782000	0.746835000	-0.047624000
H	-4.717276000	-0.402428000	-1.40656000
O	-2.243488000	-0.646792000	-1.58925500
C	1.276005000	0.964902000	-4.466459000
C	0.067122000	1.514425000	-4.667102000
C	-0.345622000	2.926108000	-5.022544000
C	0.729444000	4.012503000	-5.198309000
C	1.556109000	3.941980000	-6.502050000
C	2.086259000	2.564887000	-6.939449000
C	3.110793000	1.883956000	-6.020198000
C	2.639186000	1.616327000	-4.568434000
H	1.285348000	-0.103290000	-4.247921000
H	-0.787502000	0.842508000	-4.568300000
H	-1.051163000	3.259541000	-4.246852000
H	-0.955583000	2.873485000	-5.938104000
H	0.218733000	4.983648000	-5.188864000
H	1.385024000	4.025985000	-4.322855000
H	0.925738000	4.318744000	-7.318878000
H	2.394033000	4.647816000	-6.420669000
H	2.550426000	2.684342000	-7.927169000
H	1.238466000	1.886410000	-7.090149000
H	4.028033000	2.486513000	-5.975753000
H	3.394304000	0.928534000	-6.480600000
H	2.661438000	2.552428000	-4.005342000
H	3.376113000	0.965067000	-4.084673000

^{4}**TS**$_{43}$

Fe	-0.065605000	-0.378810000	0.232845000
N	0.098297000	-0.090731000	2.299288000
N	1.981454000	-0.464010000	0.327938000
N	0.143547000	1.772929000	0.313065000
N	-0.285363000	-2.387259000	0.964942000
C	2.787767000	-0.560153000	-0.746321000
C	4.166983000	-0.479705000	-0.628013000
C	4.718695000	-0.281696000	0.639428000
C	3.877966000	-0.182828000	1.745972000
C	2.501876000	-0.285997000	1.558324000
C	0.452207000	2.576323000	-0.716866000
C	0.678923000	3.936643000	-0.533985000
C	0.595361000	4.464274000	0.754313000
C	0.279965000	3.621807000	1.821259000
C	0.051804000	2.274721000	1.559679000
C	-0.138546000	-3.510162000	0.245014000
C	-0.270251000	-4.767652000	0.823557000
C	-0.553145000	-4.850966000	2.186934000
C	-0.699557000	-3.679485000	2.931790000
C	-0.565233000	-2.457340000	2.282121000

C	1.538010000	-0.283844000	2.715196000
C	-0.397419000	1.291755000	2.609085000
C	-0.772821000	-1.123621000	2.953134000
H	2.296967000	-0.695273000	-1.703488000
H	4.788200000	-0.562396000	-1.511572000
H	5.793244000	-0.204049000	0.764961000
H	4.278490000	-0.033949000	2.742150000
H	0.520117000	2.112827000	-1.696452000
H	0.922471000	4.560411000	-1.385838000
H	0.777882000	5.519093000	0.929844000
H	0.209639000	3.999768000	2.834793000
H	-0.147803000	-5.655850000	0.215355000
H	-0.653439000	-5.817438000	2.669197000
H	-0.914059000	-3.711529000	3.993826000
H	0.089196000	-3.380999000	-0.807164000
H	1.616890000	-1.249798000	3.221919000
H	1.809786000	0.479239000	3.448295000
H	-1.490288000	1.254734000	2.601475000
H	-0.082347000	1.589646000	3.612848000
H	-1.812552000	-0.814465000	2.817046000
H	-0.571778000	-1.164981000	4.027494000
O	-0.132467000	-0.642065000	-1.40779400
O	-2.036863000	-0.164726000	0.257949000
C	-2.584486000	-0.290014000	-0.881326000
C	-4.079988000	-0.158099000	-1.012899000
H	-4.540543000	-0.944380000	-0.40843500
H	-4.372110000	0.812438000	-0.603874000
H	-4.398134000	-0.245631000	-2.05017600
O	-1.932527000	-0.529413000	-1.94417000
C	1.494812000	1.400957000	-4.408297000
C	0.364337000	2.103028000	-4.588851000
C	0.128907000	3.577049000	-4.837174000
C	1.327718000	4.538407000	-4.908859000
C	2.173992000	4.467762000	-6.199675000
C	2.555965000	3.074526000	-6.730783000
C	3.468873000	2.212580000	-5.846465000
C	2.926812000	1.892940000	-4.430136000
H	1.373507000	0.326203000	-4.271325000
H	-0.565030000	1.531137000	-4.560132000
H	-0.551018000	3.930574000	-4.047564000
H	-0.460802000	3.668619000	-5.762851000
H	0.933787000	5.559792000	-4.833641000
H	1.956286000	4.408474000	-4.023212000
H	1.611150000	4.972413000	-6.996623000
H	3.084064000	5.065247000	-6.051797000
H	3.059487000	3.212599000	-7.696575000
H	1.641237000	2.511849000	-6.951194000
H	4.446962000	2.699926000	-5.736062000
H	3.655626000	1.268223000	-6.374275000
H	3.040298000	2.774894000	-3.795149000
H	3.568786000	1.124575000	-3.984054000

^{2}**5**

Fe	-0.179572000	-0.419158000	0.377186000
N	0.094492000	-0.040550000	2.399260000
N	1.793388000	-0.607154000	0.365024000
N	0.021535000	1.564235000	0.266793000
N	-0.346222000	-2.293082000	1.045817000
C	2.501427000	-0.894964000	-0.745775000
C	3.881687000	-1.015055000	-0.712848000
C	4.544651000	-0.831328000	0.502143000
C	3.804534000	-0.535307000	1.642273000
C	2.418391000	-0.429549000	1.542192000
C	0.279643000	2.247086000	-0.860832000
C	0.426463000	3.629334000	-0.845352000
C	0.313361000	4.308183000	0.366857000
C	0.052414000	3.587588000	1.532284000
C	-0.097425000	2.208230000	1.449920000
C	-0.255600000	-3.388730000	0.274930000
C	-0.356017000	-4.663425000	0.818981000
C	-0.543636000	-4.795458000	2.194178000
C	-0.631111000	-3.650858000	2.986739000
C	-0.536498000	-2.403860000	2.379860000
C	1.559327000	-0.118029000	2.739200000
C	-0.455672000	1.334729000	2.623476000
C	-0.692521000	-1.097001000	3.112657000
H	1.932364000	-1.023275000	-1.658321000
H	4.418890000	-1.247353000	-1.624386000
H	5.624196000	-0.917605000	0.559776000
H	4.285178000	-0.386791000	2.602741000
H	0.366918000	1.670934000	-1.775697000
H	0.630710000	4.152518000	-1.771674000

H	0.431890000	5.385484000	0.408154000
H	-0.036084000	4.081625000	2.493033000
H	-0.282010000	-5.527874000	0.170435000
H	-0.615937000	-5.777924000	2.647833000
H	-0.771329000	-3.718506000	4.059208000
H	-0.104836000	-3.220871000	-0.78443300
H	1.709815000	-0.884577000	3.503761000
H	1.876713000	0.829535000	3.181921000
H	-1.543789000	1.253510000	2.680977000
H	-0.098708000	1.750510000	3.569334000
H	-1.745056000	-0.804334000	3.086730000
H	-0.389164000	-1.170514000	4.160283000
O	-0.362783000	-0.731212000	-1.22072400
O	-2.082016000	-0.189799000	0.607256000
C	-2.801124000	-0.323861000	-0.438768000
C	-4.295224000	-0.154149000	-0.306023000
H	-4.661144000	-0.892677000	0.412032000
H	-4.494129000	0.844800000	0.090265000
H	-4.791242000	-0.284953000	-1.26624300
O	-2.332448000	-0.592625000	-1.57688600
C	1.435303000	1.021427000	-4.417439000
C	0.178072000	1.428713000	-4.655547000
C	-0.376042000	2.773025000	-5.074496000
C	0.580853000	3.954078000	-5.313997000
C	1.418257000	3.896211000	-6.610885000
C	2.110377000	2.566305000	-6.959040000
C	3.188101000	2.060389000	-5.989317000
C	2.720497000	1.813884000	-4.532033000
H	1.557096000	-0.029495000	-4.153686000
H	-0.601672000	0.673966000	-4.537412000
H	-1.107732000	3.071795000	-4.308909000
H	-0.981699000	2.613901000	-5.980467000
H	-0.029838000	4.864539000	-5.361118000
H	1.226767000	4.088442000	-4.441601000
H	0.753852000	4.142741000	-7.450219000
H	2.166643000	4.699812000	-6.575622000
H	2.576358000	2.681854000	-7.946385000
H	1.348029000	1.787825000	-7.079887000
H	4.027215000	2.768562000	-5.963464000
H	3.591464000	1.122730000	-6.393388000
H	2.626760000	2.773444000	-4.018023000
H	3.515197000	1.273541000	-4.005163000

^{4}**5**

Fe	-0.214152000	-0.403945000	0.300274000
N	0.018736000	-0.056378000	2.342016000
N	1.787455000	-0.549652000	0.347776000
N	-0.013890000	1.572479000	0.210585000
N	-0.341711000	-2.285627000	0.913111000
C	2.532524000	-0.797594000	-0.749770000
C	3.913962000	-0.867330000	-0.681169000
C	4.537549000	-0.672765000	0.553562000
C	3.758922000	-0.419336000	1.678823000
C	2.373512000	-0.365708000	1.544980000
C	0.246111000	2.270081000	-0.909038000
C	0.358602000	3.653968000	-0.873844000
C	0.204453000	4.314824000	0.344360000
C	-0.064018000	3.576968000	1.497629000
C	-0.178340000	2.195748000	1.403239000
C	-0.229225000	-3.357780000	0.110315000
C	-0.331615000	-4.644647000	0.621126000
C	-0.548859000	-4.811259000	1.988526000
C	-0.665902000	-3.688904000	2.809600000
C	-0.567623000	-2.424591000	2.242953000
C	1.472480000	-0.120832000	2.724014000
C	-0.553017000	1.308763000	2.561992000
C	-0.766853000	-1.141704000	3.007336000
H	1.991430000	-0.935054000	-1.677466000
H	4.483100000	-1.068813000	-1.580464000
H	5.617793000	-0.718667000	0.637869000
H	4.209114000	-0.266008000	2.653075000
H	0.364192000	1.706723000	-1.828805000
H	0.567317000	4.193255000	-1.789641000
H	0.295575000	5.394120000	0.399281000
H	-0.187364000	4.059885000	2.460109000
H	-0.238142000	-5.491651000	-0.04739400
H	-0.623829000	-5.805426000	2.415239000
H	-0.833600000	-3.786587000	3.875707000
H	-0.059351000	-3.160337000	-0.94037900
H	1.615485000	-0.921221000	3.454617000
H	1.759119000	0.808713000	3.221827000

H	-1.641013000	1.216001000	2.590479000
H	-0.222236000	1.724908000	3.516958000
H	-1.823702000	-0.869060000	2.962306000
H	-0.488334000	-1.243239000	4.059300000
O	-0.259783000	-0.708332000	-1.32467100
O	-2.027938000	-0.191735000	0.556365000
C	-3.011770000	-0.605635000	-0.262127000
C	-4.357207000	-0.067475000	0.174164000
H	-4.558486000	-0.362584000	1.207304000
H	-4.341990000	1.025481000	0.137447000
H	-5.136347000	-0.452043000	-0.48333600
O	-2.840504000	-1.332665000	-1.21828700
C	1.454795000	0.988978000	-4.425369000
C	0.223041000	1.461285000	-4.678539000
C	-0.256604000	2.834301000	-5.095760000
C	0.762125000	3.967453000	-5.309209000
C	1.616944000	3.876993000	-6.593122000
C	2.244104000	2.515617000	-6.943264000
C	3.281060000	1.947766000	-5.963543000
C	2.780476000	1.714878000	-4.514928000
H	1.518340000	-0.069359000	-4.171304000
H	-0.595158000	0.745602000	-4.579126000
H	-0.986566000	3.163263000	-4.340942000
H	-0.852994000	2.711554000	-6.013404000
H	0.198890000	4.907849000	-5.358964000
H	1.398730000	4.062662000	-4.424903000
H	0.980112000	4.165412000	-7.440389000
H	2.405763000	4.639749000	-6.538235000
H	2.728618000	2.614281000	-7.923462000
H	1.444655000	1.778110000	-7.080105000
H	4.154828000	2.611764000	-5.920331000
H	3.641517000	0.993645000	-6.369587000
H	2.728950000	2.674342000	-3.994782000
H	3.538291000	1.130099000	-3.981157000

^{2}**TS**$_{ep}$

Fe	0.836574000	0.358761000	-0.031196000
N	2.518989000	1.115799000	-1.054977000
N	1.068726000	-1.158763000	-1.330152000
N	-0.088927000	1.501389000	-1.392269000
N	2.244415000	-0.509025000	1.087195000
C	0.337848000	-2.288074000	-1.279567000
C	0.591527000	-3.363509000	-2.117616000
C	1.644396000	-3.271042000	-3.028782000
C	2.401915000	-2.104742000	-3.070273000
C	2.085980000	-1.058645000	-2.204853000
C	-1.388162000	1.406801000	-1.712489000
C	-1.972207000	2.255970000	-2.644593000
C	-1.179171000	3.221681000	-3.262655000
C	0.171988000	3.310027000	-2.928845000
C	0.691197000	2.437804000	-1.977679000
C	2.015906000	-1.502736000	1.960565000
C	3.053216000	-2.099590000	2.666460000
C	4.357232000	-1.656547000	2.448314000
C	4.584126000	-0.624238000	1.539016000
C	3.500295000	-0.058961000	0.874547000
C	2.823567000	0.251824000	-2.242557000
C	2.119401000	2.486226000	-1.496103000
C	3.626991000	1.123268000	-0.052820000
H	-0.454684000	-2.303267000	-0.545271000
H	-0.022646000	-4.253133000	-2.046208000
H	1.874538000	-4.096648000	-3.693442000
H	3.229250000	-1.996000000	-3.762302000
H	-1.947592000	0.635217000	-1.200673000
H	-3.025319000	2.151619000	-2.876553000
H	-1.603522000	3.894439000	-4.000067000
H	0.819963000	4.043384000	-3.395175000
H	2.834029000	-2.897568000	3.365644000
H	5.189028000	-2.109946000	2.976582000
H	5.584715000	-0.255595000	1.344345000
H	0.982839000	-1.803004000	2.080839000
H	3.901640000	0.087804000	-2.319595000
H	2.524459000	0.787844000	-3.147993000
H	2.177060000	3.149926000	-0.631515000
H	2.795913000	2.866911000	-2.266509000
H	3.530060000	2.034999000	0.541790000
H	4.603807000	1.146913000	-0.543682000
O	-0.470501000	-0.241475000	0.737390000
O	0.965354000	1.924924000	1.075303000
C	0.427330000	1.941957000	2.259349000
C	0.587375000	3.241983000	3.028299000
H	1.148474000	3.043015000	3.945321000

H	1.107904000	3.990222000	2.431020000
H	-0.401355000	3.610464000	3.312976000
O	-0.179361000	0.988222000	2.755989000
C	-3.275249000	-1.748127000	-0.225498000
C	-2.806670000	-1.635841000	1.063081000
C	-3.206936000	-0.724449000	2.173682000
C	-4.376975000	0.257124000	2.008907000
C	-5.787006000	-0.374202000	1.979927000
C	-5.998391000	-1.616492000	1.096766000
C	-5.801554000	-1.446538000	-0.415494000
C	-4.382822000	-0.975540000	-0.867652000
H	-2.833538000	-2.540421000	-0.826538000
H	-2.041170000	-2.353953000	1.351077000
H	-2.293717000	-0.160865000	2.425361000
H	-3.369070000	-1.360941000	3.058825000
H	-4.339933000	0.941878000	2.864020000
H	-4.211197000	0.890110000	1.133013000
H	-6.050845000	-0.660258000	3.006218000
H	-6.504661000	0.404303000	1.689487000
H	-7.025015000	-1.968107000	1.256832000
H	-5.353465000	-2.429831000	1.454059000
H	-6.523532000	-0.723638000	-0.81335600
H	-6.013765000	-2.404916000	-0.90298700
H	-4.286705000	0.090541000	-0.64909700
H	-4.315491000	-1.088080000	-1.95348400

^{4}TS$_{ep}$

Fe	0.446785000	0.036067000	-0.123768000
N	-0.018965000	0.083054000	1.938127000
N	2.332448000	-0.140969000	0.594694000
N	0.509471000	2.021938000	0.185452000
N	0.228132000	-1.930304000	0.177426000
C	3.413007000	-0.286620000	-0.194637000
C	4.682723000	-0.484455000	0.327345000
C	4.837445000	-0.540632000	1.713375000
C	3.718181000	-0.386328000	2.524790000
C	2.473178000	-0.181901000	1.930244000
C	1.096575000	2.907828000	-0.632331000
C	1.098721000	4.269810000	-0.355102000
C	0.481891000	4.717771000	0.812050000
C	-0.115274000	3.790506000	1.665055000
C	-0.092153000	2.442443000	1.320218000
C	0.666644000	-2.882789000	-0.658528000
C	0.530756000	-4.233359000	-0.362395000
C	-0.070839000	-4.599750000	0.840896000
C	-0.517641000	-3.604836000	1.709033000
C	-0.358540000	-2.270776000	1.345708000
C	1.237437000	0.052337000	2.757692000
C	-0.756620000	1.365700000	2.139522000
C	-0.868679000	-1.120429000	2.176310000
H	3.225770000	-0.235732000	-1.258588000
H	5.526453000	-0.594884000	-0.343325000
H	5.815256000	-0.700548000	2.154891000
H	3.798816000	-0.418427000	3.605763000
H	1.567876000	2.497598000	-1.515522000
H	1.580327000	4.955419000	-1.041999000
H	0.472503000	5.773485000	1.061169000
H	-0.593042000	4.101171000	2.587346000
H	0.895591000	-4.974278000	-1.063628000
H	-0.184874000	-5.645699000	1.104740000
H	-0.982120000	-3.852661000	2.656683000
H	1.130929000	-2.535824000	-1.571502000
H	1.151175000	-0.710925000	3.535552000
H	1.343594000	1.010014000	3.275290000
H	-1.774513000	1.227684000	1.771922000
H	-0.803831000	1.631118000	3.199492000
H	-1.884376000	-0.879580000	1.855290000
H	-0.905670000	-1.373006000	3.239762000
O	0.931939000	0.031015000	-1.710796000
O	-1.446422000	0.260874000	-0.399021000
C	-2.248718000	-0.402041000	-1.196331000
C	-3.701075000	0.033343000	-1.051342000
H	-4.332528000	-0.527525000	-1.74082200
H	-4.042158000	-0.133354000	-0.02516900
H	-3.792120000	1.104024000	-1.255416000
O	-1.907955000	-1.274575000	-1.99145200
C	2.302225000	0.453834000	-4.028864000
C	1.059456000	-0.219750000	-3.953219000
C	-0.282094000	0.207242000	-4.407099000
C	-0.566298000	1.655773000	-4.823457000
C	-0.079790000	2.047870000	-6.238439000
C	1.316890000	1.570760000	-6.674446000

C	2.522366000	2.136023000	-5.913538000
C	2.534099000	1.875789000	-4.364719000
H	3.176991000	-0.167250000	-3.847391000
H	1.128054000	-1.278760000	-3.725417000
H	-0.967522000	-0.128040000	-3.61433400
H	-0.526006000	-0.488228000	-5.23148700
H	-1.653740000	1.783576000	-4.802452000
H	-0.186894000	2.343612000	-4.063326000
H	-0.795474000	1.640830000	-6.963282000
H	-0.138864000	3.139232000	-6.334560000
H	1.446124000	1.840300000	-7.729228000
H	1.354414000	0.473268000	-6.652861000
H	2.579452000	3.222800000	-6.037923000
H	3.440626000	1.714679000	-6.334945000
H	1.773608000	2.510965000	-3.907697000
H	3.510421000	2.180706000	-3.979987000

^{2}**P**

Fe	0.237196000	0.380817000	-0.131183000
N	-0.064365000	0.120620000	1.832829000
N	2.189163000	0.349919000	0.319073000
N	0.241799000	2.312386000	0.416644000
N	0.300391000	-1.628140000	-0.148574000
C	3.207759000	0.466329000	-0.554540000
C	4.531157000	0.403012000	-0.145409000
C	4.806881000	0.209573000	1.209499000
C	3.750405000	0.093172000	2.107792000
C	2.444361000	0.171601000	1.627848000
C	0.793004000	3.338915000	-0.249521000
C	0.741572000	4.640032000	0.235910000
C	0.115150000	4.874946000	1.459244000
C	-0.421630000	3.800131000	2.167768000
C	-0.340910000	2.525332000	1.618374000
C	0.837843000	-2.437151000	-1.074778000
C	0.845558000	-3.818251000	-0.934468000
C	0.287707000	-4.378953000	0.214044000
C	-0.245959000	-3.538139000	1.188832000
C	-0.224349000	-2.163266000	0.978439000
C	1.260794000	0.073572000	2.555168000
C	-0.884654000	1.290383000	2.284405000
C	-0.801858000	-1.175626000	1.958113000
H	2.933443000	0.623028000	-1.588953000
H	5.323221000	0.503829000	-0.877532000
H	5.831258000	0.151995000	1.561349000
H	3.926716000	-0.054888000	3.167211000
H	1.291558000	3.096835000	-1.178642000
H	1.192893000	5.442806000	-0.334503000
H	0.062238000	5.878420000	1.867484000
H	-0.888422000	3.941304000	3.135781000
H	1.286567000	-4.432164000	-1.710399000
H	0.281459000	-5.454116000	0.356622000
H	-0.669123000	-3.935107000	2.104354000
H	1.276333000	-1.962100000	-1.940333000
H	1.319756000	-0.851105000	3.134715000
H	1.300699000	0.895051000	3.275143000
H	-1.911064000	1.124546000	1.954275000
H	-0.877512000	1.371290000	3.374720000
H	-1.848003000	-0.987481000	1.710234000
H	-0.760578000	-1.550499000	2.984279000
O	0.640275000	0.791204000	-2.095778000
O	-1.645450000	0.465986000	-0.334104000
C	-2.457701000	-0.221889000	-1.118776000
C	-3.911586000	0.179499000	-0.949415000
H	-4.233025000	-0.011422000	0.078952000
H	-4.026527000	1.251729000	-1.132098000
H	-4.540065000	-0.383478000	-1.63948700
O	-2.100162000	-1.094404000	-1.90179300
C	0.424311000	0.055245000	-3.375409000
C	-0.253103000	1.344990000	-3.157978000
C	0.042776000	2.706122000	-3.753403000
C	1.346932000	2.936560000	-4.531804000
C	1.327511000	2.425989000	-5.993805000
C	0.671463000	1.060861000	-6.272330000
C	1.389532000	-0.182233000	-5.724825000
C	1.664543000	-0.179041000	-4.207098000
H	-0.224961000	-0.804443000	-3.22773300
H	-1.291433000	1.250197000	-2.853911000
H	-0.051534000	3.437115000	-2.942821000
H	-0.813422000	2.914397000	-4.409168000
H	1.520464000	4.017804000	-4.563784000
H	2.195758000	2.530177000	-3.974481000
H	0.785103000	3.167926000	-6.593316000

H	2.355656000	2.421889000	-6.377994000
H	0.597947000	0.943734000	-7.360219000
H	-0.366962000	1.073238000	-5.917355000
H	2.356565000	-0.300265000	-6.228054000
H	0.799113000	-1.069899000	-5.982598000
H	2.417948000	0.571860000	-3.966018000
H	2.092127000	-1.148727000	-3.927267000

^{4}P

Fe	0.243346000	0.152116000	-0.066432000
N	-0.078728000	-0.049293000	2.130587000
N	2.190214000	0.134889000	0.536376000
N	0.190102000	2.120735000	0.542716000
N	0.276853000	-1.889727000	0.149205000
C	3.224901000	0.206067000	-0.325869000
C	4.541957000	0.160999000	0.103347000
C	4.797095000	0.034400000	1.469688000
C	3.725627000	-0.034760000	2.352988000
C	2.422357000	0.022057000	1.857665000
C	0.702040000	3.148196000	-0.154627000
C	0.600604000	4.460036000	0.291399000
C	-0.034920000	4.705452000	1.508032000
C	-0.531700000	3.631101000	2.243982000
C	-0.406681000	2.342112000	1.732806000
C	0.760256000	-2.745038000	-0.768688000
C	0.762464000	-4.118032000	-0.566717000
C	0.253860000	-4.619233000	0.631069000
C	-0.233422000	-3.729135000	1.584877000
C	-0.213504000	-2.363132000	1.314934000
C	1.244626000	-0.016118000	2.809087000
C	-0.924810000	1.123632000	2.459346000
C	-0.774667000	-1.346630000	2.282081000
H	2.969766000	0.308418000	-1.372291000
H	5.342913000	0.222285000	-0.623454000
H	5.815434000	-0.008366000	1.840604000
H	3.884831000	-0.129175000	3.421434000
H	1.206819000	2.898331000	-1.078657000
H	1.022200000	5.261963000	-0.302588000
H	-0.125604000	5.717042000	1.888819000
H	-1.005458000	3.780734000	3.207552000
H	1.160604000	-4.770329000	-1.334430000
H	0.245711000	-5.686529000	0.824086000
H	-0.626160000	-4.079703000	2.532497000
H	1.151748000	-2.316095000	-1.680826000
H	1.344470000	-0.883335000	3.468587000
H	1.296302000	0.864679000	3.456653000
H	-1.939924000	0.913165000	2.114067000
H	-0.964138000	1.302393000	3.538886000
H	-1.832506000	-1.192907000	2.053796000
H	-0.714503000	-1.717548000	3.310692000
O	0.747024000	0.670016000	-2.118630000
O	-1.616417000	0.224142000	-0.342688000
C	-2.325875000	-0.564631000	-1.141532000
C	-3.820097000	-0.394502000	-0.959680000
H	-4.103294000	-0.652788000	0.065015000
H	-4.097345000	0.650956000	-1.121539000
H	-4.355480000	-1.033066000	-1.66214400
O	-1.830578000	-1.331006000	-1.95661200
C	0.724049000	-0.084698000	-3.400732000
C	-0.081406000	1.141004000	-3.262774000
C	0.160015000	2.525247000	-3.832267000
C	1.486684000	2.845442000	-4.538183000
C	1.599539000	2.311988000	-5.986913000
C	1.108189000	0.881045000	-6.273654000
C	1.908853000	-0.270864000	-5.646227000
C	2.050079000	-0.218845000	-4.111294000
H	0.144631000	-1.000688000	-3.303070000
H	-1.132908000	0.956699000	-3.055870000
H	-0.014643000	3.237144000	-3.017102000
H	-0.671090000	2.694219000	-4.530089000
H	1.573681000	3.936823000	-4.583620000
H	2.329781000	2.519900000	-3.922445000
H	1.016947000	2.983524000	-6.630393000
H	2.642570000	2.411574000	-6.314464000
H	1.122737000	0.737470000	-7.360832000
H	0.051915000	0.792399000	-5.988856000
H	2.920803000	-0.290308000	-6.068117000
H	1.438753000	-1.219473000	-5.933066000
H	2.705852000	0.603736000	-3.823374000
H	2.531535000	-1.140181000	-3.764301000

References

1. Lim, M.H. et al. *Proc. Natl. Acad. Sci. USA.* **100**, 3665-3670 (2003).

2. Chen, H., Yai, W., Lao, J. & Shaik, S. *J Chem. Theory Comput.* **7**, 3049-3053 (2011)

3. Zimmermann, R.; Huynh, B.H.; Münck, E.; Lipscomb, J.D. *J. Chem. Phys.* **69**, 5463-5467 (1978).

Chapter VII – Characterization of a High-Spin Nonheme Fe^{III}-OOH Intermediate and Its Quantitative Conversion to an Fe^{IV}=O Complex

Published: Li, F.; **Meier, K.K.**; Cranswick, M.A.; Chakrabarti, M.; Van Heuvelen, K.M.; Münck, E.; Que, Jr., L. "Characterization of a High-Spin Non-Heme Fe^{III}-OOH Intermediate and Its Quantitative Conversion to an Fe^{IV}=O Complex." *J. Am. Chem. Soc.* 2011, 133, pp 7256-7259.

Author Contributions: F.L., K.K.M., M.A.C., M.C., K.M.V.H., E.M., and L.Q. conceived and designed the experiments. F.L., K.K.M., M.A.C., M.C., and K.M.V.H. performed the experiments. F.L., K.K.M., M.A.C., M.C., K.M.V.H., E.M., and L.Q. analyzed the data. K.K.M. performed DFT calculations with the help of Emile Bominaar. All authors participated in the writing of the paper.

Abstract

We have generated a high-spin Fe^{III}–OOH complex supported by tetramethylcyclam via protonation of its conjugate base and characterized it in detail by various spectroscopic methods. This Fe^{III}–OOH species converts quantitatively to an Fe^{IV}=O complex via O–O bond cleavage, which represents the first example of such a conversion. This conversion is promoted by two factors: the strong Fe^{III}–OOH bond that inhibits Fe–O bond lysis and the addition of protons that facilitate O–O bond cleavage. This example provides a synthetic precedent for how O–O bond cleavage of iron(III)-peroxo intermediates of nonheme iron enzymes may be promoted.

Introduction

Cleavage of the O–O bond of iron(III)-hydroperoxo (Fe^{III}–OOH) species is a key step in the O_2 activation mechanisms of cytochrome P450,[1] Rieske dioxygenases,[2] and even methane monooxygenase (MMO),[3] leading to high-valent iron-oxo species that effect organic substrate oxidation. On the other hand, Fe–O bond cleavage must occur to release H_2O_2 in the catalytic cycle of superoxide reductase (SOR)[4] and for cytochrome P450 reactions that exhibit uncoupling.[1] While protonation of the proximal O atom of the Fe^{III}–OOH unit can be readily envisioned as the step needed to release H_2O_2, the mechanism for O–O bond cleavage is not as simple. For heme peroxidases and cytochrome P450, it is generally accepted that protonation of the distal O atom of the low-spin Fe^{III}–OOH intermediate facilitates the heterolysis of the O–O bond.[1] This notion should also apply to nonheme iron systems, but the likely *high-spin* state of iron-peroxo species in nonheme enzymes could raise the barrier for O–O bond lysis relative to that for *low-spin* counterparts in heme enzymes.[5] The scarcity of experimental evidence further limits insights into O–O bond scission by nonheme enzymes. The only mechanistically relevant information available is for MMO, where the conversion of the peroxodiiron(III) intermediate to the diiron(IV) oxidant exhibits a pH dependence and a H/D solvent kinetic isotope effect;[3] emphasizing the key role played by a proton in O–O bond cleavage. Among synthetic complexes, there are only a few nonheme Fe^{III}–OOH complexes that are spectroscopically well characterized,[6,7] but none of them have been directly observed to generate a high-valent iron-oxo intermediate, thus making it difficult to obtain mechanistic insights into this key step in iron-catalyzed oxygen activation.

To obtain the first example of a Fe^{III}–OOH complex that can undergo O–O bond cleavage to generate a high-valent iron-oxo complex, we have focused on trapping $[Fe^{III}(TMC)(OOH)]^{2+}$ (**2**; see Scheme 1A for a structure of TMC), a yet elusive species invoked in the reactions of O_2 with $[Fe^{II}(TMC)(CH_3CN)]^{2+}$ that afford $[Fe^{IV}(O)(TMC)(CH_3CN)]^{2+}$ (**3**) in 60-80% yield as the final product.[8] Herein we report the high-yield generation of **2** by protonation of the previously reported $[Fe^{III}(TMC)(O_2)]^{+}$ complex (**1**)[9] at –40 °C, its detailed spectroscopic characterization, and kinetic studies that shed mechanistic light on the quantitative conversion of **2** to **3** (Scheme 1B).

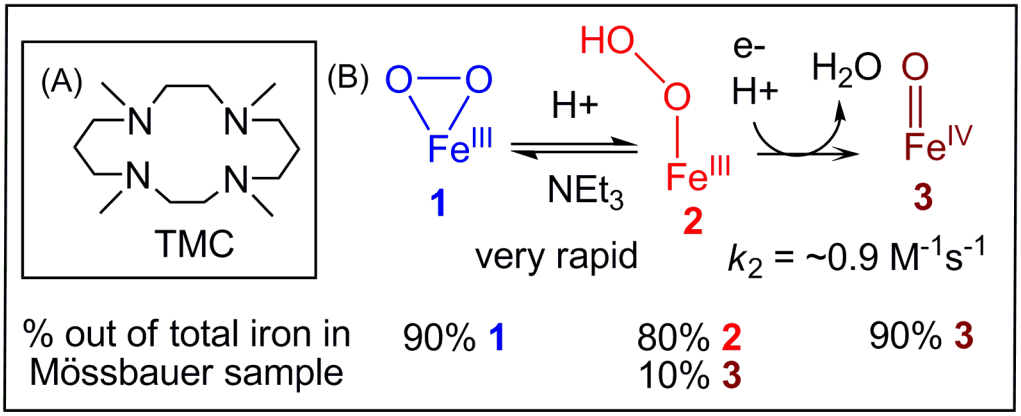

Scheme 1. (A) **TMC ligand used in this study.** (B) **Conversion of** 1 **to** 2 **and then to** 3.

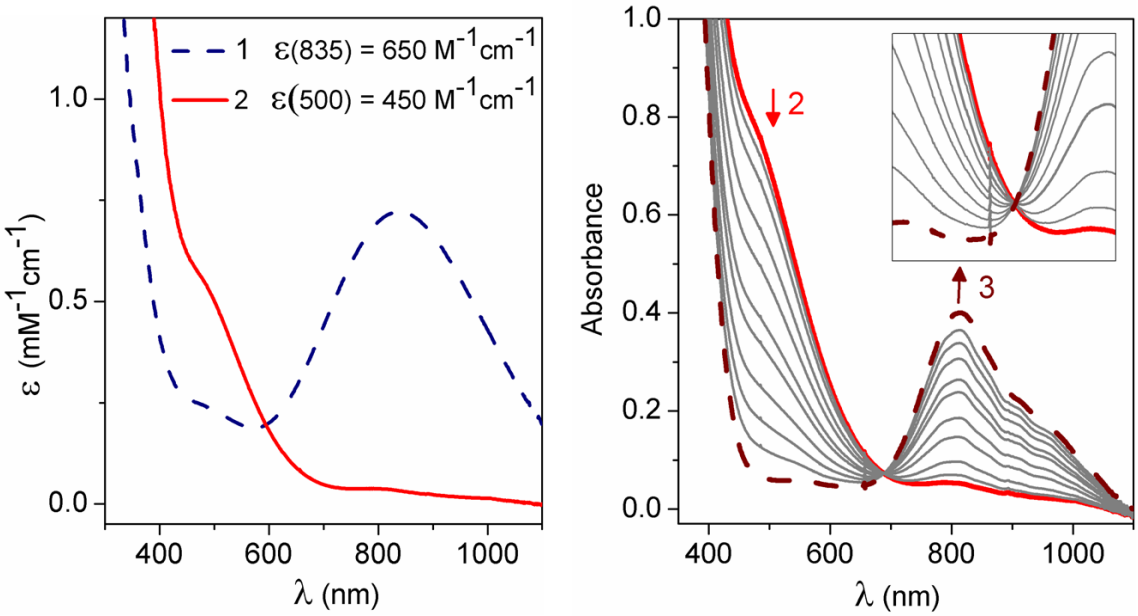

Figure 1. Left: UV-visible absorption spectra of $[Fe^{III}(TMC)(O_2)]^+$ (1) (blue dashed line) and $[Fe^{III}(TMC)(OOH)]^{2+}$ (2) (red solid line) in CH_3CN. Right: UV-visible absorption spectra during the conversion of 2 (red solid line) to $[Fe^{IV}(O)(TMC)(CH_3CN)]^{2+}$ (3) (brown dashed line) via the addition of *ca.* 20 equiv. $HClO_4$ in CH_3CN at –40 ºC. *b* = 1 cm. Inset: Close-up view to show the isosbestic point at ~695 nm.

Results and Discussion

Complex **1** was generated using the published procedure[7] by treating 2.0 mM $[Fe^{II}(TMC)(CH_3CN)]^{2+}$ in CH_3CN with 10 equiv. NEt_3 followed by 20 equiv. H_2O_2 in CH_3CN at –40 °C. Complex **1** exhibits a λ_{max} of 835 nm (Figure 1 left panel) with an ε value of 650 M^{-1} cm^{-1}, established with the aid of Mössbauer data (*vide infra).* Upon addition of 20 equiv. $HClO_4$ at –40 ºC, **1** converted immediately to a short-lived ($t_{1/2}$ ~ 1 min) maroon intermediate (**2**) with a shoulder-like absorption feature at ~500 nm (ε = 450 $M^{-1}cm^{-1}$), which in turn decayed to give the signature absorption feature of **3** (Figure 1). The significant blue shift observed in the conversion of **1** to **2** has been noted previously in the protonation of other nonheme $Fe^{III}(\eta^2\text{-}O_2)$ species, consistent with the weaker basicity of the hydroperoxo monoanion compared to the peroxo dianion.[6a-b] The conversion between **1** and **2** is reversible. Addition of excess NEt_3 to the solution of **2** instantly results in the near-quantitative regeneration of **1**, as shown by its characteristic absorption band. This cycle can be repeated several times (see Figure S1). These results further underscore that **2** is the conjugate acid of **1** and can be formulated as $[Fe^{III}(TMC)(OOH)]^{2+}$.

The Mössbauer samples of **1**, **2** and **3** contain large fractions of the designated complexes. At least 90% of total Fe in Figure 2A belongs to **1**, while 80% of the Fe in Figure 2B can be assigned to **2** with 10% of the iron belonging to Fe^{IV}=O complex **3**. Analysis of a sample of **2** that was allowed to decay for 5 min after addition of $HClO_4$ shows that >90% of the total Fe corresponds to **3**. Thus, the overall conversion of **1** to **3** is essentially quantitative.

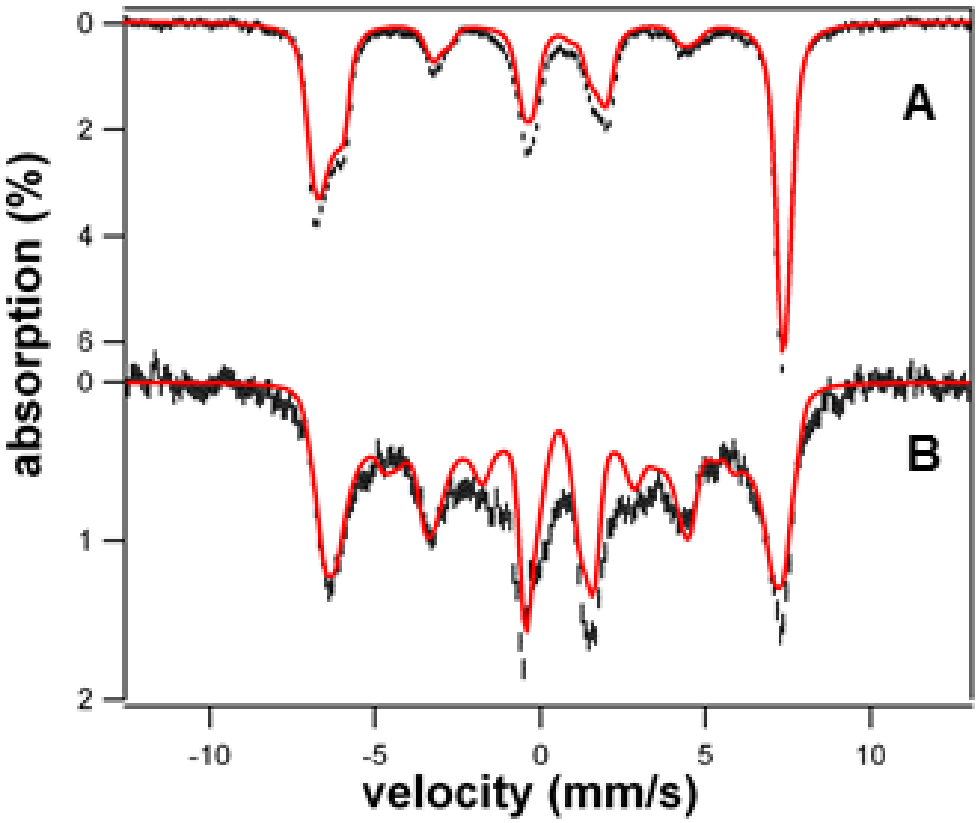

Figure 2. 4.2 K Mössbauer spectra of 1 and 2 in 3:1 PrCN/MeCN (v/v) recorded in parallel applied fields (black lines) and simulations (red lines); simulation parameters and comments are given in Table S1 and Supporting Information. (A) 8.0 T spectrum of 1; same batch as used for EPR shown in Fig. 3A. (B) 1.2 T spectrum of 2. The red line is a spectral simulation, assuming slow relaxation of the electronic system. 10% of 3 was removed from the data. Approximately 80% of the Fe in the sample belongs to 2.

The electronic structures of **1** and **2** were established by EPR and Mössbauer spectroscopy. Both complexes are high-spin Fe^{III} with quite different zero field splitting (ZFS) parameters and isomer shifts (Tables S1). We have analyzed the data with the S = 5/2 spin Hamiltonian, eq 1, where D and E are the axial and rhombic ZFS parameters, A is the ^{57}Fe magnetic hyperfine tensor and H_Q describes the nuclear quadrupole interactions.

$$\mathcal{H} = D(S_z^2 - 35/4) + E(S_x^2 - S_y^2) + \beta \boldsymbol{S} \cdot \boldsymbol{g} \cdot \boldsymbol{B} + \boldsymbol{S} \cdot \boldsymbol{A} \cdot \boldsymbol{I} - g_n \beta_n \boldsymbol{B} \cdot \boldsymbol{I} + \mathcal{H}_Q \quad \textbf{(1)}$$

The X-band EPR spectrum of **1** exhibits, for the middle Kramers doublet, signals at g_{eff} = 4.58, 4.38, and ≈ 4.1 (Figures 3A and S4–7). Mössbauer analysis (details in Supporting Information) shows that $D \approx -0.9$ cm^{-1} and E/D = 0.28(1). With E/D fixed, the explanation of the EPR features of **1** requires inclusion of substantial fourth-order ZFS parameters, eq 2.

$$H_{4th} = \frac{F}{180}[35S_z^4 - 30S(S+1)S_z^2 + 25S_z^2 - 6S(S+1) - 3S^2(S+1)^2] + \frac{a}{6}[S_x^4 + S_y^4 + S_z^4 - \frac{1}{5}S(S+1)(3S^2 + 3S - 1)] \quad (2)$$

For the simulation of Figure 3A, we used $F = -0.108$ cm^{-1} and $a = -0.017$ cm^{-1}. Large fourth-order parameters, namely a = 0.074 cm^{-1} and F = 0.043 cm^{-1}, have been reported for Fe superoxide dismutase-azide,[10] together with D = 0.46 cm^{-1} and E/D = 0.255. An 8.0 T Mössbauer spectrum of **1** together with a spectral simulation is shown in Figure 2A (see Figure S2–3 for additional spectra). The shoulder on the low energy feature (at ~ –6 mm/s Doppler velocity) and the fairly sharp high-energy line show that the ^{57}Fe A-tensor is anisotropic. The spectrum shown gives a value for the isomer shift of **1**, δ = 0.58 mm/s, similar to that of the side-on peroxo complex $[Fe^{III}(N4Py)(\eta^2\text{-}O_2)]^+$ (δ = 0.61 mm/s).[6b] See SI for additional details of the spectral analysis.

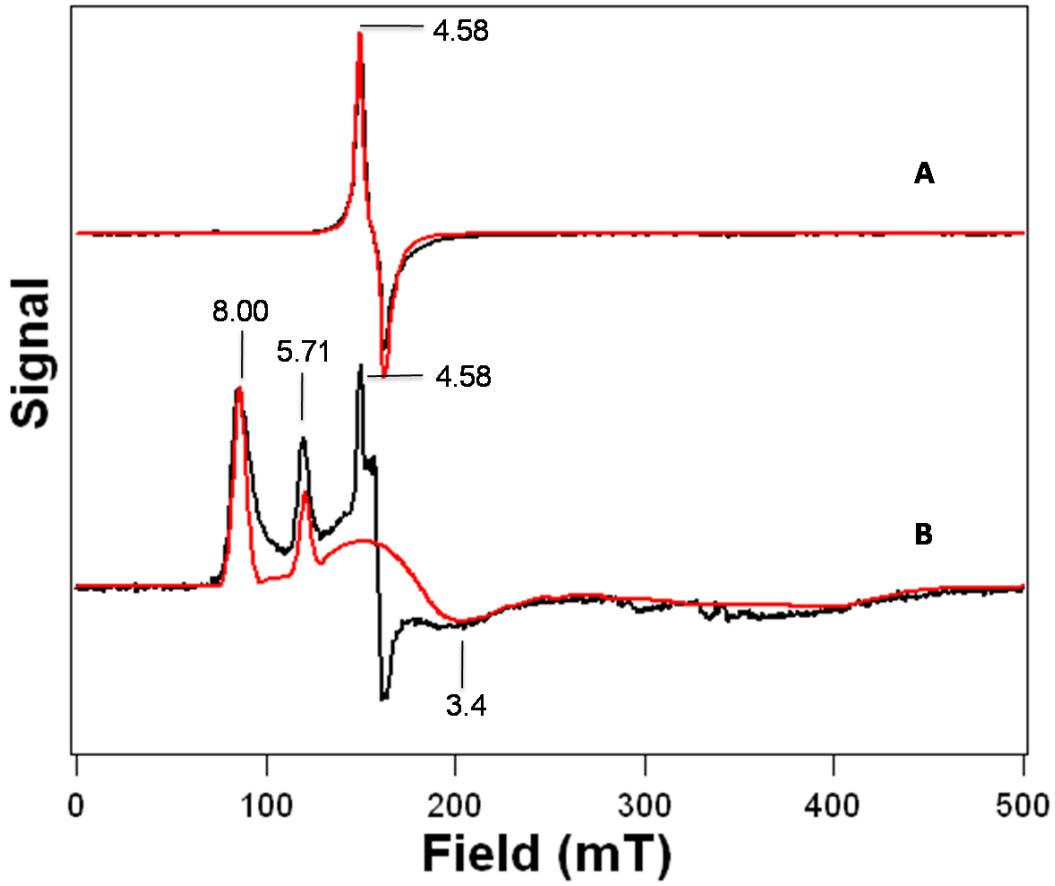

Figure 3. **X-band EPR spectra of** 1 **and** 2 **in 3:1 PrCN/MeCN (v/v) shown in black lines** (A) **Complex** 1**. T = 15 K, microwave power, 0.02 mW, 1 mT modulation. The red line is a simulation using** D **= –0.91 cm^{-1},** E/D **= 0.28, fourth-order parameters** F **= –0.108 cm^{-1} and** a **= –0.017 cm^{-1} (see Supporting Information),** g **= (2.04, 1.98, 2.03) and distributed** E/D **with** $\sigma_{E/D}$ **= 0.038.** (B) **Complex** 2**. T = 10 K, microwave power, 2.0 mW, 1 mT modulation. The red line is a simulation using** D **= 2.5 cm^{-1},** E/D **= 0.097,** g **= (2.00, 2.00, 2.00), and** $\sigma_{E/D}$ **= 0.02. The sharp features at** g_{eff} **= 4.58 and 4.36 represent remaining** 1**, corresponding to (only) 1% of total Fe.**

Analysis of the Mössbauer spectra of **2** shown in Figures 2B and S8 yielded D = +2.5 cm^{-1}, E/D = 0.097(7) and δ = 0.51 mm/s. The EPR spectrum of **2** exhibits signals at g_{eff} = 8.00 (ground doublet), 5.71 (middle) and 3.4 (ground), consistent with the above D and E/D values (Figure 3B). The parameters used for the simulations of **1** and **2** are listed in Table S1.

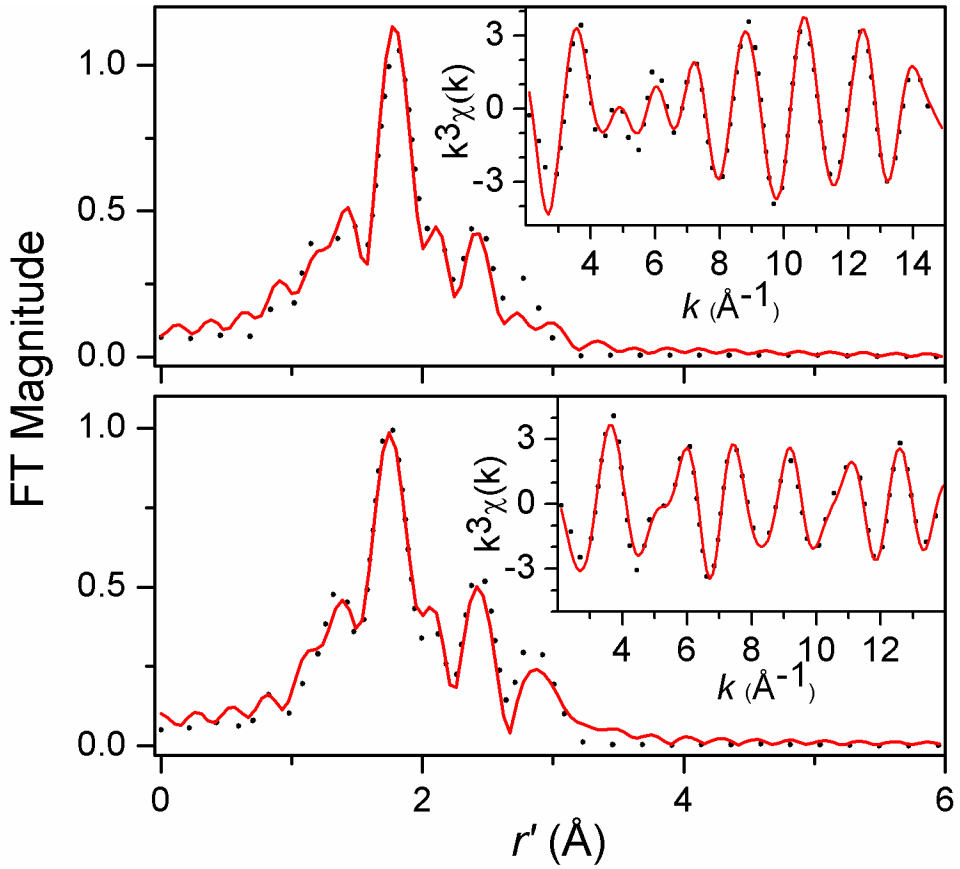

Figure 4. Top: Fourier transform of Fe K-edge EXAFS of 1 (dotted line) over a k-range of 2-15 Å-1 and a back-transformation range of 0.3–3.0 Å-1. Inset: Fourier-filtered k3χ(k) EXAFS data (dotted line). Solid lines represent fit 9 in Table S2. Bottom: Fourier transform of Fe K-edge EXAFS of 2 (dotted line) over a k-range of 2-14 Å-1 and a back-transformation range of 0.3–3.2 Å-1. Inset: Fourier-filtered k3χ(k) EXAFS data (dotted line). Solid lines represent fit 9 in Table S3.

We also carried out Fe K-edge X-ray absorption spectroscopic (XAS) studies to obtain structural information and metric parameters for both **1** and **2** (Figure 4, Tables S1–3). The EXAFS spectrum of **1** is best fit by two N/O scatterers at 1.93 Å and four N/O scatterers at 2.20 Å, while the best fit for **2** consists of one N/O scatterer at 1.92 Å and four N/O scatterers at 2.15 Å. Interchanging the number of O scatterers in the best fits of **1** and **2** significantly worsened the overall fit quality for both complexes with unacceptable Debye-Waller factors for the O sub-shell in both cases (Tables S2–3). These results lead to the respective assignments of an η^2-binding mode to the dianionic

peroxo ligand in **1** and an η^1-binding mode to the monoanionic hydroperoxo ligand of **2**. This conclusion is supported by the observed 0.05-Å decrease in the average Fe-NTMC distance from **1** to **2**.[11]

Resonance Raman studies of **1** and **2** provide additional insight into how the difference in binding mode affects the two high-spin iron(III)-peroxo units. Resonance enhanced vibrations are found for **1** at 826 and 493 cm^{-1} and for **2** at 870 and 676 cm^{-1} (Figures 5, S9). These features can be assigned respectively to ν(O–O) and ν(Fe–O) modes on the basis of downshifts observed upon ^{18}O-labeling, which conform to predictions for diatomic harmonic oscillators by Hooke's Law.[12] The observed vibrational modes compare favorably to those reported for related complexes (Tables 1 and S4). The sole exception is the ν(Fe–O) of **2** at 676 cm^{-1}, which lies above the range of ν(Fe–O) values (420–620 cm^{-1}) found for other high-spin Fe^{III}–OOH complexes studied thus far (Tables 1). We speculate that the high ν(Fe–O) value for **2** may reflect the weaker electron donating ability of the presumed CH_3CN ligand trans to the hydroperoxo unit relative to those of the other complexes in Table 1. The stronger Fe–O bond suggested by the high ν(Fe–O) value for **2** is also likely to be an important factor that contributes to the observed cleavage of its O–O bond. In contrast, the Fe^{III}–OOH units of oxyhemerythrin[13] (oxyHr) and superoxide reductase (SOR),[14] with ν(Fe–O) values that are at least 100 cm^{-1} smaller, undergo Fe–O bond cleavage in the course of their respective functions.

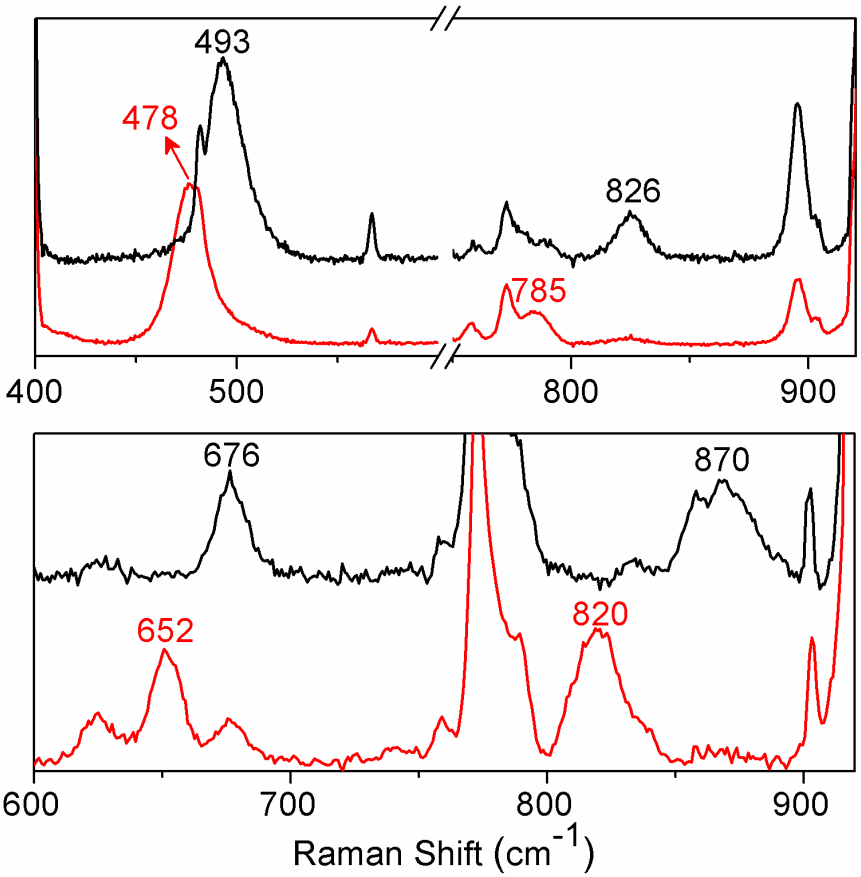

Figure 5. Top: resonance Raman spectra of 1 prepared with H_2O_2 (black line) or $H_2{}^{18}O_2$ (red line) and obtained with λ_{exc} = 647.1 nm. Bottom: resonance Raman spectra of 2 prepared with H_2O_2 (black line) or $H_2{}^{18}O_2$ (red line) and obtained with λ_{exc} = 514.5 nm.

Table 1. Vibrational frequencies of high-spin Monoiron(III)-η^1-hydroperoxo species.
[a] this work; H_2bppa = bis(6-pivalamido-2-pyridyl-methyl)(2-pyridyl- methyl)amine; oxyHr = oxyhemerythrin; SOR = superoxide reductase; cyclam-PrS-H = 1-(3'-mercaptopropyl)-1,4,8,11-tetraazacyclotetradecane.

	ν(Fe–O), cm^{-1} (Δ^{18}O)	ν(O–O), cm^{-1} (Δ^{18}O)	ref
2	676 (-24)	870 (-50)	[a]
[Fe(H_2bppa)(OOH)]$^{2+}$	621 (-22)	830 (-17)	7a
E114A SOR	567 (-4)[b]	838 (-23)[b]	14
oxyHr	503 (-24)	844 (-48)	13
[Fe(cyclam-PrS)(OOH)]$^{+}$	419 (-19)	891 (-35)	7b

After its formation from **1**, **2** quickly decayed and underwent O–O bond cleavage to form $[Fe^{IV}(O)(TMC)(CH_3CN)]^{2+}$ (**3**)[15] in essentially quantitative yield (*vide supra*). The decay of **2** (monitored at 500 nm) occurred concomitantly with the appearance of **3** (monitored at 820 nm), with an isosbestic point at ~695 nm (Figure 1 right panel). The time courses of the absorbance changes at both 500 and 820 nm could be fit with a simple first-order kinetic model (Figure 6 left panel), affording rate constants (k_{obs}) that were found to be identical within experimental error. The temperature dependence of the k_{obs} values was determined between –40 ºC to –20 ºC (Figure S10) and gave rise to an Eyring plot with activation parameters of $\Delta H^{\ddagger} = 44(2)$ kJ/mol and $\Delta S^{\ddagger} = -90(10)$ J/mol•T. These parameters are quite distinct from those determined for the reaction of $[Fe^{II}(TMC)(CH_3CN)]^{2+}$ with H_2O_2 in CH_3CN in the presence of 2,6-lutidine to form **3** ($\Delta H^{\ddagger} = 29(2)$ kJ/mol and $\Delta S^{\ddagger} = -144(10)$ J/mol•T), which involves a direct Fe^{II}/Fe^{IV}=O conversion.[16] On the other hand, the intermediacy of the Fe^{III}–OOH complex **2** has been postulated in the reactions of $[Fe^{II}(TMC)(NCCH_3)]^{2+}$ with O_2 in the presence of an H-atom donor or its equivalent that afford **3** as the final product, but **2** has been elusive in these reactions.[8] Our results thus provide the first direct evidence to support this hypothesis.

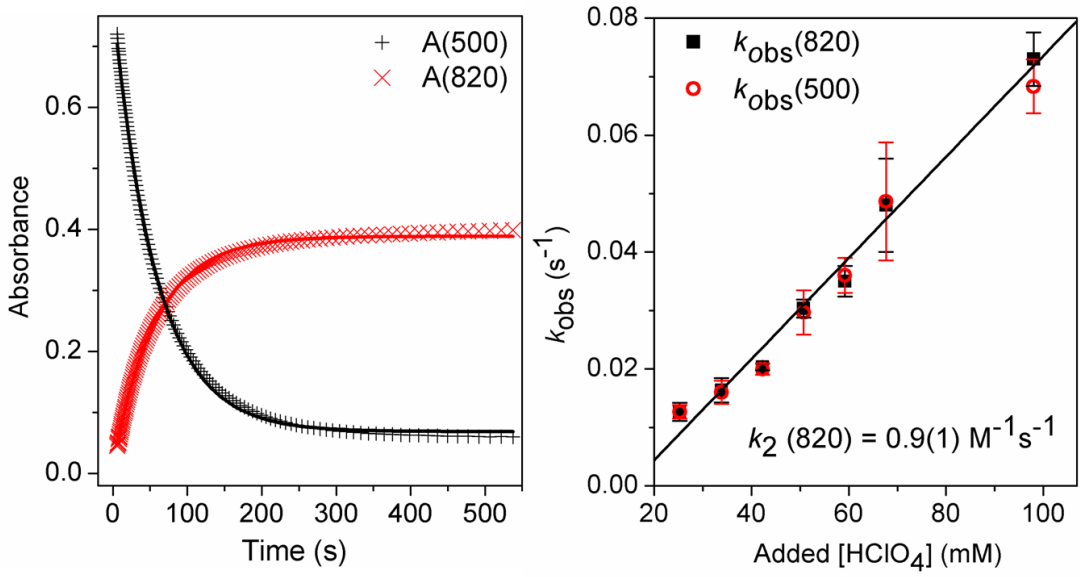

Figure 6. Left: Plots of absorbance at 500 nm and 820 nm vs. time for the conversion of **2** to **3**. Solid lines represent fits of reaction progress (absorbance at 500 nm and 820 nm) against time to typical first-order rate equations. Experimental conditions: 1.5 mM **2**, 34 mM $HClO_4$, –40 °C, in CH_3CN. **Right:** Plot of k_{obs}(820) and k_{obs}(500) vs. added [$HClO_4$] for the conversion of **2** to **3**. Experimental conditions: 1.5 mM **2**, –40 °C, in CH_3CN. The black line is a linear fit for k_{obs}(820). See Supporting Information for additional experimental details.

This first unequivocal example of converting a high-spin Fe^{III}–OOH species to an Fe^{IV}=O complex provides an opportunity to discern what factors promote O–O bond cleavage in such species. Importantly, the conversion of **2** to **3** is found to be *proton-dependent*. As shown in Figure 6 right panel, the values for both k_{obs}(500) and k_{obs}(820) increase linearly with [$HClO_4$] added, and a second-order rate constant k_2 of 0.9(1) $M^{-1}s^{-1}$ at –40 °C can be extracted from the slope of this plot. Also of significance is the observation that the quantitative yield of **3** from **1** is not affected even at the highest amounts of acid added, indicating that the added protons do not lead to Fe–O bond cleavage in **2** to release H_2O_2. The observed proton dependence in the formation of **3** strongly suggests that a proton promotes O–O bond cleavage.

Proton-assisted O–O bond cleavage has generally been associated with O–O bond heterolysis,[1,17,18] as protonation of the terminal oxygen atom of the Fe–OOH moiety converts hydroxide into a much better leaving group. Indeed this is the generally accepted mechanism for the generation of the high-valent iron-oxo intermediate Compound I in heme enzymes.[1,17] Protons also promote the conversion of the peroxo intermediate of MMO into the corresponding diiron(IV) oxidant **Q**.[3] In model systems, it has been demonstrated that acid facilitates O–O bond heterolysis for the conversion of acylperoxoiron(III) porphyrin complexes to oxoiron(IV) porphyrin cation radical species.[18] Proton-assisted O–O bond heterolysis of Fe^{III}–OOH intermediates to generate Fe^{V}=O oxidants is also proposed in the mechanisms of nonheme iron catalysts that use H_2O_2 as oxidant to carry out C–H hydroxylation, C=C epoxidation and *cis*-dihydroxylation, and aromatic ring hydroxylation.[19] The fact that many of the oxidations are highly stereoselective argues against the involvement of HO• species that would be produced from O–O bond homolysis.[19] Indeed a EPR signal that could be assigned to Fe^{V} oxidant has been reported.[20] On the other hand, DFT calculations of Solomon and co-workers reveal a very significant barrier for O–O bond homolysis of high-spin Fe^{III}–OOH(R) species.[5] Taken together, the points presented above and our observed proton dependence for the conversion of **2** into **3** lead us to favor a heterolytic cleavage mechanism that would initially afford a formally Fe^{V}=O species. Unfortunately, our attempts to intercept the putative Fe^{V}=O species have not been successful. It is perhaps not surprising for the putative $[Fe^{V}(O)(TMC)]^{3+}$ species to have such a short lifetime due to the neutral nature of the TMC ligand, and it must be rapidly reduced by one of several possible reductants present in the reaction mixture such as H_2O_2, NEt_3, or even the

CH_3CN solvent to afford **3** that is experimentally observed (Scheme 1B). Indeed the only well characterized Fe^{V}=O complex to date is supported by a tetraanionic macrocyclic ligand that significantly extends the lifetime of the Fe^{V}=O unit.[21]

Conclusions

In summary, we report here the first example of a synthetic high-spin Fe^{III}–OOH complex that quantitatively converts to an oxoiron(IV) complex via O–O bond cleavage. This transformation is promoted by two factors: a) the stronger Fe–O bond found for **2** as indicated by its high Raman frequency, which appears to prevent Fe–O bond scission even in the presence of 0.1 M $HClO_4$, and b) the key role of protons. Irrespective of the precise nature of the cleavage mechanism, the conversion of **2** to **3** demonstrates that O–O bond cleavage can indeed occur readily at a high-spin iron(III) center, even at –40 °C. This example thus serves as a synthetic precedent for the proton-assisted conversion of high-spin Fe^{III}–OOH intermediates to high-valent iron-oxo oxidants in the proposed mechanisms of dioxygen-activating nonheme enzymes such as the *cis*-dihydroxylating Rieske dioxygenases[2] and bacterial multi-component monooxygenases like MMO[3] and toluene monooxygenase.[22]

Acknowledgements

We are grateful for support provided by NIH grants GM-33162 and GM-38767 (L.Q.) and EB-001475 (E.M.), NIH postdoctoral fellowships ES017390 (M.A.C.) and GM093479 (K.V.H.), and a University of Minnesota Doctoral Dissertation Fellowship (F. L.). We are indebted to Dr. Erik R. Farquhar for helpful guidance and discussion on the XAS analysis of **1** and **2** and to Dr. Jason England for insightful discussions.

References

1. (a) Denisov, I. G.; Makris, T. M.; Sligar, S. G.; Schlichting, I. *Chem. Rev.* **2005**, *105*, 2253-2278. (b) Sligar, S. G.; Makris, T. M.; Denisov, I. G. *Biochem. Biophys. Res. Commun.* **2005**, *338*, 346-354. (c) Watanabe, Y.; Nakajima, H.; Ueno, T. *Acc. Chem. Res.* **2007**, *40*, 554-562.

2. (a) Kovaleva, E. G.; Neibergall, M. B.; Chakrabarty, S.; Lipscomb, J. D. *Acc. Chem. Res.* **2007**, *40*, 475-483. (b) Neibergall, M. B.; Stubna, A.; Mekmouche, Y.; Münck, E.; Lipscomb, J. D. *Biochemistry* **2007**, *46*, 8004-8016.

3. (a) Lee, S.-K.; Lipscomb, J. D. *Biochemistry* **1999**, *38*, 4423-4432. (b) Tinberg, C. E.; Lippard, S. J. *Biochemistry* **2009**, *48*, 2145-12158.

4. (a) Kurtz Jr, D. M., *J. Inorg. Biochem.* **2006,** *100*, 679-693. (b) Kovacs, J. A.; Brines, L. M. *Acc. Chem. Res.* **2007**, *40*, 501-509.

5. (a) Solomon, E. I.; Decker, A.; Lehnert, N. *Proc. Nat. Acad. Sci. USA* **2003,** 100, 3589-3594. (b) Lehnert, N.; Ho, R. Y. N.; Que, L., Jr.; Solomon, E. I. *J. Am. Chem. Soc.* **2001**, *123*, 12802-12816.

6. Low-spin Fe^{III}–OOH complexes: (a) Simaan, A. J.; Döpner, S.; Banse, F.; Bourcier, S.; Bouchoux, G.; Boussac, A.; Hildebrandt, P.; Girerd, J.-J. *Eur. J. Inorg. Chem.* **2000**, 1627-1633. (b) Roelfes, G.; Vrajmasu, V.; Chen, K.; Ho, R. Y. N.; Rohde, J.-U.; Zondervan, C.; la Crois, R. M.; Schudde, E. P.; Lutz, M.; Spek, A. L.; Hage, R.; Feringa, B. L.; Münck, E.; Que, L., Jr. *Inorg. Chem.* **2003**, *42*, 2639-2653. (c) Mairata i Payeras, A.; Ho, R. Y. N.; Fujita, M.; Que, L., Jr. *Chem.–Eur. J.* **2004**, *10*, 4944-4953. (d) Shearer, J.; Scarrow, R. C.; Kovacs, J. A. *J. Am. Chem. Soc.* **2002**, *124*, 11709-11717.

7. High-spin Fe^{III}–OOH complexes: (a) Wada, A.; Ogo, S.; Nagatomo, S.; Kitagawa, T.; Watanabe, Y.; Jitsukawa, K.; Masuda, H. *Inorg. Chem.* **2002**, *41*, 616-618. (b) Kitagawa, T.; Dey, A.; Lugo-Mas, P.; Benedict, J. B.; Kaminsky, W.; Solomon, E.; Kovacs, J. A. *J. Am. Chem. Soc.* **2006**, *128*, 14448-14449.

8. (a) Kim, S. O.; Sastri, C. V.; Seo, M. S.; Kim, J.; Nam, W. *J. Am. Chem . Soc.* **2005**, *127*, 4178-4179. (b) Thibon, A.; England, J.; Martinho, M.; Young, V. G.; Frisch, J. R.; Guillot, R.; Girerd, J.-J.; Münck, E.; Que, L. Jr.; Banse, F. *Angew. Chem., Int. Ed.* **2008**, *47*, 7064-7067. (c) Hong, S.; Lee, Y.-M.; Shin, W.; Fukuzumi, S.; Nam, W. *J. Am. Chem. Soc.* **2009**, *131*, 13910-13911. (d) Lee, Y.-M.; Hong, S.; Morimoto, Y.; Shin, W.; Fukuzumi, S.; Nam, W. *J. Am. Chem. Soc.* **2010**, *132*, 10668-10670.

9. Annaraj, J.; Suh, Y.; Seo, M. S.; Kim, S. O.; Nam, W. *Chem. Commun.* **2005**, 4529-4531.

10. Schmidt, M; Scherk, C; Iakovleva, O.; Nolting, H. F.; Meier, B.; Parak, F. *Inorg. Chim. Acta.* **1998**, *275*, 65-72.

11. The high-spin state for **2** results from constraints imposed by the TMC macrocycle that prevent formation of shorter Fe–N bonds required for a low-spin iron(III) center.

12. Downshifts of 1 cm^{-1} are observed for both the ν(Fe–O) and ν(O–O) of **2** when prepared with $D_2O_2/DClO_4$ rather than $H_2O_2/HClO_4$, which are within uncertainty of our Raman experiments.

13. (a) Brunold, T. C.; Solomon, E. I. *J. Am. Chem. Soc.* **1999**, *121*, 8277-8287. (b) Shiemke, A. J.; Loehr, T. M.; Sanders-Loehr, J. *J. Am. Chem. Soc.* **1984,** *106*, 4951-4956.

14. Katona, G.; Carpentier, P.; Nivière, V.; Amara, P.; Adam, V.; Ohana, J.; Tsanov, N.; Bourgeois, D. *Science* **2007**, *316*, 449-453.

15. Rohde, J.-U.; In, J.-H.; Lim, M. H.; Brennessel, W. W.; Bukowski, M. R.; Stubna, A.; Münck, E.; Nam, W.; Que, L., Jr. *Science* **2003**, *299*, 1037-1039.

16. Li, F.; England, J.; Que, L., Jr. J. *J. Am. Chem. Soc.* **2010**, *132*, 2134-2135.

17. (a) Aikens, J.; Sligar, S. G. *J. Am. Chem. Soc.* **1994**, *116*, 1143-1144. (b) Vidakovic, M.; Sligar, S. G.; Li, H.; Poulos, T. L. *Biochemistry* **1998**, *37*, 9211-9219. (c) Dunford, H. B.; Hewson, W. D.; Steiner, H. *Can. J. Chem.* **1978**, *56*, 2844-2852.

18. Groves, J. T.; Watanabe, Y. *J. Am. Chem. Soc.* **1988**, *110*, 8443-8452.

19. (a) Chen, K.; Costas, M.; Kim, J.; Tipton, A. K.; Que, L., Jr. *J. Am. Chem. Soc.* **2002**, *124*, 3026-3035. (b) Mas-Ballesté, R.; Que, L., Jr. *J. Am. Chem. Soc.* **2007**, *129*, 15964-15972. (c) Das, P.; Que, L., Jr. *Inorg. Chem.* **2010**, *49*, 9479-9485. (d) Makhlynets, O. V.; Das, P.; Taktak, S.; Flook, M.; Mas-Ballesté, R.; Rybak-Akimova, E. V.; Que, L. *Chem.–Eur. J.* **2009,** 15, 13171-13180. (e) Makhlynets, O. V.; Rybak-Akimova, E. V. *Chem.–Eur. J.* **2010**, *16*, 13995-14006.

20. Lyakin, O. Y.; Bryliakov, K. P.; Britovsek, G. J. P.; Talsi, E. P. *J. Am. Chem. Soc.* **2009,** *131*,10798-10799.

21. Tiago de Oliveira, F.; Chanda, A.; Banerjee, D.; Shan, X.; Mondal, S.; Que, L., Jr.; Bominaar, E. L.; Münck, E.; Collins, T. J. *Science* **2007**, *315*, 835-838.

22. Song, W. J.; McCormick, M. S.; Behan, R. K.; Sazinsky, M. H.; Jiang, W.; Lin, J.; Krebs, C.; Lippard, S. J., *J. Am. Chem. Soc.* **2010**, *132*, 13582–13585.

Supporting Information

Materials and Syntheses. All reagents including the 1,4,8,11-tetramethyl-1,4,8,11-tetraazacyclotetradecane (TMC) ligand, H_2O_2 (30 wt. % in H_2O) and anhydrous grade acetonitrile (99.5%) were purchased from commercial sources such as Sigma-Aldrich and Fisher Chemical and used as received unless otherwise noted. $H_2{}^{18}O_2$ (10 wt. % in H_2O; 90% ^{18}O incorporation), D_2O_2 (30 wt. % in D_2O; 98% D), and DClO4 (68%. in D_2O, 99% D) for resonance Raman sample preparation were purchased from ICON Isotopes or Sigma-Aldrich. $Fe^{II}(TMC)(CH_3CN)(OTf)_2$ was prepared by literature methods in a nitrogen-filled glove-box.[1] The concentrations of H_2O_2 were confirmed by ^1H NMR in CD_3CN as solvent.[2] For kinetic experiments, commercially available 30 wt. % H_2O_2 in H_2O (~10 M) and 11.5 M $HClO_4$ in H_2O were diluted to 1 M and 1.15 M with CH_3CN prior to use, respectively. Solutions of 2 used for proton dependence analysis and Eyring plot were typically obtained by treating ~2.0 mM $[Fe^{II}(TMC)(CH_3CN)]^{2+}$ in 1.5 mL CH_3CN with 10 equiv. NEt_3 (e.g. 60 μl of a 0.5-M solution) followed by 20 equiv. H_2O_2 (e.g. 60 μl of a 1-M solution) in CH_3CN at –40 °C. Aliquots of a 1.15-M $HClO_4$ solution were then added to these solutions without removing the excess NEt_3 and H_2O_2.

Physical Methods. UV-Vis spectra were recorded on a HP8453A diode-array spectrometer equipped with a cryostat from Unisoku Scientific Instruments (Osaka, Japan) for temperature control. Mössbauer spectra were recorded with two spectrometers, using Janis Research Super-Varitemp dewars that allowed studies in applied magnetic fields up to 8.0 T in the temperature range from 1.5 to 200 K. Mössbauer spectral simulations were performed using the WMOSS software package v2.5 (WEB Research, Edina, MN) as well as a modified version of SPHMOSS.[3] Isomer shifts are quoted

relative to Fe metal at 298 K. X-band EPR spectra were obtained on a Bruker Elexsys E-500 spectrometer equipped with an Oxford ESR-910 cryostat. EPR spectral simulations were carried out using a Windows software package (SpinCount v3.1.2) available from Professor Michael Hendrich of Carnegie Mellon University. Fe K-edge XAS data were collected for frozen solution samples of **1** and **2** at beamline 7-3 of the Stanford Synchrotron Radiation Lightsource (SLAC National Accelerator Laboratory, Menlo Park, CA). The data were collected in fluorescence mode using a 30-element germanium detector (Canberra) at a sample temperature of *ca.* 10 K over the energy range of 6.9–8.0 keV, as previously described.[4] Nine total scans were collected at a single sample spot for **1**, while nine total scans at three different sample spots were obtained for **2**. The raw XAS data were examined, average, and processed for analysis with EXAFSPAK.[5] The energies were referenced against an internal Fe foil reference at 7112.0 eV. No deglitching was carried out, nor were any points deleted from the raw XAS data. A unit-weighted average was used for both data sets. For both **1** and **2**, 17 out of 30 detector elements were included in the average. Individual scans were examined for photoreduction; no evidence of photoreduction was found for either sample based on the lack of changes in either edge energy or pre-edge intensity. The $k^3\chi(k)$ EXAFS data was analyzed using EXAFSPAK with phase and amplitude parameters obtained from FEFF 8.40.[6] The goodness-of-fit parameter F defined as $\Sigma(\chi_{calcd} - \chi_{expt})^2$. A second goodness-of-fit parameter F' is defined as $F' = F^2 / \nu$, where $\nu = N_{IDP} - \rho$. N_{IDP} is the number of independent data points ($N_{IDP} = 2\Delta k \Delta r/\pi$), while ρ is the number of floated variables in each optimization step.[7] F' is a measure of whether an added shell significantly improves the fit. In all analyses, the coordination number of a given shell was a fixed parameter,

and was varied iteratively while bond lengths and Debye-waller factors were allowed to freely float. The amplitude reduction factor S_0 was fixed at 0.9, while the edge shift parameter E_0 was allowed to float but was constrained to a common value for all shells. Thus in any given fit, $\rho = (2 \times \text{number of shells}) + 1$. Resonance Raman spectra were collected on an ACTON AM-506M3 monochromator with a Princeton LN/CCD data collection system (LN-1100PB) using a Spectra Physics Model 2060 krypton laser or a Spectra Physics Beamlok 2065-7S argon laser, and Kaiser Optical holographic super-notch filters. Low-temperature spectra of **1** and **2** in CH_3CN were obtained at 77 K using a 135° backscattering geometry. Samples were frozen onto a gold-plated copper cold finger in thermal contact with a Dewar flask containing liquid nitrogen. The Raman frequencies were referenced to indene. Slits were set for a band-pass of 4 cm^{-1} for all spectra. Raman spectra were baseline corrected, and intensity corrected to the 773 cm^{-1} solvent peak.

Progress of the conversion of $[Fe^{III}(TMC)(OOH)]^{2+}$ **(2)** to $[Fe^{IV}(O)(TMC)(CH_3CN)]^{2+}$ **(3)** was followed by monitoring the changes in absorbance at 500 nm for the decay of **2** and at 820 nm for the formation of **3**.[1] Reactions were monitored for more than six half lives. Fitting plots of reaction progress (absorbance at 500 nm and 820 nm) against time into typical first-order rate equations gave good fits and allowed the determination of observed rate constant for the decay of **2** and for the formation of **3** (k_{obs}). Errors associated with reaction rates were determined from at least three independent trials. Second order rate constants (k_2) were extracted from the linear plots of k_{obs} vs. $[HClO_4]$. Linear fits were obtained by using the *Fit Linear* function in Origin v8.07773. Activation parameters were extracted from a standard Eyring plot.

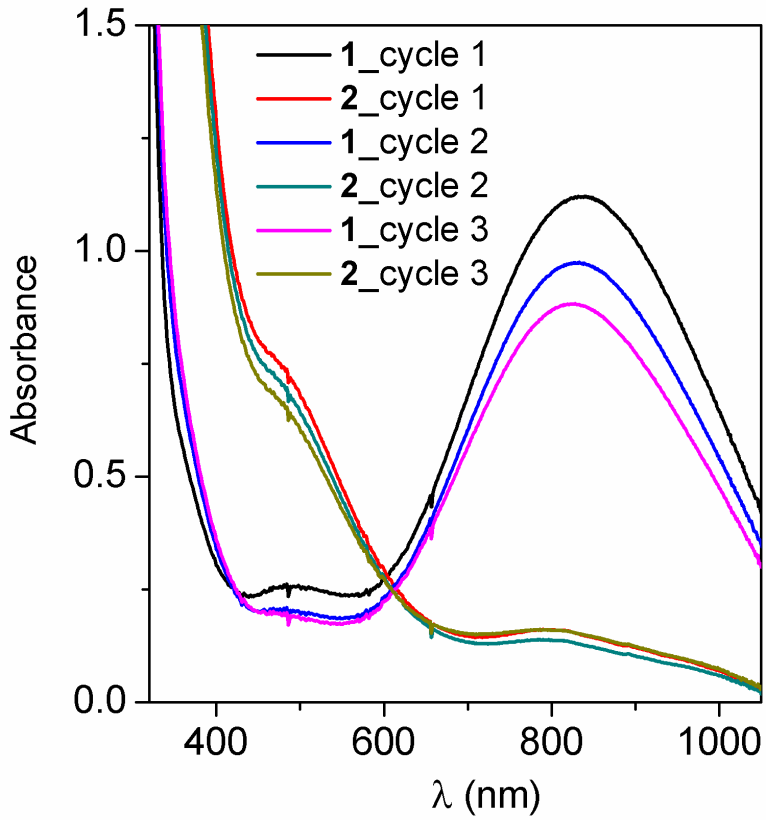

Figure S1. The interconversion between **1** and **2** upon addition of 15 equiv. $HClO_4$ or 15 equiv. NEt_3 in CH_3CN at –40 ºC. *b* = 1 cm. The concentration of **1** or **2** was diluted by as factor of 0.93 between adjacent cycles due to the addition of aliquots of $HClO_4$ and NEt_3. Considering the dilution effect, the recovery yield is >95% between adjacent cycles.

Comments on the Mössbauer and EPR spectra.

Side-on peroxo Complex **1** - We have analyzed the Mössbauer spectra of **1** and **2** with the Hamiltonian:

$$\mathcal{H} = D(S_z^2 - 35/4) + E(S_x^2 - S_y^2) + \mathcal{H}_{4th} + \beta \boldsymbol{S}\cdot\boldsymbol{g}\cdot\boldsymbol{B} + \boldsymbol{S}\cdot\boldsymbol{A}\cdot\boldsymbol{I} - g_n\beta_n\boldsymbol{B}\cdot\boldsymbol{I} + \mathcal{H}_Q \qquad (1)$$

where

$$H_{4th} = \frac{F}{180}[35S_z^4 - 30S(S+1)S_z^2 + 25S_z^2 - 6S(S+1) - 3S^2(S+1)^2] + \frac{a}{6}[S_x^4 + S_y^4 + S_z^4 - \frac{1}{5}S(S+1)(3S^2 + 3S - 1)] \qquad (2)$$

Figure S2 shows two Mössbauer spectra of **1**. The 1.7 K spectrum originates from the ground Kramers doublet ($g_z \approx 9.8$, g_x, $g_y < 1$) of **2**. The magnetic splitting of the 6-line pattern is solely determined by E/D and A_z.[8] While the fourth-order terms, a and F, strongly affect the properties of the middle Kramers doublet, their effect on the properties of the ground and upper Kramers doublets is negligible. The Mössbauer spectrum of the ground doublet yields the z component of the electric field gradient (EFG) tensor; the y-component is obtained at 10 K from the upper Kramers doublet (this doublet also yields a 6-line pattern; the second line from the left in Figure S2B originates from the upper doublet and the associated high-energy line coincides with the high-energy line of the ground doublet). As the EFG tensor is traceless, all principal components are now known. It can be seen that the 1.7 K spectrum has broad unresolved background absorption. This feature, representing roughly 30 % of the Fe, is also present in the low-field 4.2 K and 10 K spectra. Yet, for applied fields $\geq$ 3.0 T (Figure S3A-C) there is no evidence of a second species. The high field data show that this broad feature must belong to **1**. On first sight one might suspect that the shoulder at the low energy band in Figure 2A reflects the presence of a second species. However, analysis of the progression of 3.0, 4.0 and 8.0 T spectra shows that the shoulder comes about as follows: At low field, Figure S2, the magnetic hyperfine field of the ground doublet is along z, as the expectation value of S along z, $\langle S_z \rangle$, is large and $\langle S_x \rangle$ and $\langle S_y \rangle$ are small ($\langle S_i \rangle = g_i/4$). For increasing applied magnetic field $\langle S_x \rangle$ and $\langle S_y \rangle$ increase and the magnetic hyperfine field becomes more isotropic, following the applied field (for B > 3.0 T only the spin-down level of the ground doublet is appreciably populated at 4.2 K). The shoulder on the low energy feature arises from molecules for which the hyperfine field is close to the xy plane. The

intensity of the shoulder increases with increasing applied field, as <S> becomes more isotropic. We suspect that the broad feature in Figure S2 represents an aggregated subpopulation of **1**. Aggregation would give rise to spin-dipolar interactions that could broaden the low field spectra but would be decoupled (i. e. suppressed) at B >3.0 T. The EPR spectrum of **1** indicates the presence of only one species but, interestingly, our spin quantification accounts only for about 66 % of the iron (1.04 mM spin/1.56 mM Fe). This "missing" fraction is in accord with the Mössbauer data, suggesting that the iron contained in the broad species does not contribute an EPR signal in X-band. We have observed partial aggregation in other projects. Sometimes the problem can be overcome by dilution. However, **1** became unstable upon 10-fold dilution.

We have indicated in the caption of Figure S2 that we have distributed A_z to account for the line width. The slightly broadened lines of the 1.7 K spectrum could be accounted for by distributing *E/D* (relaxation can be excluded as the spin system of **1** is in the slow relaxation limit even at 120 K). However, the 8.0 T spectrum requires the distribution of some quantity, and as this spectrum does not depend on zero field splitting parameters (the electronic Zeeman term dominates), only a distribution of the components of the A-tensor can produce the desired broadening. Since distributing A_z produces the correct broadening both at 8.0 T and 50 mT, we have distributed this quantity, rather than all three components of A, using $\sigma_z/A_z = 0.02$. In order to obtain the right splitting for the 1.7 K/50 mT and 4.2K/8.0 T spectra we had to use an average $A_z/g_n\beta_n$ = -20.9 T and *E/D* = 0.28 ± 0.01.

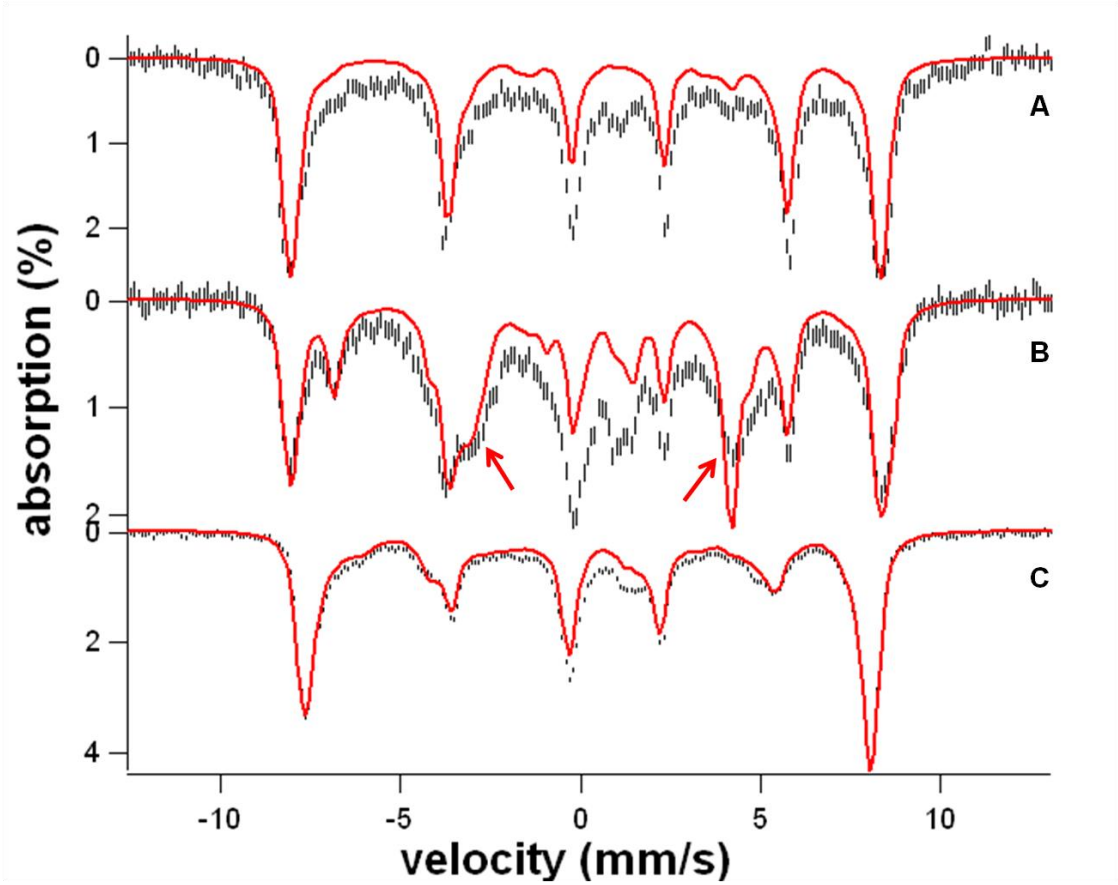

Figure S2. Mössbauer spectra of **1** in 3:1 PrCN/MeCN (black lines) recorded in magnetic fields applied parallel to the γ-rays at **(A)** 1.7 K and 50 mT; **(B)** 12K and 50 mT; **(C)** 4.2 K and 3.0 T. The red lines are spectral simulations based on eqs S1 and S2, using D = –0.91 cm^{-1}, E/D = 0.27, a = –0.017 cm^{-1}, F = –0.108 cm^{-1}, $A_x/g_n\beta_n$ = –19.7 T, $A_y/g_n\beta_n$= –20.2 T and $A_z/g_n\beta_n$ = –20.9 T, ΔE_Q = –0.92 mm/s, η = 0.47, δ = 0.58 mm/s. In all simulations we have used a Gaussian distribution of A_z with σ_z/A_z = 0.02. The arrows in (B) point to the outermost features of the spectrum associated with the middle Kramers doublet.

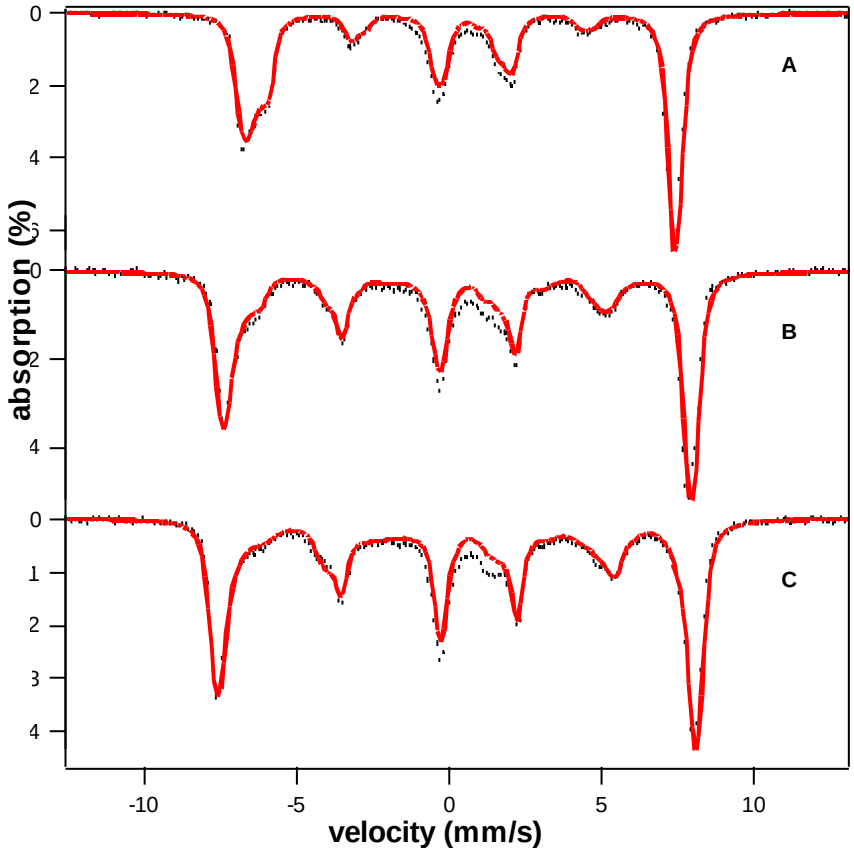

Figure S3. Mössbauer spectra of **1** recorded at 4.2 K in applied fields of 8.0T **(A)**, 4.0T **(B)** and 3.0T. The red lines are spectral simulations using the parameters quoted in Figure S1.

We next comment on the EPR spectrum associated with the middle Kramers doublet of **1**. Figure S4 shows an expanded view of the spectrum of Figure 3A (black line) of the main text, and Figure S5 shows a plot of the effective g-values of the middle Kramers doublet as a function of *E/D* without inclusion of fourth-order terms. The horizontal lines, approximately, mark the experimental g_{eff}-values. In order to match the experimental g-values one could increase the intrinsic g-values to $g_x = 2.06$, $g_y = 2.01$ and $g_z = 2.04$, thus using a g_x value which seems unreasonably high. However, use of these g-values would not solve the problem as we require slopes $dg_{eff}/d\sigma_{E/D}$ that severely broaden $g_{eff,x}$ and $g_{eff,y}$ but keep the feature at $g_{eff,z}$ fairly sharp; see below. We therefore have added the fourth order terms.

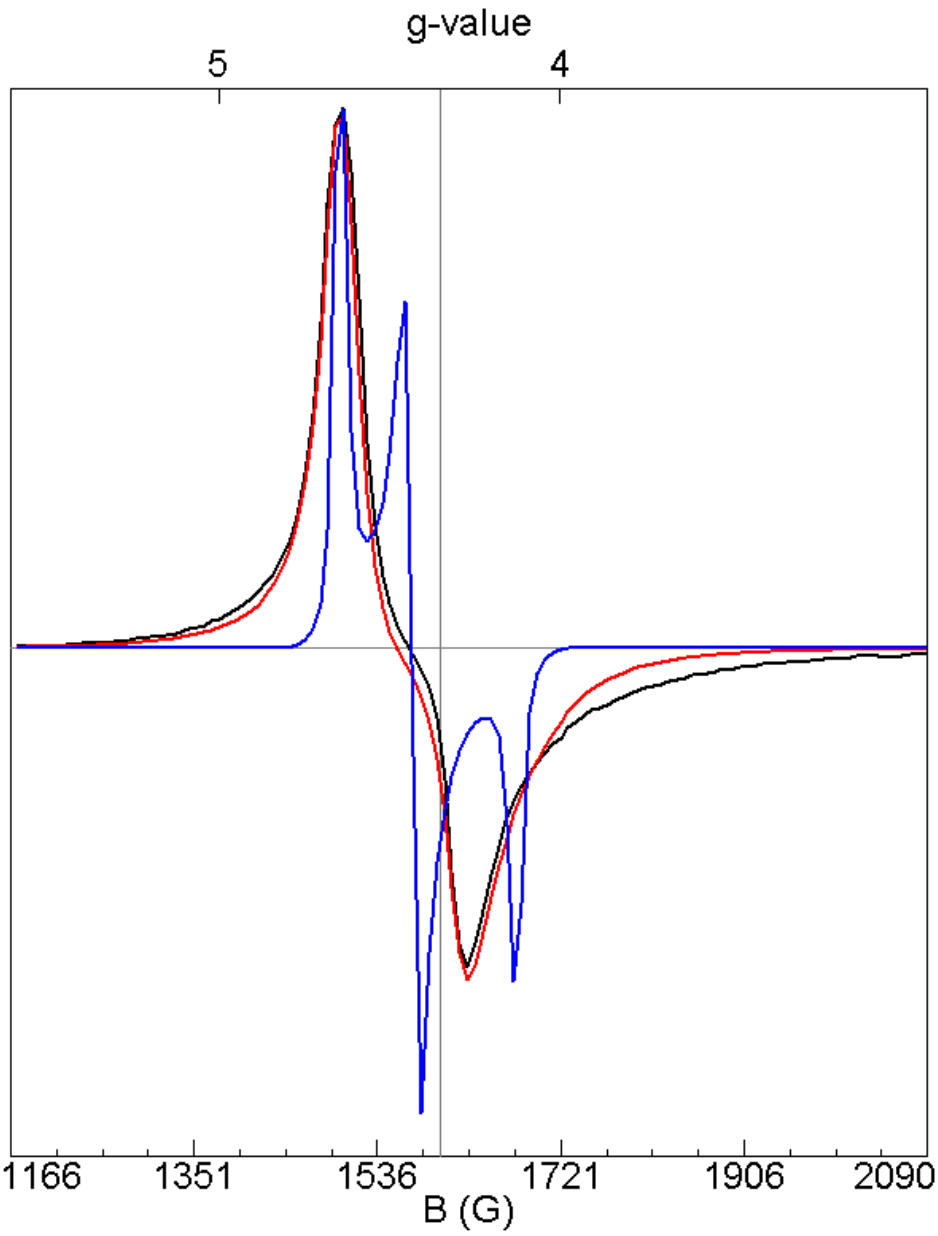

Figure S4. Expanded view of the EPR spectrum (black) of Figure 3A of the main text. The red line is the spectral simulation given in the main text. The blue line is a simulation for $\sigma_{E/D} = 0$ and a smaller packet line width.

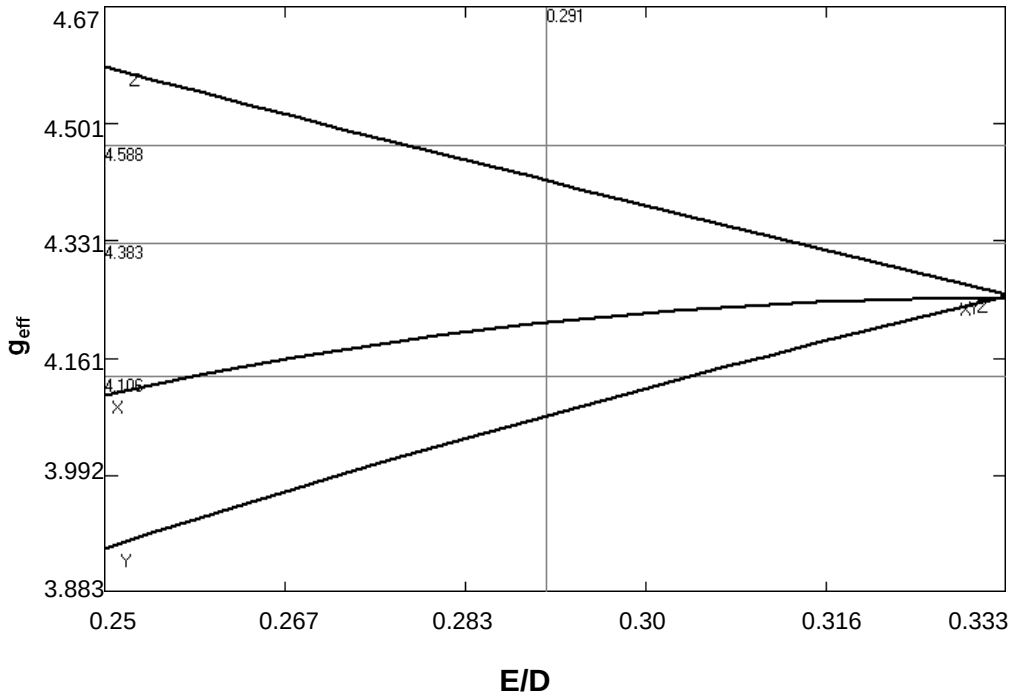

Figure S5. Effective *g*-values for the middle Kramers doublet of an $S = 5/2$ system as a function of *E/D* in the limit $\beta B/|D| << 1$ for $g_x = g_y = g_z = 2.00$. The horizontal lines indicate the "experimental" *g*-values; the vertical line indicates the *E/D* value of complex **1**, see text.

It should be pointed out that there will not be a unique solution to fitting the spectrum of Figure S4, because the effective g-values of the middle Kramers doublet depend on *E/D*, *a*, *F*, g_x, g_y, g_z and to some extent on *D*. Unfortunately, the Mössbauer spectrum of the middle Kramers doublet is broadened by distributed parameters (at least A_z and *E/D*, and possibly A_x, A_y, and *F*). If the broadening were minor, as in the Mössbauer spectra of Fe superoxide dismutase-azide,[9] we could determine *a* and *F* from the Mössbauer spectra. We have explored the parameter space of *a* and *F* and found solutions for typical small *a*-values of –(0.01 – 0.02) and $F = -(0.10 - 0.16)$ cm^{-1}, the particular value for *F* depending on how much one allows *g* to deviate from 2.00. Figure S6 shows a plot of the effective *g*-values versus *E/D* for $F = -0.108$ cm^{-1}; for other

parameters see caption. This value of F not only produces the right g_{eff}, it also produces slopes $dg_{eff}/d(E/D)$ that broaden the resonances in a desirable way when E/D is distributed: thus, $g_{eff,x}$ remains quite sharp (the experimental feature at $g_{eff} = 4.58$) while $g_{eff,y}$ and $g_{eff,z}$ broaden significantly.

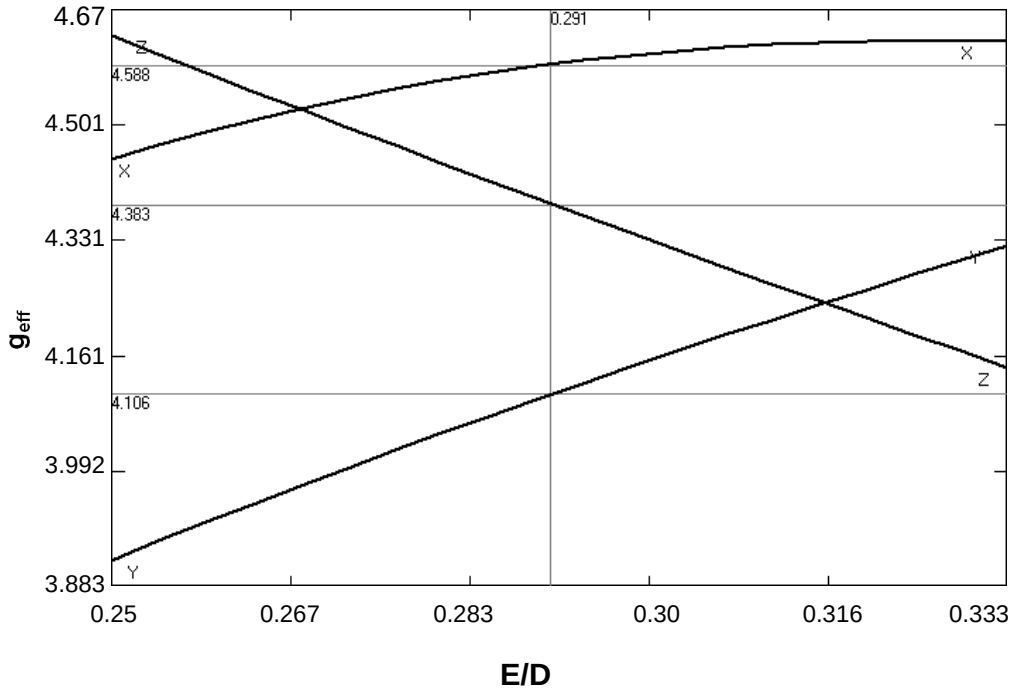

Figure S6. Effective g-values for the middle Kramers doublet for $F = -0.108$ cm^{-1}, $a = -0.017$ cm^{-1} and $g = (2.04, 1.98, 2.03)$ versus E/D, calculated for B = 0.15 T. The horizontal lines indicate the "experimental" g-values; the vertical line indicates E/D value of complex **1**, see text.

A comparison of spectra simulated with and without $\sigma_{E/D}$ illustrates how the experimental trough at $g = 4.23$ arises, namely by merging of the negative portion of the derivative feature at $g_{eff} = 4.39$ with the negative "absorption-type" feature at $g_{eff} = 4.11$ through broadening by $\sigma_{E/D}$ (the trough does not correspond to a principal direction of g_{eff}). We have also obtained acceptable fits by increasing F to –0.130 cm^{-1}, which allows one to keep the g-values a bit closer to $g = 2.00$ (2.02, 2.00, 2.02). By allowing $g_x = 2.05$

we found a solution for $F = –0.08$ cm^{-1} and $a = –0.07$ cm^{-1}. One can trade g-values for *F*- and *a*- values, but it is nevertheless apparent that a substantial *F*-term is required to explain the shape of the EPR feature. What gives rise to the large fourth-order terms will be the subject of future studies. Perhaps, mixing of the S = 3/2 states into the ground sextet (a Maltempo model in low symmetry) yields a mixed-spin state for which eq 1 is to be treated as an effective Hamiltonian.

One of the reviewers suggested to show, for the benefit of the reader, a "best" fit of the EPR spectrum without using the quartic terms; a least squares fit is shown in Figure S7. Despite the use of six free parameters the fit is inferior to the one obtained by inclusion of quartic terms. Worst, in order to get the proper width, the fit requires that g_y is distributed by $\sigma_{gy} = 0.06$, implying g_y values above and below g = 2.00, which is quite implausible in any model.

The arrows in the 10 K Mössbauer spectrum of Figure S2B mark the major absorption features associated with the middle Kramers doublet (The reader may keep in mind the presence of the above-mentioned background). With some additional broadening, perhaps by distributing *F*, the high energy feature could be broadened sufficiently to fit the data (without affecting the spectra of the ground and upper doublet).

Hydroperoxo complex **2** - The *D* and *E/D* parameters of complex **2** are such that the Mössbauer and EPR spectra would be quite insensitive to fourth-order terms. In fact, the Mössbauer and EPR spectra of **2** are quite ‘normal’. The 8.0 T spectrum shown in Figure S8 is well simulated with the parameters of Table S1. For the simulations shown we have distributed A_y using $\sigma_{Ay}/A_y = 0.05$. The EPR spectrum of Figure 2B is well represented by the simulations. The simulations do not account for some of the

absorption between the two low field peaks. This absorption might be captured by using asymmetric distributions of *E/D*, but since the transition probability steeply rises as *E/D* decreases, the absorption not represented by the simulation likely represents only a minor fraction of the molecules. Mössbauer samples trapped for **2** contain ~80% 2 and ~10% of **3** ($\Delta E_Q \approx 1.4$ mm/s and $\delta \approx 0.20$ mms/s).

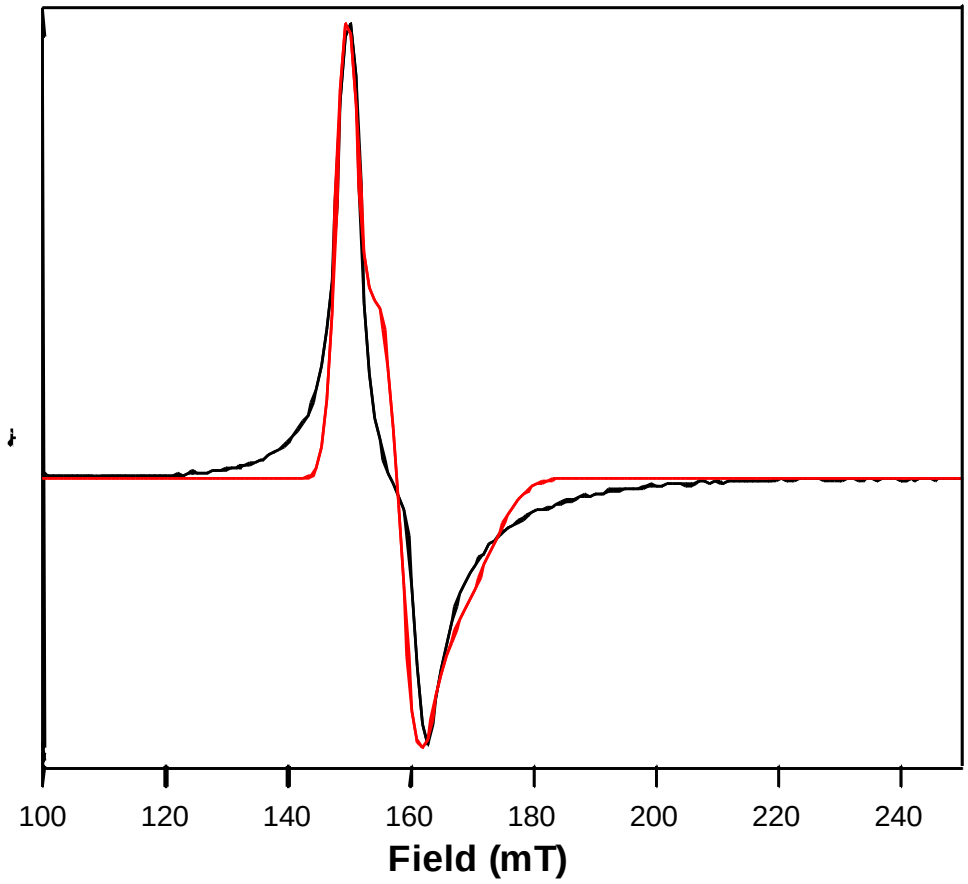

Figure S7. Simulation of the EPR signal of **1** without inclusion of fourth-order terms (red line), where the black line represents the experimentally observed spectrum. For the simulation we fixed E/D = 0.29 as obtained from the Mössbauer data. The g-values were treated as free parameters and each of the three g-values was allowed to be distributed on a Gaussian of width σ_g. The best fit yielded g_x =2.06, g_y =2.01 g_z =2.04, σ_{gx}=0.03, σ_{gy} =0.06 and σ_{gz} 0.02.

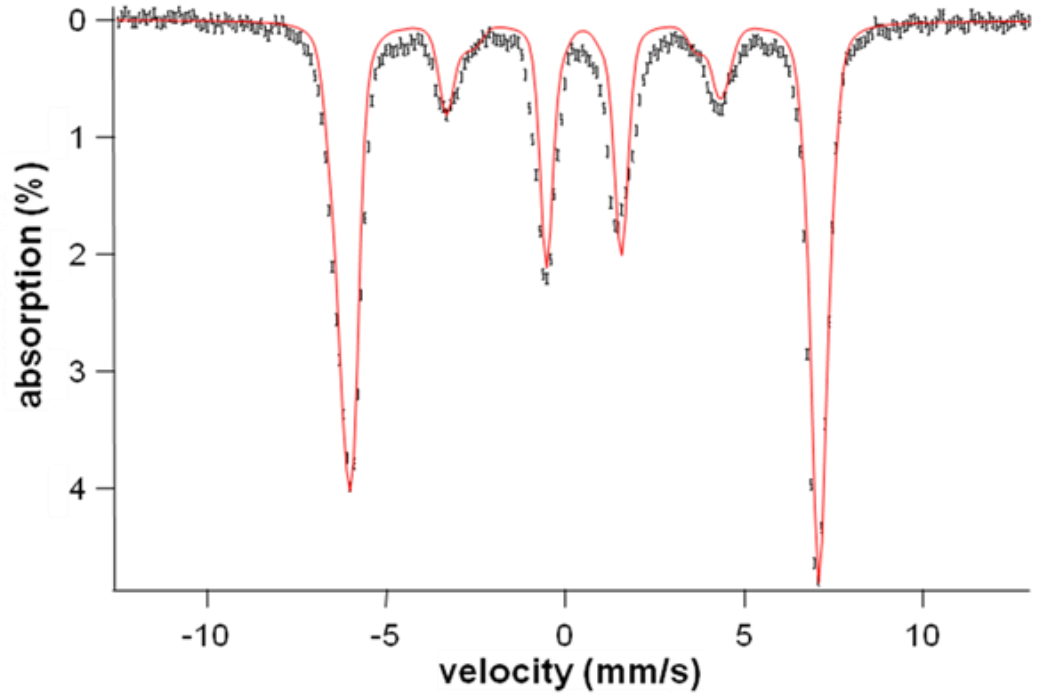

Figure S8. 4.2 K Mössbauer spectrum of **2** in 3:1 PrCN/MeCN recorded in a parallel field of 8.0 T (black line) and its simulation (red line). We have removed features corresponding to 10% of **3** from the data; the absorption of this species is confined to the velocities between –1.5 and +1.5 mm/s.

Table S1. Spectroscopic properties of **1** and **2**.

	λmax, nm (ε, $M^{-1}cm^{-1}$)	ν(O–O), cm^{-1} ($\Delta^{18}O$)	ν(Fe–O), cm^{-1} ($\Delta^{18}O$)	δ, mm/s	ΔEQ, mm/s	E/D	D, cm^{-1}	$A_{iso}/g_n\beta_{n,T}$	η	r(Fe–O), Å	r(Fe–N), Å
1	835 (730)	826 (-41)	493 (-15)	0.58	–0.92	0.28	–0.91	–20.3	0.47	1.93	2.20
2	500 (500)	870 (-50)	676 (-24)	0.51	–0.2	0.097	2.5	–20.0	3	1.92	2.15

Table S2. EXAFS fits for $[Fe^{III}(TMC)(\eta^2\text{–}O_2)]^+$ (**1**).[a]

	Fe–N/O			Fe–O			Fe•••C				
fit	*n*	*r*	σ^2	*n*	*r*	σ^2	*n*	*r*	σ^2	*F* [b]	*F'* [b]
1	6	2.21	40.4							425.5	9353
2	5	2.21	32.9							427.5	9442
3	4	2.23	3.0							341.3	6018
4	4	2.21	3.6	2	1.94	1.7				92.64	494.4
5	5	2.22	6.9	1	1.94	-1.4				149.2	1282
6	4	2.22	4.4	1	1.94	-1.1				118.1	803.6
7	5	2.21	5.4	2	1.93	1.3				117.0	788.7
8	4	2.21	3.5	2	1.94	1.7	4	3.07	8.4	60.34	237.1
9	4	2.20	3.2	2	1.93	2.5	4	2.98	2.5	27.58	56.95
							4	3.13	2.7		

[a] Fourier transform range k = 2.0 –15.0 Å^{-1} (resolution = 0.12 Å). r is in units of Å; σ^2 is in units of 10^{-3} Å^2. All fits shown here were to Fourier-filtered data employing a back transformation range of 0.3-3.0 Å. Bolded fit parameters represent the best fit.

[b] Goodness-of-fit parameter F defined as $\Sigma(\chi_{exptl}-\chi_{calc})^2$. *F'* is defined as $F' = F^2 / \nu$, where $\nu = N_{IDP} - \rho$. N_{IDP} is the number of independent data points, while ρ is the number of floated variables in each optimization step. *F'* is a measure of whether an added shell significantly improves the fit.

Table S3. EXAFS fits for $[Fe^{III}(TMC)(\eta^1\text{-}OOH)]^{2+}$ (**2**).[a]

	Fe–N/O			Fe–O			Fe•••C				
fit	*n*	*r*	σ^2	*n*	*r*	σ^2	*n*	*r*	σ^2	*F* [b]	*F'* [b]
1	5	2.17	5.2							127.5	848.2
2	6	2.17	7.3							156.0	1270
3	4	2.16	2.8	1	1.93	4.9				93.4	508.1
4	5	2.15	4.3	1	1.91	3.3				96.4	541.3
5	5	2.15	3.7	2	1.92	8.6				104.6	637.4
6	4	2.16	2.6	2	1.94	10.6				98. 7	567.2
7	4	2.15	2.7	1	1.93	4.5	3	2.91	4.8	24.18	44.41
							3	3.50	4.1		
8	5	2.15	4.3	1	1.91	2.9	3	2.91	4.5	28.61	62.17
							3	3.50	4.1		
9	4	2.15	2.9	1	1.92	5.5	3	2.92	3.0	14.92	19.94
							3	3.52	4.0		
							2	3.13	1.0		
10	5	2.15	4.6	1	1.90	3.2	3	2.92	2.6	17.78	28.31
							3	3.52	3.7		
							2	3.13	0.6		

[a] Fourier transform range k = 2.0 – 14.0 Å^{-1} (resolution = 0.13 Å). r is in units of Å; σ^2 is in units of 10^{-3} Å^2. All fits shown here were to Fourier-filtered data employing a back transformation range of 0.3-3.2 Å. Bolded fit parameters represent the best fit.

[b] Goodness-of-fit parameter F defined as $\Sigma(\chi_{exptl}\text{-}\chi_{calc})^2$. *F'* is defined as $F' = F^2 / \nu$, where $\nu = N_{IDP} - \rho$. N_{IDP} is the number of independent data points, while ρ is the number of floated variables in each optimization step. *F'* is a measure of whether an added shell significantly improves the fit.

Table S4. Vibrational frequencies of high-spin iron(III)-peroxo species.

	ν(Fe–O), cm^{-1} ($\Delta^{18}O$)	ν(O–O), cm^{-1} ($\Delta^{18}O$)	ref
Monoiron(III)-η^1-hydroperoxo			
2	676 (-24)	870 (-50)	[a]
$[Fe(H_2bppa)(OOH)]^{2+}$	621 (-22)	830 (-17)	10
E114A SOR	567 (-4)[b]	838 (-23)[b]	11
oxyHr	503 (-24)	844 (-48)	12
$[Fe(cyclam\text{-}PrS)(OOH)]^{+}$	419 (-19)	891 (-35)	13
Monoiron(III)-η^1-alkylperoxo			
$[Fe(6\text{-}Me_3\text{-}TPA)(OO^tBu)]^{2+}$	637 (-25)	860[c]	14
$[Fe(H_2bppa)(OO^tBu)]^{2+}$	629	873/838	15
$[Fe(Tp)(OO^tBu)]^{+}$	625 (-42)	860[c]	16
$[Fe(15\text{-}TMC)(OTf)(OO^tBu)]^{+}$	612 (-21)	871 (-49)	17
$[Fe(15\text{-}TMC)(SPh)(OO^tBu)]^{+}$	584 (-19)	872 (-57)	17
Monoiron(III)-η^2-peroxo			
1	493 (-15)	826 (-41)	[a]
$[Fe(N4Py)(\eta^2\text{–}O_2)]^{+}$	495 (-17)	827 (-47)	18
$[Fe(tmpIm)(\eta^2\text{–}O_2)]^{-}$	475 (-20)	807 (-49)	19
E47A SOR	438 (-23)	850 (-48)	20

[a] this work; [b] data obtained in crystallo; [c] data from -OOtBu-d9 complex; H_2bppa = bis(6-pivalamido-2-pyridyl-methyl)(2-pyridylmethyl)amine; oxyHr = oxyhemerythrin; SOR = superoxide reductase; cyclam-PrS-H = 1-(3'-mercaptopropyl)-1,4,8,11-tetraazacyclotetradecane; 6-Me_3-TPA = tris(6-methyl-2-pyridyl- methyl)amine; Tp = hydrotris(3-tert-butyl-5-isopropyl-1-pyrazolyl)borate; 15-TMC = 1,4,8,12-tetramethyl-1,4,8,12-tetraazacyclo-pentadecane; N4Py = N,N-bis(2-pyridylmethyl)-N-bis(2-pyridyl)methyl-amine; tmpIm = 5,10,15-tris(2',4',6'-trimethylphenyl)-20-(2'-(3"-imidazolylmethyl)-benzamido)phenyl) porphyrinate dianion.

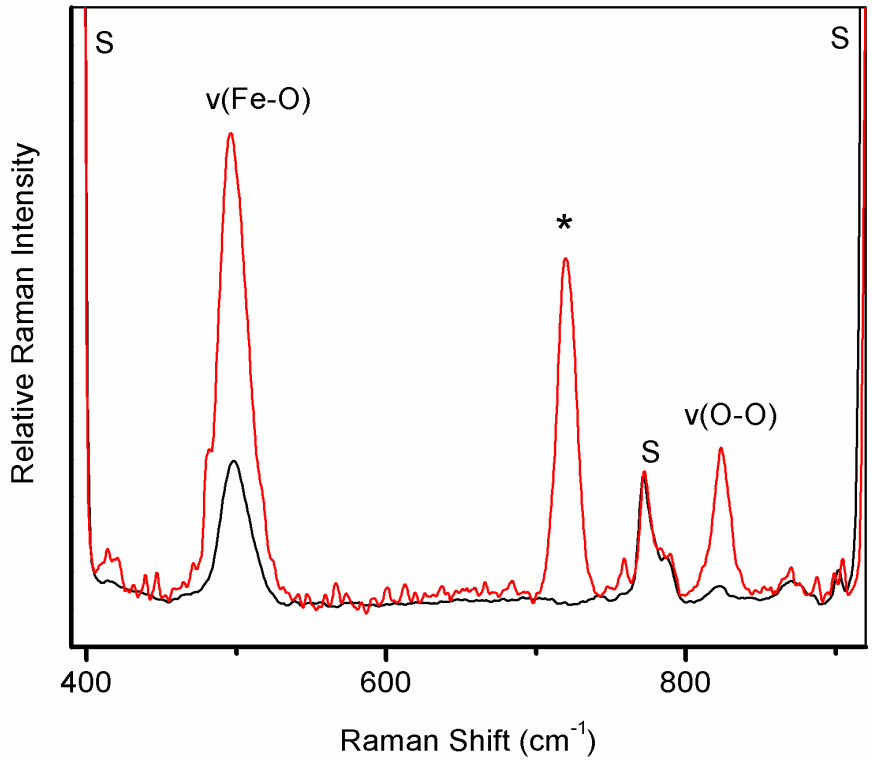

Figure S9. The resonance Raman spectra of **1** obtained with λ_{exc} = 647.1 nm (red) and 514.5 nm (black). "S" indicates peaks derived from CH_3CN solvent; asterisk denotes peaks derived from 647.1 nm notch filter. The spectra have been normalized according the 773 cm^{-1} peak of CH_3CN.

Due to the very low intensity of the peaks belonging to *ν*(Fe–O) and *ν*(O–O) of **2** (relative to the solvent peak) and the high susceptibility to photobleaching of the sample, we could not acquire very good data for both 647 nm and 514 nm laser line on the same frozen sample; the transient nature of the hydroperoxo in solution precluded comparisons between different frozen solution samples.

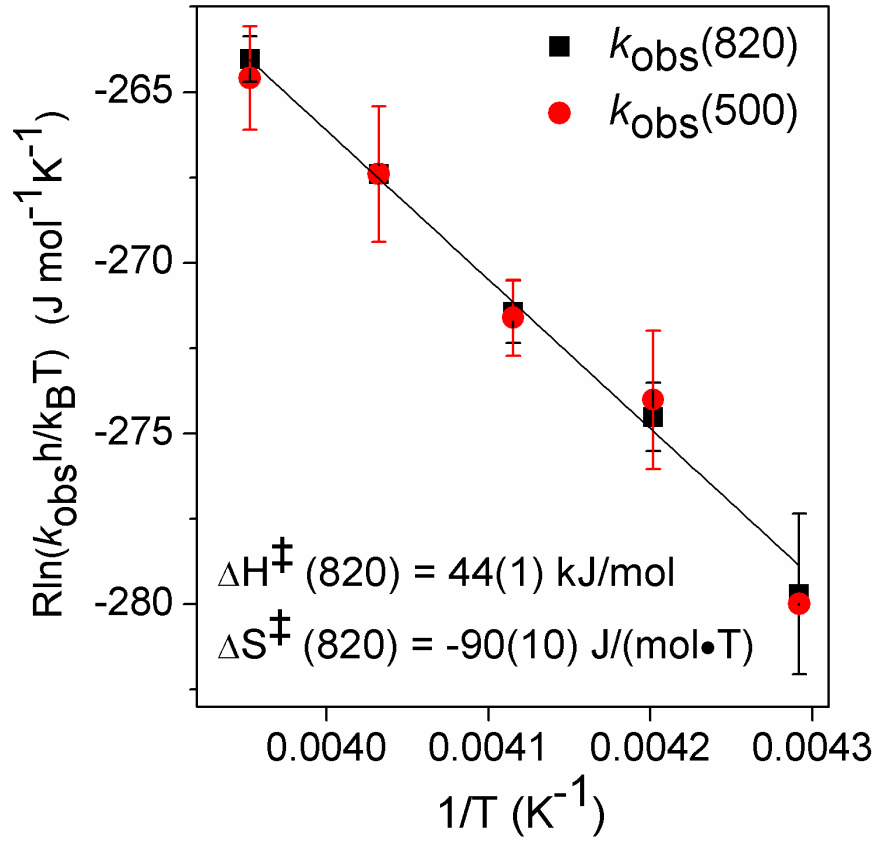

Figure S10. Eyring plot for the conversion of **2** to **3**. Experimental conditions: 1.5 mM **2**, 34 mM $HClO_4$, in CH_3CN; k_{obs} values were measured over the range of –40 °C to –20 °C. The black line is a linear fit for values of k_{obs}(820).

References

1. Rohde, J.-U.; In, J.-H.; Lim, M. H.; Brennessel, W. W.; Bukowski, M. R.; Stubna, A.; Münck, E.; Nam, W.; Que, L., Jr. *Science* 2003, *299*, 1037–1039.

2. (a) Stephenson, N. A.; Bell, A. T. *Anal. Bioanal. Chem.* 2005, 381, 1289−1293. (b) Stephenson, N. A.; Bell, A. T. *J. Am. Chem. Soc.* 2005, *127*, 8635–8643.

3. Münck, E.; Groves, J. L.; Tumolillo, T. A.; Debrunner, P. G. *Comput. Phys. Commun.* 1973, *5*, 225–238.

4. England, J.; Martinho, M.; Farquhar, E.; Frisch, J.; Bominaar, E.; Münck, E.; Que, L. Jr. *Angew. Chem., Int. Ed.* 2009, *48*, 3622–3626.

5. George, G. N. *EXAFSPAK*; Stanford Synchrotron Radiation Laboratory, Stanford Linear Accelerator Center: Stanford, CA, 2000.

6. Ankudinov, A. L.; Ravel, B.; Rehr, J. J.; Conradson, S. D. *Phys. Rev. B: Condens. Matter Mater. Phys.* 1998, *58*, 7565–7576

7. Riggs-Gelasco, P. J.; Stemmler, T. L.; Penner-Hahn, J. E. *Coord. Chem. Rev.* 1995, *144*, 245–286.

8. Wickman H. H.; Klein, M. P; Shirley, D. A. *Phys. Rev.* 1966, *152*, 345–357.

9. Schmidt, M; Scherk, C; Iakovleva, O.; Nolting, H. F.; Meier, B.; Parak, F. *Inorg. Chim. Acta.* 1998, *275*, 65–72.

10. Wada, A.; Ogo, S.; Nagatomo, S.; Kitagawa, T.; Watanabe, Y.; Jitsukawa, K.; Masuda, H. *Inorg. Chem.* 2002, *41*, 616–618.

11. Katona, G.; Carpentier, P.; Nivière, V.; Amara, P.; Adam, V.; Ohana, J.; Tsanov, N.; Bourgeois, D. *Science* 2007, *316*, 449–453.

12. Shiemke, A. J.; Loehr, T. M.; Sanders-Loehr, J. *J. Am. Chem. Soc.* 1984, *106*, 4951–4956.

13. Kitagawa, T.; Dey, A.; Lugo-Mas, P.; Benedict, J. B.; Kaminsky, W.; Solomon, E.; Kovacs, J. A. *J. Am. Chem. Soc.* 2006, *128*, 14448–14449.

14. Zang, Y.; Kim, J.; Dong, Y.; Wilkinson, E. C.; Appelman, E. H.; Que, L., Jr. *J. Am. Chem. Soc.* 1997, *119*, 4197–4205.

15. Wada, A.; Ogo, S.; Watanabe, Y.; Mukai, M.; Kitagawa, T.; Jitsukawa, K.; Masuda, H.; Einaga, H. *Inorg. Chem.* 1999, *38*, 3592–3593.

16. Lehnert, N.; Fujisawa, K.; Solomon, E. I. *Inorg. Chem.* 2003, *42*, 469–481.

17. Namuswe, F.; Hayashi, T.; Jiang, Y.; Kasper, G. D.; Sarjeant, A. A. N.; Moënne-Loccoz, P.; Goldberg, D. P. *J. Am. Chem. Soc.* 2009, *132*, 157–167.

18. Roelfes, G.; Vrajmasu, V.; Chen, K.; Ho, R. Y. N.; Rohde, J.-U.; Zondervan, C.; la Crois, R. M.; Schudde, E. P.; Lutz, M.; Spek, A. L.; Hage, R.; Feringa, B. L.; Münck, E.; Que, L., Jr. *Inorg. Chem.* 2003, *42*, 2639–2653.

19. Liu, J.-G.; Ohta, T.; Yamaguchi, S.; Ogura, T.; Sakamoto, S.; Maeda, Y.; Naruta, Y. *Angew. Chem., Int. Ed.* 2009, *48*, 9262–9267.

20. Mathé, C.; Mattioli, T. A.; Horner, O.; Lombard, M.; Latour, J.-M.; Fontecave, M.; Nivière, V. *J. Am. Chem. Soc.* 2002, *124*, 4966–4967.

Chapter VIII – Sc^{3+}-triggered oxoiron(IV) formation from O_2 and its nonheme iron(II) precursor via a Sc^{3+}-peroxo-Fe^{3+} intermediate

Published: Li, F.; Van Heuvelen, K.M.; **Meier, K.K.**; England, J.; Münck, E.; Que, Jr., L. "Sc^{3+} triggered oxoiron(IV) formation from O_2 and its nonheme iron(II) precursor via a Sc^{3+}-peroxo-Fe^{3+} intermediate." *J. Am. Chem. Soc.* 2013, 135, pp 10198-10201.

Author Contributions: F.L., K.M.V.H., K.K.M., J.E., E.M., and L.Q. conceived and designed the experiments. F.L., K.M.V.H., K.K.M. (Mössbauer, EPR), J.E. performed the experiments. F.L., K.M.V.H., K.K.M., J.E., E.M., and L.Q. analyzed the data. All authors participated in the writing of the paper.

Abstract

We report that redox-inactive Sc^{3+} can trigger O_2 activation at a ferrous center supported by the nonheme tetramethylcyclam (TMC) ligand to generate an oxoiron(IV) complex in the presence of BPh_4^- as an electron donor. To probe the role of Sc^{3+} in this reaction, we generated a transient Sc^{3+}-adduct to $[Fe^{III}(\eta^2\text{-}O_2)(TMC)]^+$, which was able to convert to the oxo-iron(IV) complex. This new intermediate was further established to contain a Fe^{III}-(μ-η^2:η^2-peroxo)-Sc^{3+} core. Our results have important implications for the role a Lewis acid can play in facilitating redox reactions in chemical and biological systems.

Introduction

There is much current interest in investigating the ability of redox-inactive metal ions to modulate redox reactions by virtue of their Lewis acidity, particularly with respect to their possible roles in O_2 evolution[1] and activation.[2,3] For example, the oxygen-evolving complex of Photosystem II requires a redox-inactive Ca^{2+} ion to produce O_2.[1] In addition, redox-inactive ions have been found to affect the stability and reactivities of high-valent metal-oxo complexes in biomimetic systems[2] as well as to accelerate O_2 activation by Fe^{II} and Mn^{II} complexes.[3] For the latter, heterometallic O_2 adducts and high-valent metal-oxo species are presumably involved but have not been observed. We previously demonstrated that $[Fe^{II}(TMC)(NCCH_3)]^{2+}$ **(1)** (TMC = 1,4,8,11-tetra-methylcyclam) reacts with O_2 in CH_3CN in the presence of stoichiometric H^+ and BPh_4^- to form $[Fe^{IV}O(TMC)(NCCH_3)]^{2+}$ **(4)**.[4] Herein, we report that a redox-inactive Sc^{3+} ion can replace the strong acid in this reaction to *trigger* the formation of **4**. An unprecedented Sc^{3+} adduct **(3)** of $[Fe^{III}(\eta^2\text{-}O_2)(TMC)]^+$ **(2)** was trapped, spectroscopically characterized in detail, and found to convert to **4** (Scheme 1).

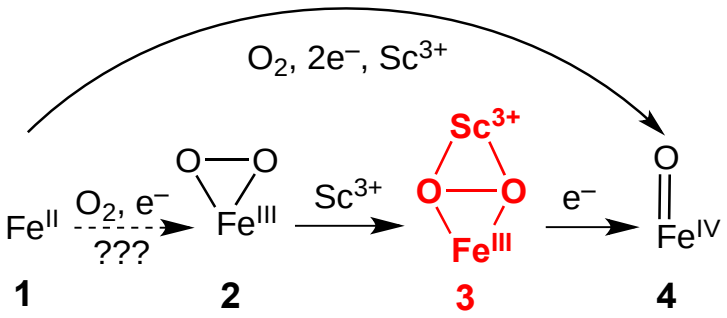

Scheme 1. Proposed mechanism for the formation of **4** from **1** and O_2.

Results and Discussion

Complex **1** is air stable in acetonitrile solution for days. However, the addition of 1 equiv. $Sc(OTf)_3$ together with 1 equiv. $NaBPh_4$ to an aerobic solution of **1** resulted in the formation of **4** in >70% yield over the course of ~1 h at 0 ºC, indicated by its signature near-IR band at 820 nm (Figure 1A).[5] Electrospray ionization mass spectra of the solution revealed the evolution of a prominent peak at m/z = 477.0, assigned to the $\{[Fe^{IV}(O)(TMC)](OTf)\}^+$ ion based on its position and isotope distribution pattern (Figure S1). When the reaction was carried out with $^{18}O_2$, the *m/z*= 477 peak showed an upshift of 2 units (Figure S2), confirming that the oxo moiety of **4** derived from dioxygen *and* that O–O bond cleavage must occur for the formation of **4** from **1** and O_2.

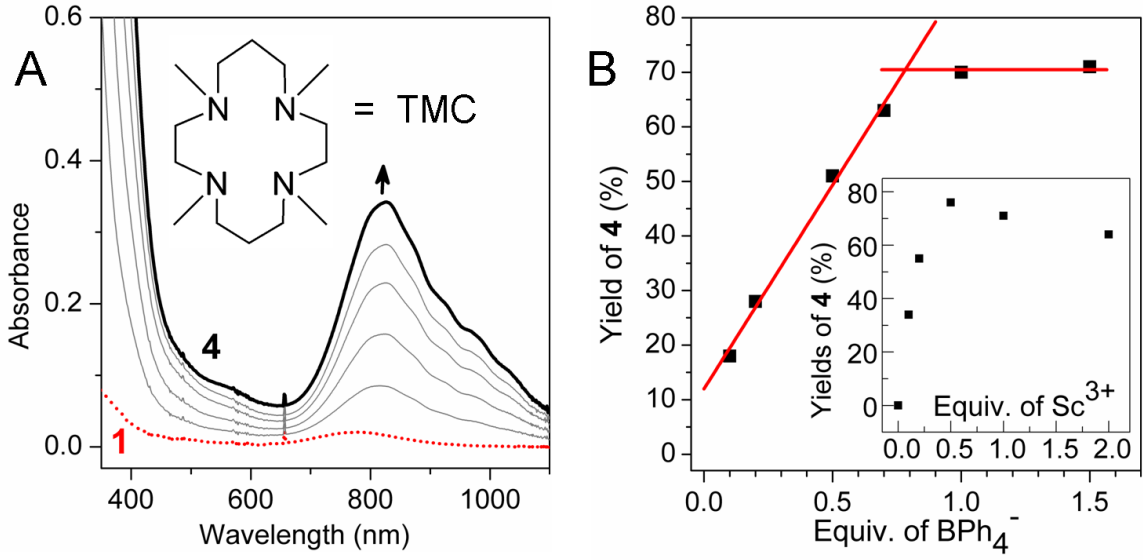

Figure 1. Reaction of 0.96 mM **1** with $NaBPh_4$ and $Sc(OTf)_3$ in aerobic CH_3CN at 0 ºC. **(A)** UV-visible spectral changes observed with 1 equiv. $NaBPh_4$ and 1 equiv. $Sc(OTf)_3$. **Inset:** TMC ligand. **(B)** Plot of the yield of **4** vs. equiv. BPh_4^- in the presence of 1 equiv. Sc^{3+}. **Inset:** plot of the yield of **4** vs. equiv. of Sc^{3+} with 1 equiv. BPh_4^-.

Further investigation demonstrated the requirement for both Sc^{3+} and BPh_4^- for the formation of **4** from **1**, as addition of either BPh_4^- or Sc^{3+} alone to **1** in air-saturated

CH_3CN solution did not elicit any detectable change in the UV-visible spectra. In addition, the yield of **4** correlated linearly with the amount of BPh_4^- added, plateauing at 1.0 equiv. BPh_4^- (Figure 1B). ^{1}H-NMR studies of the final solution showed that BPh_4^- had decomposed to 1,1'-biphenyl (Figure S3) with a stoichiometry of 0.95±0.15 equiv. relative to **1**, demonstrating that BPh_4^- provides the two electrons needed to convert **1** and O_2 into **4**. On the other hand, a sub-stoichiometric amount of Sc^{3+} was sufficient for the maximal formation of **4** (Figure 1B inset), suggesting that Sc^{3+} can act somewhat 'catalytically'.

As shown in Figure 1A, no intermediates are evident in the UV-Vis spectra during the conversion of **1** to **4**.[6] To account for the role of Sc^{3+} in this transformation, we propose the formation of a Sc^{3+}-peroxo-Fe^{3+} adduct that is reminiscent of the Fe^{III}–OOH species proposed in the H^+-and-BPh_4^--promoted generation of **4** from O_2 and **1**.[4,7] To test this hypothesis, $Sc(OTf)_3$ was added to a solution of the blue $Fe^{III}(\eta\text{-}O_2)$ complex **2** (purified via precipitation as its BPh_4 salt; see SI for details), which resulted in the immediate generation of a magenta intermediate **(3)** and its subsequent conversion to **4** in ~70% yield over the course of ~1 h at –10 ºC (Figure 2A).

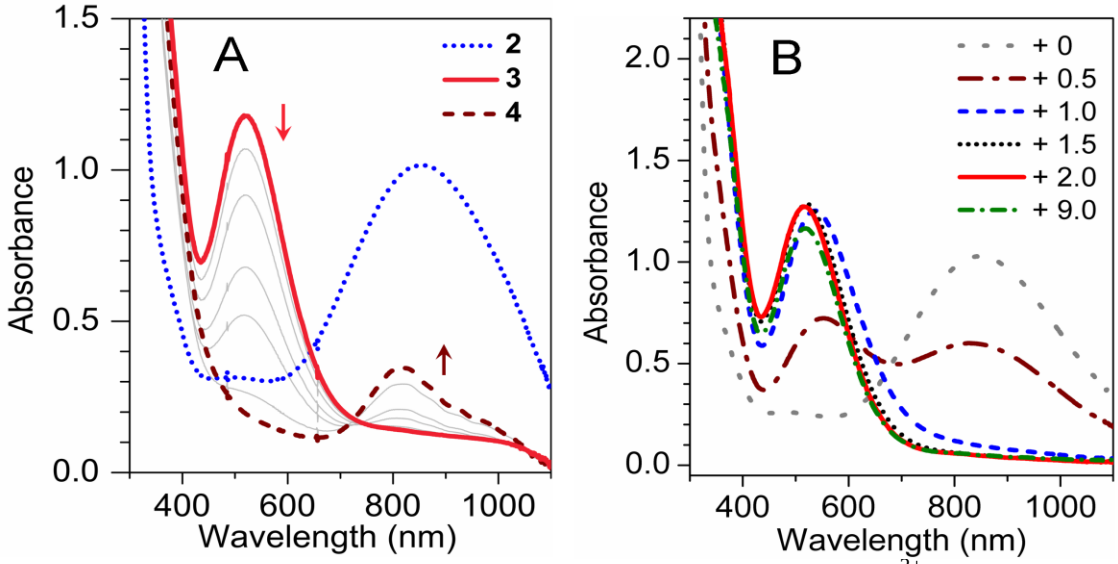

Figure 2. (A) UV-visible spectral changes upon addition of 3 equiv. Sc^{3+} to 1.5 mM *purified* **2** (ε_{835} = 650 $M^{-1}cm^{-1}$) in CH_3CN at –10 ºC instantly generating **3** (ε_{520} = 780 $M^{-1}cm^{-1}$), which in turn decayed to **4**. **(B)** UV-visible changes upon titration of 1.5 mM **2** in CH_3CN at –40 ºC with Sc^{3+} (0, 0.5, 1.0, 1.5, 2.0, 9.0 equiv, respectively).

*What is the identity of **3**?* Complex **3** exhibits a λ_{max} of 520 nm (ε_{520} = 780 $M^{-1}cm^{-1}$) established from its UV-visible spectrum (Figure 2A) and Mössbauer analysis. The large blue shift observed for the peroxo-to-Fe(III) charge transfer band of **2** (λ_{max} 835 nm) is reminisent of that seen upon protonation of **2** to form $[Fe^{III}(TMC)(\eta^1\text{-}OOH)]^{2+}$ in CH_3CN **(5)**,[7a] indicating partial neutralization of the negative charge of the peroxo ligand. Titration of **2** with $Sc(OTf)_3$ showed that 1 equiv $Sc(OTf)_3$ was nearly sufficient to cause the 835-nm band of **2** to disappear, suggesting a 1:1 stoichiometry for the Sc^{3+}-adduct of **2** (Figure 2B). The EPR spectrum of **3** shows features at g = 9.1, 5.1, 3.6 and ~2, consistent with an S = 5/2 iron(III) center with an E/D of 0.18 (Figure 3 left), compared to E/D values of 0.28 and 0.097 for **2** and **5**,[7a] respectively. The Mössbauer spectra of **3** (Figure 3 right) are typical of high-spin iron(III); their analysis is described in the SI and Mössbauer parameters are listed in Table 1 and Figure 3 caption. A comparison of the

spectroscopic properties in Table 1 shows that **3** is quite different from **2** and **5**, indicating that Sc^{3+} significantly affects the properties of the peroxoiron(III) unit.

We also carried out Fe K-edge X-ray absorption spectroscopic (XAS) studies to investigate the structural features of **3**. Complex **3** exhibits an Fe K-edge at 7125.3 eV and a pre-edge feature at 7113.3 eV, which are comparable to those of **2** and **5** obtained in CH_3CN solvent (Figure S4, Table S1).[7a] The pre-edge feature of **3** has an area of 14.4(6) units, compared to 17.9 for 2 and 22.4 for **5** (Table S1). As the pre-edge area reflects the extent to which the iron center deviates from centrosymmetry, the coordination environment of **3** must be closer to that of **2** with an η^2-peroxo ligand than that of **5** with an η^1-OOH ligand.

Analysis of the EXAFS data of **3** provides additional structural insight. Best fits reveal 4 N scatterers at 2.18 Å and 4 C scatterers each at 3.00 and 3.15 Å; all these features arise from the TMC ligand and have distances close to those found for **2** (Figure 4, Table S2). In addition, there is an O subshell at 1.98(1) Å arising from the peroxo ligand. Notably, the Fe–O distance of **3** is significantly longer than the 1.91-Å distance found for **2**,[7a] implying the addition of Sc^{3+} significantly weakens the iron-peroxo interaction. This 0.07-Å lengthening is inconsistent with conversion of the η^2-peroxo ligand to an η^1-isomer, as related η^1-peroxo complexes **5** and **6** both have shorter Fe–O distances (Table 2). Cu^{II} adducts to (η^2-peroxo)heme complexes also have one short Fe–O bond of ~1.93 Å in a highly unsymmetric η^2-peroxo ligand that binds to the iron.[9] Thus, the 0.07-Å lengthening of the *r*(Fe–O) of **3** relative to that of **2** favors a symmetric η^2-peroxo binding mode for 3. This conclusion is also supported by a comparison of fits 7 and 8 in Table S2, where the 2-O subshell in fit 7 has a σ^2 value of ~4, while the 1-O

subshell in fit 8 has a σ^2 value of –0.4. A negative σ^2 value for the latter indicates that either a bond is more rigid than would be expected for its distance or that there are too few scatterers associated with that shell.[10] A negative σ^2 value was also found when only one O-scatterer (instead of two) was used in fitting the EXAFS data for **2**. Our EXAFS results thus demonstrate that the binding of Sc^{3+} retains the symmetric side-on binding mode of the peroxo ligand in 3 but elongates the *r*(Fe–O) by 0.07 Å.[11]

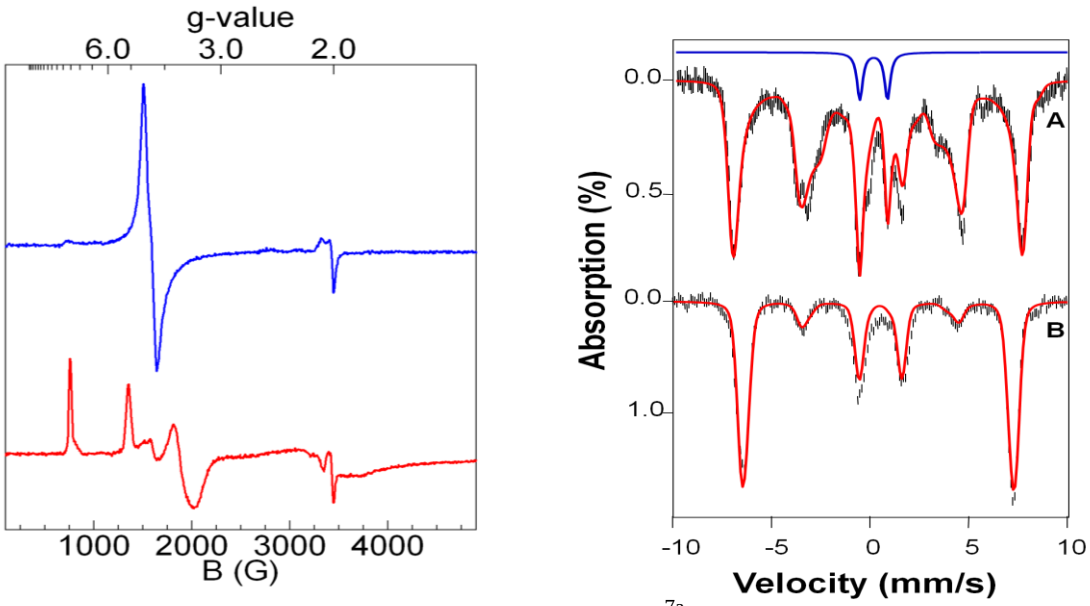

Figure 3. Left panel: EPR spectra of **2** (blue line, top)[7a] and **3** (red line, bottom) at 2 K and 0.2 mW microwave power. **Right panel:** 4.2 K Mössbauer spectra of **3** in MeCN recorded in parallel applied fields of 0.5 T **(A)** and 8.0 T **(B)**. The red lines in (A) and (B) are theoretical curves based on eq 1 of the SI, using the following parameters: D = +1.3 cm^{-1}, E/D = 0.18, g_0 = 2.00, $A_x/g_n\beta_n$ = −20.0T, $A_x/g_n\beta_n$ = −20.6 T $A_x/g_n\beta_n$ = −19.9 T , ΔE_Q = 0.50 mm/s, η = −0.5, δ = 0.47 mm/s. The Mössbauer sample contained 90% **3**[8] and 10% Fe^{IV}=O species (blue line).

Table 1. Spectroscopic comparison of Fe^{III}(TMC)-peroxo complexes (S = 5/2) in CH_3CN

	λ_{max}, nm	ΔE_Q, mm/s	δ, mm/s	D, cm^{-1}	E/D	Pre-edge area	ref
2	835	–0.92	0.58	–0.91	0.28	17.9	7a
3	520	0.50	0.47	1.3	0.18	14.4	*
5	500	0.20	0.51	2.5	0.097	22.4	7a

* this work.

The final key piece of evidence for the identity of **3** comes from resonance Raman spectroscopy. Laser excitation into the intense 520-nm band of **3** reveals two prominent peaks at 807 and 543 cm^{-1} (Figure 5) that correspond to ν(O–O) and ν(Fe–O) modes, respectively. These assignments are corroborated by ^{18}O-labeling, resulting in respective downshifts of 45 and 23 cm^{-1} that correlate well with Hooke's Law predictions for these modes and support the presence of an iron-bound peroxo ligand in **3**. The ν(O–O) of **3** is the lowest of any nonheme high-spin peroxoiron(III) complex thus far observed (Table 2). Relative to its precursor **2**,[7a] **3** has a ν(O–O) that is downshifted by 19 cm^{-1} and a ν(Fe–O) that is upshifted by 50 cm^{-1}, consistent with the retention of the η^2 binding mode of the peroxo ligand. Taken together, the spectrosopic data lead us to propose a $Fe^{3+}(\mu\text{-}\eta^2\text{:}\eta^2\text{-}O_2)Sc^{3+}$ core for **3**, analogous to the $Ni^{2+}(\mu\text{-}\eta^2\text{:}\eta^2\text{-}O_2)K^+$ core found in a complex characterized crystallographically by Limberg, Driess, and coworkers.[12,13]

Table 2. Comparison of Structural and Raman data for S = 5/2 Fe^{III}-peroxo complexes.

Complexes	*r*(Fe–N) (Å)	*r*(Fe–O) (Å)	ν(O–O) (cm^{-1})	Ref.
3[#]	2.18	1.98, 1.98	807	*
nonheme Fe^{III}-η^2-peroxo			816–827	7, 14
2 (2')[#]	2.20 (2.21)	1.91, 1.91 (1.91, 1.91)	826 (825)	7a (7b)
nonheme Fe^{III}-η^1-peroxo			830–891	7, 15[&]
5 (5')[#]	2.15 (2.16)	1.92 (1.85)	870 (868)	7a (7b)
6[$]	2.17	1.89		16
(heme)Fe^{III}-(μ-η^2:η^1-O_2)Cu^{II}	2.09	1.92, 2.09	788–808	9a, 9b
(heme)Fe^{III}-(μ-η^2:η^2-O_2)Cu^{II}	2.09	1.94, 2.09	747–767	9a, 9b

[#] **2**, **3**, and **5** in CH_3CN; **2'** and **5'** in a 3:1 (v:v) mixture of acetone:CF_3CH_2OH. [*] This work. [&] See also Table S4 of ref 7a; [$] **6** = [$Fe^{III}$(TMCS)($\eta^1$-$O_2$)].

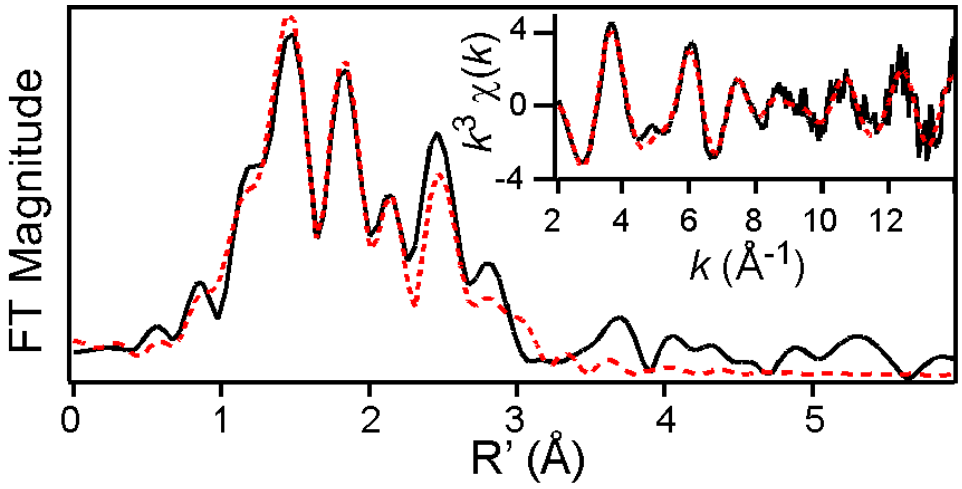

Figure 4. Fourier transform of Fe K-edge EXAFS data for **3** over a *k*-range of 2-14 Å^{-1}, with $k^3\chi(k)$ vs *k* data shown in the inset. The solid black lines represent the experimental data, while the red dashed lines correspond to the best fit with 2 O @ 1.98 Å and 4 N @ 2.18 Å (fit #22 in Table S3).

With the nature of **3** characterized, an important question that remains is whether it is involved in the conversion of **1** to **4** by O_2 activation. The requirement for both Sc^{3+} and two electrons to trigger O_2 activation of **1** suggests the likely formation of a Sc^{3+}-peroxo-Fe^{3+} species like **3** as an intermediate (Scheme 1). However the fact that this species does not accumulate during O_2 activation (Figure 1A) suggests that **3** may correspond to a more stable isomer of the actual intermediate involved in the O_2 activation reaction. Nevertheless, **3** represents a rare example of a heterobimetallic complex bridged by a peroxo ligand[9,12] and the only one thus far involving a nonheme iron center.

Conclusions

The spectroscopic characterization of **3** as a complex with an $Fe^{3+}(\mu\text{-}\eta^2\text{:}\eta^2\text{-}O_2)Sc^{3+}$ core provides a plausible mechanism for a Lewis acid to promote O–O bond cleavage. This insight points to another role the second iron center can play in diiron enzymes besides serving as an electron source: functioning as a Lewis acid to facilitate formation of high-valent iron-oxo intermediates such as Q and X in the respective oxygen activating cycles of methane monooxygenase and Class 1A ribonucleotide reductases.[17] This report of the Sc^{3+}-peroxo-Fe^{3+} intermediate **(3)** also augments the recent literature focused on the effects of redox-inactive Lewis acidic metal ions on redox transformations.[1,2,3] Prominent among these are their accelerative properties in oxidations by high-valent metal-oxo complexes discovered by Fukuzumi and Nam[2a-f] as well as the role of Ca^{2+} in forming an O–O bond from water during photosynthesis.[1] Relevant to the latter, Borovik recently showed that group II metal ions (M^{II}) can enhance the rates of O_2 activation by Fe^{II} and Mn^{II} complexes to afford well characterized M^{II}–(μ-OH)–(Mn^{III}/Fe^{III}) products, presumably via heterobimetallic O_2 adducts.[3] Our results herein demonstrate that Sc^{3+} can turn "on" the activation of O_2 at a nonheme iron center *and* that a transient Sc^{3+}–peroxo–Fe^{3+} species **(3)** could be a viable intermediate leading to O–O bond cleavage.

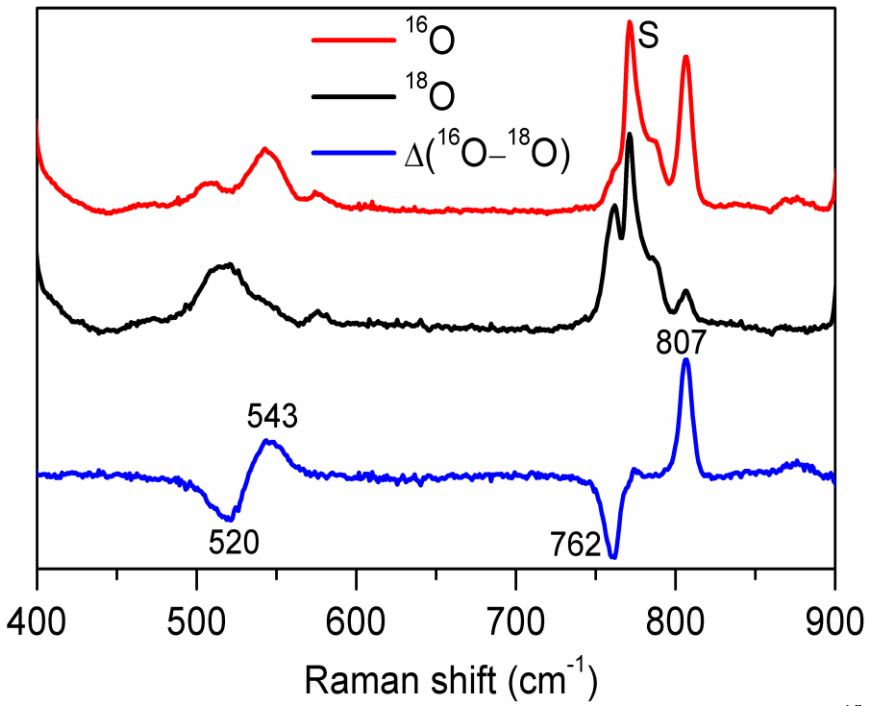

Figure 5. Resonance Raman spectra of **3** prepared in CH_3CN with $H_2{}^{16}O_2$ (red, top) and $H_2{}^{18}O_2$ (black, middle) obtained with 514.5 nm excitation, 100 mW. The $^{16}O - {}^{18}O$ difference spectrum is shown in blue (bottom). S = solvent.

Acknowledgements

This work was supported by the National Science Foundation (grant CHE1058248 to L.Q.) and the National Institutes of Health (grant EB001475 to E.M. and postdoctoral fellowship GM093479 to K.M.V.H.). F.L. acknowledges a doctoral dissertation fellowship from the University of Minnesota. XAS data were collected at beamline X3B of the National Synchrotron Light Source at the Brookhaven National Laboratory and beamline 7-3 of the Stanford Synchrotron Radiation Lightsource, both supported by NIH and DOE.

References

1. (a) Yocum, C. F. *Coord. Chem. Rev.* 2008, *252*, 296-305. (b) Umena, Y.; Kawakami, K.; Shen, J.-R.; Kamiya, N. *Nature* 2011, *473*, 55-60. (c) Tsui, E., Y.; Tran, R.; Yano, J.; Agapie, T. *Nature Chem.* 2013, *5*, 293-299.

2. (a) Fukuzumi, S. *Coord. Chem. Rev.* 2013, *257*, 1564-1575. (b) Fukuzumi, S.; Morimoto, Y.; Kotani, H.; Naumov, P.; Lee, Y.-M.; Nam, W. *Nature Chem.* 2010, *2*, 756-759. (c) Morimoto, Y.; Kotani, H.; Park, J.; Lee, Y.-M.; Nam, W.; Fukuzumi, S. *J. Am. Chem. Soc.* 2011, *133*, 403-405. (d) Park, J.; Morimoto, Y.; Lee, Y.-M.; Nam, W.; Fukuzumi, S. *J. Am. Chem. Soc.* 2011, *133*, 5236-5239. (e) Morimoto, Y.; Kotani, H.; Park, J.; Lee, Y.-M.; Nam, W.; Fukuzumi, S. *J. Am. Chem. Soc.* 2011, *133*, 403-405. (f) Chen, J.; Lee, Y.-M.; Davis, K. M.; Wu, X.; Seo, M. S.; Cho, K.-B.; Yoon, H.; Park, Y. J.; Fukuzumi, S.; Pushkar, Y. N.; Nam, W. *J. Am. Chem. Soc.* 2013, *135*, 6388-6391. (g) Leeladee, P.; Baglia, R. A.; Prokop, K. A.; Latifi, R.; de Visser, S. P.; Goldberg, D. P. *J. Am. Chem. Soc.* 2012, *134*, 10397-10400.

3. (a) Park, Y. J.; Ziller, J. W.; Borovik, A. S. *J. Am. Chem. Soc.* 2011, *133*, 9258-9261. (b) Park, Y. J.; Cook, S. A.; Sickerman, N. S.; Sano, Y.; Ziller, J. W.; Borovik, A. S. *Chem. Sci.* 2013, *4*, 717-726.

4. Thibon, A.; England, J.; Martinho, M.; Young, V. G., Jr.; Frisch, J. R.; Guillot, R.; Girerd, J.-J.; Münck, E.; Que, L., Jr.; Banse, F. *Angew. Chem. Int. Ed.* 2008, *47*, 7064-7067.

5. Rohde, J.-U.; In, J.-H.; Lim, M. H.; Brennessel, W. W.; Bukowski, M. R.; Stubna, A.; Münck, E.; Nam, W.; Que, L., Jr. *Science* 2003, *299*, 1037-1039.

6. No intermediates were observed as well in the previously reported reactions of 1 and O_2 to form 4, irrespective of whether it was promoted by H^+/BPh_4^-,[4] NADH analogs (Hong, S.; Lee, Y.-M.; Shin, W.; Fukuzumi, S.; Nam, W. *J. Am. Chem. Soc.* 2009, *131*, 13910-13911), or cycloalkene (Lee, Y.-M.; Hong, S.; Morimoto, Y.; Shin, W.; Fukuzumi, S.; Nam, W. *J. Am. Chem. Soc.* 2010, *132*, 10668-10670).

7. (a) Li, F.; Meier, K. K.; Cranswick, M. A.; Chakrabarti, M.; Van Heuvelen, K. M.; Münck, E.; Que, L., Jr. *J. Am. Chem. Soc.* 2011, *133*, 7256-7259. (b) Cho, J.; Jeon, S.; Wilson, S. A.; Liu, L. V.; Kang, E. A.; Braymer, J. J.; Lim, M. H.; Hedman, B.; Hodgson, K. O.; Valentine, J. S.; Solomon, E. I.; Nam, W. *Nature* 2011, *478*, 502-505. (c) Liu, L. V.; Hong, S.; Cho, J.; Nam, W.; Solomon, E. I. *J. Am. Chem. Soc.* 2013, *135*, 3286-3299.

8. We had difficulties obtaining simulations that simultaneously fit the 0.5 and 8.0 T. spectra. We suspect that the Hamiltonian requires the introduction of quartic terms as we found for 2.[7a]

9. (a) Halime, Z.; Kieber-Emmons, M. T.; Qayyum, M. F.; Mondal, B.; Gandhi, T.; Puiu, S. C.; Chufán, E. E.; Sarjeant, A. A. N.; Hodgson, K. O.; Hedman, B.; Solomon, E. I.; Karlin, K. D. *Inorg. Chem.* 2010, *49*, 3629-3645. (b) Chufán, E. E.; Puiu, S. C.; Karlin, K. D. *Acc. Chem. Res.* 2007, *40*, 563-572. (c) Chishiro, T.; Shimazaki, Y.; Tani, F.; Tachi, Y.; Naruta, Y.; Karasawa, S.; Hayami, S.; Maeda, Y. *Angew. Chem. Int. Ed.* 2003, *42*, 2788-2791.

10. Scott, R. A. In *Physical Methods in Bioinorganic Chemistry. Spectroscopy and Magnetism*; Que, L., Jr., Ed.; University Science Books: Sausalito, CA, 2000, p 465-503.

11. We also attempted to include in fits of 3 a Sc scatterer at 3.6-3.7 Å. Fits 13 and 14 in Table S2 show that a Sc scatterer of 3.8 Å with a reasonable Debye-Waller factor (σ^2 ~ 4) can be added, but only a slight improvement in GOF was obtained. Similar results were obtained in the EXAFS analysis of a Sc-O-Co complex (Pfaff, F. F.; Kundu, S.; Risch, M.; Pandian, S.; Heims, F.; Pryjomska-Ray, I.; Haack, P.; Metzinger, R.; Bill, E.; Dau, H.; Comba, P.; Ray, K. *Angew. Chem. Int. Ed.* 2011, *50*, 1711-1715).

12. Yao, S.; Xiong, Y.; Vogt, M.; Grützmacher, H.; Herwig, C.; Limberg, C.; Driess, M. *Angew. Chem. Int. Ed.* 2009, *48*, 8107-8110.

13. A related $Fe^{3+}(\mu\text{-}\eta^2\text{:}\eta^2\text{-}O_2)H^+$ core was postulated by Nam et al. for a short-lived (<2 ms) species (λ_{max} 527 nm) observed at –40 °C upon treatment of 2 with strong acid in its conversion to 5.[7b]

14. (a) Girerd, J.-J.; Banse, F.; Simaan, A. J. *Struct. Bonding* 2000, *97*, 145-177. (b) Roelfes, G.; Vrajmasu, V.; Chen, K.; Ho, R. Y. N.; Rohde, J.-U.; Zondervan, C.; la Crois, R. M.; Schudde, E. P.; Lutz, M.; Spek, A. L.; Hage, R.; Feringa, B. L.; Münck, E.; Que, L., Jr. *Inorg. Chem.* 2003, *42*, 2639-2653.(c) Simaan, A. J.; Döpner, S.; Banse, F.; Bourcier, S.; Bouchoux, G.; Boussac, A.; Hildebrandt, P.; Girerd, J.-J. *Eur. J. Inorg. Chem.* 2000, 1627-1633. (d) Neese, F.; Solomon, E. I. *J. Am. Chem. Soc.* 1998, *120*, 12829-12848.

15. (a) Brunold, T. C.; Solomon, E. I. *J. Am. Chem. Soc.* 1999, *121*, 8288-8295.(b) Wada, A.; Ogo, S.; Nagatomo, S.; Kitagawa, T.; Watanabe, Y.; Jitsukawa, K.; Masuda, H. *Inorg. Chem.* 2002, *41*, 616-618. (c) Kitagawa, T.; Dey, A.; Lugo-Mas, P.; Benedict, J. B.; Kaminsky, W.; Solomon, E.; Kovacs, J. A. *J. Am. Chem. Soc.* 2006, *128*, 14448-14449. (d) Katona, G.; Carpentier, P.; Nivière, V.; Amara, P.; Adam, V.; Ohana, J.; Tsanov, N.; Bourgeois, D. *Science* 2007, *316*, 449-453.

16. McDonald, A. R.; Van Heuvelen, K. M.; Guo, Y.; Li, F.; Bominaar, E. L.; Münck, E.; Que, L., Jr. *Angew. Chem. Int. Ed.* 2012, *51*, 9132-9136.

17. (a) Tinberg, C. E.; Lippard, S. J. *Acc. Chem. Res.* 2011, *44*, 280-288. (b) Stubbe, J.; Nocera, D. G.; Yee, C. S.; Chang, M. C. Y. Chem. Rev. 2003, *103*, 2167-2201.

Supporting Information

Materials and Syntheses. All reagents including the TMC ligand, $NaBPh_4$, $Sc(OTf)_3$, HPLC-grade acetonitrile (99.9%) were purchased from commercial sources such as Sigma-Aldrich and Fisher Chemical, and were used as received unless otherwise noted. $[Fe^{II}(TMC)(OTf)](OTf)$ (**1**) was prepared by literature methods in a nitrogen-filled glove-box.[1] $[Fe^{III}(TMC)(\eta^2\text{-}O_2)](OTf)$ was generated by a literature method involving the addition of 10 equiv. NEt_3 and 20 equiv. H_2O_2 to the solution of $[Fe^{II}(TMC)(OTf)](OTf)$ in CH_3CN at –40 ºC.[2]

Oxygenation of 1. CH_3CN solutions of **1** were prepared by dissolving solid **1** in CH_3CN solution under aerobic conditions. To a 1.5 mL CH_3CN solution of 1.0 mM **1** under aerobic conditions, aliquots of both $NaBPh_4$ and $Sc(OTf)_3$ solutions in CH_3CN were injected (e.g. 30 μl of a 50 mM solution of $NaBPh_4$ or $Sc(OTf)_3$ to achieve 1 equiv.) to trigger the formation of **4** in >70% yield, as indicated by its signature absorption bands at 820 nm within 1 h at 0 ºC. Addition of only $NaBPh_4$ or only $Sc(OTf)_3$ to solutions of **1** under aerobic conditions did not alter the UV-visible spectrum of **1** over the same 1-h period at 0 ºC. While the reactant O_2 was provided in the form of air-saturated CH_3CN, the formation of **4** can also occur by bubbling O_2 into CH_3CN solution of **1** under anaerobic conditions in the presence of $NaBPh_4$ and $Sc(OTf)_3$. **4** was the only observed Fe-containing product of this oxygenation reaction of **1** in the presence of $NaBPh_4$ and $Sc(OTf)_3$ in CH_3CN carried between –40 to 25 ºC.

Generation of *purified* $[Fe^{III}(TMC)(\eta^2\text{-}O_2)](BPh_4)$: A 15–20 mM solution of **1** in methanol was prepared by dissolving ~20 mg of this complex in ~1.8 mL MeOH. At –40

ºC, 10 equiv. NEt_3 and 20 equiv. H_2O_2 were added, and the solution was stirred for approximately 15 minutes to allow full formation of $[Fe^{III}(TMC)(\eta^2\text{-}O_2)](OTf)$. The solution was then decanted into a pre-cooled vial containing 5–10 equiv. $NaBPh_4$ and stirred continuously. The blue precipitate of $[Fe^{III}(TMC)(\eta^2\text{-}O_2)](BPh_4)$ formed immediately, and the suspension was stirred for an additional ~60 seconds to make sure that all the solid $NaBPh_4$ had dissolved and the formation of the blue precipitate was complete. The suspension was quickly filtered using a glass-fritted funnel pre-cooled in dry ice to collect the blue precipitate. The precipitate was washed with cold diethyl ether several times. The funnel (containing the blue precipitate) was connected by a rubber adapter to the top of a Schlenk flask, the bottom of which was kept cold with dry ice. Cold CH_3CN (–40 ºC) was then added to the funnel to re-dissolve the precipitate, and vacuum was briefly applied to the Schlenk flask to collect the blue solution into the flask after filtration. The yield of the purified $[Fe^{III}(TMC)(\eta^2\text{-}O_2)](BPh_4)$ complex in the solid state relative to the starting $[Fe^{III}(TMC)(\eta^2\text{-}O_2)](OTf)$ complex in solution was typically about 60–75%. The blue precipitate of $[Fe^{III}(TMC)(\eta^2\text{-}O_2)](BPh_4)$ was re-dissolved in cold CH_3CN at –40 ˚C to make a stock solution of 1.0–1.5 mM with its concentration based on $\varepsilon_{835} = 650\ M^{-1}cm^{-1}$. The blue precipitate of $[Fe^{III}(TMC)(\eta^2\text{-}O_2)](BPh_4)$ prepared in this manner was fairly stable under anaerobic conditions as long as it was kept at –40 ºC. In contrast, if precipitated out from CH_3CN rather than MeOH, the blue precipitate of $[Fe^{III}(TMC)(\eta^2\text{-}O_2)](BPh_4)$ decomposed into a yellowish material shortly after precipitation, even at low temperatures. This protocol thus enables the isolation of purified $[Fe^{III}(TMC)(\eta^2\text{-}O_2)](BPh_4)$ in a form that is not contaminated by excess NEt_3 or H_2O_2.

Sc^{3+} adduct of $[Fe^{III}(TMC)(\eta^2\text{-}O_2)]^+$ (3). **3** can be generated by two methods with method A starting with $[Fe^{III}(TMC)(\eta^2\text{-}O_2)](OTf)$ generated in solution *and* method B using re-dissolved $[Fe^{III}(TMC)(\eta^2\text{-}O_2)](BPh_4)$. **Method A**: after the generation of $[Fe^{III}(TMC)(\eta^2\text{-}O_2)](OTf)$ in CH_3CN from 10 equiv. NEt_3 and 20 equiv. H_2O_2 (e.g. 1.5 mM) at –40 ºC,[2] addition of >10 equiv. $Sc(OTf)_3$ afforded **3** instantly with the absorption band shifting from 835 nm to 520 nm in the UV-visible spectra. While **3** prepared by this method was fairly stable at –40 ºC, addition of <10 equiv. Sc^{3+} resulted in an unstable form of **3** that quickly decayed to a purple species within a minute. **Method B**: addition of ≥1.0 equiv. $Sc(OTf)_3$ to a solution of $[Fe^{III}(TMC)(\eta^2\text{-}O_2)](BPh_4)$ (see last paragraph for details) immediately generated **3**. Preparations of **3** generated by these two methods exhibited identical UV-visible features, EPR signals, and Mössbauer parameters (using ^{57}Fe-enriched precursors). Resonance Raman studies of **3** were conducted on samples prepared from Method A for economical purposes; titration and decay reactions were monitored with **3** prepared by Method B to prevent possible complications from NEt_3 and H_2O_2. Oxygenation reactions of **1** were followed by monitoring the increase in absorbance at 820 nm in UV-visible spectra due to the formation of $[Fe^{IV}(O)(TMC)]^{2+}$ (**4**). Yields of **4** were determined by its absorbance at 820 nm (ε_{820} = 400 $M^{-1}cm^{-1}$).[1]

For the identification and quantification of the decay product of BPh_4^-, the same reactions were carried out in CD_3CN at 0 ºC in the presence of 1 equiv. $NaBPh_4$ and 1 equiv. $Sc(OTf)_3$ followed by running the product solution through a mini-column filled with basic alumina to remove iron complexes. The ^{1}H NMR spectrum of the resulting colorless solution afforded a set of resonances that matched very well with the standard spectra of biphenyl. An internal standard (either 2,6-dimethyl-4-methoxy-phenol or 2,4,6-

trimethyl-phenol) was then added to quantify the concentrations of biphenyl. The internal standards were purified according to published procedures.[3]

Physical methods. UV-Vis spectra were recorded on a HP8453A diode-array spectrometer equipped with a cryostat from Unisoku Scientific Instruments (Osaka, Japan) for temperature control. X-band EPR spectra were obtained at liquid helium temperatures (4K) on a Bruker Elexsys E-500 spectrometer equipped with an Oxford ESR-910 cryostat. ^{1}H NMR was collected on a Varian Inova 300 MHz spectrometer at room temperature. Electrospray ionization mass spectrometry (ESI-MS) studies were conducted on a Bruker BioTof II instrument under positive ion mode with a typical *m*/*z* range of 100 – 1250. Mössbauer spectra were recorded with two spectrometers, using Janis Research Super-Varitemp dewars that allowed studies in applied magnetic fields up to 8.0 T in the temperature range from 1.5 to 200 K. Mössbauer spectral simulations were performed using the WMOSS software package v2.5 (WEB Research, Edina, MN).

We have analyzed the Mössbauer spectra of **3** with the Hamiltonian of equation 1.

$$\mathcal{H} = D\left(S_z^2 - \frac{35}{4}\right) + E(S_x^2 - S_y^2) + g_0\beta \boldsymbol{S}\cdot\boldsymbol{B} + \boldsymbol{S}\cdot\boldsymbol{A}\cdot\boldsymbol{I} - g_n\beta_n \boldsymbol{B}\cdot\boldsymbol{I} + \mathcal{H}_Q \qquad \textbf{(1)}$$

where *D* and *E* are the axial and rhombic ZFS parameters, *A* is the ^{57}Fe magnetic hyperfine tensor and H_Q describes the nuclear quadrupole interactions:

$$\mathcal{H}_Q = \frac{eQV_{zz}}{12}\left[3I_z^2 - I(I+1) + h\left(I_x^2 - I_y^2\right)\right] \qquad (2)$$

where *e* is the proton charge, V_{zz} is an element of the electric field gradient tensor, and η is the asymmetry parameter.[2]

Resonance Raman spectra were collected on an ACTON AM-506M3 monochromator with a Princeton LN/CCD data collection system (LN-1100PB) using a Spectra Physics Model 2060 krypton laser or a Spectra Physics Beamlok 2065-7S argon laser, and Kaiser Optical holographic super-notch filters. Low-temperature spectra of **3** in CH_3CN were obtained at 77 K using a 135° backscattering geometry. Samples were frozen onto a gold-plated copper cold finger in thermal contact with a Dewar flask containing liquid nitrogen. The Raman frequencies were referenced to indene. Slits were set for a band-pass of 4 cm^{-1} for all spectra. Raman spectra were baseline corrected, and intensity corrected according to the 773 cm^{-1} solvent peak of CH_3CN.

Fe K-edge X-ray absorption spectroscopic studies of **3** were conducted at beamline X3B of the National Synchrotron Light Source (NSLS) at the Brookhaven National Lab in Upton, NY. The sample consisted of a 4.3 mM solution of **3** frozen in acetonitrile in a large tandem Mössbauer/XAS sample cup. The sample was run in fluorescence mode using a new 31-element Canberra Ge detector. The sample was maintained at ~ 19 K during data collection. In order to prevent possible photoreduction, data were collected on three different spots on a single sample. Three scans were collected on the first spot, and two additional scans were collected on each of two additional spots. The raw XAS data were examined, average, and processed for analysis with EXAFSPAK.[4] No channels were excluded from the analysis. No points were excluded from the raw data. Due to noise in the data at high *k* values, deglitching was performed at *k*~11.7, 13.4, and 13.7 by fitting the EXAFS data with a cubic function in EXAFSPAK, which allowed us to consider a *k* range of 2-14 $Å^{-1}$ (resolution = 0.132 Å). To confirm that deglitching did not influence the fit, both the "raw" data and the

deglitched data were fit with the same parameters. Fits were generated using the opt program in EXAFSPAK. The energies were referenced against an internal Fe foil reference at 7112.0 eV. A unit-weighted average was used for both data sets. The $k^3\chi(k)$ EXAFS data was analyzed using EXAFSPAK with phase and amplitude parameters derived from FEFF 8.40.[5] The goodness-of-fit parameter F is defined as $[\Sigma k^6(\chi_{expt} - \chi_{calc})^2 / \Sigma k^6(\chi_{expt})^2]^{1/2}$. A second goodness-of-fit parameter F' is defined as $F' = F^2 / \nu$, where $\nu = N_{IDP} - \rho$. N_{IDP} is the number of independent data points ($N_{IDP} = 2\Delta k \Delta r/\pi$), and ρ is the number of floated variables in each optimization step.[6] F' is a measure of whether an added shell significantly improves the fit. In all analyses, the coordination number of a given shell was kept as a fixed parameter, and varied iteratively when bond lengths, Debye-waller factors, and the edge shift parameter E_0 were allowed to freely float. The scale factor S_0 was set to 0.9

X-ray Absorption Near Edge Structure (XANES) data **3** were taken on a frozen solution sample (~4.3 mM in CH_3CN) at beamline 7-3 of Stanford Synchrotron Radiation Lightsource (SLAC National Accelerator Laboratory, Menlo Park, CA). Pre-edge analysis of **2** and **6** were carried out for XAS data that were also collected at 7-3 beamline of SSRL, with the corresponding sample descriptions and XAS analyses previously published.[2] The data were collected in fluorescence mode using a 30-element germanium detector (Canberra) at a sample temperature of *ca.* 10 K. The pre-edge region was curve-fitted using SSExafs to generate pre-edge areas according to published protocols.[7,8] The heights, positions, and widths of preedge peaks were refined using a Gaussian function and all parameters were allowed to float freely for the final fit.

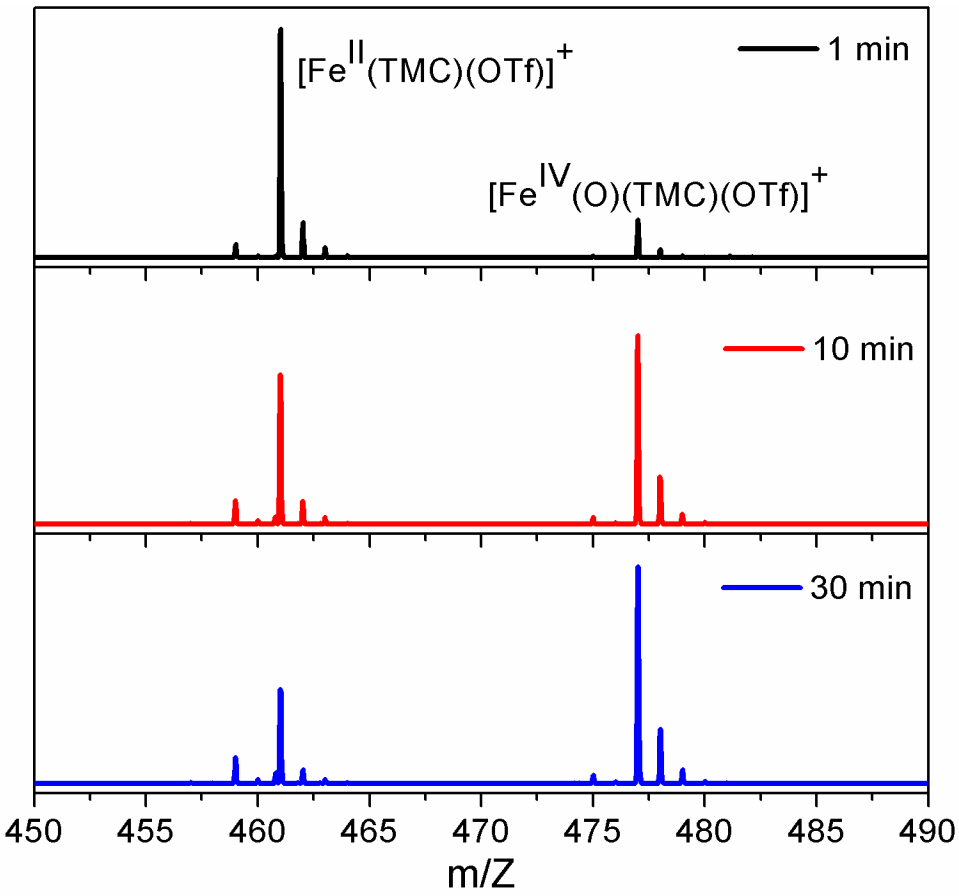

Figure S1. Electrospray ionization (ESI) mass spectra for the reactions of $[Fe^{II}(TMC)(NCCH_3)](OTf)_2$ with O_2/$Sc(OTf)_3$/$NaBPh_4$ in CH_3CN at 25 ºC. Small aliquots of the solution were collected at 1-min, 10-min, and 30-min time-points after the reaction was initiated and injected into an ESI mass spectrometer in positive ion mode.

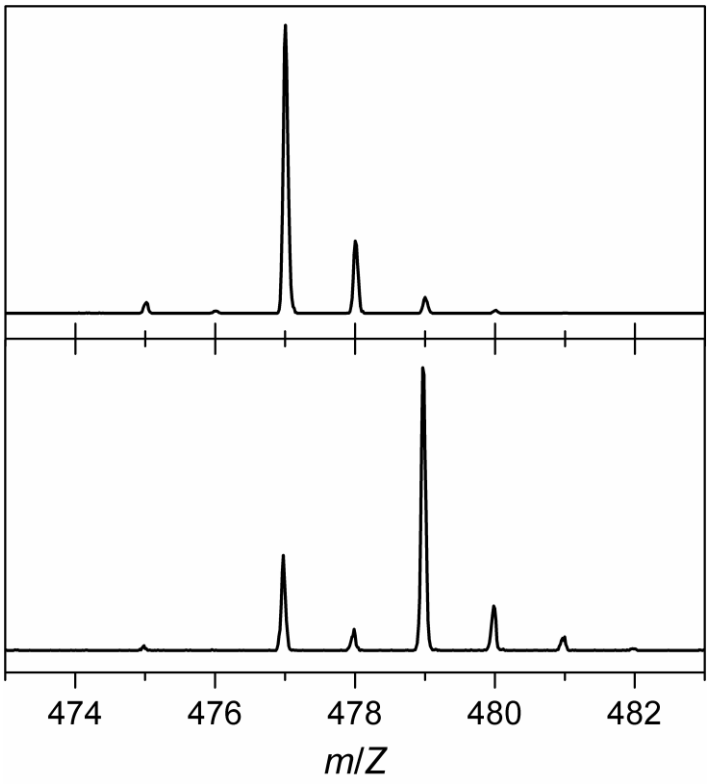

Figure S2. Electrospray ionization mass spectra of $\{[Fe^{IV}(O)(TMC)](OTf)\}^{+}$ prepared from acetonitrile solution of **1**, Sc^{3+}, BPh_4^-, and O_2 ($^{16}O_2$ in the top panel:and$^{18}O_2$ in the bottom panel).

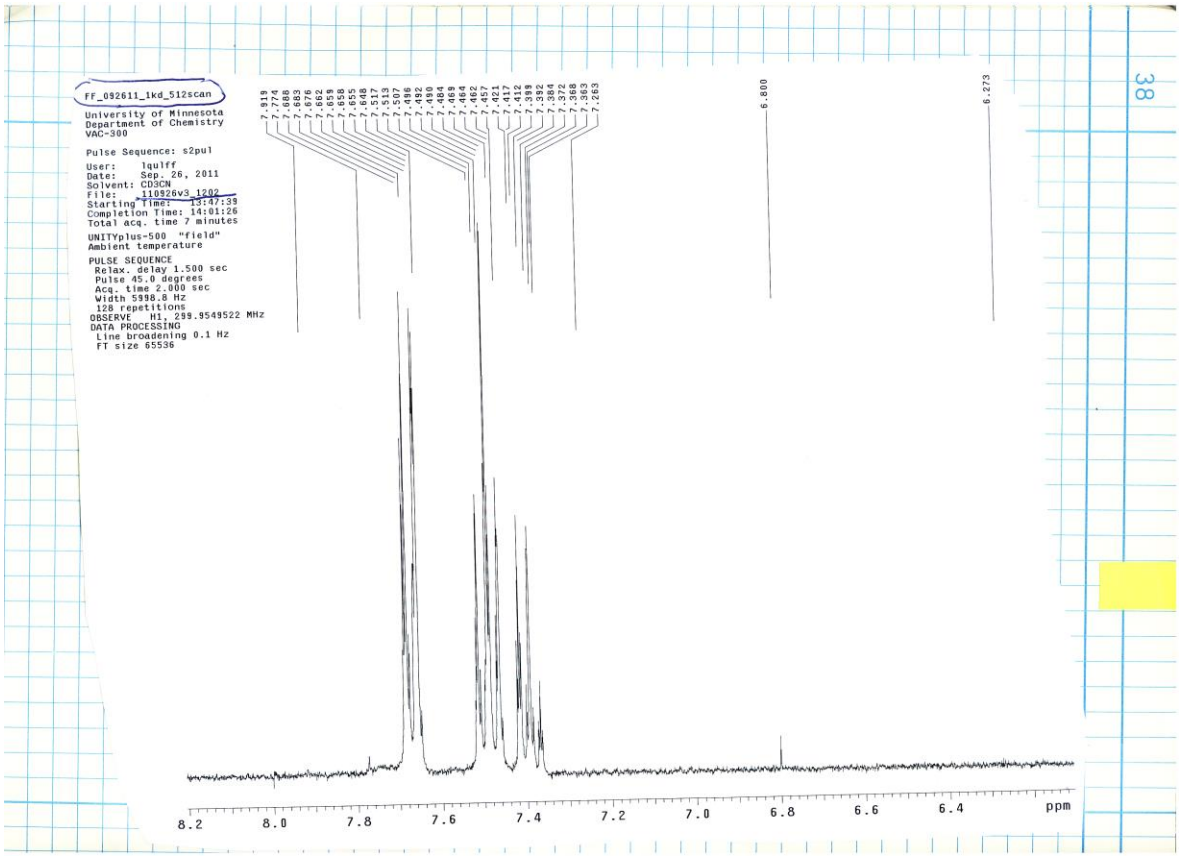

Figure S3. ^{1}H NMR spectrum of organic products in CD_3CN generated from the oxygenation reaction of **1** in the presence of 1 equiv. $Sc(OTf)_3$ and 1 equiv. $NaBPh_4$ (reaction temperature is 0 ºC) followed by filtering out any iron complexes by a flash column of alumina (basic). Only peaks derived from 1,1'-biphenyl were observed in the ^{1}H NMR spectrum.

XAS analysis and results. As shown in Figure S4 and listed in Table S1, the first inflection point of the Fe K-edge occurs at 7125.3 eV, which was taken as the edge energy. In comparison, $[Fe^{III}(O_2)(TMC)]^{+}$ (**2**) and $[Fe^{III}(OOH)(TMC)]^{2+}$ (**5**) both had an edge energy of 7125.1 eV.

Table S1. Pre-edge analysis of **2**, **3**, and **5**.

	E_0 (eV)	$E_{pre\text{-}edge}$ (eV)	Height	Width	Area*
2	7125.1	7113.5	0.057(2)	2.13(10)	12.9 (7)
		7115.4	0.022(2)	2.13 (10)	5.0 (4)
3	7125.3	7113.3	0.056(2)	2.40(10)	14.4(6)
5	7125.1	7114.1	0.076(1)	2.78(5)	22.4(4)

*Pre-edge areas have been multiplied by a factor of 100.

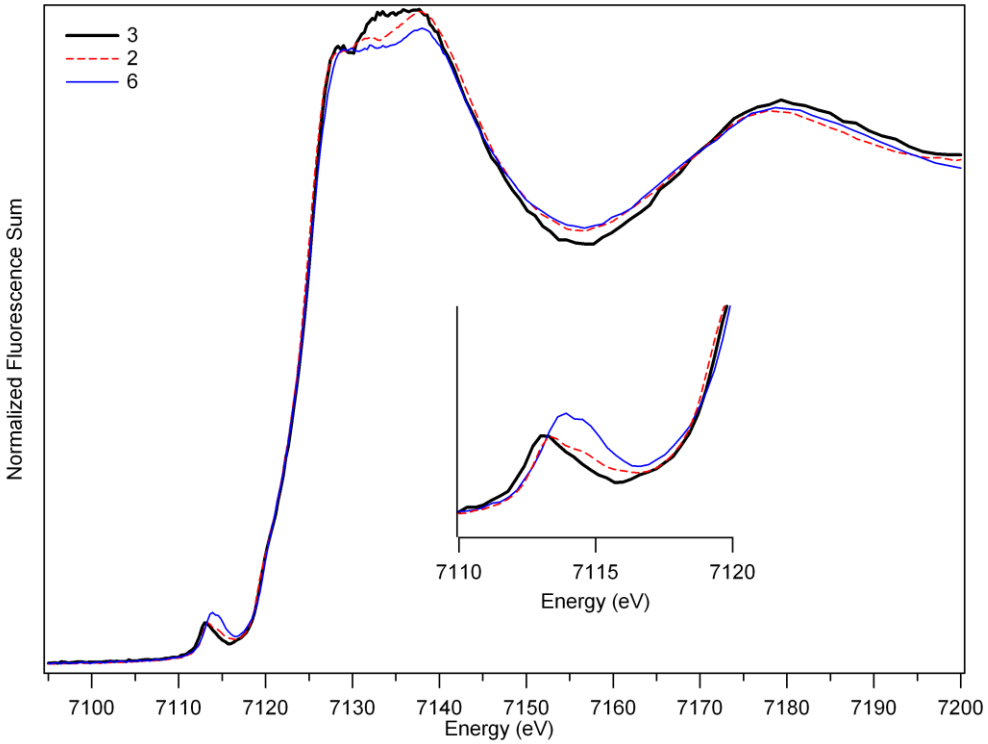

Figure S4. Fe *K*-edge XANES spectra for **2** (red dashed line), **3** (black solid line), and **5** (blue solid line).

The best fits of the EXAFS data corresponding to **3** include four N/O scatterers at ~2.18 Å that are assigned to the TMC macrocycle. Increasing the coordination number to five yielded an unreasonably large σ^2 value of ~12 (Fit 3 in Table S2) and suggests the axial site *trans* to the peroxo moiety is vacant. The overall quality of fits, as measured by the goodness-of-fit parameter F and the edge shift (E_0), is greatly improved by the addition of a second shell at ~1.98 Å, which is derived from peroxo ligand (Fits 4 and 5 in Table S2). The inclusion of a single O/N scatterer at ~1.98 Å (Fit 4) produces an unreasonable σ^2 value of less than 0. On the other hand, the inclusion of two such scatterers (Fit 5) produces a reasonable σ^2 value of ~3 that is comparable to that found for **2**, indicating that the peroxo ligand coordinated in a symmetric side-on (η^2) fashion. Carbon scatterers attributed to the TMC ligand are apparent at ~2.99 and 3.15 Å, reminiscent of EXAFS fits of $[Fe^{III}(O_2)(TMC)]^+$ and $[Fe^{III}(OOH)(TMC)]^{2+}$.[2]

We also attempted to include a scandium scatterer in the EXAFS model. A slight improvement in GOF (fits 13 and 14 in Table S2) was obtained with the inclusion of a Sc scatterer of 3.8 Å that has a reasonable Debye-Waller factor in the unfiltered data set (σ^2 ~ 4). Such an Fe•••Sc distance can be compared with the Fe•••Cu distance of 3.6-3.7 Å found for a Cu(μ-η^2:η^2-peroxo)heme complex by EXAFS and DFT.[9] However, the following two considerations prevented us from unambiguously identifying the Sc scatterer. First, inclusion of the Sc scatterer only marginally improves the F-factor, probably due to the low intensity of distant scatterers in the outer shell; Second, different Fe•••Sc distances yielded comparable values of F and E_0. For example, while the best fit placed the Sc^{3+} scatterer at ~3.82 Å from the iron center, moving the heavy atom to ~4.09 Å produced a fit of comparable quality (Table S2, fits 14 and 15). Therefore, we

conclude that the Sc scatterer could not be definitively located in the EXAFS analysis. It is not surprising that the effect of the Sc scatterer is not more pronounced because that scandium is not a particularly heavy scatterer and distant scatterers in the Fourier-transformed spectrum typically result in low intensity unless fixed by strong interactions. Moreover, the dynamic vibrational disorder experienced by **3** could lead to different Fe•••Sc distances. Similarly, EXAFS analysis of $[Co^{IV}(O)(TMG_3tren)(ScOTf_3)]^{2+}$ (recently reformulated as $[Co^{III}(OH)(TMG_3tren)(ScOTf_3)]^{2+}$ by Borovik[10]) also did not reveal a scandium scatterer.[11]

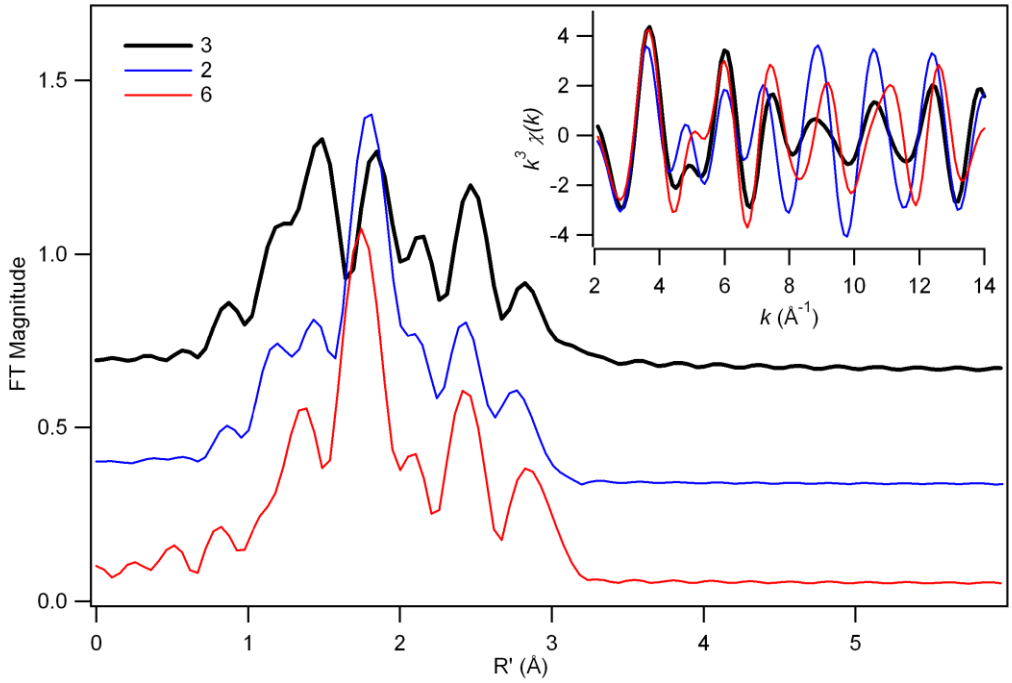

Figure S5. Fourier transform of Fe *K*-edge EXAFS data for **3** (black line, offset 0.65), **2** (blue line, offset 0.40), and **5** (red line, offset 0.00) over a *k*-range of 2-14 Å^{-1} with $k^3\chi(k)$ vs *k* data shown in the inset. Back-transform range: 0.3 to 3.0 Å (2), 0.75 to 3.2 Å (3), and 0.3–3.2 Å^{-1} (5).

Table S2. EXAFS fitting results for **3**, considering the unfiltered data, k = 2 – 14 Å (resolution 0.132 Å).

	Fe–N/O			Fe–O/N			Fe•••Sc			Fe•••C			Fe•••C					
Fit	*N*	r (Å)	$\sigma^{2(a)}$	*N*	r (Å)	σ^2	*N*	r (Å)	σ^2	*N*	r (Å)	σ^2	*N*	r (Å)	σ^2	E_0	F	F’
1	3	2.20	5.07													8.05	447.8	785.8
2	4	2.20	8.12													5.95	431.7	771.5
3	5	2.17	12.88													4.20	423.1	763.8
4	4	2.18	4.31	1	1.98	-0.40										2.23	246.9	583.5
5	4	2.19	3.22	2	1.98	2.83										0.55	250.8	588.1
6	4	2.19	3.19	2	1.98	2.76				4	3.11	6.58				0.10	181.4	500.1
7	**4**	**2.18**	**3.57**	**2**	**1.98**	**2.85**				**4**	**3.00**	**2.25**	**4**	**3.15**	**1.10**	**-1.30**	**141.30**	**441.5**
8	5	2.17	6.50	1	1.96	-0.40				4	3.02	2.33	4	3.16	1.13	-0.33	149.50	454.1
9	4	2.18	3.94	2	1.98	3.17	1	3.26	0.47	4	2.99	-1.30	4	3.12	-3.00	-1.33	123.80	413.2
10	4	2.19	3.24	2	1.98	2.80	1	3.15	7.92							0.15	207.30	534.7
11	4	2.19	3.21	2	1.98	2.86	1	3.82	6.24							0.67	246.80	583.4
12	4	2.19	3.19	2	1.98	2.77	1	3.82	6.26	4	3.11	6.55				0.20	177.90	495.2
13	4	2.18	3.61	2	1.98	2.92	1	3.82	4.36	4	3.00	1.95	4	3.15	0.77	-1.19	136.60	433.9
14	4	2.18	3.60	2	1.98	2.90	1	3.82	4.60	4	3.00	1.98	5	3.15	1.85	-1.27	134.40	430.5
15	4	2.18	3.61	2	1.98	2.87	1	4.10	4.13	4	3.00	2.05	5	3.15	2.04	-1.40	134.10	430.1

F = goodness of fit parameter = $[\Sigma^6(\chi_{expt} - \chi_{calc})^2 / \Sigma k^6(\chi_{expt})^2]^{1/2}$. F’ = weighted F factor = F^2 / ν, where $\nu = N_{IDP} - \rho$. N_{IDP} is the number of independent data points ($N_{IDP} = 2\Delta k \Delta r/\pi$), and ρ is the number of floated variables in each optimization step

Table S3. EXAFS fitting results for **3**, considering the deglitched, unfiltered data, k = 2 – 14 Å (resolution 0.132 Å).

	Fe–N/O			Fe–O/N			Fe•••Sc			Fe•••C			Fe•••C				
Fit	*N*	r (Å)	$\sigma^{2(a)}$	*N*	r (Å)	σ^2	*N*	r (Å)	σ^2	*N*	r (Å)	σ^2	*N*	r (Å)	σ^2	E_0	F
16	3	2.21	4.60													7.47	358.1
17	4	2.19	8.97													5.60	356.1
18	5	2.17	13.05													4.11	344.7
19	4	2.18	4.79	1	1.97	-0.10										2.00	196.1
20	4	2.19	3.64	2	1.98	3.20										0.30	199.4
21	4	2.19	3.62	2	1.98	3.11				4	3.10	6.46				-0.21	128.7
22	**4**	**2.18**	**3.78**	**2**	**1.98**	**3.08**				**4**	**3.02**	**3.36**	**4**	**3.16**	**2.40**	**-1.17**	**95.91**
23	4	2.19	3.65	2	1.98	3.10	1	3.14	7.93							-0.26	155.10
24	4	2.18	3.74	2	1.97	2.90	1	3.20	3.60	4	3.03	3.41				-1.43	104.20
25	4	2.18	3.99	2	1.98	3.12	1	3.25	0.24	4	2.98	-0.50	4	3.11	-2.60	-1.64	82.89
26	4	2.19	3.62	2	1.98	3.19	1	3.80	6.64							0.37	195.50
27	4	2.19	3.59	2	1.98	3.09	1	3.80	6.62	4	3.10	6.41				-0.13	125.20
28	4	2.18	3.79	2	1.98	3.09	1	3.81	6.07	4	3.01	3.29	4	3.16	2.24	-1.13	92.58
29	4	2.18	3.79	2	1.97	3.08	1	3.80	6.13	4	3.00	3.32	5	3.15	3.24	-1.24	89.97

Table S4. EXAFS fitting results for **3**, considering the filtered data, k = 2 – 14 Å (resolution 0.132 Å) with a back-transform range of 0.75 to 3.2 Å.

	Fe–N/O			Fe–O/N			Fe•••Sc			Fe•••C			Fe•••C				
Fit	*N*	r (Å)	$\sigma^{2(a)}$	*N*	r (Å)	σ^2	*N*	r (Å)	σ^2	*N*	r (Å)	σ^2	*N*	r (Å)	σ^2	E_0	F
30	4	2.20	8.19													6.48	157.3
31	4	2.18	4.64	1	1.97	0.00										2.00	74.62
32	4	2.19	3.55	2	1.98	3.12										-0.11	76.99
33	4	2.19	3.50	2	1.98	3.13				4	3.10	7.22				-0.17	36.79
34	4	2.18	3.83	2	1.97	3.18				4	3.01	1.51	4	3.16	0.62	-1.33	8.23
35	**4**	**2.18**	**3.83**	**2**	**1.97**	**3.14**				**4**	**3.00**	**1.38**	**5**	**3.15**	**1.61**	**-1.46**	**6.88**
36	4	2.18	3.87	2	1.97	3.18	1	3.83	26.07	4	3.00	1.46	5	3.15	1.69	-1.43	6.50

References

1. Rohde, J.-U.; In, J.-H.; Lim, M. H.; Brennessel, W. W.; Bukowski, M. R.; Stubna, A.; Münck, E.; Nam, W.; Que, L., Jr. *Science* **2003**, *299*, 1037-1039.

2. Li, F.; Meier, K. K.; Cranswick, M. A.; Chakrabarti, M.; Van Heuvelen, K. M.; Münck, E.; Que, L. *J. Am. Chem. Soc.* **2011**, *133*, 7256-7259.

3. Armarego, W. L. F.; Perrin, D. D. *Purification of Laboratory Chemicals*; Butterworth-Heinemann: Oxford, 1997.

4. George, G. N.; Pickering, I. J.; Stanford Synchrotron Radiation Laboratory, Stanford Linear Accelerator Center: Stanford, California, 2000.

5. Ankudinov, A. L. R., B.; Rehr, J. J.; Conradson, S. D. *Phys. Rev. B: Condens. Matter Mater. Phys.* **1998**, *58*, 7565–7576.

6. Riggs-Gelasco, P. J.; Stemmler, T. L.; Penner-Hahn, J. E. *Coord. Chem. Rev.* **1995**, *144*, 245-286.

7. Scarrow, R. C.; Trimitsis, M. G.; Buck, C. P.; Grove, G. N.; Cowling, R. A.; Nelson, M. J. *Biochemistry* **1994**, *33*, 15023-15035.

8. Shan, X.; Rohde, J.-U.; Koehntop, K. D.; Zhou, Y.; Bukowski, M. R.; Costas, M.; Fujisawa, K.; Que, L., Jr. *Inorg. Chem.* **2007**, *46*, 8410-8417.

9. Halime, Z.; Kieber-Emmons, M. T.; Qayyum, M. F.; Mondal, B.; Gandhi, T.; Puiu, S. C.; Chufán, E. E.; Sarjeant, A. A. N.; Hodgson, K. O.; Hedman, B.; Solomon, E. I.; Karlin, K. D. *Inorg. Chem.* **2010**, *49*, 3629-3645.

10. Lacy, D. C.; Park, Y. J.; Ziller, J. W.; Yano, J.; Borovik, A. S. *J. Am. Chem. Soc.* **2012**, *134*, 17526-17535.

11. Pfaff, F. F.; Kundu, S.; Risch, M.; Pandian, S.; Heims, F.; Pryjomska-Ray, I.; Haack, P.; Metzinger, R.; Bill, E.; Dau, H.; Comba, P.; Ray, K. *Angew. Chem. Int. Ed.* **2011**, *50*, 1711-1715.

Chapter IX – Spectroscopic Identification of an Fe^{III} Center, not Fe^{IV}, in the Crystalline Sc−O−Fe Adduct Derived from $[Fe^{IV}(O)(TMC)]^{2+}$

Published: Prakash, J.; Rohde, G. T.; **Meier, K. K.;** Jasniewski, A. J.; Van Heuvelen, K. M.; Münck, E.; Que, Jr., L. "Spectroscopic Identification of an Fe^{III} Center, not Fe^{IV}, in the Crystalline Sc–O–Fe Adduct Derived from $[Fe^{IV}(O)(TMC)]^{2+}$." *J. Am. Chem. Soc.* 2015, 137, pp 3478-3481.

Author Contributions: J.P., G.T.R., K.K.M., A.J.J., K.M.V.H., E.M., and L.Q. conceived and designed the experiments. J.P., G.T.R., K.K.M., A.J.J., K.M.V.H. performed the experiments. J.P., G.T.R., K.K.M., A.J.J., K.M.V.H., E.M., and L.Q. analyzed the data. All authors participated in the writing of the paper.

Abstract

The apparent Sc^{3+} adduct of $[Fe^{IV}(O)$-$(TMC)]^{2+}$ (**1**, TMC = 1,4,8,11-tetramethyl-1,4,8,11-tetraazacyclotetradecane) has been synthesized in amounts sufficient to allow its characterization by various spectroscopic techniques. Contrary to the earlier assignment of a +4 oxidation state for the iron center of **1**, we establish that **1** has a high-spin iron(III) center based on its Mössbauer and EPR spectra and its quantitative reduction by 1 equiv of ferrocene to $[Fe^{II}(TMC)]^{2+}$. Thus, **1** is best described as a Sc^{III}−O−Fe^{III} complex, in agreement with previous DFT calculations (Swart, M. *Chem. Commun*. 2013, 49, 6650.). These results shed light on the interaction of Lewis acids with high-valent metal-oxo species.

Introduction

The role of redox-inactive Lewis-acidic metal ions in modulating the chemistry of redox-active metal-oxo centers has recently attracted considerable attention due to the requirement for a Ca^{2+} or Sr^{2+} ion to be an integral part of the oxygen evolving Mn_4O_5 cluster of photosystem II.[1–3] Seminal efforts of Agapie have addressed how the binding of Lewis acidic metal ions can affect properties of manganese-oxo clusters,[4–6] while complementary investigations of Fukuzumi and Nam have demonstrated the significant acceleration by up to 8 orders of magnitude in some cases) of various oxidative transformations carried out by Fe^{IV}=O complexes upon addition of Lewis acidic metal ions, particularly Sc^{3+}.[7,8] Sc^{3+} binding has also been shown to facilitate trapping high-valent metal-oxo and imido complexes of late first row transition metal ions,[9–11] and heterobimetallic complexes with M^{III}–(μ-OH)–M^{II} cores (M^{III} = Fe, Mn, Ga; M^{II} = Ca, Sr, and Ba) have also been structurally characterized.[12]

An exciting development was the report of a crystal structure of the Sc^{3+}-bound $[Fe^{IV}(O)(TMC)]^{2+}$ adduct (TMC = 1,4,8,11-tetramethyl-1,4,8,11-tetraazacyclotetradecane) by Fukuzumi and Nam in 2010,[13] which provided the first crystallographic evidence for Sc^{3+} binding to an $Fe^{IV}(O)$ moiety and formulated the adduct as the neutral [(TMC)-(Fe^{IV}–O–Sc^{III})$(OTf)_4$(OH)] complex (**1**). However, scrutiny of the crystallographic data led to some concern about the iron(IV) oxidation state assignment.[14] Specifically, the observed average Fe–NTMC bond length of 2.18 Å was 0.08 Å longer than that found in the crystal structure of the bona fide $[Fe^{IV}(O)(TMC)(NCMe)]^{2+}$ complex.[15] Additionally, the observed Sc–O bond length of 2.19 Å was more typical of Sc–OH_2 than Sc–OH distances.[16] These discrepancies

prompted Swart to carry out DFT calculations to investigate the oxidation state of the Fe atom.[14] An iron(III) oxidation state was required to reproduce the metal−ligand bond lengths found in the crystal structure, leading Swart to conclude that the adduct should instead be formulated as $[(TMC)Fe^{III}–O–Sc^{III}(OTf)_4(OH_2)]$.

Although there are obviously methods for ascertaining iron oxidation state, **1** has only been characterized by X-ray crystallography. We surmised that the absence of additional data to characterize this intriguing complex was probably due to a lack of sufficient material, so we embarked on an effort to obtain larger amounts of the complex. Via a modification of the preparation method, we were able to obtain the desired adduct in about 50% yield, an amount sufficient to carry out characterization of the complex by Mössbauer and X-ray absorption spectroscopy of the crystals as well as electrospray ionization mass spectrometry and EPR spectroscopy of the solutions obtained from these crystals. Taken together, our studies establish the iron center in the adduct to be high-spin Fe(III). We thus confirm Swart's formulation of adduct **1** as $[(TMC)Fe^{III}–O–Sc^{III}(OTf)_4(OH_2)]$.

Results and Discussion

Our attempts to obtain larger amounts of **1** led us to make a small modification of the procedure reported by Fukuzumi et al.[13] and afforded a structural analogue of the target complex, designated **1a**, in which the apical water-derived Sc^{3+} ligand was replaced by MeCN (Figure 1). Instead of PhIO, 2-($tBuSO_2$)-C_6H_4IO (ArIO dissolved in trifluoroethanol)[17] was used as oxidant in the synthetic procedure, resulting in a dramatic increase in the yield of these crystals to ~50%. Upon reaction of $Fe^{II}(TMC)(OTf)_2$ with ArIO, the characteristic blue-green chromophore of the oxoiron(IV) complex was obtained as expected. Subsequent addition of 1 equiv of $ScOTf_3$ elicited no immediate change in the near-IR band of the Fe^{IV}=O precursor, but the solution turned yellow over the course of a week, during which time yellow crystals of **1a** were obtained by vapor diffusion of Et_2O into the reaction solution at −20 °C. The crystals of **1a** used for spectroscopic analysis were harvested by decanting off most of the mother liquor followed by carefully removing the remaining mother liquor with tissues; the crystals were then washed quickly with cold diethyl ether and dried under vacuum at −20 °C.

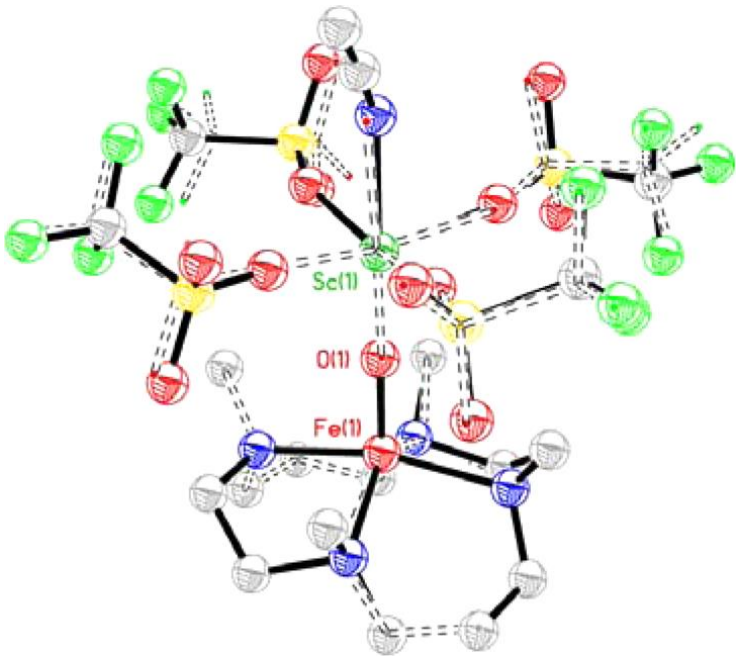

Figure 1. Overlay of X-ray structures of **1a** (solid lines) and **1** (dashed lines). For clarity, the atoms of **1a** were drawn as spheres to the 25% probability level and the atoms of **1** were drawn as small dots. Hydrogen atoms were omitted in both structures. The rmsd between the Sc, μ-O, Fe, and all non-hydrogen TMC atoms was found to be 0.0742 Å and is illustrated by the small deviation in bonds drawn above. The crystallographic R-factor (R1) is 0.0791, and complete XRD experimental and refinement details are reported in the SI.

In addition to X-ray crystallography, we were able to characterize **1a** in the solid state by X-ray absorption and Mössbauer spectroscopy, and in MeCN solution by EPR, ICP-MS, and ESI-MS techniques. X-ray analysis of the crystals of **1a** confirmed the earlier structure reported by Fukuzumi et al.,[13] except for the replacement of the water-derived ligand on the Sc^{3+} in **1** by CH_3CN in **1a**. Despite this change, the crystallographic parameters (Figure S1 and Tables S1A and S1B) obtained for the $(N_4)Fe{-}O{-}Sc(OTf)_4$ core are essentially identical, a conclusion illustrated by the overlay of the two structures (Figure 1). The root-mean-square deviation (rmsd, calculated by OFIT SHELX) for the overlay of the equivalent atoms in the two structures, namely Sc, μ-O, Fe, and all non-

hydrogen atoms of the TMC macrocycle, is remarkably small at 0.0742 Å. As previously noted, the oxo bridge is coordinated syn to the TMC methyl groups, opposite to the anti configuration found for $[Fe^{IV}(O)(TMC)(NCMe)]^{2+}$.[15a] Importantly, key bond distances are in close agreement, such as the Fe−O distances of 1.748(5) Å for **1a** and 1.753(3) Å for **1** and an average Fe−NTMC distance of 2.167(6) Å for **1a** and 2.175(3) Å for **1**. The Fe−O bond lengths are typical of 5-coordinate Fe^{III}−O−Fe^{III} complexes,[18] while the Fe−NTMC distances are associated with Fe^{III}(TMC) complexes.[19−21] Importantly, the apical CH_3CN ligand in **1a** removes the ambiguity of assigning the iron oxidation state based solely on the presence or absence of protons on the solvent-derived apical ligand, which is not advisable with X-ray diffraction experiments. Indeed, two triflate oxygen atoms in the structure of **1** are found at appropriate distances to act as hydrogen bond acceptors for the water derived ligand in **1** (Figure S2), supporting its assignment as a neutral aqua species, rather than a hydroxide as proposed in ref 13.

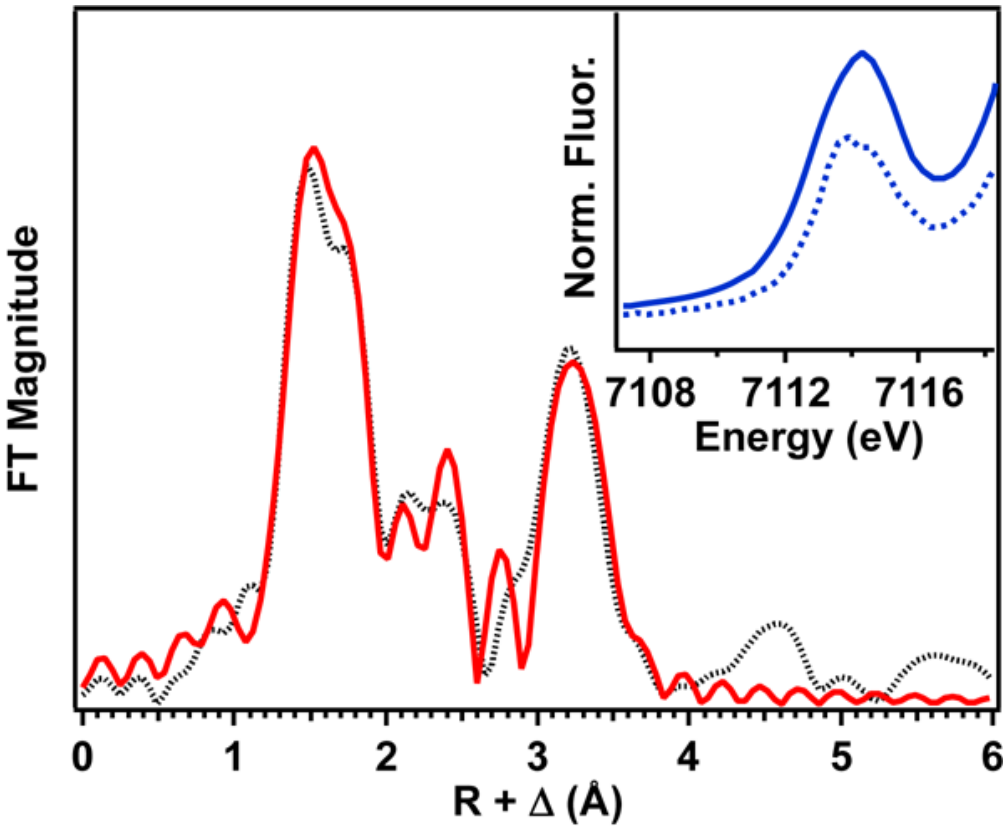

Figure 2. Fourier transform of the Fe K-edge EXAFS data for **1a** over a k range of 2−14.5 $Å^{-1}$ (the black dotted line is experimental data; the solid red line is the best fit with one O scatterer at 1.74 Å, four N scatterers at 2.17 Å, and one Sc scatterer at 3.69 Å). The inset compares the pre-edge features of **1a** (solid line) and $[Fe^{III}(\eta^1\text{-}OOH)(TMC)]^{2+}$ (dotted line).

Fe K-edge X-ray absorption spectroscopic studies were also performed on a solid sample of **1a**. The Fe K-edge of **1a** is observed at 7122.6 eV (Figure S3), which falls within the range of known high-spin Fe(III) species.[20,22−24] Moreover, there is a pre-edge peak at 7114.3 eV (Figure 2 inset) with an area of 32 units, which is by far the largest pre-edge area known for any 5- or 6-coordinate high-spin Fe(III) species in the literature.[20,22−24] This large area indicates a high degree of distortion from centrosymmetry upon scandium binding, reflecting the square-pyramidal geometry around the iron(III) ion that moves the Fe 0.53 Å away from the mean N_4-plane of the TMC framework. Although not

as large as **1a**, the pre-edge areas of related $[Fe^{III}(TMC)(\eta^1\text{-}OOH)]^{2+}$ (**2**) and $[Fe^{III}(TMC)(\eta^2\text{-}O_2)]^{+}$ (**3**) complexes are also quite large (22.4 and 17.9 units, respectively),[20] reflecting the large differences between the bond lengths Fe−NTMC (∼2.2 Å) and Fe−O (1.74 Å for **1a**,1.92 Å for **2**, and 1.93 Å for **3**) and the number of O ligands. An EXAFS analysis was performed on this solid sample to ensure that the bulk solid contained the same material as the single crystal of **1a**. Fits of the EXAFS region (Figures 2 and S4 and Table S2) revealed four N scatterers at 2.17 Å, one O scatterer at 1.74 Å, and one Sc scatterer at 3.69 Å, in excellent agreement with the X-ray structure. Importantly, the Sc scatterer in this sample exhibits a much more prominent feature in the Fourier transformed data than in the spectrum of the Sc^{3+} adduct of $[Fe^{III}(TMC)(\eta^2\text{-}O_2)]^{+}$.[20b,21]In order to gain insight into the iron oxidation state, we have studied Mössbauer and EPR spectra of **1a**. Mössbauer spectra of crystals of **1a** were collected at 4.2 K in parallel-applied magnetic fields, B, up to 7.5 T. For B < 2 T the spectra were found to be broadened due to spin−spin interactions between neighboring molecules in the crystals. For B > 4 T, however, the applied field sufficiently decouples these interactions so that well-resolved spectra were obtained. The spectra shown in Figure 3 unambiguously show that **1a** is a high-spin ferric complex. The red lines in Figure 3 are spectral simulations based on the S = 5/2 spin Hamiltonian,

$$H = D\left[S_z^2 - \frac{35}{12} + \left(\frac{E}{D}\right)\left(S_x^2 - S_y^2\right)\right] + g_0\beta\vec{S}\cdot\vec{B} + A_o\vec{S}\cdot\vec{I} - g_n\beta_n\vec{B}\cdot\vec{I} + H_Q \qquad (1)$$

where

$$H_Q = \frac{eQV_{zz}}{12}\left[3I_z^2 - \frac{15}{4} + \eta\left(I_x^2 - I_y^2\right)\right] \qquad (2)$$

and all symbols have their conventional meanings; the parameters used are listed in the caption of Figure 3.

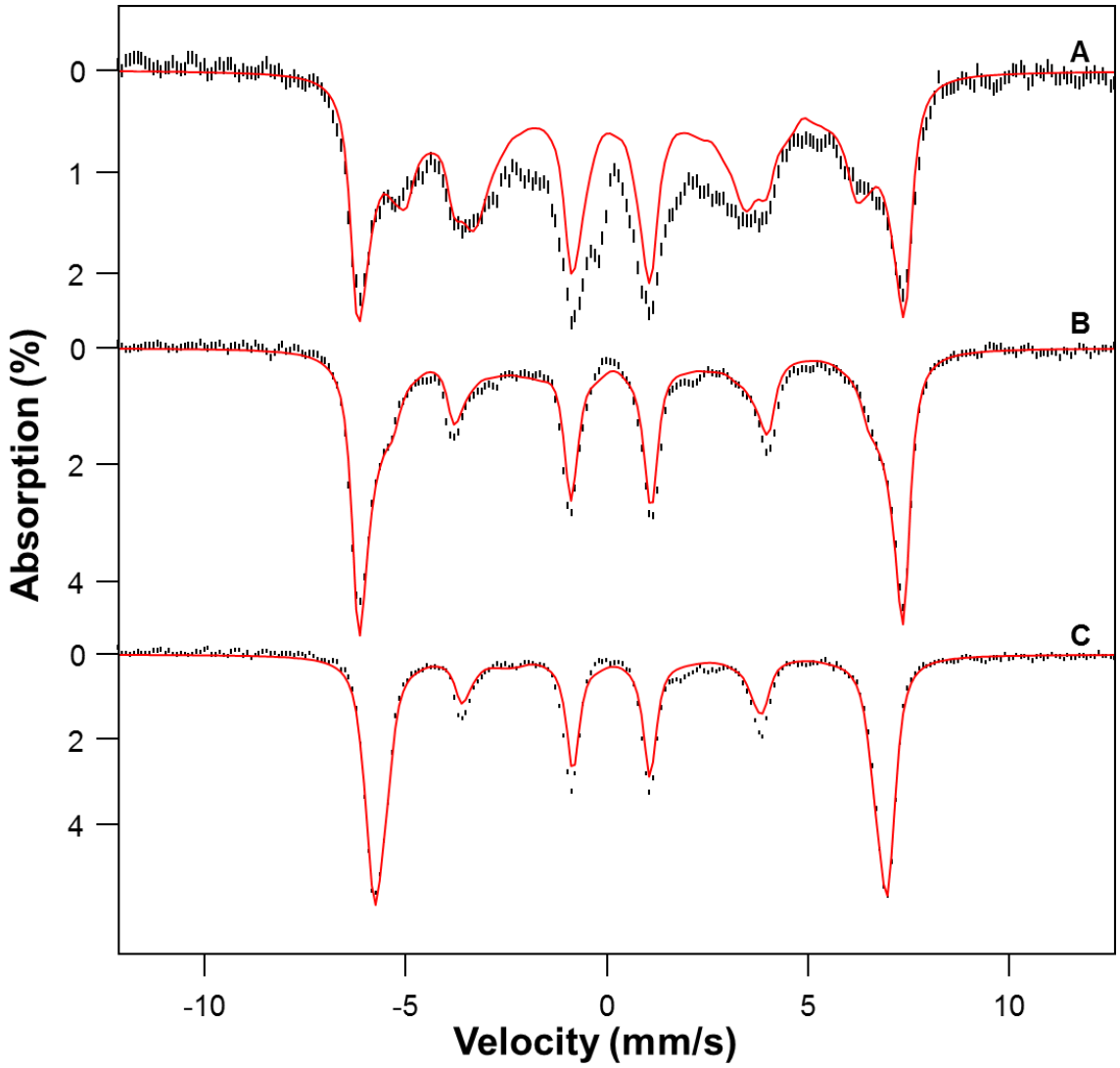

Figure 3. 4.2 K Mössbauer spectra of crystals of **1a** recorded in parallel-applied fields of 1.0 **(A)**, 4.0 **(B)**, and 7.5 T **(C)**. From spectral simulations using an S = 5/2 spin Hamiltonian, we obtained D = 3.25 cm^{-1}, E/D = 0.14(2), g0 = 2.00, $A_0/gn\beta n$ = −19.1(2) T, ΔE_Q = −1.02(5) mm s^{-1}, $\eta \approx 0$, and δ = 0.36(3) mm s^{-1}. We have subtracted from the data a spectral simulation for two Fe^{IV}=O contaminants (representing 8% of Fe), namely $[Fe^{IV}(O)(TMC)(NCMe)]^{2+}$ (5%) and $[Fe^{IV}(O)(TMC)(OH)]^{+}$ (3%), using the parameters reported in ref 15.

The salient features of the spectra are as follows. Complex **1a** has an isomer shift δ = 0.36(3) mm s^{-1} and a quadrupole splitting ΔE_Q = −1.02(5) mm s^{-1}, and the major component of the electric field gradient tensor is negative ($\Delta E_Q < 0$). The δ and

ΔE_Q values agree within the experimental uncertainty with respective values of 0.39(5) and −0.99(50) mm s^{-1} from DFT calculations of Swart who postulated **1** to be a high-spin ferric complex.[14] The ^{57}Fe A-tensor of **1a** is isotropic as expected for high-spin Fe^{III}. The zero-field splitting parameter $D \approx +3-4$ cm^{-1} was determined from the intensities of the nuclear $\Delta m = 0$ transitions (lines 2 and 5 counting from the left). The rhombicity parameter E/D was determined as follows. The splitting between the outermost lines of the B = 1.0 T spectrum reflects the internal magnetic field, $B_{int} = \langle S_y \rangle A_0/g_n\beta_n$, associated with the ground Kramers doublet. The expectation value of $\langle S_y \rangle$, like the effective g-value $g_{eff,y}$ of the doublet, depends sensitively on E/D ($\langle S_y \rangle = -g_{eff,y}/4$ for $\beta B/D \ll 1$ for the spin-down level). With A_0 known from the 4.0 and 8.0 T spectra (which are quite insensitive to E/D along the critical y direction), the magnetic splitting of the 1.0 T spectrum can be used to determine E/D. We found E/D = 0.14 ± 0.02, in excellent agreement with the EPR value E/D = 0.14 obtained for **1a** dissolved in MeCN (see below), showing that both in the solid state and in frozen solution **1a** has a high-spin Fe^{III} site, with the same structure. At least 90% of the iron in the sample can be attributed to **1a**; the sample contains two Fe^{IV}=O contaminants (see Figure 3 caption), estimated to represent ~8% of the Fe in the sample.

The findings obtained by Mössbauer spectroscopy are fully corroborated by the EPR spectra of **1a** obtained in frozen MeCN solution (Figure 4), which display resonances arising from two Kramers doublets of a high-spin Fe^{III} system with D > 0 and E/D = 0.14. A simulation of the whole spectrum (red) is shown in Figure 4, together with a simulation (blue) of the signal associated with the first excited Kramers doublet.

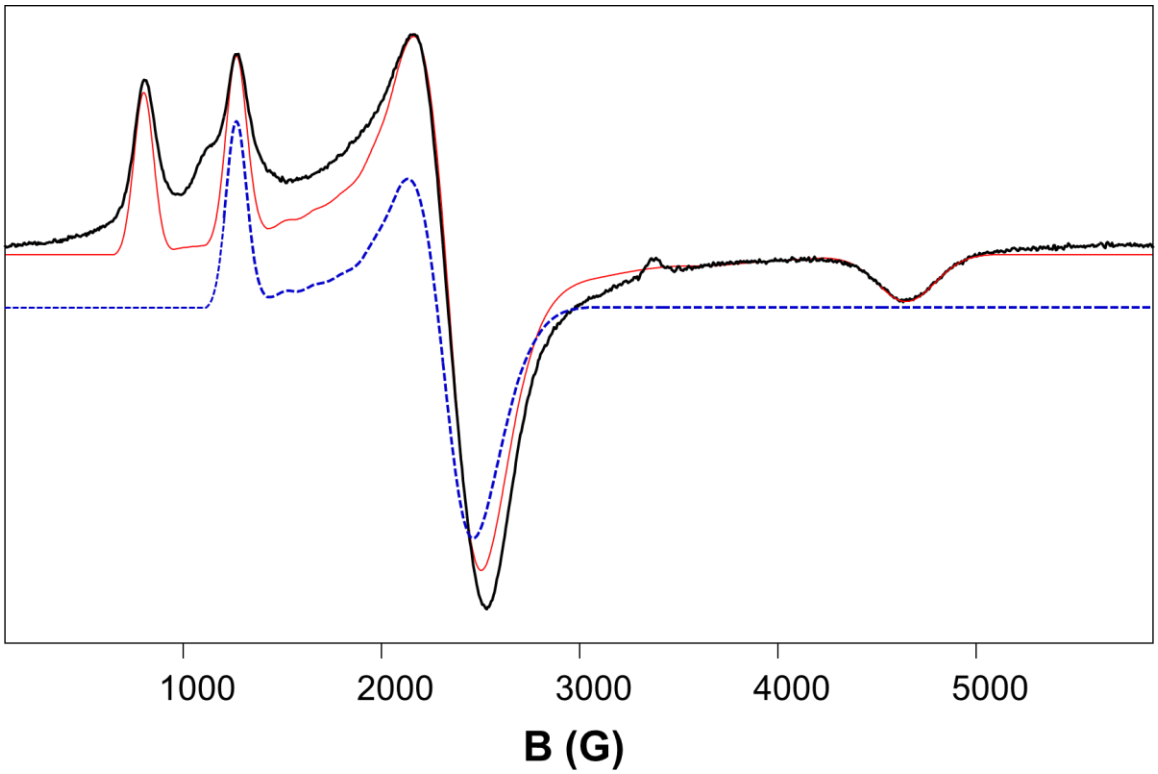

Figure 4. X-band EPR spectrum (black trace) of **1a** in MeCN. The red line is a SpinCount simulation using D = 3.25 cm^{-1}, E/D = 0.14, and g_0 = 2.00. Two of the Kramers doublets of the high-spin iron(III) center contribute to the spectrum. For E/D = 0.14 the ground doublet has g_{eff}= (2.87, 8.57, 1.48), while the spectrum of the middle doublet has g_{eff} = (3.00, 2.64, 5.4) (dashed blue line, offset for clarity). The upper doublet would yield a very weak resonance (not seen) at g_{eff} =9.95. Conditions: T = 30 K; microwave power, 20 μW; modulation amplitude, 1 mT.

The ground Kramers doublet of **1a** gives rise to a signal with effective g-values at g_{eff} = 2.87, 8.57, 1.48), the intensities of which increase as the temperature is decreased from 30 to 2 K (Figure S5). Concomitantly, the intensity of the g_{eff} = (3.00, 2.64, 5.4) signal decreases, which assigns this feature as the g_{max} signal of the middle Kramers doublet. Some features of the EPR spectrum of **1a** are worth noting. First, the sample lacks a signal at g = 4.3 often associated with rhombic Fe^{III}. Second, complex **1a** is one of the rare examples of a high-spin Fe^{III} species with intermediate E/D for which all of the

expected signals from the ground Kramers doublet are clearly resolved. Finally, the EPR results establish that the iron center has a +3 oxidation state in solution.

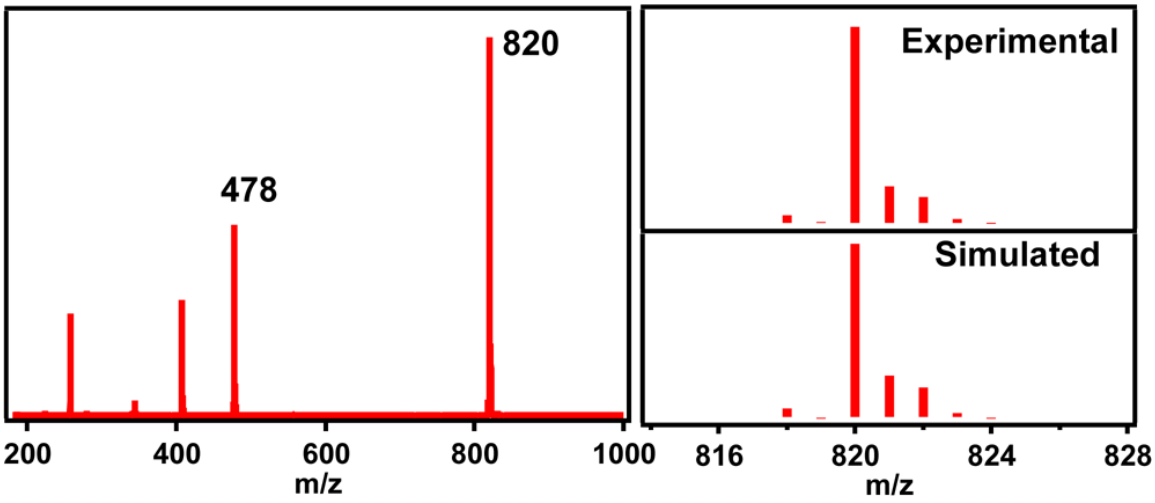

Figure 5. ESI-MS spectrum of **1a** crystals dissolved in MeCN obtained by injecting the solution at −30 °C into the mass spectrometer preset at a low dry gas temperature of 25 °C.

We have characterized other properties of **1a** in MeCN solution. Consistent with the assignment of an iron(III) oxidation state for **1a**, its electronic absorption spectrum (Figure S6) did not exhibit the NIR feature characteristic of $[Fe^{IV}=O)(TMC)(NCMe)]^{2+}$ (λ_{max}= 824 nm).[15] The only feature observed was an intense UV band at λmax= 307 nm (ε=9500 $M^{-1}cm^{-1}$) that is likely associated with the Fe−O−Sc unit of **1a**. Low-temperature ESI-MS analysis showed a prominent ion luster peak at m/z= 820 and an associated isotope pattern corresponding to the formulation $[(TMC)\text{-}(Fe)(O)(Sc)(OTf)_3]^+$ (Figure 5), confirming the persistence of the solid state structure in solution. There was also a less intense peak at m/z = 478 corresponding to the [(TMC)-(Fe)(OH)(OTf)]+ ion, presumably due to a small amount of hydrolysis of **1a** under the experimental conditions.

An ICP-MS analysis of **1a** in MeCN solution revealed a Sc:Fe ratio of 0.9, consistent with the Mössbauer finding showing that **1a** represents 90% of the Fe in the bulk sample. $[Fe^{IV}(O)(TMC)(NCMe)]^{2+}$ was previously shown to under-go 2-e− reduction by 2 equiv of ferrocene in the presence of Sc^{3+}.[13] In contrast, **1a** was reduced by only 1 equiv of ferrocene (even when excess ferrocene is used, Figure S7), affording $[Fe^{II}(TMC)]^{2+}$ quantitatively, as indicated by the quantitative formation of $[Fe^{IV}(O)(TMC)(NCMe)]^{2+}$ upon treating the ferrocene-reduced sample with PhIO. There was also a significant difference in the rates of ferrocene oxidation between $[Fe^{IV}(O)(TMC)(NCMe)]^{+}$ and **1a**. At -20°C, the oxidation of 1 equiv of ferrocene by $Fe^{IV}(O)(TMC)$-$NCMe)]^{2+}$ in the presence of 1 equiv of Sc^{3+} takes∼4h, but the corresponding reaction with **1a** was complete within 10 min, making **1a** 24-fold more reactive than $[Fe^{IV}(O)(TMC)$-$(NCMe)]^{2+}$ in the presence of 1 equiv Sc^{3+} . These results also provide support for the assignment of a +3 oxidation state for the iron center in **1a**.

Conclusions

In summary, we have re-investigated the nature of the apparent Sc^{3+} adduct of $[Fe^{IV}(O)(TMC)]_2^{+3}$ by obtaining sufficient amounts of the isolated complex to allow thorough spectroscopic investigation in both the solid state and in solution. Our studies conclusively establish that the iron center in **1a** is not iron(IV) as was previously assigned on the basis of X-ray crystallography data alone,[13] but is in fact in a high-spin iron(III) state as proposed by Swart.[14] This oxidation state assignment is also supported by the observation that only 1 equiv of ferrocene is required to reduce **1a** to $[Fe^{II}(TMC)]^{2+}$. We are actively pursuing studies to address important mechanistic questions regarding the identity of the 1-e^- reductant that converts $[Fe^{IV}(O)(TMC)]^{2+}$ to **1a** upon Sc^{3+} binding and how the oxo atom becomes coordinated syn to the methyl groups on the TMC ligand.

Acknowledgements

This work was supported by grants from the NSF (CHE-1361773 to L.Q. and CHE-1305111 to E.M.) We thank the University of Minnesota for a dissertation fellowship to G.T.R. and the NIH for a postdoctoral fellowship (GM-093479) to K.M.V.H. XAS data were collected on beamline X3B at the National Synchrotron Radiation Lightsource, which is supported by the U.S. Department of Energy under Contract No. DE-AC02-98CH10886. Use of beamline X3B was made possible by the Center for Synchrotron Biosceinces grant, P30-EB-00998, from the National Institute of Biomedical Imaging and Bioengineering. Lastly, we thank Prof. M. Swart and Dr. Victor G. Young, Jr. for valuable discussions.

References

1. Yano, J.; Yachandra, V. Chem. Rev. 2014, 114, 4175.

2. Umena, Y.; Kawakami, K.; Shen, J.-R.; Kamiya, N. Nature 2011, 473, 55.

3. Rivalta, I.; Brudvig, G. W.; Batista, V. S. Curr. Opin. Chem. Biol. 2012, 16, 11.

4. Kanady, J. S.; Tsui, E. Y.; Day, M. W.; Agapie, T. Science 2011, 333, 733.

5. Tsui, E. Y.; Tran, R.; Yano, J.; Agapie, T. Nat. Chem. 2013, 5, 293.

6. Tsui, E. Y.; Agapie, T. Proc. Natl. Acad. Sci. U.S.A. 2013, 110, 10084.

7. Fukuzumi, S. Coord. Chem. Rev. 2013, 257, 1564.

8. Park, J.; Morimoto, Y.; Lee, Y.-M.; Nam, W.; Fukuzumi, S. Inorg.Chem. 2014, 53, 3618.

9. Chen, J.; Lee, Y.-M.; Davis, K. M.; Wu, X.; Seo, M. S.; Cho, K.-B.;Yoon, H.; Park, Y. J.; Fukuzumi, S.; Pushkar, Y. N.; Nam, W.J. Am. Chem. Soc. 2013,135, 6388.

10. (a) Pfaff, F. F.; Kundu, S.; Risch, M.; Pandian, S.; Heims, F.;Pryjomska-Ray, I.; Haack, P.; Metzinger, R.; Bill, E.; Dau, H.; Comba,P.; Ray, K. Angew. Chem., Int. Ed. 2011, 50, 1711. (b) Kundu, S.;Miceli, E.; Farquhar, E.; Pfaff, F. F.; Kuhlmann, U.; Hildebrandt, P.; Braun, B.; Greco, C.; Ray, K. J. Am. Chem. Soc. 2012,134, 14710.

11. Hong, S.; Pfaff, F. F.; Kwon, E.; Wang, Y.; Seo, M.-S.; Bill, E.; Ray, K.; Nam, W. Angew. Chem., Int. Ed. 2014, 53, 10403.

12. (a) Lacy, D. C.; Park, Y. J.; Ziller, J. W.; Yano, J.; Borovik, A. S. J.Am. Chem. Soc. 2012, 134, 17526. (b) Park, Y. J.; Cook, S. A.; Sickerman, N. S.; Sano, Y.; Ziller, J. W.; Borovik, A. S. Chem. Sci. 2013, 4, 717.

13. Fukuzumi, S.; Morimoto, Y.; Kotani, H.; Naumov, P.; Lee, Y.-M.; Nam, W. Nat. Chem. 2010, 2, 756.

14. Swart, M. Chem. Commun. 2013, 49, 6650.

15. (a) Rohde, J.-U.; In, J.-H.; Lim, M. H.; Brennessel, W. W.; Bukowski, M. R.; Stubna, A.; Münck, E.; Nam, W.; Que, L., Jr. Science 2003, 299, 1037. (b) Jackson, T. A.; Rohde, J.-U.; Seo, M. S.; Sastri, C. V.; DeHont, R.; Stubna, A.; Ohta, T.; Kitagawa, T.; Münck, E.; Nam, W.; Que, L., Jr. J. Am. Chem. Soc. 2008, 130, 12394.

16. Meehan, P. R.; Aris, D. R.; Willey, G. R. Coord. Chem. Rev. 1999, 181, 121.

17. Macikenas, D.; Skrzypczak-Jankun, E.; Protasiewicz, J. D. J. Am. Chem. Soc. 1999, 121, 164.

18. Kurtz, D. M., Jr. Chem. Rev. 1990, 90, 585.

19. Cho, J.; Jeon, S.; Wilson, S. A.; Liu, L. V.; Kang, E. A.; Braymer, J. J.; Lim, M. H.; Hedman, B.; Hodgson, K. O.; Valentine, J. S.; Solomon, E. I.; Nam, W. Nature 2011, 478, 502.

20. (a) Li, F.; Meier, K. K.; Cranswick, M. A.; Chakrabarti, M.; Van Heuvelen, K. M.; Münck, E.; Que, L., Jr. J. Am. Chem. Soc. 2011, 133,7256. (b) Li, F.; Van Heuvelen, K. M.; Meier, K. K.; Münck, E.; Que, L., Jr. J. Am. Chem. Soc. 2013, 135, 10198.

21. Lee, Y.-M.; Bang, S.; Kim, Y. M.; Cho, J.; Hong, S.; Nomura, T.; Ogura, T.; Troeppner, O.; Ivanovic-Burmazovic, I.; Sarangi, R.; Fukuzumi, S.; Nam, W. Chem. Sci. 2013, 4, 3917.

22. (a) Shan, X.; Rohde, J.-U.; Koehntop, K. D.; Zhou, Y.; Bukowski, M. R.; Costas, M.; Fujisawa, K.; Que, L., Jr. Inorg. Chem. 2007, 46, 8410. (b) Koehntop, K. D.; Rohde, J.-U.; Costas, M.; Que, L., Jr. Dalton Trans. 2004, 3191.

23. Westre, T. E.; Kennepohl, P.; DeWitt, J. G.; Hedman, B.; Hodgson, K. O.; Solomon, E. I. J. Am. Chem. Soc. 1997, 119, 6297.

24. Roe, A. L.; Schneider, D. J.; Mayer, R. J.; Pyrz, J. W.; Widom, J.; Que, L., Jr. J. Am. Chem. Soc. 1984, 106, 1676.

Supporting Information

General Considerations. All reagents were purchased from commercial sources and used as received, unless otherwise noted. $[Fe^{II}(TMC)(OTf)][OTf]$ and 2-(tert-butylsulfonyl)iodosylbenzene(2-($^{t}BuSO_2$)C_6H_4IO) were synthesized according to previously published procedures.[1] All moisture and oxygen sensitive compounds were prepared using standard Schlenk-line techniques, and a nitrogen-filled glove box was used for any subsequent manipulation and storage of these compounds.

Preparation of [(TMC)FeOSc(OTf)4(NCMe)] (1a):[$Fe^{II}(TMC)(OTf)][OTf]$(25 mg, 0.04 mmol) as dissolved in MeCN(anhydrous, 1.0 mL),and 2-($^{t}BuSO_2$)C_6H_4IO (13.9 mg, 0.04 mmol) dissolved in trifluoroethanol (anhydrous, 100-150 μL) was added to it. The solution immediately turned to blue-green in color indicative of the formation of $[Fe^{IV}(O)(TMC)(NCMe)]^{2+}$. $ScOTf_3$ (20.2 mg, 0.04 mmol) dissolved in MeCN (anhydrous, 200 μL), was then added to it with no further color change of the solution. The solution was kept for vapor-diffusion (inside Et_2O bath) at -20 °C which afforded yellow crystals of **1a** over the period of a week. The crystals of **1a** were obtained by carefully soaking the solution using Kim wipes, quickly washing them few times with diethyl-ether and drying them under vacuum at -20 °C. Yield: 20-25 mg (50-60 %).UV-vis in MeCN at -20 °C (λ_{max}= 307 nm, ε= 9500 $M^{-1}cm^{-1}$)

Physical Methods: UV-vis spectroscopic measurements were performed using a HP8453A diode array spectrometer equipped with a cryostat rom Unisoku Scientific Instruments (Osaka, Japan).

Electrospray-ionization mass spectrometry (ESI-MS) experiments were carried out on a Bruker BioTOF II mass spectrometer keeping a carrier gas temperature of 25℃.

Mössbauer spectra were recorded with spectrometers using Janis Research Super-Varitemp dewars, which allow studies in the temperature range from 1.5 K to 200K in applied magnetic fields up to 8.0T. Mössbauer spectral simulations were performed using the WMOSS software package (SEE Co, Edina, MN), and isomer shifts (δ) are quoted relative to Fe metal at 298 K.

X-band EPR spectra were collected on a Bruker Elexsys E-500 spectrometer equipped with an Oxford SR-910 cryostat. EPR spectral simulations were carried out using a Windows software package (SpinCount v3.1.2).

X-ray Crystallography Data collection: A crystal (approximate dimensions 0.15 x 0.10 x 0.08 mm^3) was placed onto the tip of a 0.1 mm diameter glass capillary and mounted on a Bruker APEX-II CCD diffractometer for data collection at 102(2) K.[2] The crystal was placed on a slide precooled with liquid nitrogen to lower the possibility of solvent loss from the crystal prior to transferring to the crystal to the diffractometer. A preliminary set of cell constants was calculated from reflections harvested from three sets of 12 frames. These initial sets of frames were oriented such that orthogonal wedges of reciprocal space were surveyed. This produced initial orientation matrices determined from 311 reflections. The data collection was carried out using Mo Kα radiation (graphite monochromator) with a frame time of 25 seconds and a detector distance of 6.0 cm. A randomly oriented region of reciprocal space was surveyed to the extent of one sphere and to a resolution of 0.84 Å. Four major sections of frames were collected with 0.50º steps in w at four different f settings and a detector position f -28º in 2θ. The intensity

data were corrected for absorption and decay (SADABS).[3] Final cell constants were calculated from the xyz centroids of 5457 strong reflections from the actual data collection after integration (SAINT).[4] Please refer to Table S1 for additional crystal and refinement information.

Structure solution and refinement: The structure was solved using SHELXS-97 and refined using SHELXL-97.[5] The space group Pbam was determined based on systematic absences and intensity statistics, [6] and solutions in lower symmetry space groups did not provide meaningful results. A direct-methods solution was calculated, which provided most non-hydrogen atoms from the E-map. Full-matrix least squares / difference Fourier cycles were performed, which located the remaining non-hydrogen atoms. All non-hydrogen atoms were refined with anisotropic displacement parameters, unless stated below. All hydrogen atoms were placed in ideal positions and refined as riding atoms with relative isotropic displacement parameters. The final full matrix least squares refinement converged to R1 = 0.0791 and wR2 = 0.2196 (F^2, all data). The Fe complex is disordered by a 90° rotation over a mirror plane bisecting the Fe-O-Sc axis causing alternating ethylene and propylene groups to be disordered. The volume occupied by the two carbon chains is very similar and the occupancy of each position refined to a 50.3(4):49.7(4) ratio. Disordered pairs of Fe-N distances were restrained to be equal and allowed to refine freely. The internal symmetry of the TMC ligand was utilized and chemically equivalent 1-2 and 1-3 bond distances were restrained to be the same. The 90-degree disorder was also propagated in the apical CH_3CN molecule bound to the Sc. This resulted in four positions for the acetonitrile. The occupancies of the bound CH_3CN were set at 0.25 because it was disordered over a 2/m special position. The four positions of the

CH3CN molecule were modeled with two CH_3CN molecules disordered over the mirror plane with the Part-X statement. The bound CH_3CN positions were consistent with the four possible positions of the CH_3CN as a result of the 90° rotation, and were modeled with isotropic displacement parameters. The Fe complex packs in a head-to-head arrangement, and two positions of the bound CH_3CN are utilized to allow for proper packing with pairs of α-carbons of CH_3CN ~3.6 Å apart. The Sc-N($NCCH_3$) distances were restrained to be equal and allowed to refine freely. The pairs of N-C and C-C bond distances of the bound CH_3CN were restrained to be equal and freely refined to 1.129 Å and 1.445 Å, respectively. Additionally, the sum of the C-N and C-C bonds were restrained to be equal to the N-C(alpha) distance to maintain linearity. One CH_3CN solvent molecule was found in the symmetric unit disordered over four positions in a solvent channel located on the ab plane at c=0. The occupancies were set to 25% and refined with isotropic displacement parameters. Hard bond distance restraints were employed with the solvent CH_3CN molecules using 1.211 Å for the N-C distance and 1.464 Å for the C-C distance and were also restrained to be linear. The two bound triflate anions in the asymmetric unit were disordered over two and four positions, respectively. The Sc-O distances were restrained to be the equal and were allowed to refine freely. The internal symmetry was utilized and chemically equivalent 1-2 and 1-3 bond distances were restrained to be the same. The CF3 group on the triflate disordered over 4 positions was modeled with isotropic displacement parameters. The displacement parameters for all atoms in close proximity were constrained to be the same. See the cif file for more details.

X-ray Absorption Spectroscopy: Iron K-edge X-ray absorption spectra were collected on beam line X3B at the National Synchrotron Light Source (NSLS) at Brookhaven National Lab (BNL) using a 31 element solid state Ge detector (Canberra) with a storage ring current of ~100-300 mA at a power of 2.8 GeV. A sagittally focused Si (111) double crystal monochromator was used for energy selection, with a downstream nickel-coated mirror providing vertical focusing and rejection of higher harmonics. Four (4) scans of the fluorescence excitation spectra were collected from 6882 eV to 8000 eV at a temperature (20 K) that was controlled by closed-system liquid helium Displex cyrostat. An iron foil was placed in the beam pathway prior to I_0 and scanned concomitantly for an energy calibration, with the first inflection point of the edge assigned to 7112.0 eV. A "9 μm" Mn filter and was used to increase the signal to noise ratio of the spectra. Photoreduction was monitored by scanning the same spot on the sample twice and comparing the first derivative peaks associated with the edge energy during collection, but none was observed in the present study.

The detector channels from the scans were examined, calibrated, averaged, and processed for EXAFS analysis using EXAFSPAK to extract χ (k). Theoretical phase and amplitude parameters for a given absorber-scatterer pair were calculated using FEFF 8.40 and were utilized by the "opt" program of the EXAFSPAK package during curve fitting.[7] Parameters for **1a** were calculated using similar coordinates from the available crystal structure of the complex. In all analyses, the coordination number of a given shell was a fixed parameter and was varied iteratively in integer steps, while the bond lengths (R) and mean-square deviation (σ^2) were allowed to freely float. The amplitude reduction factor S_0 was fixed at 0.9, while the edge-shift parameters E_0 was allowed to float as a

single value for all shells. Thus, in any given fit, the number of floating parameters was typically equal to (2 x num shells) + 1.

Pre-edge analysis was performed on data normalized in the "process" program of the EXAFSPAK package,[7] and pre-edge features were fit between 7108 eV to 7118 eV using the Fityk program with pseudo-Voigt functions composed of 50:50 Gaussian/Lorentzian functions.[8]

Table S1a. Crystal data and structure refinement for **1a**.

Empirical formula	$C_{24}\ H_{41}\ F_{12}\ Fe\ N_7\ O_{13}\ S_4Sc$	
Formula weight	1092.69	
Temperature	102(2) K	
Wavelength	0.71073 Å	
Crystal system	Orthorhombic	
Space group	Pbam	
Unit cell dimensions	a = 18.0006 (13) Å	α = 90°
	b = 22.0279(15) Å	β = 90°
	c = 11.4933(8) Å	γ = 90°
Volume	4557.3(6) $Å^3$	
Z	4	
Density (calculated)	1.593 Mg/m^3	
Absorption coefficient	0.760 mm^{-1}	
F(000)	2228	
Crystal color, morphology	yellow, block	
Crystal size	0.15 x 0.10 x 0.08 mm^3	
Theta range for data collection	1.77 to 25.37°	
Index ranges	$-21 \le h \le 21$, $-26 \le k \le 26$, $-13 \le l \le 13$	
Reflections collected	43189	
Independent reflections	4399 [R(int) = 0.0703]	
Observed reflections	3154	
Completeness to theta = 27.50°	99.9%	
Absorption correction	Multi-scan	
Max. and min. transmission	0.7452 and 0.6659	
Refinement method	Full-matrix least-squares on F^2	
Data / restraints / parameters	4399 / 547 / 426	
Goodness-of-fit on F^2	1.043	
Final R indices [I>2sigma(I)]	$R1$ = 0.0791, $wR2$ = 0.1984	
R indices (all data)	R1 = 0.1080, wR2 = 0.2196	
Largest diff. peak and hole	0.829 and -0.539 e.$Å^{-3}$	

Table S1b. Select bond lengths of **1a**, Å

Fe-O_{oxo}	1.748(5)
Fe-N_{ave}	2.167(6)
Sc-O_{oxo}	1.888(5)
Sc-$O_{OTf(ave)}$	2.083(4)
Sc-N_{NcMe}	2.310(10)
Sc···Fe	3.6358(17)
<Sc-O-Fe	179.11(36)°

Table S2. Fits of the EXAFS region of **1a**.

	Fe-N/O			Fe-O			Fe···C			Fe···Sc					
Fit	N	R (Å)	σ^2 ($x10^{-3}$)	N	R (Å)	σ^2 ($x10^{-3}$)	N	R (Å)	σ^2 ($x10^{-3}$)	N	R (Å)	σ^2 ($x10^{-3}$)	E_0	F	F'
1	6	2.15	7.43										-11.2	504	737
2	5	2.15	6.12										-11.0	487	725
3	4	2.15	4.78										-9.86	483	721
4	3	2.16	3.35										-8.63	498	732
5	4	2.17	5.25	1	1.74	2.80							-4.67	379	638
6	5	2.16	6.83	1	1.74	2.94							-5.82	381	640
7	4	2.16	5.26	1	1.73	2.79				1	3.74	0.25	-7.58	279	548
8	4	2.17	5.29	1	1.74	2.90				1	3.68	1.18	-5.00	252	521
9	4	2.17	5.29	1	1.74	2.71				1	3.62	2.51	-3.54	285	555
10	4	2.18	5.40	1	1.74	2.80	5	3.07	14.11	1	3.62	2.68	-2.81	244	512
11	4	2.18	5.39	1	1.74	2.80	3	3.08	11.19	1	3.62	2.68	-2.70	254	523
12	4	2.18	5.34	1	1.74	2.73	3	3.00	4.38	1	3.62	3.22	-2.39	203	467
							3	3.18	0.77						
13	4	2.18	5.35	1	1.74	2.76	3	2.99	3.50	1	3.62	3.07	-2.59	202	466
							4	3.17	2.16						
14	4	2.17	5.37	1	1.74	2.83	3	2.97	2.32	1	3.69	1.12	-3.83	186	448
							4	3.15	2.22						

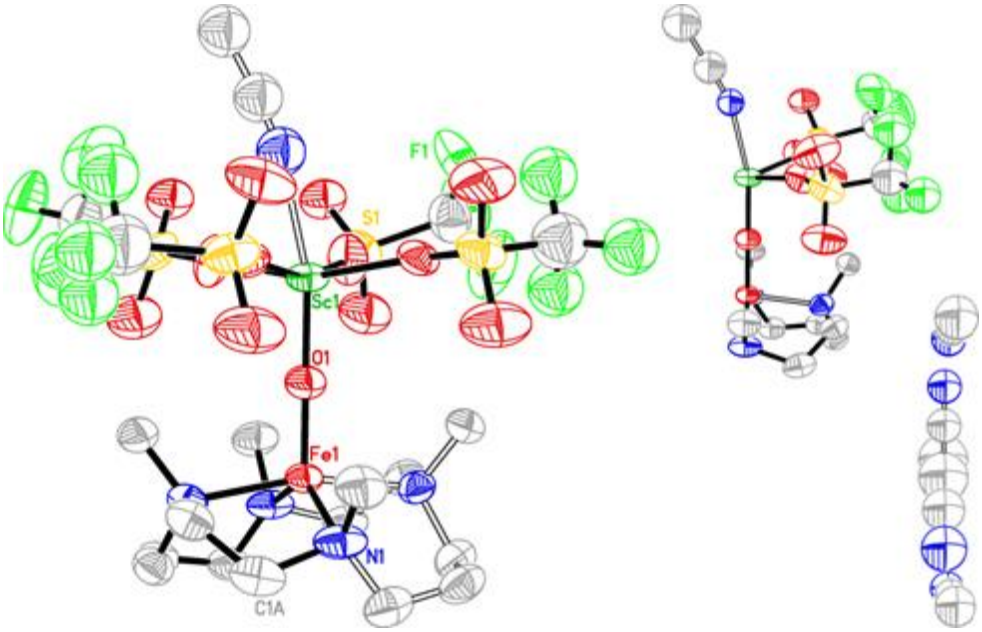

Figure S1. Left: Structure of **1a** with ellipsoids drawn to the 50% probability level with the hydrogen atoms removed for clarity. Only one half of the molecule of interest is unique and it was found to be disordered and modeled over two positions. The full complex was generated by combining the two disordered parts over the mirror plane that bisects the molecule of interest. **Right:** Asymmetric unit displaying the molecule of interest. Only one of the disordered parts of the complex is displayed for clarity. The molecule of interest is located on the mirror plane that results in a disordered macrocyclic ligand. Also in the asymmetric unit is a MeCN solvent channel, which is located on an adjacent mirror plane.

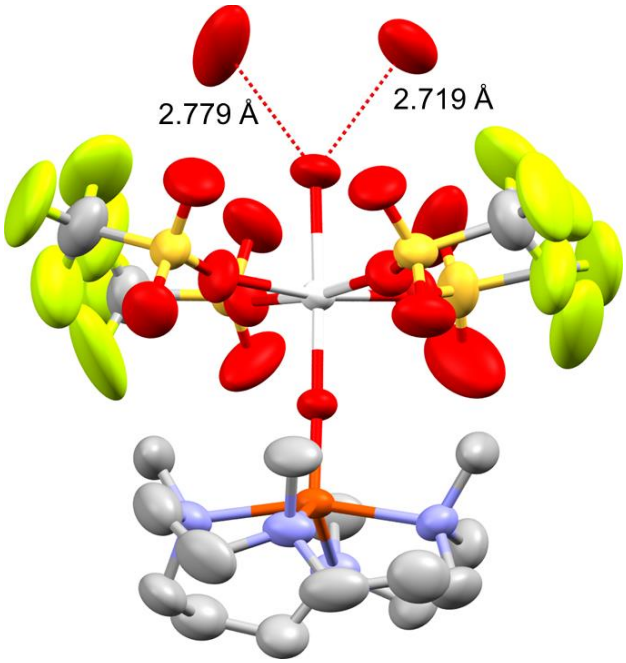

Figure S2. Detail of the crystal structure of **1** reported in the SI of ref. 9 showing O•••O contact distances consistent with H-bond donor-acceptor interactions between the triflate counterions and the apical water-derived ligand to Sc^{3+}.

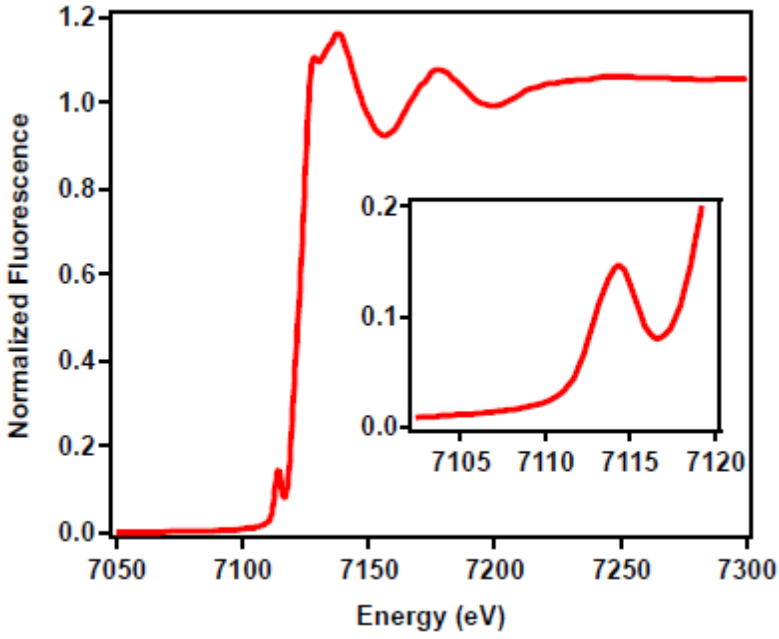

Figure S3. The XANES data for **1a**. **Inset:** The pre-edge feature for **1a**.

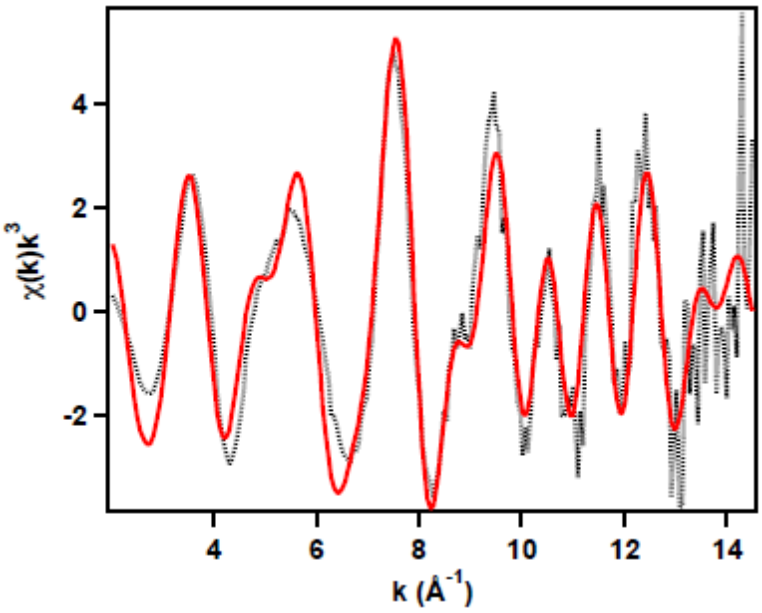

Figure S4. The *k*3-weighted EXAFS data (χ(*k*)) for **1a** over a *k* range of 2−14.5 Å−1. The black dotted line is experimental data, while the solid red line represents the best fit with one O atom at 1.74 Å and four N scatterers at 2.17 Å.

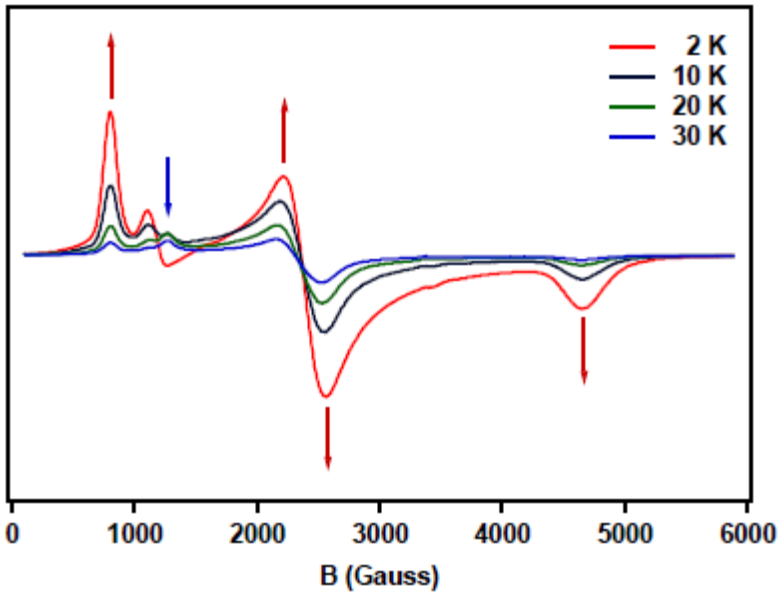

Figure S5. Variable-temperature X-band EPR spectra of **1a** in MeCN. Spectral simulations for the 30 K spectrum are shown in Figure 4 of the main text.

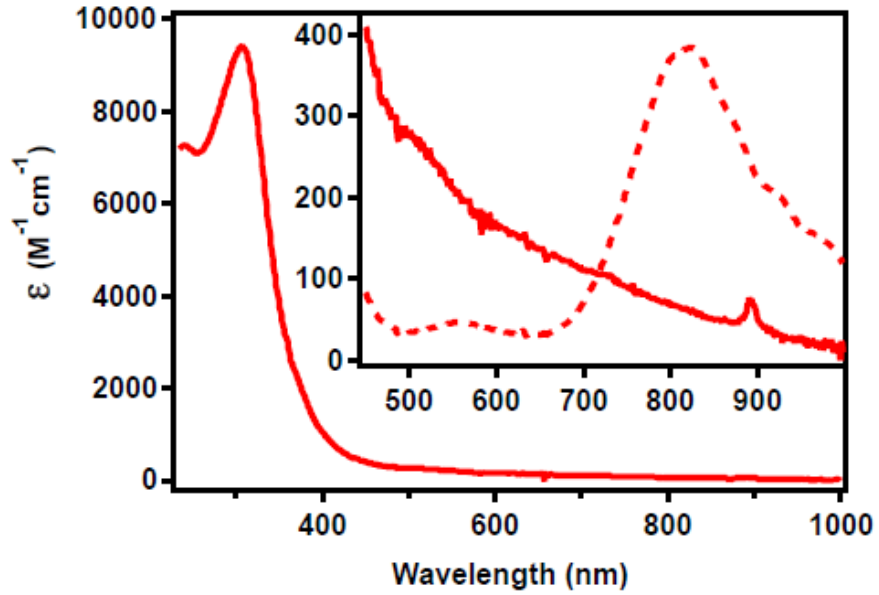

Figure S6. UV-vis spectra of **1a** (solid line) and $[Fe^{IV}(O)(TMC)(NCMe)]^{2+}$ (dotted line) in MeCN at -20 °C.

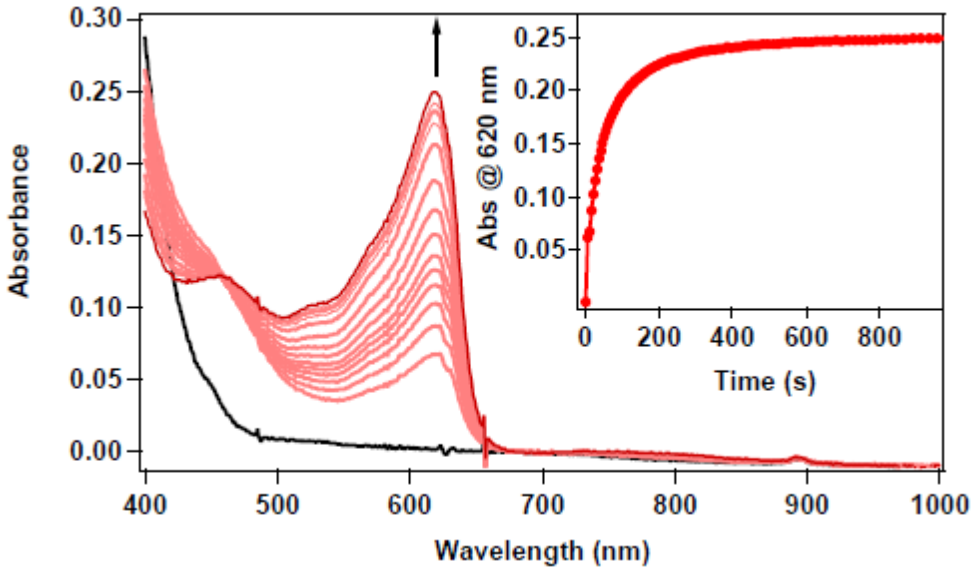

Figure S7. UV-vis spectral changes of the reaction of **1a** (0.5 mM, black line) with ferrocene (1 mM, 2 equiv.) in MeCN at -20 °C. Based on the absorbance increase of 0.25 units at 620 nm and the extinction coefficient of ferrocenium ion (Fc+) of 500 $M^{-1}cm^{-1}$ in MeCN, it can be concluded that only one equivalent of Fc^{+} ion was formed, even though 2 equivalents of ferrocene were present in the solution. Thus **1a** acts a 1-e^{-} oxidant.

References

1. (a) Rohde, J.-U.; In, J.-H.; Lim, M. H.; Brennessel, W. W.; Bukowski, M. R.; Stubna, A.; Münck, E.; Nam, W.; Que, L., Jr. *Science* **2003**, *299*, 1037. (b) Macikenas, D.; Skrzypczak-Jankun, E.; Protasiewicz, J. D. *J. Am. Chem. Soc.***1999**, *121*, 7164.

2. APEX2 V2012.4-3, Bruker Analytical X-ray Systems, Madison, WI (2012).

3. An empirical correction for absorption anisotropy, Blessing R. *Acta Cryst.* **1995**, *A51*, 33-38.

4. SAINT+ V8.18c, Bruker Analytical X-Ray Systems, Madison, WI (2011).

5. SHELXTL V2008/4, Bruker Analytical X-Ray Systems, Madison, WI (2008).

6. XPREP V2008/2, Bruker Analytical X-Ray Systems, Madison, WI (2008).

7. EXAFSPAK: A Suite of Computer Programs for Analysis of X-ray Absorption Spectra, George, G. N. and Pickering, I. J. 2000.

8. Fityk: a general-purpose peak fitting program, Wojdyr, M. *J. Appl. Cryst.* **2010**, *43*, 1126-1128.

9. Fukuzumi, S.; Morimoto, Y.; Kotani, H.; Naumov, P.; Lee, Y.-M.; Nam, W. *Nat.Chem.* **2010**, *2*, 756

Chapter X – One-electron Oxidation of an Oxoiron(IV) Complex to Form an $[O=Fe^{V}=NR]^{+}$ Center.

Published: Van Heuvelen, K.M.; Fiedler, A.T.; DeHont, R.; Shan, X.; **Meier, K.K.**; Bominaar, E.; Münck, E.; Que, Jr. L. "One-electron oxidation of an oxoiron(IV) complex to form an $[O=Fe^{V}=NR]^{+}$ center." *PNAS*. 2012, 109, pp 11933-11938.

Author Contributions: K.M.V.H., A.T.F., R.D., X.S., K.K.M., E.B., E.M., and L.Q. conceived and designed the experiments. K.M.V.H., A.T.F., R.D., X.S., K.K.M. performed the experiments. K.M.V.H., A.T.F., R.D. (Mössbauer, EPR), X.S., K.K.M. (Mössbauer, EPR), E.B., E.M., and L.Q. analyzed the data. A.T.F., R.D., K.K.M., E.B. carried out computational studies. All authors participated in the writing of the paper.

Abstract

Formally oxoiron(V) oxidants are postulated in the catalytic cycles of several iron enzymes that carry out difficult oxidations. Most prominent of these are cytochromes P450, which can hydroxylate strong C–H bonds (1-3), even those of methane (1, 2). Recent evidence has demonstrated that the active oxidant can be best described as having an oxoiron(IV) unit supported by a porphyrin cation radical (4). On the other hand, the Rieske dioxygenases activate O_2 at an active site with a 2-His-1-carboxylate facial triad motif to effect the *cis*–dihydroxylation of C=C bonds in the biodegradation of aromatic complexes (5). For these nonheme iron enzymes, the proposed $Fe^{V}=O$ oxidant is as yet unobserved. However, unlike the porphyrin ligand in cytochrome P450, none of the ligands in the nonheme iron active site appears likely to undergo one-electron oxidation to stabilize the high-valent state. $Fe^{V}=O$ oxidants are also implicated in alkane hydroxylation (6, 7), olefin epoxidation and *cis*-dihydroxylation (8-10), and water oxidation (11) by bio-inspired nonheme iron catalysts supported by neutral tetradentate

ligands, and direct evidence for the formation of oxoiron(V) oxidants has been obtained in two cases by mass spectrometry (10, 12). Despite the wealth of synthetic oxoiron(IV) complexes identified during the last decade (13), to date there is only one spectroscopically well characterized example of an oxoiron(V) complex, $[Fe^{V}(O)(TAML)]^{-}$, which is stabilized by the tetraanionic nature of the TAML ligand (14). Given the ligand environments of the Rieske dioxygenases and the synthetic iron catalysts, we have been investigating the feasibility of generating an oxoiron(V) complex supported by a polydentate ligand of lower charge. Towards this end, we have focused on the one-electron oxidation of the oxoiron(IV) complex $[Fe^{IV}(O)(TMC)(NCCH_3)]^{2+}$ (**1**, see Figure 1), where the oxoiron(IV) moiety is supported by the neutral macrocyclic TMC ligand (15). We chose complex **1** as a starting point for this effort because it is structurally well-characterized and exhibits good thermal stability (16). One-electron oxidation of **1** could be affected by the addition of *tert*-butyl hydroperoxide and strong base, and our novel observations are reported herein.

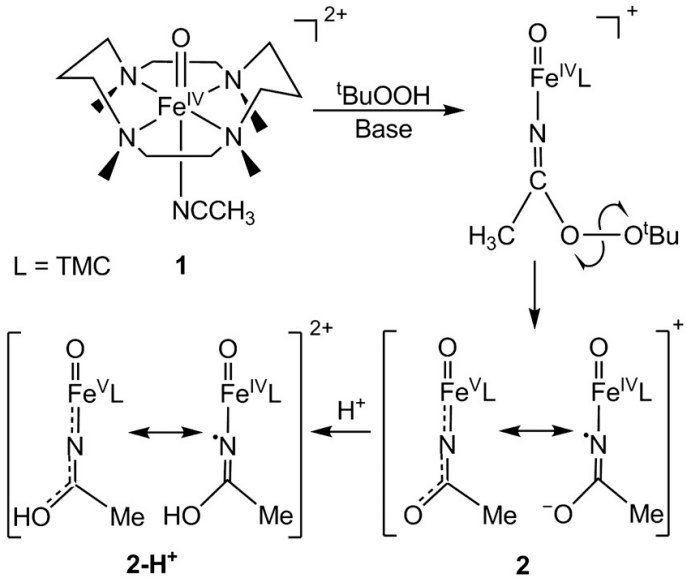

Figure 1. Proposed steps in the one-electron oxidation of **1**.

Introduction

Formally oxoiron(V) oxidants are postulated in the catalytic cycles of several iron enzymes that carry out difficult oxidations. Most prominent of these are cytochromes P450, which can hydroxylate strong C–H bonds (1-3), even those of methane (1, 2). Recent evidence has demonstrated that the active oxidant can be best described as having an oxoiron(IV) unit supported by a porphyrin cation radical (4). On the other hand, the Rieske dioxygenases activate O_2 at an active site with a 2-His-1-carboxylate facial triad motif to effect the *cis*–dihydroxylation of C=C bonds in the biodegradation of aromatic complexes (5). For these nonheme iron enzymes, the proposed Fe^{V}=O oxidant is as yet unobserved. However, unlike the porphyrin ligand in cytochrome P450, none of the ligands in the nonheme iron active site appears likely to undergo one-electron oxidation to stabilize the high-valent state. Fe^{V}=O oxidants are also implicated in alkane hydroxylation (6, 7), olefin epoxidation and *cis*-dihydroxylation (8-10), and water oxidation (11) by bio-inspired nonheme iron catalysts supported by neutral tetradentate ligands, and direct evidence for the formation of oxoiron(V) oxidants has been obtained in two cases by mass spectrometry (10, 12). Despite the wealth of synthetic oxoiron(IV) complexes identified during the last decade (13), to date there is only one spectroscopically well characterized example of an oxoiron(V) complex, $[Fe^{V}(O)(TAML)]^{-}$, which is stabilized by the tetraanionic nature of the TAML ligand (14). Given the ligand environments of the Rieske dioxygenases and the synthetic iron catalysts, we have been investigating the feasibility of generating an oxoiron(V) complex supported by a polydentate ligand of lower charge. Towards this end, we have focused on

the one-electron oxidation of the oxoiron(IV) complex $[Fe^{IV}(O)(TMC)(NCCH_3)]^{2+}$ (**1**, see Figure 1), where the oxoiron(IV) moiety is supported by the neutral macrocyclic TMC ligand (15). We chose complex **1** as a starting point for this effort because it is structurally well-characterized and exhibits good thermal stability (16). One-electron oxidation of **1** could be effected by the addition of *tert*-butyl hydroperoxide and strong base, and our novel observations are reported herein.

Experimental Methods

Preparation of 1, 2, and 2-H$^+$. All reagents and solvents were purchased from commercial sources and used as received unless otherwise noted. As previously reported (15), a solution of [Fe^{II}(TMC)(OTf)](OTf) in acetonitrile was reacted with 1.2 equivalents of PhIO solubilized in methanol to obtain **1** in quantitative yield, as monitored by the appearance of its distinctive chromophore at 820 nm. Compound **2** was prepared at -44 °C in acetonitrile by the addition of at least 3 equivalents of *tert*-butyl hydroperoxide followed by the addition of 1-2 equivalents of NBu_4OH or KO^tBu. Subsequent addition of at least five equivalents of strong acid, HBF_4 or $HClO_4$, yielded **2-H$^+$**. 40% ^{17}O-enriched H_2O was used to prepare the ^{17}O EPR samples.

Physical Methods. An HP 8453A diode-array spectrometer equipped with a Unisoku Scientific Instruments cryostat to maintain a constant temperature was employed to collect electronic absorption spectrum. Resonance Raman spectra were generated via excitation with Kr^+ and Ar^+ lasers (Spectra Physics BeamLok 2060-RM) with a power of < 10 mW at the samples, and the spectra were collected using an ACTON AM-506M3 monochromator and a LN/CCD-1340 x 400 PB detector. X band (9.28 GHz) EPR spectra were recorded on a Bruker ESR 300 spectrometer equipped with an Oxford ESR 910 liquid Helium cryostat and an Oxford temperature controller. Mössbauer spectra were recorded using Janis Research Super-Varitemp dewars that allowed studies in applied magnetic fields up to 8.0 T. Mössbauer spectral simulations were performed using the WMOSS software package (SEE Co, Edina, MN), and EPR spectra were simulated with SpinCount of M. Hendrich.Isomer shifts are quoted relative to Fe metal at 298 K.

Electrospray ionization mass spectrometry experiments were conducted using a Bruker BioTOF II mass spectrometer. The spray chamber voltage was set to 4000 V and the gas carrier temperature was set at 60°C.

Results and Discussion

The reaction of **1** in CH_3CN at -44°C with at least 3 equivalents ^tBuOOH followed by the addition of 1-2 equivalents strong base (KO^tBu or NBu_4OH) generates an orange complex (**2**) that exhibits distinct UV-visible features at 410 nm (ε = 4,000 M^{-1} cm^{-1}) and 780 nm (ε = 430 M^{-1} cm^{-1}) (Figure 2A). Subsequent addition of 5 equivalents strong acid, e.g. HBF_4 or $HClO_4$, produces a green species (**2-H**$^+$) associated with spectral features at 425 nm (ε = 4,100 M^{-1} cm^{-1}), 600 nm (ε = 680 M^{-1} cm^{-1}), and 750 nm (ε = 530 M^{-1} cm^{-1}) (Figure 2A). (The molar extinction coefficients shown are based on samples for which Mössbauer quantification of the relevant chromophores has been carried out.) Reaction of **2-H**$^+$ with an excess of strong base readily regenerates **2**, indicating that **2** and **2-H**$^+$ comprise a conjugate acid/base pair. These complexes are generated in ~50% yield relative to **1**, as determined by Mössbauer spectroscopy (*vide infra*). Unlike **1**, which is stable in MeCN at -44 °C, **2** and **2-H**$^+$ decay with $t_{1/2}$ = 60 and 30 min, respectively. Notably, both **2** and **2-H**$^+$ are S = ½ species that exhibit very similar rhombic EPR spectra (Figure 2A, inset) with g_{ave} ~ 2.0, suggesting that the S = 1 species **1** has undergone one-electron oxidation to form **2**.

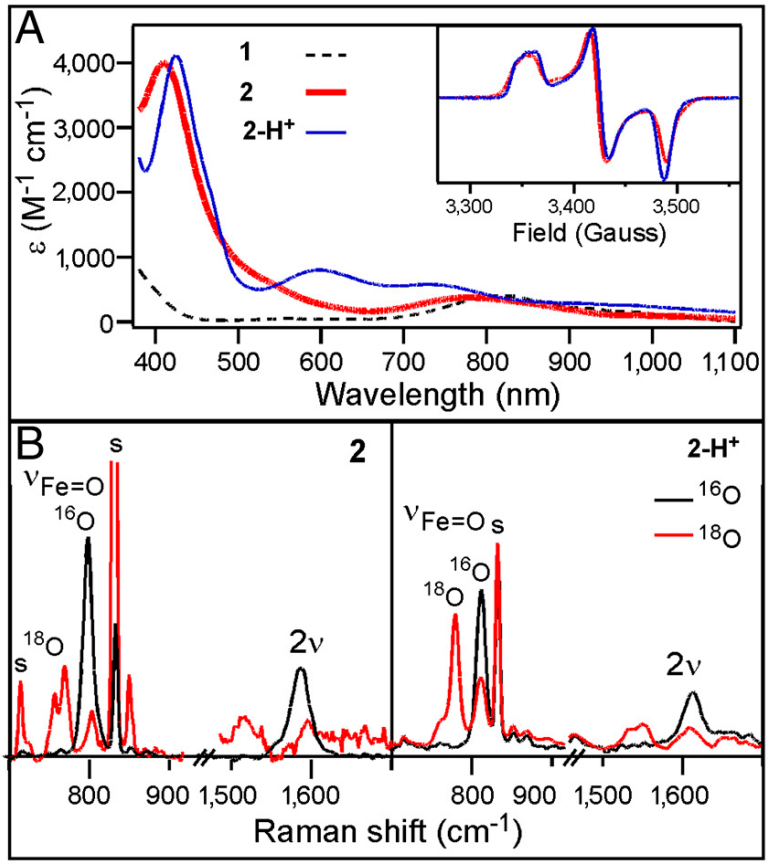

Figure 2. Spectroscopic data for **2** and **2-H**$^{+}$. **A.** UV-visible spectra of **1** (black dashed line), **2** (thick red line) and **2-H**$^{+}$ (blue solid line) collected at -44°C. **Inset:** EPR spectra of **2** in CD_3CN and **2-H**$^{+}$ in 1:9 CH_3CN:CH_2Cl_2. **B.** Resonance Raman spectra of **2** (left) and **2-H**$^{+}$ (right) collected at 77 K using 413-nm laser excitation for frozen solution samples prepared with ^{16}O (black line) and ^{18}O (red line). Acetonitrile solvent peaks are marked as "s".

The resonance Raman (rR) spectra of **2** and **2-H**$^{+}$ obtained with 413-nm excitation show features associated with an Fe=O unit. Complex **2** exhibits an intense vibrational feature at 798 cm^{-1} with an associated overtone at 1587 cm^{-1} (Figure 2B); corresponding features for **2-H**$^{+}$ are observed at 811 and 1613 cm^{-1}. All four features downshift when ^{18}O-labeled **1** is used as the precursor; the observed downshifts are in accord with values calculated for an Fe=O diatomic oscillator using Hooke's law (e.g. $\Delta\nu$= -35 and -36 cm^{-1}, respectively). The observed vibrational frequencies of 798 and 811 cm^{-1} fall at the low

end of the range of $\nu_{Fe=O}$ values previously observed for **1** (839 cm^{-1}) and its axial-ligand-substituted derivatives $[Fe^{IV}(O)(TMC)(N_3)]^+$ (814 cm^{-1}) and $[Fe^{IV}(O)(TMC)(CF_3CO_2)]^+$ (854 cm^{-1}) (16). Thus the lower $\upsilon_{Fe=O}$'s of **2** and **2-H$^+$** suggest the presence of a highly basic *trans* anionic ligand that weakens the Fe=O bond.

In order to obtain further insight into the nature of the S = ½ species, we have studied samples of **2** and **2-H$^+$** with Mössbauer spectroscopy. In a typical sample, **2** and **2-H$^+$** represented 40-55% of the total Fe in a sample. Figure 3A shows a 4.2 K Mössbauer spectrum of **2** recorded in a 50 mT field applied *parallel* to the observed γ rays. In addition to **2**, which accounts for ~55% of Fe, the sample contained several S = 1 Fe^{IV} species yielding quadrupole doublets for **1** (green, ΔE_Q = 1.23 mm/s, δ = 0.17 mm/s, ~8%), $[Fe^{IV}(O)(TMC)(OH)]^+$ (**1-OH:** blue, ΔE_Q = 0.16 mm/s, δ = 0.15 mm/s, 16%), and an unidentified Fe^{IV} species (ΔE_Q ~ 0.6 mm/s, δ ~ 0.15 mm/s, ≈ 10%). There is also a high-spin Fe^{III} species (g ~ 6.9, 5.1, ca. 10% of Fe), which, fortunately, absorbs mostly outside the spectral region of **2**. Similarly, the sample of **2-H$^+$** studied here contained the following species: S = ½ complex **2-H$^+$** (41%), two S = 1 complexes **1** (27%) and **1-OH** (2%), and S = 5/2 Fe^{III} (30%, see SI Appendix).

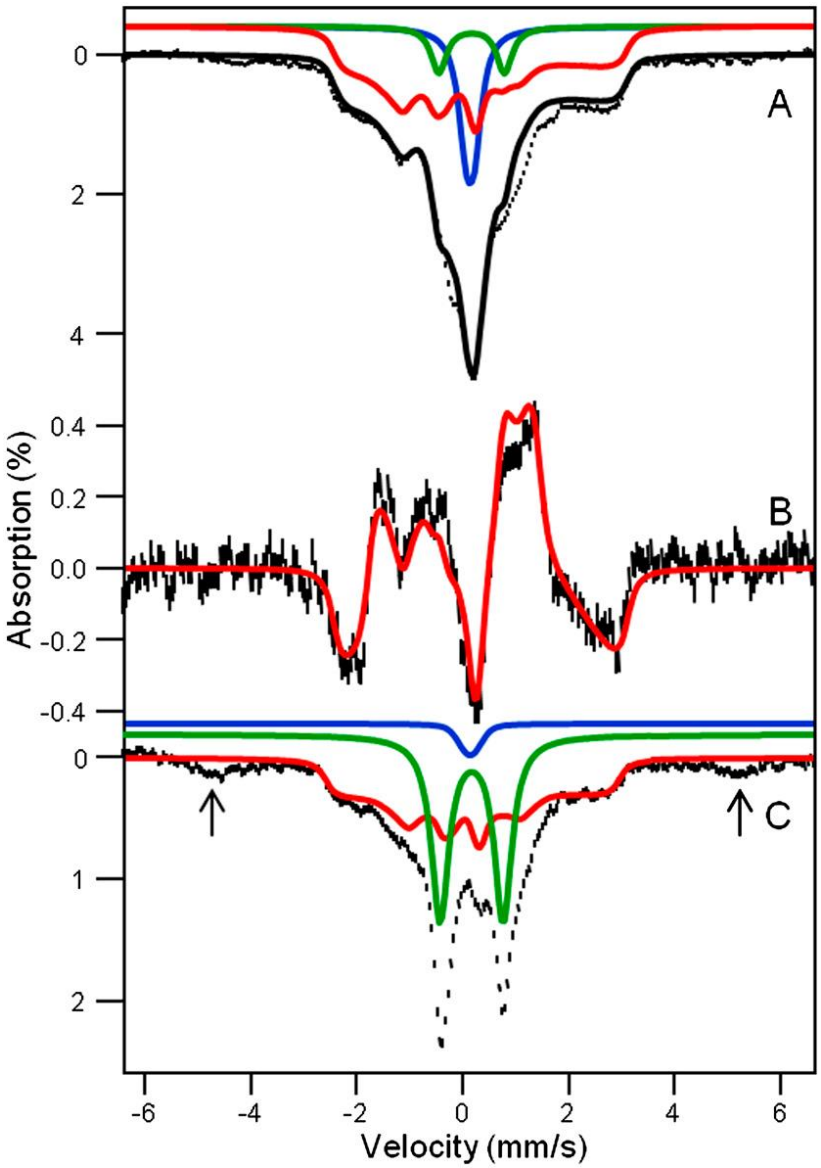

Figure 3. 4.2 K Mössbauer spectra of **2** and **2-H**$^{+}$. Mössbauer spectra of samples containing **2 (A)** and **2-H**$^{+}$ **(C)** recorded in a 50 mT field applied parallel to the observed γ rays. **(B)** Difference spectrum "parallel minus perpendicular", representing **2**, obtained with 50 mT applied fields. Red lines are simulations for **2** and **2-H**$^{+}$ based on eq 1, using the parameters listed below and in Table 1. The major Fe^{IV}=O "contaminants" are shown by the green **(1)** and blue **(1-OH)** lines. The black solid line in (A) is a spectral simulation for the sum of **2** (55% of Fe), **1**(8%) and **1-OH**(16%). The doublets in (C) represent 27% of **1** and 2% of **1-OH**. The arrows in (C) point to absorption due to a high-spin Fe^{III} contaminant (30%). The δ, ΔE_Q, and η values used in the simulations are: +0.10(4) mm/s, -0.5 mm/s, and -3, respectively for **2** and +0.10(4) mm/s, -0.2 mm/s, and -3, respectively for **2-H**$^{+}$.

The presence of multiple contaminants in the sample for **2** complicates the analysis of the $S = ½$ species of interest. However, two Mössbauer attributes allow us to uniquely associate a spectral component with the S = 1/2 species, and to eliminate the S = 1 and S = 5/2 contaminants (15). First, we can record spectra by applying a weak (e. g. 50 mT) magnetic field either parallel or perpendicular to the observed γ-rays. If the intensities of the absorption lines are different between parallel and perpendicular field, the species *must* be associated with an EPR active species; in this way a unique association between an S = 1/2 EPR signal and a Mössbauer spectral component is established (15). Second, for a difference spectrum thus taken, all contributions from species yielding quadrupole doublets cancel, leaving us with the analysis of a pure S = ½ paramagnetic species. This procedure yielded the difference spectrum of Figure 3B, which represents **2**.

Table 1. g- and A-tensors (in MHz) experimentally observed for **2**, **2-H**$^+$ and $[Fe^V(O)(TAML)]^{1-}$ and calculated for **2** and **2-H**$^+$.

	g			A (^{57}Fe)			A (^{17}O)			A (^{14}N)		
Compound	**x**	**y**	**z**	**x**	**y**	**z**	**x**	**y**	**z**	**x**	**y**	**z**
HRP Cpd I	-	-	-	-26[*]	-26[*]	-8[*]	35[t]	36[t]	ND	-	-	-
1	-	-	-	-28[‡]	-28[‡]	-4	-27[§]	-27[§]	+61[§]	-	-	-
2[¶]	2.053	2.010	1.971	-47(2)	-17(2)	0(5)	25(15)	128(3)	≈20	29(2)	11(3)	11(3)
2 (DFT) [|]	2.03	2.00	1.97	-43.5	-18.5	3.3	-1.0	-70.8	75.7	-39.3	10.8	6.1
2-H$^+$[¶]	2.054	2.011	1.975	-47(2)	-17(2)	0(5)	25(15)	133(3)	23(10)	30(2)	11(3)	10(3)
2-H$^+$ (DFT) [|]	2.03	2.00	1.97	-45.1	-14.0	-6.0	18.4[**]	-91.4	84.7	-35.5[|]	-1.2	3.9
$[Fe^V(O)(TAML)]^{1-}$[tt]	1.99	1.97	1.74	-49.3	-1.5	-16.3[‡‡]	-	-	-	-	-	-

ND, not determined

[*] From Mössbauer data analyzed with an S=1 Hamiltonian (17).

[t] From ENDOR data, S=1 (18).

[‡] Refit of Mössbauer data reported in ref. 15 using g values and zero-field splitting parameters derived from more recent high-field EPR data reported.

[§] This work; B3LYP calculations yield a good match for **A**(^{57}Fe).

[¶] This work; data analyzed with Eq. 1; 4.2 K Mössbauer spectra recorded at 2.0, 4.0, and 8.0 T show that $A_x(^{57}Fe)$ and $A_y(^{57}Fe)$ of **2** are negative, see *SI Appendix*, Fig. S4. The z axis is along the Fe-O bond in all systems. Results for **2** apply to the majority species.

[|] Values for the ***2(Fe^V)*** model obtained from DFT calculations using BP86 functionals (see below).

[**] Relative to **g**, **A**(^{17}O) and **A**(^{14}N) are rotated 8° around the z axis of the g-tensor.

[tt] From ref. 12.

[‡‡] Correcting A_z for the orbital contribution, which is proportional to $(g_z - 2)$, would yield $A_z \sim 0$.

To simulate the Mössbauer and EPR spectra, we used the $S = 1/2$ spin Hamiltonian:

$$H = \mathbf{g}\beta\mathbf{B}\bullet\mathbf{S} + \mathbf{S}\bullet A(^{57}Fe)\bullet\mathbf{I} - g_n\beta_n\mathbf{B}\bullet\mathbf{I} + H_Q + \Sigma_n\,\mathbf{S}\bullet A(n)\bullet\mathbf{I}(n) \qquad \textbf{(1)}$$

where $A(^{57}Fe)$ is the ^{57}Fe magnetic hyperfine tensor, **I** is the ^{57}Fe nuclear spin operator and H_Q describes the ^{57}Fe quadrupole interaction. As needed, the last term will be used to describe ligand hyperfine interactions observed by EPR; n = ^{14}N, ^{15}N, or ^{17}O. From extensive simulations of the spectra of **2** and **2-H**$^+$, we obtained the parameters listed in Table 1 and SI Appendix (Figure S6). **2** and **2-H**$^+$ exhibit the same isomer shifts within the uncertainties, namely $\delta = +0.10(4)$ mm/s. The δ values are smaller than those reported for $S = 1$ $Fe^{IV}(O)(TMC)$ complexes (range 0.15 - 0.19 mm/s) (16), suggesting that the oxidation state of the iron site in **2** and **2-H**$^+$ is above Fe^{IV}. More importantly, **2** and **2-H**$^+$

exhibit unusual ^{57}Fe A tensors with large x/y anisotropy, suggesting an electronic structure that differs significantly from that of **1**.

We have conducted extensive EPR studies of **2** and **2-H**$^+$. The use of glassing solvent mixtures (1:3 CH_3CN:CH_2Cl_2 or 1:3 CH_3CN:butyronitrile) sharpened the spectra considerably (4 gauss line width). The higher resolution provided decisive clues about the ligand structure of **2** and **2-H**$^+$**,** as well as important magnetic hyperfine structure data. Selected spectra are displayed in Figure 4. We found that **2** reproducibly displayed two *S* = ½ species in essentially constant proportions (ca. 2:1 in all preparations studied); the minority species is recognized by a shoulder on the high-field feature in Figure 4A. Our studies revealed that these two species did not differ in any significant way. The minor species, **2**^{m}, has g-values at 2.04, 1.99, and 1.96. As **2-H**$^+$ was found to be free of EPR-active contaminants in the g = 2.0 region, we focus here on this species. (EPR analysis of **2**, summarized in Table 1 and detailed in the SI Appendix, afforded similar conclusions.) For **2-H**$^+$ (Figure 4B), the signal at g_x = 2.045 exhibits a 1:1:1 hyperfine triplet, corresponding to a single ^{14}N nucleus with $|A_x(^{14}N)|$ = 28.5 MHz and $|A_{y,z}(^{14}N)| \cong 11$ MHz (the signs of $A_{x,y,z}$ cannot be determined by EPR). A nearly identical pattern can be discerned in the spectrum of **2** shown in Figure 4A. This splitting pattern changed to a 1:1 doublet with $|A_x(^{15}N)|$ = 40 MHz (Figure 4C) when **2-H**$^+$ was prepared using 1:3 $^{15}NCCH_3$:CH_2Cl_2 as solvent, unequivocally demonstrating that the observed hyperfine structure arises from a nitrogen atom derived from acetonitrile. This procedure yielded the parameters listed in Table 1.

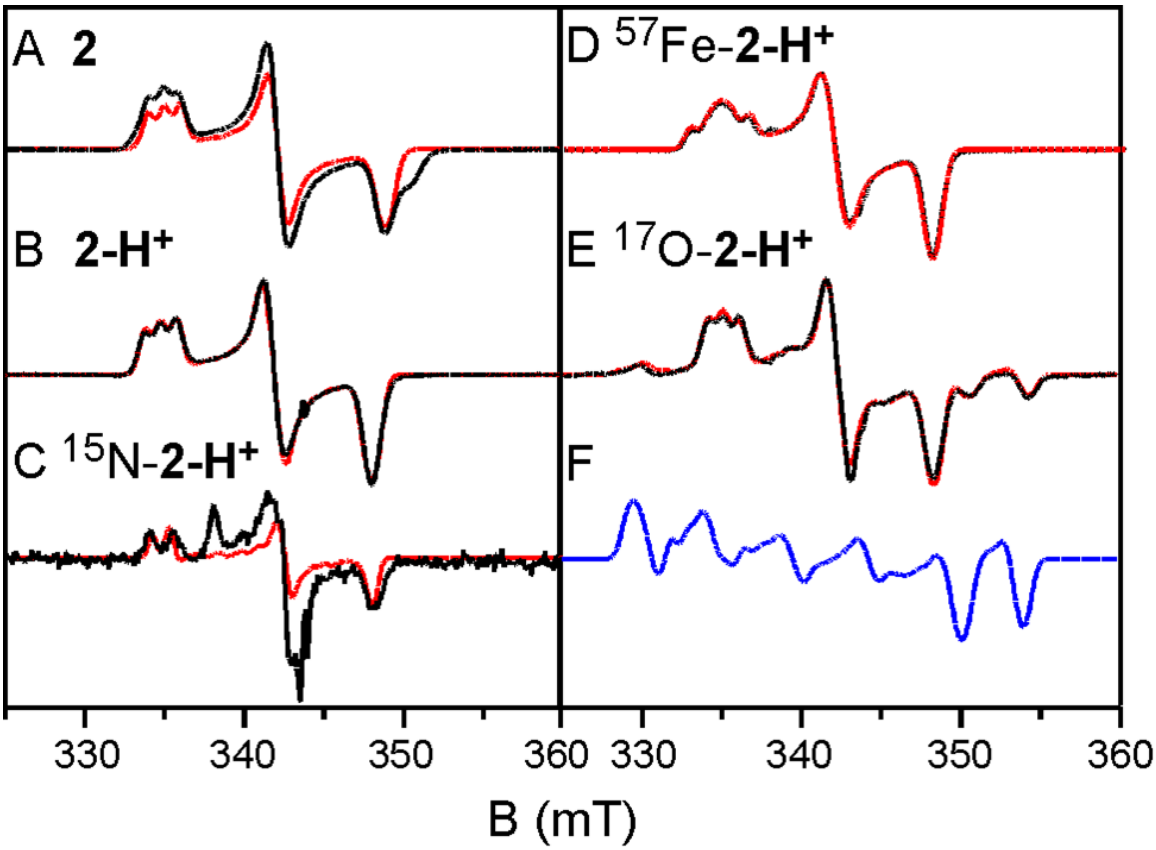

Figure 4. X-band EPR spectra of **2** and **2-H**$^+$. Experimental data (solid black lines) obtained in 1:3 CH_3CN:butyronitrile **(A, B, D, E)** or 1:3 CH_3CN:CH_2Cl_2 **(C)** and recorded at 40 K. Conditions: 9.62 GHz; microwave power, 20 μW; modulation, 0.3 mT. The red lines are theoretical curves generated with the parameters listed in Table 1. The ^{17}O enrichment in **(E)**, obtained from EPR, is ≈ 30%. For **2** only the simulation for the majority species is shown. Panel **F** shows the spectral simulation of **2-H**$^+$ assuming 100% ^{17}O enrichment.

2-H$^+$ obtained from ^{17}O-labeled **1** gave rise to a spectrum for which the (middle) g = g_y = 2.01 feature was split to afford satellite features at both low and high field (Figure 4E); these features arise from ^{17}O superhyperfine splitting with $|A_y(^{17}O)|$ = 133 MHz. We have studied two preparations, with ^{17}O enrichment of 10% and 30%; a spectrum of the latter shown in Figure 4E. To analyze this spectrum we have taken the results of the fit of Figure 4B and added an ^{17}O hyperfine tensor. After obtaining a sufficient understanding of the splitting pattern, we have fitted the spectrum, visually focusing on the resolved two high-field peaks and the low-field feature. The simulation of Figure 4F (plotted for 100%

^{17}O enrichment) indicates the complexity of the spectrum, which stems to a major extent from the fact that the ^{17}O splitting along y does not belong to a unique direction and that the splitting covers the entire Δg range. The final fit, obtained after exploring tensor rotations, gives a good value for $A_y(^{17}O)$ and an upper limit for $A_z(^{17}O)$. Although the calculated intensity for the low field feature is a bit high, this could be alleviated by increasing $A_x(^{17}O)$ together with a distribution of that parameter.

Lastly, the ^{57}Fe-enriched sample (Figure 4D) exhibits significant broadening of the g_x feature corresponding to $|A_x(^{57}Fe)| = 40$ MHz, a value in good agreement with the largest A-tensor component of -47 MHz observed in the Mössbauer spectra of **2** and **2-H**$^+$ **(**EPR can only give the magnitude of the A-values); our EPR spectral simulations show that A_y and A_z are at least a factor of two smaller than A_x. Most importantly, the EPR spectra of the ^{57}Fe-enriched sample establish that the largest ^{57}Fe A-tensor component is along x, the same direction for which the largest ^{14}N splitting is observed. It should be noted that the EPR spectra establish a spatial correlation between the dominant components of the ^{57}Fe, ^{17}O, and ^{14}N hyperfine tensors that provides insight into the electronic structure of **2** and **2-H**$^+$.

Our accumulated spectroscopic data suggest that **2** and **2-H**$^+$ are one-electron oxidized derivatives of **1** and consist of an (TMC)Fe=O unit with an axial ligand derived from acetonitrile. In Figure 1, we propose that **2** is formed by the attack of the *t*-butylperoxide anion on the bound acetonitrile to form a peroxyimidic ester intermediate (17) that then undergoes homolytic cleavage of the O–O bond. To verify that homolysis occurs in this instance, we replaced ^{t}BuOOH with 2-methyl-1-phenylpropan-2-yl hydroperoxide (MPPH), a useful mechanistic probe to distinguish between homolytic and

heterolytic O–O bond cleavage (18). While substitution of MPPH for ^{t}BuOOH did not diminish the yield of **2**, product analysis by GC showed quantitative conversion of MPPH to benzaldehyde. This result demonstrates that O–O bond homolysis occurs to generate **2**. The formulation of **2** as shown in Figure 1 is supported by low temperature ESI-MS studies of **2** that reveal a feature at m/z 385.2, consistent with the formulation of **2** as $[Fe(O)(TMC)(NCCH_3) + O]^+$ (SI Appendix, Figures S8 and S9). This feature shifts to m/z 388.2 upon preparation of **2** in CD_3CN and disappears after the sample is allowed to decay. We postulate in Figure 1 two possible limiting electronic descriptions for **2**: an oxoiron(IV) unit with an axial acetaminyl radical ligand (***2***$(Fe^{IV}N\bullet)$ at one end, and an iron(V) center with *trans* oxo and acetylimido ligands (***2***(Fe^{V}) at the other end. Our efforts to refine electronic descriptions for **2** and **2-H**$^+$ more precisely are discussed below.

The unusual A-tensor anisotropies in the xy plane listed in Table 1 for **2** and **2-H**$^+$ indicate that their electronic structures must be significantly different from that of **1**. The ^{57}Fe and ^{17}O tensors of **1** as well as those of horseradish peroxidase compound 1, an $S = 1$ Fe^{IV}=O species antiferromagnetically coupled to a porphyrin radical (19), are axial with respect to the Fe=O bond, the z axis in our coordinate frames. The axial anisotropy observed reflects the $(d_{xz})^1(d_{yz})^1$ electronic configuration associated with the $S = 1$ Fe^{IV}=O unit. In contrast, **2** and **2-H**$^+$ have drastically different A-tensor components along x and y, indicating substantially different unpaired spin densities on the d_{xz} and d_{yz} orbitals. This distribution can be achieved by transferring the electron from d_{xz} to the p_x orbital of the aminyl ligand to create an Fe^{V}=O center with a *trans* imido ligand, a notion

supported by the similar ^{57}Fe A-tensor anisotropy observed for the bona fide Fe^{V}=O complex $[Fe^{V}(O)(TAML)]^{-}$ (Table 1) (14).

DFT studies of **2** and **2-H**$^{+}$ lend substantial support to the above conclusion (see SI Appendix for full computational details, Tables S1-7). For comparison DFT calculations were also carried out for the experimentally characterized complexes **1** and $[Fe^{V}(O)(TAML)]^{-}$ as well as the hypothetical iron(V) species $\boldsymbol{1_{ox}}$ (a computational model obtained by removing one electron from **1**; italics denote purely computational models). The use of the hybrid functional B3LYP led to the ***2***$(Fe^{IV}N\bullet)$ description, which is similar to that reported for HRP Cpd I, but with the radical *trans* rather than *cis* to the oxo group. This Fe^{IV}-aminyl radical description with an iron $(d_{xz})^1(d_{yz})^1$ electron configuration predicts **2** and **2-H**$^{+}$ to have essentially axial ^{57}Fe and ^{17}O A-tensors, inconsistent with the experimental data. In stark contrast, the use of the "pure" functional BP86 generated the ***2***(Fe^{V}) limiting description with an iron $(d_{yz})^1(d_{xz})^0$ electron configuration and yielded solutions that reproduce the observed anisotropies of the ^{57}Fe A-tensor and rationalize the essential features of the entire data set. In this model, the acetaminyl radical becomes an acetylimido ligand, and **2** and **2-H**$^{+}$ are best formulated as complexes having $[O=Fe^{V}=NR]^{+}$ units (see Figure 1). The dependence of the calculated ground state on whether a hybrid (B3LYP) or pure (BP86) functional is used may be related to the propensity of Hartree-Fock exchange to stabilize high-spin states in the case of the former functional. A similar dependence on the type of functionals used has been reported for the description of electronic structures of $\{FeNO\}^7$ and $\{FeO_2\}^8$ complexes, systems involving a non-innocent ligand radical (see for example references (20) and (21)). In all cases, the functional chosen for further investigation most closely reproduced

the experimentally observed spectroscopic parameters to generate an experimentally validated computational model.

Table 2. Calculated unpaired spin populations n = $n_\alpha - n_\beta$ of Fe-d_{xz}, Fe-d_{yz} and N_{axial}-p_x orbitals.

	$Fe^V(O)(TAML)^*$	$\mathbf{1}_{ox}$ $(Fe^V)^t$	**2** (Fe^V)	**1**	**2** $(Fe^{IV}N\cdot)^§$
Fe-d_{xz}	0.07	0.15	0.23	0.58	0.58
Fe-d_{yz}	0.57	0.63	0.53	0.58	0.58
N_{axial}-p_x	-	~0	-0.30	0	-0.85

*Tiago de Oliveira et al. (14).
[t] Computational model obtained by removing one electron from **1**.
[‡] BP86 solution.
§ B3LYP solution, S=1 Fe^{IV}=O coupled to S=1/2 radical on N of axial ligand.

Table 2 compares the unpaired spin populations calculated for key orbitals of several complexes. Interestingly, while the d_{yz} spin population remains more or less constant at about 0.58 across the series, the d_{xz} spin population is equal to the d_{yz} spin population for **1** and ***2**(Fe^IV N●)* but decreases progressively for ***2**(Fe^V)*, $\mathbf{1}_{ox}$, and $[Fe^V(O)(TAML)]^-$. As viewed from the progression of d_{xz} spin density listed in Table 2, the electronic configuration of **2** more closely resembles that of $\mathbf{1}_{ox}$ and $[Fe^V(O)(TAML)]^-$ than of **1** and ***2**(Fe^IV N●)*. Since the transfer of electron density from the metal d_{xz} orbital to the singly occupied p_x orbital of the acetaminyl radical is not complete, the axial nitrogen retains a net β spin population in p_x (n = -0.30), which is much smaller than the value (n = -0.85) calculated for ***2**(Fe^IV N●)*. Consistent with these ideas, the Mulliken Fe spin populations for ***2**(Fe^V)* and ***2**(Fe^V)*-$\mathbf{H}^+$ are calculated to be 0.86 and 0.77, respectively, which is lower than the 1.30 value calculated for **1**. The expectation value of the operator $\mathbf{S}^2$ provides quantitative insight into the oxidation state predicted by DFT. ***2**(Fe^V)* was found to have $\langle\Psi_{BP86}|\mathbf{S}^2|\Psi_{BP86}\rangle = 0.94$, which is close to

the ideal value of S(S+1) = 0.75 for $S = ½$ Fe^{V} but considerably smaller than the value of 1.75 anticipated for the broken symmetry state (BS) of ***2(*** $Fe^{IV}N\bullet$***)***. Using the expansion $|\Psi_{BP86}> = c\,|Fe^{V}, S = 1/2> + (1 - c^2)^{1/2}\,|Fe^{IV}N\bullet, BS>$ and the expectation values $<S = 1/2|\mathbf{S}^2|S = 1/2> = 0.75$ and $<BS|\mathbf{S}^2|BS> = 1.75$, we obtain $c^2 = 0.81$ from $<\Psi_{BP86}|\mathbf{S}^2|\Psi_{BP86}> = 0.75\,c^2 + 1.75\,(1 - c^2) = 0.94$. As spin unrestricted calculations show always some degree of spin contamination, the Fe^{V} character of **2** (and **2-H$^+$)** is greater than 80%.

If we view **2** and **2-H$^+$** as Fe^{V} complexes, the spin densities at the axial ligand atoms must originate from covalent spin polarization (22). Interaction of the oxo $O(p_y)$ electron pair with the $Fe(d_{yz})$ orbital results in partial transfer of a β oxo electron to pair off some of the α spin density associated with the unpaired $Fe(d_{yz})$ electron, leaving a net α spin population in $O(p_y)$ (blue in Figure 5). The imido $N(p_x)$ electron pair transfers net α spin density to the empty $Fe(d_{xz})$ orbital, "guided" by Hund's rule, leaving a net β spin population in $N(p_x)$ (red in Figure 5). The electron pair in the out-of-plane $N(p_y)$ orbital of the imido ligand is calculated by DFT to be 10,000 cm^{-1} lower in energy than the redox-active in-plane $N(p_x)$ orbital and thus is much less involved in covalent delocalization to the metal.

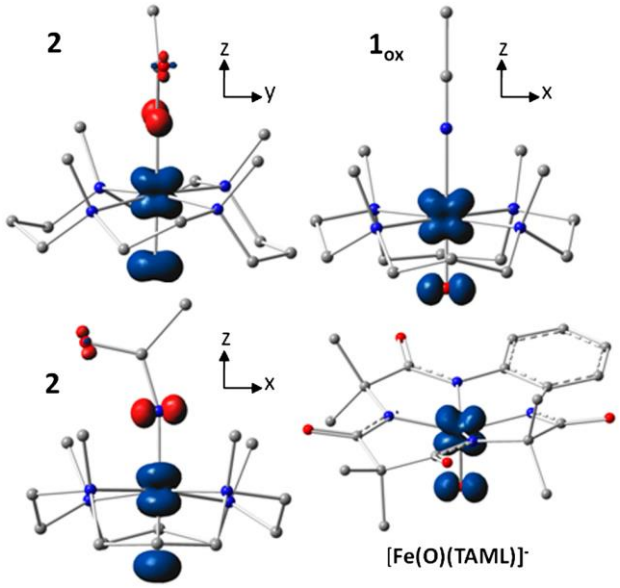

Figure 5. Spin density plots of geometry optimized BP86 solutions for ***2(Fe^{V})***, ***1$_{ox}$*** and [Fe(O)(TAML)]$^{-}$. The plot for ***2(Fe^{V})***, shown in two views, reveals the contours of the orbitals carrying spin density: from top to bottom, p_x (N_{am}), d_{yz} (Fe), and p_y (^{17}O). For ***1$_{ox}$***, the TMC ligand has been rotated by ~ 90º around the Fe=O bond relative to the orientation shown for ***2(Fe^{V})***. Majority spin α in blue; minority spin β in red.

The resulting spin densities shown in Figure 5A rationalize the spatial pattern observed in the A-tensors for ^{17}O, ^{57}Fe, and ^{14}N. Thus, the net β spin population of the N(p_x) gives a magnetic hyperfine tensor with a large component along x and two smaller components along y and z for **2 (**and **2-H**$^{+}$), with calculated $A_{x,y,z}$ values of (-39, 11, 6) MHz for ^{14}N in good agreement with the data. The net α spin population of Fe(d_{yz}) produces a spin-dipolar hyperfine contribution with a large negative component along x, which together with the negative Fermi contact term yields a magnetic hyperfine tensor of which the dominant component is along x; the calculated $A_{x,y,z}$ values of (-44, -19, 3) MHz (Table 1) are also in excellent agreement with the results obtained for **2** and **2-H**$^{+}$. Finally, the net α spin population of O(p_y) gives an ^{17}O A-tensor that has a large component along y, with $A_{x,y,z}$ values of (-1, -71, +76) MHz. The agreement for ^{17}O between experiment and calculations is not as good as that for ^{57}Fe and ^{14}N; A_y is still too

small and A_z comes out too large but, importantly, the calculated tensor lacks axial symmetry around z and exhibits the x/y anisotropy observed experimentally. Finally, the g-values calculated for ***2(Fe^V)*** reported in Table 1 match both in magnitude and direction of the experimental data for **2** and **2-H$^+$**. Thus the congruence of the experimental EPR results with the ***2(Fe^V)*** model provides a strong rationale for the description of **2** and **2-H$^+$** as Fe^V complexes.

In contrast, the $\nu_{Fe=O}$ frequencies hint at an Fe^{IV} oxidation state for **2** and **2-H$^+$,** and therefore may at first glance favor ***2(Fe^{IV}N●)*** over ***2(Fe^V)***. It should be noted, however, that $\nu_{Fe=O}$ is a spectroscopic parameter that reflects the length of the Fe-oxo bond (23). The Fe-O bond in the DFT model ***2(Fe^V)*** (1.70 Å) is longer than the oxoiron(V) bond in ***1$_{ox}$*** (1.60 Å) and the oxoiron(IV) bond in ***1*** (1.66 Å) due to delocalization of electron density over the oxo-iron-imido moiety[⊥] (see Figure 6) and is therefore predict to exhibit a lower $\nu_{Fe=O}$ than ***1$_{ox}$***. The ***2(Fe^V)*** model predicts $\nu_{Fe=O}$ values of 785 cm^{-1} for ***2(Fe^V)*** (ν_{exp} = 798 cm^{-1}) and of 829 cm^{-1} for ***2(Fe^V)*-H$^+$** (ν_{exp} = 811 cm^{-1}) in excellent agreement with the trend observed in our experimental data, indicating that the imido ligand exerts a sizable *trans* influence on the Fe-O unit.

Similarly, the weaker Fe=O bonds of **2** and **2-H$^+$** are expected to give rise to higher Mössbauer isomer shifts, as this spectroscopic parameter reflects the 3s electron density at the ^{57}Fe nucleus and the extent to which the 3s electrons are shielded by 3d electrons. Thus, we expect that δ value of **2** to be more positive than that of an Fe^V complex with an O=Fe–NCCH$_3$ unit. As a further test of the *trans* influence of the

[⊥] Unfortunately, our Raman experiments have not been able to identify vibrational modes that can be associated with the Fe=NR unit. This may not be surprising, as vibrational data are also not available for the only previously reported six-coordinate Fe=NR complex, although Raman data for four-coordinate Fe=NR complexes have been obtained.

O=Fe=N–C(O)–R unit on the value of δ, we calculated the properties for the hypothetical 1-electron reduced **2** (denoted ***2*$_{red}$**) and obtained an Fe–O bond length of 1.767 Å, which is 0.10 Å longer than the Fe–O distance 1.664 Å calculated for **1**. The increase in bond length is indeed accompanied by an increase of the δ value by 0.09 mm/s and a 164 cm^{-1} decrease in $\nu_{Fe=O}$. The significant *trans* influence of the acetylimido ligand is also manifested in the comparison of the calculated values for ***2***(Fe^{V}) (r_{Fe-O} = 1.701 Å, δ = 0.03 mm/s, $\nu_{Fe=O}$ = 785 cm^{-1}) and ***1*$_{ox}$** (r_{Fe-O} = 1.603 Å, δ = –0.08 mm/s, $\nu_{Fe=O}$ = 944 cm^{-1}). These calculations support our view that $\nu_{Fe=O}$ and δ are poor indicators for the oxidation state of **2** and **2-H**$^{+}$, without properly accounting for the *trans* influence of the axial ligand. Judged from the full data set, **2** and **2-H**$^{+}$ are best described as Fe^{V} complexes.

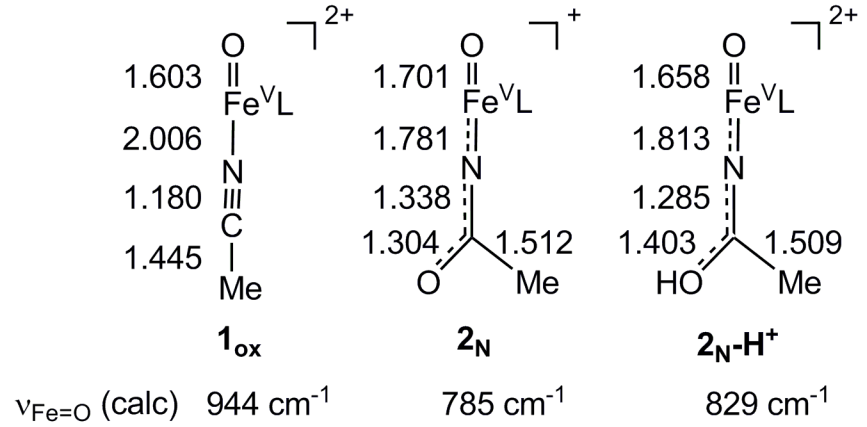

Figure 6. Calculated geometric and spectral parameters for the energy-minimized BP86 models ***1*$_{ox}$**, ***2***, and ***2-H***$^{+}$. Bond lengths are reported in Å. "L" denotes the TMC ligand.

The characterization of **2** and **2-H**$^{+}$ reported in this paper increases to three the number of synthetic oxoiron(V) complexes for which detailed spectroscopic and electronic structure information is available. Such complexes demonstrate that it is possible to stabilize such a high-valent state in an iron coordination complex. For $[Fe^{V}(O)(TAML)]^{-}$, the iron(V) oxidation state was achieved by the use of a tetraanionic

tetraazamacrocyclic ligand that mitigates the high charge of the metal center (14). In contrast, **2** and **2-H**$^{+}$ are supported by a neutral tetraazamacrocycle, so the stabilization of the iron(V) state, it would seem, must derive from the presence of the charged axial oxo and imido ligands. The structure we favor for **2** is closely related to that of $[Mn^{V}(O)_2(TPFPP)]^{-}$ (TPFPP = *meso*-tetrakis(pentafluorophenyl)porphinate dianion), which is the only known example of a first row transition metal containing an $[M^{V}(O)_2]$ moiety (26). Examples of nitridoiron(V) and nitridoiron(VI) complexes have also been reported, demonstrating the ability of the N^{3-} ligand to allow access to high-valent iron complexes, even with supporting polydentate ligands that are neutral or monoanionic (27-31). Lastly, the characterization of **2** and **2-H**$^{+}$ demonstrates the possibility of a neutral nonheme ligand to support an Fe(V) center and lends credence to mechanistic proposals for $Fe^{V}(O)(OH)$ oxidants in arene *cis*-dihydroxylation by Rieske dioxygenases (5) and in alkane, olefin, and water oxidation by a series of bio-inspired synthetic iron catalysts (6-9, 11). For the latter, evidence for the fleeting iron(V) intermediates has been obtained from low temperature spectroscopic analysis of catalytic reactions by EPR (32, 33) and by mass spectrometry. (10, 12)

Acknowledgements

This work was supported by National Institutes of Health Grants GM33162 and GM38767 (to L.Q.) and EB001475 (to E.M.) and postdoctoral fellowships GM-093479 (to K.M.V.H.) and GM-0079839 (to A.T.F.) and National Science Foundation Grant CHE1058248 (to L.Q.) and Grant CHE070073 (to E.L.B.) through TeraGrid resources provided by the National Center for Supercomputing Applications and Pittsburgh Supercomputing Center. We thank Professor Thomas C. Brunhold at the University of Wisconsin-Madison for kindly providing access to his computer cluster. We are particularly grateful to two of the reviewers for suggesting a key improvement in our proposed mechanism in Figure 1.

References

1. Denisov IG, Makris TM, Sligar SG, & Schlichting I (2005) Structure and Chemistry of Cytochrome P450. *Chem. Rev.* 105: 2253-2278.

2. Zilly FE, Acevedo JP, Augustyniak W, Deege A, Hausig UW, & Reetz MT (2011) Tuning a P450 Enzyme for Methane Oxidation. *Angew. Chem. Int. Ed* 50: 2720-2724.

3. Kawakami N, Shoji O, & Watanabe Y (2011) Use of Perfluorocarboxylic Acids To Trick Cytochrome P450BM3 into Initiating the Hydroxylation of Gaseous Alkanes *Angew. Chem. Int. Ed.* 50: 5315–5318.

4. Rittle J & Green MT (2010) Cytochrome P450 Compound I: Capture, Characterization, and C-H Bond Activation Kinetics. *Science* 330: 933-937.

5. Kovaleva EG & Lipscomb JD (2008) Versatility of biological non-heme Fe(II) centers in oxygen activation reactions. *Nature Chem. Biol.* 4: 186-193.

6. Chen K & Que L, Jr. (2001) Stereospecific Alkane Hydroxylation by Nonheme Iron Catalysts: Mechanistic Evidence for an Fe^{V}=O Active Species. *J. Am. Chem. Soc.* 123: 6327-6337.

7. Company A, Gomez L, Guell M, Ribas X, Luis JM, Que L, Jr., & Costas M (2007) Alkane Hydroxylation by a Nonheme Iron Catalyst that Challenges the Heme Paradigm for Oxygenase Action *J. Am. Chem. Soc.* 129: 15766-15767.

8. Chen K, Costas M, Kim J, Tipton AK, & Que L, Jr. (2002) Olefin *cis*-Dihydroxylation versus Epoxidation by Nonheme Iron Catalysts: Two Faces of an Fe^{III}-OOH Coin. *J. Am. Chem. Soc.* 124: 3026-3035.

9. Company A, Feng Y, Güell M, Ribas X, Luis JM, Que L, Jr., & Costas M (2009) Olefin-Dependent Discrimination Between Two Nonheme HO-Fe^{V}=O Tautomeric Species in Catalytic H_2O_2 Epoxidations. *Chem. Eur. J.* 15: 3359-3362.

10. Chow TW-S, Wong EL-M, Guo Z, Liu Y, Huang J-S, & Che C-M (2010) cis-Dihydroxylation of Alkenes with Oxone Catalyzed by Iron Complexes of a Macrocyclic Tetraaza Ligand and Reaction Mechanism by ESI-MS Spectrometry and DFT Calculations. *J. Am. Chem. Soc.* 132: 13229-13239.

11. Fillol JL, Codola Z, Garcia-Bosch I, Comex L, Pla JJ, & Costas M (2011) Efficient water oxidation catalysts based on readily available iron coordination complexes. *Nature Chem.* 3: 807-813.

12. Prat I, Mathieson JS, Güell M, Ribas X, Luis JM, Cronin L, & Costas M (2011) Observation of Fe(V)=O using Variable Temperature Mass Spectrometry and its Enzyme-like C-H and C=C Oxidation Reactions. *Nature Chem.* 3: 788-793.

13. Que L, Jr. (2007) The Road to Non-Heme Oxoferryls and Beyond. *Acc. Chem. Res.* 40: 493-500.

14. Tiago de Oliveira F, Chanda A, Banerjee D, Shan X, Mondal S, Que L, Jr., Bominaar EL, Münck E, & Collins TJ (2007) Chemical and Spectroscopic Evidence for an Fe^{V}-Oxo Complex. *Science* 315: 835-838.

15. Rohde J-U, In J-H, Lim MH, Brennessel WW, Bukowski MR, Stubna A, Münck E, Nam W, & Que L, Jr. (2003) Crystallographic and Spectroscopic Evidence for a Nonheme Fe^{IV}=O Complex. *Science* 299: 1037-1039.

16. Jackson TA, Rohde J-U, Seo MS, Sastri CV, DeHont R, Ohta T, Kitagawa T, Münck E, Nam W, & Que L, Jr. (2008) Axial Ligand Effects on the Geometric and Electronic Structures of Nonheme Oxoiron(IV) Complexes. *J. Am. Chem. Soc.* 130: 12394-12407.

17. Payne GB, Deming PH, & Williams PH (1961) Reactions of Hydrogen Peroxide. VII. Alkali-Catalyzed Epoxidation and Oxidation Using a Nitrile as Co-reactant. *J. Org. Chem.* 26: 659-663.

18. MacFaul PA, Arends IWCE, Ingold KI, & Wayner DDM (1997) Oxygen Activation by Metal Complexes and Alkyl Hydroperoxides. Applications of Mechanistic Probes to Explore the Role of Alkoxyl Radicals in Alkane Functionalization. *J. Chem. Soc., Perkin Trans. 2*: 135-145.

19. Roberts JE, Hoffman BM, Rutter R, & Hager LP (1981) ^{17}O ENDOR of Horseradish Peroxidase Compound I. *J. Am. Chem. Soc.* 103: 7654-7656.

20. Schenk G, Pau MYM, & Solomon EI (2004) Comparison between the Geometric and Electronic Structures and Reactivities of $\{FeNO\}^{7}$ and $\{FeO_2\}^{8}$ Complexes: A Density Functional Theory Study. *J. Am. Chem. Soc.* 126: 505-515.

21. Hopmann KH, Conradie J, & Ghosh A (2009) Broken-Symmetry DFT Spin Densities of Iron Nitrosyls, Including Roussin's Red and Black Salts: Striking Differences between Pure and Hybrid Functionals. *J. Phys. Chem. B* 113: 10540-10547.

22. Drago RS (1992) *Physical Methods for Chemists* (Saunders, Philadelphia).

23. Green MT (2006) Application of Badger's Rule to Heme and Non-Heme Iron−Oxygen Bonds: An Examination of Ferryl Protonation States. *J. Am. Chem. Soc.* 128: 1902-1906.

24. Klinker EJ, Jackson TA, Jensen MP, Stubna A, Juhász G, Bominaar EL, Münck E, & Que L, Jr. (2006) A Tosylimido Analogue of a Nonheme Oxoiron(IV) Complex *Angew. Chem. Int. Ed.* 45: 7394-7397.

25. Mehn MP, Brown SD, Jenkins DM, Peters JC, & Que L, Jr. (2006) Vibrational Spectroscopy and Analysis of Pseudo-tetrahedral Complexes with Metal Imido Bonds. *Inorg. Chem.* 45: 7417–7427.

26. Jin N, Ibrahim M, Spiro TG, & Groves JT (2007) Trans-dioxo Manganese(V) Porphyrins. *J. Am. Chem. Soc.* 129: 12416-12417.

27. Meyer K, Bill E, Mienert B, Weyhermüller T, & Wieghardt K (1999) Photolysis of cis- and trans-$[Fe^{III}(cyclam)(N_3)_2]^+$ Complexes: Spectroscopic Characterization of a Nitridoiron(V) Species. *J. Am. Chem. Soc.* 121: 4859-4876.

28. Grapperhaus CA, Mienert B, Bill E, Weyhermüller T, & Wieghardt K (2000) Mononuclear (Nitrido)iron(V) and (Oxo)iron(IV) Complexes via Photolysis of $[(cyclam\text{-}acetato)Fe^{III}(N_3)]^+$ and Ozonolysis of $[(cyclam\text{-}acetato)Fe^{III}(O_3SCF_3)]^+$ in Water/Acetone Mixtures. *Inorg. Chem.* 39: 5306-5317.

29. Aliaga-Alcalde N, George SD, Mienert B, Bill E, Wieghardt K, & Neese F (2005) The Geometric and Electronic Structure of $[(cyclam\text{-}acetato)Fe(N)]^+$: A Genuine Iron(V) Species with a Ground-State Spin S=1/2. *Angew. Chem. Int. Ed.* 44: 2908-2912.

30. Berry JF, Bill E, Bothe E, George SD, Mienert B, Neese F, & Wieghardt K (2006) An Octahedral Coordination Complex of Iron(VI). *Science* 312: 1937-1941.

31. Scepaniak JJ, Vogel CS, Khusniyarov MM, Heinemann FW, Meyer K, & Smith JM (2011) Synthesis, Structure, and Reactivity of an Iron(V) Nitride. *Science* 331: 1049-1052.

32. Lyakin OY, Bryliakov KP, Britovsek GJP, & Talsi EP (2009) EPR Spectroscopic Trapping of the Active Species of Nonheme Iron-Catalyzed Oxidation. *J. Am. Chem. Soc.* 131: 10798-10799.

33. Lyakin OY, Bryliakov KP, & Talsi EP (2011) EPR, ^1H and ^2H NMR, and Reactivity Studies of the Iron-Oxygen Intermediates in Bioinspired Catalyst Systems. *Inorg. Chem.* 50: 5526-5538.

Supporting Information

Preparation of 1, 2, and 2-H+. All reagents and solvents were purchased from commercial sources and used as received unless otherwise noted. Compound **1** was prepared using previously reported procedures.{Rohde, 2003 #291} In brief, a solution of $[Fe^{II}(TMC)(OTf)](OTf)$ in acetonitrile was reacted with 1.2 equivalents of PhIO solubilized in methanol to yield **1** in quantitative yield. The formation of **1** was monitored by the appearance of its distinctive chromophore at 820 nm. Compound **2** was prepared at -44°C in acetonitrile by the addition of at least 3 equivalents of *tert*-butylhydroperoxide followed by the addition of 1-2 equivalents of strong base, typically NBu_4OH, NBu_4OMe, or KO^tBu. Further addition of at least five equivalents of strong acid, (HBF_4, $HClO_4$, or CF_3COOH), yielded **2-H**$^+$. Notably, while **2** and **2-H**$^+$ can both be generated in mixed solvent systems, such as 3:1 CH_2Cl_2:MeCN, neither species can be generated in the absence of acetonitrile.

Physical Methods. An HP 8453A diode-array spectrometer equipped with a unisoku Scientific Instruments cryostat to maintain a constant temperature was employed to collect electronic absorption spectrum. Resonance Raman spectra were generated via excitation with Kr^+ and Ar^+ lasers (Spectra Physics BeamLok 2060-RM) with a power of < 10 mW at the samples, and the spectra were collected using an ACTON AM-506M3 monochromator and a LN/CCD-1340 x 400 PB detector. EPR spectra were recorded on a Bruker ESR 300 spectrometer equipped with an Oxford ESR 910 liquid Helium cryostat and an Oxford temperature controller. Mössbauer spectra were recorded with two spectrometers, using Janis Research Super-Varitemp dewars that allowed studies in

applied magnetic fields up to 8.0 T in temperature range from 1.5 to 200 K. Mössbauer spectral simulations were performed using the WMOSS software package (SEE Co, Edina, MN). Isomer shifts are quoted relative to Fe metal at 298 K. X band (9.28 GHz) Electrospray ionization mass spectrometry experiments were conducted using a Bruker BioTOFF II mass spectrometer. The spray chamber voltage was set to 4000 V and the gas carrier temperature was set at 60°C.

DFT Calculations. The DFT calculations presented in **Tables S1-S7** and **Figures S1-S3** were performed Gaussian '09, Revision B.01, M. J. Frisch, G. W. Trucks, H. B. Schlegel, G. E. Scuseria, M. A. Robb, J. R. Cheeseman, G. Scalmani, V. Barone, B. Mennucci, G. A. Petersson, H. Nakatsuji, M. Caricato, X. Li, H. P. Hratchian, A. F. Izmaylov, J. Bloino, G. Zheng, J. L. Sonnenberg, M. Hada, M. Ehara, K. Toyota, R. Fukuda, J. Hasegawa, M. Ishida, T. Nakajima, Y. Honda, O. Kitao, H. Nakai, T. Vreven, J. A. Montgomery, Jr., J. E. Peralta, F. Ogliaro, M. Bearpark, J. J. Heyd, E. Brothers, K. N. Kudin, V. N. Staroverov, T. Keith, R. Kobayashi, J. Normand, K. Raghavachari, A. Rendell, J. C. Burant, S. S. Iyengar, J. Tomasi, M. Cossi, N. Rega, J. M. Millam, M. Klene, J. E. Knox, J. B. Cross, V. Bakken, C. Adamo, J. Jaramillo, R. Gomperts, R. E. Stratmann, O. Yazyev, A. J. Austin, R. Cammi, C. Pomelli, J. W. Ochterski, R. L. Martin, K. Morokuma, V. G. Zakrzewski, G. A. Voth, P. Salvador, J. J. Dannenberg, S. Dapprich, A. D. Daniels, O. Farkas, J. B. Foresman, J. V. Ortiz, J. Cioslowski, D. J. Fox, Gaussian, Inc., Wallingford CT, 2010.

Table S1. Mulliken spin populations P(X), idealized valence state formulation, ^{57}Fe isomer shifts, quadrupole splitting, and asymmetry parameter from DFT.

Functional	Complex	P(Fe)	P(^{17}O)	P(N_{am})	Formulation [e]	δ (mm/s)	ΔE_Q [d] (mm/s)	η
B3LYP [a]	**2**	1.34	0.70	-0.85	$Fe^{IV}N\bullet$	0.14	-0.48	0.75
B3LYP [a]	**2-H$^+$**	1.25	0.79	-0.92	$Fe^{IV}N\bullet$	0.13	0.52	0.66
B3LYP [b]	**1**	1.34	0.79	–	Fe^{IV}	0.18	1.17	0.09
B3LYP [c]	**1_{ox}**	0.35	0.65	–	$Fe^{IV}O\bullet$	-0.09	2.83	0.93
BP86 [a]	**2**	0.86	0.51	-0.30	Fe^{V}	0.03	1.08	0.47
BP86 [a]	**2-H$^+$**	0.77	0.55	-0.31	Fe^{V}	-0.05	-1.17	0.48
BP86 [b]	**1**	1.30	0.76	–	Fe^{IV}	0.16	1.08	0.17
BP86 [c]	**1_{ox}**	0.90	0.27	–	Fe^{V}	-0.08	2.52	0.92

[a] $[Fe(O)(NC(Me)O(H))(TMC)]^{1+(2+)}$. [b] $Fe^{IV}(O)(NCMe)(TMC)$. [c] $Fe^{V}(O)(NCMe)(TMC)$. [d] Used Q(^{57}Fe) = 0.16 barn. [e] Based on spin populations and $\langle \mathbf{S}^2 \rangle$ values.

The spin populations calculated for **2** and **2-H$^+$** are given in **Table S1** and show that hybrid functional B3LYP yields solutions that are best described as iron(IV)-radical, $Fe^{IV}N\bullet$, species, while the BP86 solutions are best described as Fe^{V}. The difference in the performance of B3LYP and BP86 in predicting the valencies of the atoms in these systems is probably rooted in their respectively "hybrid" and "pure" natures (the pure functionals PBEVWN and OLYP gave similar results as BP86, results not shown). The functional dependence of the results may be related to the propensity of Hartree-Fock exchange toward stabilizing high-spin states. Applied to the present situation, the HF-exchange contribution included in the B3LYP functional explains why this functional favors the $Fe^{IV}N\bullet$ formulation (three unpaired electrons of which two are on iron) over the Fe^{V} formulation (one unpaired electron). The Fe^{IV}-radical state for B3LYP and the Fe^{V} state for BP86 are strongly supported by the expectation values $\langle \Psi_{B3LYP}|\mathbf{S}^2|\Psi_{B3LYP}\rangle$ = 1.63 (ideally 1¾ for the broken symmetry state of the Fe^{IV}-radical model) and $\langle \Psi_{BP86}|\mathbf{S}^2|\Psi_{BP86}\rangle$ = 0.94 (ideally ¾ for the Fe^{V} model).

The isomer shift, δ, and quadrupole splitting, ΔE_Q, have no clear preference for any of the two functionals. The solutions with Fe^{IV}-radical character (B3LYP solutions) give isomer shifts that are higher than the observed value (δ_{exp} = 0.10 (4) mm/s) while those with Fe^{V} character, all obtained with BP86, are somewhat lower than in experiment. The quadrupole splittings for B3LYP are in slightly better agreement with experiment than those for BP86 but the discrepancies for the latter functional are also within the commonly observed error margin for this quantity (±0.5 mm/s). Also included in **Table S1** are the results for the starting material **1** (Fe^{IV}=O) and its hypothetical 1-electron oxidized adduct $\mathbf{1_{ox}}$ (Fe^{V}=O). The isomer shifts for **2** and $\mathbf{2\text{-}H^+}$ with Fe^{IV}-radical character are consistent with the isomer shift of the Fe^{IV}=O starting material. The isomer shift calculated for the Fe^{V} solution of **2** (δ = +0.03 mm/s) is considerably larger than computed for the hypothetical Fe^{V}(O)(NCMe)(TMC) complex $\mathbf{1_{ox}}$ (δ = -0.08 mm/s), in spite of having rather similar spin populations. Apparently, the replacement of the acetonitrile ligand in $\mathbf{1_{ox}}$ with an acetimido ligand, gives rise to a significant increase in the isomer shifts, even if the oxidation state remains Fe^{V}, as in the BP86 solution for **2**. Thus, as it has already been noted earlier in the literature, the isomer shift is a poor indicator of iron valence state unless the ligand effect on this quantity is properly accounted for. The difference of the δ values for **2** (δ = 0.03 mm/s) and experiment (δ = 0.10 mm/s) is within the standard error of the BP86 isomer shift calibration (Δδ = 0.09 mm/s). The negative change in the isomer shift observed upon protonation ($\mathbf{2\text{-}H^+}$) has the sign expected for the anticipated increase in Fe^{V} character but is not unambiguously supported by the data. The quadrupole splittings obtained with the two functionals for $\mathbf{1_{ox}}$ are significantly larger (~2.5 mm/s) than observed in **2** and $\mathbf{2\text{-}H^+}$ by Mössbauer

($\Delta E_{Q,exp}$ ~ 0.50 mm/s). This observation does not preclude Fe^{V} as iron valence state in **2** and **2-H$^+$**, because the BP86 states for **2** and **2-H$^+$**, while clearly Fe^{V} on the basis of spin density and $<\mathbf{S}^2>$, have dramatically smaller values for ΔE_Q (~ 1 mm/s vs. 2.5 mm/s in **1_{ox}**). This difference shows that quadrupole splitting ΔE_Q, like isomer shift δ, is sometimes an ambiguous reporter for the iron oxidation state because of its ligand dependence. DFT supports this assessment: the replacement of acetonitrile with the redox labile acetimido nitrogen *trans* to the oxo ligands gives a large change in the calculated values for ΔE_Q.

The *Fe^{IV}-radical* solutions for **2** and **2-H$^+$** obtained with B3LYP and the *Fe^{V}* solutions obtained with BP86 require different treatments of the magnetic hyperfine interactions. In the Fe^{IV}-radical formulation, the magnetic hyperfine interaction of ^{14}N nucleus arises from the magnetic coupling of this nucleus with a π radical electron centered at this nucleus, $\mathbf{S}_R \cdot a_R \cdot \mathbf{I}_R$. The radical spin is coupled to the S_{Fe}=1 spin of the iron to give a total spin S=1/2, introducing spin projection factors of 4/3 (Fe^{IV}, S_{Fe}=1) and -1/3 (N•, S_R=1/2) in the expression for the magnetic hyperfine coupling constants in the coupled S = 1/2 representation. In order to express the DFT calculated quantities with those obtained by analyzing the data with an S = ½ spin Hamiltonian, the DFT quantities have to be expressed in the coupled representation: $\mathbf{S} \cdot A_X \cdot \mathbf{I}_X$ (X = Fe, N, O) where **S** is the coupled S=1/2 system spin, $|\{S_{Fe}=1, S_R=1/2\}S=1/2>$. For the ^{57}Fe and the ^{17}O of the oxo group, the DFT output for the A-tensors has to be divided by 2 (to refer the values to the S_{Fe}=1 Hamiltonian) and then multiplied by the spin projection factor 4/3. For ^{14}N the signs of the a_R values have to be reversed (it is a β spin) and then multiplied by spin projection factor -1/3. This yields the entries in rows 1-4 of **Table S2,** which allows

direct comparison between the calculated and experimental A-values. Note that the calculated ^{57}Fe A-tensors are quite axial around z, in contrast to the experimental data.

In the Fe^{V} model the DFT calculated A-tensors can be directly compared with the experimental A-tensors. For a final comparison we wish to make one adjustment. It is well known that DFT often underestimates the magnitude of the Fermi contact interaction, A_{FC}, and researchers have either introduced correction factors (as much as 1.7) or used the experimentally determined contact term. Since the g-values of **2** and **2-H^+** are close to g = 2, orbital contributions to the A-tensor are negligible, and thus we can use $A_{iso} = (A_x + A_y + A_z)/3$ for A_{FC}. Using the experimental value A_{iso} (^{57}Fe) = (- 48 - 17 + 0)/3 MHz = -21.7 MHz for **2** and **2-H^+** further improves an already excellent agreement with experiment as can be seen by inspection of **Table S3**.

Table S2. Magnetic hyperfine coupling constants (in MHz, Fermi contact + spin dipolar) deduced from DFT using for each complex the model suggested by Table S1.

Functional	Complex	State [b]	^{57}Fe			$^{14}N_{ax}$			^{17}O		
			A_x	A_y	A_z	A_x	A_y	A_z	A_x	A_y	A_z
B3LYP [a]	**2**	$Fe^{IV}N\bullet$	-24.7	-27.5	6.3	-32.7	2.2	3.3	-56.1	-57.0	54.4
B3LYP [a]	**2-H$^+$**	$Fe^{IV}N\bullet$	-24.2	-19.2	4.8	-35.6	-0.9	3.2	-57.9	-62.5	63.1
BP86 [a,c]	**2**	Fe^{V}	**-35.5**	**-10.7**	**4.5**	**-39.3**	**10.8**	**6.1**	**-1.0**	**-70.8**	**75.7**
BP86 [a,c]	**2-H$^+$**	Fe^{V}	**-35.5**	**-4.4**	**3.6**	**-35.5**	**-1.2**	**3.9**	**18.4**	**-91.4**	**84.7**
Exp.	**2**, **2-H$^+$**		-48	-17	0	29	11	11	30	133	20

[a] $[Fe(O)(NC(Me)O(H))(TMC)]^{1+(2+)}$. [b] State used for interpreting DFT results for magnetic hyperfine interactions (cf. **Table S1**). [c] Rows having most satisfactory agreement with experimental data for **2** and **2-H$^+$** are in bold face.

None of the computed A-value sets listed for the $Fe^{IV}N\bullet$ state (**Table S2**) gives a satisfactory agreement with experiment. The A-values obtained for ^{57}Fe and ^{17}O in the $Fe^{IV}N\bullet$ state are nearly axial along z and not rhombic (^{57}Fe) or quasi axial along y (^{17}O) as observed.

The experimental magnetic hyperfine data for ^{14}N, ^{57}Fe, and ^{17}O for **2** and **2-H$^+$** reveal A-values with a characteristic set of spatially correlated anisotropies. The A tensor for $^{14}N_{ax}$ has one large and two small components. Let us define the direction with the large $^{14}N_{ax}$ A-component as the x axis. The A values for both ^{57}Fe and ^{17}O show marked anisotropies. ^{57}Fe has one large, one intermediate, and one vanishing A-component. The largest component of A(Fe) is along x and we define the eigenvector of the intermediate component as the y axis (this choice of axes assigns the vanishing component to the z axis, as in Fe^{IV}(O)(TMC)(NCMe) (-25 T, -20 T, -3 T) where z is along the Fe-O bond. $^{17}O_{ax}$ has one large and two smaller A-components, with the large component being along the y axis. B3LYP consistently fails to reproduce the anisotropies of both the ^{57}Fe and ^{17}O A-values (**Table S2**). This property is anticipated from **Table S1**, which shows that the spin densities calculated with B3LYP for the Fe=O unit in **2** and **2-H$^+$** are similar to

those for starting complex **1**, and share with them nearly z-axial A-values. Clearly, there is no Fe^{IV} solution for **2** and **2-H$^+$**. The best agreement with the experimental results is obtained for the Fe^{V} state predicted by BP86 for **2** and **2-H$^+$** (bold faced rows of **Table S2**), which have similar A values.

Table S3. Section of Table S2 but using the experimental A_{iso} (^{57}Fe) value instead of the calculated Fermi contact term.

Functional	Complex	State	^{57}Fe			$^{14}N_{imido}$			^{17}O		
			A_x	A_y	A_z	A_x	A_y	A_z	A_x	A_y	A_z
BP86	**2**	Fe^{V}	**-43.3**	**-18.5**	**3.3**	**-39.3**	**10.8**	**6.1**	**-1.0**	**-70.8**	**75.7**
BP86	**2-H$^+$**	Fe^{V}	**-45.1**	**-14.0**	**-6.0**	**-35.5**	**-1.2**	**3.9**	**18.4**	**-91.4**	**84.7**
Exp.	**2, 2-H$^+$**		-48	-17	0	29	11	11	30	133	20

Observations from **Table S4**: (i) B3LYP and BP86 give for the iron site in the hypothetical $Fe^{IV}N\bullet$ complex similar A-values. (ii) B3LYP and BP86 give for the iron(V) site in $\mathbf{1_{ox}}$ similar A values. (iii) The corresponding differences between the A-values for ^{17}O are somewhat larger than for iron. (iv) B3LYP and BP86 give for $Fe^{IV}N\bullet$ axial ^{57}Fe and ^{17}O A-values. (v) B3LYP and BP86 give ^{57}Fe and ^{17}O A-values for $\mathbf{1_{ox}}$ that show similar spatial anisotropies. (vi) B3LYP gives essentially the same results for **2** and $Fe^{IV}N\bullet$. This observation shows that the Fe site in the B3LYP solution of **2** is best described as an Fe^{IV}-radical system (this conclusion is supported by the spin populations obtained with B3LYP given in **Table S1**). (vii) BP86 gives excellent agreement between **2** and Fe^{V}. This observation shows that the Fe site in the BP86 state for **2** is best described as Fe^{V} (this conclusion is supported by the spin populations obtained with BP86 given in **Table S1**). Thus, the difference between B3LYP and BP86 is not so much in the calculation of the properties *per se* but in the balance between the Fe^{IV}-radical and

Fe^{V} configurations, which is tipped toward Fe^{IV}-radical by B3LYP and toward Fe^{V} by BP86 (see discussion below **Table S1**). (viii) *The B3LYP results for **2** are in poor agreement with experiment*; in particular, they fail to reproduce the anisotropic A tensors observed. The reason for this shortcoming is that the B3LYP solution for **2** is an Fe^{IV}-radical state in which the Fe^{IV}=O moiety retains the axial features of starting complex **1**. (ix) The BP86 results for **2** are in good agreement with experiment; in particular, they reproduce the rhombic A tensors (the agreement for iron is excellent; for ^{17}O the agreement is fine, except for a discrepancy in the z component). The reason for the improved agreement is that the BP86 solution for **2** has predominant Fe^{V} character. (NB. If B3LYP is forced into the Fe^{V} state, as in the calculation for $\mathbf{1_{ox}}$, a similarly good agreement is found for this functional as well). The A-values are explained on the basis of the Fe^{V} formulation in the discussion of **Figure 5** of main text.

Table S4. $A_{x,y,z}$-values (in MHz, Fermi contact + spin dipolar) from experiment compared with results deduced from DFT with Fe^{IV}-radical model and Fe^{V} model (shaded) for **2**, and two hypothetical complexes containing Fe^{IV}-radical ($Fe^{IV}N\bullet$) and Fe^{V} sites.

Nucleus	Axis	Exp	B3LYP				BP86			
			2 [c]	$Fe^{IV}N\bullet$ [a]	**2** [f]	Fe^{V} [b,d]	**2** [c]	$Fe^{IV}N\bullet$ [a]	**2** [d,f]	Fe^{V} [b,d]
^{57}Fe	x	-48	-24.7	-27.1	N.A.[g]	**-46.4**	N.A.[h]	-23.7	**-35.5**	**-40.0**
	y	-17	-27.5	-26.5		**16.0**		-25.3	**-10.7**	**-4.7**
	z[e]	0	6.3	2.4		**-1.1**		1.7	**4.5**	**3.3**
^{17}O	x	30	-56.1	-60.2		**-27.9**		-36.9	**-1.0**	**78.7**
	y	133	-57.0	-60.3		**-100.5**		-35.7	**-70.8**	**-118.3**
	z[e]	20	54.4	65.0		**75.9**		81.0	**75.7**	**47.4**

[a] A-values obtained on the basis of the $A(^{57}Fe)$ and $A(^{17}O)$ calculated for a hypothetical system in which an Fe^{IV}=O (S_{Fe}=1) site as in **1** is coupled to a (amidyl) radical (S_R=1/2) to give total spin S=½. [b] A-values for $\mathbf{1_{ox}}$. [c] A-values for **2** obtained with Fe^{IV}-radical model in coupled representation. [d] Columns showing data resembling the experimental data for **2** and **2-H**$^+$ are in bold face. [e] z is along the Fe-^{17}O vector. [f] A-values obtained with Fe^{V} model. [g] Fe^{V} model not applicable. [h] Fe^{IV}-radical model not applicable

Table S5. Fe-O stretch frequencies and axial bond lengths from DFT.

functional	Complex	State	$\nu_{Fe\text{-}O}$ (cm^{-1})	Fe-^{17}O (Å)	Fe-N_{ax} (Å)
B3LYP [a]	**2**	$Fe^{IV}N\bullet$	855	1.669	1.905
B3LYP [a]	**2-H**$^+$	$Fe^{IV}N\bullet$	898	1.642	1.985
B3LYP [b]	**1**	Fe^{IV}	910	1.641	2.097
B3LYP [c]	$\mathbf{1_{ox}}$	Fe^{V}	1256	1.584	2.022
BP86 [a]	**2**	Fe^{V}	**785** [d]	1.701	1.781
BP86 [a]	**2-H**$^+$	Fe^{V}	**829** [d]	1.658	1.813
BP86 [b]	**1**	Fe^{IV}	**853** [d]	1.664	2.037
BP86 [c]	$\mathbf{1_{ox}}$	Fe^{V}	944	1.603	2.006

[a] $[Fe(O)(NC(Me)O(H))(TMC)]^{1+(2+)}$. [b] $Fe^{IV}(O)(NCMe)(TMC)$. [c] $Fe^{V}(O)(NCMe)(TMC)$. [d] Numbers having most satisfactory agreement with the experimental data for **2**, **2-H**$^+$ and **1** are in bold face.

Table S5 shows that B3LYP gives consistently stronger the Fe-^{17}O bonds than BP86 for all complexes listed, resulting in shorter bond lengths and higher Fe-O stretch frequencies for the former functional. The Fe-O stretch frequencies obtained with BP86 are in better agreement with experiment than those calculated with B3LYP, which are

significantly higher than observed. Both functionals reproduce the increasing trend in the experimental Fe-O frequencies for **2**, **2-H**$^{+}$ and **1**: 798 cm^{-1} < 811 cm^{-1} < 839 cm^{-1}. Irrespective of the functional used, the frequencies calculated for **2** and **2-H**$^{+}$ are considerably smaller than for the Fe^{IV}=O bond in **1** and the Fe^{V}=O bond in $\mathbf{1_{ox}}$, suggesting the Fe-O stretch frequency to be a poor reporter for the oxidation state of iron in the present case where iron is coordinated by a redox labile imido *trans* to the oxo ligand. The induced weakening of the Fe-O bond correlates with the increase in isomer shift (see main text).

Table S6. $A_{x,y,z}$-values (in MHz, Fermi contact + spin dipolar) deduced from DFT using Fe^{IV}-Radical model and Fe-N_{ax} distances (in Å) from relaxed B3LYP/6-311G scan along Fe-O_{ax}.

Fe-O_{ax} [a]	Fe-N	^{57}Fe [b]			^{57}Fe [c]			^{14}N			^{17}O		
		x	y	z	x	y	z	x	y	z	x	y	z
1.669 [d]	1.904	-17.1	-12.3	29.4	-24.7	-21.5	6.3	-71.0	33.7	37.3	-54.5	-56.4	110.9
1.699	1.897	-17.0	-12.1	29.1	-24.6	-21.3	6.1	-70.7	33.7	37.0	-54.9	-56.7	111.6
1.729	1.891	-17.0	-11.9	28.9	-24.5	-21.1	6.1	-70.6	33.8	36.8	-55.2	-57.1	112.3
1.759	1.884	-16.9	-11.6	28.5	-24.4	-20.9	5.9	-70.4	33.9	36.5	-55.4	-57.6	113.0
1.789	1.878	-16.8	-11.3	28.1	-24.2	-20.5	5.7	-70.2	34.0	36.2	-55.2	-58.6	113.8
1.819	1.871	-17.0	-10.6	27.6	-24.2	-19.9	5.5	-70.1	34.2	35.9	-61.8	-53.0	114.8

[a] Value of imposed distance in optimization.
[b] Using for ^{57}Fe a^{FC} = -16.25 MHz ($\mathbf{I}\cdot a^{FC}\cdot\mathbf{S}_{Fe}$, S_{Fe} = 1), the value obtained from the average of the experimental A values by multiplication with 3/4.
[c] Using the DFT calculated A^{FC}.
[d] Distance in the B3LYP/6-311G optimized structure; other distances of relaxed scan are defined by incrementing five times by 0.03 Å.

The DFT-functional dependence of the bond distances raises the possibility that the differences in the performance of the functionals in the A-value calculations arise from differences in the bond distances in the optimized geometries obtained with these functionals. In **Table S6** we have listed the results for the A-values from a relaxed B3LYP/6-311G scan along the Fe-^{17}O coordinate. The changes in the A-values appear to be remarkably small given the broad range of Fe-O distances considered. A similar insensitivity of the A-values is observed in a relaxed scan along the Fe-N_{ax} coordinate (not shown). These results together with the insensitivity of the A-values to basis set changes (we used 6-311G, 6-311G*, TZVP, results not listed) corroborate with the conclusion that the computational differences between the A values obtained with B3LYP versus BP86 and two other pure functionals (PBEVWN and OLYP, results not shown) are rooted in the type of solution obtained with these functionals (see discussion below **Table S1**).

Table S7. Mulliken spin (first row) and total (second row) populations of 3d orbitals at Fe and 2p orbitals at N_{ax} and O_{ax}, for the Fe^{V} $|d_{x2-y2}^{2}\ d_{yz}^{1}|$ BP86 solution for 2. Axes: z is along N-Fe-O_{ax} bonds and x is here the intersection of TMC-nitrogen plane and acetamide NCO plane.[a]

Fe					N_{ax}			O_{ax}		
x^2-y^2	xz [b]	yz [c]	xy	z^2	x	y	z	x	y	z
0.01	0.23	**0.53**	0.06	0.02	**-0.30**	0.03	-0.02	0.18 [d]	**0.32**	0.01
1.82 [e]	1.21	1.42	0.82 [e]	0.94	1.19	1.45	1.20	1.55	1.59	1.41

[a] Dominant spin densities are given in bold face.
[b] α spin population = 0.71, β spin population 0.49.
[c] α spin population = 0.97, β spin population 0.44.
[d] This number is not zero because the donation of electron density into the formally empty d_{xz} orbital is not completely spin balanced due to the presence of the α spin electron in d_{yz}.
[e] These values approach 2.0 and 0.6 by rotating x and y slightly around z as to make x and y more accurately bisect the equatorial N-Fe-N angles.

The spin and total populations for the BP86 solution for **2** concur with earlier DFT studies in that the formally empty metal d orbitals in high-valent iron complexes acquire large electronic populations due to covalent interactions with the ligands.

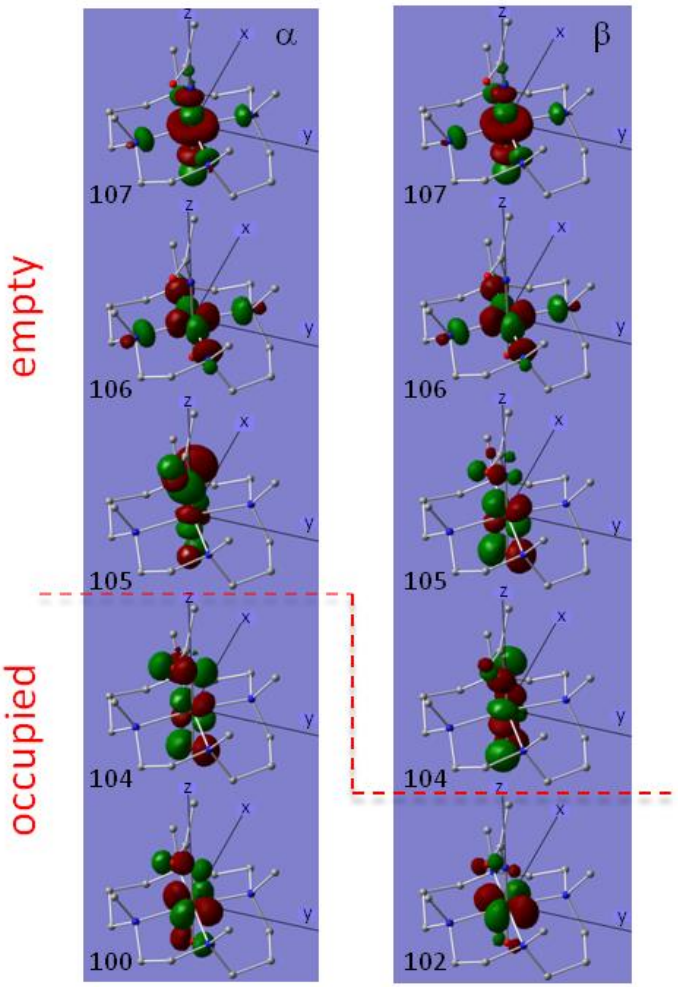

Figure S1. 3d-type molecular orbitals of the Fe^{V} $|d_{x2-y2}{}^{2}\ d_{yz}{}^{1}|$ BP86 solution for **2**.

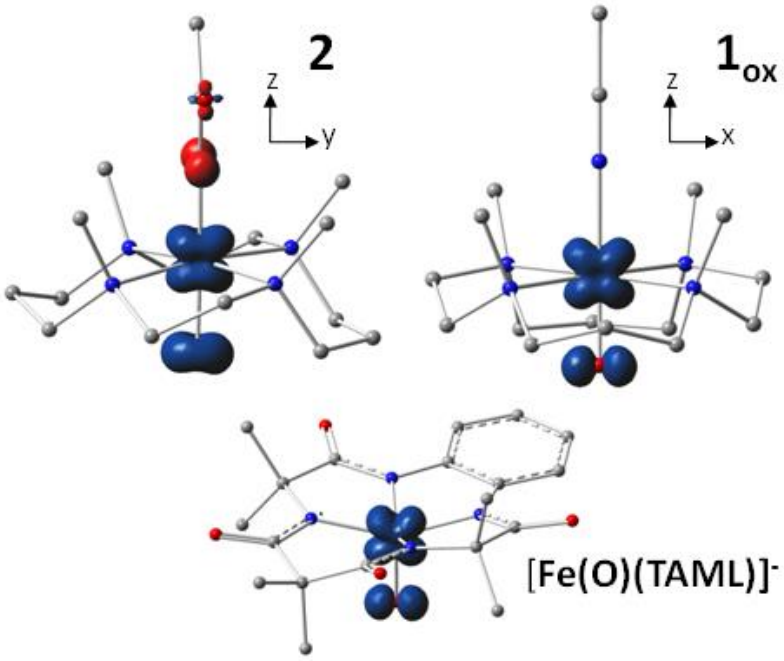

Figure S2. Spin density contour plots obtained with BP86/6-311G for three low-spin Fe^{V}-oxo complexes: complex **2**, the computational complex for the 1e-oxidized starting material $\mathbf{1_{ox}}$, and the truncated TAML complex $[Fe^{V}(O)B^{*}]^{1-}$ (F. Tiago de Oliveira, A. Chanda, D. Banerjee, X. Shan, S. Mandal, L. Que, Jr., E. L. Bominaar, E. Münck, T. J. Collins, *Science*, 2007, 315, 835) all viewed approximately along the normal to the plane containing the unpaired electron containing orbital, labeled d_{yz} (**2**) and d_{xz} ($\mathbf{1_{ox}}$).

The spin density profiles shown in **Figure S2** corroborate the classification of **2** as an Fe^{V} complex. The spin density at the Fe=O moiety in **2** resembles the spin densities for the only Fe^{V}=O species, $[Fe^{V}(O)B^{*}]^{1-}$, reported in the literature and the computational complex $\mathbf{1_{ox}}$, which is an Fe^{V} species as all ligands therein (MeCN, O^{2-}, TMC) are redox innocent. The p_y like contour of the spin density at the oxo atom in **2** is slightly blurred by the presence of some spin density in the p_x orbital of oxygen (**Table S7**) donated by the redox non-innocent imido nitrogen.

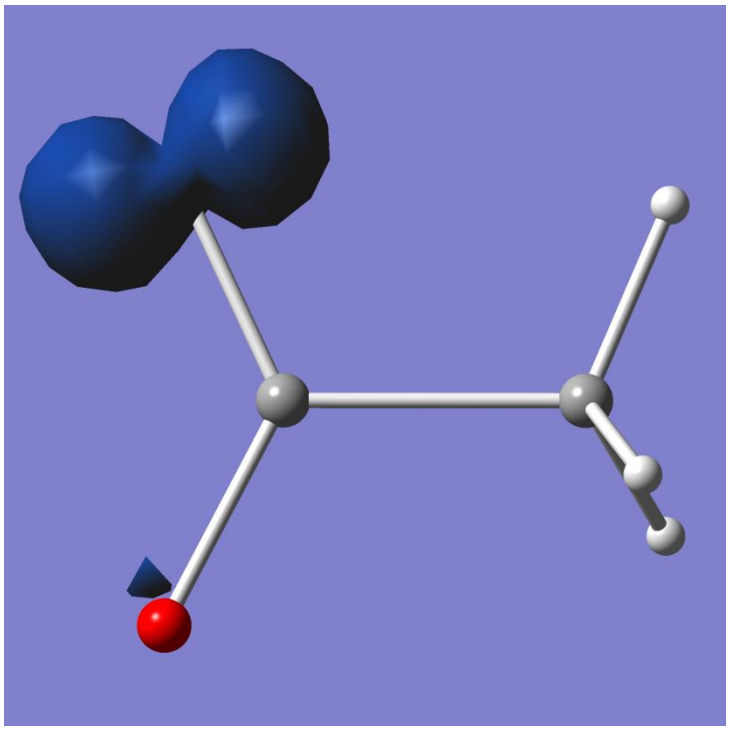

Figure S3. Plot of spin density in acetamidyl radical obtained with BP86 revealing the contour of the in-plane p orbital at nitrogen (labeled p_x in text) containing the unpaired electron.

Table S8. BP86 optimized structure for **2**

Fe	-0.01024099	0.02306683	-0.09676283
N	-1.17725984	1.79683954	-0.25838780
N	1.70147703	1.32326218	-0.18781458
N	1.24788782	-1.71937391	-0.17896251
N	-1.64958483	-1.32346469	-0.24927041
C	-0.22538889	2.73632556	-0.97653287
C	1.13350707	2.73295991	-0.31166926
C	2.48552484	0.96919266	-1.44510015
C	3.07159865	-0.45288621	-1.47149840
C	2.07292973	-1.62287157	-1.45261501
C	0.28028651	-2.89566926	-0.25109017
C	-1.01205607	-2.51712182	-0.94027235
C	-2.76092048	-0.83353673	-1.16064998
C	-3.34520464	0.52456157	-0.77642209
C	-2.40708660	1.67341700	-1.13985877
C	-1.58273952	2.36561082	1.07472857
C	2.62601819	1.36498493	1.00369954
C	2.16058930	-2.03551189	0.98720274
C	-2.25119711	-1.74304869	1.07040823
H	-0.64901529	3.75636444	-0.98310138
H	-0.15325115	2.37603244	-2.00869548
H	1.07409387	3.14835530	0.70297737
H	1.84284066	3.36092941	-0.87742810
H	3.30982356	1.70088430	-1.53684436
H	1.79575591	1.09343972	-2.28797093
H	3.62612662	-0.53472721	-2.42252407
H	3.83661553	-0.57935295	-0.68975147
H	1.37167123	-1.52058717	-2.28818943
H	2.62929944	-2.57272642	-1.55665785
H	0.77041764	-3.73378275	-0.77507854
H	0.09247804	-3.21006711	0.78296390
H	-1.71780112	-3.36580370	-0.92541474
H	-0.83344712	-2.22055315	-1.97982802
H	-3.54785643	-1.60885145	-1.15914278
H	-2.33529388	-0.76765408	-2.16975299
H	-3.65775398	0.55880825	0.27853673
H	-4.27102476	0.66305761	-1.35970031
H	-2.04204242	1.52149903	-2.16375698
H	-2.93898896	2.64111024	-1.09937846
H	-2.08639165	3.33644700	0.93151582
H	-0.70549037	2.49358628	1.71302746
H	-2.26000378	1.67043351	1.57900361
H	3.28452376	2.24613677	0.92733861
H	3.25159157	0.47389949	1.04727787
H	2.02571361	1.41831227	1.91660690
H	2.65615123	-3.00186872	0.79084278
H	1.56477083	-2.10515680	1.90413999
H	2.93049962	-1.27450408	1.10624736
H	-3.03126389	-2.50110729	0.88808564
H	-2.70216168	-0.87290256	1.55769434
H	-1.48497279	-2.13666742	1.74613582
C	-0.01203733	-0.39560906	2.96186581
N	0.00000000	0.00000000	1.68375635
C	-0.03346059	0.59798308	4.10178657
H	0.82068506	0.40332148	4.76743487
H	0.00593297	1.64220747	3.76336590
H	-0.94658200	0.45121239	4.69844472
O	0.00000000	-1.67578230	3.21192172
O	-0.05858361	0.01033995	-1.79669894

Comments on EPR and Mössbauer Spectra. In the following we add some details of the Mössbauer and EPR spectra we recorded. The appropriate comments are given in the captions of the figures. In the caption of Figure 3 we indicated that the sample for **2-H**$^+$ contains a 30% high-spin Fe^{III} contaminant. The 8.0 T spectrum of **Figure S4** proves this assertion. The spectrum also shows that A_x and A_y of **2** are negative. The magnitude of A_z of **2** and **2-H**$^+$ is small and we could not determine its sign.

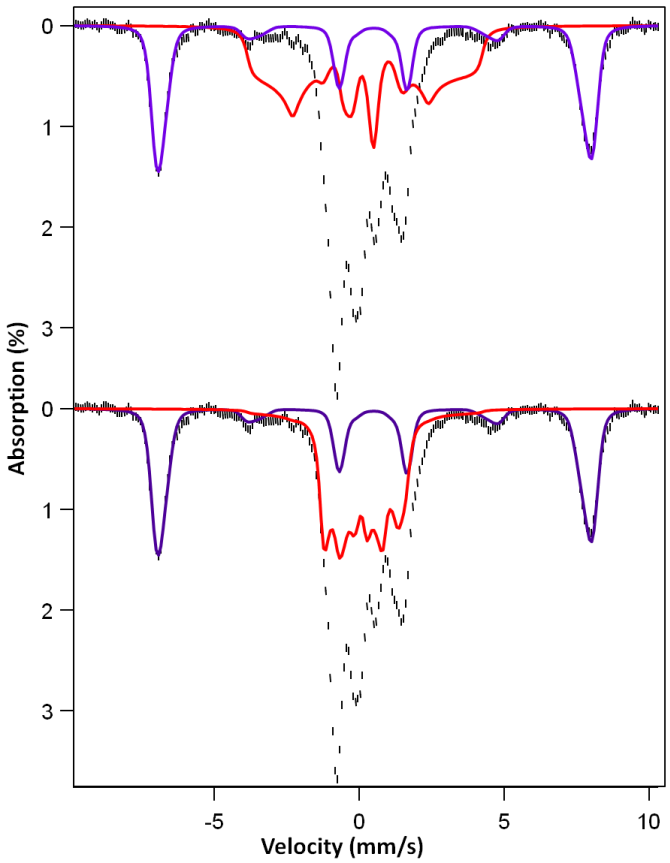

Figure S4. 4.2 K/8.0 T Mössbauer spectrum of the sample containing **2-H**$^+$ (Sample from Figure 3C). The purple line is a spectral simulation outlining the high-spin Fe^{III} contaminant (30% of Fe). The EPR spectra of this sample shows two high-spin Fe^{III} species with a positive zero-field splitting parameter D, $|D| < 2$ cm^{-1}, and E/D = 0.04 and 0.05. The red line in the bottom panel is a spectral simulation for **2-H**$^+$ assuming that A_x and A_y of **2** are negative. As shown in top panel, positive A_x and A_y values do not fit the data. A_z is too small, $|A_z| < 5$ MHz to determine its sign.

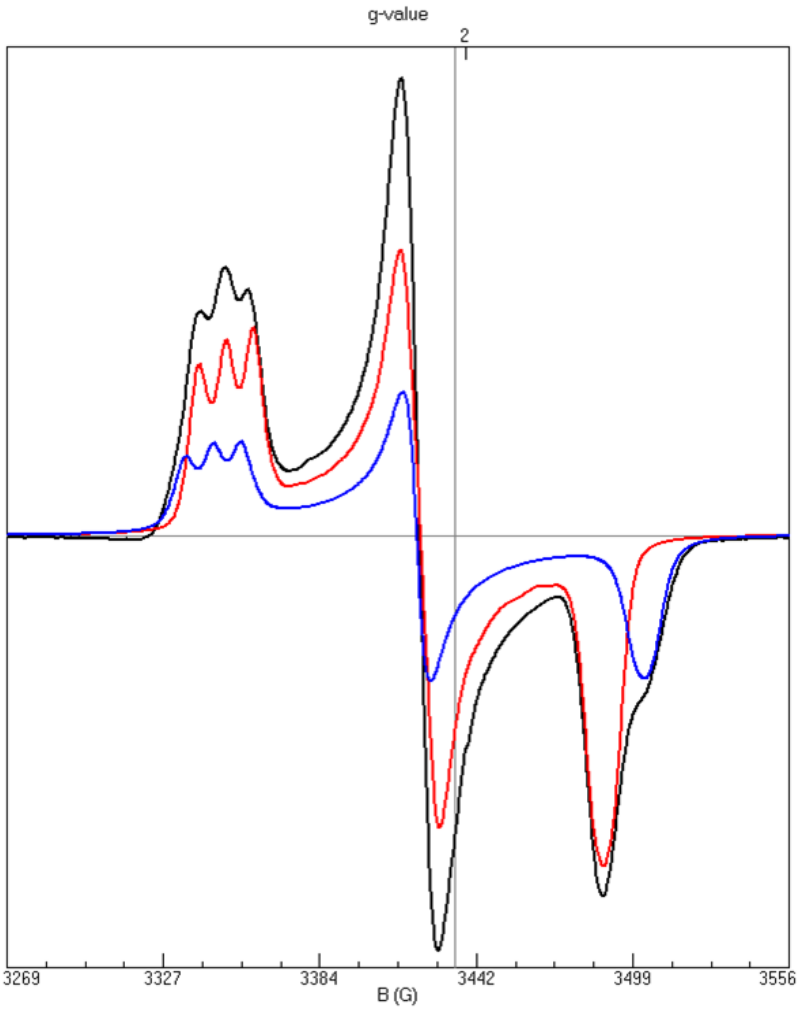

Figure S5. The black line shows a 40 K spectrum of **2** (same spectrum as shown in Figure 4A of the main text). The red line is a SpinCount simulation of the majority species, **2**. For the simulation the concentration of **2** was chosen to fit its high-field feature. It can be seen that this simulation does not produce sufficient amplitude for the low-field and middle resonances. The difference must be contributed by minority species $\mathbf{2^m}$ (blue line). Thus, the g-values of $\mathbf{2^m}$ are essentially known. $\mathbf{2^m}$ must also exhibit a ^{14}N hyperfine triplet, otherwise its low field feature would show a strong central peak due to the non-split line. Species $\mathbf{2^m}$ must be quite similar to **2**, but presently we do not know the conformational difference between the species (possibly different orientations of the imido ligand). Protonation always yields only one species $\mathbf{2\text{-}H^+}$. There is no hint in our data indicating that the Mössbauer spectra of **2** and $\mathbf{2\text{-}H^+}$ differ.

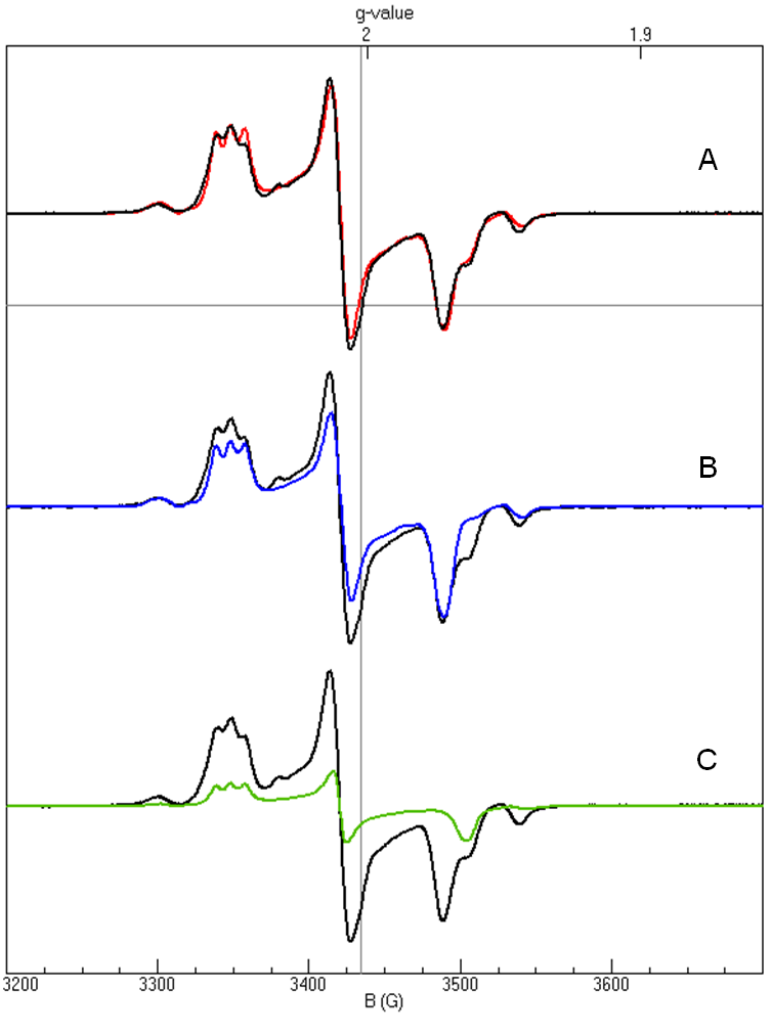

Figure S6. X-band EPR spectrum of ^{17}O labeled **2** (black lines) obtained in 3:1 PrCN:MeCN at 40 K. **(A)** SpinCount simulations of **2** and **2^{m}** added in 2:1 ratio (red line). In **(B)** and **(C)** are shown the individual simulations of for **2** (blue) and **2^{m}** (green) separately, in 2:1 proportions. Parameters used for **2** and **2^{m}** (italics): $g_{x,y,z}$ =2.054, 2.010, 1.971 (*2.054, 2.011, 1.963*); $A_{x,y,z,}$(^{14}N, MHz) = 28.5, 10.5, 12 (*28.5, 2.6, 11)*, $A_{x,y,z,}$ (^{17}O, MHz) = 30, 130, 20 (*30, 130, 20)*, Lorentzian line width = 4 gauss.

Comments on Resonance Raman Data. As ^{18}O labeling of **2** yielded two features centered at 762.5 cm^{-1}, we conducted additional labeling experiments to determine if these vibrations could be attributed to a Fermi doublet. Preparation of **2** using $PhI^{18}O$ to ensure that only one ^{18}O atom was incorporated into the final product also yielded the previously observed doublet, while generation of **2** using ^{17}O produced a single resonance-enhanced vibrational feature at 780 cm^{-1}. Thus, the pair of features at 762.5 cm^{-1} can be conclusively assigned as a Fermi doublet.

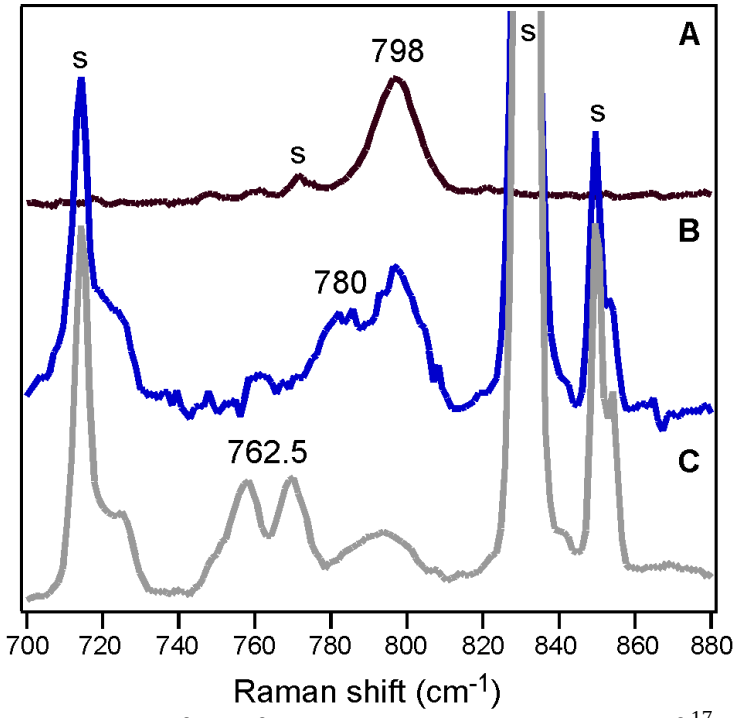

Figure S7. (A) rR spectrum of **2** in frozen CH_3CN. **(B)** rR spectra of ^{17}O-labeled **2** in CD_3CN. This sample was prepared by treating **1** with 100 equivalents of 60:40 $H_2{}^{16}O$:$H_2{}^{17}O$ at RT for 10 minutes, followed by addition of TBHP and base at -44 ^{o}C. **(C)** rR spectra of ^{18}O-labeled **2** prepared with solid $PhI^{18}O$ in CD_3CN. A small amount of unlabeled complex is also evident at ~798 cm^{-1}. All spectra were obtained with 457.9 nm laser excitation (~100 mW at source). S = solvent-derived peaks.

Comments on Low-temperature ESI-MS Experiments. The use of the solvent mixture 3:1 CH_2Cl_2:CH_3CN allowed us to cool our system to -80°C and thus sufficiently stabilize **2** to conduct low-temperature ESI-MS experiments. The reaction vessel was immersed in dry ice, and a 0.4 mM solution of **2** was infused directly into the Bruker BioTOFFII in order to minimize sample decay. Parallel samples were prepared, one using 3:1 CH_2Cl_2:CH_3CN and the other 3:1 CH_2Cl_2:CD_3CN (Figure S8). Consistent with the results of Mössbauer analysis, ESI-MS investigations reveal a distribution of species (Figure S9).

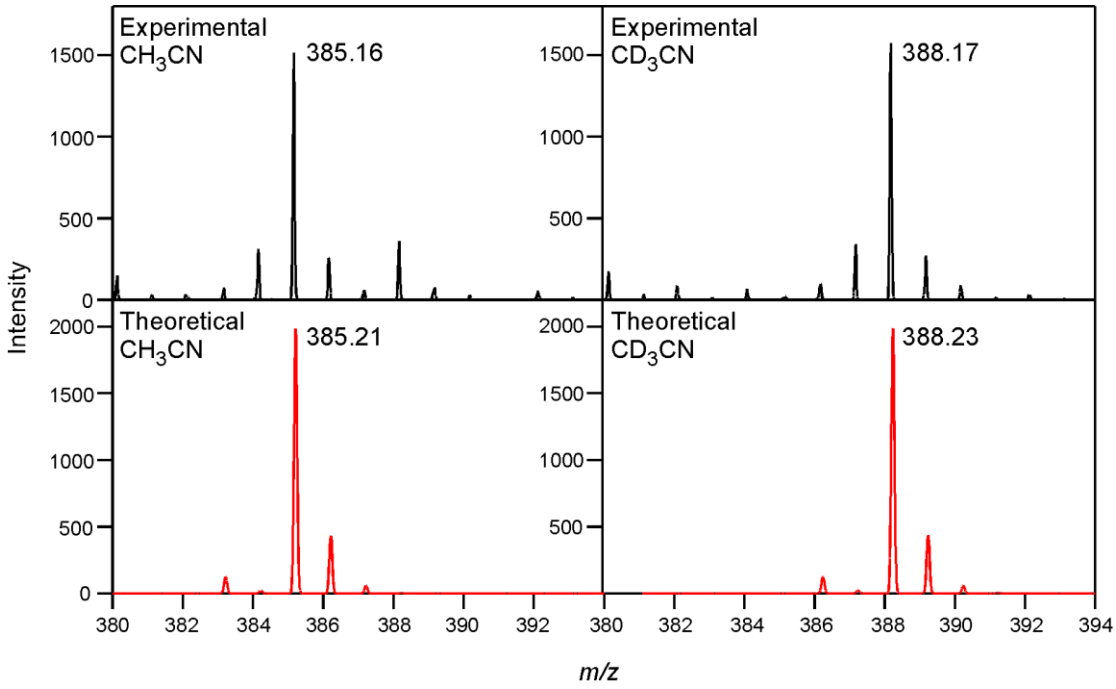

Figure S8. The electrospray ionization mass spectra (ESI-MS) of samples of **2** prepared in **(left)** 3:1 CH_2Cl_2:CH_3CN and **(right)** 3:1 CH_2Cl_2:CD_3CN. The theoretical spectra correspond to the expected isotope patterns of the cation $[Fe(O)(TMC)(NCOCH/D_3)]^+$.

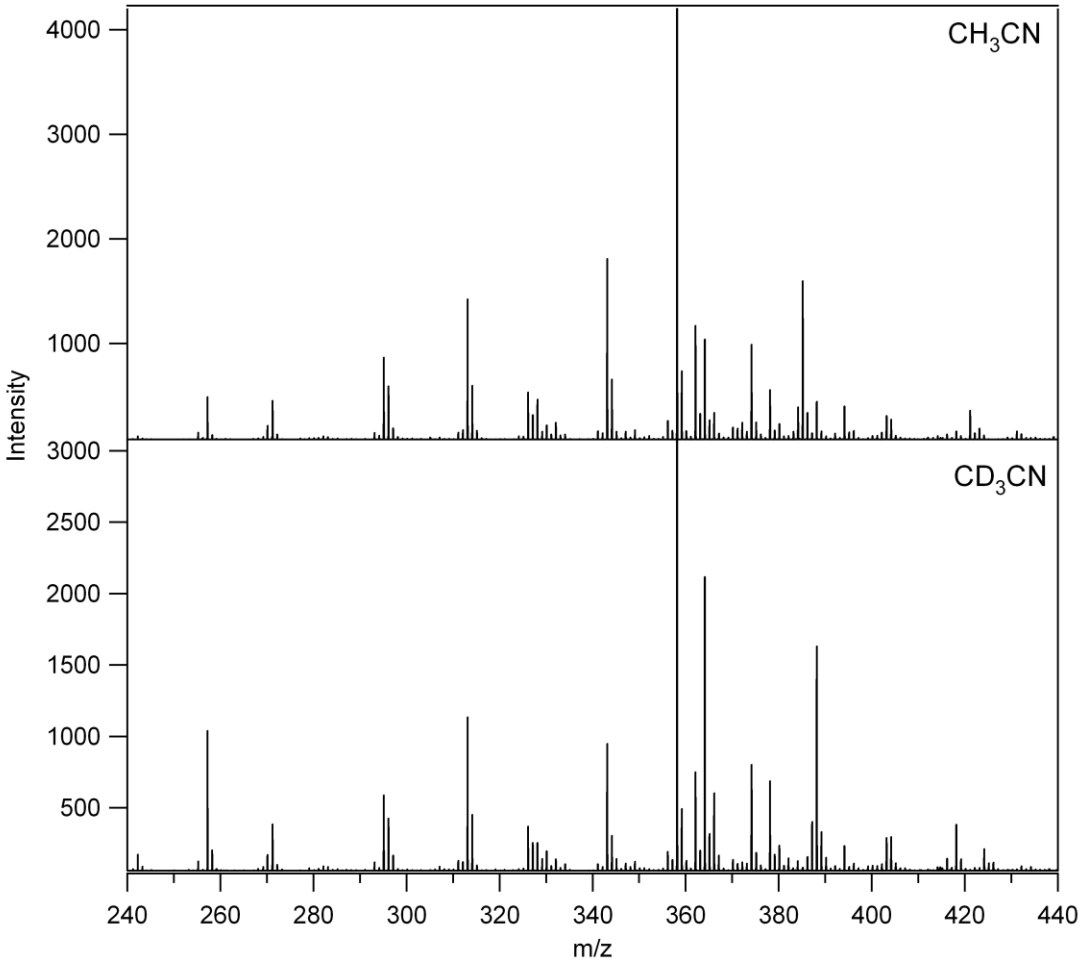

Figure S9. The electrospray ionization mass spectra (ESI-MS) of samples of **2** prepared in **(top)** 3:1 CH_2Cl_2:CH_3CN and **(bottom)** 3:1 CH_2Cl_2:CD_3CN.

List of Publications

1. **Meier, K. K.**; Rogers, M.; Kovaleva, E. G.; Bominaar, E.; Lipscomb, J. D.; Münck, E. "Detailed characterization of the resting and ES states in H200C homoprotcatechuate 2,3-dioxygenase by Mössbauer, EPR, and DFT methods." *(in preparation – to be submitted to Inorg. Chem.)*

2. **Meier, K. K.**; Rogers, M.; Kovaleva, E. G.; Bominaar, E.; Lipscomb, J. D.; Münck, E. "Characterization of a new, long-lived intermediate in the H200C mutant of homoprotocatechuate 2,3-dioxygenase by Mössbauer, EPR, and DFT methods." *(in preparation – to be submitted to Inorg. Chem.- Chapter III)*

3. Prakash, J.; Rohde, G. T.; **Meier, K. K.**, Münck, E.; Que, Jr., L. "The Two Faces of the Tetramethylcyclam Ligand in Oxoiron(IV) Chemistry: the *syn*-Isomer of $[Fe^{IV}(O)(TMC)]^{2+}$." (*in preparation)*

4. Prakash, J.; Rohde, G. T.; **Meier, K. K.;** Jasniewski, A. J.; Van Heuvelen, K. M.; Münck, E.; Que, Jr., L. "Spectroscopic Identification of an Fe^{III} Center, not Fe^{IV}, in the Crystalline Sc–O–Fe Adduct Derived from $[Fe^{IV}(O)(TMC)]^{2+}$." *J. Am. Chem. Soc.* 2015, 137, pp 3478-3481.

5. Biswas, A. N.; Puri, M. **Meier, K. K.**; Oloo, W. N.; Rohde, G. T.; Münck, E.; Que, Jr., L. "Modeling TauD-J: a high-spin nonheme oxoiron(IV) complex with high reactivity towards C–H bonds." *J. Am. Chem. Soc.* 2015, 137, pp 2428-2431.

6. Makris, T. M.; Vu, V. V.; **Meier, K. K.**; Komor, A.; Rivard, B. S.; Münck, E.; Que, Jr., L.; Lipscomb, J. D. **"**An Unusual Peroxo Intermediate of the Arylamine Oxygenase of the Chloramphenicol Biosynthetic Pathway." *J. Am. Chem. Soc.* 2015, 137, pp 1608-1617.

7. Liu, J.; **Meier, K.**; Tian, S.; Zhang, J.; Guo, H.; Schulz, C. E.; Robinson, H.; Nilges, M. J.; Münck, E.; Lu, Y. "Redesigning the Blue Copper Azurin into a Redox-Active Mononuclear Nonheme Iron Protein: Preparation and Study of Fe(II)-M121E Azurin." *J. Am. Chem. Soc.* 2014, 136, pp 12337-12344.

8. Chiang, C.-W.; Kleespies, S. T.; Stout, H. D.; **Meier, K. K.**; Li, P.-Y.; Bominaar, E. L.; Que, Jr., L.; Münck, E.; Lee, W.-Z. "Characterization of a Paramagnetic Mononuclear Nonheme Iron-Superoxo Complex." *J. Am. Chem. Soc.* 2014, 136, pp 10846-10849.

9. England, J.; Bigelow, J.O.; Van Heuvelen, K.M.; Farquhar, E.R.; Martinho, M.; **Meier, K.K.**; Frisch, J.R.; Münck, E.; Que, Jr., L. "An Ultra-Stable Oxoiron(IV) Complex and Its Blue Conjugate Base." *Chem. Sci.* 2014, 5, pp 1204-1215.

10. Oloo, W.N.; **Meier, K.K.**, Wang, Y.; Shaik, S.; Münck, E., Que Jr., L. "Identification of a low-spin acylperoxoiron(III) intermediate in bio-inspired nonheme iron-catalysed oxidations." *Nature Commun.* 2013, 5, pp 3046-3054.

11. Li, F.; Van Heuvelen, K.M.; **Meier, K.K.**; England, J.; Münck, E.; Que, Jr., L. "Sc^{3+} triggered oxoiron(IV) formation from O_2 and its nonheme iron(II) precursor via a Sc^{3+}-peroxo-Fe^{3+} intermediate." *J. Am. Chem. Soc.* 2013, 135, pp 10198-10201.

12. Banerjee, R.; **Meier, K.K.**; Münck, E.; Lipscomb, J.D. "Intermediate P* from Soluble Methane Monooxygenase Contains a Diferrous Cluster." *Biochemistry.* 2013, 52, pp 4331-4342.

13. Mbughuni, M.M.; **Meier, K.K.**; Münck, E.; Lipscomb, J.D. "Substrate-Mediated Oxygen Activation by Homoprotocatechuate 2,3-Dioxygenase: Intermediates Formed by a Tyrosine 257 Variant." *Biochemistry*. 2012, 51, pp 8743-8754.

14. Cranswick, M.A.; **Meier, K.K.**; Shan, X.; Stubna, A.; Kaizer, J.; Mehn, M.P.; Münck, E.; Que, Jr., L. "Protonation of a Peroxodiiron(III) Complex and Conversion to a Diiron (III/IV) Intermediate: Implications to Proton-assisted O-O Bond Cleavage in Nonheme Diiron Enzymes." *Inorganic Chemistry*. 2012, 5, pp 10417-10426.

15. Van Heuvelen, K.M.; Fiedler, A.T.; DeHont, R.; Shan, X.; **Meier, K.K.**; Bominaar, E.; Münck, E.; Que, Jr. L. "One-electron oxidation of an oxoiron(IV) complex to form an $[O=Fe^{V}=NR]^{+}$ center." *PNAS*. 2012, 109, pp 11933-11938.

16. Mbughuni, M.M.; Chakrabarti, M.; Hayden, J.A.; **Meier, K.K.**; Dalluge, J.J.; Hendrich, M.P.; Münck, E.; Lipscomb, J.D. "Oxy-intermediates of homoprotocatechuate 2,3-dioxygenase: facile electron transfer between substrates." *Biochemistry*. 2011, 50, pp 10262-10274.

17. Li, F.; **Meier, K.K.**; Cranswick, M.A.; Chakrabarti, M.; Van Heuvelen, K.M.; Münck, E.; Que, Jr., L. "Characterization of a High-Spin Non-Heme Fe^{III}-OOH Intermediate and Its Quantitative Conversion to an Fe^{IV}=O Complex." *J. Am. Chem. Soc.* 2011, 133, pp 7256-7259.